

AN OVERVIEW OF UNOCAL'S LOW EMISSIONS GASOLINE RESEARCH PROGRAM

Peter J. Jessup, Michael C. Croudace, Tim Wusz
Unocal Corporation, Science & Technology Division,
376 S. Valencia Ave., Brea, CA 92621

Keywords: automobile emissions, gasoline, fuel properties

SINCE THE MID-1980s, oil companies, government agencies and automobile manufacturers have extolled the emissions improvements possible by changing the composition of gasolines used in spark ignition engines. The promise has been that, by changing the composition and physical properties of fuels, vehicle emission systems will work more cooperatively with the fuel to limit the output and reactivity of pollutants.

Some regulations which specify fuel formulations as a method for emissions reduction from automobile exhausts are currently in effect. For example, several western states that are unable to meet regulated wintertime carbon monoxide (CO) levels for ambient air quality standards, as prescribed in the Clean Air Act, already impose mandatory oxygen content of gasoline. Other regulations being considered include the reduction of Reid vapor pressure to limit the evaporative emissions of hydrocarbons from vehicles.

It was the purpose of the work described here to evaluate a fuller set of fuel properties than has previously been done to gain a more complete understanding of the interactions between fuels and emissions systems. Our program was unique in that there was a greater focus on the fuel matrix design than in any other previously published work. We pursued our emissions testing using a linear screening design for the fuels in which ten properties were varied independently within the bounds placed by four multivariable constraints (see Table 1). No up-front assumptions were made as to which gasoline properties were important.

The fuels we prepared for this program had chemical compositions typical of gasolines sold in commerce. These gasolines were made from eleven gasoline blending stocks which are widely used in refineries. All blends included a highly effective gasoline detergent to minimize deposit related deterioration of the fuel, engine and emission system. All car/fuel combinations were tested at least twice in random order. Other constraints which have been included in these fuels are limitations on the octane sensitivity (RON-MON) and distillation properties of the blends to make the products more typical of commercial gasolines. These constraints limited the possibility of designing a gasoline that improved emissions while limiting the performance of the vehicle in other areas. Finally, a limit was placed on the amount of aromatics plus MTBE present in any blend so that octane was limited to normal levels.

The fuels were each run at least twice in random order, including no back to back duplication, to limit systematic errors and effects from uncontrolled variables. A control fuel was run frequently to evaluate possible time sequence error. This showed that no significant changes were seen in any individual vehicle emissions over the time span of our experiments.

Results from two separate emission test programs using the fifteen fuel test matrix have shown that changes in gasoline distillation characteristics, olefin content and Reid vapor pressure

(RVP) can produce major changes in total tailpipe exhaust emissions. All other variables examined, including oxygen content and aromatic content of the fuels, did not directly or greatly affect the tailpipe emissions of carbon monoxide, nitrogen oxides, or hydrocarbons. From these results a generalized mathematical model was produced which predicts tailpipe emission changes from key fuel properties. The model was verified in a separate, 13 vehicle study.

The single vehicle test program was performed with a 1988 Oldsmobile Regency 98 equipped with a current technology closed-loop three-way catalyst and adaptive learning emission system. Sixty three FTP tests were performed in this vehicle during this stage of our experimentation. The car was selected because it represented a high sales volume product that was close to current state of the art in emission technology.

This vehicle is representative of those that use the technology in which it would be expected to be most difficult to effect gross emissions by changing the fuel. This is because the emissions from this vehicle are already very low and there are limited effects one might expect from fuel compositional changes. Further, the adaptive learning feature of this technology tends to reduce the effect of changing fuel composition. Finally, tests were run in this car because it was felt that it contained the major types of vehicle emission technology that will be in the marketplace in the mid-1990s and beyond. Major changes in gasoline composition would take until the mid- to late-1990s, at the minimum, to implement.

All emissions testing was performed in the Unocal emissions testing facility in Brea, California. The fifteen fuel test matrix that was used was uniquely designed to screen 10 properties independently through a linear screening, statistical designed experiment. Emissions of carbon monoxide (CO), hydrocarbons (HC) and oxides of nitrogen (NOx) were determined with the 1975 Federal Test Procedure (FTP). Changes by a factor of 1.5 to 3.0 in these emissions were observed across the range of test gasolines used. The main variables that we found that affect the FTP tailpipe emissions are distillation characteristics, olefin content, and RVP. The results of these experiments strongly suggest that through simple changes in the formulations of gasolines, fuel and vehicle systems can work more effectively together, producing less total emissions.

Figures 1, 2, and 3 show the hydrocarbon, carbon monoxide, and nitrogen oxides emissions, respectively, observed for the Oldsmobile Regency 88 over the range of the 15 experimental design fuels. The average of two or more independent measurements on each fuel are plotted with 95% confidence intervals. The confidence intervals were calculated using a pooled standard deviation over all the fuels so all confidence intervals are identical. Also plotted, as a horizontal reference line on each Figure, are the average emissions observed for the Auto/Oil RF-A, industry average gasoline (1), flanked with 95% confidence interval reference lines. This fuel is identical to the reference gasoline described in the 1991 Clean Air Act.

It can readily be seen from an examination of the confidence levels on these three Figures that the range of observed emissions, relative to the repeatability of the experimental data, is high. In addition, while the observed order of fuels, from lowest to highest, is similar, but not identical, for hydrocarbon (HC) and carbon monoxide (CO) emissions, it is quite different for nitrogen oxides (NOx) emissions.

This way of presenting the experimental data leads to the observation that quite different fuel properties are controlling NO_x emissions compared to the HC and CO emissions, but that the properties controlling HC and CO emissions are probably similar.

The set of linear models that fits this single car data quite well are as follows:

$$\text{HC (gm/mile)} = 0.00245(\text{olefins vol\%}) + 0.00109(\text{T}_{50}) - 0.00104(\text{RON})$$

$$\text{CO (gm/mile)} = 0.00937(\text{T}_{50}) + 0.00133(\text{T}_{90}) - 0.00828(\text{saturates vol\%})$$

$$\text{NO}_x \text{ (gm/mile)} = 0.00503(\text{olefins vol\%}) - 0.0006(\text{saturates vol\%}) \\ + 0.00087(\text{T}_{10}) + 0.0159(\text{RVP})$$

Fitting the experimental data is only one measure of the value of these equations. A second measure is their ability to make predictions about fuels not in the experimental matrix. Table 2 contains the observed properties of four gasolines that were used as check points to test the predictive equations. At least two FTP runs were made using each of these four fuels. A comparison between average measured and predicted emissions for each fuel is shown in Table 3. This shows that, at least for these four fuels, the predicted emissions are always within two standard deviations of the mean measured emissions.

The startling range of emissions observed over our set of test fuels, coupled with the success of simple linear models in predicting emissions of gasolines outside the test fuel set used to generate the models, lead to the conclusion that the properties of gasolines can have a dramatic effect on tailpipe emissions. This prompted the acquisition of a ten car fleet to test our single-car conclusions for generality.

The confirmatory ten car fleet test was run at Southwest Research Institute in San Antonio, Texas. In this test fifteen fuels, with similar fuel characteristics to those used in the single car experiment, were evaluated using the FTP. The ten cars tested were selected from the list of post-1980 model vehicles used in the Auto/Oil test fleet (1). Details of the fleet are shown in Table 4. The results supported the conclusions from the single car study. Olefins, RVP and distillation were major influences of vehicle emissions over the entire ten car fleet.

Fifteen new test gasolines were blended in accordance with those used in our previous single car test. Again, they were designed to vary each of the ten properties, shown in Table 1, independently. New blending stocks for these fuels were obtained from the Unocal Los Angeles refinery. Physical characteristics had changed slightly over our initial blending streams, so the final blends produced varied slightly in physical properties from our fifteen initial blends. The experimental protocol was identical to that used in the testing performed with the single car described above.

Preliminary analysis of the FTP data showed that the older technology cars responded to fuel changes differently to the newer cars. Consequently, for further analysis the fleet was split into two categories. The Suburban, Tempo, Caprice, and Accord were grouped together as older technology cars while the remaining six cars were grouped as newer technology vehicles.

The data confirmed some of the observations made concerning the emissions of the single car in our earlier program. For all ten cars we have seen very big changes in bulk emissions as we

have varied fuel properties within our experimental design set of gasolines. We observe spreads between lowest and highest emissions by factors of 1.5 to 2 on a fleet averaged basis.

Initial regression analysis of the emissions data outlined above using the cars as groups was not very satisfactory. For example, regression models tended to give poor predictability. To get around this we reverted to the type of analysis that was completed for the single car study. We built individual, empirical regression models for each car. The results of these regression analyses are shown in Tables 5, 6, and 7. These Tables show which variables have a significant effect on HC, CO, or NO_x emissions respectively, by car. In the Tables, a + indicates a property that has the effect of raising the tailpipe emission if the value of that property is increased. Similarly, a - indicates that if the property value is increased, the associated emission decreases.

It is readily apparent from these Tables that the property that has the most universal effect is on HC and CO emissions is the distillation T₅₀ point. For NO_x emissions there were three properties with almost universal effect. These were olefin content, distillation T₁₀ point, and Reid vapor pressure (RVP).

There are many ways in which individual car effects can be combined to yield a predictive equation for the fleet. We chose to combine individual regression equations by taking simple averages of all the individual car equations. This gave the following set of three equations:

$$\text{HC} = -0.000474(\text{aromatics vol}\%) + 0.00248(\text{olefins vol}\%) \\ - 0.00212(\text{research octane number}) + 0.00207(\text{T}_{50} \text{ distillation point})$$

$$\text{CO} = -0.00682(\text{saturates vol}\%) + 0.0128(\text{T}_{50} \text{ distillation point}) + 0.00123(\text{T}_{90} \text{ distillation point})$$

$$\text{NO}_x = 0.005595(\text{olefin vol}\%) - 0.000282(\text{saturates vol}\%) \\ + 0.002715(\text{T}_{10} \text{ distillation point}) + 0.02765(\text{Reid vapor pressure})$$

In order for this predictive model to be useful to a refiner the model needs to be capable of predicting formulations that meet emissions reduction targets that can be blended in the refinery. We set up to run our Los Angeles refinery using the predictive model as part of the refinery linear program (LP). The goal was to produce a fuel that had a emissions of 15% below the emissions of the CAA reference gasoline. A premium unleaded gasoline was formulated for testing that was part of the overall refinery balance. Properties of the experimental and reference fuels are shown in Table 9.

The testing was performed at Southwest Research Institute vehicle emissions test facility in San Antonio, Texas and NIPER's emission test facility in Bartlesville, Texas. Exhaust emissions were evaluated through the EPA's 1975 Federal Test Procedure (FTP).

Thirteen vehicles were selected to represent the major vehicle emission technology classes since 1970 and to mimic the present day California fleet. These vehicles are listed in Table 8. The experimental protocol was identical to that used in the testing performed with the single car described above.

The results of this strategy are shown in Figure 4. In this Figure the average emissions reductions of all 13 cars, along with pooled 85% confidence levels, are plotted for the experimental gasoline. These reductions are shown as a percentage of the reference gasoline emissions levels. The 85% confidence levels for the reference fuel are shown as a variable-width band across the center of the chart, centered about zero. The 85% confidence level was chosen for this comparison because, at the time, it was the value that the California Air Resources Board was contemplating using for this type of comparison.

The experimental emissions reductions for the whole 13 car fleet are plotted as three vertical bars at the left side of the chart. It can be seen that we achieved the substantial emissions reduction that we were aiming for. Not only did we greatly reduce both HC and CO emissions but we *SIMULTANEOUSLY* reduced NOx emissions.

Although the HC and CO emissions reductions met our expectations, the overall NOx emissions reduction did not. Considering that the predictive equations we used were based on data collected with post-1980 cars, we decided to split this experimental data and recalculate NOx emissions reductions for two groups of cars. These reductions are plotted as vertical bars on the right side of the chart in Figure 4. The 13 car fleet was split into its pre-1980 and post-1980 components.

The result of this exercise shows that we did indeed achieve the NOx emissions reductions that we had expected, but only in the post-1980 fleet. That is, in the cars with the types of technology that we had done all our previous experimental work with. In the older cars the test gasoline exhibited NOx emissions that were not statistically different from the NOx emissions of the reference fuel. We believe that this difference in NOx emissions between the older and newer car fleets may be caused by the presence of oxygenate in the test gasoline. This would be in agreement with published literature concerning the effect of oxygenates on the emissions from pre-1980 cars (2).

The authors would like to acknowledge the contributions to this work of J. M. Kulakowski and S. Vincent of Unocal's planning staff for help with the refinery LP work, S. T. Woods and G. W. Phillips, for fuels preparation, G. E. Brooks and Jim Smith of the Unocal emission test facility, Lawrence R. Smith and Matthew S. Newkirk of Southwest Research Institute, and William F. Marshall of NIPER.

REFERENCES

Vehicle Emissions by Technology (1973 to 1989)", SAE Paper 910380, February 1991.

1. Vaughn R. Burns, et al., "Description of Auto/Oil Air Quality Improvement Research Program", SAE Paper 912320, October 1991.
2. William J. Koehl, et al., "Effects of Gasoline Composition and Properties on Vehicle Emissions: A Review of Prior Studies - Auto/Air Quality Improvement Research Program", SAE Paper 912321, October 1991.

Table 1
Fuel Variables And Their Ranges

Variable or Constraint	Min.	Max.
aromatics (vol%)	10	45
olefins (vol%)	0	15
paraffins (vol%)	40	90
MTBE (vol%)	0	15
Research Octane # (RON)	90	95
Motor Octane # (MON)	84	87
Distillation 10% Point (°F) T10	130	160
Distillation 50% Point (°F) T50	170	240
Distillation 90% Point (°F) T90	290	350
Reid Vapor Pressure (psi) RVP	8	10
RON-MON	5	8
Aromatics + MTBE	0	50
T50 - T10	50	
T90 - T50		150

Table 2
Check Fuel Properties

Property	#1	#2	#3	#4
aromatics (vol%)	40.9	20.7	58.3	30.0
olefins (vol%)	11.1	10.8	0.4	9.2
paraffins (vol%)	48.0	61.4	30.4	60.8
MTBE (vol%)	0.0	7.1	10.9	0.0
RON	96.4	92.8	107.0	92.1
MON	85.2	84.0	95.7	82.4
T10	120	125	160	112
T50	214	198	218	200
T90	339	348	229	315
RVP	8.2	8.0	5.4	8.7

Table 3
Check Fuel Emissions

Emission	Fuel #	Measured g/mile	Calculated g/mile	Difference g/mile	Standard Deviation
Carbon Monoxide	1	2.127	2.059	0.067	0.205
	2	1.584	1.810	0.226	
	3	1.901	2.096	0.195	
	4	2.319	2.009	0.310	
Nitrogen Oxides	1	0.266	0.261	0.005	0.016
	2	0.263	0.256	0.007	
	3	0.200	0.207	0.007	
	4	0.286	0.260	0.026	
Hydrocarbons	1	0.178	0.161	0.017	0.014
	2	0.139	0.146	0.007	
	3	0.142	0.126	0.014	
	4	0.189	0.165	0.024	

Table 4
Ten Vehicle Fleet Details

OEM	Model	Engine Size (l)	Fuel System ¹	EGR ²	Catalyst System	Year
GM	Cutlass	2.3	PFI	no	3-way	1989
GM	98 Regency	3.8	PFI	yes	3-way	1988
Ford	Tempo	2.3	TBI	yes	3-way	1985
Ford	Lincoln	5.0	PFI	yes	3-way, dual bed, close coupled	1990
GM	Caprise	2.0	Carb	yes	3-way, dual bed	1984
Honda	Accord	2.0	Carb	yes	3-way	1988
Ford	Taurus	3.0	PFI	no	3-way, close coupled	1989
Dodge	Shadow	2.5	TBI	yes	3-way, close coupled	1990
GM	Suburban	2.5	Carb	yes	oxidation	1985
Toyota	Camry	2.0	PFI	yes	3-way, close coupled	1990

- 1) PFI = Port Fuel Injected, TBI = Throttle Body Injected, Carb = carburetted
2) EGR = Exhaust Gas Recirculation

Table 5
Individual vehicle effects of fuel properties
in the 10 car fleet on **Hydrocarbon** emissions

Car	arom vol%	olef vol%	RON	T50
GM Cutlass		+	-	+
GM 98 Regency			-	+
Ford Tempo			-	+
Ford Lincoln	-			+
GM Caprice	-			+
Honda Accord	-			+
Ford Taurus		+	-	+
Dodge Shadow	-			+
GM Suburban	-			+
Toyota Camry		+	-	+

Table 6
Individual vehicle effects of fuel properties
in the 10 car fleet on **Carbon Monoxide** emissions

Car	arom vol%	para vol%	T50	T90
GM Cutlass		-	+	
GM 98 Regency		-	+	
Ford Tempo		-	+	
Ford Lincoln			+	
GM Caprice	-		+	
Honda Accord			+	
Ford Taurus			+	
Dodge Shadow		-	+	+
GM Suburban		+	+	-
Toyota Camry		-	+	

Table 7
Individual vehicle effects of fuel properties
in the 10 car fleet on **Nitrogen Oxide** emissions

Car	olef vol%	paraf vol%	T10	RVP
GM Cutlass	+	-	+	+
GM 98 Regency	+		+	+
Ford Tempo	+		+	+
Ford Lincoln	+		+	+
GM Caprice	+		+	+
Honda Accord	+	-	+	+
Ford Taurus	+		+	+
Dodge Shadow	+		+	+
GM Suburban	+		+	+
Toyota Camry	+		+	

Table 9
Reference and Reformulated Gasoline Properties

Property	Reformulated Premium Gasoline	CAA Reference Gasoline
aromatics (vol%)	44.1	32.0
olefins (vol%)	3.3	9.2
paraffins (vol%)	45.4	58.8
mtbe (vol%)	7.2	0.0
RON	97.5	92.0
T10 (°F)	136	128
T50 (°F)	208	218
RVP (psi)	8.0	8.7

Table 8
13 Car Fleet Details For Reformulated Commercial Gasoline Test Program

OEM	Model	Engine Size (l)	Fuel System ¹	EGR	Catalyst System	Year
GM	98 Regency	3.8	PFI	yes	3-way	1988
Ford	Tempo	2.3	TBI	yes	3-way	1985
Ford	Lincoln	5.0	PFI	yes	3-way, dual bed, close coupled	1990
Honda	Accord	2.0	Carb	yes	3-way, dual bed	1988
Toyota	Camry	2.0	PFI	yes	3-way, close coupled	1990
Dodge	Shadow	2.5	TBI	yes	3-way, close coupled	1990
Chrysler	Diplomat	5.2	Carb	yes	oxidation	1979
GM	Monte Carlo	5.0	Carb	yes	oxidation	1978
GM	Caprice	5.7	Carb	yes	oxidation	1979
GM	Delta 88	7.4	Carb	yes	non-catalyst	1974
Ford	LTD	6.6	Carb	yes	non-catalyst	1974
Chrysler	Dart	3.7	Carb	yes	non-catalyst	1973
Ford	Cougar	5.8	Carb	yes	oxidation	1975

1) PFI = Port Fuel Injected, TBI = Throttle Body Injected, Carb = carburetted.

Figure 1
Hydrocarbon Emissions of Experimental Fuels
in Oldsmobile 98 Regency

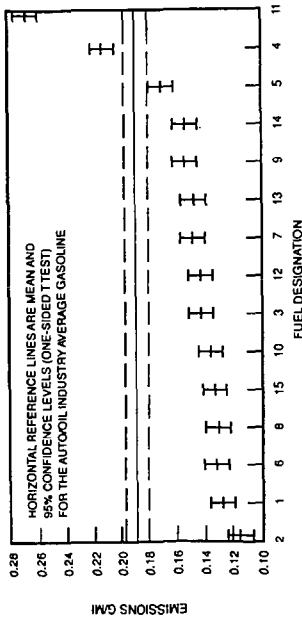


Figure 2
Carbon Monoxide Emissions of Experimental Fuels
in Oldsmobile 98 Regency

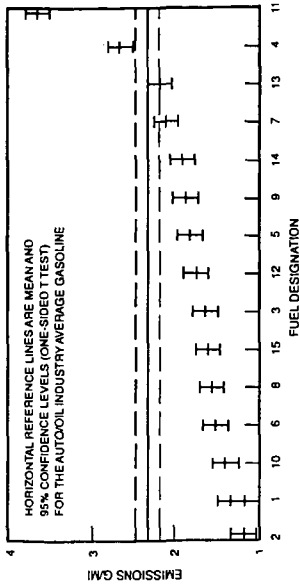


Figure 3
Nitrogen Oxide Emissions of Experimental Fuels
in Oldsmobile 98 Regency

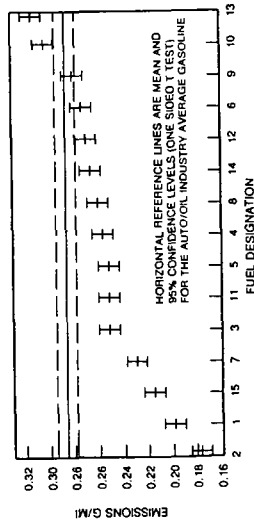
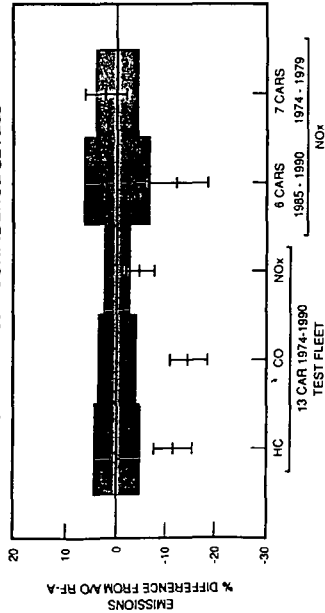


Figure 4
Comparison of Emissions of Predicted Low Emission Gasoline
With the CAA Reference Gasoline
EMISSIONS WITH 85% CONFIDENCE LEVELS



METHODS FOR DETERMINING AROMATICS AND BENZENE IN REFORMULATED GASOLINES

R. E. Pauls and G. J. Weight
Amoco Research Center
150 West Warrenville Road
Naperville, IL 60563-8460

Keywords: Aromatics, Gasoline, Gas Chromatography

ABSTRACT

The recently passed Clean Air Act places a number of restrictions upon the composition of gasolines marketed in ozone and CO nonattainment areas. These restrictions include upper limits on the total aromatic and benzene contents of the reformulated gasolines. As a result, reliable, routine analytical methods will be required to certify the aromatic and benzene content of gasolines.

Although a number of different approaches are available for the determination of these properties, many are unsuited for routine analysis, especially in smaller refineries. This presentation will review chromatographic methods currently available for these measurements. In addition, the accuracy and precision of several of these methods for the determination of the aromatic and benzene content of reformulated fuels will be discussed.

INTRODUCTION

The effects of motor vehicle exhaust and running losses upon urban air quality has prompted the regulation of the composition of automotive fuels. The recently passed Clean Air Act places restrictions in a number of instances upon the maximum aromatic and benzene content of gasolines. Concerns over benzene arise because it is a known carcinogen and it along with 1,3-butadiene, formaldehyde and acetaldehyde are the major toxic compounds found in vehicle exhaust. To meet the requirements of these regulations, the oil industry will need reliable analytical methods. Among the requirements of these methods are acceptable precision, freedom from bias, and freedom from interferences due to oxygenates.

BENZENE METHODS

A number of different chromatographic methods are currently available for the determination of benzene in gasoline. For comparison purposes, these can be subdivided into 4 classes:

- 1) Single column gas chromatographic methods
- 2) Column switching gas chromatographic methods
- 3) Multi-column PIONA methods
- 4) Liquid chromatographic methods

Single column methods may employ either long capillary columns containing non-polar stationary phases or, alternately, columns containing highly polar stationary phases such as TCEP. The former are commonly referred to as single column PONA methods and typically employ 100 m columns with internal diameters of 0.25 mm and a film thickness of 0.5 μm methyl silicone stationary phase (1). These columns rely on their high inherent separation power to resolve benzene from other closely boiling components such as 1-methylcyclopentene. Separation of benzene from other hydrocarbons on TCEP columns (2) is based upon the significantly greater retention of aromatic compounds relative to non-aromatics of similar boiling point on polar stationary phases. Both these single column methods suffer limitations due to long analysis times and possible co-elution of

other components.

An example of a column switching approach to determine benzene is ASTM D 3606 (3). The method employs a non-polar column to perform an initial separation based upon boiling point followed by a polar column to separate benzene and toluene from other, closely boiling hydrocarbons. Heavier components are backflushed to waste. Figure 1 illustrates a typical separation of gasoline by D 3606. Note the rapid analysis time and good resolution of benzene and toluene from other components. MTBE is not an interference in this method. There is some partial overlap with methanol and ethanol but resolution is sufficient to permit accurate quantitative measurement (4).

Multi-column PIONA methods provide a distribution of paraffins, iso paraffins, olefins, naphthenes and aromatics by carbon number (5). As benzene is the only C_6 aromatic, benzene values can be obtained directly from PIONA methods. However, when only benzene values are of interest, this is a costly and time consuming approach.

Benzene may also be rapidly determined by liquid chromatography employing C_{18} reversed-phase columns and water/acetonitrile mobile phases with refractive index detection (6). Figure 2 contains a plot comparing the results obtained on approximately 100 samples with D 3606 and the LC method. The slope and intercept are close to unity and zero, respectively indicating little relative or fixed bias between the two methods. In our laboratory, we prefer to employ D 3606 because it has demonstrated better precision than the LC method. Table 1 contains a comparison of the repeatability obtained in our laboratory of these two methods for a gasoline sample:

TOTAL AROMATICS

The accurate measurement of total aromatics is considerably more difficult to achieve than the determination of benzene. The ideal requirements for a total aromatics method would include that it be simple, inexpensive, accurate, precise and free from oxygenate interferences. The same 4 basic approaches discussed above for measuring benzene can also be employed to measure total aromatics. In addition, the traditional FIA method, ASTM D 1319 (7) is widely employed for this purpose. This method is based upon displacement chromatography with fluorescent dyes to indicate boundary regions between saturates, olefins and aromatics. Although widely employed for a number of years, this method suffers from a number of deficiencies including poor precision, operator dependency, long analysis times, and difficulties with automation. Additional chromatographic methods for measuring total aromatics include supercritical fluid chromatography (SFC) and an EPA proposed method that employs GC/MS. Recently SFC with flame ionization detection has been employed to measure aromatics in diesel and jet fuels (8). A similar approach may be suitable for gasoline. GC/MS approaches have not been widely employed because of their additional complexity, difficulties with calibration, and the high cost of such methods.

The two different single column approaches described above for benzene are also suitable for total aromatics. The PIONA approach requires that all aromatic peaks be assigned and the total summed. In contrast, an advantage of using a highly polar stationary phase such as Carbowax derivatives or TCEP for measuring total aromatics is that the aromatics tend to be isolated into the end of the chromatogram. These can be summed as a group. Except for the early eluting peaks, benzene and toluene, it is not necessary to identify each individual aromatic peak. Figure 3 illustrates the separation of a gasoline on a DB-Wax megabore capillary column. Although LC methods have been employed to monitor hydrocarbon types in fuels, this approach has in general been limited by detector

response problems (9).

Most of our recent efforts in this area have been devoted toward developing a rugged, routine column switching method for measuring total aromatics. Such a method could be more suitable for refinery applications than previously discussed approaches. ASTM Method D 4420 was employed as the basis for our work. It was modified in 4 ways: an internal standard was added, a flame ionization detector was employed, a different column set was employed than that specified in the D 4420 method, and the analysis was performed in two steps to minimize interferences from non-aromatics. The first two changes were made to enhance the quantitative aspects of the analysis. The column set was modified to incorporate the same columns as used by ASTM D 4815, a method to determine oxygenates in gasoline. These columns are a 1/16 inch TCEP packed column and a methyl silicone megabore column. This change was implemented to enhance resolution and speed.

Figure 4 illustrates the valve configuration employed in this method. We perform this analysis in two steps. Initially the sample is injected through injector B onto the TCEP column. Non-aromatics compounds, out to approximately n-decane, elute prior to benzene and are vented to waste through a thermal conductivity detector. Six seconds prior to the elution of benzene, the valve is actuated and components not eluted from the TCEP column are backflushed onto a methyl silicone megabore column. Once C_8 aromatics have eluted from the megabore column, the valve is switched to its original position and C_9+ aromatics are backflushed to the detector. All measurements of aromatics are made with the flame ionization detector. Figure 5 contains a chromatogram resulting from this analysis. Only the benzene and toluene values are used from this first analysis.

The analysis is repeated a second time with the valve switching time increased to a time 6 seconds prior to the elution of ethyl benzene from the TCEP column. This step is performed to reduce the possibility of interference due to high boiling non-aromatics. These compounds would normally be found in the C_9+ fraction. Figure 6 contains a chromatogram resulting from this analysis. Note the differences in the peaks of the C_9+ fractions in Figures 5 and 6. Table 2 contains a comparison of the C_9+ results from the first and second analyses. T90 values are also provided. As expected, lower values were obtained for C_9+ aromatics with the longer cut time. This is due to the exclusion of some higher boiling non-aromatics. The greatest discrepancy was observed for the samples with the highest endpoint. The C_8 and C_9+ values from the second run are combined with the benzene and toluene values obtained on the first run to obtain total aromatics. Comparisons of this method with alternate approaches such as PIONA indicate a high correlation between total aromatics for the two methods. Common oxygenates including MTBE, methanol and ethanol do not interfere with the aromatic peaks in the modified D 4420.

SUMMARY

A number of different chromatographic approaches are available for the measurement of benzene and total aromatics. In our laboratory, we prefer to employ D 3606 to determine benzene because of its high precision and fast analysis times. A wide range of alternative methods may be employed to measure total aromatics. Our current work has focused upon modification of ASTM D 4420 to provide a rugged, reliable method using proven column switching methodology.

REFERENCES

1. Data Sheet and Column Performance Information for Petrocol DH Column, Supelco, Bellefonte, PA.
2. ASTM Method D 2267. Standard Test Method for Aromatics in Light Naphthas

- and Aviation Gasolines by Gas Chromatography, ASTM Manual on Hydrocarbon Analysis, ASTM, Philadelphia, PA.
3. ASTM Method D 3606. Standard Test Method for Benzene and Toluene in Finished Motor and Aviation Gasoline by Gas Chromatography. ASTM Manual on Hydrocarbon Analysis, ASTM, Philadelphia PA.
 4. R. E. Pauls, G. J. Weight, and P. S. Munowitz, *J. Chromatogr. Sci.*, 30, 1 (1992).
 5. P. van Arkel, J. Beens, H. Spaans, D. Grutterink, and R. Verbeek, *J. Chromatogr. Sci.*, 25, 141 (1987).
 6. R. E. Pauls, *J. Chromatogr. Sci.*, 23, 197 (1985).
 7. ASTM Method 1319. Standard Test Method for Hydrocarbon Types in Liquid Petroleum Products by Fluorescent Indicator Adsorption. ASTM Manual on Hydrocarbon Analysis, ASTM, Philadelphia PA.
 8. F. P. Di Sanzo and R. E. Yoder, *J. Chromatogr. Sci.*, 29, 4 (1991).
 9. J. C. Suatoni, H. R. Garber, and B. R. Davis, *J. Chromatogr. Sci.*, 13, 367 (1975).

Table 1. Comparison of the Precision of ASTM D 3606 and an LC Method for the Determination of Benzene

	D 3606 ^a	LC ^b
Mean (wt%)	0.73	0.72
Standard Deviation (wt%)	0.007	0.022
Relative Standard Deviation (%)	0.96	3.1
Repeatability (wt%)	0.019	0.061
Number of measurements	24	50

Table 2. Effect of Cut Time on C₈ and C₉+ Aromatics Measurements by Modified D 4420

Sample	Vol% C ₈ Aromatics		Vol% C ₉ + Aromatics		T90(°F)
	Cut Time 1	Cut Time 2	Cut Time 1	Cut Time 2	
A	11.6	11.3	16.4	15.5	330
B	4.25	4.12	15.0	11.9	357
C	6.32	6.22	5.89	5.19	280
D	5.75	5.70	22.0	19.7	350

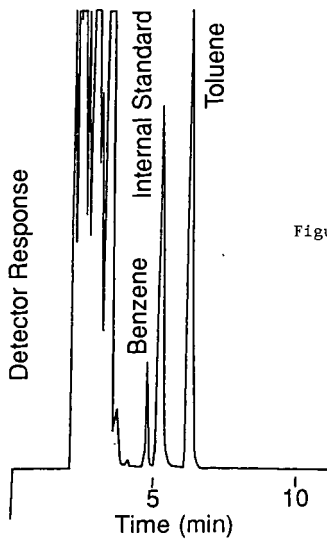


Figure 1 Chromatogram of a gasoline by ASTM Method D 3606

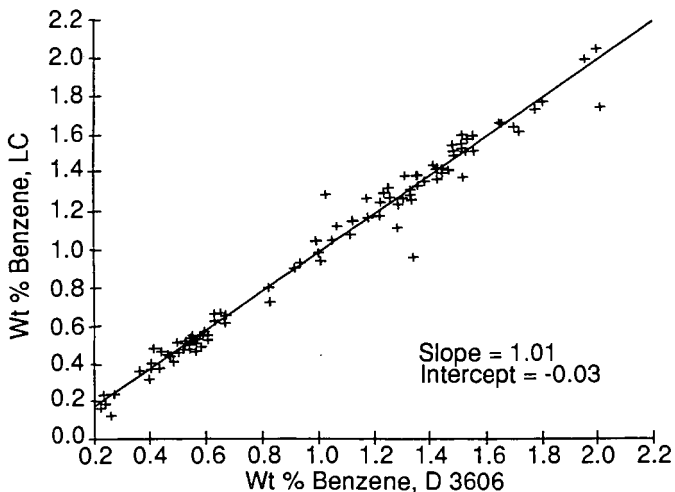


Figure 2 Comparison between D 3606 and Liquid Chromatography for the determination of benzene in gasoline blending stocks.

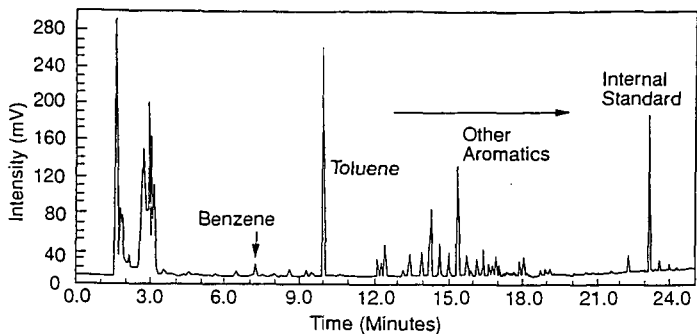


Figure 3 Chromatogram of a gasoline on a DB-Wax capillary column. Gasoline diluted with benzene-free carbon disulfide.

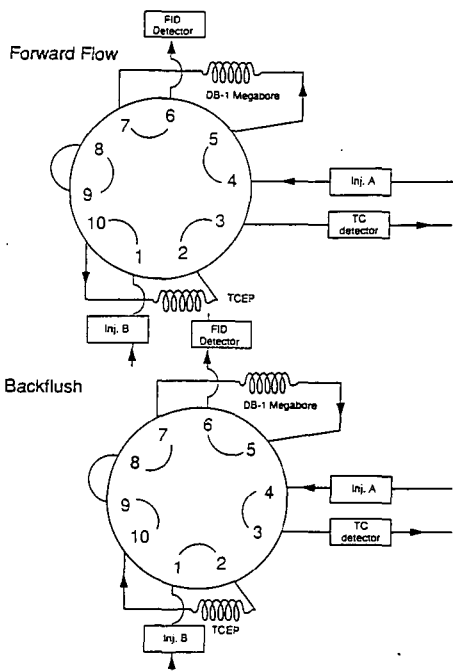


Figure 4 Valve configuration for modified D 4420

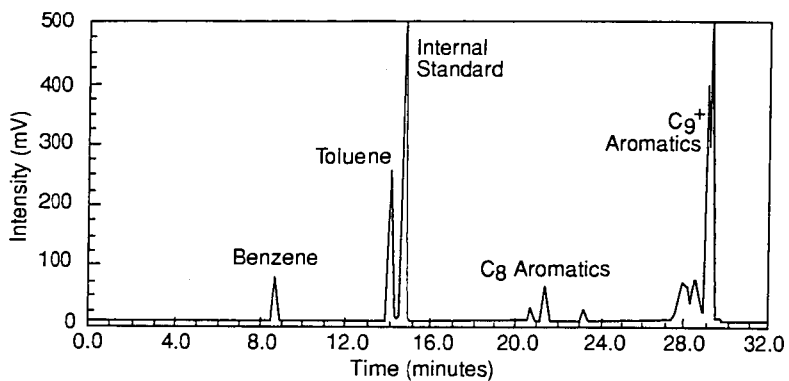


Figure 5 Chromatogram of gasoline with first valve cut time.

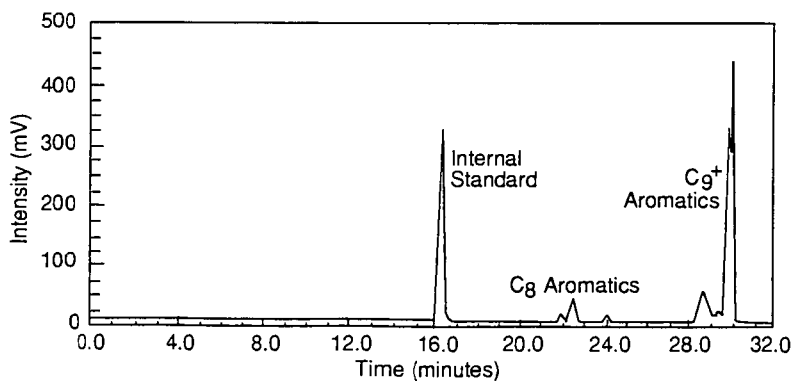


Figure 6 Chromatogram of gasoline with second valve cut time.

THE IMPACT OF CHEMICAL AND PHYSICAL PROPERTIES OF FUELS ON DIESEL
ENGINE EMISSIONS

David G. Leddy, Linda D. Gratz, Susan T. Bagley
Michigan Technological University
1400 Townsend Drive
Houghton, MI 49931

KEYWORDS: Diesel Emissions, Fuel Effects on Diesel Emissions,
Control of Diesel Emissions

ABSTRACT: Studies considering engine type and mode of operation as the most important factors in the characteristics of diesel emissions may be valid when looking at the gross emission parameters: total particulate matter (TPM), soluble organic fraction (SOF), and solids. Recently, we have concentrated on quantifying specific chemical species, such as polynuclear aromatic hydrocarbons (PAH), which have lead us to believe that chemical composition of the fuel plays a major role in determining the concentration of these species in the emissions.

This paper is a summary of studies where sufficient data have been obtained to allow us to test for relationships between fuel composition and emission parameters. Data obtained from samples collected at Michigan Technological University and the United States Bureau of Mines were analyzed. Four number 2 diesel fuels were investigated which varied in cetane number, sulfur and aromatic content. Specific PAH, TPM, SOF, volatile organics (XOC), sulfates, hydrocarbons (HC) and nitrogen oxides (NOx) data were tested in this study. The results show that fuel composition may have effects on specific pollutant emissions.

INTRODUCTION: Diesel fuels are characterized on the basis of: 1) physical properties (such as density, viscosity, and distillation profile); 2) a performance property (cetane number); and 3) chemical properties (such as sulfur, aromatic and olefin content). Blending of distillates or feedstocks may be used to produce fuels with desired properties to meet the demands of the users and to satisfy the engine emission standards promulgated by government agencies.

In previous studies (1-4), we have proposed that the type of engine and mode of operation are the most important factors in determining emission characteristics. This may be valid when looking at gross characteristics of emissions such as total particulate matter (TPM), soluble organic fraction (SOF), and sulfate. More recently, however, we have concentrated on quantifying specific chemical species, such as certain polynuclear aromatic hydrocarbons (PAH), which may have human health impacts, and proposing that chemical composition of the fuel plays a major role in determining the concentration of these species in emissions.

Studies on fuel effects have been carried out by Baranescu (5), Wall et. al (6) and Ullman et. al (7). Baranescu (5) and Wall et. al (6) investigated the impact of fuel sulfur on emissions and both concluded that sulfur must be removed from diesel fuel for effective particle emission control. Ullman et. al (7), on the other hand, studied the impact of cetane number and aromatic content showing that as cetane number increased there were significant decreases in

both gaseous and particle emissions, while aromatic content reductions produced varied results on the diesel emissions studied. Weaver et. al (8) have reviewed the literature and have concluded that the most important emission-related properties of diesel fuel are sulfur and aromatic content. The emissions of PAH compounds, however, were not considered in these fuel evaluations.

This study is a summary of results of research activities where sufficient data have been obtained to allow us to test for significant relationships between a number of parameters. Data obtained at Michigan Technological University (MTU) and from samples provided by the Twin Cities Research Center of the United States Bureau of Mines (USEM), Minneapolis, MN were primarily used as the basis of the study. Fuel studied consisted of types where cetane number, sulfur content and aromatic content were varied in fuels with the physical properties of a number 2 standard blend. Specific PAH, TPM, SOF, volatile organics (XOC), sulfates, nitrogen oxides (NOx), and hydrocarbons (HC) were measured in most studies.

EXPERIMENTAL: Four fuels were used in gathering the data used for this paper. The data from the MTU engine studies were obtained using Amoco regular sulfur fuel (ARS) and a Chevron low sulfur (CLS) fuel. Data from the USEM engine studies were obtained using a specially prepared low aromatics diesel fuel manufactured by Chevron (CLAD) at its El Segundo refinery, and another Chevron cetane-adjusted diesel (CCAD), a commercially available fuel used in California which had its cetane number adjusted from an initial value of 45 to 53 by the addition of 0.3 weight percent Naltane 5308 cetane improver (to the same level as the CLAD fuel). Properties of these fuels are summarized in Table 1. Fuel analyses were provided by the supplier and analysis methods (where available) are indicated in Table 1.

Emission data analyzed were from engine test runs conducted at MTU and USEM. Engines used were a Cummins 1988 Model L-10 224 kw direct-injection diesel engine at MTU, representative of on-highway, heavy-duty diesel engines, and a 3304 Caterpillar 75 kw, indirect-injection engine at USEM representative of current mining engines. The MTU engine was operated at EPA steady-state modes 9 and 11 (rated speed at 75% and 25% load, respectively) while the USEM engine was operated a light-duty transient cycle representing mining engine operation. The specifics on the engines, dynamometers, and emissions collection systems are described in references 9 and 10. The emissions parameters measured were TPM, sulfate, SOF, semi-volatile organics, collected on XAD-2 resin (XOC), HC, and PAH (fluoranthene, pyrene, benz[a]anthracene, chrysene, benzo[b]fluoranthene, benzo[k]fluoranthene, and benzo[a]pyrene). All TPM, sulfate, SOF, XOC and PAH analyses were carried out at MTU. NOx and HC were measured at both sites.

Sampling for TPM, SOF and sulfate was done on Teflon-coated Pallflex filters, XOC was collected on XAD-2 resin directly downstream from the Pallflex filter. TPM and SOF were determined gravimetrically from filter masses before and after exposure and by the mass of material extracted, respectively. Sulfates were measured by ion chromatography of the aqueous extract of the Pallflex filter using a conductance detector. HC were measured using a heated flame ionization detector and NOx were analyzed using a chemiluminescence analyzer. PAH were analyzed from a fraction

taken from the methylene chloride extract that was subsequently cleaned-up using column chromatography and analyzed by high performance liquid chromatography (HPLC) with fluorescence detection. The sampling and analysis procedures for these parameters are described in detail in reference 9.

The MTU data for NOx, HC, TPM, SOF, sulfate and XOC were analyzed using a 3-way analysis of variance (ANOVA) to determine if significant differences in test variables (mode, fuel, or aftertreatment device) could be detected within an entire data set (9). Two way ANOVAs for the same parameters were used for the USBM data to test for fuel or aftertreatment device effects (10). All null hypotheses being tested stated that there were no significant differences due to mode, fuel or aftertreatment device for the MTU data or fuel or aftertreatment device for the USBM data. A significance level of 0.05 was used for all statistical comparisons. The statistical treatment of the PAH data sets was further complicated due to the presence of less than minimum detection limit (MDL) data. These data sets were also analyzed using ANOVA techniques, with the less than MDL values replaced by the MDL values divided by two (9). In this paper, only the effects of fuel and mode are considered for the MTU data and only fuel for the USBM data.

RESULTS AND DISCUSSION: The results of the chemical analyses for the engine emissions parameters TPM, SOF, sulfate, XOC, NOx and HC are reported in Table 2. Particle- and vapor phase-associated PAH values are given in Table 3. Each of these tables is separated into two portions with the upper and lower portions, representing the values from the MTU studies and the USBM studies, respectively. Since the data were obtained on two different engines with MTU operating at steady-state conditions and USBM operating under transient mode conditions, the data were analyzed separately. However, comparisons on a relative basis can be made between the studies to assess fuel composition effects on emissions.

Gaseous Emissions -The values for the gaseous emissions from the MTU study are given in Table 2. All emissions values have been converted to mg/std m³ (25°C, 101 KPa). USBM data are given in ppm.

For the MTU NOx data a significant difference was found for both mode and fuel. Both low (CLS) and conventional sulfur (ARS) fuels gave a mode 9 to mode 11 difference in NOx of 68% with the lower value at mode 9 attributed to higher combustion temperatures compared to mode 11. A significant difference is illustrated in the NOx data between fuel types, particularly at mode 9. The USBM data gave a 9% decrease in NOx when the low aromatic fuel was used. Differences in fuel cetane number may also be responsible for this trend in the MTU study, while the USBM study utilized fuels with the same cetane number. Ullman et. al (7) have shown an inverse NOx correlation in their studies of cetane number, as well as a direct relationship between NOx and fuel aromatic content. These observations are consistent with our findings.

The HC emissions from the MTU study were also dependent on both fuel and mode. Mode 9 compared to mode 11 emissions (Table 2) for the CLS and AHS fuels were 20% and 53% lower, respectively. Mode-dependent differences are again explained by the increased temperatures of mode 9 and subsequently, more of the fuel is

oxidized. Fuel-dependent differences in HC may also be related to the cetane number of the fuels. Ullman et. al (7) also showed an inverse relationship between cetane number and HC emissions.

TPM, SOF, SULFATE, and XOC Emissions - The mean values for these emissions from the MTU data and the USBM data are also reported in Table 2 for all fuels studied. The variability of all measurements were within the normal expected ranges for these measured values.

The only significant effect of fuel type on TPM composition was on the sulfate concentrations which were at or below the minimum detection limit (MDL) for all of the MTU low sulfur (CLS) fuel samples and close to the MDL for the USBM low sulfur (CLAD and CCAD) fuel samples. Within the conventional (ARS) fuel data sets, significant differences in sulfate were detected between modes 9 and 11 (50% lower at mode 11). The USBM study did not utilize any conventional high sulfur fuel for comparison. The TPM concentrations were significantly affected by mode but not fuel type (based on the MTU data). This may be attributed in part to the higher aromatics, lower cetane number, and higher 90% volatility temperature of the CLS fuel (Table 1). These fuel properties might tend to cause increased formation of solid particulate matter as a result of the combustion process. The increase in solids due to fuel properties would then balance, to some extent, the sulfate reduction attributed to the low sulfur fuel. The USBM studies emphasized fuels with significant differences in aromatic content and their results gave a significant difference for TPM with a 13% decrease in TPM for the CLAD compared to CCAD.

Significant differences were not detected in SOF concentrations for mode or fuel in the MTU studies. USBM fuels were significantly different in terms of SOF emissions with a reduction of 17% when comparing the low aromatic fuel (CLAD) to the higher aromatics fuel (CCAD).

Despite the higher variability in XOC measurements, some significant relationships were found between fuels and modes in the MTU studies. Use of the conventional sulfur fuel (ARS) resulted in lower (27%) XOC concentrations than with the low sulfur fuel (CLS) at mode 9; mode 11 showed no fuel dependency. This is similar to the situation with the HC measurements where the differences are more likely due to differences in fuel composition other than fuel sulfur levels. Data for USBM fuels show a significantly different amount of XOC (31% higher) with the CLAD fuel as compared to the CCAD fuel.

PAH Measurements - The particle and vapor phase PAH emissions for all fuels studied are presented in Table 3. For the complete statistical treatment of these data the reader is referred to reference 9 which includes a discussion on handling data below minimum detection levels.

There were numerous significant differences in particle-associated PAH emissions (as determined by analysis of SOF samples) in the MTU study where the CLS fuel gave PAH levels higher than the conventional ARS fuel. Benz[a]anthracene, benzo[b]fluoranthene, benzo[k]fluoranthene, pyrene, chrysene, and benzo[a]pyrene emissions for the two fuels were significantly different when comparing like modes. The only significant difference between modes for vapor phase associated PAH (as analyzed in XOC samples) was for

benz[a]anthracene; this difference was significant for both fuels. For both fuels, the only detectable levels of benzo[k]fluoranthene and benzo[a]pyrene were particle-associated.

For the USBM data set, significantly different PAH values were found for chrysene, pyrene, benz[a]anthracene, and benzo[b]fluoranthene with the higher levels found with lower aromatics (CLAD) fuel as compared to the higher aromatics (CCAD) fuel when the SOF and XOC values were summed to determine the total emissions.

CONCLUSION: From these results, we have provided additional evidence to support the proposal that fuel composition has effects on specific pollutant emissions from diesel engines. More detailed analysis of fuels (including quantification of important PAH compounds and potential PAH precursors in fuel) is necessary in order to further define the correlation of fuel parameters and emissions.

ACKNOWLEDGMENTS: Funding for this study was provided in part by the Health Effects Institute, the United States Bureau of Mines Health and Safety research program, and the National Institute for Occupational Safety and Health. The engine at MTU was donated by Cummins Engine Co.

"Research described in this article was conducted under contract to the Health Effects Institute (HEI), and organization jointly funded by the United States Environmental Protection Agency (EPA) (Assistance Agreement X-812059) and the automotive manufacturers. The contents of this article do not necessarily reflect the views of the HEI, nor do they necessarily reflect the policies of EPA, or the automotive manufacturers."

References

1. Frisch, L.E., Johnson, J.H., Leddy, D.G., SAE Publication 790417 (1979)
2. Funkenbusch, E.F., Leddy, D.G., Johnson, J.H., SAE Publication 790418 (1979)
3. Campbell, J., Scholl, J., Hibbler, F., Bagley, S., Leddy, D., Abata, D., Johnson, J., SAE Publication 810263 (1981)
4. Bagley, S.T., Gratz, L.D., Leddy, D.G., Johnson, J.H., Preprints ACS Div. of Fuel Chemistry, Vol. 36, pp 311-318 (1991)
5. Baranescu, R.A., SAE Publication 881174 (1988)
6. Wall, J.C., Shimpi, S.A., Yu, M.L., SAE Publication 872139 (1987)
7. Ullman, T.L., Mason, R.L., Montalvo, D.A., SWRI Final Report to CRC, Project VE-1 (1990)
8. Weaver, C.S., Miller, C., Johnson, W.A., Higgins, T.S., SAE Publication 860622 (1986)
9. Kantola, T.C., Bagley, S.T., Gratz, L.D., Leddy, D.G., Johnson, J.H., SAE Publication 920565 (1992)
10. McClure, B.T., Bagley, S.T., Gratz, L.D., SAE Publication 920371 (1992)

Table 1. Comparison of Properties of Fuels*

Property	ARS	CLS	CLAD	CCAD
API Gravity	38.4	34.5		
Dist. Profile (°C)				
Initial B.P.	162	183	208	
10%	195	224	251	
50%	254	269	284	
90%	307	317	317	
95%	318	331		
Final B.P.	327	352	355	
Composition				
Carbon (wt.%)	85.6		86.1	
Hydrogen (wt.%)	13.3		13.85	
Sulfur (wt.%)	0.317	0.010	0.03	0.04
Oxygen (wt.%)	0.06			
Total N (ppm)	40	26.9	98	
Hydrocarbon Type (vol.%)				
Paraffins/Napthenes	73.0	67.8	88.9	
Olefins	3.5	2.3		
Aromatics				
FIAM Analysis	23.5	29.9	11	20
Mass Spectrometry		23.7		
HPLC			11.2	
Cetane Number	52.8	42.4	53	53

* Analyses provided by fuel suppliers.

ARS = Amoco conventional sulfur fuel, CLS = Chevron low sulfur fuel
 CLAD = Chevron low aromatic content fuel, CCAD = Chevron cetane
 adjusted fuel available in California

Table 1. Comparison of Properties of Fuels*

Property	ARS	CLS	CLAD	CCAD
API Gravity	38.4	34.5		
Dist. Profile (°C)				
Initial B.P.	162	183	208	
10%	195	224	251	
50%	254	269	284	
90%	307	317	317	
95%	318	331		
Final B.P.	327	352	355	
Composition				
Carbon (wt.%)	85.6		86.1	
Hydrogen (wt.%)	13.3		13.85	
Sulfur (wt.%)	0.317	0.010	0.03	0.04
Oxygen (wt.%)	0.06			
Total N (ppm)	40	26.9	98	
Hydrocarbon Type (vol.%)				
Paraffins/Napthenes	73.0	67.8	88.9	
Olefins	3.5	2.3		
Aromatics				
FIAM Analysis	23.5	29.9	11	20
Mass Spectrometry		23.7		
HPLC			11.2	
Cetane Number	52.8	42.4	53	53

* Analyses provided by fuel suppliers.

ARS = Amoco conventional sulfur fuel, CLS = Chevron low sulfur fuel
 CLAD = Chevron low aromatic content fuel, CCAD = Chevron cetane
 adjusted fuel available in California

Table 3. Summary of PAH Emissions Data (ng/m³-std)
Particle Associated PAH

Fuel	Mode	n	FLU	PYR	BaA	CHR	BbF	BkF	BaP
ARS	9	2	1300 (56)	31 (91)	140 (89)	120 (9.1)	94 (54)	3.6 (100)	4.4 (92)
	11	2	600 (16)	79 (20)	170 (19)	120 (9.1)	47 (24)	5.5 (8.7)	4.3 (3.5)
CLS	9	4	800 (33)	2300 (12)	1100 (61)	600 (74)	260 (28)	110 (84)	150 (82)
	11	4	1200 (5.6)	2000 (9.0)	730 (18)	180 (24)	240 (2.9)	140 (69)	220 (12)
CLAD	t ^a	6	950 (8.8)	2300 (9.0)	180 (1.7)	730 (22)	1500 (15)	240 (14)	140 (18)
CCAD	t ^a	5	940 (33)	2100 (43)	190 (40)	370 (36)	910 (39)	250 (58)	370 (63)

Vapor Phase Associated PAH (mg/m³-std)

Fuel	Mode	n	FLU	PYR	BaA	CHR	BbF	BkF	BaP
ARS	9	2	1700 (22)	300 (84)	120 (89)	18 ^b	<3 ^b	<3 ^b	<3 ^b
	11	2	2700 (22)	470 (22)	200 (17)	12 ^b	<4 ^b	<5 ^b	<5 ^b
CLS	9	4	2300 (51)	1800 (28)	320 (29)	240 (28)	4.6 ^b (52)	<6 ^b	<9 ^b
	11	4	1200 (14)	910 (14)	250 (7.3)	270 (55)	6.5 (18)	<5 ^b	<7 ^b
CLAD	t ^a	5	1400 (10)	1800 (15)	180 (28)	15 (37)	32 (24)	<2 ^b	<2 ^b
CCAD	t ^a	6	1200 (6.4)	1100 (18)	29 (47)	24 (58)	28 (13)	7.5 (32)	<2 ^b

FLU = fluoanthene, PYR = pyrene, BaA = benz[a]anthracene,
CHR = chrysene, BbF = benzo[b]fluoranthene, BaP = benzo[a]pyrene,
BkF = benzo[k]fluoranthene

^a light-duty transient cycle

^b less than minimum detection limit, no CV reported

CORRELATIONS BETWEEN DIESEL FUEL PROPERTIES AND ENGINE EMISSIONS

E. LOIS and S. STOURNAS

Fuels and Lubricants Laboratory, National Technical University,
157 73 Zografou, Athens, Greece

ABSTRACT

The oil industry and motor manufacturers are currently facing similar problems with diesel engines, namely restrictions on fuel quality for environmental reasons. It would thus be of value if some of the most important pollutants, such as NO_x and particulate matter (PM), could be predicted from basic fuel properties. This paper presents expressions from which the cetane number of the diesel fuel (without additives) and its aromatic content, are evaluated from the distillation curve and density, with very good accuracy, the correlation coefficient in the first case being 0.98 and in the latter 0.99. Subsequently NO_x and PM emitted for two types of engines are evaluated, both for hot and cold conditions, from the fuel aromaticity. This gives a direct measure of the pollutants as the fuel cetane number varies in the range 25-65, making it possible to adjust the fuel distillation curve to meet emission standards.

INTRODUCTION

In diesel fuels the cetane number is a property measured in a standard CFR engine (1) and for calculation purposes it can be approximated by methods such as the Calculated Cetane Index (2) or the Diesel Index (3), both of which are computed from the API gravity and either the mid-boiling point or the aniline point of the fuel. More recently, ASTM has introduced a method (4) that employs three points of the distillation curve, whereas numerous reports have appeared in the literature (5-7) that rely on instrumental methods such as NMR and HPLC for the estimation of cetane number. The reason for this approximation is the necessity of a rather cumbersome and expensive engine test for the measurement of the cetane number, which describes accurately the fuel ignition behavior. It would thus be of value if a simple method is developed to calculate the actual cetane number of a gasoil from other characteristics less troublesome to measure. A simple method was developed here, which accurately predicts the cetane number from five points of the distillation curve, i.e. the initial boiling point, the 10%, 50%, 90% and end point, the density and aromaticity of the fuel.

An effort was also made to predict the fuel aromaticity from the distillation curve and the density, making the evaluation of the cetane number dependent only on these two properties. The fuel aromaticity is important since it influences directly or indirectly many other specifications. If one examines the nature of the aromatic components found in gasoils (8), it is easy to see the diverse nature of the various aromatic, alkylaromatic or polyaromatic components, whose molecular weights and structures are such that they span the entire boiling point range of the middle

distillate fuels. The concentrations of each aromatic family also varies in each distillation fraction without following a specific pattern. The conclusion of this approach was that the prediction of the aromatic content depends on the method used to evaluate it. Accurate predictions were made following this method, whereas a global prediction effort was less successful.

Finally, we have attempted to correlate the cetane number with engine emissions. The emittants are directly dependent not only on the fuel specifications, but also on the type of engine used and the running conditions (9-12). Our effort was to correlate some of the most important emittants, i.e. NOx and particulate matter for hot and cold conditions, for two types of engines, a Detroit diesel engine of 315 hp (9), and a Cummins diesel engine of 400 hp (9). NOx and particulate emission values were obtained from the fuel aromatic content and the 90% point of the distillation curve, from equations referring to the above engines (5). The value of such correlations lies in the fact that given the level of the emittants set by regulations, and the dependence of the cetane number on the distillation curve and density, the refinery can adjust the distillation curve to meet these regulations for specific types of engines.

CETANE NUMBER

The parameters chosen to predict the cetane number were the fuel aromaticity, the distillation curve and the density. Other parameters such as viscosity, sulfur content etc., were excluded from the calculation since they did not seem to affect the results further.

For this reason a matrix of 26 fuels was analysed, Table 1. None of the fuels considered contained any additives and the distillation characteristics were measured either according to the IP or the ASTM standards (8, 13-15).

The relationship found to describe the cetane number best is the following:

$$\text{Cetane Number} = a.IP + b.D10 + c.D50 + d.D90 + e.(1/EP) + f.(1/DENS^2) + g.(1/AROM^4) + h \quad (1)$$

where, IP = Initial boiling point, °C
 Dn = n% vol. recovered, °C
 EP = End boiling point, °C
 DENS = Specific gravity, 15/4 °C
 AROM = Aromatics, wt%

and,

a = -0.011
 b = 0.092554
 c = 0.119366
 d = 0.130821
 e = 7083.031
 f = 110.258
 g = 16096.35
 h = -219.705

The correlation obtained between the measured and the calculated cetane number (r = 0.983) was good, where in over 92% of the cases the error was less than 5%, and for the rest 8% of the

points the error was less than 6%. In absolute numbers, the calculated cetane number of 24 of the fuels was within two units of the experimentally determined value, i.e. within the accuracy limits of the measuring method; the maximum error in the other two fuels was 2.9 units. It is worth noting that ASTM D-976 estimations of the same 26 fuels fall within two units in only eleven of the cases, and the maximum error is in excess of five cetane number units. The results are depicted in Figure 1.

FUEL AROMATICITY

The aromaticity of fuels 1-8, Table 1, was measured using the FIA method (IP Method No 156/70) (8) whereas the aromatic content of fuels 9-16 was evaluated using the HPLC method (14); the method employed for the rest of the fuels was not specified (15). The equation found to fit best the data of the 26 fuels was the following:

$$\begin{aligned} \text{AROM} = & a.\text{IP} + b.\text{D10} + c.(\text{d50})^{0.5} + d.\text{D90} \\ & + e.\text{EP} + f.(1/\text{DENS}^2) + g \end{aligned} \quad (2)$$

where, $a = -0.25931$
 $b = 0.514474$
 $c = -13.157$
 $d = -0.03947$
 $e = 0.059787$
 $f = -166.654$
 $g = 400.452$

The results are shown in Figure 2, and the correlation coefficient between the measured and the calculated aromatic fuel content would not exceed 0.91, regardless of the number of points selected from the distillation curve. The high degree of scatter of the results does not allow an accurate estimate of the aromatic content.

However, much better results were obtained if one considers the results of each individual method separately, even in the case that only one point was selected to represent the distillation curve, Figure 3. The equations used to evaluate the aromaticity content are the following:

$$\begin{aligned} \text{AROM wt}\% = & 236.323 \times 10^{-3} \times \text{D50} + 396.9 \times \text{DENS} \quad (3) \\ \text{AROM wt}\% = & -144.17 \times 10^{-3} \times \text{D50} + 583.6 \times \text{DENS} \quad (4) \end{aligned}$$

It is worth mentioning that in both cases very good results were obtained, irrespective of the point selected from the distillation curve, the correlation coefficients being always at least 0.99.

ENGINE EMISSIONS

The equations set forward for two types of engines (9), a Cummins NTCC 400, six cylinder engine, 14 liter displacement, direct-injection, in-line, turbocharged, intercooled, rated power 400 hp at 2100 rpm, and fuel consumption of 153 lb/hr and a Detroit diesel DDC 60-11-315, six cylinder engine, 11 liter displacement, in-line, direct injection, turbocharged, intercooled, rated power

315 hp at 1800 rpm, and fuel consumption of 105 lb/hr, were utilized in this analysis:

<u>Cummins</u>	PMCS(g/hp-hr) = $0.436563 + 5.375 \times 10^{-3} \times (\% \text{Aromatics})$	(5)
	PMHS(g/hp-hr) = $0.370001 + 3.947 \times 10^{-3} \times (\% \text{Aromatics})$	(6)
	NOxCS(g/hp-hr) = $3.911810 + 11.89 \times 10^{-3} \times (\% \text{Aromatics})$	(7)
	NOxHS(g/hp-hr) = $4.28257 + 12.7932 \times 10^{-3} \times (\% \text{Aromatics})$	(8)
<u>DDC</u>	NOxCS(g/hp-hr) = $9.3563 + 28.5266 \times 10^{-3} \times (\% \text{Aromatics})$	
	- $88.5758 \times 10^{-4} \times (90\% \text{ Boiling point})$	(9)
	NOxHS(g/hp-hr) = $6.45922 + 26.8833 \times 10^{-3} \times (\% \text{Aromatics})$	
	- $43.0576 \times 10^{-4} \times (90\% \text{ Boiling point})$	(10)

where PMCS = Particulate Matter Cold-Start
 PMHS = Particulate Matter Hot-Start
 NOxCS = NOx Cold-Start
 NOxHS = NOx Hot-Start
 g/hp-hr = gram per brake horsepower-hour

The data from Table 1 were applied to the above equations, and the results obtained are depicted in Figures 4-6. It can be seen that for the two engines, as the cetane number increases in the range 25-65, both NOx and particulate matter decrease, irrespective of hot or cold conditions. An equation of the type

$$y = a \cdot \exp(-b \cdot \text{CN}) \quad (11)$$

where CN is the fuel cetane number, was found to fit reasonably well the points of the above figures. The values of a and b for the various emittants are listed in Table 2.

CONCLUSIONS

Equations were presented which predict the gasoil aromatic content from the density and the distillation curve, and its cetane number from the density, aromaticity and the distillation characteristics.

Subsequently the cetane number was correlated to NOx and particulate emittants for two types of engines, making it thus possible to adjust the fuel characteristics to meet current or future legislation.

REFERENCES

1. Test for Ignition Quality of Diesel Fuels by the Cetane Method, ASTM D-613.
2. Calculated Cetane Index of Distillate Fuels, ASTM D-768.
3. Diesel Index, IP 21-80.
4. ASTM Method D-4737-87.
5. B. K. Bailey et al. SAE Paper 861521, 1986
6. T. H. DeFries et al., Ind. Eng. Chem. Res. 1987, 26, 188-193.
7. S. G. Pande and D. R. Hardy, Energy Fuels 1989, 3, 308-312.
8. G.Mills, J.Howarth and A.Howard, J.Inst.Energy, Vol. LVII, No 430, pp.273-286, 1984.
9. J.Courtis, Technical Support Document, Air Resources Board, State of California, 1988.
10. R.Burt and K.Troth, "Influence of fuel properties on diesel

- exhaust emissions", Institute of Mechanical Engineers, 1968.
11. E.Yoshida, H.Nomura and M.Sekimoto, SAE-paper 860619, 1986.
 12. CONCAWE, Concawe report No 10/87, 1987.
 13. Automotive Emissions/Fuel Characteristics AE/STF-2, Concawe report, 7th Draft, 1989.
 14. M.Kagami et al. SAE-paper 841082, 1984.
 15. K. Weidmann et al. SAE-paper 881649, 1989.

TABLE 1. THE FUEL MATRIX

NO OF FUEL	CETANE NUMBER	AROM wt%	DENSITY gr/cm ³	IP °C	D10 °C	D50 °C	D90 °C	EP °C
1	50.6	19.43	0.8438	197	230	279	329	355
2	65.1	8.18	0.8170	220	253	274	308	322
3	47.9	25.70	0.8557	214	245	292	346	364
4	47.2	34.94	0.8727	220	248	297	346	364
5	38.0	44.63	0.8917	220	257	299	345	368
6	37.3	54.87	0.9137	220	266	303	349	368
7	28.1	66.36	0.9471	257	280	310	351	368
8	45.0	32.00	0.8722	231	257	286	330	351
9	56.0	23.80	0.8230	191	219	255	322	348
10	57.0	28.20	0.8392	192	243.5	295.5	349	369
11	57.0	34.60	0.8570	211	270	320.5	366.5	393
12	58.0	37.80	0.8647	230	288.5	329	369	398
13	30.0	65.30	0.8996	175	236	273	312.5	335
14	34.0	59.70	0.8884	180	239	275	315	337
15	40.0	54.20	0.8764	184	241.5	276.5	317	338
16	44.0	45.00	0.8640	193	245	279.5	318	340
17	34.3	48.40	0.8486	83	165	221	304	350
18	39.7	31.70	0.8331	112	166	220	303	346
19	44.8	15.50	0.8181	138	166	220	302	346
20	35.0	53.00	0.8683	71	176	251	328	359
21	39.1	40.10	0.8532	72	178	250	328	359
22	44.6	26.80	0.8380	76	177	250	328	359
23	35.1	58.90	0.8931	107	201	285	340	358
24	39.8	47.70	0.8825	126	211	285	342	368
25	44.2	38.90	0.8641	108	209	291	341	367
26	45.5	24.70	0.8522	172	221	263	312	340

TABLE 2. VALUES OF THE CONSTANTS a and b

		a	b
<u>Cummins</u>	PMCS	1.127440	0.0118222
	PMHS	0.876955	0.0109310
	NOxCS	5.27345	0.0039207
	NOxHS	5.74554	0.0038658
<u>DDC</u>	NOxCS	7.69730	0.0096137
	NOxHS	7.21377	0.0086266

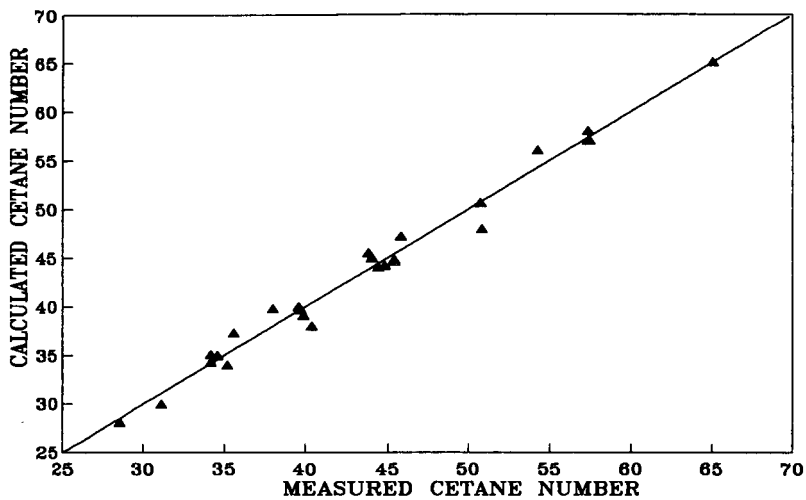


FIGURE 1. Calculated vs. Experimental Cetane Number

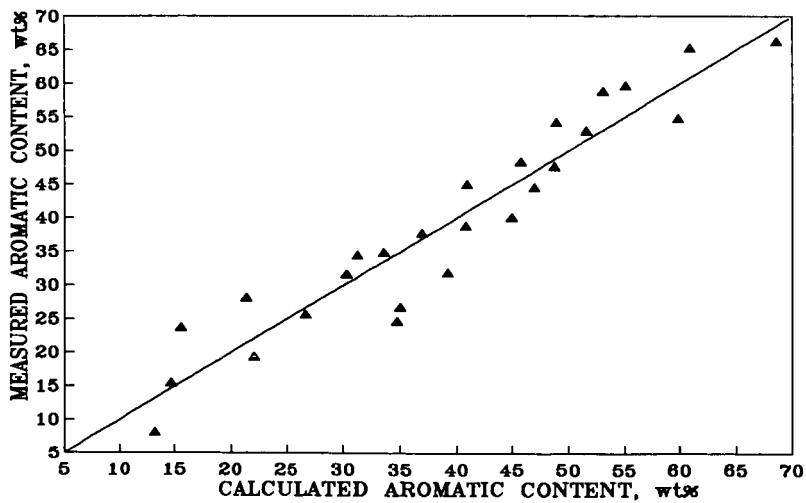


FIGURE 2. Calculated vs. Experimental Aromaticity

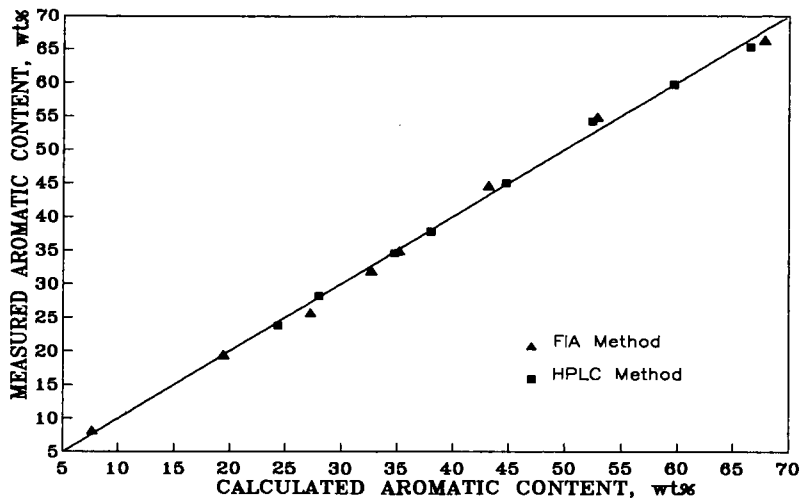


FIGURE 3. Calculated vs. Experimental Aromaticity, with the method of measurement taken into account

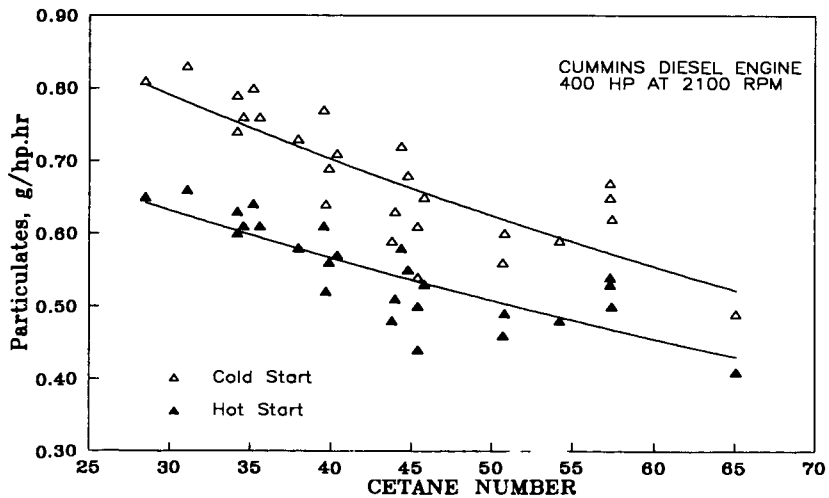


FIGURE 4. Particulate Emissions

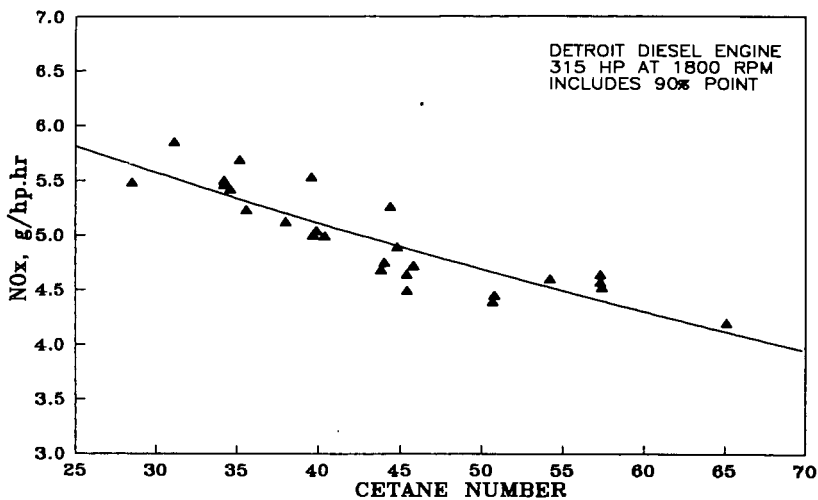


FIGURE 5. NOx Emissions (Hot Start)

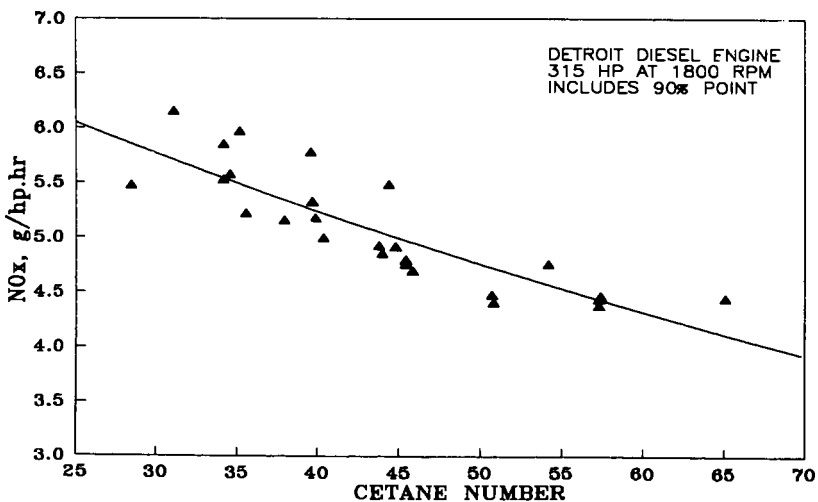


FIGURE 6. NOx Emissions (Cold Start)

INFLUENCE OF CATALYST ON SULFUR DISTRIBUTION IN FCC GASOLINE

Robert R. Gatte^a, Robert H. Harding^a, Thomas G. Albro^a,
Don S. Chin^b and Richard F. Wormsbecher^b
W. R. Grace and Co.

^aResearch Division

^bDavison Chemical Division

Washington Research Center

7379 Route 32, Columbia, MD 21044

Keywords: Catalytic Cracking, Sulfur, Reformulated Gasoline

In an effort to learn more about the role of the catalyst on the sulfur content and distribution in FCC gasoline, several catalysts have been tested, and the resulting gasoline range sulfur species examined in detail. In addition, model compound studies have been conducted to examine the cracking of thiophene over the same catalysts. It has been found that catalysts which produce widely different hydrocarbon distributions during FCC produce only marginally different sulfur distributions in the gasoline range. In addition, catalysts which have significant hydrogen-transfer activity more effectively convert thiophene to H₂S than those with low hydrogen-transfer activity. These findings show that the FCC catalyst may have a role to play in the production of low-sulfur reformulated gasoline.

Introduction

The reformulated gasoline regulations mandated by the Clean Air Act Amendment of 1990 have set new limits on the composition of gasoline to be sold in many parts of the U.S.¹. Meeting the requirements of the Act (as specified by the EPA) will present a considerable challenge to the refining industry over the course of the next decade². Besides setting limits on the levels of oxygenates and aromatics (particularly benzene) in reformulated gasoline, it is anticipated that the EPA will set an additional limit on the level of gasoline sulfur^{2,3}. A recent report from the Auto/Oil Air Quality Improvement Research Program clearly showed that reduction in the gasoline sulfur level from 500 ppm to 50 ppm had a significant favorable impact on tailpipe emissions^{4,5}. The reason is that sulfur emissions poison the active noble metal in emission control catalysts, thus, lower sulfur results in a more effective catalytic converter.

FCC naphtha contributes the largest fraction of sulfur to the total gasoline pool. In fact, 75% to 90% of pool sulfur can be traced to the FCC unit, while only 35% to 40% of the pool volume is FCC gasoline^{6,7}. Thus, any move to reduce gasoline sulfur content will invariably impact the FCC unit in some way. Of the possible options, hydrotreating either the FCC feedstock or the FCC naphtha is the most obvious. However, with the concomitant need to reduce the aromatic content of the reformulated gasoline pool, reformer severity will probably be reduced which will limit the refinery's hydrogen supply. In addition, in order to reduce the gasoline sulfur content to the proposed levels (30-50 ppm), "deep" hydrotreating will most likely be required.

A potentially less expensive option is the catalytic removal of sulfur compounds in the FCC unit. In order to examine this alternative, we have studied the impact of the FCC catalyst on the gasoline sulfur content. Previous workers have examined the sulfur distributions resulting from thermal cracking of gas oils⁸, while others have focussed on the effect of the feedstock and operating conditions on the final sulfur distribution⁹⁻¹². However, to date, no study of the effect of the FCC catalyst on gasoline sulfur content has been reported.

In this study, we explored the impact of variations in FCC catalyst properties on the concentration and distribution of gasoline range sulfur compounds in FCC naphtha. In addition, we examined the conversion of thiophene in a thiophene/hexadecane mixture over the same catalysts in order to determine the extent and importance of secondary cracking reactions, i.e. overcracking¹³, on the final sulfur distribution.

Experimental

The catalysts used for this study are typical of the types of faujasite-based materials which are commercially available, and were chosen to provide a wide variation of hydrogen-transfer (H-T) activity¹⁴⁻¹⁶. Catalyst properties are given in Table I. The REY catalyst showed the highest steamed unit cell size, and was expected to have the highest H-T activity. In contrast, the USY/Matrix and USY-G catalysts had the lowest steamed unit cell size and thus, the lowest H-T activity. The REUSY catalyst showed properties intermediate between the REY and USY's. All of the catalysts were steam-deactivated for 4 hours at 1500°F prior to testing.

Gas oil cracking experiments were run in the Davison Circulating Riser (DCR¹⁷) which was run in the adiabatic mode with a riser outlet temperature of 970°F. The feed used in the DCR was a sour heavy gas oil which contained 2.67 wt% sulfur¹⁸. H₂S in the light gas fraction was determined by GC analysis. Feed and liquid-product sulfur contents were measured using a LECO sulfur analyzer. Sulfur on coke was determined by measuring SO₂ content of the regenerator flue gas. Sulfur material balances between 99% and 102% were consistently obtained.

Detailed identification of the gasoline range sulfur compounds was obtained using a HP 5890 GC equipped with a PONA capillary column and an Atomic Emission Detector (GCAED). In this system, the separated compounds from the column exit are broken down into constituent elements and excited in a plasma. The various atoms then emit light at characteristic wavelengths and quantitative element-specific information is obtained by monitoring the wavelength(s) characteristic of a specific element. Individual sulfur compound identifications were made using a combination of GCAED and GC-MS. A typical chromatogram is shown in Figure 1.

The hexadecane and thiophene used in the model compound experiments were 99+ % purity gold label Aldrich products. Hexadecane conversion was determined by GC analysis (HP 5890 equipped with a 19091S-001 50 m Fused Silica Capillary column). The reactor system had a standard fixed-bed configuration and the liquid mixture was pumped into the reaction chamber with a syringe infusion pump at the rate of .6 g/min. Nitrogen was co-fed with the hydrocarbons at the rate of 10 cc/min. Contact time was fixed at 3 minutes, and weight hourly space velocity (WHSV) was varied by changing the amount of catalyst in the reactor tube. To maintain constant reactor heat capacity the catalyst was diluted with alundum (EM Science, calcined for 2 hrs. at 1300 °F) to a constant bed volume of 4 ml. Alundum alone shows less than 1 % conversion for this pseudocomponent mixture.

Liquid products were collected in an ice bath and then analyzed by GC. The volume

of the gas products was determined by water displacement. The gas products were analyzed by FID and TCD on a Varian Vista 6000 Gas Chromatograph equipped with a 50 m Chrompack Fused Silica column 7515. Coke levels were determined by mass difference between the catalyst after 100 °C calcination and 540 °C calcination for 1 hour. Only mass balances above 97% are reported in this study.

Results and Discussion

Table I contains a constant (70 wt%) conversion comparison of the four catalysts tested in the Davison Circulating Riser (DCR). A more detailed analysis of the DCR data is given in a previous paper¹⁸. From the data, it appears that all of the catalysts are equally efficient at converting feed sulfur from LCO/HCO into lighter products, with the exception of USY-G which shows somewhat lower sulfur conversion activity. No significant differences in product yields are observed: The majority (about 40%) of the feed sulfur is converted into H₂S, about 3% is converted into coke, while roughly 2% ends up in the gasoline fraction. However, on closer analysis of the sulfur distribution in the gasoline fraction, some differences are observed. For all catalysts, the majority of the gasoline range sulfur compounds are thiophene derivatives. However, the catalysts with high hydrogen-transfer activity (REY, REUSY) produced about 8% less gasoline sulfur than those with low hydrogen-transfer activity (USY, USY-G). This result was unexpected, since thiophene is aromatic and hydrogen-transfer over FCC catalysts typically results in the formation, not the destruction, of aromatic molecules¹⁴⁻¹⁶. Another difference between the two catalyst types is the molecular weight distribution of the gasoline range sulfur products. While the amounts of lighter products (mercaptans, thiophene, tetrahydrothiophene) is similar for all four, the low H-T catalysts produced larger amounts of the heavier species (propylthiophenes, butylthiophenes, benzothiophene).

In addition to sulfur content, future reformulated gasoline regulations will also include T90 (the distillation temperature at which 90% of the fuel has boiled away) as a variable in the "complex model" to be used for gasoline certification. Lowering T90 reduces the average molecular weight of gasoline which allows for better vaporization and cleaner combustion in automobile engines. In our study, reduction of T90 from the current level of 380°F (430°F endpoint) to the proposed level of 300°F (340°F endpoint) has the effect of removing the heavy sulfur compounds from the resulting gasoline. All of the benzothiophene and butylthiophenes and some of the propylthiophenes are removed by this change in T90. This effectively eliminates the differences in gasoline sulfur distribution shown by the four catalyst systems¹⁸.

In an attempt to determine the extent and importance of secondary cracking reactions on the final sulfur distribution, model compound cracking experiments were run for three of the catalysts. Thiophene was tested as a mixture with hexadecane in an effort to mimic a typical hydrocarbon environment during the cracking reactions. The mixture contained 0.5 wt% (5000 ppm) sulfur. Results from this set of experiments are shown in Figures 2 and 3 and Table II.

The data show that, for all catalysts, the conversion of thiophene is low and independent of the conversion of hexadecane (which ranged in conversion from 20-80%). For our data, there is a linear relationship between $-\ln(1-\text{thiophene conversion})$ and the reciprocal of space velocity (1/WHSV). The linear yield curves, shown for the REY catalyst in Figure 2, further demonstrate that the product selectivity of the thiophene is unaffected by the changes in hexadecane product distribution over this range of conversion. Although we expect the alkylthiophenes to be direct reaction products of thiophene with hexadecane product precursors, these species must be in

great excess with respect to the thiophene if they do not affect either the conversion or the selectivity of the thiophene.

To determine the relative cracking rates of hexadecane and thiophene, we used a technique for the cracking kinetics of model compound mixtures which is described in detail elsewhere¹⁹. The cracking of the mixture can be represented by two coupled nonlinear equations:

$$\frac{dC_H}{dt} = \frac{K_H \sum_j k_{Hj} C_H [1+G\tau]^{-N}/[VE]}{1+[K_H C_H + K_T C_T + \sum_j [C_{H0}-C_H] K_{Hj} n_{Hj} + \sum_j [C_{T0}-C_T] K_{Tj} n_{Tj}]/[VE]}, \quad (1)$$

$$\frac{dC_T}{dt} = \frac{K_T \sum_j k_{Tj} C_T [1+G\tau]^{-N}/[VE]}{1+[K_H C_H + K_T C_T + \sum_j [C_{H0}-C_H] K_{Hj} n_{Hj} + \sum_j [C_{T0}-C_T] K_{Tj} n_{Tj}]/[VE]}, \quad (2)$$

where subscripts H and T represent Hexadecane and Thiophene respectively, C is the concentration, K is the Langmuir-Hinshelwood-Hougen-Watson (LHHW) adsorption constant, k_j is the first order reaction through the j th reaction pathway, G and N are the decay parameters for time on stream τ , C_0 is the initial concentration in the reaction mixture, K_j is the adsorption constant of the products through reaction pathway j , n_j is the stoichiometry of reaction pathway j , and [VE] represents the volume expansion of the mixture. Equations 1 and 2 can be simplified by solving for dC_H/dC_T to obtain:

$$\left(\frac{C_H}{C_{H0}} \right) = \left(\frac{C_T}{C_{T0}} \right)^{\frac{K'_H}{K'_T}} \quad (3)$$

By using equation (3) to examine the relative conversions of hexadecane and thiophene, we can obtain a ratio of effective rate constants K' that is independent of the catalyst deactivation rate, most competitive sorption terms, and the volume expansion of the mixture. In Figure 2 we plot C_H vs. C_T for the REY (high H-T) and USY (low H-T) catalysts along with the curve fitted to equation (3). The data show that hexadecane cracks approximately 10.4 times faster than thiophene under these conditions. No difference is observed between the two faujasite types, which indicates that the increased hydrogen-transfer kinetics of the REY does not alter the relative cracking rates of the thiophene and the hexadecane.

While analysis of the kinetic data show no difference between the rates of thiophene cracking over the high and low H-T catalysts, there is a difference between the product selectivities of the catalysts. Table II shows the product distributions for the four catalysts interpolated to a constant 4 mol% conversion. At this low conversion, only primary products are expected to form. The product selectivity varies smoothly with the hydrogen-transfer activity of the catalysts. With REY, tetrahydrothiophene is the most abundant product, while ethylthiophene is the major product over USY. REUSY shows behavior intermediate between the other two. This is consistent with the riser data (Table I) which showed increased levels of the heavier thiophene derivatives for the low H-T catalysts. It is also interesting to note that there is some formation of H_2S , a secondary reaction product, over the REY and REUSY catalysts, even at this low conversion level.

There appear to be two different mechanisms for the conversion of thiophene over faujasite-based FCC catalysts. The dominant mechanism over the high H-T catalysts is the hydrogenation of thiophene to tetrahydrothiophene, followed by the cracking of this product to form H₂S. Conversely, the dominant mechanism over the low H-T catalysts is the alkylation of thiophene to methyl, ethyl and propyl thiophene. Thus, the lower the H-T activity, the higher the average molecular weight of the sulfur products. Also, it appears that the relative importance of the two reaction pathways varies smoothly with H-T activity, since the REUSY shows behavior intermediate between the other catalysts.

Conclusions

Examination of the role of catalyst properties on the distribution of sulfur compounds present in FCC gasoline has shown that only small differences exist between catalyst types, and the primary impact of the catalyst is on the molecular weight distribution of the thiophene derivatives which are produced. Model compound experiments have shown that thiophene can be either alkylated or hydrogenated over FCC catalysts under cracking conditions, albeit at an extremely low rate. Catalysts with high site-density and therefore high hydrogen-transfer activity preferentially hydrogenate thiophene to tetrahydrothiophene which can then be cracked to H₂S. In contrast, catalysts with low site density and low hydrogen-transfer activity favor alkylation of thiophene to higher molecular weight products. However, the small differences between catalyst types indicate that alternative materials will be required to significantly affect the sulfur content of FCC gasoline.

Acknowledgements

The authors wish to thank Petrea Erbe for assistance in the analysis of the DCR data, and Pam Gore and Ted Peders for collecting the model compound data. We also wish to thank W. R. Grace & Co.-Conn for permission to publish this work.

References

1. "Provisions: Clean Air Act Amendments," Congressional Quarterly, 48, p. 3934 (1990).
2. Reilly, W. K., Fuel Reformulation, 1(1), p. 18 (1991).
3. Sharpless, J., Fuel Reformulation, 1(2), p. 8 (1991).
4. Corbett, R. A., Fuel Reformulation, 1(1), p. 46 (1991).
5. "Effects of Fuel Sulfur Levels on Mass Exhaust Emissions," Auto/Oil Air Quality Improvement Research Program, Technical Bulletin No. 2, February 1991.
6. NPRA Gasoline Survey, Section A, Revised Sulfur Data, National Petroleum Refiners Association, March 1991.
7. Stokes, G. M., Wear, C. C., Suarez, W. and Young, G. W., Oil and Gas J., p. 58, July 2, 1990.
8. Barron, J. M., Vanderploeg, A. R. and McReynolds, H., Ind. Eng. Chem., 41, p. 2687 (1949).
9. Sterba, M. J., Ind. Eng. Chem., 41, p. 2680 (1949).
10. Wollaston, E. G., Forsythe, W. L., and Vasalos, I. A., Oil and Gas J., p. 64, August 2, 1971.

11. Huling, G. P., McKinney, J. P., and Readal, T. C., *Oil and Gas J.*, p. 73, May 19, 1975.
12. Campagna, R. J., Krishna, A. S., and Yanik, S. J., *Oil and Gas J.*, p. 128, October 31, 1983.
13. Rawlence, D. J. and Dwyer, J., in "Fluid Catalytic Cracking II: Concepts in Catalyst Design", M. L. Occelli, Ed., ACS Symp. Series 452, American Chemical Society, Washington, D.C., p. 56 (1991).
14. Pine, L. A., Maher, P. J., and Watcher, W. A., *J. Catal.*, **85**, p. 44 (1984).
15. Ritter, R. E., *Catalagram*, **74**, (1986), (Published by the Davison Chemical Division of W. R. Grace & Co.-Conn.).
16. Young, G. W., Suarez, W., Roberie, T. G., and Cheng, W.-C., paper AM-91-34, presented at the NPRA Annual Meeting, San Antonio, March 1991.
17. Young, G. W., and Weatherbee, G. D., "FCCU Studies with an Adiabatic Circulating Pilot Unit," presented at the AIChE Annual Meeting, San Francisco, November, 1989.
18. Wormsbecher, R. F., et al, presented at NPRA Annual Meeting, New Orleans, 1992.
19. Harding, R. H., Gatte, R. R. and Pereira, C. J., submitted to *I&EC Res.*, January, 1992.

Table I.
Distribution of Sulfur Products from
DCR Cracking of Gas Oil over FCC Catalysts

Liquid Conversion = 70 wt%

Catalyst Properties	REY	REUSY	USY/MATRIX	USY-G
Re ₂ O ₃ , wt%	4.73	2.79	0.02	0.04
Unit Cell*, Å	24.49	24.30	24.19	24.24
Zeolite SA, m ² /g	38	131	81	196
Matrix SA, m ² /g	24	23	55	25
Sulfur Conversion (wt%)	45.5	44.5	45.0	42.5
Product Yields (wt%)				
H ₂ S	40.1	39.1	40.1	36.7
Gasoline	2.0	2.0	2.0	2.2
LCO/HCO	54.5	55.5	55.0	57.5
Coke	3.3	3.3	3.0	3.7
Gasoline Sulfur (ppm S)	1175	1175	1280	1280
mercaptans	169	61	169	167
thiophene	62	168	59	59
tetrahydrothiophene	17	17	17	17
methylthiophenes	150	148	160	158
ethylthiophenes	171	169	176	174
propylthiophenes	120	119	145	144
butylthiophenes	133	142	164	174
benzothiophene	353	351	389	385

* After 4 hr, 1500°F steam deactivation

Table II.

Sulfur Product Yields from Cracking of Thiophene in Hexadecane, Interpolated to 4 vol% Thiophene Conversion

Operating Conditions: 500°C, 1 atm

Product Yields	<u>REY</u>	<u>REUSY</u>	<u>USY-G</u>
Tetrahydrothiophene	1.7	1.5	1.0
Alkylthiophenes	2.2	2.4	3.0
Methylthiophene	1.2	1.3	1.4
Ethylthiophene	1.0	1.1	1.6
Hydrogen Sulfide	0.1	0.1	0.0

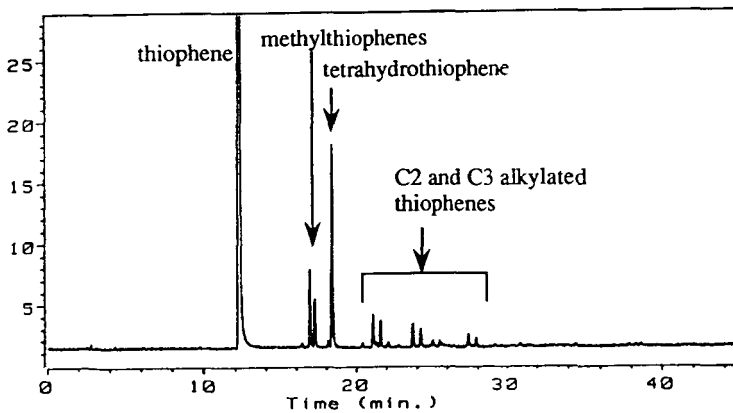


Figure 1 Sulfur GCAES Chromatogram from Cracking of Thiophene in Hexadecane

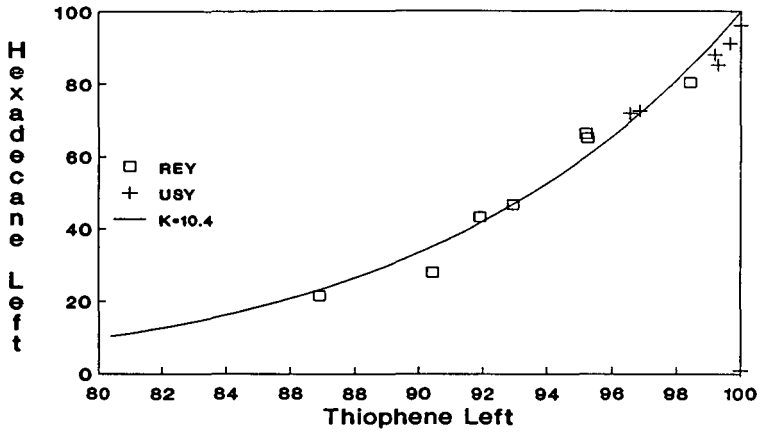


Figure 2 Product Yields from Cracking of Thiophene in Hexadecane over REY Catalyst

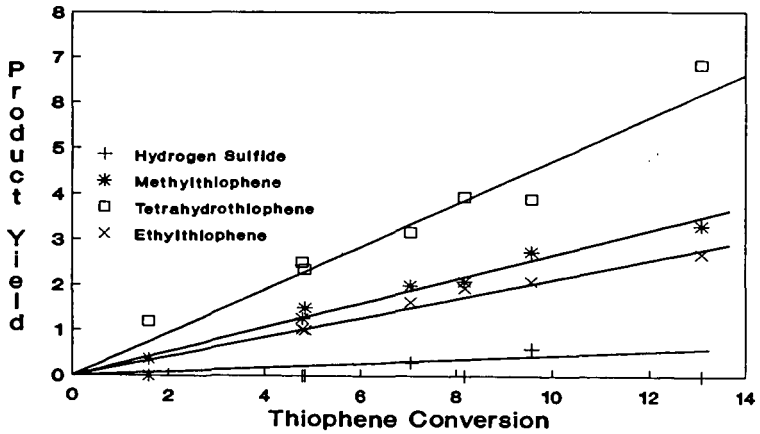


Figure 3 Relative Conversion of Thiophene and Hexadecane from Cracking of Mixture

**DIESEL AROMATICS SATURATION:
A COMPARATIVE STUDY OF FOUR CATALYST SYSTEMS**

Barry H. Cooper, Antony Muthu Stanislaus, Peter N. Hannerup
Haldor Topsøe A/S Research Laboratories
DK-2800 Lyngby, Denmark

Keywords: Diesel aromatics saturation; hydroprocessing catalysts, sulfur tolerant noble-metal catalyst.

INTRODUCTION

It has previously been reported that a high aromatics content in diesel fuel both lowers the fuel quality and contributes significantly to the formation of undesired emissions in exhaust gases (1, 2). Because of the health hazards associated with these emissions, environmental regulations governing the composition of diesel fuels are being tightened in Europe and the USA (3, 4). There is, however, a large span in the stipulated maximum level of aromatics. The 1990 Amendments to the Clean Air Act will limit aromatics in the USA to 35%v or a minimum cetane number of 40 from 1993, whilst in California a maximum of 10%v will be enforced. In Sweden there are three diesel specifications in operation with a limit of 5%w aromatics in class 1, 20%w in class 2 and 25%w in class 3. In Denmark a minimum cetane number of 52 is likely to be required for city diesel.

At the same time the aromatics content of diesel feedstocks can vary widely: S.R. stocks typically contain 20-40%v aromatics and cracked stocks 40-70%v. Thus the requirements for aromatics saturation range from moderate to severe depending on refinery location and feedstock availability. Existing middle distillate hydrotreaters designed to reduce sulfur levels are capable of reducing aromatics content only marginally (5-7), and as such considerable attention has in recent years been paid to new catalysts and processes for aromatics saturation.

In this paper results obtained on four catalyst systems are reported. The systems investigated are:

- conventional hydrotreating catalysts in single-stage operation,
- NiMo/NiW in two-stage operation,
- Pt/Al₂O₃ in two-stage operation,
- sulfur-tolerant noble-metal catalyst in two-stage operation.

A comparison of the conditions necessary to obtain given aromatic specifications is made for all four systems.

EXPERIMENTAL

The hydrogenation runs were performed in a stainless steel tubular fixed-bed reactor (50 ml) operating in the down-flow mode. Once-through pure hydrogen gas was used. The feedstocks used in the present study and their properties are summarized in Table 1.

FEED CUT	A HGO	B Pretr. HGO	C Pretr. HGO	D Pretr. HGO	E LGO	F Pretr. LGO
SG	0.865	0.845	0.839	0.841	0.839	0.832
S, wppm	17,000	1400	1.5	300	1270	90
N, wppm	225	60	2	46	38	15
D86, °F						
IBP/10%	425/532	397/505	390/485	390/485	376/429	385/426
50/90%	624/710	600/703	600/689	597/689	480/547	478/545
EP	720	717	705	730	590	587
<u>Aromatics</u>						
FIA, %v	33.0	23.5	19.0	19.5	30.0	25.5
HPLC, %w						
total	36.0	25.0	20.0	21.0	32.5	28.0
mono-	20.5	19.0	16.5	17.0	17.5	17.0
di-	13.0	5.0	3.0	3.5	11.0	7.5
tri-	2.5	1.0	0.5	0.5	4.0	3.5
Aromatic carbon, %w	13.5	9.3	7.7	7.9	10.3	9.3

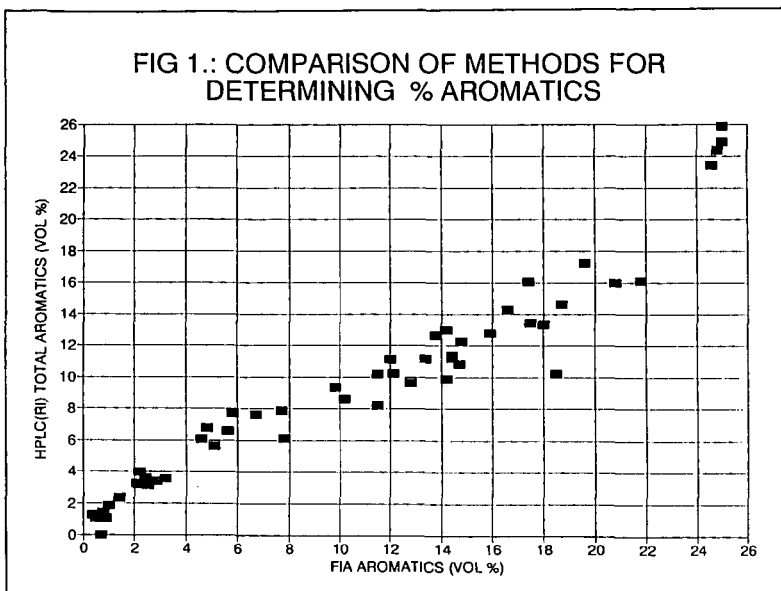
TABLE 1: Properties of Feedstocks.

Aromatics content in feed and products was measured by FIA, HPLC and Dhulesia's correlation (8). ^{13}C NMR was used to check the results of Dhulesia's correlation. These two methods give the total content of aromatic carbon in wt%. The HPLC method uses two types of detectors, namely ultraviolet (UV) and refractive index (RI) to measure quantitatively different types of aromatics (i.e. mono-, di-, tri- and total aromatics) in feed and products. The FIA method (ASTM D1319) that has been prescribed by the EPA as a standard method for specifying aromatics levels in diesel fuels does not give any breakdown of aromatics type distribution, but gives the total aromatics content in vol%. Different methods usually give different absolute aromatics levels than those by FIA. Correlations between aromatics measured by FIA and other methods have been developed by several workers (5, 9). However, such correlations differ significantly with variations in feedstocks.

Among the various methods used in our laboratory for aromatics determination, the best agreement for total aromatics content was found between HPLC (RI) and FIA methods. A plot of total aromatics as measured by FIA and HPLC (RI) is shown in Figure 1.

The HPLC (RI) method is a standard IP method (IP 391/90). It can be used for routine aromatics analysis as well as a research tool to follow changes in concentration of different types of aromatics and reactions during hydrodearomatization.

FIG 1.: COMPARISON OF METHODS FOR DETERMINING % AROMATICS



RESULTS AND DISCUSSION

1. Conventional Catalysts in Single-Stage Operation

Tests were carried out on a commercial catalyst, TK 561, using a Kuwait HGO as feedstock. TK 561 is a catalyst containing Ni and Mo on alumina. The HGO is a straight run cut used as a feed to a commercial diesel hydrotreater with a high sulfur content and 36 wt% aromatic compounds (Feed A in Table 1). The tests were run at a wide range of conditions: hydrogen pressure 4.5-12.5 MPa (650-1815 psi); temperature 593-673K (608-752°F); LHSV 1-2.5 h⁻¹.

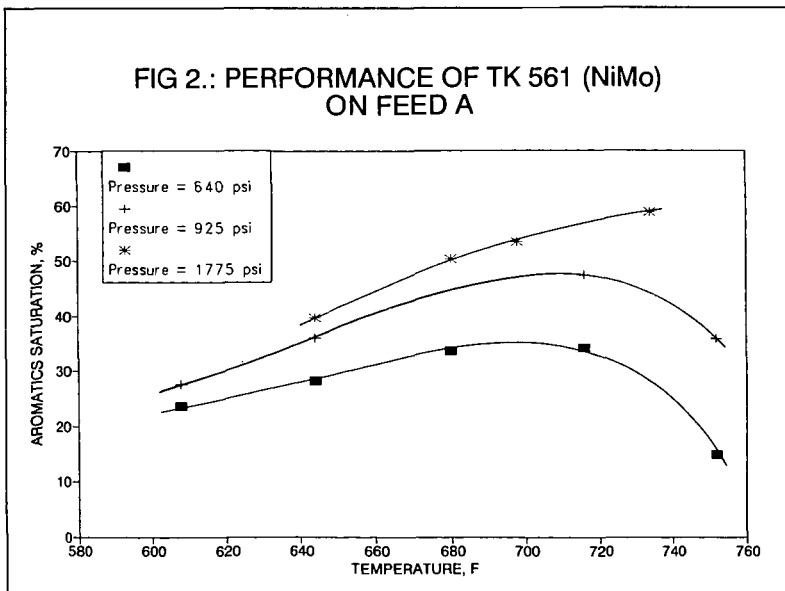
It was found that the degree of aromatics saturation increased with increase in reactor temperature up to a maximum level. The temperature at which the maximum conversion was obtained was a function of pressure and space velocity. Further increase in temperature resulted in a decrease in aromatics saturation. These results are illustrated in Fig. 2 in which the degree of aromatics saturation (as measured by ¹³C NMR) is plotted against temperature for three different pressure levels (LHSV held constant). The existence of a maximum conversion at a given pressure indicates a limitation imposed by thermodynamic equilibrium. This is supported by the HPLC aromatics analysis which shows that at high temperatures, the equilibrium between monoaromatic species and naphthenes is established. As seen in Figure 2, the maximum occurs at higher

temperatures as the pressure is increased, which is consistent with a shift in the equilibrium concentration.

A number of other catalysts were investigated over the same range of conditions, including CoMo and NiW (all on alumina) and TK 525, which is NiMo on a special carrier (the molar concentration of W and Mo is the same for the catalysts). Using only the data obtained at or below 633K (680°F) - below which temperature dehydrogenation reactions are negligible - and assuming first order kinetics, a comparison of the relative average activity of the catalysts was made (Table 2).

Catalyst Type	Relative Hydrogenation Activity
NiMo (TK 561)	100
NiW (TK 547)	90
CoMo	90
NiMo (TK 525)	125

TABLE 2: Traditional Hydrotreating Catalysts in Single-Stage Operation on Feed A.



It is seen that NiW gives lower activity than the NiMo catalysts in single-stage operation even though the difference in activity of the catalysts is not large.

The results show that when using these catalysts in single-stage operation it is necessary to operate at high pressures, which is in agreement with the conclusions of (10, 11).

2. NiMo/NiW Catalysts in Two-Stage Operation

Several workers (12, 13) have shown that H₂S inhibits aromatics saturation reactions. Our own studies indicated that the extent of inhibition depends on the catalyst system under investigation: NiW catalysts are more affected by H₂S than NiMo catalysts. This is illustrated by test runs on a pretreated HGO (Feed B, Table 1). This feedstock was obtained by hydrotreating a portion of Feed A using TK 561. Feed B contains about 10% of the sulfur and 70% of the aromatics in Feed A. Note, however, that the concentration of monoaromatics is about the same for the two feeds.

Using average first order rate constants, the performance of a NiW catalyst, TK 547, and TK 561 was compared. The results are shown in Table 3.

Catalyst Type	Relative Hydrogenation Activity	
	Feed A, S=1.7 wt%	Feed B, S=0.14 wt%
NiMo (TK 561)	100	100
NiW (TK 547)	90	225

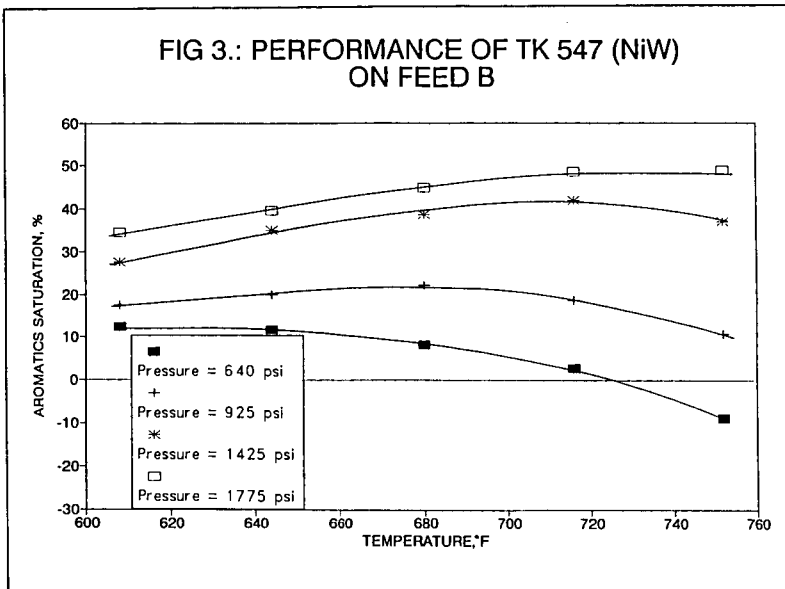
TABLE 3: Comparison of NiMo and NiW Catalyst Activity for Two Feed Sulfur Levels.

On Feed B, TK 547 is twice as active as TK 561. This opens up the possibility of a two-stage process with a NiMo-type catalyst in the first stage and NiW in the second with removal of H₂S between the stages.

The performance of TK 547 on Feed B at various temperatures and pressures is shown in Figure 3. Since there is a higher fraction of monoaromatics (the most refractive aromatic species) in Feed B, the overall levels of aromatics saturation are lower than those obtained with TK 561 on Feed A. It is seen that there is a maximum degree of saturation that can be achieved at a given pressure level and that the temperature at which the maximum occurs increases with increasing temperature.

It was found that it is possible to achieve higher levels of saturation at a given space velocity using NiMo + NiW in a two-stage process rather than NiMo in a single-stage process. However, high pressures or low space velocities are also needed with this catalyst system to obtain reasonable levels of aromatics reduction (see section entitled Comparison of Operating Conditions).

FIG 3.: PERFORMANCE OF TK 547 (NiW)
ON FEED B



3. Pt on Alumina in Two-Stage Operation

It is well known that catalysts based on Pt/Al₂O₃ exhibit excellent hydrogenation activity but are poisoned by quite small quantities of sulfur compounds in the feedstock (14). A severe pretreatment is therefore necessary to reduce the sulfur content to a level that does not affect the performance of the Pt/Al₂O₃ catalyst, which will normally mean reduction of sulfur content to below 2 ppm.

Feed C is a batch of Feed A that has been pretreated to give 1.5 ppm sulfur. The feed contains 20% aromatics which are almost all monoaromatics. A Pt/Al₂O₃ catalyst containing 0.6% Pt was tested on this feed at a variety of conditions. It was found that up to 60-70% reduction in aromatics content could be achieved at moderate conditions: pressure 4.5-6.0 MPa (650-870 psi); temperature 550-590K (530-600°F) and LHSV 0.75-1.5. However, as discussed later, the low space velocities that are required in the pretreatment stage to obtain sufficient reduction in sulfur content make this alternative economically unattractive for most applications.

4. Sulfur-Tolerant Noble Metal Catalyst in Two-Stage Operation

The sulfur tolerance of a noble metal can be increased e.g. by supporting it on zeolite as reported by (15, 16). It is therefore not necessary to pretreat so severely when using this type of catalyst. A process using TK 908, a noble-metal catalyst on a special carrier is described in (17). The sulfur tolerance of TK 908 is illustrated

by tests on two different feedstocks. The first test was made on Feed D which was obtained by hydrotreating a batch of Feed A. Feed D contains 300 ppm S and 21% aromatics (Table 1). Using this feed, 55% reduction in aromatics content (corresponding to 9% aromatics in the product) was achieved at 5.0 MPA (725 psi) and 600-620K (625-655°F)

The second feedstock Feed E (Table 1) is a hydrotreated diesel, the origin of which is a North Sea and Middle East LGO (Feed F, Table 1) The low end-point makes the cut suitable for class 1 Swedish diesel but the aromatics content needs to be reduced from 28%w to below 5%. Test results are shown in Figure 4 and it is seen that this goal can be achieved at a hydrogen pressure of 5.0 MPA (725 psi) and between 575-590K (580-600°F) depending on the H₂/oil recycle ratio.

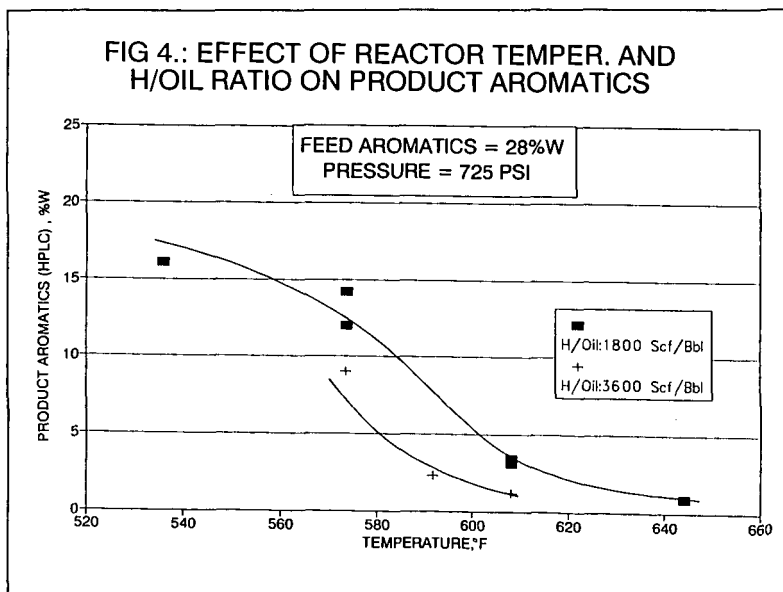
COMPARISON OF OPERATING CONDITIONS

Calculations have been made for each catalyst system to compare the relative reactor volumes needed to obtain a given product quality. The calculation basis was as follows:

Feedstock to first stage = Feed A (36%w aromatics).

Average reactor temperature = 625°F.

Product aromatics: for non-noble metal systems = 18%w, for noble metal systems = 10%w.



The results are presented in Table 4.

Catalyst System	NiMo	NiMo + NiW		CoMo+ Pt/Al ₂ O ₃	NiMo + TK 908	
No. of Stages	one	two		two	two	
Case	1	2	3	4	5	6
Feedstock	A	A	A	A	A	E
Aromatics in feed, %w	36	36	36	36	36	32.4
H ₂ pressure, psi	1450	1450	925	925	725	725
Average temp., °F	625	625	625	625	625	600
Aromatics in product, %w	18	18	18	10	10	5
Relative reactor volume NiMo=1.0	1.0	0.7	2.8	3.0	1.0	0.55

TABLE 4: Comparison of Operating Conditions.

The reactor volumes are relative to NiMo, single-stage operation = 1.0. In all other cases the relative reactor volume is for combined first and second stage. The size of the first-stage reactor is determined by the required level of sulfur in the feed to second stage.

It is seen that using NiMo + NiW in two stages results in a 30% reduction in reactor volume as compared with NiMo alone. This system is very sensitive to hydrogen pressure as is seen by comparing cases 2 and 3.

The use of a sulfur tolerant catalyst instead of a Pt/Al₂O₃ catalyst reduces the reactor volume by a factor of 3 (case 4 and 5) despite a lower operating pressure. It is also seen that the NiMo + TK 908 system results in 8% fewer aromatics in the product than NiMo alone at half the pressure and without increase in reactor volume. Furthermore, the feed used in this comparison has an unusually high sulfur content (1.7%w) and end boiling point (720°F). The NiMo + TK 908 system performs even better on lower sulfur feeds such as Feed E as seen in case 6.

Which of these systems should be used for a given service will depend on a large number of factors, but generally speaking, the NiMo + NiW system will be preferred at moderate levels of saturation, whilst for deep aromatics saturation the system employing the sulfur tolerant noble metal catalyst TK 908 will be preferred.

REFERENCES

- 1) Ullman, T.L., "Investigation of the Effects of Fuel Composition on Heavy-Duty Diesel Engine Emissions", SAE Paper 892072, International Fuels and Lubricants Meeting and Exposition, Baltimore, Maryland, September 26-28, 1989.
- 2) Miller, C., Weaver, C.S., and Johnson, W., "Diesel Fuel Quality Effects on Emissions, Durability and Performance", Final Report EPA Contract 68-01-65443, Sept. 30, 1985.
- 3) Crow, P. and Williams, B., "U.S. Refiners Facing Squeeze Under New Federal, State Air Quality Rules", Oil and Gas J., January 23, 1989, p. 15.
- 4) Parkinson, G., "Stricter Standards for California diesel Fuel", Chemical Engineering, January 1989, vol. 96, No. 1, p. 42.
- 5) Assim, M.Y. and Yoes, J.R., "Confronting New Challenges in Distillate Hydrotreating", AM-87-59, NPRA AM March 1987.
- 6) Johnson, A.D., "Study Shows Marginal Cetane Gains From Hydrotreating", Oil and Gas J., May 30, 1983, p. 79.
- 7) McCulloch, D.C., Edgar, M.D. and Pistorious, J.T., "High Severity Diesel Hydrotreating", AM-87-58, NPRA AM, March 1987.
- 8) Dhulesia, H., "New Correlations Predict FCC Feed Characterizing Parameters", Oil and Gas J., January 13, 1986, p. 51.
- 9) Somogyvari, A.F., Oballa, M.C. and Herrera, P.S., "Industrial Catalysts for Aromatics Reduction in Gas Oil", ACS Preprints, New York, August 1991, p. 1878.
- 10) Assim, M.Y., Keyworth, D.A., Zoller, J.R., Platenga, F.L. and Lee, S.L., AM-90-19, NPRA AM, March 1990.
- 11) Nash, R.M., Oil and Gas J., May 29, 1989, p. 47.
- 12) Le Page, J.F., "Applied Heterogeneous Catalysis", Technip, Paris (1987), p. 373.
- 13) Spare, A.V. and Gates, B.C., I.E.C. Process Des. Dev. 21 (1982) 86.
- 14) Barbier, J., Lamy-Pitara, Marecot, P., Boitiaux, J.P., Cosyns, J. and Verna, F., "Role of Sulfur in Catalytic Hydrogenation Reactions", Advances in Catalysis, 37 (1990) 279.
- 15) Gallezot, P., Catal. Rev. Sci. Eng. 20 (1979) 121.
- 16) Gallezot, P. and G. Bergeret in "Catalyst Deactivation" (E.E. Peterson and Bell, A.T., Eds), Dekker, New York (1987), p. 263.
- 17) Sogaard-Andersen, P., Cooper, B.H., Hannerup, P.N., "Topsøe's Process for Improving Diesel Quality", NPRA AM, New Orleans 1992.

**MOLECULAR MODEL OF REFORMING CHEMISTRY
AT REFORMULATED GASOLINE CONDITIONS.**

John H. Shinn
Chevron Research and Technology Company
Richmond, CA 94802

Keywords: Reforming, Gasoline, Benzene

ABSTRACT

The Clean Air Act Amendments of 1990 mandate a reduced benzene content and the incorporation of oxygenates in gasoline, and set emissions performance standards for gasoline sold in the nations worst ozone non-attainment areas. These constraints will result in significant changes in operating conditions used in commercial catalytic reformers. Reformer product octanes are expected to drop, throughputs will be reduced, and pressures (and concomitant recycle hydrogen rates) are expected to drop to allow reformers to maintain hydrogen production at reduced severity. These conditions represent a significant change from post-lead-phaseout operation in which product octanes were pushed and pressures were maintained at high levels to increase the run span of semi-regenerative reforming plants.

A pilot plant study was performed to examine the reaction network which exists in a reformer under post-reformulated gasoline operating conditions. Operations were performed at a range of severities using a paraffinic Arabian naphtha as feedstock. Detailed product analyses and careful material balancing allowed construction of a molecular picture of the reforming process at these conditions revealing the nature of yield losses, hydrogen production, and benzene production during the reforming process.

INTRODUCTION

Catalytic reforming is one of the key refinery processes involved in the production of gasoline worldwide. Reforming performs two major functions in the modern refinery: upgrading the octane value of low octane naphthas to make a high octane gasoline blending component; and providing hydrogen for hydrotreating and hydrocracking processes.

The two major reforming technologies used commercially vary by the manner in which the catalyst is regenerated; either periodically (referred to as Semi-Regenerative or semi-regen operation) or continuously (called Continuous Catalytic Reforming or CCR). For the semi-regen plants, the length of the operating cycles between regenerations is an important factor. Bimetallic reforming catalysts (platinum-rhenium on alumina being used most frequently) were developed to extend this cycle length.

Since reforming is a major source of gasoline components, reforming operations are impacted by regulations which constrain the composition of gasoline. As it became necessary to reduce the level of high-octane lead additives in gasoline during the 1970s and 1980s, reformers were required to produce products of higher octane value to compensate for this reduction. Reformers changed in response to these increased demands: improved catalyst systems were developed to allow semi-regen plants to operate with adequate cycle lengths at these more severe

conditions, and the CCR type operation became more cost-effective than it had been at moderate severities.

The Clean Air Act requirements will affect gasoline composition in a manner which is unprecedented in the history of gasoline manufacture. Unlike lead-phaseout, reformers will be likely to operate at lower product octane levels as a result of gasoline reformulation. This is because high-octane oxygenates (such as methyl-tertiary-butyl-ether, MTBE) will be required in areas where reformulated gasoline is produced. Reformulated gasolines must also meet a benzene limit of 1 wt% and must produce fewer hydrocarbon and benzene emissions, requirements which will indirectly limit the total amount of aromatics allowable in such fuels. At first glance, this would appear to make life easier for reformers. However, the reformers must also produce the hydrogen required in other refinery operations and to do so at lower throughputs and lower product octane levels will be a severe challenge. Most refiners are closely examining reducing both operating pressure and the rate of recycle hydrogen circulation to provide additional net hydrogen at the reduced severity conditions. The combined low octane, low throughput, low pressure, low recycle operation is atypical of commonly-practiced reformer operation and is correspondingly an area infrequently examined in reforming studies.

To provide information on the nature of reforming operations under these new conditions a reaction study was conducted. Pilot plant tests were performed using an Arabian Naphtha. The tests were performed using Chevron's commercial Rheniforming F catalyst at 100-150 psig, 1.5 liquid hourly space velocity, and a 2.5:1 molar hydrogen-to-hydrocarbon recycle gas ratio. A continuous reforming pilot plant was employed for the test which consisted of a 1" OD steel tube reactor charged with 80 cc of catalyst.

Samples of the debutanizer overhead ("low-gas") and high-pressure separator gas ("high-gas") were analyzed by packed-column chromatography and their flowrates were measured to provide the rates of C4- product generation. The debutanizer bottoms (C5+ liquid product) were analyzed by capillary column gas chromatography to determine liquid composition.

PRODUCT COMPOSITION AS A FUNCTION OF OCTANE

Figures 1 through 5 provide a schematic molecular view of product composition as a function of research octane number (RON). These figures illustrate the changes in molar composition by showing the number of moles of each molecule present per 10000 gms of original feed. For example, in Figure 1 we see that the in 10000 gms of the original feed are contained roughly 2 moles n-pentane, 3 moles n-hexane, 2 moles iso-hexanes, 1 mole benzene, etc. This feed has a measured RON of 42.9 and is comprised predominantly of C7 and C8 components (about 70 mole % of the feed). The feed is paraffin-rich as well (about 2/3 of the feed molecules) and aromatics-poor (16 mole% aromatics).

Upon conversion to 72.9 RON (Figure 2) a substantial number of the C7+ naphthenes have disappeared along with a roughly equivalent molar amount of paraffins. In contrast, C6 naphthenes are apparently untouched. For the most part, there is a rough agreement between the appearance of aromatics of a given carbon number and the disappearance

of paraffins and naphthenes of that carbon number. For the C7 and C8 molecules, a few more paraffins + naphthenes have disappeared than the number of aromatic molecules which have appeared. C5 and C6 paraffins have each increased by 1 mole per 10000 gm feed. In addition, a mole of benzene and a mole of C11 aromatic (dimethyl indan?) have appeared where no corresponding conversion of feed paraffin or naphthene seems to have occurred.

When product octane is raised to 83.5 RON (Figure 3), disappearance of C8+ paraffins is the dominant reaction. 75% of the C7 paraffins present in the feed still remain. Additional C5 and C6 paraffins are produced. The product is now 50 mole-% aromatics.

By 94.7 RON (Figure 4), virtually all of the C9+ paraffins and 80% of the C8 paraffin have been converted. Only about half of the C7 paraffins have been converted, however. Of the naphthenes, only the C6s remain. The largest gains in the aromatics are seen in the C8+. The liquid product is 62 mole % aromatics.

In raising product octane to 100 RON (see Figure 5), C7 paraffin conversion finally begins to accelerate significantly reaching a level of 75% conversion. The C6 naphthenes are finally converted. More C5 paraffins are generated and the first signs of disappearance of heavy aromatics is seen (destruction of a C10 aromatic). The product is over 70 mole % aromatic with the balance being entirely composed of C7-paraffins.

REACTION CHEMISTRY

By matching the appearance of various molecules with the disappearance of others as the reaction proceeds, one may predict the reaction network which is occurring as severity is increased.

In order to produce such a network, certain assumptions are necessary. The assumptions used herein are as follows:

- 1) 100% of the converted naphthenes produce an aromatic of the same carbon number.
- 2) The remainder of the aromatics produced for a given carbon number are derived from dehydrocyclization of a paraffin of the same carbon number.
- 3) Other imbalances in the number of aromatics of a given carbon number are caused by side-reactions of aromatics which result in changes in carbon number of the aromatics.
- 4) Converted paraffins above those needed to form aromatics contribute to light product formation.

Figure 6 provides the net reaction network which evolves from the application of these reaction rules to the changes in product composition provided above. In going from 43 to 73 RON (first column in Figure 6), both dehydrogenation and dehydrocyclization share in the production of aromatics and hydrogen (numerals in circles at the bottom right-hand corner of each section of the table indicate the total contribution to hydrogen production for given set of reactions - for instance at 73 RON, dehydrogenation contributes a total of 39 moles H₂

while dehydrocyclization contributes a total of 40 moles H₂). C₇ paraffin reactions are limited to isomerization and cracking (all of the toluene production is explainable from naphthene dehydrogenation). One molecule of C₈ paraffin is also left to produce gas while four C₈-paraffin molecules produce aromatics. There is an additional net aromatic reaction needed to explain the presence of benzene and a C₁₁ aromatic - this is assumed to occur through disproportionation (or transalkylation) of a C₈ and a C₉ aromatic to a C₁₁ plus a C₆ aromatic followed by a dehydrogenation of the monoaromatic C₁₁ to a diaromatic C₁₁.

Between 73 and 84 RON, dehydrocyclization of C₈ and C₉ paraffins is the primary source of aromatics and hydrogen. The t-butyl-benzene is converted and a diethyl-benzene appears in its place. Gases are produced from C₇ to C₁₀ paraffins.

Between 84 and 95 RON, dehydrocyclization continues with participation of C₇ paraffins in the reaction scheme. The gas production continues to pick up and most of the cracked paraffins must now experience multiple cracking events in order to explain the gas yields. Two additional reactions are needed to explain the redistribution of aromatics: the disappearance of a diethyl-benzene with the appearance of a naphthalene; and an additional benzene is produced which is matched with the disappearance of propyl-benzene.

Between 95 and 100 RON the cracking reactions take over. Some additional aromatics are generated from C₆ naphthene conversion and dehydrocyclization, but gas production takes a steep upturn and most of the converted molecules contribute to the cracking reactions. In order to explain the gas production, almost 90% of the cracked molecules must experience multiple cracking events. The hydrogen produced from the dehydrogenation and dehydrocyclization is consumed by the large number of cracking events.

BENZENE PRODUCTION

For reformulated gasoline production, it is of specific interest to understand the origin of benzene in reformate. The evidence above shows that substantial benzene is produced prior to any significant conversion of C₆ naphthenes. Figure 7 presents the conversion data on C₆ components versus octane for a range of conditions and catalysts tested on this feedstock (including data from various catalysts at pressures ranging from 100-200 psig, and recycle rates ranging from 2.5 to 3.5 molar H₂/HC, at 1.5 LHSV). This data confirms that under a broad range of conditions, benzene is produced from sources other than C₆ naphthenes or paraffins. It is true that benzene production does turn up considerably with the conversion of C₆ naphthenes above 90 RON, thus removal of these materials from the feedstock does have a significant impact on benzene production. However, it is also true there is considerable benzene produced without the contribution from C₆ precursors and even complete removal of C₆ components from the reformer feed may not totally eliminate benzene production.

Examination of the relationship between production of benzene and other aromatics shows that benzene production appears most closely correlated to toluene and naphthalene (see Figures 8 and 9). A possible interpretation is that benzene is produced from transalkylation reactions which increase the amount of aromatics with a low degree of

substitution (benzene, toluene and naphthalene) at the expense of those with a higher degree of substitution (poly-methyl-, or poly-methyl-alkyl- benzenes). The most likely sources of benzene from transalkylation would be aromatics with the largest side chains and/or highest degree of substitution.

CONCLUSIONS

The model illustrates the progression of reactions which occur in reforming of a paraffinic naphtha. The three major classes of reactions are naphthene dehydrogenation, paraffin dehydrocyclization, and paraffin cracking. As expected, naphthenes convert most readily generating aromatics primarily of the same carbon number. Hydrogen production from this conversion is about 75% complete by 73 RON and accounts for about half of the hydrogen produced at this severity. Additional aromatics and hydrogen are generated from the dehydrocyclization of paraffins. The selectivity of conversion of paraffins to aromatics increases with increasing carbon number - 20% for C7s, 60% for C8s, 85% for C9+. C7 paraffins convert slowly until higher severities and appear to be responsible for about 2/3 of the gas formed at 100 RON. Other reactions have a very minor role in explaining the distribution of products observed. Benzene production is observed to begin well before significant disappearance of C6 naphthenes occurs which implies that removing C6s from reformer feeds while substantially reducing benzene production will not totally eliminate it from reformer products.

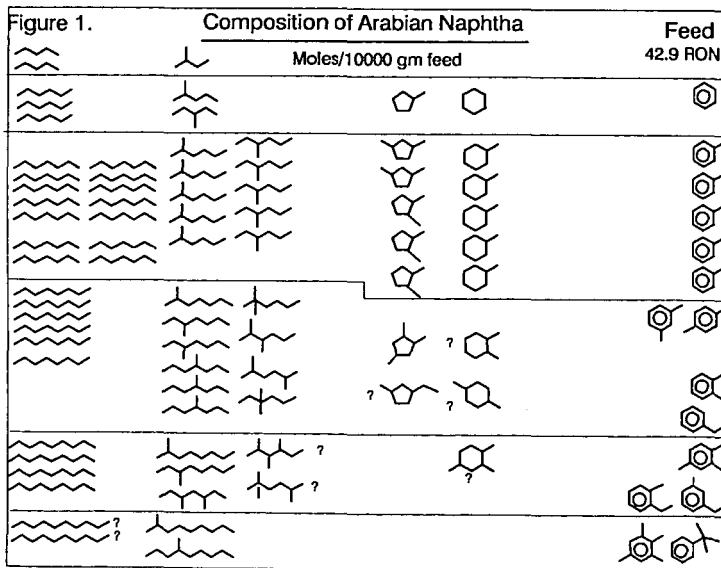
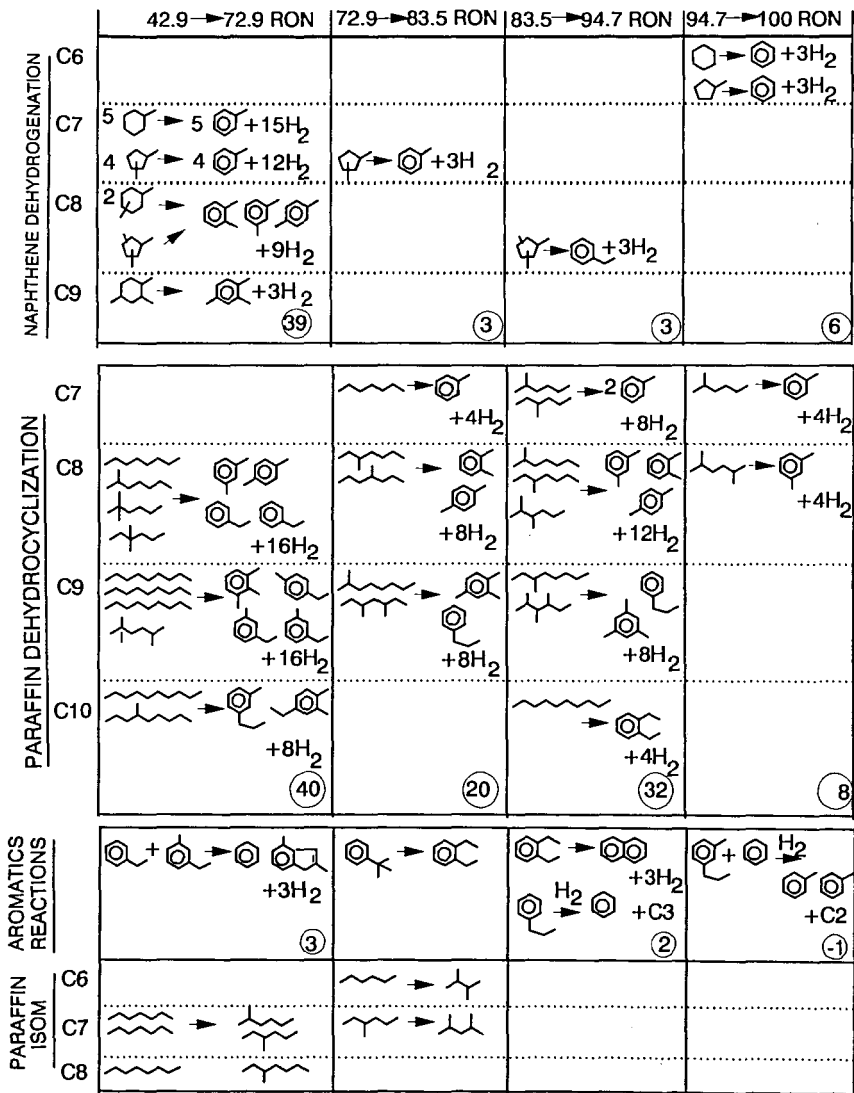


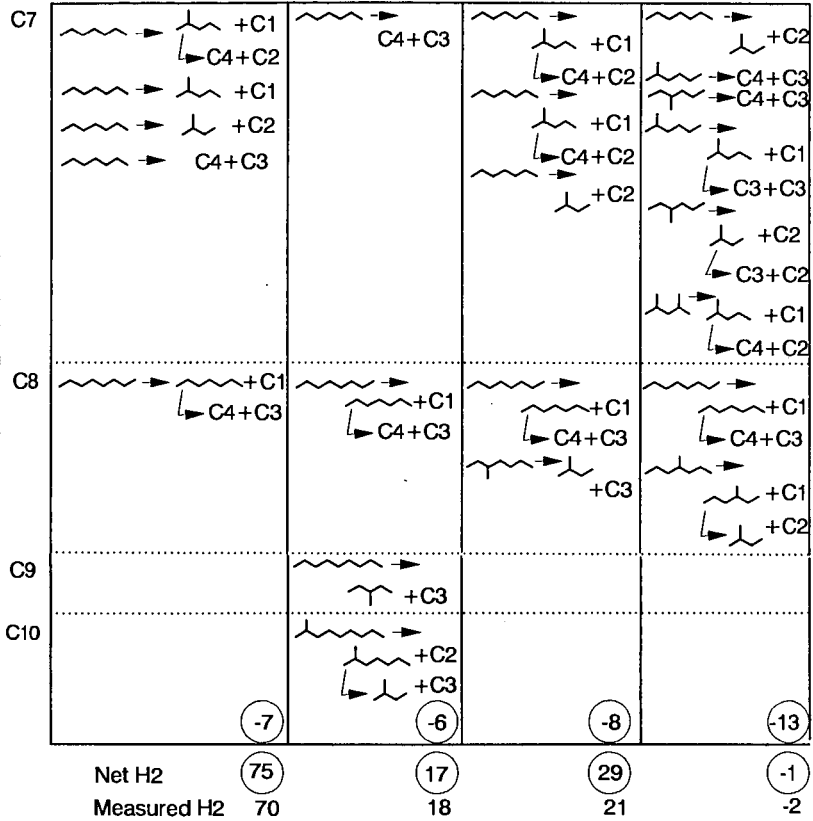
Figure 2.		Composition of 72.9 Octane Reformate				Product
		Moles/10000 gm feed				72.9 RON
70 H2	C1 C1	C2 C2	C3 C3	C4 C4	C4 C4	

Figure 3.		Composition of 83.5 Octane Reformate				Product
		Moles/10000 gm feed				83.5 RON
85 H2	C1 C1 C1	C2 C2 C2 C2	C3 C3 C3 C3 C3	C4 C4 C4 C4 C4	C4 C4	

Figure 6
Reforming Reactions as a Function of Severity



PARAFFIN CRACKING AND HYDROCRACKING



C4- Yields above are different from those actually produced as noted below (differences caused by C balance).

An extra C1 is shown.

A C3 should be a C2.

(In balance)

2 additional C1s needed.

Figure 7.
Conversion of C6 Components
Versus Reformate Octane

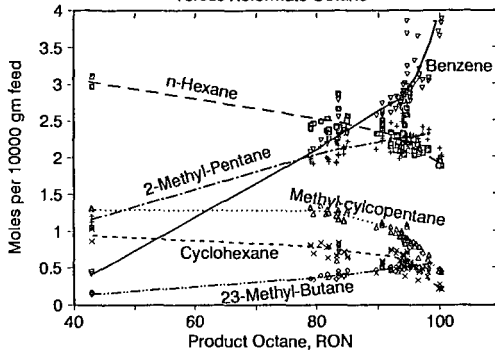


Figure 8.
Correlation Between Reformate
Benzene and Toluene Content

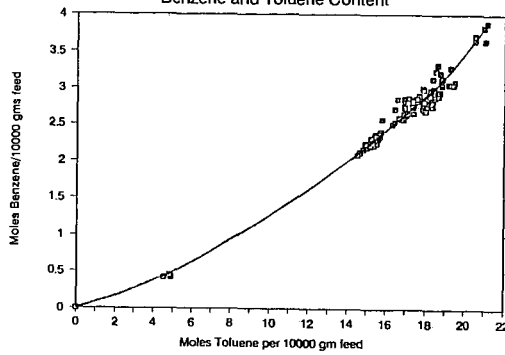
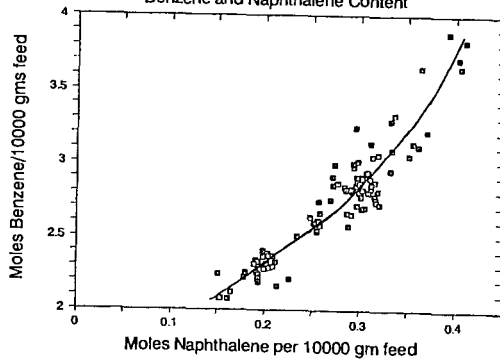


Figure 9.
Correlation Between Reformate
Benzene and Naphthalene Content



THE EFFICIENT USE OF NATURAL GAS IN TRANSPORTATION

Frank Stodolsky¹ and Danilo J. Santini
Argonne National Laboratory
9700 South Cass Avenue
Argonne, IL 60439

The submitted manuscript has been authored by a contractor of the U. S. Government under contract No. W-31-109-ENG-38. Accordingly, the U. S. Government retains a nonexclusive, royalty-free license to publish or reproduce the published form of this contribution, or allow others to do so, for U. S. Government purposes.

Keywords: Natural gas, Energy efficiency, Greenhouse gases

INTRODUCTION

Concerns over air quality and greenhouse gas emissions have prompted discussion as well as action on alternative fuels and energy efficiency. Natural gas and natural gas derived fuels and fuel additives are prime alternative fuel candidates for the transportation sector. The Clean Fuel Vehicle provisions of the Clean Air Act of 1990 (CAA) set the stage for "clean alternative fuels" from natural gas, such as compressed natural gas (CNG), liquefied natural gas (LNG), methanol, and liquefied petroleum gas (LPG). Methyl tertiary butyl ether (MTBE) is a popular gasoline additive used to lower Reid Vapor Pressure (RVP) to comply with the oxygenate requirements of the CAA. Currently, most MTBE capacity has been met by captive refinery plants using existing isobutylene streams and butanes from fluid catalytic cracking units in petroleum refineries (Unzelman 1991). However, there is growing evidence that additional capacity will be met by natural gas-derived butanes, as suggested by construction of new MTBE facilities at major gas fields (New Fuels Report 1990). Alkylate is another low RVP, high octane blending component which can be derived from natural gas-derived butanes.

It has been argued by C. Marchetti of the International Institute of Applied Systems Analysis and D. Santini of Argonne that natural gas will be the next dominant world fuel (Santini et al. 1989). During most of the 1980s rates of gas discoveries exceeded those of crude oil, as noted by Santini et al. (1989). If this prediction turns out to be true, natural gas will be the feedstock for much of transportation. This paper examines what the natural gas-based fuel might become.

APPROACH

In this study, we reexamine and add to past work on energy efficiency and greenhouse gas emissions of natural gas fuels for transportation (DeLuchi 1991, Santini et al. 1989, Ho and Renner 1990, Unnasch et al. 1989). We add to past work by looking at MTBE (from natural gas and butane component of natural gas), alkylate (from natural gas butanes), and gasoline from natural gas. We also reexamine CNG, LPG, LNG, and methanol based on our analysis of vehicle efficiency potential. We compare the results against nonoxygenated gasoline.

¹ 370 L'Enfant Promenade, S.W., Suite 201A, Washington, D.C. 20024

We obtained from the literature estimates of extraction, refining, and distribution efficiency for CNG, LNG, LPG, methanol, and baseline gasoline. We obtained an average efficiency of the natural gas-to-gasoline pathway for the Shell Middle Distillate Synthesis (SMDS) process (van der Burgt et al. 1989). From discussions with and information from refinery equipment manufacturers, we constructed a hypothetical natural gas-to-MTBE pathway (Wilcher 1991). Similarly, we constructed a hypothetical natural gas butane-to-alkylate pathway (Wilcher 1991). For the MTBE and alkylate pathways, we considered the path of a "parcel" of original natural gas taken from extraction at the well to blending with crude oil-derived gasoline and finally to combustion in a vehicle. The combustion of both MTBE and alkylate would occur at that efficiency obtained by the vehicle burning the mixture of gasoline and the natural gas-derived component. For pathways that do not utilize the entire natural gas stream, such as the LPG (using propane and butane only) and alkylate pathway (using butane only), we assume the balance of the natural gas components (mainly methane) would more than likely be converted at higher efficiencies compared to internal combustion engine vehicles if used in industrial/commercial/residential space heating or industrial cogeneration applications. Therefore, we did not investigate the pathway of these other components.

We considered passenger cars only. Two vehicle cases were considered: (1) constant performance acceleration vehicles; and (2) constant range vehicles (defined below). Finally, we compare the overall ("feedstock to tailpipe") efficiency of each natural gas fuel with baseline gasoline.

For each pathway, we estimated emissions and the warming effects of carbon dioxide (CO_2), methane (CH_4), and nitrous oxide (N_2O), three major greenhouse gases. We used the preliminary warming indices for CH_4 and N_2O at the 20 year and 100 year time horizons developed in 1990 by the Intergovernmental Panel on Climate Change (IPCC) (Renner and Santini 1991). For CH_4 , we used a 20-year warming index of 63, and a 100-year warming index of 21. For N_2O , we used a 20-year warming index of 270, and a 100-year warming index of 290. We did not consider warming effects beyond 100 years. Renner and Santini (1991) observed that a very large percentage of the cumulative warming effects due to CH_4 emissions occur in the first few decades. Renner and Santini also estimated that the discounting of economic damage over time implies the warming effects beyond a century has very little influence on average warming effects.

There are some differences between this analysis and the others mentioned above that are worth noting. Unnasch et al. 1989 argues that natural gas fuels could be produced from natural gas currently being flared, and this would greatly reduce greenhouse gas emissions. His study shows CNG and methanol from currently wasted gas is superior in reducing greenhouse gas emissions over crude oil-derived gasoline. Santini et al. (1989) supports Unnasch's findings in part by suggesting that for the short-term, using currently vented and flared natural gas for reinjection or transportation far outweighs global warming reduction opportunities available through substitution of one natural-gas-based fuel for another. However, they estimate that the elimination of

flaring and venting could only substitute for a small percentage of potential alternative fuel energy needs. As reported by Ho and Renner (1990), worldwide gas being flared has been reduced by 70% since 1978, and what remains is unlikely to be a major feedstock source due to geographic and economic hurdles. Because this analysis focuses on longer term (year 2010 and beyond) applications for natural gas based fuels, we assumed venting and flaring of natural gas and crude oil production occurs as calculated by Ho and Renner (1990). However, for comparison, we also show the impact of eliminating all venting and flaring for each pathway.

We did not consider emissions attributable to vehicle manufacture. Differences in these emissions are negligible when considering the fuels investigated here.

We did not look at the effects of additional criteria pollutants (NO_x , CO, and nonmethane hydrocarbons). For example, we did not examine NO_x emissions resulting from high compression ratios. We assumed that each dedicated vehicle was designed to meet the same emission standards for criteria pollutants so these emissions would not cause differences among the fuels examined. We did not consider the potential benefits of lower sulfur and nitrogen from natural gas derived gasoline (van der Burgt et al. 1989). Nor did we consider the economics and fuel distribution logistics. Consideration of geographical distribution of natural gas and crude oil resources and associated economics could significantly alter the conclusions reached in this study. Fuel shipping distances can have an important effect, especially when remote feedstock locations compete with domestic supplies.

Fuel Process

Generalized MTBE, alkylate, and natural gas-derived gasoline process flows are illustrated in Figure 1. Table 1 shows the energy efficiency for feedstock to fuel, vehicle efficiency, and overall (fuel and vehicle) efficiency. Energy efficiency of transforming feedstock to fuel (feedstock production and transport, preparation, conversion/refining, and fuel transport and distribution) is shown in the top section of Table 1. Process details and assumptions for CNG, LPG, methanol, and gasoline extraction and production are described in detail in Ho and Renner (1990) and DeLuchi (1991). For simplicity, we used the average of the Ho and Renner conversion/refining estimates for advanced and base technologies.

We assume MTBE is made from natural gas butanes and natural-gas-derived methanol. First, field butanes with an assumed composition of 70% n-butane and 30% isobutane is isomerized to yield 95% isobutane. An energy efficiency of 86% (product energy divided by the sum of feedstock energy and process energy) was calculated by the authors based on generic process efficiencies and yields obtained from UOP for their Butamer process (Wilcher 1991). The isobutane is dehydrogenated to isobutylene assuming generic process efficiencies and yields of the UOP Oleflex process (Hydrocarbon Processing 1991). The energy efficiency of natural gas to methanol via steam reforming to produce synthesis gas (syngas) and subsequent methanol synthesis is assumed to be 70% based on the average conversion/refining data presented in Ho and Renner (1990). The energy efficiency of the MTBE plant, utilizing the isobutylene and

methanol feedstocks, was estimated to be 93%, based on generic process efficiencies and yields of the UOP Ethermax process (Wilcher 1991). Approximately 80% (vol) isobutylene and 34% (vol) methanol yields 100% (vol) MTBE, which results in a calculated process energy efficiency of 76% (excluding natural gas production and transport, and fuel product transport and distribution efficiencies). We assume the MTBE is mixed with baseline gasoline and combusted with the same efficiency as the baseline gasoline (minor improvements would actually be expected). Within practical limits, it is not necessary to know the ratio of MTBE (or other natural gas derived additives such as butane alkylate) to gasoline since we are following a "parcel" of natural gas which "sees" the thermal efficiency achieved by the engine when burning the reformulated gasoline.

We assume natural gas butanes are isomerized and are fed into a hydrofluoric acid (HF) alkylation plant having an energy efficiency of 86% to make alkylate. We assume the HF alkylation plant has the same efficiency as when it is receiving raffinate from the MTBE plant described by Wilcher (1991). An overall energy efficiency of 78% (excluding natural gas production and transport, and fuel product transport and distribution efficiencies) for alkylate production is estimated.

For natural gas to gasoline, an efficiency of 63% was used, typical for the SMDS process (van der Burgt 1989). Efficiency is highly dependent on the mix of gasoil, kerosene, and naphtha desired. Additional process study is required to determine the effects of product slate on energy efficiency.

To estimate greenhouse gas emissions, the average of base and advanced technology data presented by Ho and Renner (1990) was used for baseline gasoline, CNG, LPG, and methanol. For the LNG pathway, it was assumed that CO₂, CH₄ and N₂O emissions when in the form of CNG were identical to the CNG pathway. The LNG pathway emissions were increased by using the ratio of CNG conversion efficiency to that of LNG.

For MTBE, alkylate, and gasoline from natural gas, we assume feedstock CO₂, CH₄, and N₂O emission rates (per million btu of fuel) are those given by Ho and Renner (1990) for domestic natural gas production and transport. CO₂ and N₂O emissions for the preparation and conversion stage were adjusted according to the energy efficiency ratio between the baseline gasoline and the natural gas process. Transportation emissions for the natural gas products are those used for baseline gasoline. As mentioned, the portion attributable to venting and flaring estimates are presented separately.

Vehicle

We assume each vehicle alternative is optimized to run on one fuel, i.e., there are no efficiency penalties typical of flexible-fueled vehicle operation. The baseline vehicle is assumed to be the hypothetical, maximum technology model year 2001 Ford Taurus as described by the Office of Technology Assessment (U.S. Congress 1991), weighing 2810 lbs and achieving a fuel consumption of 35.3 miles per gallon. Engine-only performance

estimates for all fuels are shown in Table 2. Vehicle assumptions and efficiency estimates are shown in the lower section of Table 1. Compression ratios were estimated by multiplying the baseline vehicle compression ratio by the ratio between dedicated CNG and methanol fueled engine compression ratios and conventional engine compression ratios presented in Santini et al. (1989). The compression ratio for LPG was obtained in the same manner using data from the National Propane Gas Association (undated). It was assumed that the compression ratio is not changed for engines running on reformulated fuels (MTBE and alkylate) and gasoline from natural gas. Actually, a slight increase in compression ratio is expected with higher octane alternatives, but our assumption does not materially affect the results. Air standard thermal efficiencies were then calculated, and adjusted for changes in volumetric efficiency for the gaseous fuels. For fuel containing MTBE and alkylate, we assumed a 2% increase in thermal efficiency based on mileage improvement data (DeLuchi 1991). We assumed that gasoline from natural gas is the same as that of the nonoxygenated, baseline gasoline. Efficiency of the methanol engine was adjusted because the high latent heat of vaporization cools the intake charge which increases volumetric efficiency. Finally, adjustments were made to account for the differences in mean effective pressure.

For the constant performance case, we assumed: (1) constant acceleration (i.e., all vehicles have the same power-to-vehicle-weight ratio); (2) constant fuel volume; and (3) the same platform design (no increase or decrease in passenger space and cargo volume). We assume the engine displacement (measured as the swept volume by the piston) is adjusted to keep the power-to-vehicle weight constant. The results include an adjustment for the weight of the tank, fuel, and engine. This case assumes acceleration characteristics are important and that consumers will not trade down for poorer performing vehicles, especially if they cost more. Positioning the Impact electric vehicle as a performance commuter car by General Motors, for example, accounts for particular attributes of electric vehicles (Amann 1990). Instead of designing for long-range travel (batteries replacing cargo volume), GM engineers focused on developing a lightweight vehicle with a relatively low vehicle weight-to-power ratio of 19.3. Due to large tank weights and volume, CNG vehicles are similarly penalized if designed for conventional range. Like the Impact, CNG vehicles could meet consumer expectations for acceleration while meeting typical daily commuting ranges and cargo volumes if designed accordingly. The social cost of frequent refueling (time and convenience considerations) and refueling emissions were not assessed.

The constant range case assumes range is more important than acceleration characteristics and cargo volume or passenger space. For this case, we assumed (1) all vehicles are capable of traveling 350 miles between refueling; (2) engine displacement is constant; and (3) the same platform design (i.e., to allow for larger tanks, passenger space and/or cargo volume will decrease). We assume the engine displacement is kept constant. The results include an adjustment for the weight of the tank and fuel.

Greenhouse gas emissions attributable to the vehicle were estimated using Ho and Renner (1990) assumptions. We adjusted CO₂ g/mi emissions in proportion to vehicle energy efficiency. We assumed CH₄ emissions for CNG and LNG vehicles are

controlled to a 1.5 g/mi level. We assumed vehicles running on the other fuels emit 0.08 g/mi of CH_4 . We assumed all vehicles emit 0.1 g/mi of N_2O .

RESULTS AND DISCUSSION

Fuel Processing Energy Efficiency

The top portion of Table 1 summarizes fuel processing energy efficiency. Based on our assumptions, production of gasoline is more efficient than natural gas fuel production for transportation, which is the conclusion also reached by Ho and Renner (1990). Because additional processing is needed, oxygenation and alkylation of the baseline gasoline should decrease energy efficiency. Our estimates support this hypothesis. Our estimates also suggest that conversion and refining of alkylate is slightly more efficient than MTBE conversion and refining, assuming natural gas is used as a feedstock. Although we calculate higher efficiencies for the MTBE plant over the HF alkylation plant, the syngas step required to produce methanol feedstock for MTBE reduces overall energy efficiency below that of the overall alkylation process. The volume of feedstock requiring isomerization greatly affects the calculation of efficiency of alkylate production. For example, for high iso- to n-butane ratios typically found in petroleum refinery catalytic cracking units, alkylate production efficiencies of up to 86% (for a volume ratio of 3:1) are predicted, compared to 78% theoretically obtained from natural gas feedstock containing 30% (vol) iso- and 70% (vol) n-butane.

Overall energy efficiency of LPG is estimated to be higher than that of CNG because of higher fuel transport and distribution efficiency. Overall energy efficiency of CNG is estimated to be higher than that of LNG primarily because less energy is required for compression. Methanol's overall energy efficiency is lower than LPG, CNG, and LNG because the syngas process is relatively energy intensive, even after accounting for the highly exothermic methanol synthesis step. The gasoline from natural gas process is estimated to have the lowest conversion/refining energy efficiency (and hence the lowest overall energy efficiency) because, like methanol, syngas is produced in an intermediate step, and implied by our assumptions, less heat is liberated by the Fischer-Tropsch reaction than in the methanol synthesis reaction. Further analysis is required to determine actual component efficiencies of the natural gas-to-gasoline pathway.

Vehicle Efficiency

Table 1 summarizes the results of the constant performance and constant range vehicle cases. Both cases yield the same relative ranking in terms of vehicle energy efficiency relative to baseline gasoline except for CNG. Similar to the findings of other researchers, CNG vehicles face the greatest penalty when compared on a constant range basis (DeLuchi 1991, Ho and Renner 1990, Santini et al. 1989). Our results suggest that CNG vehicle performance (acceleration) and utility (passenger space and cargo volume) is comparable to a gasoline-fueled vehicle if the range between refueling is shortened to about 85 miles. The engine displacement could be downsized by 2%, while vehicle weight could be reduced slightly. Energy efficiency would be 6% higher. For short-range commuting of under 20 miles-per-round-trip, refueling would occur about once per workweek. Assuming the CNG vehicle is designed for a 350 mile range, vehicle weight increases by about 190 pounds, and no improvement is seen in energy efficiency

compared to a conventional vehicle. The LNG vehicle is also penalized if compared on a constant range basis, but still maintains improved performance over the baseline gasoline vehicle.

The methanol-fueled vehicle is estimated to have the highest energy efficiency, 14% higher than the baseline vehicle for the constant acceleration case, and 12% higher for the constant range case. For the same acceleration as a gasoline-fueled vehicle, the methanol engine can be downsized by 8% (or about 0.16 liter [L]). Since methanol contains less energy per gallon than gasoline, the range of the methanol vehicle is estimated to be about 62% of the gasoline vehicle. Efficiency of the LPG vehicle is slightly greater than CNG and LNG for the constant performance case, but is much better than these fuels for the constant range case since LPG has a greater energy density than CNG or LNG.

Process and Vehicle Efficiency

The lower portion of Table 1 shows the combined process and vehicle efficiency of each natural gas fuel relative to gasoline for the constant performance and constant range vehicle cases. Results suggest that the LPG pathway is superior over the others for both cases, with an overall efficiency improvement of 5% over the baseline gasoline pathway. The highest overall efficiency is calculated for LPG because of its high fuel transport and distribution efficiencies relative to CNG and LNG. Fuel transport and distribution energy is based on the relative energy content of each fuel, and LPG has greater energy density than either. Compression energy is accounted for under distribution energy in the table. Compression energy requirements for LPG is lower than CNG or change of state (gas to liquid) requirements and state maintenance requirements for LNG.

CNG processing energy efficiency is lower than baseline gasoline processing energy efficiency offsetting by an equal amount the gain in efficiency from designing the CNG vehicle for constant performance and short range. The constant range design assumption for CNG vehicles severely penalizes efficiency, also noted in other studies (Santini et al. 1989). For LNG, we assumed domestic sources, and therefore do not include LNG boil-off during shipment and regassification.

The overall energy efficiency of the alkylate pathway is estimated to be approximately the same as the MTBE pathway energy efficiency. The overall energy efficiency of the baseline gasoline pathway is greater than for either additive. For MTBE, this is expected because the steam reforming process used to produce the methanol feedstock is relatively energy intensive. For alkylate, the combined isomerization, dehydrogenation, and alkylation conversion of butanes in natural gas are less efficient than baseline gasoline production from crude oil.

Methanol is combusted in the vehicle with high efficiency compared to the baseline gasoline vehicle. However, our results suggest that the overall efficiency is lower than all pathways except for gasoline from natural gas because of the syngas step.

Based on our assumptions, the least energy efficient pathway for domestic natural gas is the production of gasoline. Overall energy efficiency is 32% below that of baseline gasoline, primarily as a result of the low efficiency assumed for the conversion/refining step.

Greenhouse Gas Emissions, Expressed in CO₂ Equivalents, Constant Performance Case

Figures 2 and 3 summarize the greenhouse gas emission estimates using the 20 year IPCC warming indices for CH₄ and N₂O, assuming the constant performance vehicle case. The IPCC warming indices present the estimated warming effect of a unit of mass of CH₄ or N₂O relative to that from a unit of mass of CO₂, integrated over the time period of interest. Applying the warming factor to CH₄ or N₂O converts it to "CO₂ equivalent" units. Figures 4 and 5 show the same results using the 100 year warming indices. (CH₄ and N₂O emission rates discussed below are expressed in term of CO₂ equivalent.) The CH₄ increment shown is the amount estimated from venting and flaring from natural gas and crude oil production. The results for the constant range vehicle case (not shown here) show that the greatest increase in emissions would be for CNG and could change CNG's position in the 100-year case. No change in relative ranking of greenhouse gas emissions from other fuels are predicted for the constant range case. Results from using the 20 year indices for the constant performance vehicle case are discussed immediately below, followed by comparative discussion of the results using 100 year indices.

CNG and LNG are estimated to produce the most greenhouse gas emissions when 20 year indices are used, primarily because of the high CH₄ emissions (Figure 2). Including CH₄ emissions associated with venting and flaring at natural gas fields, emissions are about 26% higher than baseline gasoline, which, aside from LPG, produces the least amount of greenhouse gas emissions per mile. Assuming all methane is utilized at the natural gas field (eliminating the "CH₄ increment" illustrated in the figure), greenhouse gas emissions are still 12% higher than baseline gasoline because of the high assumed tailpipe CH₄ emissions. Figure 3 shows that CNG and LNG estimates are greatly affected by the assumed CH₄ and N₂O emissions and venting/flaring increment. Although we estimate that the overall CNG energy efficiency is greater than overall LNG energy efficiency, emissions are approximately the same for both fuels because we assume most emissions are actually a result of fuel transportation and not from processing. We assume LNG has the same fuel transportation efficiency as CNG (DeLuchi 1991), both being moved within the domestic natural gas transmission system. We assume conversion to LNG close to final distribution/sales, consistent with our domestic production assumption.

Our findings show LPG emits the lowest level of greenhouse gas emissions because of high vehicle efficiency combined and low emissions of CH₄ from fuel processing and tailpipe emission assumptions. LPG emissions are about 3% lower than baseline gasoline emissions including the CH₄ increment, and about 22% lower when compared against CNG or LNG. Excluding the CH₄ increment, LPG emits 13% less greenhouse gas emissions than baseline gasoline. Greenhouse gas emissions from alkylate are higher than baseline gasoline. Alkylate greenhouse gas emissions are

comparable to MTBE greenhouse gas emissions. Methanol produces lower greenhouse gas emissions than alkylate and MTBE because methanol vehicle efficiency is high. However, methanol fuel production emissions (on a CO₂ gram-per-btu fuel basis) are almost 10% higher. Greenhouse gas emissions from gasoline produced from natural gas are lower than CNG or LNG because gasoline tailpipe CH₄ emissions are assumed to be very low. However, greenhouse gas emissions from natural gas-based gasoline are higher than alkylate or MTBE greenhouse gas emissions because of higher CO₂ emissions.

The 100 year indices assume a lower warming potential for CH₄ emissions. As shown in Figures 4 and 5, LPG produces less greenhouse gas emissions than baseline gasoline, and CNG and LNG perhaps slightly less. If CH₄ emissions from venting and flaring are excluded, methanol also produces less greenhouse gases. The efficiency of the methanol vehicle counteracts the relatively low efficiency of the syngas process, resulting a small (2%) net decrease in greenhouse gas emissions, excluding venting and flaring emissions. Greenhouse gas emissions from MTBE and alkylate are about the same, and higher than baseline gasoline because of lower fuel processing efficiency. Natural gas-based gasoline produces the most greenhouse gases because of low fuel processing efficiency.

CONCLUSIONS

Our findings suggest that over the long-term (a century), dedicated use of LPG, CNG, LNG and methanol in transportation can lower overall greenhouse gas emissions compared with the use of gasolines with MTBE or alkylate. A CNG vehicle designed for shorter range but with adequate acceleration would improve overall energy efficiency and decrease greenhouse gas emissions over a vehicle designed to compete with gasoline on a range basis. In the short-term (20 years), CNG and LNG are estimated to cause more warming, especially if we assume venting and flaring will occur. If CNG and LNG are to realize greenhouse gas reductions both in the short- and long-term, very strict regulation of emissions from the tailpipe would be necessary. Use of LPG is the most energy efficient pathway, according to our estimates. However, since LPG is a relatively small component of natural gas compared with methane, there may be supply constraints by the year 2010. The efficiency of the baseline gasoline pathway is high. On a short term basis, baseline gasoline pathway greenhouse gas emissions are low. While the use of oxygenates such as MTBE may reduce tailpipe emissions, no clear benefits exist from an energy efficiency and greenhouse gas perspective over the use of alkylate as a high octane, low RVP additive. Methanol is the most desirable from a vehicle efficiency perspective. However, the syngas to methanol production step significantly reduces overall energy efficiency. Improvements in the syngas step will benefit efficiencies of producing methanol, MTBE (methanol feedstock) and natural gas-derived gasoline. Production of gasoline from natural gas is the least energy efficient pathway, according to our estimates, and results in the highest greenhouse gas emissions over the long-term. Our findings are greatly affected by assumptions of the global warming effect of CH₄, emissions rates of CH₄ from the tailpipe and from venting associated with gas extraction, and vehicle efficiency. Our findings are also affected by fuel transportation energy assumptions. Fuel conversion/refining efficiency assumptions affects results to a lesser degree.

ACKNOWLEDGMENTS

This work was supported by the U.S. Department of Energy, Office of Environmental Analysis, Deputy Under Secretary for Policy, Planning and Analysis, under contract W-31-109-Eng-38.

REFERENCES

- Amann 1990. The Passenger Car and the Greenhouse Effect, Society of Automotive Engineers technical paper 902099.
- DeLuchi 1991. (Center for Energy and Environmental Studies, Princeton University) Unpublished information.
- Ho and Renner 1990. Global Warming Impact of Gasoline vs. Alternative Transportation Fuels, SAE paper 901489.
- Hydrocarbon Processing 1991. Petrochemical Handbook '91 (March).
- National Propane Gas Association (undated). Fact Sheet, Using LP-Gas as an Alternative Fuel.
- New Fuels Report 1990. Increased World MTBE Output May Cut Butane for U.S., Hamper Domestic MTBE. October 8.
- Renner and Santini 1991. Issues in the Estimation of Global Warming Effects of Natural-Gas-Based Passenger Car Fuels, presentation at SAE Government/Industry Meeting, Washington, D.C., May 15-17 (contact principal author for information).
- Santini et al. 1989. Greenhouse Gas Emissions from Selected Alternative Transportation Fuels Market Niches, Argonne National Laboratory, Center for Transportation Research, (August 20-23).
- U.S. Congress 1991. Improving Automobile Fuel Economy: New Standards, New Approaches, Office of Technology Assessment report OTA-E-504 (Washington, DC: U.S. Government Printing Office, October).
- U.S. Department of Energy 1992. Limiting Net Greenhouse Gas Emissions in the United States: Vol. I, Energy Technologies, U.S. Department of Energy, Office of Policy, Planning and Analysis (in press).
- Unnasch et al. 1989. Comparing the Impacts of Different Transportation Fuels on The Greenhouse Effect, California Energy Commission Report P500-89-001 (April).
- Unzelman 1991. U.S. Clean Air Act Expands Role for Oxygenates, 89 (15) Oil & Gas Journal, 44-48.
- van der Burgt et al. 1989. "The Shell Middle Distillate Synthesis Process," updated paper originally presented in Syntfuels Worldwide Symposium, Washington, D.C. (November).
- Wilcher 1991. Personal communication. (Marketing Engineer, Petrochemical Processes, UOP, Des Plaines, Ill.) (October).

Table 1. Feedstock-to-fuel efficiency, vehicle parameters and efficiency, and fuel cycle efficiency of natural gas fuel pathways.

FEEDSTOCK-TO-FUEL EFFICIENCY	CNG a	LNG b	LPG a	MEOH a	MTBE c	GASOLINE FROM NG e	ALKYLATE c	BASE a
Feedstock Production	0.96	0.96	0.96	0.96	0.96	0.96	0.96	0.97
Feedstock Transport	1.00	1.00	1.00	1.00	1.00	1.00	1.00	0.98
Preparation	0.97	0.85	0.89	0.97	0.97	0.97	0.97	0.91
Conversion/Refining	1.00	1.00	1.00	0.70	0.76 d	0.63 f	0.78 d	1.00
Fuel Transport	0.95	0.95	0.97	0.95	0.98	0.98	0.98	0.98
Fuel Distribution	0.89	0.89	0.99	0.98	0.98	0.99	0.99	0.99
Feedstock-to-fuel efficiency	0.78	0.68	0.82	0.60	0.68	0.57	0.70	0.83
VEHICLE PARAMETERS								
CONSTANT PERFORMANCE VEHICLE g	CNG	LNG	LPG	MEOH	MTBE	GASOLINE FROM NG	ALKYLATE c	BASE
Engine displacement, fraction of baseline	0.98	0.97	0.94	0.92	1.00	1.00	1.00	1.00
Fuel+tank weight increment over baseline	-25	-45	11	0	0	0	0	0
Range (mi)	85	111	289	213	350	350	350	350
Vehicle weight (lbs)	2783	2761	2814	2799	2810	2810	2810	2810
Vehicle efficiency (Btu/mi) h	3102	3083	3079	2890	3233	3281	3233	3281
Vehicle efficiency relative to baseline	1.06	1.06	1.07	1.14	1.01	1.00	1.01	1.00
CONSTANT RANGE VEHICLE i								
Engine displacement, fraction of baseline	1.00	1.00	1.00	1.00	1.00	1.00	1.00	1.00
Fuel+tank weight increment over baseline	189	50	37	55	0	0	0	0
Range (mi)	350	350	350	350	350	350	350	350
Vehicle weight (lbs)	2999	2860	2847	2865	2810	2810	2810	2810
Vehicle efficiency (Btu/mi) h	3302	3172	3102	2937	3233	3281	3233	3281
Vehicle efficiency relative to baseline	1.00	1.03	1.06	1.12	1.01	1.00	1.01	1.00
FUEL CYCLE EFFICIENCY (FUEL AND VEHICLE)								
RELATIVE TO BASELINE								
CONSTANT PERFORMANCE VEHICLE	1.00	0.88	1.05	0.83	0.83	0.68	0.86	1.00
FUEL CYCLE EFFICIENCY (FUEL AND VEHICLE)								
RELATIVE TO BASELINE								
CONSTANT RANGE VEHICLE	0.95	0.86	1.05	0.82	0.83	0.68	0.86	1.00
NOTES:								
a Average of base and advanced technology from Ho and Renner (1990).								
b Ho and Renner (1990) values for CNG used except for preparation (liquefaction) efficiency. Liquefaction efficiency of 83.19% estimated by Deluchi (1991) was used.								
c Ho and Renner (1990) feedstock data for natural gas; Fuel transport data for baseline gasoline; Conversion and refining efficiency based on process information by Wilcher (1991).								
d Assumes butanes obtained from natural gas field.								
e Efficiency of gasoline/diesel fuel mix from natural gas. Gasoline fuel transport and distribution efficiency is assumed.								
f Average efficiency of Shell two stage synthesis process., from van der Burgt et al. (1989).								
g Constant power-to-vehicle weight ratio and platform size (constant passenger space volume and tank volume). Engine is downsized to keep power constant.								
h Assumes a 0.23% increase in fuel consumption per 1% increase in power to vehicle weight ratio (Santini et al. 1989). Assumes a 0.64% increase in fuel consumption per 1% increase in vehicle weight (U.S. Department of Energy 1992).								
i Constant range. Constant platform size, but tank volume varies at expense of cargo space. Constant engine displacement (power-to-vehicle weight varies).								

Table 2. Engine Assumptions

Parameter	CNG	LNG	LPG	MeOH	MTBE	GASOLINE FROM N.G.	ALKY.	BASE b
Compression ratio a	14.55	14.55	15.02	12.50	10.00	10.00	10.00	10.00
Unadjusted thermal efficiency	1.07	1.07	1.08	1.09	1.02	1.00	1.02	1.00
Power ratio, volumetric efficiency	0.90	0.90	0.94	1.00	1.00	1.00	1.00	1.00
Power ratio, heat of vaporization	1.00	1.00	1.00	1.04	1.00	1.00	1.00	1.00
Power ratio, mean pressure effects	1.04	1.04	1.04	1.03	1.00	1.00	1.00	1.00
Power ratio, net change from baseline	1.01	1.01	1.07	1.09	1.02	1.00	1.02	1.00

NOTES
a Data obtained from Santini et al. (1989), Amann (1990), DeLuchi (1991), and Ho and Renner (1990).
b Baseline vehicle is a hypothetical Ford Taurus as described by U.S. Congress (1991).

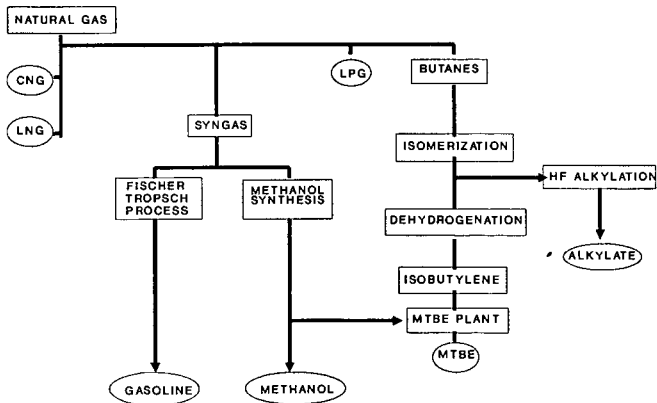


Figure 1. Schematic of natural gas fuel production pathways.

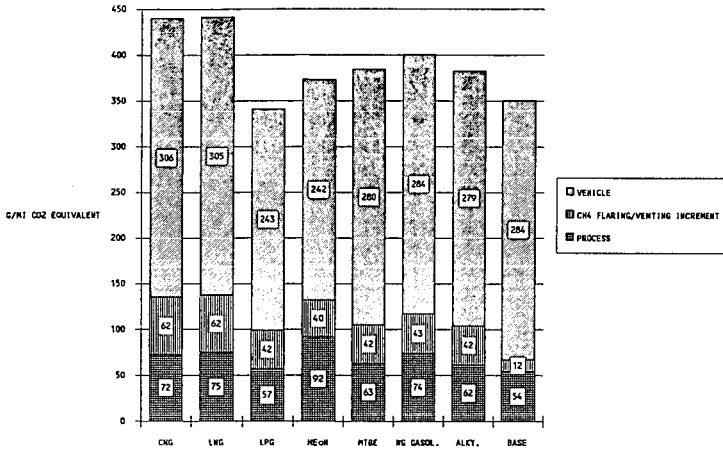


Figure 2. 20-year CO₂ equivalent emissions for constant performance case: vehicle, methane flaring/venting, and process contributions. (Venting/flaring increment assumes CH₄ is emitted during extraction of natural gas feedstock. N₂O emissions from venting/flaring assumed negligible.)

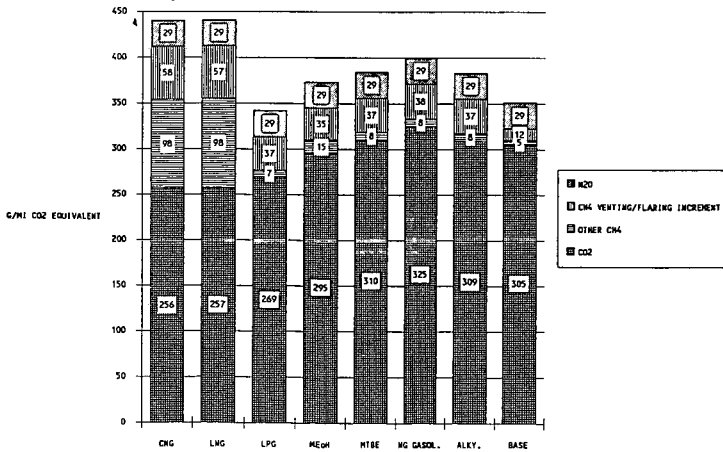


Figure 3. 20-year CO₂ equivalent emissions from natural gas fuel pathways: contributions from different greenhouse gases, constant performance case. (Venting/flaring increment assumes CH₄ is emitted during extraction of natural gas. N₂O emissions from venting/flaring assumed negligible. Other CH₄ is emitted from process conversion/refining and/or from the vehicle tailpipe.)

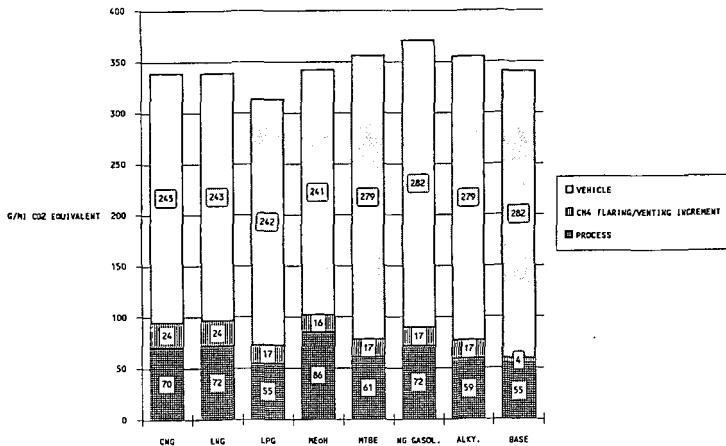


Figure 4. 100-year CO₂ equivalent emissions for constant performance case: vehicle, methane flaring/venting, and process contributions. (Venting/flaring increment assumes CH₄ gas is emitted during extraction of natural gas. N₂O emissions from venting/flaring assumed negligible.)

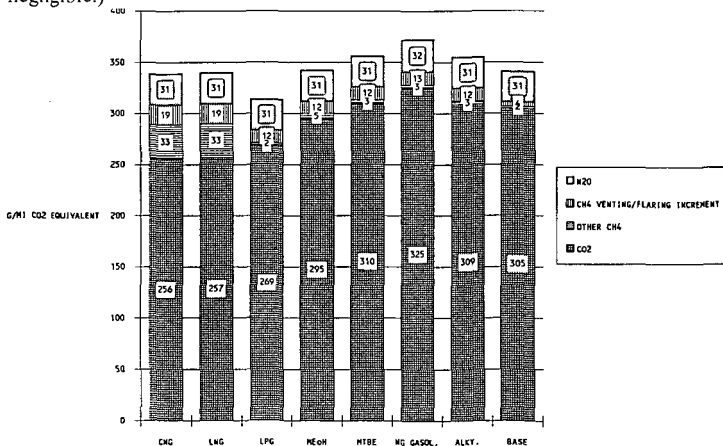


Figure 5. 100-year CO₂ equivalent emissions from natural gas fuel pathways: contributions from different greenhouse gases, constant performance case. (Venting/flaring increment assumes CH₄ is emitted during extraction of natural gas feedstock. N₂O emissions from venting/flaring assumed negligible. Other CH₄ is emitted from process conversion/refining and/or from the vehicle tailpipe.)

THE EFFECT ON DIESEL ENGINE EMISSIONS WITH HIGH CETANE ADDITIVES FROM BIOMASS OILS

D.W. Soveran, M. Sulatisky
Saskatchewan Research Council
515 Henderson Drive
Regina, Saskatchewan S4N 5X1
Canada

K. Ha, W. Robinson
ORTECH International
2395 Speakman Drive
Mississauga, Ontario
Canada

M. Stumborg
Agriculture Canada
P.O. Box 1030
Swift Current, Saskatchewan
Canada

KEYWORDS: Engine emissions, cetane additives, biomass

ABSTRACT: A process to convert plant oils (e.g. vegetable oils), tree oils (e.g. palm, tall oil) and other similar biomass oils to valuable high cetane blending components (supercetane) has been under development at the Saskatchewan Research Council (SRC) for approximately six years. The SRC recently completed a long-term conversion test (40 days) to demonstrate the process operability and catalyst activity maintenance. Sufficient product was generated for a fuel evaluation program that was performed at ORTECH International in Mississauga, Ontario. Two groups of blends were tested in a single cylinder diesel engine. The program compared the effects on fuel blends of converted vegetable oil and commercial cetane additives. The supercetane proved to be as effective as typical commercial additives. In addition, it was more effective on low cetane base fuels (e.g. light cycle oil) than commercial additives.

1. INTRODUCTION

The Saskatchewan Research Council has been performing research on the conversion of biomass oils into transportation fuels for more than a decade. In the mid-1980's the focus of the work turned to converting vegetable oils to diesel fuel. Convinced that the well-established conversion method of esterification of triglyceride oils was not attractive to conventional petroleum refiners, conversion techniques based on conventional petroleum conversion technology

were tested. The petroleum refining industry is a capital-intensive and complex. It was likely that an unconventional feedstock and an unknown conversion technology would have a difficult time finding acceptance within the industry. By developing a conversion method similar to those already in use at most refineries, renewable feedstocks would stand a better likelihood of utilization.

The first project demonstrated that hydroprocessing technology was flexible enough to convert triglyceride oils to a diesel fuel. Conversion products were expected to have cetane numbers in the 50-60 range (similar to esterified oils), but hydroprocessed vegetable oils have cetane numbers in the 90-100 range. It was quickly recognized that the product had more value as a diesel cetane improver. The process has since been patented.¹

Subsequent projects have continued the development of the conversion process. A variety of triglyceride oils (most plant and some tree oils) have been tested. Most limitations of the process have been determined. The actual chemistry of the conversion process is quite simple. Figure 1 provides a simple representation of the reactants and significant products. The fatty acid chains are broken off the triglyceride molecule, oxygen is removed (either as water or carbon dioxide), and any other double bonds saturated. A saturated paraffin is the predominant product. Other products include propane, carbon dioxide, carbon monoxide and water. As much as 85 wt. % of the feed is converted to a diesel product. The cetane value of the final product is a function of the fatty acid chain length. Most common vegetable oils have 16-20 carbon atom chains. This will yield a product with a cetane value of 90-100.

One non-triglyceride oil, tall oil, has been tested as well.² Derived from the pulping of pine trees, it is a mixture of free fatty acids and diterpene based compounds. The conversion product has a lower cetane value, around 70. Tall oil does have a very significant advantage though, it has a much lower cost than any vegetable oil.

In parallel to the experimental program, several economic analyses were performed to identify potential opportunities for application of this technology.^{2,3} The objective of this segment of the work was to find the applications available in the current energy market. Most renewable fuels (e.g. ethanol) rely on special tax breaks to be economically viable; getting these considerations for triglyceride oils would delay implementation of the technology. There was a belief at the SRC that there may exist economically attractive opportunities. A market survey of vegetable oil and other biomass oil production identified the plentiful and low cost oils. The most promising candidate, from a Canadian perspective, was tall oil. Canadian tall oil has a lower acid content than most other tall oils. Consequently, most is burned at the individual pulp mills because there is no market for the material.

Tall oil has become the focus of a commercial application in Canada. A process licence has been granted to a Canadian consulting company who is working with a tall oil fractionation company to develop a conversion facility.

Other economic analyses have identified potential scenarios for higher cost vegetable oils. These scenarios were directed to the situation faced by many Canadian refiners. With light oil production decreasing in Canada, refiners are having to use lower quality crude oils to meet their

market needs. The cetane value of many middle distillate products does not meet the requirements of the market. Cetane additives are relied on to bring these products to the necessary levels. Most commercial additives are expensive and cannot be added in the large quantities sometimes required. Some refiners are finding that it is necessary to hydrotreat their middle distillates to achieve the desired cetane numbers. One analysis has identified that it is much cheaper to hydroprocess a small volume of vegetable oil than it is to hydrotreat a large volume of middle distillate to reach the same cetane increase.

Because the conversion product is more than a straight diesel replacement, an accurate measure of its value is more difficult to determine. Some very limited engine tests indicated that conventional diesel fuels containing a small percentage of converted vegetable oil improved engine performance beyond those that could be attributed to the cetane number increase. For development to continue, a better definition of the product value was required.

This background information provides the basis for the work discussed in this paper. The areas to be covered include the demonstration of a longer operating period for the conversion process and a systematic program of comparing fuel blends.

2. EXPERIMENTAL

2.1 Production of Supercetane

Prior to this project the conversion process had been tested for short periods of time. Five days had been the longest period of operation. Catalyst deactivation was measurable in that short period. Although it was much quicker than conventional petroleum conversion, this problem was not expected to delay technology application. This project presented the opportunity to operate a conversion unit for a much longer period of time allowing some experimentation with techniques to prolong catalyst activity. To produce sufficient quantities for the engine testing, a larger laboratory hydroprocessing unit was operated for 45 days. Some techniques to alleviate catalyst deactivation were tested during this period.

Most of the developmental work was performed with a 30-mL trickle bed reactor system. A similar apparatus with a 100-mL trickle bed reactor was used for the project. Figure 2 provides a simplified schematic of the unit. The liquid product was collected at 24-hour intervals and analyzed for middle distillate content. Analysis of the gas product was done approximately three times per 24-hour period. Daily mass balances were performed to monitor conversion and product yields.

The feedstock for the conversion operation was canola oil. Canola oil (still called rapeseed oil in many other countries) is grown extensively in western Canada. It is a low euristic acid oil, with a predominant fatty acid chain length of 18 carbon atoms. An analysis is provided in Table 1.

The liquid products were distilled at an outside laboratory to produce a middle distillate fraction boiling in the 210-343°C range. The distillation technique complied with ASTM method

D-2982. Approximately 120 L of conversion product (referred to as "supercetane" at SRC) was prepared. An analysis of supercetane is shown in Table 1.

2.2 Engine Testing

A systematic engine testing program was set-up with the advice of ORTECH International. When testing diesel fuels, several factors are investigated. Increasing environmental awareness is focusing most work on engine emissions. Unburned hydrocarbons, carbon monoxide, nitrous oxides and particulate emissions are the key items in fuel evaluation. Other factors tied to engine performance are included as well: fuel consumption, thermal efficiency and power output.

A single cylinder engine was utilized to perform steady-state emissions testing for six fuels containing various amounts of cetane improver. Engine test conditions selected corresponded with those required by EPA 13-mode testing. Gaseous and particulate emissions were collected during the 13-mode test conditions consisting of 5-modes at rated engine speed, 5-modes at an intermediate speed, and at idle speed of the engine. The EPA 13-mode test is a recommended practice for determining the gaseous emission levels of heavy-duty diesel engines and was adapted for the test program. Emissions collected were measured in accordance with the recommended Society of Automotive Engineers (SAE) practices.

Because of the small size of the test engine and its low exhaust flow rate, available dilution tunnel/particulate sampling equipment could not be used. For this reason, particulate sampling was conducted from the raw or undiluted exhaust of the engine. Figure 3 is a schematic of the system.

From the Ricardo engine manufacturer's performance curves, and from running the reference fuels, engine conditions were determined as shown in Table 2. The engine timing was set according to the engine manufacturer's specifications. The poor quality of the B reference fuel necessitated a timing change at idle conditions. The other blends in the B fuel group were also run at the same conditions as the B reference fuel. Engine timing was not optimized for the fuel blends tested.

The Saskatchewan Research Council supplied ORTECH International with a total of 210 L of each of the six fuels to be evaluated for engine emissions. The fuels were divided into two series, the first fuel of each series was identified as Reference A and Reference B. These were considered to be the baseline fuel for each series from which all emission comparisons were performed and calculated. The remaining fuels were identified as A1, A2, B1 and B2, respectively. Compositions of all the test fuels were made available to ORTECH after all testing was completed and results tabulated. This was to ensure that all testing performed was unbiased.

Two reference fuels were chosen with the aid of a Canadian refiner. The first was a typical commercial grade diesel with a cetane number of 43.6. The second was a low cetane, high aromatic content middle distillate (light cycle oil) obtained from the fluid catalytic cracking of gas oil (343-525°C). The light cycle oil (LCO) had a cetane value 31.7. Neither fuel had any

commercial cetane additives. From each reference fuel two blends were made. The cetane value was increased by four to 48 in the fuel A series. The LCO blends had the cetane number increased to 43 with the additives. Table 1 gives an analysis of each fuel blend, as well as the amount and type of cetane additive. A commonly used commercial cetane additive was used for comparison. It is based on an alkyl nitrate compound. The cetane value of the supercetane is 90.7. All cetane determinations were performed using the ASTM standard engine technique.

3. RESULTS AND DISCUSSION

3.1 Supercetane Production

The production of supercetane required 45 days of continuous operation. As many as three catalyst replacements were expected because of activity loss, but conditions were altered to maintain activity. Product yields and quality were kept at a constant level for almost the entire period of operation. A change in conditions was made at day 40. Changes in gas yields were observed by the end of the run indicating that activity was deteriorating.

Figure 4 summarizes the distillate, water and gas yield on a daily basis. Gas yields for the first three days of operation were quite low because of an undetected gas leak. Distillate yields were nearly stoichiometric for the entire run.

3.2 Engine Testing of the Fuel Blends

Evaluation of the different fuel blends was performed at ORTECH International in Mississauga. ORTECH is an internationally recognized engine and fuel testing facility. Most engine testing is now done on heavy-duty, multicylinder diesel engines. Producing sufficient supercetane for multi-cylinder engine analysis would have been too costly for the purposes of this project. The single cylinder Recardo engine is a proven research tool which will provide reliable results. The data generated using this engine are not directly translatable to larger, more modern engines. It is, however, a useful tool for comparing the effects of different fuels on engine operation. The same trends would be observable on large multicylinder engines.

All the data reported were calculated using the EPA 13-mode weightings and calculations. Not all the information generated by the test program is presented here, only the more significant items of greatest interest (primarily emissions). Factors that also best illustrate the effect of the supercetane additive are also given.

Gas emissions are summarized in Table 3. Carbon dioxide (CO₂) emissions were similar for all the fuels with a cetane number above 40. The reference B fuel had a much higher CO₂ emission rate (per power output) than the other fuels. Fuels A1 and A2, those with the highest cetane number, had the lowest CO₂ emissions. A similar observation was possible with carbon monoxide (CO) emissions. The A1 and A2 blends were marginally better than A, B1 and B2 fuels. Total oxides of nitrogen were similar for all fuel blends.

Brake specific fuel consumption (BSFC) values were similar to the gaseous emission data. With the exception of the B reference fuel, which was higher, all the other fuels were very similar.

Total hydrocarbon emissions clearly showed the effect of increasing cetane values. The A1 and A2 blends had 10% lower emission rates. The B1 and B2 blends were similar to the A series fuels. Their emissions were 40% of the B reference fuel.

Particulate emissions are summarized in Table 4. Particulates are categorized as containing two separate fractions, a soluble (in methylene chloride) fraction and an insoluble fraction. The soluble fraction is considered to be more toxic because it will contain aromatic organic compounds, and therefore carcinogenic. For the A series fuels, the total particulates increased for the higher cetane blends. Almost all of the increase was in the insoluble fraction. The total particulates for the B blends decreased with the B1 and B2 fuels. The soluble fraction was reduced significantly while the insoluble increased by more than 100%.

The engine testing program provided reliable data on the effects of adding supercetane to conventional diesel fuel blends. Although its primary effect on fuel performance was related to the impact it had on cetane value, the project provided additional insights into what fuel characteristics have the most impact on engine emissions.

4. CONCLUSIONS

Improvements to the conversion process were developed in the project. A catalyst activity maintenance technique successfully kept the activity constant for 40 days of continuous operation. It is expected that catalyst life for this process will be similar to that used for hydrotreating of petroleum fractions (at least one year).

The fuel evaluation program proved that supercetane is an effective cetane improver for a wide range of middle distillate fractions. It can be blended to high or low cetane base fuels and have the same impact on cetane value. Commercial additives are less effective as the cetane number of the base fuels decreases.

Engine emissions are most affected by the cetane value of the fuel. Other researchers have also observed this phenomenon.^{4,5,6} In recent times there has been much concern focused on the aromatic content of diesel fuels and their contribution to emissions. The results clearly demonstrate that fuels produce similar emissions even though there are large differences in aromatic content. For example, the B2 fuel contains 38 vol % aromatics and A2 contains only 21.6 vol %, while emissions are very similar in almost every respect for these two fuels.

Supercetane does have two negative effects on the fuels it is added to. Both are related to the basic chemical nature of supercetane. Supercetane is a normal paraffin, boiling at the upper end of the middle distillate range, with 16-20 carbon atoms. Pure supercetane has a pour point of 21°C, which results in an increased pour and cloud point for each fuel it is added to. This limits its use in Canada and the northern United States to summertime fuel blends. It also limits the amount that can be blended with a fuel. Adding 8 vol % is all that is possible without

a dramatic effect on pour point. In the southern half of the United States it is less of a consideration.

Supercetane's high molecular weight also increases engine particulate emissions. Fortunately it increases only the insoluble portion, but since particulates are also quite visible it may make them appear less attractive.

The fuel evaluation study provided no evidence that the supercetane additive had other positive effects on engine performance other than those related to the cetane value increase. Limited engine testing done in other projects showed some performance benefits. These benefits were related to the higher cetane value of the fuel with supercetane added.

Development of this process is continuing at the Saskatchewan Research Council. A larger-scale pilot plant operation is in the planning stages. Further engine testing in large-scale multicylinder engines is expected to follow the pilot plant program. Other biomass oils such as waste animal oils and pyrolysis oils are being considered for evaluation. The commercialization with a tall oil feedstock is proceeding in parallel to these other activities. The SRC is also studying other potential applications.

ACKNOWLEDGEMENT

The authors gratefully acknowledge the financial, technical and moral support provided the development of the process by the Bioenergy Development Program, Energy, Mines and Resources Canada.

REFERENCES

1. Craig, W.K., Soveran, D.W. **Production of Hydrocarbons with a Relatively High Cetane Rating**, United States Patent No. 4,992,605
2. Soveran, D.W., Coxworth, E., Craig, W.K., Uloth, V.C., McBride, G.E. **Conversion of Tall Oil Derivatives to Premium Quality Transportation Fuels**, Confidential Report to Energy, Mines and Resources Canada, 580 Booth Street, Ottawa, Ontario K1A 0E4, Canada
3. Soveran, D.W., Coxworth, E., Sulatisky, M., Robinson, W., Ha, K. **Fuel Properties and Engine Performance of Fuel Additives Produced by Hydrotreating Triglyceride Oils**, Confidential Report to Energy, Mines and Resources Canada, 580 Booth Street, Ottawa, Ontario K1A 0E4, Canada
4. Ullman, T.L., Mason, R.L., Montalvo, D.A. **Effects of Fuel Aromatics, Cetane Number, and Cetane Improver on Emissions from a 1991 Prototype Heavy-Duty Diesel Engine**, International Fuels and Lubricants Meeting and Exposition, Tulsa, Oklahoma, October 22-25, 1990

5. Sienicki, E.J., Jass, R.E., Slodowske, W.J. **Diesel Fuel Aromatic and Cetane Number Effects on Combustion and Emissions from a Prototype 1991 Diesel Engine**, International Fuels and Lubricants Meeting and Exposition, Tulsa, Oklahoma, October 22-25, 1990
6. Cunningham, L.J., Henly, T.J., Kulinowski, A.M. **The Effects of Diesel Ignition Improvers in Low-Sulfur Fuels on Heavy-Duty Diesel Emissions**, International Fuels and Lubricants Meeting and Exposition, Tulsa, Oklahoma, October 22-25, 1990

Table 1 Analysis of Canola Oil, Supercetane and Fuel Blends

Analysis	Canola	Supercetane	Fuel A	Fuel A1	Fuel A2	Fuel B	Fuel B1	Fuel B2
Density @ 15°C	920.4		824.0	820.6	824.0	860.9	844.3	859.8
Cloud Point (°C)		24	-29	6	-32	-38	8	-16
Pour Point (°C)		21	-47	-16	-47	-53	-4	-49
Sulphur (wt. %)	0.02	0.0015	0.032	0.026	0.027	0.023	0.018	0.025
Flash Point (°C)		138	63	62	63	75	76	75
Corrosion (Cu, 3 hr. @ 50°C)		none	none	none	none	none	none	none
Viscosity @ 40°C, cSt	37.0	3.74	1.74	1.91	1.76	1.92	2.25	1.97
Carbon Residue (wt. %)		0.05	0.08			0.24		
Ash (wt. %)		<2 x 10 ⁻³	<2 x 10 ⁻³			<2 x 10 ⁻³		
Cetane number		90.7	43.6	47.7	47.7	31.7	43.3	42.3
Paraffins			15.8	23.5	16.0	4.7	23.7	13.2
Naphthenes			60.7	54.7	61.7	49.5	39.7	46.3
Olefins			1.0	0.7	0.7	1.3	1.3	2.4
Aromatics			22.5	21.1	21.6	44.5	35.3	38.1
Supercetane (vol %)				8.0			22.0	8.0
Cetane Additive (vol %)					0.1			0.2

Table 2 Engine Test Matrix

Fuel I.D.	Engine Test Conditions											
	Rated				Intermediate				Idle			
	Speed (rpm)	Torque (Nm)	Timing (°)	Speed (rpm)	Torque (Nm)	Timing (°)	Speed (rpm)	Torque (Nm)	Timing (°)	Speed (rpm)	Torque (Nm)	Timing (°)
A	3600	17.5	19	2400	18.5	16	780	1.8	14			
A1	3600	17.5	19	2400	18.5	16	780	1.8	14			
A2	3600	17.5	19	2400	18.5	16	780	1.8	14			
B	3600	17.5	19	2400	18.5	16	780	3.5	18			
B1	3600	17.5	19	2400	18.5	16	780	3.5	18			
B2	3600	17.5	19	2400	18.5	16	780	3.5	18			

Table 3 EPA 13-Mode Brake Specific Emissions (Gaseous)

Fuel I.D.	Total Hydrocarbons as CH ₄ (g/kW-hr)	% Change	Carbon Monoxide (g/kW-hr)	% Change	Total Oxides of Nitrogen (g/kW-hr)	% Change	Carbon Dioxide (g/kW-hr)	% Change
A	6.74	-	8.90	-	9.53	-	1140	-
A1	6.09	-10	6.97	-22	8.32	-13	1145	0
A2	6.08	-10	6.47	-27	9.21	-3	1153	1
B	15.64	-	23.89	-	9.94	-	1316	-
B1	5.83	-63	7.33	-69	9.50	-4	1192	-9
B2	6.39	-59	7.23	-70	10.08	1	1176	-11

Table 4 EPA 13-Mode Brake Specific Emissions (Particulates)

Fuel I.D.	Total Partis (g/kW-hr)	% Change from Base Fuel	Soluble Fraction (g/kW-hr)	% of Total Part.	% Change from Base Fuel	Insoluble Fraction (g/kW-hr)	% of Total Part.	% Change from Base Fuel
A	0.472	-	0.188	40	-	0.284	60	-
A1	0.588	25	0.196	33	4	0.392	67	38
A2	0.574	22	0.192	33	2	0.382	67	35
B	1.358	-	1.035	76	-	0.323	24	-
B1	1.123	-17	0.301	27	-71	0.822	73	154
B2	0.919	-32	0.233	25	-77	0.686	75	112

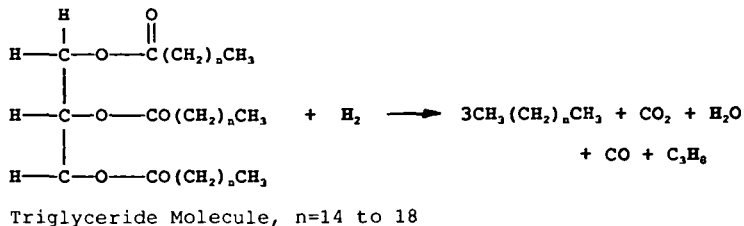


Figure 1 Conversion Reaction for Supercetane Production

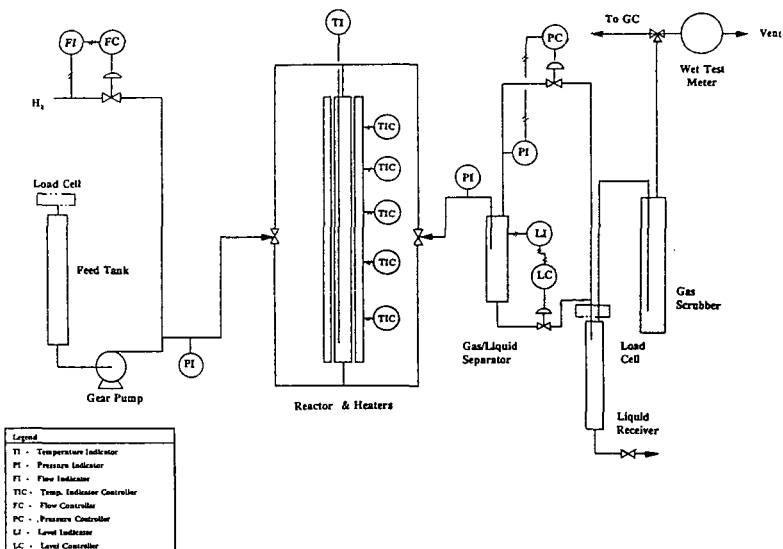


Figure 2 Schematic of Laboratory Hydroprocessing Unit - 100-mL Reactor.

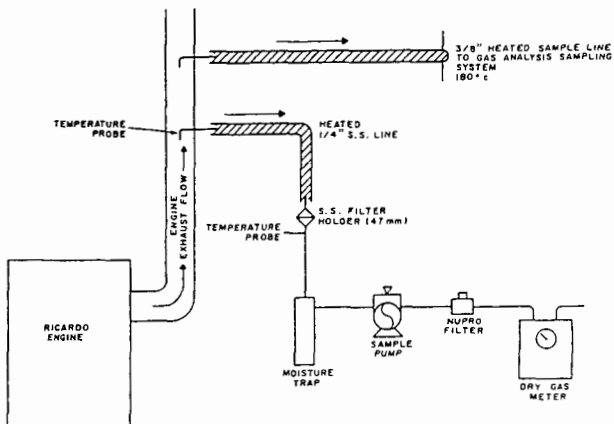


Figure 3 Particulate Sampling System - Ricardo Test Engine

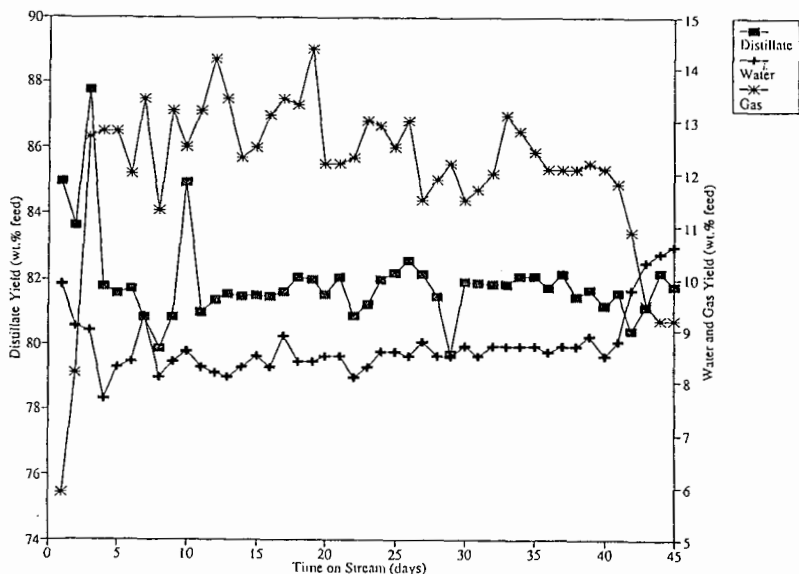


Figure 4 Liquid and Gas Yield Summary - Supercetane Production

SONOCHEMICAL TREATMENT OF FUEL COMPONENTS

Kazem M. Sadeghi, Jiunn-Ren Lin, and Teh Fu Yen
Department of Civil and Environmental Engineering
University of Southern California
Los Angeles, CA 90089-2531

Keywords: Upgrading, Ultrasound, Tar Sand, Asphalt, Heavy Oil, Oil Shale, Coal Liquid

ABSTRACT

A new method has been developed to recover upgraded lighter-hydrocarbon liquid oil from an asphaltene-containing oil material (tar sand, asphalt, heavy oil, shale oil, coal liquids, etc.). The process follows of dispersing particle of the carbonaceous material in an aqueous solution containing inorganic base (NaOH, Na_2SiO_3 , etc.) and/or surfactant at ambient temperatures and pressures. With the aid of sonication energy, the inorganic base and/or surfactant will combine with the polar components of the fuel to speed the recovery of upgraded oil material. The reaction process essentially removes and/or converts the asphaltene fraction in the bituminous material to lighter fractions. The process is highly efficient and the reaction time in minutes for the samples examined. The reaction mechanisms are related to principles of sonochemistry as well as membrane mimetic chemistry.

INTRODUCTION

The time has come for a new chemical process to improve the old refining technology that has not been revolutionized over a century. The new process has been developed and proved to recover upgraded lighter fuels from asphaltene-containing oil compounds. The writers have studied membrane mimetic chemistry and have applied the principles to sonochemistry.^{1,4,9} In most of the material studied, self-inducing, in-situ surfactants are generated or an external surfactant is introduced to initiate the process of upgrading.

The reactions initiated by ultrasonic irradiation in this country began 50 years ago.¹⁴ Since then, the mechanism of acoustic chemical reactions had remained poorly understood, thus limiting its practical application. Yet, in recent years, some considerable advances have been made in the technological generation of newer, higher intensity ultrasonic generators. Advances in ultrasonic waves are also becoming more successful in enhancing chemical processing operations by increasing the rates of individual transport phenomena involved in the overall operation.

In recent years, this problem has been reexamined, especially that part involving the application of cavitation in a microenvironment. For example, in aqueous solution, the instantaneous pressure at the center of a collapsing bubble has been estimated from theoretical considerations to be about 75,000 psi (5,100 atm).¹⁰ Experimentally, cavitation thresholds up to 300 bars (3.0×10^7 Pa) have been obtained.¹⁵ The actual cavitation temperature has been similarly measured as high as 5200 ± 560 K.³ The industry is therefore slowly being awakened to this powerfully unique manner and feasibility for large scale processes.

This new process developed by the writers^{5,8,19,20} operates at ambient temperature and atmospheric pressure. The hydrogen supply is either from the water or a stream of hydrogen bubbles. The recovered upgraded fuel is lower in heterocyclic elements content and metals can be recovered. This reduces process cost and minimizes adverse environmental impact. The fuel samples used are tar sand, asphalt, heavy oil, coal liquids and even oil shales.

EXPERIMENTAL AND RESULTS

Tar Sands

The sample used is high grade Athabasca tar sand, from McMurray Formation. The Kentucky tar sand from Edmonson Formation as well as the California tar sand from Sisquoc Formation have also been investigated.¹⁸ In the case of tar sand both separation as well as upgrading are achieved. The methodology calls for an alkaline solution with the aid of sonication. Stirring is applied only to help mix the solution with the sample and is not a major factor in the extraction. Usually, two different alkalis were used to extract

the bitumen: (1) 20:1 by volume distilled water to sodium silicate [wt. ratio $\text{SiO}_2/\text{Na}_2\text{O} = 1.80$] (PO Corporation) and (2) 0.02 M NaOH (J.T. Baker Chemical Co.) solution. The stirrer operates at 320 rpm with the blade at 2 cm above the sample. Sonication was performed in a 10-gallon 40 kHz transducerized tank (Branson model EMA30-6). Six piezoelectric transducers, made from lead zirconate titanate ceramic, were bonded to an area of about 350 cm² directly at the bottom of the tank. The six transducers consume a total power of 180 W/cm² and deliver approximately 2.0 W/cm² acoustic intensity at the transducer surface. Ultrasonic energy is directed upward through the tank. A typical example is that 200 g of tar sand are applied to 1000 mL of alkaline solution and sonicated for 20 minutes with the addition of few drops of 30% hydrogen peroxide as free-radical initiators. The solution temperature is observed at 45°C. The bitumen is skimmed from the surface solution at intervals and oven dried overnight under a vacuum at 50°C. For the upgraded bitumen, an average gravity of 15° API is found, based on a 95% cumulative recovery (see Figure 1, circles 1-6). The bitumen from Athabasca sample has an average value of 8° API in its raw state. Agglomerates are the heavier asphaltene and preasphaltenes that couple with the metals (Ti, V, etc.) to form a charcoal-like materials that precipitate (ca. 5%) to the bottom (circle 7, Figure 1). The microemulsion of micelles to form surfactants have been reported previously to be stable for many years.⁶ Figure 1 is a plot of the heterocyclic elements content X, $X = S + N + O$ versus the hydrogen enrichment, while all the elements are in atom basis. In the same figure the solvent fractionation products from the raw tar sand bitumen are also located. This indicates a positive upgrading in quantitative recovery. Material balance on the hydrogen content cannot account for the interconversion of the products from this new process alone. The extra amount of hydrogen must be derived from the water.

Asphalt

Regular paving asphalts obtained through the material bank of the Strategic Highway Research Program (SHRP) are used for the investigation.²² To isolate the asphaltene fraction, Soxhlet extractor is used with n-pentane as the eluent for more than 24 h. The n-pentane insoluble fraction is dried overnight in vacuum and used as asphaltene in this work. For each run, 0.50 g of asphaltene is dissolved in 1.0 g toluene and 30 g of water is added gradually to a 50 ml flask. To increase the interfacial surface area, vigorous stirring during the water addition is employed to form an oil in water emulsion. Model VC-500 ultrasonic processor (Sonics & Materials, Inc.) at power level 10 kW is used in the process. Instead of hydrogen gas a reducing agent, sodium borohydride, is introduced and hydrogen bubbles are evaluated. Span 20 is commonly employed as extra surfactant for the conversion reaction. After the reaction, the asphalt constituent is extracted by the dichloromethane. Both 30 mL of dichloromethane and the sample after reaction are put into the separation funnel and shaken several times. Two layers will appear in a short time. Since part of the emulsion is quite stable and hard to extract from the oil phase, shaking several times is generally required at that point. Since analysis of the asphalt content is dependent on the four fraction ratios, part of the product remaining in the water phase will not affect the analysis result. the dichloromethane with asphalt will stay in the bottom layer. After 10 minutes, the bottom layer in the separation funnel is collected for further analysis.

The composition of asphalt sample is determined through the TLC/FID analysis in this study. Before starting the analysis, a blank scan of Chromarod is required to ensure the removal of contaminants. Around 1 μl of sample is spotted on the Chromarod-SIII which is made by Iatron Laboratories, Inc. Since humidity will significantly effect the result of TLC development and reproducibility tremendously, preserving the Chromarod in the constant humidity chamber for at least 10 minutes to reach equilibrium is necessary. The constant humidity chamber is a chamber with sulfuric acid inside. Thus, the relative humidity will stay at 25% while reaching equilibrium. Two solvents with different polarities, including toluene and a mixture of dichloromethane and methanol at a ration of 95 to 5, are used to developed the sample into three fractions. The oil fraction will expanded first in the TLC development chamber by using toluene as an eluent. Using the mixture of dichloromethane and methanol as an eluent will expand the resin fraction. Since the asphaltene fraction is mostly polar, it will stay in the same spot. After development, the Chromarod is mounted on the rack and the analysis is run in the Itatrosan TH-10 analyst. Hydrogen pressure and air flow rate used for FID analysis are 0.9 in Hg and 2000 cfm, respectively. The HP 3390A integrator is connected to obtain the composition for three different fractions. Data are collected within 1 minute for each sample. The result of a typical experiment is shown in Figure 2 where various concentration of Span 20 is used. Evidently the decrease of asphaltene concentration as well as the accompanied increase of resin and gas oil

content suggest that upgrading can be accomplished in a reasonable time (time used is 15 minutes). Other types of extra-aided surfactant also has been investigated.

Heavy Oil

A California Monterey native crude oil (18°API, Well Blockmen #1) after vacuum dewatering and evaporation of light fraction obtained was used in the study. This topped crude contains 68.3% of resin and oil, 29.7% of asphaltene, and 2.0% of preasphaltene (carbene and carboid). For each run heavy oil upgrading study, 9.0 g of heavy crude is mixed with 10 mL of toluene and 250 mL of 10% aqueous sodium silicate solution. The mixture is placed into 1 L three necked-round bottom flask equipped with a mechanical stirrer and water cooling condenser. The reactor is placed in a water bath at 55°C in the Branson's ultrasonic unit with six piezoelectric transducers as described in Tar Sand Section. Sonication is continuously applied to the system for 5 to 10 hours. During the reaction, 2 mL of hydrogen peroxide is applied into the reactor. After sonication, the solution is poured into a separation funnel and the crude product was extracted by dichloromethane. The organic phase and aqueous phase separate within 5 minutes. The organic phase is subjected to vacuum evaporation to remove the dichloromethane from organic phase. The 1 L of n-pentane is added to the crude products to make sure the precipitation of asphaltene fraction. Asphaltene fraction is determined after filtration and drying in a vacuum oven. The quantity of oil and resin fraction is determined after the removal of n-pentane by vacuum evaporation. The toluene insoluble fraction is termed preasphaltene.

Figure 3 summarizes all the separate experiments and evidently the asphaltene has converted into oil and resin. After reaction, the oil and resin fraction content increases from 68.3% up to 86.0% and asphaltene content reduces from 29.7% down to 15.6%. From the mass balance, the recovery ranges 98% to 102%. Structural parameter such as H_A/H_S (from 1H NMR) and H_{M_0}/H_S (from FT-IR) for the products have been supported the upgrading.⁴

Coal Liquid

The sample employed here is from a chromatography-separated fraction (benzene-eluent) of asphaltene isolated from the coal liquid by catalytic Inc. (Willsonville, AL) from the solvent refined coal process. the coal is from Bellicap Seam, a Wyoming sub-bituminous type. For each run, a 0.2 g of sample is used dissolved in 0.4 g of toluene. The asphaltene solution is mixed with 30 mL of spent sodium silicate solution (recovered from Tar Sand Experiment Section). For every 15 m. of sonication a quantity of 0.3 g of sodium borohydride is added for maintaining a constant hydrogen bubbling activities. The results are summarized in Figure 4.

From the results shown in the Figure 4, the coal asphaltene content reduces tremendously within a short reaction time. Within 60 minutes, the asphaltene content reduced to 45.2%. At the same time, the oil and resin content increased up to 54.8%. From chemical kinetics, it is seen that the reaction is significant within a short time.

Oil Shale

For oil shale, the process has modified¹⁶⁻¹⁷ to a simultaneous use of electrolytic oxidation and ultrasonic radiation in alkaline environment; up to 57% by weight of the oil shale system has been dissociated and suspended in a process solution. The oil shale sample used are Stuart oil shale (Brick Kiln Member, Queensland, Australia) and Maoming oil shale (leave shale outcrop deposits, Guangdong, China). On the basis of analytical results, the Brick Kiln member of Stuart oil shale contains approximately 19.0% (by weight) kerogen, less than 0.1% bitumen, 6.6% moisture, 3.3% combined water, and a residual mineral, mostly quartz and clays. Maoming oil shale contains approximately 25.5% kerogen, 1.25% bitumen, 1.2% moisture and 63% minerals dominant in kaolinite associated with montmorillonite interstratified with illite and amesite. Bitumen in the oil shale is extracted by using benzene/methanol (with a volume ration of 3/2) in a Soxhlet extractor for 72 h. The solvent-free bitumen is obtained after filtration and following vacuum evaporation procedures. Usually, electrolytic oxidation of oil shale is carried out by using a glass cell of 700 mL total capacity. The anode and cathode compartments are separated by a porous frit. The anode electrode is made of 50-mesh platinum gauze (3.2 X 5.0 cm²). A constant potential of 0.3 V was maintained throughout the oxidation. An ultrasonic transducer of 40 kHz (nominal) and about 60 W is mounted on the bottom of the electrolytic glass cell. Shale samples are ground to sizes between 40 and 100 mesh screen and

placed in the anode chamber together with a total of 500 mL of 3 N sodium hydroxide solution. The same solution is used in the cathode chamber. The mixture in the anode chamber is acidified with HCl to yield an precipitate. An enrichment of organic matter is found in the acid precipitate from the process solution where it contains more than 23% organic matter. The remaining residue oil shale contains only less than 12% organic matter. Therefore the enrichment of organic matter in the precipitate as well as in the process solution is evident. Furthermore, the kerogen structure is destroyed in this mild dissociation process. This is proven by using a bitumen-free shale sample, where carboxylic acids are formed by infrared (Nicolet's FT-IR) and identified by GC (Hewlett-Packard 5880A) after esterification of the process solution. The 1575 cm^{-1} represent in the organic matter recovered from dissociation process and the absence of the absorption band in kerogen and bitumen reflect that the organic matter as well as mineral aggregates have been transformed (Figure 5).

DISCUSSION

Process Mechanism

This process is unique in separating oil into upgraded asphaltene-free fractions low in metal content. Experimental results indicate that the separation process operates by the reaction of specific chemical components of the bitumen with alkaline solution (e.g., sodium hydroxide) in the presence of sonication. The in-situ surfactants formed thus to facilitate the bitumen separation by a membrane-mimetic mechanism.²¹ Both asphaltenes and resins consist of aromatic sheets with saturated and polar functional groups spaced closely on long chains. Asphaltenes in their natural state exist in micelle form, peptized with resin molecules.¹² The center of this micelle can be either metal (V, Ni, Fe, etc.) or silica (or clay), or trace water. The crucial feature is that the polar groups are concentrated towards the center. This is often called oil external-water internal or reversed micelle. Surface adhesion is mainly due to hydrogen bonding, although other intermediate bonding mechanism such as charge transfer and acid-base salt formation do exist.

Ultrasound induced cavitation causes emulsification of the asphaltene and resin molecules and reorganization of metal, polar, and non-polar components into a continuous, single phase micelle of the polar external form. The surfactants interact with resin molecules in a membrane-mimetic fashion²; that is, a selective cation (e.g., hydroxide or silicate) is activated and dissolved in the oil phase. In this manner, the molecule containing the heterocycle center is dissociated and any ionizable proton such as in COOH, SH, or NH is replaced with the cation. When the surfactant migrates into the micelle it disrupts the polar structure, forming a Hartley micelle or polar-external micelle, and consequently a gel or liquid crystal phase of vesicles may also form. The outer counter anions emulsify the oil, and the micellar structure becomes a micro-emulsion stabilized by the reagent molecules. Sonication contributes to the removal of the heteroatoms by decreasing hydrogen bonding and inducing charge transfer and salt formation, thus lowering viscosity and specific gravity and increasing and facilitating recovery of the bitumen.

Ultrasound Phenomena

The mechanisms responsible for the observed increases in transport rates and unit operation processes utilizing ultrasonic energy can be divided into two categories: (1) first-order effects of fluid particles (displacement, velocity, and acceleration); and (2) second-order phenomena (radiation pressure, cavitation, acoustic streaming, and interfacial instabilities). Usually, one or more of the second-order effects are responsible for the enhancements in the transport process.^{10,14} The ultrasonic vibration raises the solution temperature to 45°C,¹⁰ but the temperature rise has little effect on bitumen recovery.⁸ In fact, Ibishi and Brown¹³ reported a monotonic decrease in sonochemical yield with increasing temperature. Because ultrasound in both aqueous and organic media produces radicals, conventional free radical propagation, inhibition, termination occurs. Cracking of asphaltene based on Rice mechanism of pyrolysis also occurs.^{21,22}

Interfacial Hydrogenation

In some special fuels system such as oil shale the system need further operations such as swelling bonification or additional electrolytic oxidation. An interfacial reaction can enhance chemical reaction by generation of continuous renewable surfaces. The size of the microemulsion also can be controlled by the multilamellar-unilamellar vesicle formation. The fact the collision probability can be increased by 10⁴ fold

by using a membrane-mimetic agent in micellar cage is naturally of advantage. In many cases the bubble size of evolved hydrogen gas or processing hydrogen gas can also be mediated.

CONCLUSIONS

Experimental results from a wide variety of fuel sources, coal liquids, tar sands, oil shale, asphalt and heavy oils all indicate that this new upgrading technology is feasible. The remaining development work leading to any useful industrial operations still need to be followed and completed. Upon completion of development work, a second generation refining technology may be born with the minimum environmental impact since this new process can be conducted at room temperature and ambient atmosphere and all the process can be made in modules with enclosed pathways.

ACKNOWLEDGEMENTS

We would like to thank Energy and Environment Research Laboratories, Inc., for the financial support.

REFERENCES

1. Esfandiari, R.S., Sloss, J.M., Sadeghi, K.M. and Yen, T.F., 1991. *Fuel Science and Technol. Internat.*, 9(5):537.
2. Fendler, J.H., 1982. *Membrane Mimetic Chemistry*. John Wiley and Sons, New York, 522 pp.
3. Flint, E.B. and Suslick, K.S., 1991. *Science*, 253:1397.
4. Lee, A.S., Xu, X.W. and Yen, T.F., 1988. *Proc., The 4th UNITAR UNDP Internat. Conf. on Heavy Crude and Tar Sand*, Edmonton, AOSTRA, Alberta, 5:109.
5. Sadeghi, M.A., Sadeghi, K.M., Kuo, J.F., Jang, L.K. and Yen, T.F., 1988. U.S. Patent 4,765,885.
6. Sadeghi, M.A., Sadeghi, K.M., Momeni, D. and Yen, T.F., 1989. *Oil Field Chemistry: Enhanced Recovery and Production Stimulation*, ACS Symp. Ser. No. 396: Chapter 21,391.
7. Sadeghi, K.M., Sadeghi, M.A., Kuo, J.F., Jang, L.K. and Yen, T.F., 1990. *Energy Sources*, 12(2):147.
8. Sadeghi, M.A., Sadeghi, K.M., Kuo, J.F., Jang, L.K. and Yen, T.F., 1990. U.S. Patent 4, 841, 131.
9. Sadeghi, K.M. Sadeghi, M.A. and Yen, T.F., 1990. *Energy and Fuel*, 4:604.
10. Suslick, K.S., 1988. *Ultrasound, Its Chemical, Physical and Biological Effects*. VCH Publisher, Inc., New York, 336 pp.
11. Tadros, T.F., 1984. *Surfactants*. Academic Press, New York, 342 pp.
12. Yen, T.F., 1990. *Encyclopedia of Polymer Science and Engineering*, 2nd Ed., John Wiley & Sons, New York, 1-10.
13. Ibishi, M. and Brown, B., 1967. Variation of the relative intensity of cavitation with temperature. *J. Acoustical Soc. Am.*, 41(3):568.
14. Frederick, J.R., 1965. *Ultrasonic Engineering*. John Wiley and Sons, New York, 379 pp.
15. Bnggs, L.J., 1950. *J. App. Phy.*, 21:721.
16. Lee, A.S., Lian, H.J., and Yen T.F., 1988. *Proc. International Conference on Oil Shale and Shale Oil*, Chemical Industrial Press, Beijing, 112.
17. Lee, A.S., Sadeghi, M.A. and Yen, T.F., 1988. *Energy and Fuel*, 2:88.
18. Sadeghi, K.M., Sadeghi, M.A., and Yen T.F., 1990. *Proc., Eastern Oil Shale Symposium*, Institute of Mining and Mineral Research, University of Kentucky, 18.
19. Sadeghi, M.A., Sadeghi, K.M., Kuo, J.F., Jang, L.K. and Yen T.F., 1991. U.S. Patent 5,017,281.
20. Sadeghi, M.A., Sadeghi, K.M., Kuo, J.F., Jang, L.K. and Yen T.F., 1991. *Canadian Patent* 1,283,879.
21. Kuo, J.F., Sadeghi, K.M., Jang, L.K., Sadeghi, M.A., and Yen, T.F., 1986. *Appl. Phy. Commu.*, 6(2):205.
22. Yen, T.F. and Lin, J.R., 1991. *Heavy Crude and Tar Sands-Hydrocarbons for the 21 Century Upgrading, Government and Environment*, UNITAR, New York, 4:75.

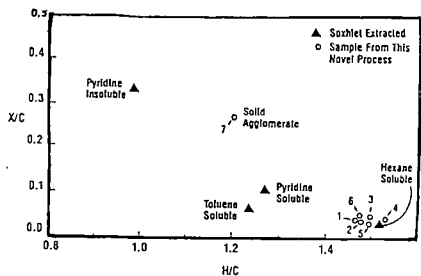


Figure 1. X/C versus H/C for various fractions of bitumen from Athabasca tar sand. Circles 1 through 6 are the recovered bitumen from the surface of solution and circle 7 is the solid agglomerate precipitate. Soxhlet extraction of the raw bitumen as reference points.

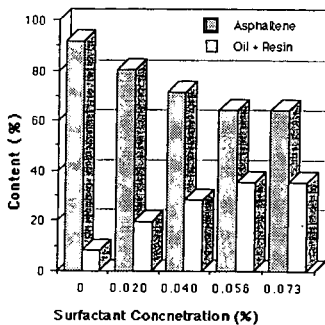


Figure 2. The conversion of asphaltene to oil and resin at various surfactant content (reaction time : 15 minutes). The asphaltene is isolated from a paving asphalt (AAX). The surfactant is Span 20.

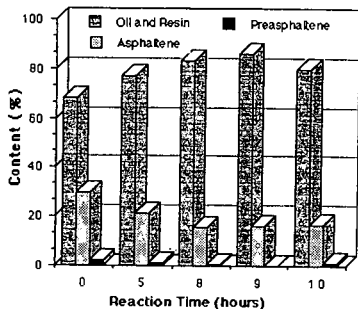


Figure 3. The composition of a Monterey native crude oil at various reaction time after sonication process. Each time interval represents a separate experiment.

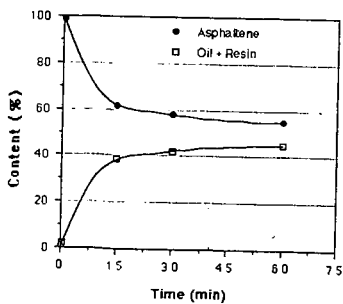


Figure 4. Conversion of a coal-derived asphaltene fraction from coal liquid with time. The sample is isolated from Catalytic Inc. at Willsville, Al.

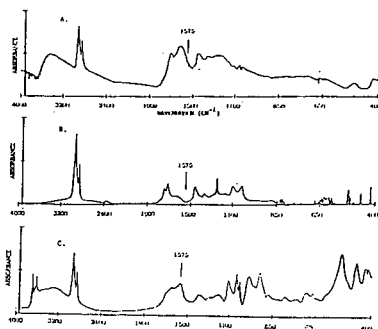


Figure 5. FT-IR spectra of a Maoming oil shale (A) isolated kerogen in KBr, (B) raw bitumen in CCl_4 , and (C) organic matter recovered from dissociation process. The 1735 cm^{-1} represent carboxylic acids.

DEPENDENCE OF PARTICULATE MATTER EMISSIONS FROM BOILERS ON QUALITY OF RESIDUAL FUEL OIL

Peter M. Walsh,* Dominick J. Mormile,† Bruce F. Piper‡

*Fuel Science Program
Department of Materials Science and Engineering
Pennsylvania State University
University Park, PA 16802

†Environmental Affairs
Consolidated Edison Co. of New York
4 Irving Place
New York, NY 10003

‡Energy Technology Consultants, Inc.
51 Virginia Avenue
West Nyack, NY 10994

Keywords: Residual fuel oil, Particulate matter emissions, Particle size distribution.

INTRODUCTION

In a recent paper, Walsh, Wei, Mormile, Piper, Olen, and Washington (1991) outlined an approach to the estimation of concentrations and size distributions of ash and unburned coke particles in flue gas from residual oil-fired electric utility boilers. Three contributions to particulate matter were considered: unburned coke, submicrometer ash formed from vapor, and ash residues left on burnout of coke. Other components of particulate, such as sulfate and soot, were not included. More detailed methods for calculating the concentrations and size distributions of unburned coke, submicrometer ash, and ash residues have been developed, as described below.

Size distributions of stack particulate were measured by Piper and Nazimowitz (1985) during combustion of 0.3 wt% sulfur oils in a 62 MW boiler of the Consolidated Edison Co. of New York. Samples were collected at the stack breeching, where gas temperature was 450 K (350°F). A representative size distribution, with indications of the materials thought to be the principal contributors to each of the three modes, is shown in Figure 1. The proposed mechanism for formation of the particles is presented in Figure 2.

RESULTS AND DISCUSSION

Unburned Coke

Under normal conditions, about 99% of the coke formed in a residual oil spray flame burns out in the furnace. The few particles which survive, do so because of extreme properties or conditions under which they make their passage through the furnace: large particle size, low reactivity, short residence time, low temperature, or rich mixture. A large part of the difficulty in simulating the process arises from the need to account for the nonuniformity of particle properties and furnace conditions.

A detailed analysis of factors controlling the combustion of petroleum coke was recently given by Stanmore (1991). For the present simulation of coke combustion in a boiler, coke residues were assumed to burn at constant size with decreasing density, according to a reaction which is first order with respect to oxygen concentration, producing carbon monoxide which burns far from the particle surface. Each particle was assumed to remain at its initial size until it disintegrated, at the critical porosity (Kerstein and Niksa, 1985). The fragments were assumed to burn instantaneously. The mean temperature was estimated from the furnace exit gas and adiabatic flame temperatures (Hotel and Sarofim, 1967). Particles and gas were assumed to be at the same temperature. Allowance was made for a distribution of residence times in the furnace (Beér and Lee, 1965).

The present calculation differs from the previous one (Walsh et al., 1991) in its consideration of a distribution of oxygen concentrations, arising from uneven distribution of fuel and air among the burners (Lawn and Godridge, 1987), from fluctuations in fuel and air flowrates, or from imperfect mixing of spray droplets with combustion air. The calculation was done by separating the gas/particle flow into two imaginary streams, one rich and one lean, whose average oxygen content is that which would be present in a perfectly mixed postflame region, after combustion of volatiles. The difference between the oxygen content of either stream and the average is the standard deviation of the oxygen concentration distribution at the onset of coke combustion. The concentration in both streams decays exponentially toward the flue gas excess oxygen as the streams are mixed. When the initial O_2 content of the rich stream was less than zero, no combustion of coke was allowed until mixing with lean gas raised its oxygen content above zero. Both the standard deviation of the initial oxygen concentration distribution and the characteristic mixing time were adjusted to fit the unburned carbon emission measurement, but the two values together were constrained by the observed O_2 distribution in flue gas, determined by a traverse at the economizer outlet. The mixing time is characteristic of the postflame flow, rather than the jet-stirred region near the burners.

The probability density function for the aerodynamic sizes of coke particles surviving at the furnace exit was obtained by integration of the contributions to each size of unburned particles from all sizes of coke particles formed in the flame. Values of the parameters having the greatest influence on the coke particle size distribution are given in Table 1. The size distributions of particles remaining unburned are shown on the right hand side of Figure 1 (peak labeled "unburned coke"). When compared with the earlier result (Walsh et al., 1991), one sees that the introduction of the oxygen concentration distribution allows smaller particles to survive, improving the agreement between model and measurements. However, the calculated sizes are still two to three times larger than observed. Two possible approaches to reconciling this discrepancy might be to account for size reduction during burnout and to allow for a distribution of furnace temperatures.

Ash Residues of Coke Fragments

Vaporized ash forms submicrometer particles, while the nonvaporized ash forms micrometer-sized residues. The extent of vaporization is expected to depend upon ash composition, temperature, oxygen concentration, and the structure of the coke (Quann and Sarofim, 1982; Senior and Flagan, 1985). We have not attempted to simulate the vaporization process, so the fraction vaporized was simply adjusted until the calculation reproduced the heights of the submicron and residue peaks.

The breakup of coke particles during burnout divides the ash retained in the coke among smaller fragments. If inorganic species were uniformly distributed through the coke, the size distribution of fragments would determine the sizes of ash residues formed when the coke burns out (Flagan, 1979; Kang et al., 1989). In the previous calculation (Walsh et al., 1991), the mean size of fragments was derived from measurements of the sizes of partially burned coke (Lawn et al., 1987). A different approach was taken here.

The cumulative mass-based fragment size distribution was assumed to take the form of a power law (Kerstein and Niksa, 1985): $F(d_f) = (d_f/d_C)^n$, in which d_f and d_C are the sizes of fragments and parent coke particle, respectively. The probability density function for the fragments was obtained by integration of the contributions to a given size from all sizes of parent particles. The exponent, n , was assigned the smallest value thought to be reasonable ($n = 1$), which implies a uniform distribution (by mass) of fragments formed from each size of particle. The ratio of ash residue size to fragment size is obtained from the ash content of the oil, the coke yield in the flame, and the densities of ash and coke. The result is shown in Figure 1 (peak labeled "ash residues"). The most probable size of residue in the calculated distribution is five times larger than that obtained in the previous calculation (Walsh et al., 1991), and about four times larger than the size at the peak in the measurements (at $\sim 1 \mu\text{m}$).

Although this calculation provides an explanation for the presence of particles having sizes in the range from 0.6 to 7 μm in the flue gas, there is not a satisfactory fundamental basis for the calculation of the coke fragment size distribution. Some measurements and analysis of the breakup of residual oil coke particles are needed. The spherical macropores in the coke are expected to have an important effect on the fragment size distribution (Kerstein and Niksa, 1985; Kang et al., 1989). The ash residue sizes may also be influenced by the sizes of inorganic particles (e.g. fluidized catalytic cracker fines and MgO) in the oil, which become incorporated in the coke.

Submicrometer Ash

Ash not assigned to the residues was assumed to vaporize during combustion of coke. Oxidation and cooling in a coke particle boundary layer cause supersaturation of the vapor. Nuclei formed from the vapor grow by condensation until the condensable species are depleted, after which growth continues by coagulation of the particles. The ultimate particle size distribution, after the relatively long residence times characteristic of combustion, is determined primarily by coagulation (Friedlander, 1977; Flagan, 1979; Neville et al., 1981).

The key to a satisfactory calculation of the most probable size of submicron particles was provided by the work of Senior and Flagan (1982, 1985) and Helble, Neville, and Sarofim (1988). Senior and Flagan (1982) pointed out that the principal mechanism for transport of submicron ash particles away from their parent coke or char particle is the convective flow arising from the increase in gas volume accompanying the reaction $2\text{C} + \text{O}_2 = 2\text{CO}$ at the coke particle surface. Because the volume fraction of submicron particles in the coke particle boundary layer is 200 times greater than after uniform mixing in the free stream, most of the coagulation and size increase occur in the vicinity of the coke. Helble et al. (1988) reached similar conclusions from consideration of convection and diffusion, when the coke particle is moving relative to the ambient gas.

In the present calculation it was assumed that submicron particles are confined to the outward flow from a coke particle as long as it is burning, but that the submicron particles

become uniformly mixed at the instant the coke burns out. Increase in size by coagulation of the well-mixed particles could not be neglected, since the mean residence time in the furnace and convective sections is 50 times longer than the burning time of the mean size of coke. A refinement of this approach, considering details of the mixing process, would be possible using the theory of Heible et al. (1988).

The average of Lee and coworkers' results for the geometric standard deviation of the sizes of coagulated aerosols formed in the continuum (Lee, 1983) and free molecule (Lee, Chen, and Gieseke, 1984) regimes was used to calculate the particle size distribution shown in Figure 1 (peak labeled "submicron ash"). In calculating the aerodynamic diameters, corrections were made for both density and the change in Cunningham correction for slip (Flagan and Seinfeld, 1988). However, the effect of the particles' not being spherical (Ulrich and Subramanian, 1977; Graham et al., 1990) was not considered. The calculated mean aerodynamic particle size was approximately 0.2 μm , compared with the peak in the measurements at 0.3 μm . This is a marked improvement over the previous calculation (Walsh et al., 1991), in which the coagulating particles were assumed to be uniformly mixed with gaseous combustion products.

Effects of Fuel Quality

The primary influence on unburned coke is the mass fraction of fuel converted to coke. There are two effects of increasing the coke yield: 1. The amount of coke to be burned increases, and 2. Particle size increases, although weakly [size is proportional to the one-third to one-half power of coke yield (Urban and Dryer, 1990b, 1991)]. Our estimate of coke yield was based on the IP 143 asphaltene analysis (Lawn et al., 1987; Holmes, 1989; Olen, 1989; Urban and Dryer, 1990a). An apparatus for the measurement of coke formation, under conditions simulating pyrolysis in a flame, is under development for routine analysis of fuel oils (McElroy, Muzio, and Carl, 1991).

Coke particle sizes depend upon the fineness of the spray, which depends upon the viscosity of oil in the atomizing tip. It is often assumed that the required temperature for a desired viscosity can be obtained from a universal viscosity-temperature relationship for fuel oils. However, there is significant variation in temperature dependence of viscosity among residual oils (Olen, 1988). Agglomerated asphaltene may influence atomization behavior (Audibert, 1989).

The ash content of fuel oil determines the total of submicron ash and ash residue contributions to particulate matter, which, for the fuel and boiler under consideration, was approximately the amount of material smaller than 10 μm (PM₁₀). To make useful calculations of collection efficiency and opacity one would require, in addition, an estimate of the proportions of vaporized ash and residues. The Consolidated Edison Co. of New York measurements indicated that the fraction of ash vaporized was 30 to 80 wt%, much greater than during pulverized coal combustion, and the fraction vaporized was not well correlated with NO_x emission (McElroy, Carr, Ensor, and Markowski, 1982). Experience in the field shows that submicron ash increases with increasing vanadium in the oil (Walsh, Olen, Mormile, and Piper, 1990). Particles suspended in the oil (FCC catalyst, MgO) are expected to contribute to 1 to 10 μm residues.

We have not included discussion of the important contributions of sulfate to particulate matter and sulfuric acid mist to stack plume opacity, because the samples under consideration were collected from flue gas at temperatures well above the acid dewpoint.

Sulfate and acid mist depend upon the sulfur, vanadium, and sodium contents of the oil, MgO treatment, and the extent to which excess air can be lowered without causing unacceptable unburned carbon emission.

CONCLUSIONS

Agreement between calculated and observed size distributions of unburned coke in flue gas was improved by the introduction of a fuel/air ratio distribution at the burners, which enabled smaller particles to remain unburned at the furnace exit. It appears, however, that allowance for particle size changes during burnout and the distribution of furnace temperatures may be needed to further improve the calculation of the size distribution of unburned particles.

Intermediate-size particles, in the range of aerodynamic sizes from 0.6 to 7 μm , were thought to be ash residues left on burnout of coke fragments. The assumption of a uniform distribution of fragment sizes formed from each size of parent coke particles roughly imitated the observed size distribution in this range. A better analysis is needed for the fragmentation behavior of particles having the structure of residual oil coke.

The growth of submicron particles by coagulation following nucleation and condensation of vapor-phase inorganic species was simulated by dividing the process into two stages. In the first stage, particles were confined to the convective flow from the coke surface, driven by combustion of the coke (Senior and Flagan, 1982). In the second stage, following burnout of the coke, the submicron particles were uniformly mixed with combustion products. High concentration of particles is characteristic of the first stage, while long residence time is characteristic of the second. The mean size of particles obtained from this calculation was in good agreement with the most probable size in the submicron peak of the measured distribution. The most important limitation on the predictive capability of this calculation is the lack of a model for vaporization of ash, which would describe the segregation of ash between residues and submicron particles.

ACKNOWLEDGMENTS

This work is supported by the Consolidated Edison Co. of New York, Electric Power Research Institute, Empire State Electric Energy Research Corp., and Florida Power & Light Co. The Project Managers are Peter E. Coffey (Empire State Electric Energy Research Corp.), Dominick J. Mormile (Consolidated Edison Co. of New York), Kenneth R. Olen (Florida Power & Light Co.), and William C. Rovesti (Electric Power Research Institute). The figures were drawn by Rick Sharbaugh and Amy Peters of Penn State University Photo/Graphics. We are indebted to Karl A. Graham for many valuable discussions.

REFERENCES

- Audibert, F.: "Particulate Emissions Related to Unusual Metallic Compounds and to Asphaltene Dispersion in Fuel Oils," Institut Français du Pétrole, Manuscript prepared for publication, 1989.
- Beér, J. M. and Lee, K. B.: Tenth Symposium (International) on Combustion, The Combustion Institute, 1965, pp. 1187-1202.

Flagan, R. C.: Seventeenth Symposium (International) on Combustion, The Combustion Institute, 1979, pp. 97-104.

Flagan, R. C. and Seinfeld, J. H.: Fundamentals of Air Pollution Engineering, Prentice-Hall, 1988.

Friedlander, S. K.: Smoke, Dust, and Haze: Fundamentals of Aerosol Behavior, Wiley, 1977.

Graham, K. A., Walsh, P. M., Beér, J. M., and Sarofim, A. F.: "Compositional Mapping of the Inorganic Submicron Aerosols Produced from the Combustion of Pulverized Coals and Residual Oils," American Association for Aerosol Research, 1990 Annual Meeting, Philadelphia, June 18-22, 1990, Paper No. 8C4.

Helble, J., Neville, M., and Sarofim, A. F.: Twenty-First Symposium (International) on Combustion, The Combustion Institute, 1988, pp. 411-417.

Holmes, R.: Central Electricity Generating Board, UK, personal communication to K. R. Olen, May 17, 1989.

Hottel, H. C. and Sarofim, A. F.: Radiant-Heat Transfer, Standard Handbook for Mechanical Engineers, T. Baumeister and L. S. Marks (Eds.), McGraw-Hill, 7th Edition, 1967, pp. 4-108 to 4-123.

Kang, S.-G., Helble, J. J., Sarofim, A. F., and Beér, J. M.: Twenty-Second Symposium (International) on Combustion, The Combustion Institute, 1989, pp. 231-238.

Kerstein, A. R. and Niksa, S.: Twentieth Symposium (International) on Combustion, The Combustion Institute, 1985, pp. 941-949.

Lawn, C. J., Cunningham, A. T. S., Street, P. J., Matthews, K. J., Sarjeant, M., and Godridge, A. M.: "The Combustion of Heavy Fuel Oils," Chapter 2 in: Principles of Combustion Engineering for Boilers, C. J. Lawn (Ed.), Academic Press, 1987, pp. 61-196.

Lawn, C. J. and Godridge, A. M.: "Matching the Combustion Equipment to the Boiler," Chapter 1 in: Principles of Combustion Engineering for Boilers, C. J. Lawn (Ed.), Academic Press, 1987, pp. 1-60.

Lee, K. W.: *Journal of Colloid and Interface Science* 92, 315 (1983).

Lee, K. W., Chen, H., and Gieseke, J. A.: *Aerosol Science and Technology* 3, 53 (1984).

McElroy, M. W., Carr, R. C., Ensor, D. S., and Markowski, G. R.: *Science* 215, 13-19 (1982).

McElroy, M. W., Muzio, L. J., and Carl, U.: "The New Coke Index Method for Characterizing Fuel Oil," EPRI, 1991 Fuel Oil Utilization Workshop, San Antonio, TX, November 6-7, 1991.

Neville, M., Quann, R. J., Haynes, B. S., and Sarofim, A. F.: Eighteenth Symposium (International) on Combustion, The Combustion Institute, 1981, pp. 1267-1274.

Olen, K. R.: "The Effect of Fuel Properties on the Viscosity Temperature Relationship for Residual Oils," EPRI, Fuel Oil Users' Newsletter, Vol. III, No. 1, April 1988, pp. 5-8.

Olen, K. R.: Florida Power & Light Co., personal communication, 1989.

Piper, B. and Nazimowitz, W.: "High Viscosity Oil Evaluation, 59th Street Station - Unit 110," Volumes 1 and 2, Prepared for the Consolidated Edison Co. of New York, Inc. by KVB, Inc., Engineering and Research Division, KVB 21640-1, March 1985.

Quann, R. J. and Sarofim, A. F.: Nineteenth Symposium (International) on Combustion, The Combustion Institute, Pittsburgh, PA, 1982, pp. 1429-1440.

Senior, C. L. and Flagan, R. C.: Aerosol Science and Technology 1, 371-383 (1982).

Senior, C. L. and Flagan, R. C.: Twentieth Symposium (International) on Combustion, The Combustion Institute, 1985, pp. 921-929.

Simmons, H. C.: Transactions of the ASME, J. Engr. for Power 99, 309-319 (1977).

Stanmore, B. R.: Combustion and Flame 83, 221-227 (1991).

Ulrich, G. D. and Subramanian, N. S.: Combustion Science and Technology 17, 119-126 (1977).

Urban, D. L. and Dryer, F. L.: "Relationship of the Coke Formation Index to Heavy Fuel Oil Properties," Joint Meeting of the Western States and Canadian Sections of the Combustion Institute, Banff, Alberta, April 29-May 2, 1990a.

Urban, D. L. and Dryer, F. L.: "Formation of Coke Particulate in the Combustion of Residual Oil: Particle Size and Mass Prediction from Initial Droplet Parameters," HTD-Vol. 142, Heat Transfer in Combustion Systems, B. Farouk, W. L. Grosshandler, D. G. Lilley, and C. Presser (Eds.), ASME, 1990b.

Urban, D. L. and Dryer, F. L.: Twenty-Third Symposium (International) on Combustion, The Combustion Institute, 1991, pp. 1437-1443.

Walsh, P. M., Olen, K. R., Mormile, D. J., and Piper, B. F.: "Size Distribution and Opacity of Particulate Matter Emissions from Combustion of Residual Fuel Oils," EPRI, 1990 Fuel Oil Utilization Workshop, Arlington, VA, October 31 to November 1, 1990.

Walsh, P. M., Wei, G., Mormile, D. J., Piper, B. F., Olen, K. R., and Washington, K. T.: "Size Distribution of Coke and Ash Particles Formed during Combustion of Residual Fuel Oil in Electric Utility Boilers," EPRI, Ninth Symposium on the Transfer and Utilization of Particulate Control Technology, Williamsburg, VA, October 15-18, 1991.

Wigg, L. D.: J. Inst. Fuel 37, 500 (1964).

Table 1. Values of parameters used in the calculation of the particle size distribution.

Parameter	Value	Source
Furnace volume	2088 m ³	furnace dimensions
Furnace plan area	91 m ²	furnace dimensions
Distance from burners to furnace exit	16.3 m	furnace dimensions
Load	62 MW	Piper and Nazimowitz (1985)
Furnace exit gas temperature	1480 K	typical
Mass median spray droplet size	120 μm	Wigg (1964)
Geometric standard deviation of the droplet size distribution	1.83	Simmons (1977)
Mass fraction of fuel oil converted to coke	0.22(IPA/100) ^{0.4}	Olen (1989), Holmes (1989)*
Apparent density of coke	690 kg/m ³	Lawn et al. (1987)
Dimensionless standard deviation of the oxygen concentration distribution	1	adjusted
Characteristic time for mixing in the postflame region	1.2 s	adjusted
Exponent in power law describing the coke fragment size distribution	1	adjusted
Sticking propability in collisions between submicrometer particles	1	assumed
Geometric standard deviation of the submicrometer ash particle size distribution	1.34	Lee (1983) Lee et al. (1984)
Apparent density of ash	2500 kg/m ³	typical of aluminosilicates
Average temperature during coagulation in the convective section	1000 K	average of furnace exit and stack
Total residence time in furnace and convective sections	10 s	estimate
Fraction of ash vaporized	60 wt%	adjusted

*IPA = IP 143 asphaltenes (wt %).

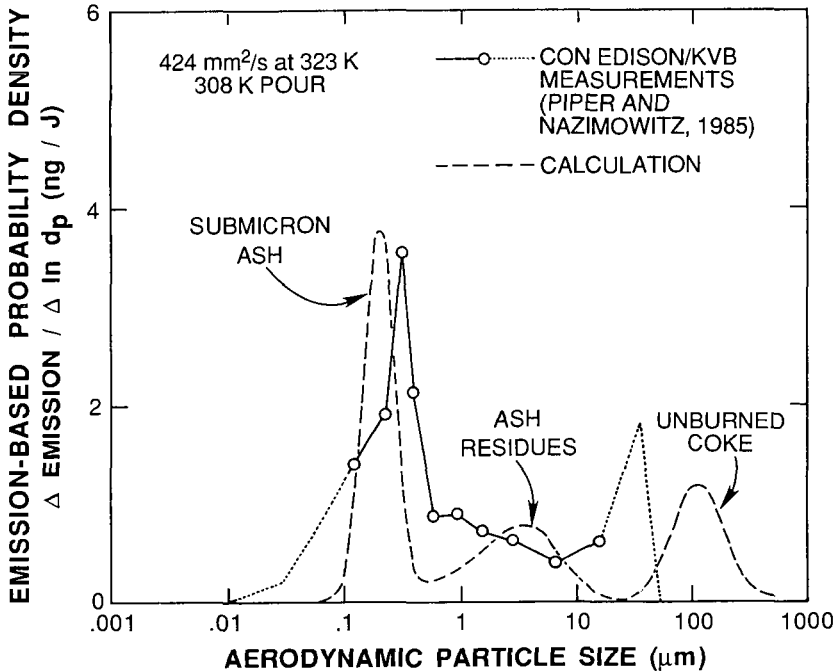


Figure 1. Emission-based size distribution of particles separated from flue gas at the stack breaching in Unit 110 at the 59th Street Station of the Consolidated Edison Co. of New York (Piper and Nazimowitz, 1985). The fuel oil properties were: viscosity at 323 K (122°F), 424 mm²/s (200 SSU); pour point, 308 K (95°F); sulfur, 0.29 wt%; ash, 0.02 wt%; IP 143 asphaltenes, 1.6 wt%; and vanadium, <10 wt ppm. The excess oxygen in flue gas was 3.1 mol%. The extreme left and right portions of the experimental curves are shown dotted, to indicate that the shape in these regions depends upon the maximum and minimum sizes assumed for the particles in the prefilter and final filter, respectively, of the cascade impactor. Although resolution of particle size in these samples might change the shapes of the curves, it would not change their areas. The dashed curve is the result of the calculation described in the text.

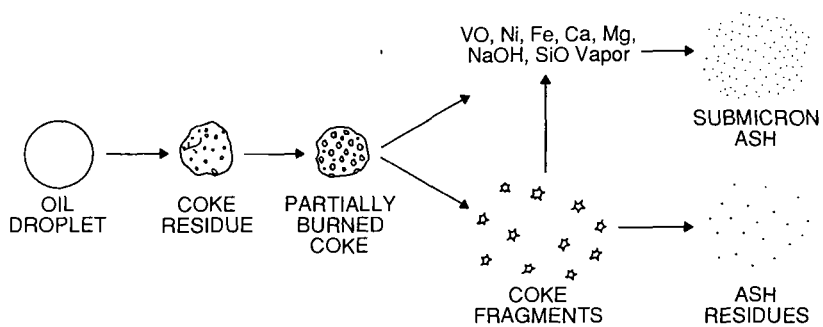


Figure 2. Mechanism for formation of particles observed in flue gas, in the absence of soot, and while temperature is still above the sulfuric acid dewpoint. Under these conditions the principal components of particulate matter are thought to be partially burned coke residues, ash residues remaining on burnout of coke fragments, and submicrometer ash formed by nucleation, condensation, and coagulation of vaporized inorganic species. Typical sizes are: oil droplets (mean), 100 to 200 μm , unburned coke, 10 to 300 μm , ash residues, 0.5 to 8 μm , and submicrometer ash, 0.1 to 0.5 μm .

THE EVOLUTION OF FUEL NITROGEN DURING RAPID COAL DEVOLATILIZATION

C. K. Man, K. J. Pendlebury and J. R. Gibbins,
Mechanical Engineering Department, Imperial College, London SW7 2BX

INTRODUCTION

Significant reductions in emissions of NO_x from pulverised fuel (PF) combustion have been achieved by low- NO_x burners employing air staging to ensure that coal volatiles are burnt under fuel-rich, reducing conditions. Almost complete suppression of NO_x formation from volatile nitrogen has been reported¹ for air-staged low- NO_x burners. Air-staging alone cannot, however, reduce the formation of oxides of nitrogen contained in the char residue during its subsequent heterogeneous combustion. The char will typically contain around 50% of the nitrogen in the coal and 10-30% of this may be converted to NO_x ^{1,2}. Techniques to reduce overall emissions of NO_x beyond this limit are available (e.g. fuel staging/reburning, SCR and SNCR) but these will incur additional installation and operating costs².

Because of its relevance for the performance of air-staged low- NO_x burners the pattern of nitrogen release from coals, and in particular the volatile/char nitrogen split, has received considerable attention. It is now well-known that conventional proximate analysis tests based on relatively slow heating of a bulk coal sample in a crucible do not give either accurate total volatile yields or nitrogen release data for devolatilization in PF combustion, where well-dispersed coal is heated rapidly (approx. 10^5 K/s) to high temperatures (approx. 1500°C).

To obtain better nitrogen release data for PF combustion, bench-scale tests based on rapid heating of coal entrained in a laminar (e.g.³) or turbulent (e.g.¹) stream of gas have been widely used. Entrained-flow tests have the advantage that heating rates and peak temperatures similar to those encountered in PF combustion can be attained, although residence times are generally limited to 1 s or less by the length of the reactors. Total volatile yields, however, usually have to be estimated using ash-tracer methods. This can introduce some uncertainty into the estimation of the total volatile yield, and hence also nitrogen release, particularly for coals with a low ash content. Entrained flow reactor studies (i.e. at high heating rates and short residence times) have generally indicated that the fraction of the coal nitrogen in the volatiles is close to the total volatile yield fraction for a wide range of final temperatures (e.g. ^{1,3,4,5}).

Wire-mesh reactors, in which the sample is held between two layers of woven wire mesh that act as an electrical resistance heater, have also been used to study the evolution of nitrogen during rapid heating. Typically samples of 5 mg or greater can be handled, sufficient for direct weighing measurement of the total volatile yield and 'conventional' micro elemental analysis of the chars. In general, heating rates (typically 10^3 - 10^4 K/s) and, more seriously, peak temperatures (usually $<1100^\circ\text{C}$) have been below values for PF combustion. Extended isothermal hold times can be used, however, with suitable reactor design. Maximum temperatures are limited mainly by the decreasing mechanical strength of the mesh material as it approaches its melting point. For the stainless steel meshes used in virtually all studies to date this limit is reached in the region of 1100°C , although workers at United Technologies Research Centre⁶ have demonstrated that higher temperatures (up to 1800°C) can be achieved with molybdenum or tungsten meshes. In the UTRC study Freihaut and Seery observed that, for a constant total run time of 10 s and a heating rate of 500-1000 K/s, at temperatures up to 1100°C the fraction of coal nitrogen volatilized was roughly equal to the total volatiles fraction but at higher temperatures there was 'a substantial increase in nitrogen evolution as HCN' with little accompanying weight loss. Nitrogen retention at high temperatures was found to be a function of rank, with higher rank coal chars retaining more.

Comparison of experimental measurements for nitrogen release in the entrained flow

and wire-mesh reactors thus suggests (in agreement with a theoretical analysis of earlier data⁷) that at temperatures of interest for PF combustion the hold time has a significant effect, while at lower temperatures the amounts evolved are insensitive to holding time. As a preliminary stage in an investigation of high-intensity coal devolatilization it was therefore decided to employ a recently-developed wire-mesh reactor with computerised temperature control, and capable of using molybdenum mesh for high-temperature experiments, to obtain more detailed measurements of the effect of holding time (and other key parameters) on nitrogen release. This information might also indicate whether or not any significant reduction in char N content (and hence subsequent char NO_x production) could be obtained from further devolatilization at elevated temperatures over timescales not achievable in present furnaces (i.e. >1 s) but perhaps feasible for specially designed systems.

EXPERIMENTAL

A rank series of two UK and a US bituminous coal was used, from low to high rank: Daw Mill (UK type 802), Kellingley (UK type 602) and Pittsburgh No. 8 (UK type 402, US HVB). The particle size range for all experiments, 150-180 μ m, was determined by the molybdenum mesh available. The Daw Mill (N 1.4% daf - analysis for prepared sample) and Kellingley (N 1.8% daf) were obtained as lump coal and ground to size in air in a motorised pestle and mortar with frequent sieving to remove undersize material. The Pittsburgh No. 8 (N 1.7% daf), from the Argonne Premium Coal Sample bank, was ground by hand. All samples were dried at 105°C overnight in a nitrogen-purged oven and stored under flowing nitrogen until used.

A modified version of the wire-mesh reactor previously developed at Imperial College⁹ was used for devolatilization experiments. The main changes in the design were the addition of a two-colour pyrometer for high-temperature measurement and a higher-current (400 A) AC power supply system. A diagram of the apparatus is shown in Fig. 1. All experiments were conducted in flowing helium at atmospheric pressure. Stainless steel mesh (AISI 304, 36 μ m wires x 63 μ m aperture) was used for runs up to 1000°C, molybdenum mesh (71 μ m wires x 140 μ m aperture) for runs at higher temperatures. Comparisons of results at 1000°C showed no significant differences between the two meshes. Total volatile yields were measured by direct weighing of the wire-mesh sample holder before and after experiments. The coal loading was 8-10 mg, spread within a 15 mm diameter circle at the centre of the sample holder.

Nitrogen contents of coals and chars were measured using a Carlo Erba elemental analyzer. Sample masses used for analysis were 0.5-0.9 mg, allowing duplicate runs in most cases on the char residue from a single wire-mesh experiment. Typically pairs of measurements (subsequently averaged) agreed within ± 0.05 percentage points. Volatile nitrogen yields were calculated by difference, from the char yields and coal and char nitrogen contents.

RESULTS AND DISCUSSION

The effect of peak temperature on total volatile and volatile nitrogen yields for heating rates of 10 K/s and 1000 K/s is shown in Fig. 2 (Daw Mill), Fig. 3 (Kellingley) and Fig. 4 (Pittsburgh No. 8, to 1000°C only). As expected, for 1000 K/s heating with zero hold time the total volatiles and volatile nitrogen values followed similar trends with temperature across the range 400°C to 1400°C.

At 10 K/s (approximately the same heating rate as the proximate VM test) total volatile yields were slightly reduced compared to the 1000 K/s data (in line with previous studies⁹) but volatile nitrogen yields were proportionally lower for both of the UK coals while for the Pittsburgh No.8 they appeared to be slightly higher. To investigate the effect of heating rate in more detail yields were measured over the range 10-4000 K/s to a final temperature of 1000°C (Figs 5-7) with a hold time of 10 s to ensure that the primary pyrolysis reactions had time to run to completion⁹. This confirmed a progressive reduction in evolved nitrogen with

decreasing heating rate for the two UK coals, but no clear trends emerged for the Pittsburgh No. 8, with any changes in yields being within experimental scatter. Overall, the effect of heating rate on nitrogen evolution appeared to decrease with increasing coal rank.

The effect of heating rate on nitrogen yields is tentatively attributed to differences in tar release, since it is well-known that the bulk of nitrogen evolved in the primary volatiles is contained in the tars⁶ and it has also been shown that it is mainly the tar yield that is affected by changes in heating rate⁹. The apparent variation with rank may then reflect the relatively lower thermal stability of (nitrogen-containing) low-rank tar precursors, which have a greater opportunity to undergo retrograde char-forming reactions during the longer periods between formation and subsequent evolution from the pyrolysing coal as tar that occur at the lower heating rate. The results confirm the inadequacy of the proximate volatile test for characterising nitrogen release under rapid-heating conditions.

Also shown in Figs 2 and 3 are total volatile and nitrogen yields for 1000 K/s heating to 1000-1400°C with 10 s hold time at peak temperature. For both coals, at 1000°C and 1200°C the total volatiles and volatile nitrogen yields with 10 s hold were virtually identical to the zero hold values. At 1400°C with 10 s hold, however, although the total volatiles were observed to increase only slightly there was a marked increase in the evolved nitrogen, in agreement with the previous observations by Freihaut and Seery⁶. The sensitivity to hold time at 1400°C is demonstrated in more detail by Figs 8 and 9, with total volatile yields unaffected by hold times up to 10 s, but nitrogen evolution progressively increasing.

The effect on the total volatiles/volatile nitrogen ratio of this enhanced loss of nitrogen at elevated temperatures is shown in Figs 10 and 11. The transition from the zero hold through intermediate holds to the 10 s values parallels differences between zero and extended hold time results from earlier studies, but obtained using a range of reactor types (e.g. ^{1,3,5,6,7}). Since the same reactor was used for all conditions in this study, however, the differences observed can be attributed entirely to the effect of hold time.

The demonstrated effects of heating rate and hold time at realistic PF combustion temperatures on nitrogen release point to the need to match the conditions in the combustor more closely for char/volatile nitrogen distribution measurements than, for example, for total volatile yield measurements. The relatively rapid initial decline in char nitrogen at 1400°C shown in Fig. 9 also suggests that a reduction in char nitrogen, and hence char NO_x formation, might be feasible with appropriate combustor design.

CONCLUSIONS

The sensitivity of coal nitrogen evolution to heating rate, final temperature and isothermal hold time during devolatilization has been investigated using a computer-controlled wire-mesh apparatus which allows these parameters to be varied independently without the need to change reactor type. The main conclusions, which agree with trends expected on the basis of previous studies are:

- (a) with zero hold time at peak temperature the fraction of coal nitrogen volatilized during rapid (1000 K/s) heating was directly proportional to total volatile yields for all temperatures up to 1400°C
- (b) with extended hold times (10s, up to 100s at 1000°C) at peak temperature the same correspondence was observed at up to 1200°C, but at 1400°C a progressive increase in nitrogen evolution occurred with longer hold times
- (c) volatile nitrogen yields from two lower-rank bituminous coals were also observed to decrease as the heating rate was reduced from 4000 K/s to 10 K/s,

but there was no significant effect of heating rate on yields from a higher-rank bituminous coal.

(d) volatile nitrogen yields exhibit greater sensitivity to experimental conditions than total volatile yields.

ACKNOWLEDGEMENTS

Financial support for this work was provided by the UK Science and Engineering Research Council under Grant GR/F89817. UK coal samples were supplied by British Coal.

REFERENCES

1. Nakamura, T, Smart, J. P., van de Kamp, W. L. and Morgan, M. E., *Effect of coal blends and qualities on the performance of a swirl stabilized internally air staged P. F. burner*, Proc. 1991 Int. Conf. on Coal Sci., Newcastle, 331-334.
2. Morrison, G. F, *Understanding pulverised coal combustion*, IEA Coal Research Report ICTIS/TR34, IEA, London, 1986.
3. Cahill, P., Smith, M. and Vallender, S. J., *Characterisation of British coals for low-NOx combustion*, Proc. 1991 Int. Conf. on Coal Sci., Newcastle, 319-322.
4. Sayre, A. N., Knill, K. J. and Smart, J. P., *Coal characterisation requirements for modelling pulverized coal flames*, Doc No F 88/y/13, IFRP, IJmuiden, Netherlands, 1991.
5. Pohl, J. H. and Sarofim, A. F., *Devolatilization and oxidation of coal nitrogen*, Sixteenth Symposium (Int.) on Combustion, The Combustion Institute, 1977, 491-501.
6. Frelhaut, J. D. and Seery, D. J., *An investigation of yields and characteristics of tars released during the thermal decomposition of coal*, ACS DFC 26(2), 1981, 133-148.
7. Solomon, P. R. and Colket, M. B., *Evolution of fuel nitrogen in coal devolatilization*, Fuel 58, 1978, 749-755.
8. Gibbins, J. R., King, R. A. W., Wood, R. J. and Kandiyoti, R., *Variable heating rate wire-mesh apparatus*, Rev. Sci. Instrum. 60, 1989, 1129-1139.
9. Gibbins, J. R. and Kandiyoti, R., *Coal pyrolysis yields from fast and slow heating in a wire-mesh apparatus with a gas sweep*, Energy & Fuels 2, 1988, 505-511.

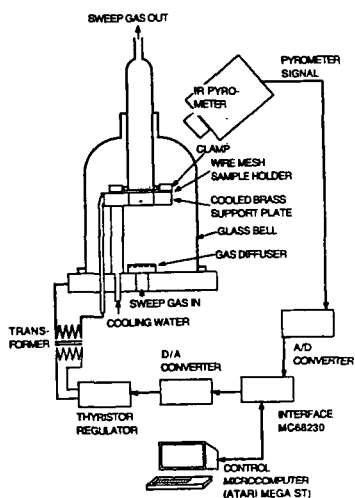


Fig. 1 Wire mesh apparatus

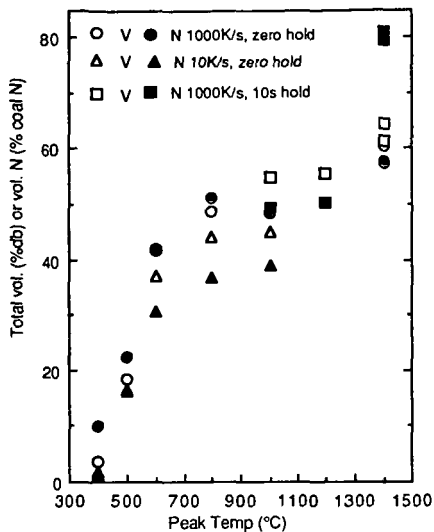


Fig. 2 Effect of peak temperature on yields from Daw Mill coal

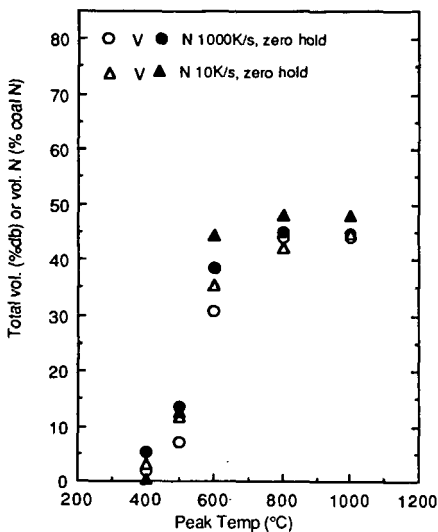


Fig. 4 Effect of peak temperature on yields from Pittsburgh No. 8 coal

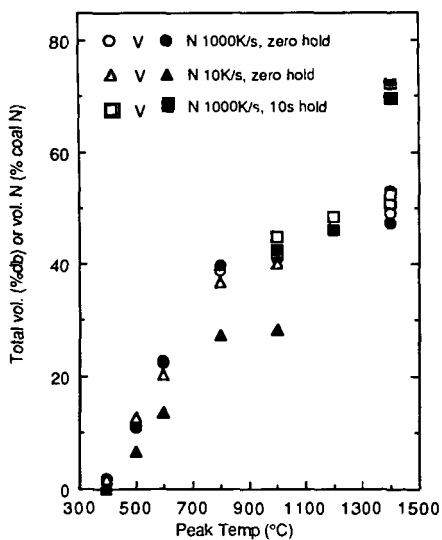


Fig. 3 Effect of peak temperature on yields from Kellingley coal

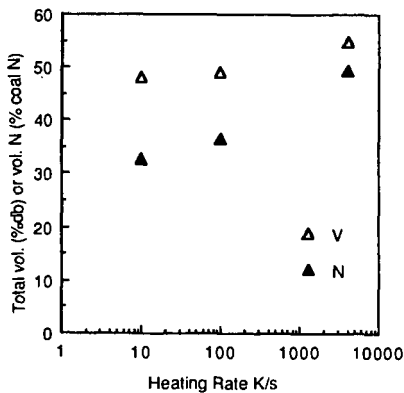


Fig. 5 Effect of heating rate on yields from Daw Mill coal

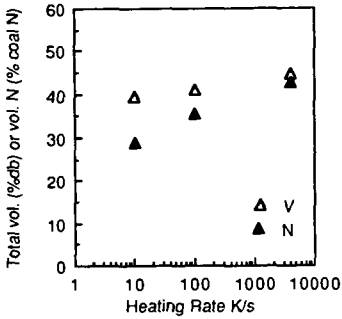


Fig. 6 Effect of heating rate on yields from Kellingley coal

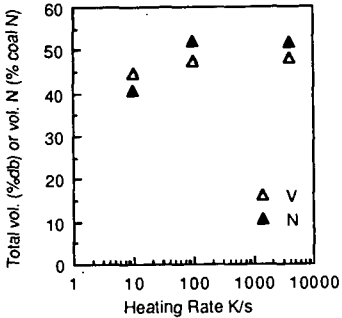


Fig. 7 Effect of heating rate on yields from Pittsburgh No.8 coal

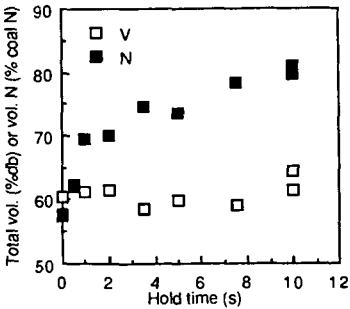


Fig. 8 Effect of hold time at 1400°C for Daw Mill coal

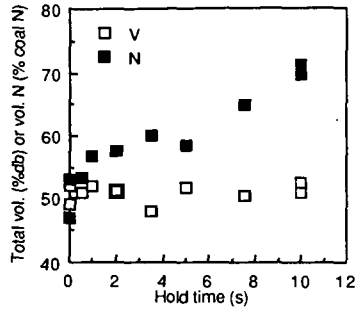


Fig. 9 Effect of hold time at 1400°C for Kellingley coal

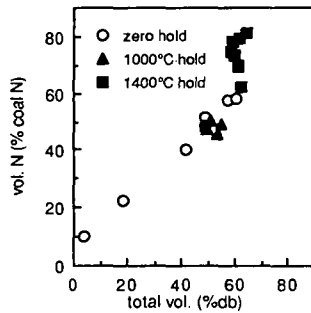


Fig. 10. Volatile N vs. total volatiles for Daw Mill coal

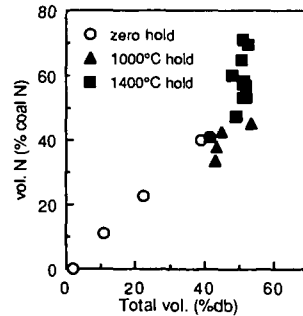


Fig. 11. Volatile N vs. total volatiles for Kellingley coal

**MONITORING OF CHLORINE IN COAL
DURING PYROLYSIS BY SIMULTANEOUS TG/FTIR TECHNIQUE**

Dakang Shao and Wei-Ping Pan
Department of Chemistry
Western Kentucky University
Bowling Green, KY 42101

Chen-Lin Chou
Illinois State Geological Survey
615 East Peabody Drive
Champaign, IL 61820

Keywords: chlorine in coal, coal pyrolysis, TG/FTIR

INTRODUCTION

At least half of the known economically minable coal resources in Illinois have a high chlorine content (>0.3%). Coal with such high chlorine content may be difficult to market because the chlorine may not only enhance boiler corrosion rate of metal tube walls in utility and industrial boilers, but also contribute to environmental pollution. However, assessing the effect of chlorine in coal on boiler corrosion is a complex problem. There are many variables which may synergistically affect the corrosion rate in a boiler, and there is a lack of data to isolate individual factors.

Boiler corrosion is controlled by several other factors, in addition to the chlorine content, including temperature, oxidizing-reducing conditions, alkali contents, sulfur content, and ash composition. For several decades, chlorine-enhanced corrosion has been attributed to the presence of chloride which prevents the formation of a protective layer of oxides on metal surfaces. Direct HCl attack is also a potential corrosion mechanism. Chlorine-enhanced corrosion is believed to be more significant under a reducing condition than an oxidizing condition. Under the oxidizing condition, the metal surface is coated with a protective oxide layer, and corrosion is constrained by diffusion of corrosive gaseous species through the protective layer. In contrast, under the reducing condition the deposits on metal surfaces are a mixture of oxides and sulfides, which do not form as good a protective layer as compact oxides. Thus, corrosion can be significant in areas under a reducing atmosphere. The mechanism of boiler corrosion is related to the relative abundances of gaseous species (HCl, NaCl, KCl, Cl₂, SO₂, H₂S, etc.) in combustion gases, which in turn are related to the composition of feed coal and combustion conditions.

Several studies have been done on the behavior of chlorine in the British coal during pyrolysis/combustion. Edgecombe concluded that chlorine in the British coals was liberated as HCl gas only in air at 200°C, whereas Daybell concluded that chlorine in the coals was liberated as HCl gas also in oxygen-free nitrogen at 200°C.

Gibb concluded, however, that the British coals gave off 97% of its chlorine as HCl gas in oxygen-free nitrogen at 258^oC. There is a lack of data concerning the behavior of chlorine in the Illinois coals during pyrolysis/combustion.

This study is part of an on-going the project: Behavior of Sulfur and Chlorine in Coal during Combustion and Boiler Corrosion. One important purpose of this project is to determine the gaseous species in pyrolysis/combustion gases and the kinetics of their release during pyrolysis/combustion. The results will lead to a better understanding of the relation between the chlorine and alkali levels in feed coal and boiler corrosion can be better understood. The purposes of this study were to identify HCl gas from the gaseous species evolved from the Illinois coals and to observe the behavior of chlorine in the coals during pyrolysis by using the simultaneous TG-FTIR techniques. We also tried to establish the relation between the amount of chlorine liberated as HCl gas and temperature.

EXPERIMENTAL PROCEDURES

Samples

Two coal samples from the Illinois Basin Coal Sample Program were used in the experiments: IBC-109 (0.42% chlorine, 1.13% sulfur) and IBC-106 (0.02% chlorine, 3.77% sulfur).

Identification of gaseous chlorine species in pyrolysis gas and determination of gas release profile using thermal gravimetry (TG) in conjunction with Fourier transform infrared spectroscopy (FTIR).

Using the TG-FTIR system, the gases produced on a DuPont-951 TGA are analyzed by FTIR spectroscopy using the Perkin Elmer-1650 FTIR spectrometer. Thermogravimetry provides a means for measurement of heating condition and weight change. The system is able to continuously monitor the weight change of a coal sample as well as to quantitatively determine the gases evolved (CO, CO₂, COS, SO₂, HCl, H₂O, NO, NO₂, NH₃, CH₄, C₂H₄, C₃H₆, etc.) during pyrolysis. The TGA furnace is connected to the 100 x 24 mm gas cell through a 1-mm Teflon tube. Both the Teflon line and the gas cell can be heated by heating coils up to 250^oC. The time lag between the sample and the gas cell is one minute with a gas flow of 50 ml/min; the spectrum can be taken every minute. This also includes the time it takes to store the spectrum on the computer. Calibration of the FTIR is made using pure gases or prepared gas mixtures.

Approximately 100 mg of coal was used in each TG-FTIR experiment. The pyrolysis was conducted with a nitrogen gas (flow rate 50 ml/min), a temperature program from ambient to 900^oC, a heating rate of 10^oC/min. The FTIR scanning period was four seconds.

Determination of gaseous chlorine release profile using ion chromatography (IC)

Several filtering test tubes with gas dispersers were connected in a series with TG-FTIR to collect the pyrolysis gases in different temperature ranges; three trapping solutions connected in a series were used for each temperature range. The HCl vapor was trapped in 90 ml of 0.01% sodium carbonate solution and the solution was diluted to 100 ml. The solution was analyzed for chlorine concentration by the Shimadzu HIC-6A ion chromatographic system.

RESULTS AND DISCUSSION

TG/DTG Analysis

The thermogravimetric curves obtained from the pyrolysis of samples IBC-109 and IBC-106 are shown in Figure 1. The temperature of the maximum rate of weight loss (T_{max}), % weight loss, and the maximum rate of the weight loss (R_{max}) in %/min are listed in Table 1. Two samples have similar curves of weight loss and weight-loss rate, but their amounts of weight loss and rates of weight loss are slightly different. Weight loss occurred in two major temperature ranges: between 20° and 150°C and between 350° and 850°C. In the 20° - 150°C range, IBC-109 had a weight loss of 4.23%, and IBC-106 6.4% as a result of the loss moisture. The second weight loss occurred in the temperature range of 350° - 850°C, IBC-109 had a weight loss of 26.1% and IBC-106 32.3%. These weight losses correspond to the loss of the volatile matter, and are comparable to the volatile matter content of the coals determined with Leco MAC-400 analyzer (32.0% of IBC-109 and of 35.9% of IBC-106 on an as-received basis).

Table 1. Results of TG/DTG analysis on coal samples IBC-109 and IBC-106.

Sample	Temp. Range	T_{max}	Weight Loss	R_{max}
IBC-109	20.0°-149.8°C	87.1°C	4.2 %	0.56 %/min
	149.8°-351.0°C		1.7 %	
	351.0°-889.7°C	450.5°C	26.1 %	1.26 %/min
IBC-106	20.0°-150.0°C	87.1°C	6.4 %	0.85 %/min
	150.0°-348.7°C		1.5 %	
	348.7°-833.1°C	422.5°C	32.3 %	2.71 %/min

FTIR Analysis

The gases evolved from coal during pyrolysis were identified by FTIR spectroscopy. In order to identify the evolved gases, we analyzed some of the pure gases by FTIR, which were suspected to be present in the evolved coal gases. Figure 2 shows the standard

FTIR spectra of the pure gases (HCl, SO₂, CO, CO₂, H₂O and CH₄). The data of FTIR for the rest of the evolved gases were taken from the literature. Figure 3 shows the FTIR spectra of two samples at about 490°C. The volatile species identified include carbon dioxide (CO₂, 2360 cm⁻¹), carbon monoxide (CO, 2175 CO cm⁻¹), sulfur dioxide (SO₂, 1360 cm⁻¹), carbon oxide sulfide (COS, 2072 cm⁻¹), water moisture (H₂O, 1683 cm⁻¹), ammonia (NH₃, 966 cm⁻¹), hydrogen cyanide (HCN, 713 cm⁻¹), nitrogen monoxide (NO, 2050 cm⁻¹), nitrogen dioxide (NO₂, 1468 cm⁻¹), methane (CH₄, 1304 cm⁻¹), ethylene (C₂H₄, 950 cm⁻¹), propylene (C₃H₆, cm⁻¹), and hydrogen chloride (HCl, 2962 cm⁻¹).

The gas release profiles from coal IBC-109 determined by TG-FTIR analysis are shown in Figure 4-1 and 4-2, respectively, and those for sample IBC-106 are shown in Figure 5-1 and 5-2, respectively. A quantitative identification of HCl, however, is not straightforward because both CH₄ and HCl absorb around 2962 cm⁻¹. In order to resolve the contribution of each gas to the peak at 2962 cm⁻¹, the standard FTIR spectra of pure HCl and CH₄ were analyzed (Figure 6). Absorption peaks of methane occur in two regions: region I with wavenumbers from 3207 to 2679 cm⁻¹, and region II from 1392 to 2679 cm⁻¹. So the absorption peaks of HCl overlap completely with the peaks in the region I of CH₄.

In determining CH₄ gas, some peaks in region II (such as 1304 or 1269 cm⁻¹) can be used; the CH₄ release profiles (peak absorbance intensity vs. temperature) for IBC-109 and IBC-106 are shown in Figures 7 and 8, respectively. The gas release profile of HCl may be established as described in the following. First, the behavior of the peaks in region I where peaks of CH₄ and HCl overlap may be compared with the peaks in region II (CH₄). The gas release profiles of IBC-109 are shown in Figure 7 for the 1304 cm⁻¹ and 1269 cm⁻¹ peaks from region II (CH₄), and the 2962 cm⁻¹ peak from region I (CH₄ + HCl). Both profiles of 1304 cm⁻¹ and 1269 cm⁻¹ (CH₄) have a peak at 550°C with different intensities. In contrast, the profile of 2962 cm⁻¹ (HCl + CH₄) has a peak at 490°C. This temperature is significantly lower than the 550°C peaks of CH₄. Thus, the 490°C peak of 2962 cm⁻¹ is mainly due to HCl, with a limited component of CH₄. Furthermore, the intensity ratio between the 2962 cm⁻¹ and 1304 cm⁻¹ peaks of the high-chlorine coal IBC-109 (0.42%) is 0.67; this is much larger than a ratio of 0.30 for the low-chlorine coal IBC-106 (Figure 8). Hence, the higher intensity of the 2962 cm⁻¹ peak of IBC-109 is caused by its higher chlorine content (0.42%) than that of IBC-106 (0.02%). The HCl release profile may be obtained by subtracting the CH₄ component from the profile of 2962 cm⁻¹. The resulting profile should be close to that of curve (b) in Figure 8. The HCl gas appears to be released between 300° and 700°C with a peak slightly below 490°C during pyrolysis.

Determination of Chlorine in Pyrolysis Gas by Ion Chromatography

Trapped in the sodium carbonate solution, the chlorine released in each temperature range during pyrolysis of the high-chlorine

coal IBC-109 was determined quantitatively by ion chromatography (IC). The data are summarized in Table II and the chlorine release profile is shown in Figure 9. The IC analysis indicates that the gaseous chlorine (mainly due to the HCl gas) is released mainly between 250^o and 700^oC with a peak in the 450^o - 500^oC range, and about 90% of chlorine in the coal was evolved during pyrolysis.

Table II. Results of determination of gaseous chlorine released in different temperature ranges by IC analysis.

Temp Range(^o C)	Amount of Cl(ug)	%Cl vs. Total Cl
100 - 250	19.95	4.75 %
250 - 300	28.30	6.74 %
300 - 350	40.02	9.53 %
350 - 400	43.19	10.28 %
400 - 450	47.05	11.20 %
450 - 500	47.42	11.29 %
500 - 550	41.87	9.97 %
550 - 600	41.33	9.84 %
600 - 650	40.70	9.69 %
650 - 700	29.88	7.11 %
Total	379.90	90.45 %

CONCLUSIONS

The pyrolysis-thermogravimetry-Fourier transform infrared (TG-FTIR) analysis was carried out on two coal samples: the high-chlorine coal IBC-109 and the low-chlorine IBC-106: The volatile species identified by the FTIR spectroscopy include CO₂, CO, NO, NO₂, NH₃, HCN, SO₂, COS, H₂O, CH₄, C₂H₄, C₃H₆, and HCl. The absorption peaks of HCl overlap with those of CH₄. However, the 2962 cm⁻¹ peak is mainly due to HCl because this peak is stronger for the high-chlorine coal IBC-109 than that of the low-chlorine coal IBC-106. The gas release profile of 2962 cm⁻¹ has a peak at 490^oC, significantly lower than that of wavenumber 1304 cm⁻¹ (CH₄). We will obtain the HCl release profile by subtracting the CH₄ component from the from the 2962 cm⁻¹ profile following appropriate calibration. The resulting profile should be close to curve (b) of Figure 8. It appears that HCl the high-chlorine coal was evolved between 300^o and 700^oC with a peak slightly below 490^oC during pyrolysis. This was consistent with the results obtained by IC analysis.

ACKNOWLEDGEMENTS

This work has been financially supported by Center for Research on Sulfur in Coal.

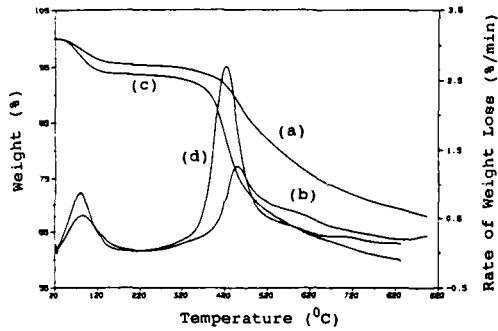


Figure 1. The thermogravimetric curves of coals IBC-109 and IBC-106. (a) TG curve of IBC-109, (b) DTG curve of IBC-109, (c) TG curve of IBC-106, and (d) DTG curve of IBC-106.

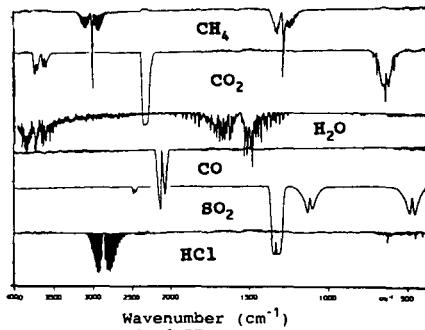


Figure 2. Standard FTIR spectra of some pure gases.

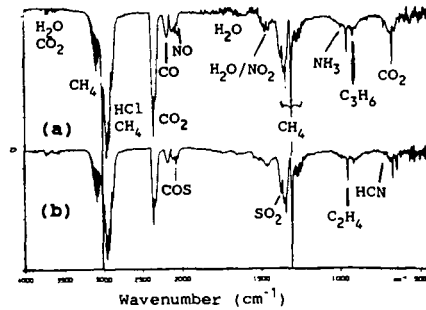


Figure 3. The TG-FTIR spectra of coals IBC-109 and IBC-106. (a) IBC-109 at about 490°C, (b) IBC-106 at about 490°C.

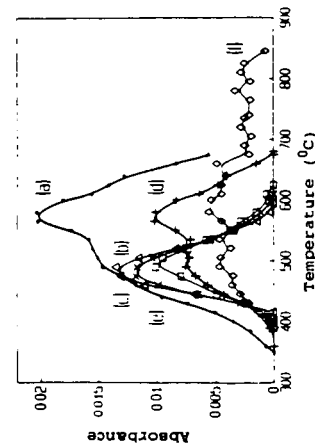


Figure 4-1. Gas release profile by TG-FTIR analysis for the high-chlorine coal IBC-109. (a) COS (2072 cm^{-1}), (b) $\text{NO}_2/\text{H}_2\text{O}$ (1468 cm^{-1}), (c) H_2O (1683 cm^{-1}), (d) NO (2050 cm^{-1}), (e) NH_3 (966 cm^{-1}), and (f) HCN (713 cm^{-1}).

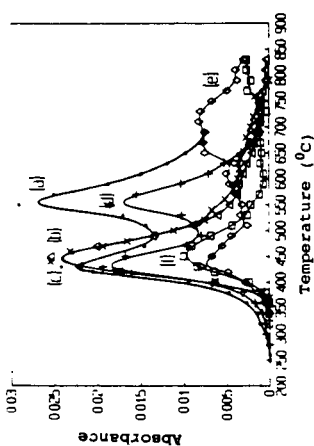


Figure 5-1. Gas release profile by TG-FTIR analysis for the low-chlorine coal IBC-106. (a) COS (2072 cm^{-1}), (b) H_2O (1683 cm^{-1}), (c) $\text{NO}_2/\text{H}_2\text{O}$ (1468 cm^{-1}), (d) NO (2050 cm^{-1}), (e) HCN (713 cm^{-1}) and (f) NH_3 (966 cm^{-1}).

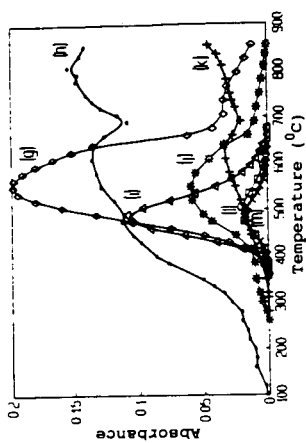


Figure 4-2. Gas release profile by TG-FTIR analysis for the high-chlorine coal IBC-109. (g) CH_4 (1304 cm^{-1}), (h) CO_2 (2360 cm^{-1}), (i) HCl/CH_4 (2962 cm^{-1}), (j) SO_2 (1360 cm^{-1}), (k) CO (2175 cm^{-1}), (l) C_2H_4 (950 cm^{-1}), and (m) C_3H_6 (912 cm^{-1}).

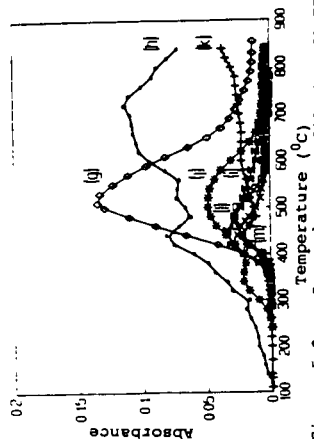


Figure 5-2. Gas release profile by TG-FTIR analysis for the low-chlorine coal IBC-106. (g) CH_4 (1304 cm^{-1}), (h) CO_2 (2360 cm^{-1}), (i) HCl/CH_4 (2962 cm^{-1}), (j) SO_2 (1360 cm^{-1}), (k) CO (2175 cm^{-1}), (l) C_2H_4 (950 cm^{-1}), and (m) C_3H_6 (912 cm^{-1}).

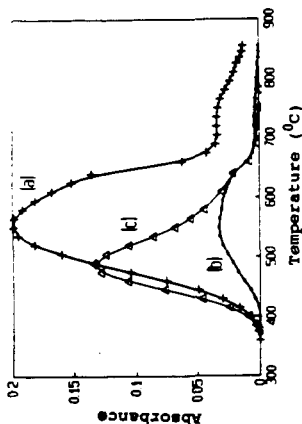


Figure 7. Release profile of CH_4 (1304 cm^{-1} , and 1269 cm^{-1}) and the $\text{HCl} + \text{CH}_4$ (2962 cm^{-1}) by TG-FTIR analysis of coal IBC-109. (a) CH_4 (1304 cm^{-1}), (b) CH_4 (1269 cm^{-1}), (c) HCl/CH_4 (2962 cm^{-1}).

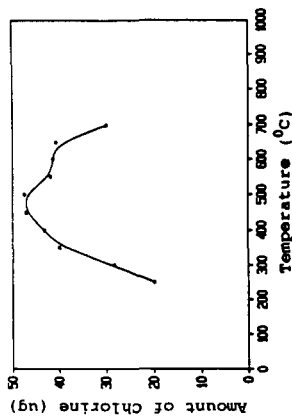


Figure 9. Gaseous chlorine release profile by IC analysis for the high-chlorine coal IBC-109.

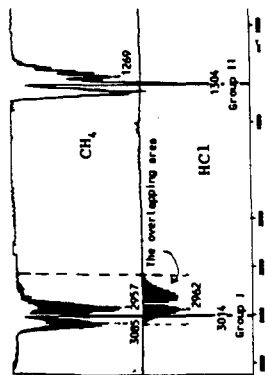


Figure 6. Comparison of the standard FTIR spectra of CH_4 and HCl .

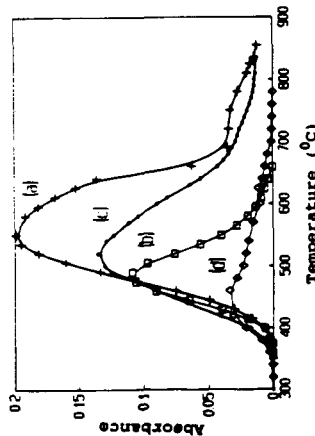


Figure 8. Comparison of gas release profiles of IBC-109 and IBC-106. (a) CH_4 (1304 cm^{-1}) from IBC-109, (b) HCl/CH_4 (2962 cm^{-1}) from IBC-109, (c) CH_4 (1304 cm^{-1}) from IBC-106 and (d) HCl/CH_4 (2962 cm^{-1}) from IBC-106.

LIQUID FUELS FROM SYNGAS - PROGRESS REPORT

G. Alex Mills
Department of Chemical Engineering
University of Delaware
Newark, DE 19716

Keywords: Syngas Catalysis, Oxy-Fuels, Synthetic Fuels

INTRODUCTION

Revolutionary changes lie immediately ahead for manufacture and use of transportation fuels. What will be their composition, technology for their manufacture and economic impact? On what basis will decisions be made? Major new requirements for fuel composition and the time table for their adoption have been set by the Clean Air Act Amendment of 1990. Fuel values have become strongly dependent on environmental performance criteria. It has slowly become realized that such criteria have changed economics of fuel values. Higher environmental performance values justifies higher prices. For instance, methyl-tertiary-butyl ether, MTBE, sells for 1.5 times the price of gasoline.

Fuels manufactured from synthesis gas (H_2 , CO, CO_2) offer special opportunities based both on environmental (decrease in CO and O_3) and energy performance (high octane or cetane ratings). Further, syngas can be made not only from abundant coal and gas, but also from biomass. Biomass has the advantage of providing a renewable energy source. It also has the special advantage of avoiding net production of CO_2 and so helps to minimize the greenhouse effect.

SOCIETAL FACTORS INFLUENCING FUELS SELECTION

Several recent events now shape the selection of fuels and, consequently, R & D relative to their manufacture and use. Pollution assessments EPA has determined that >100 city areas have not attained a sufficiently low level of CO or O_3 in their air deemed essential for health. This was influential in passage of the Clean Air Act Amendment of 1990 which requires, among other things: 1992 Gasoline in 44 city areas in which winter fuels must contain 2.7% oxygen (equivalent to 15% MTBE or 8% EtOH), 1995 Gasoline must contain 2% oxygen in 9 city areas year round, 1998 Fleets of 10 or more vehicles in ozone non-compliance areas to have at least one vehicle capable of using alternative fuel. In an understatement the administration has said that "The CAAA's of 1990 were not intended to be an energy policy, but because of their major impact on the energy industry, they will have significant effect on energy use."

Reformulated Gasoline ARCO led the way by marketing a less polluting gasoline with at least 1% O (contains MTBE) lower benzene and lower vapor pressure. M85 fuel, containing 85% methanol and 15% hydrocarbons, is increasingly marketed in California and elsewhere. Flexible Fuel Vehicles, FFV's, capable of using alcohol, gasoline, or mixtures, have been developed, tested extensively, and are near mass production. Exemption of federal tax for gasoline known as Gasohol, containing 10% agricultural ethanol (equivalent to 60 cents/gal ethanol), extended to ethyl-tertiary-butyl ether, ETBE. National Energy Strategy 1991 was issued by the U.S. Department of Energy. Increased oil production was stressed. No increase in CAFE was proposed. Increased support, incentives, and requirements were advocated for alternative fuels, particularly for renewable fuels.

NEAR TERM PROGRESS - HYDROCARBON FUELS

Several new or improved catalytic processes to provide fuel from syngas have been installed or are in an advanced development stage. Methanol-to-Gasoline The MTG process, developed by Mobil in partnership with DOE, has been in operation in New Zealand for six years. It supplies the equivalent of 1/3 of New Zealand's gasoline requirements. First, and fundamental to the concept for its installation, this plant meets the national policy of relative energy independence. Now privately owned

(25% by Mobil Oil continued) the investment debt has been paid. Gasoline is being exported to Japan, valuable there because of its high octane. Improvements in the MTG process have been made since its New Zealand installation in fixed-bed form. The TIGAS variation, developed by Topsoe (1), provides for plant savings by process integration. Alternatively, a fluid bed catalytic version of MTG, having improved economics (2), has been demonstrated on a semicommercial scale.

Slurry FT + ZSM 5 This concept consists of slurry phase FT followed by upgrading of the products over a ZSM 5 catalyst. Two modes of operation were established - a low wax and a high wax mode (3). The wax can be further upgraded to gasoline and diesel fuel. Excellent yields of high quality fuels were demonstrated, Table 1. Fixed Bed FT + Hydrocrack A problem with the usual FT process is the production of methane. The Shell Oil Company is pioneering the concept of carrying out syngas hydrogenation using a catalyst, possibly based on cobalt rather than iron, under conditions that result in a high degree of polymerization. When operated with an alpha (ASF relationship) of 0.9 or above, the reactor product consists of high molecular weight alkanes, Fig. 1 (4). Modern technology provides that the wax product can be efficiently hydrocracked to produce a kerosene and high quality diesel fuel. It is estimated that the energy efficiency of gas to product is 60%. A large plant in Malaysia is scheduled to come on stream in 1993.

Cobalt Catalysts Goodwin has pointed out (5) that a number of patents have been issued involving cobalt instead of iron for slurry FT, Table 2. It is proposed that the second metal functions by permitting reduction of the cobalt salt at a lower temperature, thereby providing a larger cobalt metal surface area and higher activity. The question of the difference between Fe and Co on removal of oxygen as H₂O or CO₂ is of considerable interest.

Slurry FT Using Landfill Gas for Syngas The Fuel Resources Development Company, a subsidiary of Public Service Company of Colorado, has built a small plant near Denver in which landfill methane is converted to syngas and then to hydrocarbon fuels using the slurry catalyst technique (6), pioneered by Koelbel in Germany (1). A Fe catalyst is used. Tests by Detroit Diesel Corp. (7) showed an excellent diesel fuel can be made, Table 3, which on combustion showed a surprisingly favorable particulate reduction. It was concluded that the presence of oxygenates contributed significantly to the particulate reduction. The fuel contained 12% oxygenates. This draws attention to the potential for oxygenates in diesel fuels.

A pilot plant trial of slurry FT is planned in 1992 at the Air Products pilot plant at La Porte, TX, inspired by the projected improved economics, discussed later.

NEAR TERM PROGRESS - OXY-FUELS

The initial rationale for use of oxygenates in fuels was based on their high octane properties. Now, the dominant benefit is regarded as environmental. It is believed that CO and O₃ pollution from automotive fuel combustion is lowered about 25% by their use. Also in their favor is the fact that they can be made from sources other than petroleum including biomass. Regulations arising from the Clean Air Act Amendments are powerful determinants. The remarkable growth of MTBE (8) dominates the changes in fuel composition and manufacture (now 6 MM gallon per day for MTBE vs. 300 for gasoline in USA) Fig. 2. Much of the technology for MTBE manufacture, Fig. 3, has long been known. One interesting technical innovation is the use of the alcohol + isobutylene to ether conversion catalyst as distillation column packing. This application helps overcome reaction equilibrium limitations and so enhances higher ether productivity.

The extensive growth in MTBE has now resulted on an impending shortage in isobutylene, generally obtained as a "by-product" from catalytic cracking. This has inspired research searching for cracking catalysts which produce larger amounts of suitable olefins. The shortage in isobutylene is being met by worldwide installation of plants for dehydrogenation of isobutane by processes licensed by United Catalysts (Houdry Catofin), Phillips Petroleum (Star), UOP, and Snamprogetti. It is of considerable interest that isobutylene can be manufactured from syngas. This involves first production of isobutanol, IBA, which is catalytically dehydrated.

The technology for hydrogenation of CO to mixed alcohols has been developed extensively. Product distributions from several processes offered commercially are shown in Table 4. It has been noted that in the Lurgi process 60% of the C₄ alcohols is isobutanol. One research report (9) claims 59% isobutanol from syngas using an optimized catalyst. The use of catalysts containing alkali, particularly cesium, increases isobutanol formation, Fig. 4 (10). A trial is planned in 1992 to test such a catalyst in slurry form in the Air Product's pilot plant in La Porte. It can be noted that mixed alcohols containing C₁, C₂, C₃ is not now well regarded. MTBE is considered to be much more fungible (ie compatible, trouble free). One important technological feature noted in Table 3 is the ability to recycle lower alcohols to produce higher alcohols. There is some evidence that C₂ and C₃ alcohols are so converted, but MeOH is converted back to syngas. However, even if the methanol is converted to syngas, this ultimately is transformed into higher alcohols. This is a distinct advantage over similar hydrocarbon synthesis where methane which is formed does not revert to syngas, but must go to a separate and costly reforming step.

A further consideration of IBA as a fuel is its potential as a competitor of MTBE. IBA has a good octane rating and lower vapor pressure, Table 5. IBA is highly hydrocarbon-soluble and so does not suffer disadvantages of lower alcohols for phase separation in the presence of water. Thus starting with IBA, is it better to use it as such or convert to MTBE? Starting with isobutylene, is it better to add H₂O or MeOH? It also should be mentioned that there are a number of other oxygenates which have potential markets. These include not only other ethers such as TAME, DME, diisopropyl ether, but also dimethyl carbonate and other oxygenates.

More economical synthesis of methanol has been developed by extensive research and pilot plant testing using a slurry catalyst system at Air Products pilot plant at La Porte with support of DOE. Extensive background practical engineering know-how information was established regarding fluid dynamics, catalyst stability, etc. Major improvements in through-put have been achieved by techniques such as more efficient gas distribution configurations. Decreased investment costs have been made possible by demonstration of simpler heat exchange equipment. Also a big step forward was catalyst systems which could catalyze shift as well as synthesis, thus providing the means of being able to use directly low H₂/CO ratio gas from modern gasifiers. Recently also, it has been demonstrated (11) that by coproduction of MeOH and dimethyl ether, DME, much higher CO conversion per pass is achieved since the same thermodynamic limitations do not apply. This provides for lower recycle costs and also potential for manufacture from DME.

It also should be noted that the Eastman plant which manufactures acetic anhydride from syngas from lignite also produces and markets methanol. It is certainly a convincing evidence of the economic viability that this plant has been expanded recently. It is claimed that the key for success is efficient integration of modern technology.

MID/LONGER TERM

A wide variety of novel syngas conversion catalysts have been investigated, testing novel concepts, particularly for synthesis of oxygenates. Technical progress reviewed in 1988 (1) included research ideas involving partial poisoning, metal dispersion control, melts, alloys, metals in zeolites, multimetals, sulfides, and biocatalysts. Only a few will be mentioned because of space limitations. Isobutanol synthesis has been referred to above. Catalysts derived from certain rare earth/copper alloys, such as CeCu₂, have been found to exhibit extraordinarily high catalytic activity for hydrogenation of CO to methanol (1). They are active at 100°C. Unfortunately, these catalysts are deactivated by low concentrations of CO₂. Possibly new methods of preparation or purification of syngas free from CO₂ can make these catalysts of practical interest.

Dual function catalysts, such as Rh-MoO_x/Al₂O₃, have been found to activate CO by Rh and hydrogen by MoO_x sites not inhibited by CO (1). The enhanced kinetics then provides highly active catalysts

and point the direction for future design of even more active catalysts for selective production of alcohols at low temperature.

There is a new interest in systems involving CO activation using base catalysts such as KOCH_3 (12). Methyl formate is the first formed which is subsequently hydrogenated to methanol by a catalyst such as copper chromite. $\text{CH}_3\text{OH} \rightarrow \text{HCOOCH}_3 + \text{H}_2 \rightarrow 2\text{CH}_3\text{OH}$. A limitation has been that such base catalyst are inactivated by H_2O or CO_2 . New interest has been sparked by the report that there is a tolerance for low levels of H_2O and CO_2 by simultaneous use of both catalysts.

For the longer term, there is promise of progress from information developed by surface science and biocatalysis studies as well as new approaches such as use of artificial intelligence or computer graphics for catalyst design.

ECONOMICS

Because of thermodynamic limitations, the energy efficiency of indirect liquefaction is lower than for direct liquefaction of coal. It has been erroneously stated that, therefore, indirect is more costly than direct liquefaction. However, the cost of a synthetic fuel is much more dependent on plant investment costs than on raw materials costs. Manufacturing charges include not only costs directly attributable to operation of an expensive plant such as maintenance and insurance, but also necessary charges for profit and taxes. For a generalized synfuels from coal plant, (13) production cost, $\$10^6$ Btu, is 3.21, made up of coal 1.42, operating costs 0.19, and capital charges of 1.60. Selling price required includes profit 1.42, taxes 1.42 equal to 6.05 (ca $\$36/\text{bbl}$). As mentioned above, a further consideration of synfuel economics is the value placed on their environmental performance qualities.

Perhaps the most striking economic news is the estimates which have been made for use for the production of diesel and gasoline from syngas using of modern gasifiers coupled with slurry FT. The resulting increase in energy efficiency and decrease in selling price is shown in Table 6 (14). The $\$42/\text{bbl}$ price for gasoline/diesel which makes slurry FT is as low or lower than direct liquefaction for the same products (not crude oil) made by direct liquefaction of coal.

It may be pertinent to notice the costs of subsidization for the Gasohol program in the USA (15). The federal tax benefit is 60 cents/gallon of alcohol used in Gasohol. In 1987 there were 55,400 barrels/day ethanol fuel sales corresponding to a subsidy of about $\$500,000,000$ annually. There is an additional subsidy in the corn used to produce the ethanol.

ACKNOWLEDGEMENT

Preparation of this report was supported by the National Renewable Energy Laboratory, Department of Energy, Contract HZ-1-11208-1.

REFERENCES

1. G. A. Mills, Catalysts for Fuels from Syngas - New Directions for Research, IEACR/09, IEA Coal Research, London, IEACR 8901, Nat. Tech. Inf. Serv., Springfield, VA 22161 (1988).
2. R. D. Srivastava, P. Zhou, G. J. Stiegel, V. U. S. Rao, G. Cinquegrane, Direct Conversion of Methane to Liquid Fuels and Chemicals, Specialists Report, Vol. 9, Catalysis, Royal Society, London (1992), *in press*
3. W. O. Haag, J. C. Kuo, I. Wender, In Coal Gasification: Direct Application and Synthesis of Chemicals and Fuels, DOE/ER-0326, DE 8800129, Nat. Tech. Info. Serv., Springfield, VA 22161 (1987).
4. F. G. A. Van den Berg, J. H. E. Glezer, W. M. H. Sachtler, J. of Catalysis, **23**, 340 (1985).
5. J. Goodwin, Preprints, Div. Fuel Chem., Am. Chem. Soc., **36**, 156 (1991).
6. A. Rowley, SYNHYTECH - Developing Environmentally Responsible Energy Resources, Proc. Indirect Liquefaction Contractors Meeting, DOE, 291 (1990).

7. J. E. Benethum, R. E. Winson, Towards Improved Diesel Fuel, SAE 912325 (1991).
8. M. B. Haigwood, Worldwide MTBE Capacity Growing at Accelerated Pace, Fuel Reformulation, 1 (1) 52 (1991).
9. W. Keim, W. Falter, Catalysis Letters, 3 (59) (1989).
10. J. G. Nunan, C. E. Bogdan, K. Klier, K. J. Smith, C. W. Young, R. G. Herman, J. Catal., 116, 195 (1989).
11. D. M. Brown, B. L. Bhatt, T. H. Hsuing, J. J. Lewnard, F. J. Waller, Catalysis Today, 8, 279 (1991).
12. V. Palekar, J. W. Tierney, I. Wender, Liquid Phase Synthesis of Methanol/Methyl Formate at Mild Conditions, A.I.C.H.E. Meeting, New Orleans, LA (March 1992).
13. G. A. Mills, C. W. Knudsen, Comparative Economics of Synthetic Hydrocarbon Sources, Proc. 10th World Petroleum Congress, Vol. 3, p. 329 (1979).
14. D. Gray, A. ElSawy, G. Tomlinson, Quantification of Progress in Indirect Coal Liquefaction, Proc. Liquefaction Contractors' Meeting, DOE, p. 344 (1991).
15. D. Sperling, New Transportation Fuels - A Strategic Approach to Technology Change, Univ. CA Press, Berkeley (1988).

TABLES

Table 1: Stages FT/ZSM 5/ Alkylation

Product	After FT	Yield, Wt After ZSM 5	After Alkylation
C ₁	7.5	7.7	7.7
C ₂ =/C ₂	1.6/3.0	1.1/3.1	1.1/3.1
C ₃ =/C ₃	8.0/2.2	4.0/5.1	0/5.1
C ₄ =	6.6	4.4	0
iC ₄ /nC ₄	0/2.0	7.8/4.3	(2.2)/4.3
C ₅ -C ₁₁	33.5	52.8	71.2*
C ₁₂₊ (Liq)	27.8	1.7	1.7
Wax	8.0	8.0	8.0

* Octane Rating: Research 90, Motor 83

Table 2: Patented Co - Based FT Catalysts

Company	Primary	Typical Constituents		Support
		Secondary 1	Secondary 2	
Gulf	Co	Ru	Oxides	Alumina
Exxon	Co	Re/Ru	Oxides	Alumina
Shell	Co	w/wo noble metal	ZrO ₂	Silica
Statoil	Co	Re	Oxides	Alumina

Table 3: Synthetic Diesel Fuel

	Composition, Wt. %
Sulfur	< 0.001
Aromatics	0
Paraffins	47
Olefins	41
Alcohols	6
Other Oxygenates	6
Cetane Index	62

Table 4: Composition of Fuel Alcohols From Syngas

Alcohol %	C ₁	C ₂	C ₃	C ₄	C ₅	Other Oxygenates	Catalyst
MAS (SEHT)	69	3	4	13	9	2	K/Zn/Cr
Substifuel (IFP)	64	25	6	2	2.5	0.5	K/Cu/Co/Al
Octamix (Lurgi)	62	7	4	8	19	--	Alkali/Cu/Zn/Cr
HAS (DOW)	26*	48	14	3.5	0.5	8	CoS/MoS ₂ /K

* Methanol can be recycled to extinction, increasing ethanol

Table 5: Properties of Some Fuel Oxygenates

	Blending RVP	Blending Octane	BTU/Gallon 1000's	Production MMgpd
MTBE	8	110	109	6.1
ETBE	4	110	117	
TAME	2	103	112	
t-Butanol	9	100	101	
iso Butanol	5	102	95	
Gasoline		87	125	300

Table 6: Improvements in Indirect Liquefaction of Coal

Processes	Lurgi + Arge FT	Shell + Arge FT	Shell + Slurry FT
Plant Output, Bpsd			
Alcohols	1,762	1,836	1,954
Propane	4,467	4,037	4,207
Butane	5,403	5,522	5,560
Gasoline	36,450	32,494	33,953
Diesel	<u>35,419</u>	<u>39,617</u>	<u>37,828</u>
Total	83,501	83,505	85,503
Energy Efficiency %	48	53	59
Required Selling Price, \$/Bbl	55	48	42

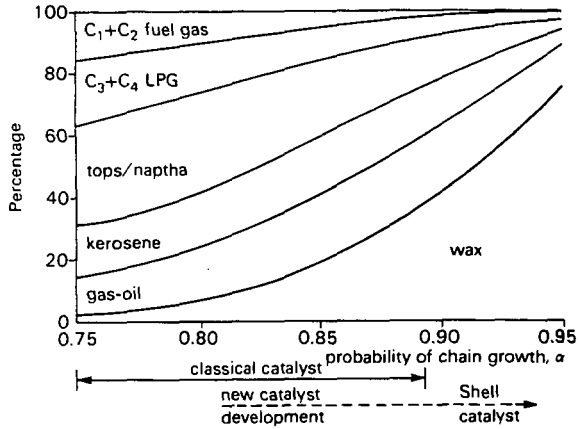


Fig. 1 Product Distribution for Fischer Tropsch Synthesis as a Function of Alpha

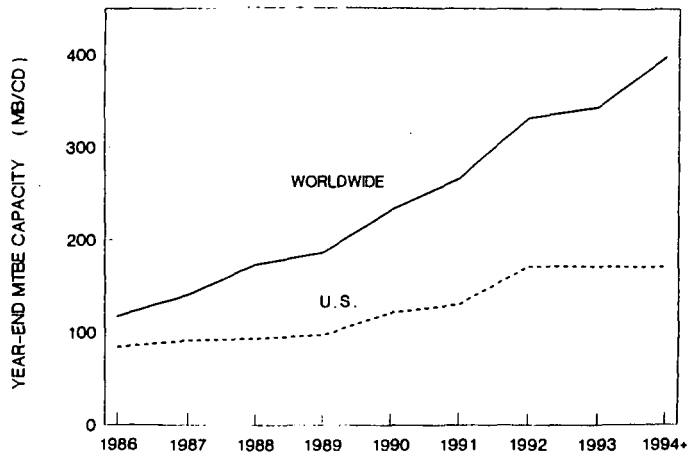
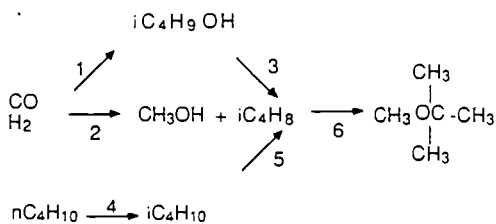


Fig. 2 U.S. and World Production Capacity of MTBE Based on Announced Additions



- | | |
|---|--|
| 1 Cu-ZnO-Al ₂ O ₃ -Alkali | 4 Pt-Cl-Al ₂ O ₃ |
| 2 Cu-ZnO-Al ₂ O ₃ | 5 Cr ₂ O ₃ -Al ₂ O ₃ |
| 3 ACID | 6 ACID RESIN |

Fig. 3 Reactions and Catalysts for MTBE Synthesis

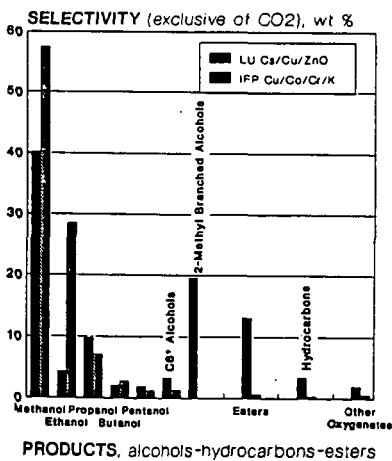


Fig. 4 Synthesis of Alcohols Over Cs / Cu / ZnO and Cu / Co / Cr / K Catalysts

CATALYSIS IN DIRECT LIQUEFACTION OF COAL

R.D. Srivastava and S.V. Gollakota
Burns and Roe Services Corporation
Pittsburgh, PA 15236
and

M.J. Baird, E.B. Klunder, S.R. Lee, and G.V. McGurl
Pittsburgh Energy Technology Center
Pittsburgh, PA 15236

Keywords: Direct Liquefaction, Catalysis, Dispersed Catalysts

INTRODUCTION

In view of the recent National Research Council study (1) and the present National Energy Strategy (2), the Pittsburgh Energy Technology Center (U.S. Department of Energy) is actively pursuing the Direct Liquefaction Program to develop technologies for producing low-cost liquid fuels from coal. A brief overview of the ongoing Direct Liquefaction Program is given below. This program broadly encompasses laboratory and bench-scale developments of promising new concepts, as well as proof-of-concept evaluation in pilot-scale, two-stage liquefaction units. Of the various areas being studied in this program, improved catalysts could play a major role in lowering thermal severity, improving product yields/selectivity, and improving process configuration. Thus, the catalysts used in the ongoing two-stage liquefaction studies and some of the current activities in the catalysis research are outlined in this paper.

OVERVIEW OF THE DIRECT LIQUEFACTION PROGRAM

The overall objective of the Pittsburgh Energy Technology Center's (PETC) Direct Liquefaction Program is to bring the liquefaction technology to commercial readiness in an environmentally acceptable manner, and some of the current activities directed toward this objective are outlined below.

Two-Stage Liquefaction Program

Direct liquefaction process testing is continuing at Hydrocarbon Research Inc. (HRI) and Amoco Oil Company. Future research will focus on the effects of coal cleaning/pretreatment, dispersed catalysts, preconversion processing, solids separation methods, bottoms processing, on-line hydrotreating, and solvent quality improvement.

Advanced Process Concepts Program

One of the main objectives of this program is to conduct fundamental studies and exploratory research to develop improved process configurations in direct liquefaction. The work being performed by some PETC contractors is briefly outlined as follows. The University of Kentucky Research Foundation is focusing on a two-stage low-rank coal liquefaction process that has oil agglomeration, fluid coking, and solvent dewaxing as the main features. Improvements in process operation, coal conversion, and product yields are anticipated. SRI is evaluating novel dispersed catalysts and improved reaction chemistry (e.g., use

of CO+H₂) for low-rank coals. This program will focus on reducing regressive reactions and increasing product quality in liquefaction. HRI is studying the merits of integrating two-stage liquefaction with fixed-bed hydrotreating to give improved products. Amoco Oil Company is evaluating the following processing steps to improve process operability during liquefaction of low-rank coals: conventional coal cleaning, coal pretreatment with aqueous SO₂ solutions to remove alkali metals from coal, impregnation of coal with a catalyst, and bottoms processing (e.g., deasphalting, coking). The Canadian Energy Development, Inc. (with Alberta Research Council) is evaluating a two-stage process consisting of oil agglomeration, coal slurry pretreatment, and hydroconversion. In this study, use of a dispersed catalyst and CO+H₂O system in a counter-flow reactor is proposed for process improvement.

Baseline Design and System Analysis

A conceptual baseline design of a two-stage direct coal liquefaction process, sponsored by PETC, is being performed by Bechtel and Amoco. This baseline study includes development of a process simulation model applicable over a certain range of capacities and process options involving coal cleaning, reactor configuration, vacuum bottoms processing, and hydrogen production methods. The model simulates a commercial liquefaction facility to predict yields and economics for different processing schemes. The data obtained at the Wilsonville Advanced Coal Liquefaction Research and Development Facility in Run 257 with Illinois No. 6 coal from Burning Star No. 2 mine and Amocat-1C catalyst in a two-stage catalytic liquefaction process is being utilized as the base case.

Coprocessing Program

Coprocessing, in which coal is processed along with a heavy petroleum residuum, is considered to be a variation of direct liquefaction. Some of the present studies in coprocessing are focusing on understanding possible synergism between coal and petroleum residuum, merits of dispersed catalysts, and recycle effects. Bench-scale studies are being carried out at UOP in a slurry reactor and at HRI in a two-stage ebullated-bed reactor system. These studies are being assessed for their technical and economic merits.

Refining, Upgrading, and End-Use Testing Program

Although the current two-stage liquefaction products are lower in heteroatom contents and higher in hydrogen compared to previous single-stage products, the two-stage products require additional refining/upgrading to meet commercial fuel specifications. Studies will be performed to produce refinery feeds and specification products in order to assess the technology required for refining and also to test the products for their emission properties.

Generic Bench-Scale Unit

An integrated, continuous-flow bench-scale unit (BSU) will be built at PETC to screen, develop, and improve new process concepts in direct liquefaction. This unit will have a capacity of 200 pounds of coal feed per day. This BSU will have the flexibility to operate over a wide range of conditions with different ranks of coals and different reactor types (i.e., slurry, ebullated-bed, fixed-bed). It is anticipated that this unit will be ready for operation by 1993. During the design and construction of this generic BSU, promising new approaches being developed by PETC contractors will be evaluated for testing in this unit.

TWO-STAGE LIQUEFACTION CATALYSTS

Catalysis plays a major role in determining coal and resid conversions and distillate selectivity in direct liquefaction. Although the inherent mineral matter in coal itself has some catalytic activity, external catalysts must be provided to obtain satisfactory reaction rates and specification products. A description of the status of liquefaction catalysis and catalysts was given in some recent reviews (3, 4). In the catalytic two-stage liquefaction process that was studied at Wilsonville and HRI in the recent past, alumina-supported transition metal catalysts were used in the ebullated-bed reactors to facilitate coal liquefaction and solvent hydrogenation. A brief description of the two-stage liquefaction process is given below to better understand the role and importance of catalysts in each reactor.

Process Description

In the close-coupled two-stage liquefaction, two ebullated-bed reactors are in series followed by a solids separation system. The pulverized feed coal is mixed with coal-derived recycle solvent and hydrogen and preheated before entering the first stage. The slurry in the first stage is continuously recirculated by the use of a pump while the catalyst extrudates are ebullated in an upflow stream. Typical reactor inlet hydrogen partial pressures and reactor average temperatures would be in the ranges of 2300 to 2500 psig and 750 to 810°F, respectively. About 90 wt% of a bituminous coal conversion generally occurs in the first stage, and the degree of hydrogenation and distillate production depend on the operating conditions such as temperature, pressure, catalyst type/charge/age, and space velocity. Depending on the liquefaction conditions, the catalyst could deactivate due to factors such as coking, deposition of minerals and basic compounds, pore mouth plugging, and sintering. To sustain steady catalytic activity in the reactor, some deactivated catalyst must be withdrawn and replaced with fresh catalyst. Because high catalyst deactivation rates require high catalyst replacement rates, developing catalysts that are resistant to rapid deactivation is desirable. Maintaining good catalyst activity in the first stage could facilitate obtaining higher coal conversions, higher solvent quality, and higher resid cracking/hydrogenation.

The first-stage products, which are gases, distillate, resid (resid is typically non-distillable at 850°F and 1 atm), unconverted coal, and ash, may be passed through an interstage separator for removing heteroatom gases (i.e., gases containing sulfur, nitrogen, and oxygen), light hydrocarbon gases, and some distillate before entering the second stage. Separating the heteroatom gases could allow maintaining higher hydrogen partial pressures in the second stage. In addition, undesirable reactions such as methanation could be minimized, especially in low-rank coal operations. The second stage is usually operated under conditions that are favorable for heteroatom removal and further upgrading of coal liquids. Depending on the operating mode, i.e., high/low or low/high, the second stage conditions could be, to some extent, in the range given above for the first stage. The second-stage products are sent to various vapor-liquid and liquid-solid separation systems for product recovery and recycle solvent preparation (5-9).

Supported Catalysts

Generally, in two-stage liquefaction, supported catalysts were used in both

stages for bituminous coals (7-9). On the other hand, a supported catalyst was used in only one stage at Wilsonville in most of the low-rank coal liquefaction studies; some tests with subbituminous coals were, however, made both at HRI and Wilsonville using supported catalysts in both stages.

At Wilsonville, Criterion 324 (Shell 324) unimodal Ni-Mo catalyst was frequently used in recent runs. In addition, Ni-Mo bimodal catalysts were also tested in some runs, e.g., Shell 317 in Run 254, Amocat-1C in Run 257, and EXP-AO-60 in Run 261 (8, 9). These catalysts typically contain 10 to 13 wt% molybdenum and 2 to 3 wt% nickel on alumina. The pore volumes in unimodal and bimodal catalysts are typically in the ranges of 0.4 to 0.5 and 0.7 to 0.8 cc/g, respectively (9). The diameters of small pores in both types of catalysts are usually in hundreds of angstroms (e.g., 100-200 Å); however, the bimodal catalysts are distinguished by the presence of additional pores having diameters in thousands of angstroms (e.g., 1000-2000 Å). The larger pores in bimodal catalysts could facilitate diffusion of large asphaltene molecules and reduce pore mouth plugging.

Satisfactory performance of Criterion 324 was observed, when it was used as the second-stage catalyst in thermal/catalytic mode, in Wilsonville subbituminous coal runs 258 and 260 (8, 10). In these runs, the catalyst replacement rate was in the range of 1.5 to 3 lb/ton coal. Significantly improved performance of the catalytic stage was observed when Criterion 324 was used in the first stage in catalytic/thermal mode in Run 260 (8). It may be pointed out that in these runs, an iron precursor was introduced with coal-solvent slurry to catalyze coal conversion.

High distillate yields and good product qualities were obtained with a deep-cleaned Pittsburgh seam coal, in Wilsonville Run 259, using Criterion 324 catalyst in both stages at a total catalyst replacement rate of 8 lb/ton coal (9). In Run 261, tests were performed with Illinois No. 6 coal using EXP-AO-60 and Criterion 324 catalysts (8). The total catalyst replacement rates in this run were in the range of 3 to 6 lb/ton coal. In Runs 259 and 261, increasing slurry viscosities limited the extent of batch deactivation with Criterion 324 catalyst. Satisfactory process performance was obtained using EXP-AO-60 catalyst at a total catalyst replacement rate of 3 lb/ton coal (8). The physical strength of the bimodal catalysts was of some concern in ebullated-bed reactor operation. For example, when 1/12-inch Amocat-1C cylindrical extrudates were used in Wilsonville Run 257, a significant amount of the initially charged catalyst was found to be broken at the end of the tests (11). However, it appeared that some other bimodal catalysts, i.e., 1/16-inch EXP-AO-60 cylindrical pellets tested in Run 261 and 1/20-inch Shell 317 trilobe pellets tested in Run 254, did not exhibit significant breakage (8, 12).

HRI developed a catalytic two-stage liquefaction process operating in low/high temperature mode using nickel-molybdenum supported catalysts (7). Some of the catalysts tested were 1/32-inch Davison Amocat-1C catalyst, 1/20-inch UOP spherical catalyst, and 1/32-inch Shell 317 cylindrical catalyst. An Illinois No. 6 coal and an Ohio No. 5/6 coal (both bituminous) and a Wyodak subbituminous coal were tested in this process development. In this low/high process, the first-stage catalytic ebullated-bed reactor was operated at low temperatures (about 750°F). At these mild temperatures, coal is thought to dissolve slowly in the recycle solvent allowing the rate of catalytic hydrogenation reactions that regenerate the solvent to be somewhat similar to the rate of coal conversion. Further conversion and upgrading of first-stage products occur in

the second stage operated at higher temperatures. Higher distillate yields and extinction recycle conversion of heavy oils (750°F+ vacuum gas oil) were said to be some of the major achievements in this low/high mode (7).

Some of the recent supported catalyst work at HRI was focused on on-line hydrotreating. On-line hydrotreating with Shell 424, NiMo catalyst, was effective in reducing the heteroatom content in the distillate product. For example, when a distillate having an end-point of about 550°F was hydrotreated, the nitrogen and sulfur contents were reduced from 1280 to 9 ppm and 230 to 14 ppm, respectively. In additional tests, the hydrotreating efficiency was found to be dependent on the feed end-point (13).

Dispersed Catalysts

At Wilsonville, a readily available iron oxide (minus 325 mesh powder) in combination with a sulfiding agent was used routinely in the liquefaction of subbituminous coals. Although this gave satisfactory operation with two-stage coal conversions in the range of 90 to 95 wt%, the iron dispersion might not have been optimum under the liquefaction conditions. In the recent past, a molybdenum precursor was used at Wilsonville in the liquefaction of the Black Thunder mine subbituminous coal (8, 14). The precursor was a complex organic compound (commercial name is Molyvan L) containing molybdenum, sulfur, phosphorous, carbon, and hydrogen. It was used primarily to test the effectiveness of dispersed molybdenum in limiting the solids buildup frequently observed at Wilsonville during the liquefaction of subbituminous coals. Based on preliminary results, it appeared that the solids buildup was mitigated to some extent when the dispersed molybdenum was used (14). Again, as was the case with the iron oxide, it was not certain that the selected molybdenum precursor, Molyvan L, gave optimum active metal dispersion.

HRI recently tested some iron precursors in combination with a supported catalyst. These iron compounds were magnetite (an oxide magnetic pigment) and a pyrrhotite. It was concluded that these compounds had limited catalytic effect (15).

The effectiveness of supported catalysts in obtaining high distillate yields (up to 75-78 wt% maf coal) and good product qualities was demonstrated both at Wilsonville and HRI; however, the application of dispersed catalysts in pilot-scale two-stage liquefaction is yet to be thoroughly examined. Some of the current activities in dispersed catalyst development are outlined below.

CATALYST DEVELOPMENT

As stated earlier, due to high deactivation rates of supported catalysts currently used in pilot-scale process development, aged catalysts must be continually replaced to sustain good catalytic activity. High catalyst replacement rates could contribute significantly to the operating costs in a commercial process. Although regeneration of these catalysts could reduce costs, effective procedures for catalyst regeneration are yet to be demonstrated in pilot-scale operations. In addition, recovery of the metals from spent catalysts is a significant process expense. Hence, PETC is sponsoring research on the development of new and improved catalysts and catalytic processes. Some of these activities are briefly described below.

Finely Dispersed Iron and Molybdenum Catalysts: In-House Research at PETC

Researchers at PETC are developing advanced procedures to obtain finely divided forms of iron and molybdenum to yield highly active catalysts for direct coal liquefaction applications. Demonstrating the effectiveness of dispersed catalysts in pilot-scale liquefaction units could allow using slurry reactors in place of ebullated-bed reactors at lower capital and operating costs.

Commercially available, low-cost iron compounds could be used as precursors for disposable liquefaction catalysts. However, the activity of catalysts derived from readily available iron oxides and iron sulfides could be low due to poor initial dispersion, low surface area, and the tendency to aggregate. PETC is focusing on preparing ultrafine particles that have significantly larger surface area and higher activity compared to the conventional catalysts.

The well-dispersed iron catalysts can exhibit superior characteristics for use in a coal dissolution reactor. In one preparation method, an initial incipient wetness impregnation of the feed coal with ferric nitrate was carried out. Subsequently, the high dispersion and interaction with the coal surfaces was maintained by conversion of the added iron to an insoluble hydrated iron oxide. Then, activation of this dispersed hydrated iron oxide at about 525°F was shown to result in an effective disposable catalyst for coal conversion (16, 17).

Under proper activation conditions, two sulfided molybdenum compounds -- ammonium tetrathiomolybdate and molybdenum trisulfide -- are very good candidates as precursors for a slurry catalyst. In contrast to alternative non-sulfided molybdenum catalyst precursors, use of these precursors could reduce the activation steps and external sulfur requirements while resulting in a highly active molybdenum disulfide catalyst. Preliminary studies at PETC indicated that both precursors thermally decompose to a high surface area molybdenum disulfide if the thermal transition was rapid. The catalytic activity was sufficient to sustain high coal conversions at molybdenum concentrations as low as 200 to 300 parts per million (18).

Laboratory liquefaction tests were made at PETC to evaluate the aforementioned iron and molybdenum catalysts. Using iron concentrations as low as 2500 ppm (based on coal), liquefaction tests were conducted with Illinois No. 6 coal slurried with coal-derived solvents. Conversions of the coal to distillate and soluble products at 425°C in H₂+3% H₂S atmosphere for 1 hr compared favorably with conversions obtained under the same conditions using 1500 ppm of molybdenum (16). HRI is also currently testing these dispersed iron catalysts prepared at PETC. Further development of these catalysts is in progress.

Hydrous Metal Oxide Catalysts

Researchers at Sandia National Laboratories are developing catalysts based on hydrous titanium oxide (HTO) ion exchangers for application in direct liquefaction. The hydrous metal oxide ion-exchangers are amorphous inorganic compounds of metals such as Ti, Zr, Nb, and Ta. They offer significant advantages as supports in the preparation of catalysts. The following are some properties of these ion-exchange compounds that make them desirable as supports for active metals: several active metals or mixtures of metals can be atomically dispersed over a wide range of concentrations; the ion exchange capacity of the materials is large, permitting high loadings of active metals; solution chemistry

can be used to provide control of the oxidation state of the active metal; and, these materials have high surface areas. For example, hydrous titanium oxide catalysts were prepared by a technique that consisted of the synthesis of sodium hydrous titanate ion exchange material followed by exchanging the sodium for active metal ions (19).

Preliminary tests indicated that the HTO catalysts, even at low active metal loadings of 1 wt%, were as effective in converting coal to low molecular weight products as a commercial Ni-Mo/Al₂O₃ catalyst containing 15 wt% active metals. In addition, for the same oil yield, the HTO catalysts used less hydrogen than the commercial catalyst (19). In recent tests at Amoco, a NiMo HTO catalyst gave similar performance compared to a commercial catalyst, but at only half of the active metal loading (20). This result suggested good dispersion of Ni and Mo on the HTO catalyst.

Metal Carbide and Nitride Catalysts

Researchers at Clarkson University are developing carbides and nitrides of transition metals to be used as catalysts specifically for nitrogen removal from coal liquids. The metal carbides and nitrides are hard, refractory materials that are resistant to corrosion. In a typical procedure, Mo₂C was prepared from MoO₃ using a CH₄/H₂ reactant gas. Initially, the precursor MoO₃ was reduced to MoO₂ producing water. In the next step, further reduction and carburization occurred giving Mo₂C having a surface area of about 50-90 m²/g while forming additional water. When ammonia was used in place of CH₄/H₂, Mo₂N having a surface area as high as 225 m²/g was produced (21).

Amoco recently compared the performances of a bulk molybdenum nitride and an alumina-supported molybdenum carbide with Amocat-1B (Mo/Al₂O₃) and Shell 324 (NiMo/Al₂O₃). These tests were conducted in packed-bed reactors (14/20 mesh catalyst size) under the following conditions: 760°F, 2000 psig total pressure, 10000 SCFB hydrogen flow rate. The feed material was a mixture of a coal-derived resid and Panasol (a refinery by-product). Coal-derived distillates were also used in some tests. This preliminary study seemed to indicate that the molybdenum carbide and nitride catalysts gave products that were better than those obtained using Shell 324 and Amocat-1B (20). Moreover, these carbide and nitride catalysts seemed to have higher activity on a per-site basis (turnover rate) compared to the commercial catalysts (21).

SUMMARY

PETC is actively pursuing an advanced, novel concepts research program in direct liquefaction to bring the technology to commercial readiness in the near future. Of the various areas being studied in this program, improved catalysts could play a major role in lowering thermal severity, improving product yields and selectivity, and improving process configuration. The catalysts used in the recent two-stage liquefaction studies at Wilsonville and HRI, and the current activities in catalysis research have been briefly reviewed. The commercial supported catalysts were found to be effective in two-stage liquefaction. Because of high deactivation rates and the need for using ebullated-bed reactors, PETC is also focusing on developing dispersed catalysts which will lead to the use of less capital intensive slurry reactors. Preliminary work at PETC was successful in obtaining finely dispersed, highly active iron and molybdenum catalysts. The PETC Project Office will continue to focus on the development of advanced liquefaction reactor systems to improve the overall economics.

REFERENCES

1. "Fuels to Drive Our Future," National Research Council, National Academy Press, Washington, D.C., 1990.
2. "National Energy Strategy," U.S. Department of Energy, Washington, D.C., First Edition, February 1991.
3. Srivastava, R.D., "Catalysis in Direct Liquefaction - A Research Needs Assessment," Technical Report, Prepared by Burns and Roe Services Corp. Under DOE Contract No. DE-AC22-89PC88400, February 1991.
4. Derbyshire, F., "Catalysis in Coal Liquefaction: New Directions for Research," IEA Coal Research, IEACR/08, London, 1988.
5. Rao, S.N.; Schindler, H.D.; McGurl, G.V., "Advances and New Directions in Direct Liquefaction," Prepr. Am. Chem. Soc. Div. Fuel Chem. 145, 33(3), 1988.
6. Gollakota, S.V.; Lee, J.M.; Davies, O.L., "Process Optimization of Close-Coupled Integrated Two-Stage Liquefaction by the Use of Cleaned Coals," Fuel Proc. Tech., 205, 22, 1989.
7. Comolli, A.G.; Duddy, J.E.; Johanson, E.S.; Smith, T.O., "Low Severity Catalytic Two-Stage Liquefaction Process," Final Report by Hydrocarbon Research, Inc. Under DOE Contract No. AC22-85PC80002, Sept. 1988.
8. Gollakota, S.V.; Vimalchand, P.; Davies, O.L.; Lee, J.M.; Cantrell, C.E.; Corser, M.C., "Wilsonville CC-ITSL Process Development," Proceedings of Liquefaction Contractors' Review Meeting, September 1991, Pittsburgh, PA.
9. "Run 259 with Pittsburgh No. 8 (Ireland Mine) Coal," Technical Progress Report Prepared by Southern Electric International Under DOE Contract No. DE-AC-82PC50041, May 1991.
10. "Run 258 with Subbituminous Coal," Technical Progress Report Prepared by Southern Electric International Under DOE Contract No. DE-AC-82PC50041, May 1991.
11. "Run 257 with Illinois No. 6 Coal," Technical Progress Report Prepared by Southern Electric International Under DOE Contract No. DE-AC-82PC50041, February 1991.
12. "Run 254 with Ohio No. 6 Coal," Technical Progress Report Prepared by Southern Electric International Under DOE Contract No. DE-AC-82PC50041, February 1990.
13. Comolli, A.G.; Johanson, E.S.; Panvelkar, S.V.; Popper, G.A., "Recent Advances in Direct Coal Liquefaction," Proceedings of the 16th International Conference on Coal & Slurry Technologies, April 1991, Clearwater, FL.
14. Wilsonville 113th Technical Review Meeting, Birmingham, AL, November 1991.

15. Comolli, A.G.; Johanson, E.S.; Panvelkar, S.V., "CTSL™ Process Studies," Proceedings of Direct Liquefaction Contractors' Review Meeting, September 1990, Pittsburgh, PA.
16. Cugini, A.V.; Krastman, D.; Hickey, R.F., "The Use of Hydrated Iron Oxide Catalysts in Coal Liquefaction," Proceedings of the 8th Annual International Pittsburgh Coal Conference, October 1991, Pittsburgh, PA.
17. Cugini, A.V.; Utz, B.R.; Krastman, D.; Hickey, R.F.; Balsone, V., "Effect of Activation Conditions on Dispersed Iron Catalysts in Coal Liquefaction," Prepr. Am. Chem. Soc. Div. Fuel Chem. 91, 36(1), 1991.
18. PETC Review, Office of Fossil Energy, U.S. Department of Energy, 51, 2, September 1990.
19. Stohl, F.V.; Dosch, R.G.; Stephens, H.P., "Development of Hydrous Metal Oxide Catalysts for Direct Coal Liquefaction," Proceedings of Direct Liquefaction Contractors' Review Meeting, October 1988, Pittsburgh, PA.
20. Sajkowski, D.J., "Second-Stage Catalyst Testing," Proceedings of Direct Liquefaction Contractors' Review Meeting, September 1990, Pittsburgh, PA.
21. Oyama, S.T., "Catalytic Hydrodenitrogenation by Molybdenum Carbide and Nitride," Proceedings of Direct Liquefaction Contractors' Review Meeting, September 1990, Pittsburgh, PA.

CATALYSIS OF LOW TEMPERATURE LIQUEFACTION BY MOLYBDENUM SULFIDES

B. C. BOCKRATH, E. G. ILLIG, AND M. J. KELLER, III

U. S. DEPARTMENT OF ENERGY
PITTSBURGH ENERGY TECHNOLOGY CENTER
PO BOX 10940
PITTSBURGH, PA 15236

KEYWORDS: Liquefaction, dispersed catalysts, molybdenum disulfide

INTRODUCTION:

The use of molybdenum sulfide catalysts in the direct liquefaction of coal is well known. Nonetheless, the development and application of more effective catalysts, particularly in first-stage liquefaction reactors, remains a high priority goal¹. When used as unsupported catalysts in first-stage reactors, molybdenum sulfides are often intended to promote the conversion of coal and to provide better quality products for further refining. Typically, temperatures ranging from 400° to 465° C are used in first-stage reactors to promote the formation of distillable products. Molybdenum catalysts used at these temperatures generally increase coal conversion and the yield of distillates, and reduce the content of heteroatoms, principally sulfur and oxygen. Results described below suggest that molybdenum catalysts might play additional roles. The conversion of coal to soluble products at low temperatures, generally around 350° C, may be promoted by active catalysts, possibly through the prevention of retrogressive reactions². With this in mind, the activity of molybdenum catalysts in low temperature liquefaction was investigated. The results indicate that it is of value to have the catalyst present in an active form when the liquefaction feed stock is brought to temperatures above 300° C.

EXPERIMENTAL:

Small-scale liquefaction reactions were carried out in 316 stainless steel autoclaves of about 40 mL capacity. A set of five microautoclaves was heated and shaken (60 cps) in a sandbath. In these experiments, the reactors were brought to temperature slowly by heating the sandbath at about 6° C/min. The usual charge was 3.5 g Illinois No. 6 coal, 7 g coal-derived liquefaction solvent, and 1200 psig hydrogen at room temperature. Larger scale experiments were carried out in a 316 stainless steel stirred autoclave of 1/2 L capacity. Typical charges were 70 g coal, 140 g solvent, and 1200 psig hydrogen at room temperature. The heating rate was about 8° C/min. Rapid cooling was achieved by flowing water through an internal cooling coil.

Coal conversions were calculated on an maf basis from weights of dry residues recovered after vacuum filtration on 8u paper with cyclohexane followed by tetrahydrofuran (THF). The catalyst was added to the coal by mixing it with about 40% of its weight of an aqueous solution of ammonium heptamolybdate or ammonium tetrathiomolybdate followed by drying in a vacuum oven at 60° C. In one case, the catalyst was simply added to the reactor as a powder without impregnation. The coal was from Burning Star mine, and had the following elemental composition: C=78.4%; H=5.1%; N=1.6%; O=11.4% (by diff.) on an maf basis with total S=3.2%. The ash content was 10.4% on a moisture free basis. The liquefaction solvent was a hydrotreated distillate (V-178) obtained from the Advanced Coal Liquefaction R & D Facility at Wilsonville, Alabama. Its carbon and hydrogen contents were C=88.2% and H=9.6%. By

D-1160 distillation, 84% distilled below 850° F.

RESULTS AND DISCUSSION:

The use of unsupported molybdenum sulfides as liquefaction catalysts is well known¹. Nonetheless, at the outset of this work, it was useful to establish whether or not catalyst activity could be observed at low temperatures, in this case about 350° C. Two sets of experiments were used to verify catalyst activity. In the first, coal conversion (THF) was measured as a function of catalyst activity. The residence time at liquefaction temperature (350° C) was 60 min. The conversion values shown in Fig. 1 increase with catalyst loading until a plateau is reached at around 2000 ppm molybdenum. Conversions with either ammonium heptamolybdate and ammonium tetrathiomolybdate were generally similar except at the lowest concentration. These differences aside, the more important observation is that the precursors may be activated and perform a catalytic function at low temperature.

In addition to increasing the conversion of coal, a catalyst may be expected to increase the rate of hydrogen consumption. In these experiments, we have no direct, real-time indication of changes in hydrogen partial pressure. However, the microautoclaves were equipped with pressure transducers allowing total pressure to be recorded as a function of reaction time. The time/temperature and time/pressure profiles for a set of autoclaves heated together in the sandbath are given in Figure 2. The pressure increased with temperature, as expected. A peak in total pressure is observed a short time after the temperature reached 350° C. Thereafter, total pressures declined.

The pressure profiles shown result from a composite of the effects of temperature changes, hydrogen uptake, and production of other gases or vapors. Despite this complexity, important information may still be derived from the profiles. Peak pressure developed shortly after reaching liquefaction temperature, indicating that the major portion of gas formation is rapid, being almost complete within several minutes of reaching reaction temperature. Analysis of the gases recovered at the end of the run indicates that the major component of the non-condensable gases evolved is CO₂, with a lesser amount of CH₄. Once gas evolution slows, a gradual decrease in total pressure is observed. This decrease is reasonably attributed to hydrogen uptake. Although the decrease is larger when catalyst has been added, it is evident even when it has not. It is possible that a native catalytic effect of coal mineral matter may contribute to the pressure decrease. Indeed, the Illinois No. 6 coal used in this work has a high iron content (1.1 wt%, mf).

The changes in total gas pressure reflect the effects of both temperature changes and chemical reactions. An attempt to factor out the former was made by estimating the pressure change that would be due to the temperature change. This estimate was based on a least squares fit of the temperature/pressure data using the first three points covering the temperature span from 15 to 219° C. The resulting linear equation was then used to calculate expected pressures for higher temperatures. This estimation assumes that the evolution of gases below 219° C is negligible. The difference between the calculated and observed pressures is a rough estimate of the combined effects of gas production and hydrogen uptake. Pressure differences calculated from the data in Figure 2 are plotted versus time in Figure 3.

The difference between catalyzed and non-catalyzed liquefaction is readily apparent. In the catalyzed cases, the pressure peak is reduced and hydrogen uptake begins to dominate within the first 15 minutes at 350° C. Coal conversions were also somewhat higher, being 91-92% for all catalyzed cases as opposed to 87% without catalyst. By cyclohexane extraction, conversions with catalyst ranged from 12% to as high as 21%

for 5000 ppm Mo. The value without catalyst was only 7%. Clearly the precursor was activated at 350° C and the resulting catalyst played an important role in the early stages of the liquefaction reaction.

The relative rates of hydrogen uptake at times beyond the pressure peak are also interesting. The rates are nearly identical for catalyst loadings of 1000 and 5000 ppm Mo. At these levels, the rate of hydrogenation seems to be limited by factors other than the amount of catalyst present. It is also apparent that the rate of hydrogen uptake falls off with time until it approaches that observed in the absence of added catalyst. This observation was grounds for asking whether or not the catalyst was progressively deactivated.

To determine if the catalysts were in fact deactivated, the tetrahydrofuran insoluble residues recovered after product work-up were mixed with fresh coal slurry and a second cycle of liquefaction was performed. For comparison, simultaneous experiments were made with and without the addition of ammonium molybdate powder. The temperature/pressure-difference profiles are shown in Figure 4. The experimental conditions were the same as the initial liquefaction experiment, except that the temperature was increased to 425° C after 120 minutes at 350° C. The pressure differences were calculated as before. As may be seen in the Figure, catalytic activity is quite apparent for the material recovered from the previous experiment. Improvements in coal conversion were also obtained by using the liquefaction residue. Values determined by THF extraction were 95% with liquefaction residue, 86% with ammonium molybdate, and 85% without catalyst. Measured by cyclohexane extraction, the values were 64%, 36%, and 38%, respectively.

It is important to note that the liquefaction residue demonstrated catalytic activity as soon as the temperature reached 350° C. The recovered catalyst was not only active, but able to participate in liquefaction reactions during the first few critical minutes. A pattern of hydrogen uptake similar to that seen in the previous experiment is repeated here. With added liquefaction residue, the rate of hydrogen uptake diminished with time until it approached that for the non-catalyzed case. However, when the temperature was increased to 425° C, the apparent hydrogen uptake was much greater in the presence of the liquefaction residue. From the results of temperature programming, it seems the catalyst acts as a cofactor in processes that are initiated by thermal reactions. Thus, as the temperature is brought up to each plateau, a new but limited burst of catalyzed hydrogen uptake initiated. These observations are in accord with the concept of catalytically controlled thermal cracking postulated for petroleum residua and other heavy hydrocarbons³. In that concept, MoS₂ was pictured as hydrogenating thermally produced free radicals, thus inhibiting the formation of coke.

Comparison of the addition of the liquefaction residue with addition of ammonium molybdate in the form of a powder illustrates the importance of dispersing the catalyst precursor. The added ammonium molybdate powder performed only marginally better than coal without added catalyst, even though twice as much molybdenum was added in the form of the powder as in the liquefaction residue. This relatively poor performance most likely resulted because no effort was made to disperse the catalyst precursor. By contrast, the precursor used to generate the catalyst in the liquefaction residue had been dispersed on the coal in the first liquefaction experiment. Thus, a major benefit of dispersing a precursor on coal is that more effective catalysts may be produced. This benefit is separate from any derived by improved contact between coal and catalyst brought about by dispersing the precursor. It should be emphasized that in the second liquefaction experiment, the added catalyst was physically associated with the liquefaction residue from the previous experiment. The degree of contact with fresh coal was then governed by the extent of mixing in the reactor. Experiments directed

toward improving the contact between the coal and catalyst thus need to take into account the effect the chosen method of dispersing the precursor might have on the physical properties of the resulting catalyst. It is also apparent that tailoring the conditions of the preparation of an unsupported catalyst may have a large effect on its performance in a process that makes use of catalyst recycle.

The recovery of the catalytic material in the previous experiments entailed the solvent separation of the liquefaction products. Thus, the catalyst was exposed to several laboratory operations that could have degraded its performance in the subsequent liquefaction cycle. These extraneous influences make it more difficult to conduct a systematic program to improve the preparation of these catalysts. A way around this problem was devised by preparing catalysts under liquefaction conditions in a microautoclave, then transferring them without work-up to a 1/2 L stirred autoclave for performance testing. In this way, a small volume of liquid product containing active catalyst can be mixed with a larger volume of fresh feed slurry before liquefaction. In this testing scheme, the precursor loading in the preparation stage must be high in order to supply enough catalyst for the performance test in the stirred autoclave. Initially, 20,000 ppm of ammonium molybdate on coal was used in the preparation, which reduced to 1000 ppm Mo after dilution with 20 times as much fresh coal in the performance test.

Initial tests of this preparation/testing scheme revealed that the introduction of active catalyst to the stirred autoclave often led to exothermic reactions as the temperature approached about 350° C. In general, the extent of these exotherms varied according to the type and amount of catalyst used. Thus, the temperature profiles were not reproducible. To obtain better control, a temperature staged testing program was adopted. One such temperature profile for a noncatalyzed liquefaction experiment in the 1/2 L stirred autoclave is illustrated in Figure 5. In this example, 20 minutes was spent at 300° C, followed by 60 minutes at 325° C, then 50 minutes each at 350° and 375° C. The total pressure rose until 10 minutes after reaching 325° C. Expected pressures were calculated based on the initial pressure change as done before. The difference between expected and observed pressures is plotted in Figure 6. For comparison, the pressure difference profile for a case with added catalyst is presented in Figure 7. The heating program was closely similar to the non-catalyzed example, but they are not identical. Several important observations may be made by comparing the two pressure difference profiles. First, in the non-catalyzed case, the onset of the pressure peak is evident as the temperature approaches the first plateau, 315° C, and it is much larger in magnitude than in the catalyzed case. This apparent increase in hydrogen uptake is further evidence that the catalyst carried in the liquefaction products of the previous run is able to function during the initial stage of the liquefaction reaction. Second, the pressure difference at the end of the heating program is much more negative with than without added catalyst. Third, the rate of pressure change in the presence of catalyst is nearly constant once the pressure peak has passed. It is striking that the rate of uptake does not seem to be affected by the changes in temperature. This is somewhat different than the profile from the microautoclave experiment shown in Figure 4, which exhibited a distinct change in rate as the temperature increased to the next plateau. It may be that the smaller temperature changes in the stirred autoclave experiment combined with a fortuitous choice of intervals between temperature changes produced a constant rate of uptake.

CONCLUSIONS:

The results obtained in this work indicate several factors are

important to using unsupported molybdenum sulfide catalysts more effectively in the first stage of liquefaction. Since catalysts are able to participate in liquefaction reactions at low temperatures, it is important that they be present in an active form rather than allow this one-time opportunity to pass while a precursor undergoes transformation. One approach to this objective is demonstrated here, namely, preparation of a catalyst from a precursor dispersed on coal in a small reactor followed by mixing the entire liquefaction product with fresh slurry for use in a larger reactor. Impregnation of the precursor on coal seems to be of benefit to generating a better catalyst. Such a prepared catalyst is able to perform well in subsequent liquefaction tests even though it is only physically mixed with coal, not impregnated in any way. It is also clear that evaluation and comparison of liquefaction catalysts is complicated by the fact that performance is governed by many factors, not just catalyst activity. For example, during typical liquefaction experiments, the catalytic properties of a precursor added with the feed undergo considerable change during the course of the reaction. For this reason, the results given above are taken as measures of overall catalyst performance rather than catalyst activity. In the present context, the latter may not be a static characteristic.

ACKNOWLEDGEMENT:

We gratefully acknowledge the assistance of Harold M. Boyer in carrying out many of the liquefaction experiments.

REFERENCES:

1. Derbyshire, F.; *Energy and Fuels*; **3**, 273 (1989).
2. Solomon, P. R.; Serio, M. A.; Deshpande, G. V.; Kroo, E.; *Am. Chem. Soc. Div. Fuel Chem., Preprints*, **34(3)**, 803 (1989).
3. Bearden, R; Aldridge, C. L.; *Energy Progress*, **1**, 44 (1981).

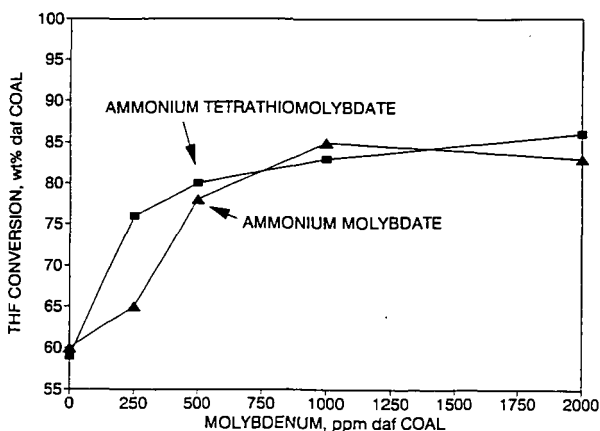


Fig. 1. Conversion versus molybdenum loading.

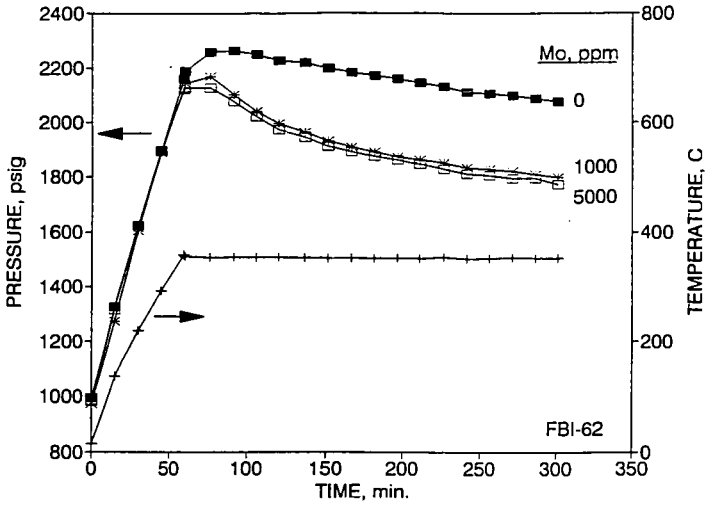


Fig. 2. Temperature and total pressure profiles.

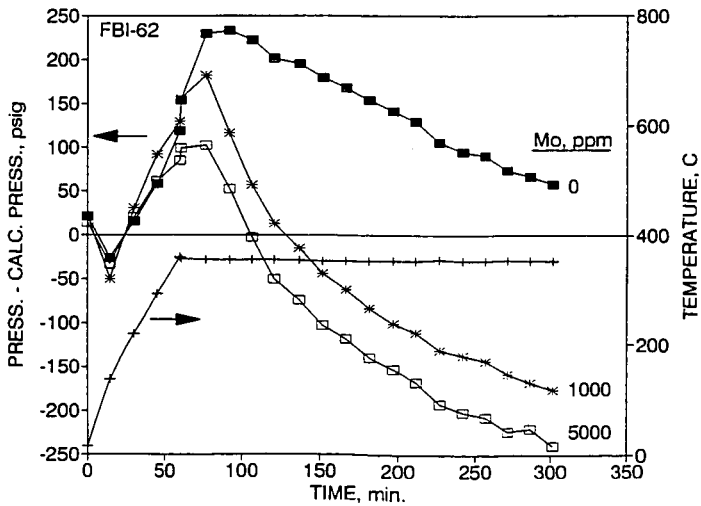


Fig. 3. Differences between calculated and total pressure.

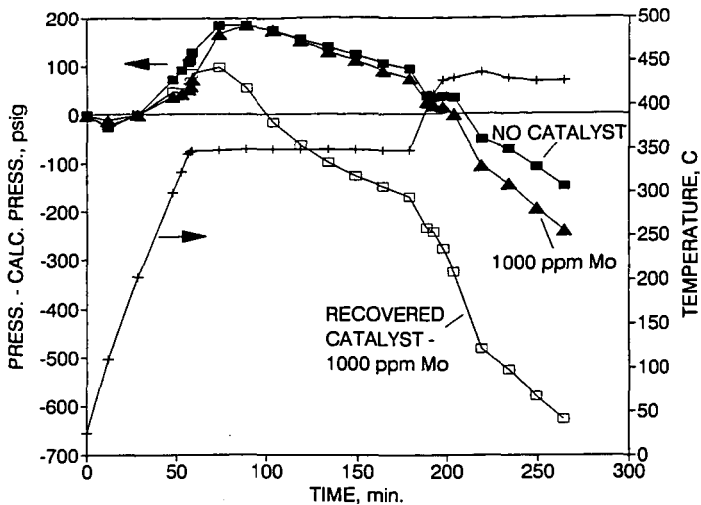


Fig. 4. Pressure difference profiles with and without catalyst.

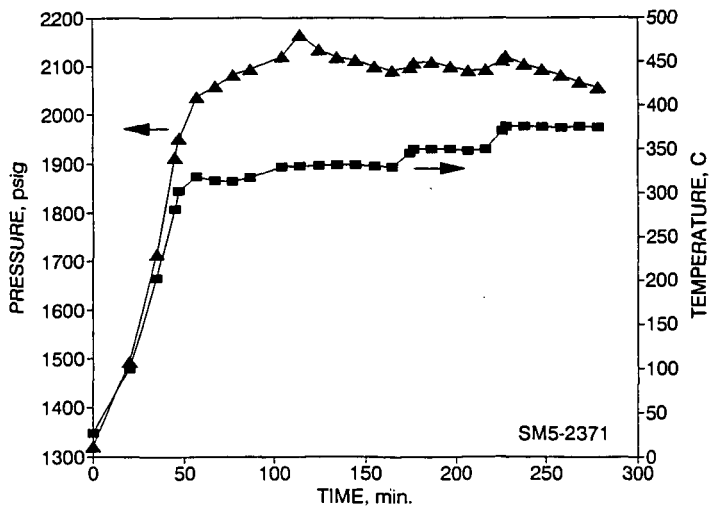


Fig. 5. Temperature and pressure profiles without added catalyst.

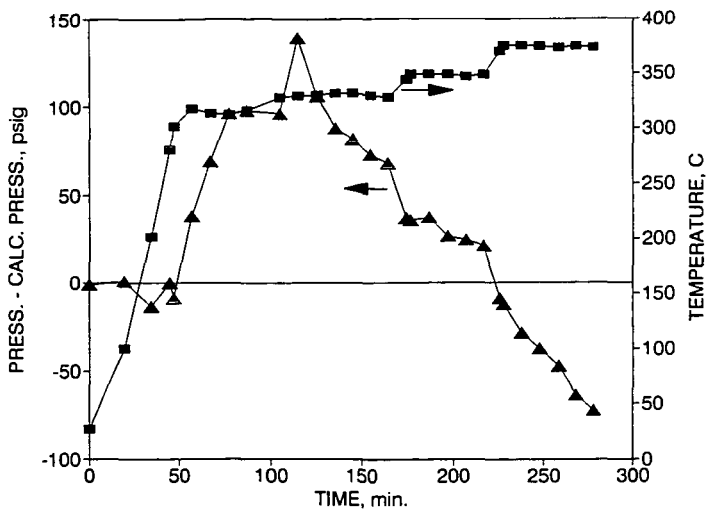


Fig. 6. Pressure difference without added catalyst.

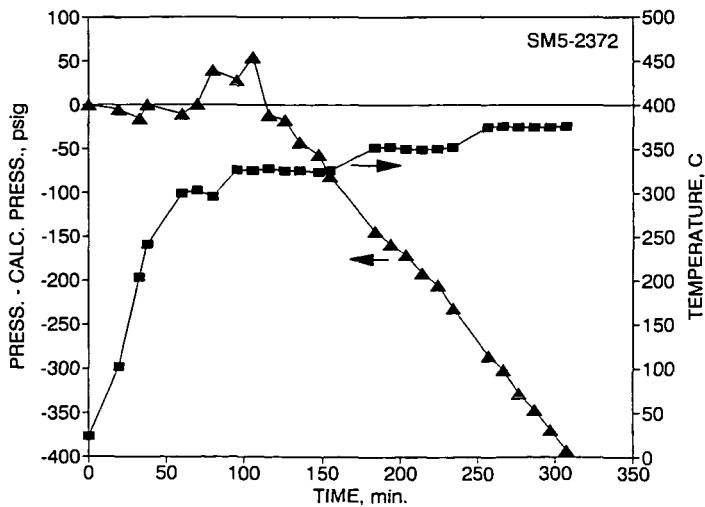


Fig. 7. Pressure difference with 1000 ppm Mo added.

DEVELOPMENT OF THIN FILM HYDROUS METAL OXIDE SUPPORTED CATALYSTS FOR DIRECT COAL LIQUEFACTION*

R. G. Dosch, L. I. McLaughlin, H. P. Stephens
Process Research Division

and T. J. Headley
Electron Optics Division

Sandia National Laboratories
Albuquerque, New Mexico

INTRODUCTION

In order to achieve optimum yields of distillate, current two-stage liquefaction processes, as evaluated in pilot research facilities consume as much 4 to 8 lbs of catalyst per ton of moisture-free coal fed to the reactors. The cost of catalyst for these replacement rates ranges from \$4 to \$6 per barrel of distillate product. If the cost of disposal of spent catalyst is considered, the cost could be substantially more. Thus a very important factor in achieving \$30/bbl liquids from coal is the development of less expensive catalysts or catalysts with better activity, selectivity and life.

The goal of this project is to develop catalysts, based on hydrous metal oxide (HMO) ion exchangers, that improve the efficiency and economics of conversion of coal to distillate products. Continuous reactor tests performed by AMOCO [1,2] have shown that preliminary formulations of one member of this class of catalysts, NiMo hydrous titanium oxide (HTO) catalysts were comparable or superior to 25 other commercial and novel formulations tested by AMOCO for second-stage upgrading of coal-derived resid. Thus efforts have focused on optimizing HTO supported catalysts, and recent research has resulted in formulation of NiMo/HTO catalysts with lower active metal loadings and increased activity. This paper reports the status of recent HTO catalyst research, especially the development of thin-film HTO-coated supports.

Although other HMOs, based on Zr, Nb or Ta may also provide good catalyst supports, HTO supports were chosen for initial development because the raw materials required to form HTOs are more readily available and less expensive than those required for other HMOs. A promising method to produce inexpensive catalysts with properties tailored to a specific process is the application of HTO catalysts as thin film coatings on other support structures. Development effort has concentrated on molybdenum as the major active metal in both the bulk and thin-film HTO catalysts. The choice of molybdenum as the major active component is based

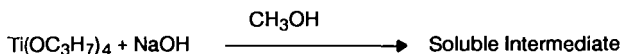
* This work was supported by the US Department of Energy at Sandia National Laboratories under contract DE-AC04-76DP000789

on the fact that the most successful liquefaction catalysts currently in use (e.g. Shell 324M and Amocat 1C) contain molybdenum as the major active metal. Catalysts developed in this program have been evaluated with laboratory micro-scale reactors, and will ultimately be evaluated with bench-scale units, such as the PETC Generic Unit, and a large-scale process development unit.

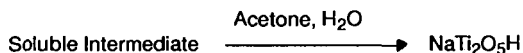
CATALYST PREPARATION

Hydrous titanium oxide catalysts are prepared by a technique that consists of synthesis of sodium hydrous titanate ion exchange material followed by ion exchange of the sodium for active metal ions [3]. The synthesis involves three steps:

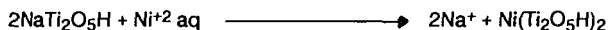
- (1) Reaction of tetraisopropyl titanate with sodium hydroxide in alcohol solution to form a soluble intermediate:



- (2) Hydrolysis of the soluble intermediate in acetone/water mixtures to form the hydrous metal oxide ion exchange material:



- (3) Ion exchange of the sodium for active metal ions in aqueous solution to form the catalyst:



In addition to the capacity to exchange metal cations, contact of the ion-exchangers with acidic solutions results in exchange of hydrogen ions, which alters the acidity and catalytic activity of the material. The materials can also function as anion exchangers in acidic solutions, allowing adsorption of metals that exist as aqueous oxygenated anions; molybdates, for example.

Catalyst preparation by coating inert supports with a thin film of a hydrous metal oxide ion-exchanger offers the potential of tailoring catalyst activity and selectivity by appropriate choice of active metal combinations and substrate physical properties such as strength, surface area, and pore size. Additionally, an excellent dispersion of active metals may be achieved by this technique.

Preparation of coated-support catalysts involves three steps:

- (1) Synthesis of the water or alcohol soluble hydrous titanium oxide as in step (1) above;

- (2) Deposition of an ion exchange coating by contacting the support with an aqueous or alcoholic solution of the soluble hydrous titanium oxide ion exchanger;
- (3) Ion exchange of the cations of the HTO coating for those of a catalytically active metal in aqueous solution as in step (3) above.

Because active metals are dispersed on HTO catalysts by ion exchange, they are chemically associated with the HTO support. Therefore activation techniques must result in release of the active metal components from the HTO support. For example, activation [4] of Mo-based HTO catalysts is performed in two steps: (1) calcination in air at 500°C to release the Mo and promoter ions from the HTO structure, followed by (2) sulfidation at 425°C with a 10% mixture of H₂S in H₂.

CATALYST TESTING

Initial tests have been conducted on powdered (-100 mesh) and particulate catalysts (granular, extrudate, or spherical) using batch microautoclaves for rapid screening of a large number of preparations to determine their activity for model reactions such as pyrene hydrogenation and dibenzothiophene desulfurization. The batch microautoclaves have liquid reactant capacities of 2 cc and a gas-phase volume of 25 cc. Four reactors can be operated simultaneously. A typical experiment is carried out as follows. After being charged with the catalyst and reactant, the reactors are heated to temperature in a fluidized sand bath while being shaken with a wrist-action motion at 200 cycles/min. Temperatures and pressures are recorded with a digital data acquisition system during the course of the experiments. Following the heating period, the reactors are rapidly quenched to ambient temperature, a gas sample is taken and the products are removed for analysis by various techniques, including gas and liquid chromatography and elemental composition. For sulfided NiMo catalysts, pyrene hydrogenation tests are typically carried out at 300°C and 500 psig cold charge hydrogen pressure, and dibenzothiophene desulfurization at 350°C and 1200 psig. For the more active noble metal catalysts such as Pd/HTO, pyrene hydrogenation experiments are typically performed at 100°C and 100 psig.

RESULTS AND DISCUSSION

Bulk-Phase NiMo/HTO Catalysts

The development of NiMo/HTO catalysts has progressed to the point where the hydrogenation activity of HTO-supported materials, as measured by the hydrogenation of pyrene, is significantly higher than that of commercially available NiMo/Al₂O₃ catalysts used for coal liquefaction. NiMo/HTO catalysts exhibiting pseudo-first-order rate constants for pyrene hydrogenation of 0.19 sec⁻¹ g cat⁻¹ (1.66 sec⁻¹ g Mo⁻¹) for the powdered catalyst (-100 mesh) can be routinely prepared.

This hydrogenation activity can be compared to that of $0.16 \text{ sec}^{-1} \text{ g cat}^{-1}$ ($1.21 \text{ sec}^{-1} \text{ g Mo}^{-1}$) for powdered Shell 324M in tests run under identical conditions.

Further advances in catalytic activity have been made via a combination of HTO substrate modification and changes in metal loading techniques. Addition of tetraethylorthosilicate in the first step of the synthesis to achieve a Ti/Si ratio of 0.2 for the ion-exchanger was found to further increase activity. The $\text{Na}_{0.5}\text{Ti}/0.2\text{Si}$ supports were converted to the $\text{H}_{0.5}\text{Ti}/0.2\text{Si}$ form prior to metal loading. Mo was introduced onto the support via an ion exchange reaction. Following drying at 100°C , Ni was introduced by wetting with a minimum amount of aqueous $\text{Ni}(\text{NO}_3)_2$ solution. With this method, most, but probably not all of the Ni is fixed on the support via ion exchange. After the Ni loading step, the materials were dried at 100°C , pelletized, calcined at 500°C , and sulfided at 425°C prior to testing. The powdered form of this catalyst (8.69% Mo, 2.95%Ni) was found to have a pseudo-first-order rate constant for pyrene hydrogenation of $0.22 \text{ sec}^{-1} \text{ g cat}^{-1}$ ($2.32 \text{ sec}^{-1} \text{ g Mo}^{-1}$). The catalyst weight basis desulfurization activity as measured by the pseudo-first-order rate constant for dibenzothiophene desulfurization ($0.027 \text{ sec}^{-1} \text{ g cat}^{-1}$) was found to be the same as that for freshly sulfided, -200 mesh Shell 324M (0.027). However, on a weight of Mo basis, the desulfurization activity is about 50% greater, because of the lower Mo loading on the Si modified HTO catalyst. It appears that the increase in activity due to silicon addition is achieved, in part, by the stabilizing effect that Si has on the surface area of the calcined and sulfided catalysts. Catalysts containing silicon have approximately 60% higher surface area than preparations without silicon (150 vs $90 \text{ m}^2/\text{g}$).

Transmission electron microscopy (TEM) of the sulfided NiMo/HTO and commercial NiMo/alumina catalysts has shown that the greater activity of the HTO catalysts appears to result from a better dispersion of the Mo sulfide crystallites. Whereas the alumina catalysts appear to contain 50 to 70 angstrom-size stacks of 4-6 MoS_2 layers supported on amorphous alumina (figure 1), the HTO catalysts contain 50 to 70 angstrom-size crystallites of only 1-2 MoS_2 layers supported on 100 to 150 angstrom diameter anatase crystallites (figure 2) formed during the calcination process.

HTO-Coated Catalyst Supports

The information obtained from the development of bulk-phase HTO catalysts was found to be directly applicable to the preparation of thin-film NiMo/HTO catalysts on pre-formed supports. Application of HTO catalysts as thin films on support material is a promising approach to preparing inexpensive catalysts, because smaller amounts of HTO ion-exchanger material and active metals are required, and inexpensive supports may be used. Initially thin-film NiMo/HTO catalysts supported on a material referred to as controlled pore glass (CPG), available in -20 mesh granular form, were prepared. Results of experiments performed to compare the hydrogenation activities of bulk-phase and thin-film Pd/HTO-coated and NiMo/HTO-coated CPG catalysts showed that the thin-film catalysts had comparable or greater activities on a weight of active metal basis.

Recently NiMo/HTO-coated catalysts have been prepared using a porous silica support in spherical form, 1.5 mm in diameter. The silica spherical support has a surface area of 55 m²/g, an average pore diameter of 77 nm, and a total pore volume of 1.00 cc/g. The spheres were first coated with a thin film of HTO followed by exchange of Mo and Ni onto the thin film to achieve nominal Mo loadings of 1% and Ni loadings of 0.3%. Following calcination and sulfidation, the catalysts were tested for their activity for hydrogenation of pyrene to 4,5-dihdropyrene at 300°C, and desulfurization of dibenzothiophene at 350°C. These spherical silica NiMo/HTO-coated catalysts had weight basis rate constants for pyrene hydrogenation of 0.032 ± 0.003 sec⁻¹-g cat⁻¹ as compared to 0.041 for Shell 324M extrudate (0.78 mm diameter by 4 mm long) and 0.038 for Amocat 1C extrudate (1.59 mm diameter by 6 mm long). On a weight of active metal (Mo) basis, the rate constants ranged from 2.6 to 3.5 sec⁻¹ g Mo⁻¹, a factor of ten greater than that of 0.31 for Shell 324M. For dibenzothiophene desulfurization, rate constants of 0.0081 ± 0.0003 sec⁻¹ g cat⁻¹ were determined for the NiMo/HTO-coated silica spheres, compared to 0.016 for Shell 324M. Thus the HTO-coated silica sphere catalysts, which contained only one-tenth as much active metal as Shell 324M, exhibited half of the dibenzothiophene desulfurization activity on a weight of catalyst basis. On a weight of Mo basis, because of the low active metal loadings, the HTO coated sphere catalysts had activities six times that of Shell 324M.

The high activity, on a weight of Mo basis, for these spherical silica HTO-coated catalysts is due, in part, to their high effectiveness factor (ratio of the rate constant for the catalyst spheres to that of the powdered catalyst), which was determined to be 0.75 (for hydrogenation), compared with the much smaller values of 0.27 and 0.22 for Shell 324M and Amocat 1C. This result is undoubtedly due, in part, to differences in the effective diffusivity resulting from the more open pore structures of the silica spheres. A factor contributing to the higher Mo weight basis activity of the NiMo/HTO-silica sphere catalysts is the better dispersion of MoS₂ achieved by the HTO coating process. TEM analysis (figures 3 and 4) has shown that, as with the case for the bulk-phase HTO catalysts, the MoS₂ crystallites for the coated catalysts consist of 50-70 angstrom-size crystallites of 1-2 layers of MoS₂ attached to small anatase crystallites. These results demonstrate that the HTO coating method can be used to produce a catalyst with a low active metal loading, satisfactory activity, and a geometry amenable to existing reactor systems.

CONCLUSIONS

Hydrous titanium oxides are extremely versatile materials for preparation of coal liquefaction catalysts. Screening tests of catalyst activity with feeds that model coal liquefaction reactions have shown that bulk HTO catalysts with activities significantly greater than commercial NiMo/alumina catalysts can be prepared. Preliminary formulations of bulk-phase NiMo/HTO catalysts have also performed well in continuous microreactor tests [1] for upgrading coal-derived resid. In addition, catalysts prepared from HTO-coated supports, containing one-tenth the active metals of commercial alumina-supported catalysts, have been found to exhibit high

hydrogenation and desulfurization activities on a weight of Mo basis. Thus, HTO-coated support materials offer a promising method to produce cost-effective catalysts with mechanical, physical and catalytic properties tailored to specific direct liquefaction process applications.

REFERENCES

1. D. J. Sajkowski, "Second Stage Catalyst Testing," Proceedings of the 1990 Direct Liquefaction Contractors' Review Meeting, U. S. Department of Energy, Pittsburgh Energy Technology Center, Pittsburgh, PA, September 24-26, 1990, p. 76.
2. R. G. Dosch, F. V. Stohl, and H. P. Stephens, "Development of Hydrous Metal Oxide-Supported Catalysts for Direct Liquefaction, Proceedings of the 1990 Direct Liquefaction Contractors' Review Meeting, U. S. Department of Energy, Pittsburgh Energy Technology Center, Pittsburgh, PA, September 24-26, 1990, p. 56.
3. R. G. Dosch, H. P. Stephens, F. V. Stohl, B. C. Bunker, and C. H. F. Peden, "Hydrous Metal Oxide-Supported Catalysts: Part I. Preparation Chemistry and Physical and Chemical Properties," SAND89-2399, Albuquerque: Sandia National Laboratories, February 1990.
4. R. G. Dosch, F. V. Stohl, and J. T. Richardson, "Activation of Hydrous Oxide-Supported Catalysts for HDS, and HDO Reactions," Novel Materials in Heterogeneous Catalysis, ACS Symposium Series 437, Edited by R. T. K. Baker and L. L. Murrell, pp. 279-288, 1990.

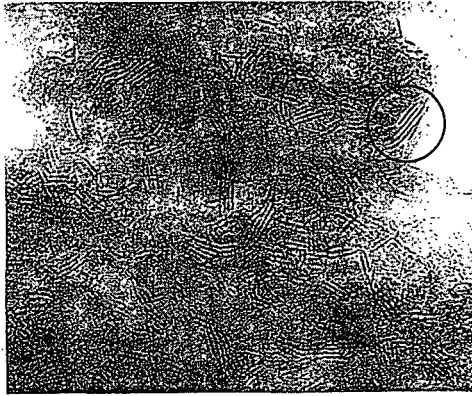


Figure 1. Transmission Electron Micrograph of sulfided NiMo/alumina catalyst containing 13.2% Mo and 2.7% Ni. A typical crystallite containing a "stack" of 4 MoS₂ layers (dark lines) is shown within circled area. Many other "stacks" of 4-6 MoS₂ layers can be observed.

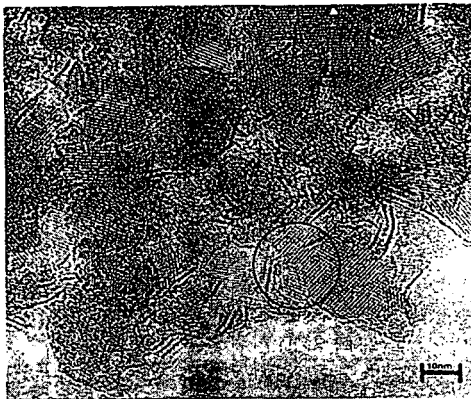


Figure 2. Transmission Electron Micrograph of sulfided NiMo/HTO catalyst containing 10.2% Mo and 3.4% Ni. Typical crystallites containing one MoS₂ layer (dark line) conforming to the shape of an anatase crystallite is shown within circled area. Many other crystallites of one MoS₂ layer can be observed.

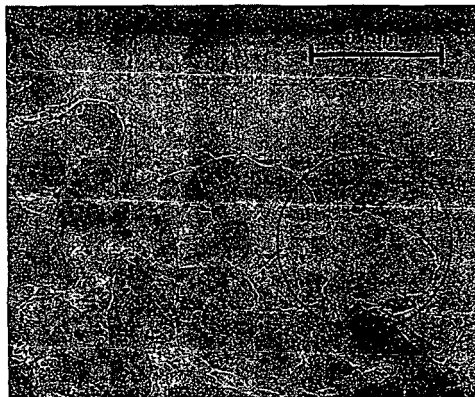


Figure 3. Transmission Electron Micrograph of sulfided NiMo/HTO supported on porous silica. This catalyst contains 1.3% Mo and 0.2% Ni. The silica support is seen as the larger irregularly shaped material (circled), approximately 100 nm in size. The smaller material (10 nm in size, darker spots) on the silica are crystallites of anatase with MoS₂ attached. The circled area is shown magnified by a factor of 3 in Figure 4.

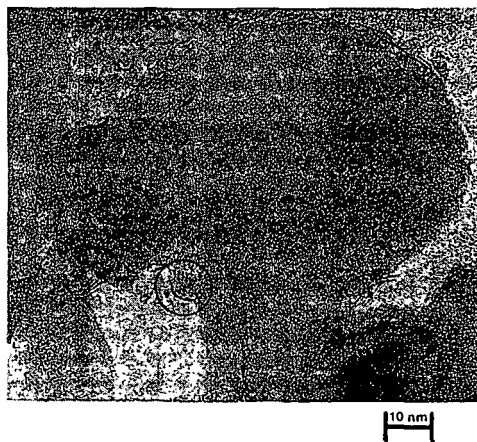


Figure 4. Transmission Electron Micrograph of sulfided NiMo/HTO supported on porous silica. The circled area shows a typical crystallite of anatase with a crystallite containing a single layer of MoS₂ (dark line) attached.

DISPERSED MOLYBDENUM CATALYSTS FOR LIQUEFACTION OF ILLINOIS NO. 6 COAL

April J. Swanson
Amoco Oil Co., H-2, P. O. Box 3011
Naperville, IL 60566-8460

Keywords: Coal, Molybdenum, Catalyst

ABSTRACT

Supported Ni/Mo catalysts have been used successfully for liquefaction of Illinois No. 6 bituminous coal at the Advanced Coal Liquefaction facility in Wilsonville, AL. In Run 261, coal conversions of 92-93% and C₄+ distillate yields of 64-65% were obtained with Akzo's EXP-A060 catalyst or Shell 324. These results are excellent, however, process costs could be decreased by use of a dispersed catalyst in a slurry reactor. Research was undertaken to evaluate dispersed Mo catalysts for liquefaction of Illinois No. 6 coal under DOE Contract DE-AC22-88PC88819.

Resid conversion improved when oil-soluble Molyvan L replaced Amocat™ LC catalyst in the first stage (192 ppm Mo/coal). Raising the first stage temperature from 800°F to 820°F increased resid conversion further. Use of Molyvan L or Mo octoate (84-192 ppm Mo) as the only catalyst also gave high resid conversion. Furthermore, about the same yield structure was obtained at half the residence time and higher temperature. With the oil-soluble Mo catalysts, distilled fractions contained more heteroatoms, which must be removed in a subsequent hydrotreating step. Based on these tests, oil-soluble Mo catalysts are recommended for liquefaction of Illinois No. 6 coal.

INTRODUCTION

Illinois No. 6 coal has served as the reference liquefaction feedstock at the Advanced Coal Liquefaction facility in Wilsonville, Alabama for several years. The process has evolved over time from single-stage high-severity to two-stage, moderate severity. Significant improvements have been made in coal conversion, energy rejection during solids separation, distillate yield, and coal throughput. The best results to date were obtained using a new catalyst, EXP-AO-60, with a pore structure similar to Amocat™ catalysts, in the two stage catalytic process. It is becoming increasingly difficult to develop a new supported catalyst that gives a large beneficial effect on process economics. Improvements are more likely to come from significant process changes. With this in mind, oil-soluble molybdenum catalysts for liquefaction of Illinois No. 6 coal were tested in this work in place of the supported catalyst in one or both stages. Use of oil-soluble catalysts would simplify reactor design and decrease reactor cost. Molyvan L (8% Mo, \$3.20/lb.) and molybdenum octoate (8% Mo, \$2.00/lb.) are commercially-available oil-soluble lubricant additives. Molyvan L was used as a first stage catalyst for liquefaction of Black Thunder coal in Wilsonville run 262 (Shell 324 in stage 2) and the only catalyst in Wilsonville run 263. This paper describes use of Molyvan L and molybdenum octoate for liquefaction of Illinois No. 6 coal. Results were very promising, suggesting that oil-soluble molybdenum compounds are good alternative catalysts for a Wilsonville-type process with Illinois No. 6 coal feed.

EXPERIMENTAL

Analyses of the Illinois No. 6 coal feed, from Wilsonville Run 257, is given in Table 1. Liquefaction solvent was a blend of V-1074 and V-203 liquids from Wilsonville Run 257. The analysis is given in Table 2. The bench-scale liquefaction runs were made in AU-135L continuous, two-stage pilot plant with 1-liter stirred autoclave reactors. Feed slurries consisted of 33/67 mixtures of

coal/liquefaction solvent. Molyvan L or molybdenum octoate were added to the feed tank without additional sulfiding agent. Two runs with dispersed catalyst were completed, one with Molyvan L added to the feed as the first stage catalyst and Amocat™ 1C catalyst in the second reactor, and one with Molyvan L or molybdenum octoate and no supported second stage catalyst. Amocat™ 1C catalyst was presulfided with 8% hydrogen sulfide in hydrogen before use. Product solubility was determined by millipore filtration, distillate yields were determined by modified D-86 and D-1160 distillation, and distilled fractions were analyzed for C, H, S, N, and O. Unconverted solids were analyzed for metals by ICP (inductively coupled plasma spectroscopy).

Molyvan L Catalyst in Stage 1/Amocat™ 1C Catalyst in Stage 2

Liquefaction of Illinois No. 6 coal may place greater demands on the catalyst for hydrogenation of aromatics than liquefaction of Black Thunder coal. This test used Molyvan L in the first stage and Amocat™ 1C catalyst in the second stage to keep hydrogenation activity high. Feed slurries contained 800 ppm of Molyvan L (192 ppm molybdenum as a fraction of coal). Operating temperatures were 800-820 °F for the first stage, and 760 °F for the second stage. Nominal residence times were 1.5 hour in each stage or 3 hours overall. The run was operated with slurry feed for 15 days, and then with solvent-only feed for 6 days.

RESULTS

Product yields are compared to those from Amocat 1C in Table 3. The run with Molyvan L in the first stage is labelled "T/C" and the run with Amocat™ 1C catalyst in the first stage is labelled "C/C". At 800°F, the resid yield was lower with Molyvan L than with Amocat™ 1C first stage catalyst (15% vs. 28%). Resid yield decreased to 7% with Molyvan L when the first stage temperature was raised from 800 to 820°F. Yields of 650-935°F distillate increased from 5% to 13% with Molyvan L, and yields of 360-650°F distillate increased from 35% to 43% at the higher first stage temperature. Hydrocarbon gas yields and hydrogen consumption increased only slightly at 820°F.

Analyses of distilled products are given in Table 5. Amocat™ 1C catalyst in the first stage gave better hydrogenation and heteroatom removal in the lightest (360-650°F) fraction than Molyvan L. This result is not surprising because smaller pore catalysts are most effective for hydrotreating light distillate fractions. The Molyvan L acts like a very large-pore catalyst.

Spent second stage catalyst analyses are given in Table 6. With Molyvan L in the first stage, second stage catalyst was in worse shape than when it was protected by Amocat™ 1C first stage catalyst. Carbon levels were higher (25% vs. 8%), the surface area was lower (84 vs. 151 m²/g), the pore volume was lower (0.21 vs. 0.38 cc/g), and metal deposits were higher. Solids appear to deposit on the first supported catalyst that is available. In fact, spent second stage catalyst from the run with Molyvan L is similar to spent first stage Amocat™ 1C catalyst. The second stage catalyst replacement rate would have to increase if Molyvan L was used in the first stage.

Dispersed Molybdenum Catalysts in Stages 1-2

Molyvan L or molybdenum octoate were tested without supported catalyst for liquefaction of Illinois No. 6 coal at 192 ppm and 84 ppm Mo:coal (64 and 26 ppm Mo:slurry) for Molyvan L, and 96 ppm Mo:coal (32 ppm Mo:slurry) for molybdenum octoate. Operating temperatures were 800-820°F for both reactors. The nominal residence times were 0.75-1.5 hour in each stage or 1.5-3.0 hours overall. Each set of conditions was maintained for 3 days to obtain representative samples.

At the end of the run, a solvent-only feed was processed with Molyvan L catalyst (48 ppm Mo:solvent).

RESULTS

Product yields from all conditions were good, see Table 3, columns labelled "slurry". Resid yields were 3-8%, C₄-935°F distillate yields were 66-72%, and coal conversions were 94-96%, which was as least as good as from the first stage test with Molyvan L. Hydrogen consumption were somewhat lower (4.8-5.7%) than from Amocat™ 1C (5.6%) or for first stage Molyvan L (5.4-6.1%).

Product yields did not change when the molybdenum level was decreased from 192 ppm to 84 ppm. Product yields were also unchanged when and the residence time was decreased from 3 to 1.5 hours and the temperature was raised from 800 to 820°F. Molybdenum octoate gave less resid than Molyvan L at the same conditions, and would be the preferred oil-soluble molybdenum catalyst because it is less expensive.

Distillate product quality, Table 4, was not as good as when Amocat™ 1C catalyst was present, however. Nitrogen and oxygen levels were higher, but sulfur and hydrogen levels were about the same. It is interesting to note that the resid plus solid fraction has a higher H/C ratio (0.98) with Molyvan L catalyst at 800°F than with Amocat™ 1C catalyst (0.95-0.96). Better hydrogenation of the heaviest components by Molyvan L is indicated. At reactor temperatures of 820°F, the H/C ratio of the resid plus solids fraction dropped to 0.92, reflecting a shift in equilibrium toward dehydrogenation. Molybdenum octoate was not as active for hydrogenation of resid plus solids, giving a H/C ratio of 0.91 at 800°F.

CONCLUSIONS

Molyvan L Catalyst in Stage 1

Overall, a process with Molyvan L catalyst in the first stage and Amocat™ 1C catalyst in the second stage gave a higher distillate yields than a process with Amocat™ 1C catalyst in both stages. Because Molyvan L catalyst can be used in a less expensive slurry reactor, it would be the preferred first stage catalyst for liquefaction of Illinois No. 6 coal. With Molyvan L in the first stage, deactivation is more rapid for supported second stage catalyst, and the catalyst addition rate would have to be increased. Also, hydrogenation of light distillate was not as good, which would require additional hydrotreating.

Molyvan L Catalyst in Stage 1/Amocat™ 1C Catalyst in Stage 2

A process with dispersed molybdenum compounds as the only catalyst offers several advantages over liquefaction with Amocat™ 1C catalyst, including less expensive reactor design and simpler operation of the reactors. Product was better than when Amocat™ 1C catalyst was used in both reactors and as good as when Amocat™ 1C was used in stage 2 with Molyvan L in stage 1. Low levels of molybdenum, 84 ppm Mo:coal, were effective. Production of a low-resid product at 1.5 hours residence time and 820°F was demonstrated. Molybdenum octoate, a less expensive dispersed molybdenum catalyst, performed well, perhaps because of the high sulfur content of Illinois No. 6 coal. Use of dispersed molybdenum catalysts for liquefaction of Illinois No. 6 coal is recommended.

ACKNOWLEDGEMENTS

This work was completed with funding from the United States Department of Energy under contract number DE-AC22-88PC88819.

TABLE 1
COAL ANALYSES

Coal	Illinois No. 6
As Received, Wt% H ₂ O	6.05
Dry, Wt%	
C	69.54
H	4.56
N	1.17
S	3.26
O (Difference)	12.03
Ash	9.44
Fe	1.19
Na	0.05
K	0.18
Ca	0.37
Mg	0.06
Al	0.99
Ti	0.05
Si	2.15

TABLE 2
SOLVENT ANALYSES

Wilsonville Run	257
Wilsonville Coal	Illinois No. 6
Elemental Analyses, Wt%	
C	89.26
H	8.83
N	0.57
S	0.08
O	1.26
Distillation, Wt%	
IBP-650°F	0.36
650-935°F	58.26
935+°F	40.45
Solubility, Wt%	
THF Insolubles	0.12
Toluene Insolubles	1.07
Hexane Insolubles	7.96

TABLE 3.
Liquefaction of Illinois No. 6 Coal: Distilled Product Yields

Process	C/C	T/C	T/C	Slurry	Slurry	Slurry	Slurry
Residence Time, Hours	3	3	3	3	3	1.5	3
Stage 1, °F	790	800	820	800	800	820	800
Stage 2, °F	760	760	760	800	800	820	800
Molyvan L, ppm	0	192	192	192	84	84	0
MoOctoate, ppm	0	0	0	0	0	0	96
Catalyst Age, Hours	180	150	310				
Yields, Wt% of MAF Coal							
C ₁ -C ₃	8.9	9.3	10.1	8.5	9.1	11.0	10.5
C ₄ -360°F	7	7	12	7	10	11	8
360-650°F	35	35	43	40	39	41	43
650-935°F	5	13	12	21	19	16	22
935°F+	28	15	7	8	8	5	3
C ₄ -935°F	47	56	67	68	66	68	72
Conversion	93.2	91.1	93.9	94.6	96.3	95.7	94.5
H ₂ Consumption	5.6	5.4	6.1	5.1	5.7	4.9	4.8

C - With Amocat™ 1C catalyst T - Without Amocat™ 1C catalyst

TABLE 4.
Liquefaction of Illinois No. 6 Coal: Product Analyses

Process	C/C	T/C	T/C	Slurry	Slurry	Slurry	Slurry
Residence Time, Hours	3	3	3	3	3	1.5	3
Stage 1 °F	790	800	820	800	800	820	800
Stage 2 °F	760	760	760	800	800	820	800
Molyvan L, ppm	0	192	192	192	84	84	0
MoOctoate, ppm	0	0	0	0	0	0	96
Catalyst Age, Hours	150	150	310				
Analyses, Wt%							
<u>360-650°F</u> Aromatic C	32	40	40	43	43	43	43
H/C	1.61	1.49	1.49	1.47	1.48	1.46	1.45
N	.25	.41	.48	.65	.56	.54	.51
O	1.5	2.3	2.4	2.9	3.3	3.1	3.1
<u>650-935°F</u> Aromatic C	42	47	47	47	48	50	51
H/C	1.28	1.28	1.27	1.25	1.27	1.22	1.22
S	.06	.07	.07	.08	.09	.09	.09
N	.30	.36	.47	.60	.61	.52	.49
O	.5	.8	.9	1.1	1.2	1.1	1.0
<u>935°F+, Solids</u>							
H/C	.96	.95	.96	.98	.98	.92	.91
S	.96	1.00	.92	1.01	.88	.35	.95
N	1.07	1.14	1.18	.97	1.06	1.09	1.12

C - With Amocat™ 1C catalyst T - Without Amocat™ 1C catalyst
Nominal residence time was about 3 hours for these periods.

TABLE 5.
 Analyses of Spent Amocat™ 1C Catalyst Samples:
 Illinois No. 6 Liquefaction

Stage	Fresh	1	2	2
Temperature, °F		790	760	760
Process		C/C	C/C	T/C
Oil-Soluble Mo, ppm				192
Run Length, Days	0	20	20	20
<u>Elemental Analyses, Wt%</u>				
<u>Primary Metals</u>				
Mo	9.10	5.9	8.10	6.50
Ni	2.22	1.25	1.63	1.37
Al	35.40	23.50	31.60	25.10
Si	1.39	.98	1.22	.99
<u>Deposits</u>				
C	--	25.35	7.86	24.98
H	--	1.59	1.50	1.42
S	.20	4.78	5.86	4.97
Ti	.00	1.54	.14	.58
Fe	.02	.44	.14	.17
Na	.08	.12	.11	.15
Mg	.00	.05	.01	.01
Ca	.00	.00	.00	.00
<u>Pore Properties</u>				
Vol. <1200 Å Diam., cc/g	.59	.16	.38	.21
BET Surface Area, m ² /g	200	65	151	84

TRANSITION METAL CARBIDES AND NITRIDES AS HYDROPROCESSING CATALYSTS

S. Ted Oyama^{1,2}, Rajat Kapoor¹
Departments of Chemical Engineering¹ and Chemistry²
Clarkson University
Potsdam, New York 13699-5705

Chakka Sudhakar
Texaco, Inc.
Research and Development
Beacon, New York 12508

INTRODUCTION

The removal of nitrogen and sulfur from petroleum and coal feedstocks is an essential step in their refining to transportation fuels. Traditional catalysts have been sulfides of Co, Mo, W and Ni in various combinations supported on alumina. Although other transition metal sulfides have been found to be more effective in hydrodesulfurization (Os, Ru, Ir, Rh), their high cost has precluded their use as commercial catalysts (1). The resemblance of early transition metal carbides and nitrides to Group 8 metals (2,3) suggested their possible application in hydroprocessing. The objective of this study was to compare the catalytic activity of selected carbides and nitrides to a commercial sulfided Ni-Mo-P/Al₂O₃ catalyst in the hydroprocessing of a diesel feedstock.

EXPERIMENTAL

The transition metal carbides and nitrides were prepared by a temperature-programmed method in which a precursor oxide was treated in a flowing reactive gas stream as the temperature was progressively raised (4,5,6). The catalysts were passivated in a stream of 0.5 mol% O₂/He after preparation. The surface areas of the catalysts were determined in a flow system by the 1-point BET method and were found to be 66 m²g⁻¹ for Mo₂C, 59 m²g⁻¹ for

Mo₂N, and 60 m²g⁻¹ for VN. Prior to catalytic evaluations the catalysts were reduced *in situ* at 723 K (450 °C) for 3h.

The performance of the carbides and nitrides was compared to that of a state-of-the-art commercial catalyst containing 14 wt% Mo, 3 wt% Ni, and 4-6 wt% P, supported on alumina. The surface area of the catalyst was 175 m²g⁻¹. This catalyst was sulfided in 10 mol% H₂S/H₂ at 623 K (350 °C) for 2 hours before the start of the reaction.

The catalysts were evaluated in a standard high pressure flow reactor system equipped with electronic flow and temperature controllers. The feedstock used for the evaluations was a finished diesel from a west coast refinery containing 0.02% S, 82 ppm N and 27 wt% aromatics. Hydrodenitrogenation was determined as N removed as ammonia as measured by the Antek N analysis of the product. Hydrodearomatization (HDA) was measured by the open column liquid chromatography (OCLC, ASTM D# 2549) method. The catalysts were compared at two conditions, moderate and severe, applied in succession to the same catalyst batch. The moderate conditions consisted of a LHSV of 3.0 h⁻¹, 4.8 MPa (700 psig), 573 K (300 °C) and a H₂ flow of 2000 SCFB. The severe conditions comprised a LHSV of 1.0 h⁻¹, 10.3 MPa (1500 psig), 653 K (380 °C), and a H₂ flow of 4000 SCFB. All catalysts were compared on an equal volume basis.

RESULTS AND DISCUSSION

The results of the catalytic evaluations are reported in Table 1 and 2. The tables also report the amounts of catalyst loaded in volume and weight. The comparisons are made at constant values of liquid hourly space velocity (LHSV), so that the hydrodenitrogenation activity (%HDN) of the different catalysts are on the basis of *equal volume*. For analysis, samples were collected at the reported time intervals, sometimes with mixing of aliquots.

Table 1 compares the performance of the catalysts at moderate conditions. The Mo₂C catalyst shows a decline in activity over the 64 h of test time. Such initial deactivation is normal in most hydroprocessing catalysts. In contrast, Mo₂N does not manifest any substantial deactivation and maintains its initial activity. The VN catalyst shows no catalytic activity at these conditions. The commercial Ni-Mo-P-S/Al₂O₃ catalyst shows the greatest HDN activity per unit volume.

Table 1
Catalytic Performance of Catalysts at Moderate Conditions
(Reactant N = 84 ppm, P = 4.8 MPa, T = 573 K, LHSV = 3.0 h⁻¹, H₂ flow = 2000 SCFB)

Catalyst	Volume cm ³	Weight g	Product N ppm	HDN %	HDA %	Comments
Mo ₂ C	4.3	5.2	68	17	-	24 h, cuts 1-3
			74	9.8	-	40 h, cuts 4,5
			77	6.1	-	64 h, cuts 6,7
Mo ₂ N	3.2	5.1	70	17	-	24 h, cuts 1,2
			71	16	-	48 h, cuts 3,4
VN	5.8	5.2	84	0	-	24 h, cuts 1-3
			84	0	-	40 h, cuts 4,5
			84	0	-	64 h, cuts 6,7
Ni-Mo-P	15	12.8	25	70	-	24 h, cuts 1,2

Table 2 reports the performance of the catalysts at severe hydroprocessing conditions. At these conditions all catalysts are active, including VN. Of the carbides and nitrides Mo₂N remains the most active, equalling the performance of the commercial Ni-Mo-P-S/Al₂O₃ in HDN and approaching it in hydrodearomatization. Interestingly, the carbide and nitride catalysts showed increased HDN activity with the progression of the test. This is contrary to what is generally found in hydroprocessing and suggests that the catalysts were not properly activated in the initial tests. This may explain the lower performance of these catalysts compared to the commercial Ni-Mo catalyst at the moderate conditions (Table 1).

It should be pointed out that comparisons of catalyst performance in HDN at the severe conditions employed in Table 2 may be misleading because of the high conversions achieved. This would tend to eliminate differences between catalysts. However, it should also be noted that in all comparisons a *volume* basis was employed. If correction is made for the surface areas of the catalysts, the carbides and nitrides would manifest higher activities.

Table 2
Catalytic Performance of Catalysts at Severe Conditions
(Reactant N = 84 ppm, P = 10.3 MPa, T = 653 K, LHSV = 1.0 h⁻¹, H₂ flow = 4000 SCFB)

Catalyst	Volume cm ³	Weight g	Product N ppm	HDN %	HDA %	Comments
Mo ₂ C	4.3	5.2	4	95	22	24 h, cut 8
			2	98	18	50 h, cut 9
Mo ₂ N	3.2	5.1	17	80	31	30 h, cut 5
			1	99	41	100h, cut 6
VN	5.8	5.2	27	68	6	24 h, cut 8
			14	83	11	50 h, cut 9
Ni-Mo-P	15	12.8	1	99	43	24 h, cut 3
			1	99	61	50 h, cut 4

ACKNOWLEDGEMENTS

This paper was written with support from the Center for Advanced Materials Processing at Clarkson University and from the U.S. Department of Energy under the Advanced Coal Research at U.S. Universities Program, Grant no DE-FG22-91PC91298. The authors also thank Texaco, Inc. for permission to publish these results.

LITERATURE CITED

- (1) Chianelli, R. R., *Catal. Rev.-Sci. Eng.*, 26, 361 (1984).
- (2) Oyama, S. T. and Haller, G. L., *Catal. Spec. Period. Rep.*, 5, 333 (1982).
- (3) Oyama, S. T., *Catal. Today*, In press.
- (4) Lee, J. S., Oyama, S. T. and Boudart, M., *J. Catal.*, 106, 125 (1987).
- (5) Oyama, S. T., Schlatter, J. C., Metcalfe, J. E. and Lambert, J., *Ind. Eng. Chem. Res.*, 27, 1639 (1988).
- (6) Kapoor, R. and Oyama, S. T., *J. Solid State Chem.*, In press.

HIGH-SEVERITY CO-PROCESSING

J. G. Gatsis, R. W. Roemisch, M. A. Miller,
C. A. Piasecki, and H. E. Fullerton

UOP
Des Plaines, Illinois

Keywords: co-processing, liquefaction, coal, petroleum resid

INTRODUCTION

UOP is continuing bench-scale research and development of coal and petroleum resid co-processing technology under the sponsorship of U.S. Department of Energy. Earlier work, under completed contract DE-AC22-84PC70002, has been reported in a series of papers and reports (1-7). The overall objectives, to evaluate the technical feasibility of the co-processing concept and to establish a co-processing data base, were met. The concept of single-stage, slurry-catalyzed co-processing was successfully demonstrated in laboratory batch experiments (1) and in continuous bench-scale operations (2). Good long-term operability with the UOP vanadium-based catalyst was demonstrated for nearly 2,000 hours on-stream (3). A method of recovering the catalyst was developed and demonstrated on a laboratory scale. Based on the long-term operability and catalyst recovery studies, a conceptual commercial design was completed for a co-processing unit integrated into a 100,000 BPSD conventional refinery (3,4).

The primary objective of the current contract, DE-AC22-87PC79818, is to extend and optimize the single-stage, slurry-catalyzed co-processing scheme. Catalyst economics plays a major role in determining the overall profitability of slurry-phase co-processing. Consequently, much work has been devoted to exploring new catalyst systems and improving catalyst activity, dispersion, and recovery techniques. Most of the early development work was done using a vanadium-based slurry catalyst. A newer molybdenum-based slurry catalyst has been developed. In autoclave testing, the molybdenum-based catalyst gave equivalent conversions and yields as the vanadium-based catalyst at one-tenth the metal concentration (8). This molybdenum-based catalyst has been evaluated in the continuous bench-scale unit. Plant modifications, including the addition of a recycle loop, have made bench-scale operations possible at much higher severities than were previously possible. Good plant operations have been achieved at temperatures up to 470°C and with catalyst concentrations as low as 500 ppm molybdenum (9). Processing at high severities for short durations has demonstrated high nondistillable conversion without excessive carbon loss to retrograde reactions and light-ends yield. This important advancement in co-processing should significantly improve the process economics. A long-term operability study at high-severity conditions was needed to demonstrate that high-severity co-processing is feasible and can be run for extended periods without major operational problems. This paper reviews the results of a recent long-term operability study at high severity.

Continuous Bench-Scale Operations

A simplified block diagram of the pilot plant is shown in Figure 1. The unit contains many of the essential features of the commercial flow scheme and is equipped to quantitatively measure the hydrogen consumption in the operations. The slurry feed (finely ground coal, petroleum vacuum resid, and catalyst) is combined with a hydrogen-rich recycle gas and is preheated before it enters the bottom of an upflow reactor. The products from the reactor are separated into gas and oil streams in the high-pressure separator (HPS). The gas stream from the HPS is combined with makeup hydrogen before being recycled back to the incoming fresh feed. A portion of the oil stream

from the HPS is recycled back to the incoming fresh feed, and the remainder is sent to a stripper. The lighter hydrocarbon stream from the stripper is sent to a debutanizer, where it is separated into C_4 and C_5 products. The heavier hydrocarbon stream from the stripper is sent to a vacuum fractionator to recover an overhead stream (light oil and vacuum gas oil) and a bottoms stream containing catalyst, coal minerals, insoluble carbonaceous material, and nondistillable hydrocarbons.

The addition of a recycle loop to the plant, i.e., the recycle of a portion of the HPS liquid back to the fresh feed, has greatly improved plant operability, especially at temperatures greater than 440°C. A recycle ratio of greater than 5:1 (based on recycle to fresh feed) is typically used. The space velocity of the fresh feed is maintained constant. The recycle results in increased liquid velocities and backmixing in the reactor. The improved mixing may help to eliminate the wall effect associated with a small bench-scale reactor. The liquid recycle also has a "flywheel" effect that helps to better withstand upsets in the fresh feed rate.

Prior to the introduction of liquid recycle, the reactor temperature in the bench-scale unit was limited to a maximum of about 425°C. As the operating temperature was increased beyond 425°C, a rapid decrease in heptane insolubles followed by coking and plugging problems made the plant increasingly difficult to operate (2).

With the addition of liquid recycle, the bench-scale unit can be run at much higher temperatures without developing coking problems (9). Temperatures of up to 470°C were achieved. The increased severity had little effect on the maximum coal conversion, which was still about 92%, but did result in about 20% increase in maximum asphaltene conversion (as measured by heptane insolubles) and an almost 30% increase in the 510°C+ nondistillable conversion.

The mechanism for improved high-temperature plant operability and conversions with liquid recycle may be due to better contacting of the reactive coal fragments with hydrogen and catalyst as a result of improved reactor backmixing or to the decrease in the relative contact between the coke precursors and the hot reactor walls as a result of greater superficial liquid velocities in the reactor. Hydrodynamic differences resulting from recycle may have also affected the flow regime, heat transfer characteristics, or gas void volume in the reactor. Further reactor modeling studies are needed to thoroughly understand these phenomena.

Feedstocks

The feedstocks used for this study were reference feedstocks Lloydminster vacuum resid, designated as R10, and Illinois No. 6 coal, designated as Cl.4. Feed properties are given in Tables 1 and 2. Lloydminster vacuum resid (950°F⁺, 120-150 Pen.) was obtained from a commercial refinery in Canada. Illinois Coal No. 6 was obtained by the Kentucky Center for Energy Research Laboratory from the Burning Star Mine. Grinding (thru 200 mesh) and drying were done by Empire Coke Company of Holt, Alabama. The preparation procedure and equipment have been previously described (5).

TEMPERATURE SURVEY STUDY

An important part of the single-stage, slurry-catalyzed processing program is to determine the optimum conversion level that produces high liquid yields by selective catalytic conversion as opposed to thermal conversion. A temperature survey study was conducted to determine the highest processing temperature attainable without excessive carbon loss to retrograde reactions and light ends (9). Standard operating conditions were used: 3000 psig, 5:1 minimum liquid recycle ratio, base WHSV, 2:1 mixture of petroleum resid to coal, and 0.12% molybdenum catalyst concentration.

The run was started at 427°C, and the temperature was increased in a stepwise manner. Six test conditions (427, 432, 438, 446, 451, and 459°C) were run. The plant operated well, even at the higher processing temperatures, and showed no evidence of either thermal degradation or reactor fouling. The conversion showed a steady increase with temperature and no sign of decrease even at 459°C. The unconverted coal showed a steady decrease with temperature (Figure 2), and the heptane-insoluble conversion increased with temperature (Figure 3). The greatest impact of the higher temperature was the 30 wt-% increase in nondistillable conversion (Figure 4) without significant carbon loss to retrograde reactions and only about 6% increase in light-ends yields (Figure 5). Table 3 compares the yields and product properties at 427, 446, and 459°C. The product distribution shows the expected trends when temperature was increased: an increase of lighter fractions (C₁-C₄, C₅-177°C, and 177-343°C) and a decrease of heavier fractions (343-510°C and 510+°C). The quality of the liquid product improved with increasing temperature. The API gravity and hydrogen content of the product increased; and heptane insolubles, sulfur, and nitrogen levels decreased.

LONG-TERM OPERABILITY STUDY

A long-term operability study at high-severity conditions was undertaken to determine if high-severity co-processing could be run continuously for extended periods without major operational problems or the gradual buildup of coke in the reactor. The run was conducted at standard operating conditions: 3,000 psig, 5:1 minimum liquid recycle ratio, base WHSV, 2:1 mixture of petroleum resid to coal, and 0.090% molybdenum catalyst concentration. The reactor temperature was held at 455°C during the initial three weeks of operation, then increased to 465°C, and maintained for 17 days. During the operation, daily weight balances were conducted to ensure the integrity of the operation.

Catalyst and coal ash balances were followed to monitor fouling or deposition in the pilot plant. Product recoveries, H₂ consumption, and catalyst and ash balances indicated stable operation. The weight recoveries versus hours on-stream are shown in Figure 6 and can be compared with the average value, shown as a solid line. The weight recoveries were good and averaged 100.3 wt-%. The average reactor bed temperature for the 455 and 465°C operation versus hours on-stream is shown in Figure 7: the solid line on the figure represents the average temperature of 455.5°C and 464.7°C. The run was ended by a planned shutdown after 38 days on-stream without any significant operational problem. Upon disassembling the reactor, the walls were found to be free of coke or any deposits.

Conversions, product distribution, and total liquid product properties are shown in Tables 4 and 5 for the 455°C operations and in Tables 6 and 7 for the 465°C operation. The average coal, heptane-insoluble, and nondistillable conversions were 90.5, 74.6, and 78.9 wt-%, respectively, for the 455°C temperature and 91.9, 86.3, and 84.2 wt-%, respectively, for the 465°C temperature. As shown in Figures 8, 9, 10, and 11 the conversions and yields are comparable to those obtained at the same temperature in the temperature survey study.

CONCLUSIONS

Long-term operability of co-processing at high-severity conditions was demonstrated. Plant operations and performance were extremely good, and no major operational problems were encountered. High nondistillable conversion was obtained without excessive carbon loss to retrograde reactions and light-end yields. The operability of co-processing at high severity represents an important advance that may significantly improve the process economics.

REFERENCES

1. J. G. Gatsis, et al., "Coal Liquefaction Co-Processing," Proceedings of DOE Direct Liquefaction Contractors' Review Meeting, Nov. 19-21, 1985.
2. J. G. Gatsis, et al., "Continuous Bench-Scale Single-Stage Slurry Catalyzed Co-Processing," Proceedings of DOE Direct Liquefaction Contractors' Review Meeting, Oct. 20-22, 1986.
3. J. G. Gatsis, et al., "Continuous Bench-Scale Single-Stage Slurry Catalyzed Co-Processing," Proceedings of DOE Direct Liquefaction Contractors' Review Meeting, Oct. 6-8, 1987.
4. D. A. Nafis, et al., "Bench-Scale Co-Processing," Proceedings of DOE Direct Liquefaction Contractors' Review Meeting, Oct. 4-6, 1988.
5. C. P. Luebke, et al., "Coal Liquefaction Co-Processing Topical Report Number 1," Prepared for the United States Department of Energy under Contract No. DE-AC22-84PC70002, June 1, 1987.
6. J. G. Gatsis, et al., "Coal Liquefaction Co-Processing Topical Report Number 2," Prepared for the United States Department of Energy under Contract No. DE-AC22-84PC70002, Aug. 19, 1988.
7. D. A. Nafis, et al., "Coal Liquefaction Co-Processing Final Report," Prepared for the United States Department of Energy Under Contract No. DE-AC22-84PC70002.
8. D. A. Nafis, et al., "UOP Co-Processing Developments," Proceedings of DOE Direct Liquefaction Contractors' Review Meeting, Oct. 2-4, 1989.
9. C. A. Piasecki, et al., "Single-Stage Slurry-Catalyzed Co-Processing with Liquid Recycle," Proceedings of DOE Direct Liquefaction Contractors' Review Meeting, Sept. 24-26, 1990.

Table 1
Analysis of Lloydminster Vacuum Resid (R10)

API Gravity	6.6
Specific Gravity	1.0246
Distillation, °C:	
IBP, vol-%	379
5	455
10	473
20	509
EP	512
Vol-% over at EP	22.0
Analysis, wt-%:	
Carbon	83.6
Hydrogen	10.3
Sulfur	4.77
Nitrogen	0.59
Heptane Insolubles	13.56
Carbon Residue (MCRT)	17.39

Table 2
Analysis of Illinois No. 6 (CL4)

Proximate Analysis: (AR Basis), wt-%	
Volatile Matter	38.84
Fixed Carbon ^a	45.80
Moisture	4.08
Ash	11.28
Ultimate Analysis (AR Basis), wt-%	
Carbon	66.75
Hydrogen ^b	4.66
Sulfur	2.91
Nitrogen	1.34
Oxygen ^a	8.98
Ash	11.28
Moisture	4.08

^a By difference

^b Corrected for Moisture

Table 3
Effect of Severity on Yields and Product Properties

Temperature, °C	427	446	459
Yields, wt-% MAFF:			
H ₂ O + CO ₂	6.7	4.0	4.3
H ₂ S	1.6	3.3	3.5
NH ₃	0.2	0.4	0.8
C ₁ -C ₄ (Light Ends)	2.5	5.5	9.1
C ₅ -177°C (Naphtha)	5.4	12.0	14.5
177-343°C (Distillate)	17.6	24.0	36.0
343-510°C (VGO)	29.3	26.1	22.9
510+°C (Resid)	34.0	24.2	10.3
Unc. MAF Coal	5.6	3.6	2.3
H ₂ Consumption	(2.8)	(2.9)	(3.6)
Total	100.0	100.0	100.0
C₅₊ Total Liquid Product:			
MAFF, wt-%	86.2	86.3	83.7
API Gravity	12.9	17.0	19.9
Carbon, wt-%	84.7	84.0	84.4
Hydrogen, wt-%	10.0	10.3	11.0
Sulfur, wt-%	2.1	1.4	1.1
Nitrogen, wt-%	0.9	0.8	0.4
Heptane Insolubles, wt-%	9.8	9.1	3.1
MCRT, wt-%	12.7	11.2	6.2

Table 4
Conversion and Product Distribution
of 455°C High-Severity Co-Processing

Normalized Conversion	Wt-%
Coal	90.5
Heptane Insolubles	74.6
Nondistillable, 510+ °C	78.9
Product Distribution	Wt-% MAFF
H ₂ O, CO ₂ , CO	3.2
H ₂ S	4.7
C ₁ -C ₄	7.5
C ₅ -177°C	13.8
177-343°C	25.8
343-510°C	24.0
510+ °C	17.7
Unc. MAF Coal	3.3
H ₂ Consumption	(1.6)
Total	100.0

Table 5
Total Liquid Product Properties
of 455°C High-Severity Co-Processing

API Gravity	17.2
Carbon, wt-%	85.1
Hydrogen wt-%	10.4
Sulfur, wt-%	1.3
Nitrogen, wt-%	0.4
Heptane Insolubles, wt-%	9.9
MCRT, wt-%	9.3

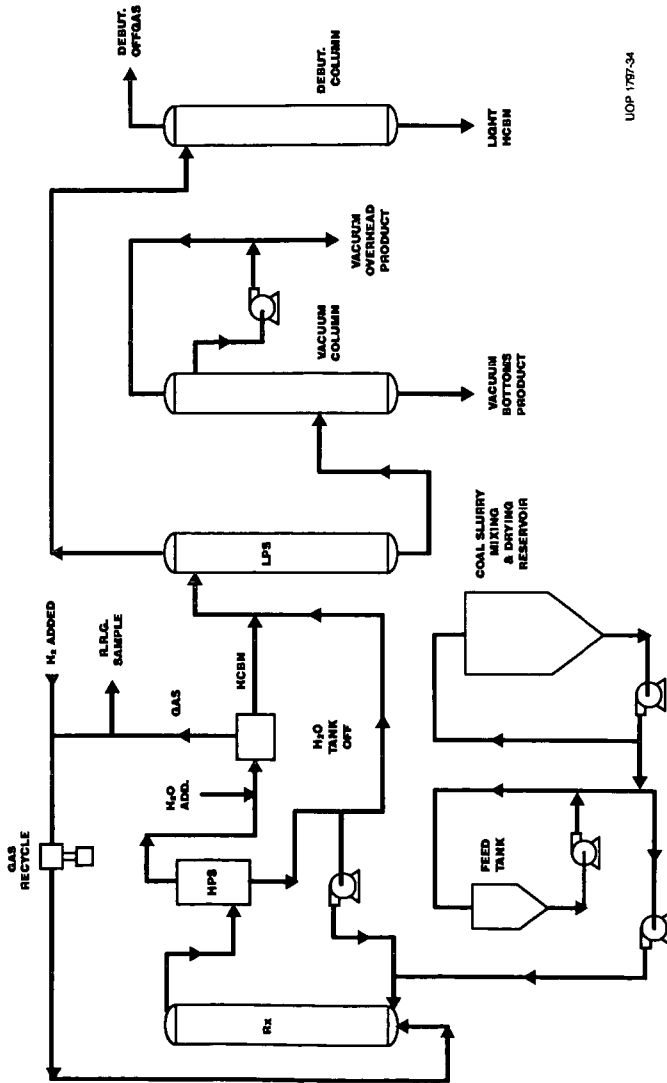
Table 6
Conversion and Product Distribution
of 465°C High-Severity Co-Processing

Normalized Conversion	Wt-%
Coal	91.9
Heptane Insolubles	86.3
Nondistillable, 510+ °C	84.2
Product Distribution	Wt-% MAFF
H ₂ O, CO ₂ , CO	5.0
H ₂ S	5.9
C ₁ -C ₄	9.9
C ₅ -177°C	19.5
177-343°C	28.2
343-510°C	17.9
510+ °C	12.8
Unc. MAF Coal	2.9
H ₂ Consumption	(2.1)
Total	100.0

Table 7
Total Liquid-Product Properties
of 465°C High-Severity Co-Processing

API Gravity	20.3
Carbon, wt-%	83.7
Hydrogen, wt-%	10.5
Sulfur, wt-%	1.0
Nitrogen, wt-%	0.4
Heptane Insolubles, wt-%	4.4
MCRT, wt-%	8.4

**FIGURE 1
CO-PROCESSING PILOT PLANT**



UOP 1967-64

FIGURE 2
UNCONVERTED COAL YIELD
vs. TEMPERATURE OF 0.12% Mo

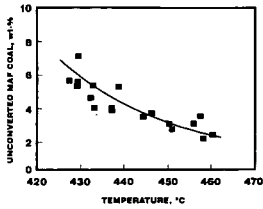


FIGURE 3
HEPTANE INSOLUBLE CONVERSION
vs. TEMPERATURE OF 0.12% Mo

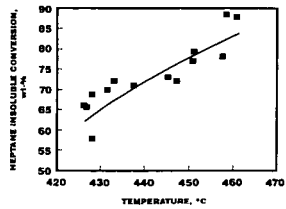


FIGURE 4
NONDISTILLABLE CONVERSION
vs. TEMPERATURE OF 0.12% Mo

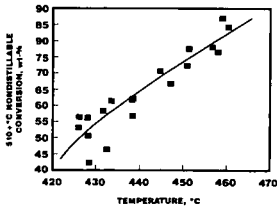


FIGURE 5
LIGHT-ENDS YIELDS
vs. TEMPERATURE OF 0.12% Mo

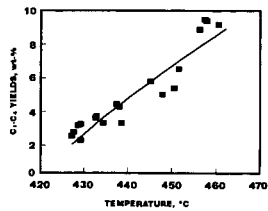


FIGURE 6
HIGH-SEVERITY CO-PROCESSING
WEIGHT RECOVERIES

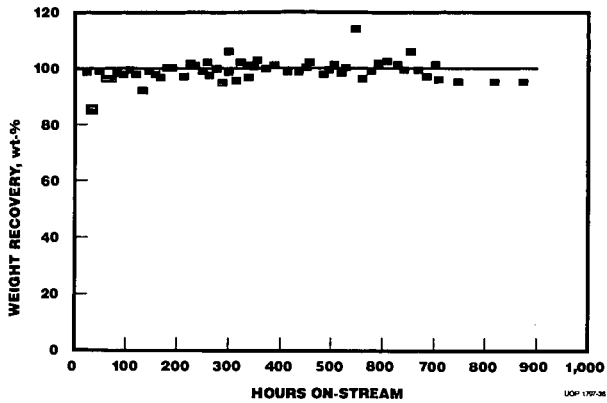


FIGURE 7
HIGH-SEVERITY CO-PROCESSING
OPERATING TEMPERATURE

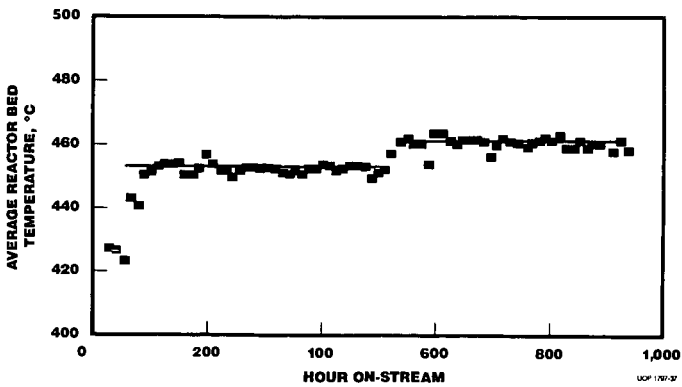


FIGURE 8
UNCONVERTED COAL YIELD
COMPARISON

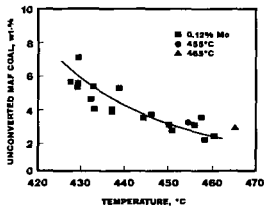


FIGURE 9
HEPTANE INSOLUBLE CONVERSION
COMPARISON

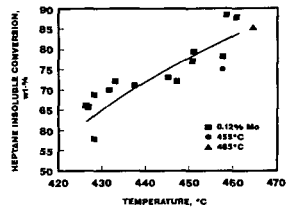


FIGURE 10
NONDISTILLABLE CONVERSION
COMPARISON

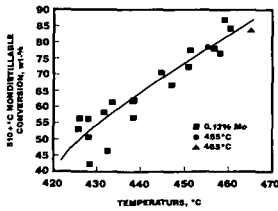
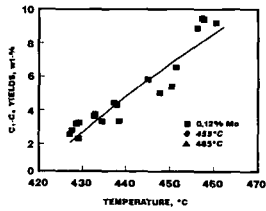


FIGURE 11
LIGHT-ENDS YIELDS
COMPARISON



THE TWO-ALPHA VALUE FOR IRON FISCHER-TROPSCH CATALYSTS: FACT OR FICTION?

Burtron H. Davis
Center for Applied Energy Research
University of Kentucky
3572 Iron Works Pike
Lexington, KY 40511

Keywords: Fischer-Tropsch Synthesis, Selectivity, Two-Alpha Plots

INTRODUCTION

The Fischer-Tropsch Synthesis may be viewed as a simple polymerization reaction, the monomer being CO or a C₁ species derived from it. Schulz (1,2) derived an equation for the distribution of molecular weights of polymers obtained by a free radical polymerization process, that is, through a one-by-one addition of monomer to a growing chain. The Schulz distribution function is applicable generally if there is a **constant** probability of chain growth, α , and $\alpha < 1$; the latter requirement applies when some reaction limits the chain growth. The probability for chain growth, α , is defined as:

$$\alpha = r_p / (r_p + \Sigma r_t) \quad [1]$$

where r_p is the rate of chain propagation and r_t is the rate of chain transfer or chain termination. The probability of the chain growth step to take place P times without termination is

$$P_p = \alpha_1 \alpha_2 \alpha_3 \dots \alpha_p = \alpha^P \quad [2]$$

The number of molecules per degree of polymerization P, n_p , is proportional to the probability of their formation

$$n_p = \text{const } \alpha^P \quad [3]$$

The mass fraction m_p is proportional to n_p as well as the molecular weight of the components of the fraction ($M_p = M_M P$, where M_M is the molecular weight of the monomer)

$$m_p = A P \alpha^P \quad [4]$$

where A contains the constant M_M . The mass fraction is defined so that

$$\Sigma m_p = 1 \quad [5]$$

The mass fraction is considered to be a continuous function so that

$$\int_0^{\infty} m_p dP = A \int_0^{\infty} P \alpha^P dP = 1 \quad [6]$$

and

$$A = 1 / \int_0^{\infty} P \alpha^P dP \quad [7]$$

Solving the integral ($\alpha < 1$, $\alpha^{\infty} = 0$) and combining equations [4] and [7] leads to

$$m_p = (\ln^2 \alpha) P \alpha^P \quad [8]$$

Rearranging gives the more familiar form

$$\log(m_p/P) = \log(\ln^2 \alpha) + (\log \alpha) P \quad [9]$$

Thus, a plot of $\log(m_p/P)$ versus P should result in a straight line.

Flory published a number of theoretical distribution functions for this and other types of macromolecular formation (e.g., reference 3). Thus, polymer scientists usually designate distributions as represented by [9] as conforming to a Schulz-Flory distribution.

Similar equations were derived, apparently independently, by catalysis scientists (4-6). Anderson continued his efforts to develop chain growth mechanisms and to account for the products formed by chain branching (7). Many catalysis scientists therefore recognize Anderson's contributions to the Fischer-Tropsch Synthesis by designating equation [9], and plots based upon it, as an Anderson-Schulz-Flory (ASF) equation or plot, and we shall follow this practice.

Anderson (8) summarized product distribution results up to about 1954. Included in this review were the results of the Schwarzheide tests using catalysts from Lurgi, Brabag, K.W.I., I.G. Farben, Ruhr Chemie, and Rheinpreussen as well as tests at the larger U.S. pilot plants, and Standard Oil Co. of New Jersey (figure 1). These results included operations with iron catalysts both in fixed and fluidized reactors. The results in figure 1 clearly indicate that a single α value does not adequately describe the data. Up to carbon number 9 to 11 the data fit one alpha value for equation [9] very well; however, a second α value is needed to describe those products higher than carbon number 9 to 11. These early workers did not have the benefit of gas chromatography to analyze the higher molecular weight products. Thus, while Anderson noted the need for two or more alpha values to describe the products from FTS using iron catalysts, it received little attention. Furthermore, FTS products from a cobalt catalyst were adequately described with a single alpha value.

Madon and Taylor (9) conducted extensive tests with a precipitated, alkali-promoted iron-copper catalyst. They reported a product distribution for the condensed products from FTS using a plug flow reactor that exhibited a two-alpha plot (figure 2) but the break occurred at a higher carbon number than those in figure 1. Madon and Taylor (9) noted that Anderson and coworkers (10) had obtained such a plot but with the break occurring at a lower carbon number. Madon and Taylor noted that Hall *et al.* (11) had suggested that in addition to stepwise growth

with a single carbon intermediate, multiple build-in of growing chains could occur and that this could affect the growth rate of heavy hydrocarbons. Madon and Taylor, after considering this explanation, suggested instead that chain growth takes place on at least two types of sites, each having a slightly different chain growth probability α .

Novak *et al.* (12) considered the impact of readsorption of α -olefins upon the products from a continuous stirred tank reactor (CSTR) and a plug flow reactor (PFR). They also considered that α -olefins could only initiate chain growth, or that they can also isomerize to internal olefins as well as be hydrogenated. For the CSTR, these authors concluded that, even with such secondary reactions, the products still exhibit an ASF plot. For the PFR, the products deviate from an ASF plot when α -olefins can undergo only chain initiation. If, however, as is the case in a more realistic situation, the α -olefin also undergoes hydrogenation and isomerization in addition to chain initiation, the distribution rapidly becomes similar to an ASF distribution. Finally, these authors considered the case where the chain growth parameter was allowed to vary along the length of a PFR by forcing the C_1 surface concentration to vary and found, in this case also, that the distribution is quite close to a Flory distribution.

Satterfield and Huff (13) initially concluded that the products for a doubly promoted catalyst (C-73, United Catalysts, Inc.) in a CSTR yielded a precise linear relationship between the log of the mole fraction of the products and the carbon number as predicted by an ASF distribution provided all products, including oxygenate species, were included. The linear relationship held over four orders of magnitude of the moles of products and for carbon numbers from 1 to about 20 over a wide range of gas compositions. The chain growth probability factor, α , increased slightly from 0.67 at 269°C to 0.71 at 234°C.

Huff and Satterfield (14), after re-examination of their previous data and a consideration of new experimental data on three different iron catalysts, reported that in some cases, the ASF distribution plot can only be well represented by two straight lines with a marked break occurring at about C_{10} . However, when the products are considered on the basis of compound classes, the situation shown in figure 1 is an oversimplification. As shown in figure 3, Huff and Satterfield found that only the paraffins deviate from the ASF plot; oxygenates and alkenes appear to follow a single ASF plot with $\alpha \sim 0.55$.

Egiebor *et al.* (15) also reported that the break in the ASF plot was due to the alkanes. These authors showed that α -olefins and cis- and trans- β -olefins all show straight line plots with different slopes. They concluded that all these compounds are primary products. The fact that only paraffins show a break in the ASF slope proves that paraffins are not secondary products derived from α -olefins. These authors advanced the view that growth of linear chains proceed at the same rate (α) for all species and that it is the termination event which is species specific. The break in the paraffin ASF plot is therefore caused by a sharp change in the rate of termination at about C_{13} . Since a number of investigators have found that the carbon number where the break occurs is about the same and since the break is observed with a variety of catalysts, they state that it may be that the phenomenon is governed by the nature of the C_{13} molecule as well as the catalyst.

Gaube and coworkers (16,17) also observed a two α plot. For an iron catalyst the $C_3 - C_{40}$ products exhibit a linear ASF plot that only required a single α value (figure 4). However, when the catalyst contained alkali (added as K_2CO_3), the ASF plot needed two α values to adequately describe the data. However, others have found the need for two alpha values for catalysts that do not contain potassium or other alkali metals (e.g., 18-21).

Donnelly *et al.* (22) extended the chain growth theory to include two growth probabilities; thus, rather than equation [4] one should write

$$m_p = AP\alpha^P + BP\alpha^P \quad [10]$$

The contribution of each growing chain will be equal at the break point. They offer this as an improved equation for analyzing FTS product distributions, and show that this equation adequately described their data.

Dictor and Bell (18) found a two-alpha plot for both reduced and unreduced iron oxide catalysts. Furthermore, these authors found that the ASF plot for n-aldehydes yielded a two-alpha plot just as was the case for the hydrocarbon products. Furthermore, the break for the aldehydes was at the same carbon number as the hydrocarbons, provided the aldehyde ASF plot was based upon n-1 rather than \bar{n} , as was used for the hydrocarbons (figure 5). This was taken to support the view that aldehydes are formed by CO insertion into a growing surface alkyl group and subsequent reductive elimination of the acyl group (23,24); hydrocarbons on the other hand are believed to be formed in a termination step that occurs by elimination of a hydrogen from an alkyl group. Since the break occurs at \bar{n} for hydrocarbons and $n + 1$ for the aldehydes, it appears that the oxygenate and hydrocarbon products are derived from a common surface species.

Donnelly and Satterfield (20) utilized a Ruhrchemie catalysts in a CSTR and found that both the n-alkanes and 1-alkenes fit a two-alpha ASF plot (figure 5) whereas earlier work from that laboratory (14) showed that only n-alkanes deviated from ASF. In contrast to Dictor and Bell (18), Donnelly and Satterfield (20) found that oxygenates followed a single alpha plot even though they now find, in contrast to earlier results, that both n-alkanes and 1-alkenes deviate from ASF. These data serve to illustrate the difficulty in deciding the one or two-alpha plot question.

Stenger (25) showed that the two site ASF equation used by Huff and Satterfield was equivalent to one based on a distributed-site model in its ability to fit the molecular weight product distribution from an iron catalyst promoted with potassium. In the promoted catalyst, a distribution of sites proportional to the concentration of potassium relative to iron is utilized. In his model, Stenger assumed a normal distribution of K on the surface and postulated an exponential dependence of alpha on the random distribution variable, X, that is proportional to the potassium distribution.

Inoui *et al.* (26) introduced a single criterion to differentiate between the two-site model (20) and a distributed site model (25). However, for typical values of α_1 and α_2 for iron catalysts (~ 0.6 and 0.8 , respectively) the fit to the ASF plot should make it difficult to distinguish the two models, even using the approach suggested by Inoui *et al.*

Kikuchi and Itoh (27) utilized an iron catalyst based upon ultrafine particles loaded with 1% K and found a break in the ASF plot at C_{10} . The data fit the model based upon two kinds of sites, A and B, with A exhibiting the lower and B exhibiting the higher growth probability. The fit of the experimental data and the calculated curve was satisfactory (figure 6).

Iglesia *et al.* (28) reported that olefins readsorb and initiate surface chains that are indistinguishable from those formed directly from CO/H₂. Diffusion enhanced olefin readsorption leads to an increase in chain growth probability, α , and in paraffin content with increasing pore

and bed residence time. Deviations from conventional (ASF) polymerization kinetics were quantitatively described by transport effects on the residence time of intermediate olefins within the liquid-filled catalyst pores without requiring the presence of several types of chain growth sites. The results reported for this study were obtained with a Ru catalyst, and not an iron catalyst.

Not all of the earlier studies require two or more α values to describe the distribution of products from FTS with iron catalysts. Three examples of this will be noted. Zwart and Vink (29) report that the product from zeolite supported iron catalysts derived from iron carbonyl complexes produced a product distribution in the C_{3-20} range which obeyed ASF statistics in all cases. Eilers et al. (30) report that in a few hundred independent FTS experiments with various catalyst formulations under different operating conditions it was confirmed that the carbon number distribution were in close agreement with the ASF kinetics (figure 7). However, neither of the two data sets for the iron catalysts cover the total range of carbon numbers where the break in the ASF plot is observed. Cannella (31) reported a linear ASF plot that only required one alpha value to fit the C_{3+} products for an unsupported iron catalyst but that a two-alpha plot was required for the K-promoted catalyst. Linear ASF plots were always obtained for the C_3^+ products produced over each of the supported iron catalysts.

Tau et al. (32) found that a doubly promoted C-73 catalyst incorporated ^{14}C labeled 1-pentanol, added to the CO/H_2 feed, into higher carbon number products. They found that product accumulation in the CSTR was not adequate to explain the deviation from a constant ^{14}C activity/mole with increasing carbon number for higher carbon number alkane products.

^{14}C labeled ethanol served only as a chain initiator; this is demonstrated by the constant ^{14}C activity/mole for the C_2 through C_4 products (figure 8). The constant activity of C_3 and C_4 that is equal to ethanol indicates that only one C_2 species derived from ethanol was incorporated into these products. These results are in agreement with the earlier data obtained by Emmett and coworkers (11, 33-37).

However, the data in figure 9 clearly indicate that the $C_{10} - C_{14}$ paraffins exhibit a different ^{14}C activity pattern with increasing carbon number than those in the $C_2 - C_4$ range. The higher carbon number products are diluted by the products accumulated in the reactor prior to the addition of ^{14}C labeled 1-pentanol. Analysis of the wax withdrawn from the reactor prior to the addition of the ^{14}C tracer provided data to calculate the impact of these products in diluting the ^{14}C content of higher carbon number products. Dilution did provide a minor contribution to the negative slope of the ASF plot in figure 9; however, the points corrected for accumulation (\blacklozenge) provided only a modest correction toward that exhibited by the lower carbon number products where ^{14}C /mole was constant with increasing carbon number (figure 8). Hence, the effect of accumulation alone cannot account for the experimental data.

Another explanation for the deviation from the ASF plot is that hydrogenolysis of higher carbon number compounds produce more lower carbon number hydrocarbon products than can be accounted for by ASF. Using the same C-73 catalyst, Huang et al. (38) used octacosane, labeled at the carbon-14 position of the chain, to show that a detectable amount of hydrogenolysis did not occur even after one week of operation at the same conditions as was used by Tau et al. (32). Thus, hydrogenolysis is eliminated as an explanation for the two-alpha ASF plot for a promoted iron catalyst.

Tau et al. (32) concluded that the two alpha values in figure 1 correspond to different product groupings. For the smaller alpha (about 0.62) the typical Fischer-Tropsch products are formed

(alkanes, alkenes, oxygenates, etc.). However, for the larger alpha (about 0.82) the only significant product obtained corresponds to alkanes. The data in figure 10, after first correcting for accumulation and then for the two different product groups, show a constant $^{14}\text{C}/\text{mole}$, causing the conclusion based upon the higher carbon alkane products to be consistent with the one based on the lower alkane products.

In conclusion, it is evident that many groups using a variety of iron catalysts have found that two or more alpha values are needed if ASF kinetics are to account for the FTS products. The summary of the two-alpha values (39) for eight studies emphasize this conclusion. It is possible for deficiencies in the analytical determinations or loss of certain carbon number ranges during sampling or testing could cause the break in the ASF plot. However, this is not possible for the ^{14}C studies since the conclusion is based upon the $^{14}\text{C}/\text{mole}$ rather than the total number of moles. Recent data using ^{14}C -ethanol (40) and analysis of a wider carbon number range than in reference 32 provide additional support for the results reported by Tau *et al.* Furthermore, similar results are obtained for the addition of ^{14}C labeled C_2 , C_3 , C_5 , C_6 and C_{10} alcohols and C_2 , C_5 and C_{10} alkenes (41,42). With emphasis on the ^{14}C tracer studies, we conclude that it is likely that at least two chains are growing independently, and that these independent chains lead to different groups of products. These in turn require at least two-alpha values for the ASF to adequately describe the FTS data.

ACKNOWLEDGMENT

This work was supported with funding from the Commonwealth of Kentucky and the U.S. Department of Energy, Pittsburgh Energy Technology Center, through Contract No. De-AC22-84PC70029.

REFERENCES

1. G. V. Schulz, *Z. Phys. Chem.*, **29**, 299 (1935); **30**, 375 (1935).
2. G. V. Schulz, *Z. Phys. Chem.*, **30**, 375 (1936).
3. P. J. Flory, *J. Amer. Chem. Soc.*, **58**, 1877 (1936).
4. E. F. G. Herrington, *Chem. Ind.*, (1946) 347.
5. R. A. Friedel and R. B. Anderson, *J. Amer. Chem. Soc.*, **72**, 1212 (1950); **72**, 2307 (1950).
6. S. Weller and R. A. Friedel, *J. Chem. Phys.*, **17**, 801 (1949).
7. R. B. Anderson, "The Fischer-Tropsch Synthesis", Academic Press, New York, 1984.
8. R. B. Anderson in "Catalysis" (P.H. Emmett, ed.) Reinhold Pub. Corp., New York, 1956, Vol. IV, pp 22-256.
9. R. J. Madon and W. F. Taylor, *J. Catal.*, **69**, 32 (1981).
10. J. F. Schulz, W. K. Hall, B. Seligman and R. B. Anderson, *J. Amer. Chem. Soc.*, **77**, 211 (1955).
11. W. K. Hall, R. J. Kokes and P. H. Emmett, *J. Amer. Chem. Soc.*, **82**, 1027 (1960).
12. S. Novak, R. J. Madon and H. Suhl, *J. Catal.*, **77**, 141 (1982).
13. C. N. Satterfield and G. A. Huff, Jr., *J. Catal.*, **73**, 187 (1982).
14. G. A. Huff, Jr. and C. N. Satterfield, *J. Catal.*, **85**, 370 (1984).
15. N. O. Egiebor, W. C. Cooper and B. W. Wojciechowski, *Canadian J. Chem. Eng.*, **63**, 826 (1985).
16. L. Konig and J. Gaube, *Chem. Ing. Tech.*, **55**, 14 (1983).
17. B. Schliebs and J. Gaube, *Ber. Bunsenges. Phys. Chem.*, **39**, 68 (1985).
18. R. A. Dictor and A. T. Bell, *J. Catal.*, **97**, 121 (1986).
19. L.-M. Tau, H. Dabbagh, B. Chawla and B. H. Davis, "Mechanism of Promotion of Fischer-Tropsch Catalysts", DOE/PC/70029-T1, Final Report, December 1987.

20. T. J. Donnelly and C. T. Satterfield, *Appl. Catal.*, **52**, 93 (1989).
21. H. Itoh, H. Hosaka and E. Kikuchi, *Appl. Catal.*, **40**, 53 (1988).
22. T. J. Donnelly, I. C. Yates and C. N. Satterfield, *Energy & Fuels*, **2**, 734 (1988).
23. H. Schulz and A. Zein El Deen, *Fuel Proc. Tech.*, **1**, 45 (1977).
24. P. Biloen, J. N. Helle and W. M. H. Sachtler, *J. Catal.*, **58**, 95 (1979).
25. H. G. Stenger, Jr., *J. Catal.*, **92**, 426 (1985).
26. M. Inoui, T. Miyake and T. Inui, *J. Catal.*, **105**, 266 (1987).
27. E. Kikuchi and H. Itoh, "Methane Conversion" (D. M. Bibby et al., eds.) Elsevier Sci. Pub., Amsterdam, 1988, pp 517-521.
28. E. Iglesia, S. C. Reyes and R. J. Madon, "Transport-Enhanced Olefin Readsorption Model of Hydrocarbon Synthesis Selectivity", 12th NAM of The Catalysis society, Abstract PC02, Lexington, KY, May 5-9, 1991.
29. J. Zwart and J. Venk, *Appl. Catal.*, **33**, 383 (1987).
30. J. Eilers, S. A. Posthuma and S. T. Sie, *Catal. Lett.*, **7**, 253 (1990).
31. W. J. Cannella, Ph.D. dissertation, U. of California, Berkeley, 1984.
32. L.-M. Tau, H. Dabbagh, S.-Q. Bao and B. H. Davis, *Catal. Lett.*, **7**, 127 (1990).
33. W. K. Hall, R. J. Kokes and P. H. Emmett, *J. Amer. Chem. Soc.*, **79**, 2983 (1957).
34. J. T. Kummer, T. W. DeWitt and P. H. Emmett, *J. Amer. Chem. Soc.*, **70**, 3632 (1948).
35. J. T. Kummer and P. H. Emmett, *J. Amer. Chem. Soc.*, **75**, 5177 (1953).
36. J. T. Kummer, H. H. Podgurski, W. B. Spencer and P. H. Emmett, *J. Amer. Chem. Soc.*, **73**, 564 (1951).
37. G. Blyholder and P. H. Emmett, *J. Phys. Chem.*, **63**, 962 (1959); **62**, 470 (1960).
38. C. S. Huang, H. Dabbagh and B. H. Davis, *Appl. Catal.*, **73**, 237 (1991).
39. D. K. Matsumoto and C. N. Satterfield, *Energy & Fuels*, **3**, 249 (1989).
40. Unpublished data.
41. L.-M. Tau, H. A. Dabbagh and B. H. Davis, *Energy & Fuels*, **5**, 174 (1991).
42. L.-M. Tau, H. A. Dabbagh and B. H. Davis, *Energy & Fuels*, **4**, 94 (1990).

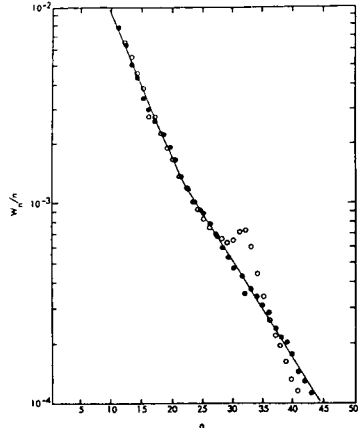
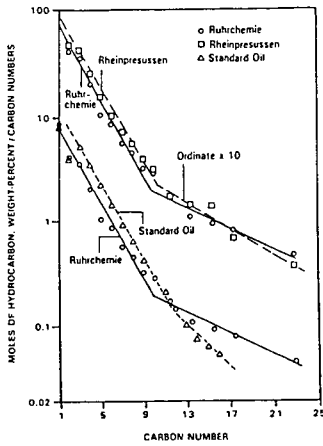


Figure 1. Anderson-Schulz-Flory (ASF) plots for the products from Schwarzheide for four sources and Standard Oil Company of New Jersey (reproduced from ref. (8), p. 208).

Figure 2. Plot of $\ln W_n/n$ versus carbon number n . Open points, unsulfided catalysts; solid points, sulfided catalyst (reproduced from ref. (9)).

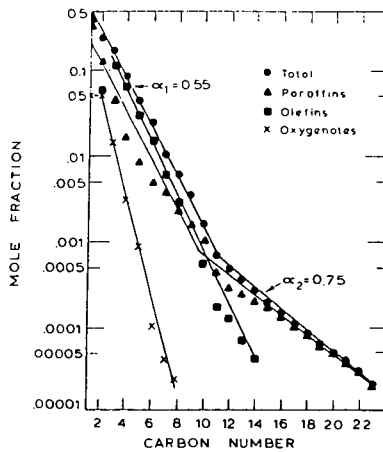


Figure 3. Flory distribution of MnO/Fe catalyst; 283°C, 1.24 MPa, $(H_2/CO)_m = 1.19$ (reproduced from ref. (14)).

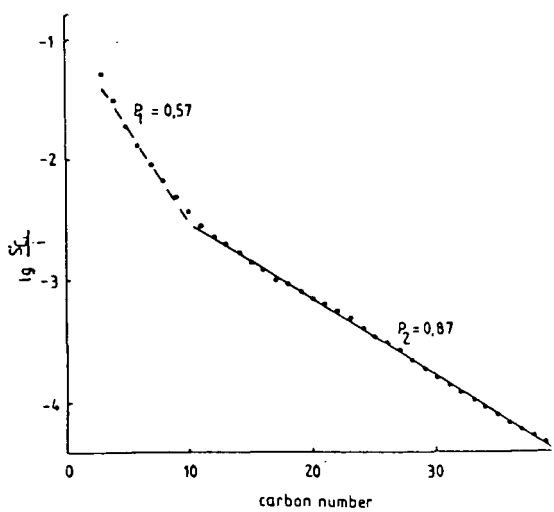
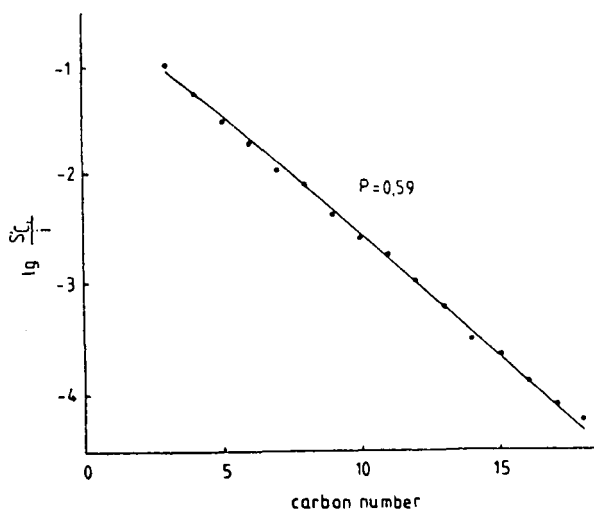


Figure 4. Product distribution from FTS using an iron (top) and potassium promoted iron catalyst (bottom) (redrawn from ref. (16)).

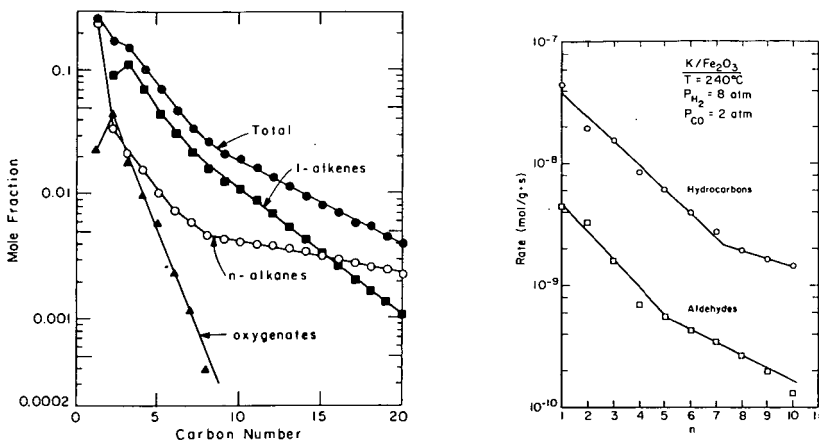


Figure 5. (left) Component Schulz-Flory diagram for overhead products. Ruhrchemie Catalyst MPa, 0.034 NI/min/g_{cat}, (H₂/CO)_{feed} = 0.7, 600 hours-on-stream (reproduced from ref. (20)). (right) Distribution of hydrocarbons and aldehydes from a common effluent sample. Each point for hydrocarbons represents the sum of 1-olefin plus n-paraffin; only straight-chain aldehydes are measured (reproduced from ref. (18)).

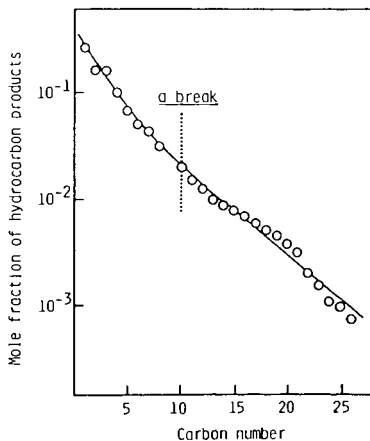


Figure 6. Flory plot of hydrocarbon products over potassium-promoted Fe UFP (ultrafine particle) catalyst. Reaction conditions: temperature, 220°C; pressure, 30 atm; H₂/CO, 1 mol/mol; W/F, 300 g-cat.min/CO-mol. Potassium addition: 1 wt.% of catalyst. Solid line represents the simulated distribution based on two-site ASF equation (reproduced from ref. (21)).

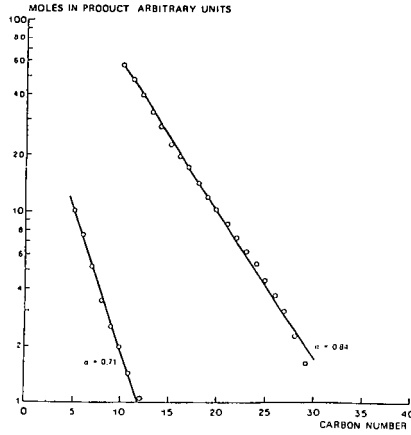


Figure 7. Typical carbon number distribution of the FTS using an iron catalyst (redrawn from ref. (30)).

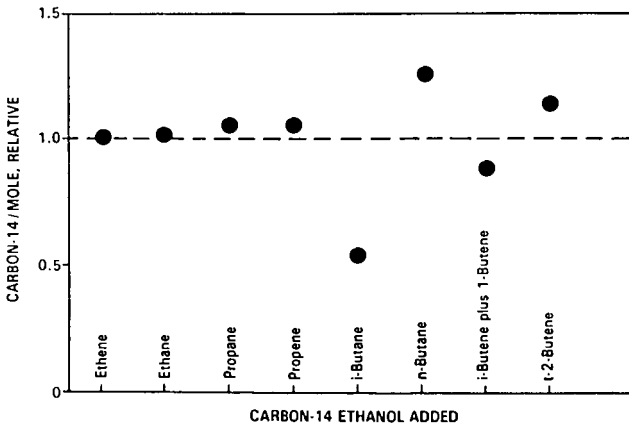


Figure 8. Relative ^{14}C /mole in gaseous products from the synthesis (7 atm, $\text{H}_2/\text{CO} = 1.2$, 262°C) with 3-volume % (based on alcohol and CO) [^{14}C -1]-ethanol was added during a 24 hour period (redrawn from ref. (32)).

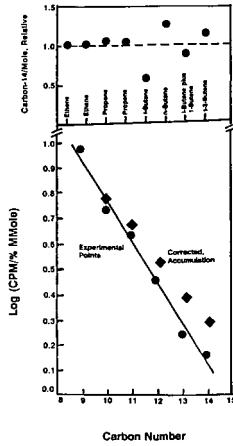


Figure 9. Composite figure showing relative radioactivity for the lower carbon number compounds (●); the measured values for the higher carbon number compounds (◆), and the values for the higher carbon number compounds (■) after correcting for reactor accumulation effects (redrawn from (41)).

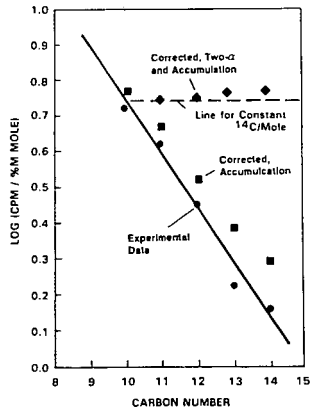


Figure 10. Radioactivity of the: alkane products (●); experimental data corrected for accumulation using data shown in Table 1 (■), and experimental data corrected for both accumulation and the two alpha mechanism (see text for details) (◆) (redrawn from ref. (41)).

IRON-BASED CATALYSTS FOR SLURRY-PHASE FISCHER-TROPSCH SYNTHESIS

V. U. S. Rao, G. J. Stiegel, A. C. Bose and G. J. Cinquegrane
U. S. Department of Energy
Pittsburgh Energy Technology Center
P. O. Box 10940
Pittsburgh, PA 15236

and

R. D. Srivastava
Burns and Roe Services Corporation
P. O. Box 18288
Pittsburgh, PA 15236

Keywords: Fischer-Tropsch, Indirect Liquefaction, Iron Catalysts

Introduction

The Pittsburgh Energy Technology Center is responsible for implementing the U.S. Department of Energy's (DOE) Indirect Liquefaction program as part of the Coal Liquefaction program. The overall goal of the Coal Liquefaction program is to develop the scientific and engineering knowledge base to help industry market economically competitive and environmentally acceptable advanced technology for the manufacture of synthetic liquid fuels from coal.

This article examines the state of knowledge in iron-based catalysts for use in slurry-phase synthesis reactors used in the Indirect Liquefaction of coal. The advantages of using iron catalysts are (1) they are inexpensive, (2) specific activity for Fischer-Tropsch (FT) synthesis is high, and (3) some iron catalysts have high water-gas-shift activity and can convert low H_2/CO ratio synthesis gas without an external shift reaction step.

Stoichiometry of the FT Reaction:

The intrinsic stoichiometry of the FT synthesis reaction is represented by eq 1. Many FT catalysts are also active for water-gas-shift (WGS) reaction represented by eq 2. Catalysts that are active for both reactions can be used to convert synthesis gas with hydrogen-to-carbon monoxide ratios as low as 0.5 into hydrocarbon products [see eq 3]. This point is significant because of the development of several advanced coal gasification processes that directly produce synthesis gas with approximately this ratio.



In current commercial practice (SASOL, South Africa), the indirect liquefaction route for the conversion of coal to liquid fuels involves four principal stages [1], namely, coal gasification, gas purification, hydrocarbon synthesis, and product upgrading.

Of these, the gasification step is the most expensive; hence, technological improvements associated with this step offer the greatest potential for reducing costs.

A number of advanced gasification processes (e.g., Texaco and Shell-Koppers), which are now in various stages of commercial development, significantly improve on SASOL technology [2] which uses the conventional Lurgi gasifier. The advanced gasifiers not only exhibit improved efficiencies but also produce a smaller proportion of undesirable by-products (e.g., CH_4 , CO_2 , and H_2S). At the same time, however, the hydrogen-to-carbon monoxide ratio of the synthesis gas produced is much lower (0.5-0.9, compared to 2.1 for Lurgi). It has been shown that hydrocarbon products can be produced at reasonable reaction rates from this low H_2/CO synthesis gas [3-5], provided the catalyst is active for both reactions 1 and 2.

Depending on the process configuration, the desired products from slurry-phase FT synthesis could be liquid fuels (e.g., gasoline, diesel, jet fuel), light olefins, and/or wax. The light olefins could be oligomerized to liquid fuels through known processes such as MOGD [6]. The wax could be treated by catalytic hydrocracking to provide liquid fuels [7].

Slurry Phase FT Synthesis: The development of a slurry-phase Fischer-Tropsch process using an iron-based catalyst has drawn considerable attention. The advantages of the slurry-phase reactor system are (1) the ability to use low H_2/CO ratio synthesis gas produced by the advanced gasification processes, (2) the ability of the liquid phase to withdraw heats of reaction efficiently and thereby control reaction temperature, (3) high catalyst and reactor productivity, (4) favorable conditions for catalyst regeneration, and (5) simple construction and low investment costs.

Initial evaluation of FT catalysts for slurry bubble column reactors is performed in bench-scale, mechanically-stirred, slurry reactors. These reactors offer excellent temperature control and flexibility in operating conditions. Descriptions of such reactors and their operation are available [8]. Since the internal composition of such reactors is uniform, they facilitate development of kinetic models without the complications involved in the analysis of integral data obtained in a fixed bed reactor. The kinetic models will permit the prediction of performance of the catalyst in a slurry-bubble column reactor.

The production of hydrocarbons using traditional FT catalysts, such as Fe or Co, is governed by chain growth or polymerization kinetics. This can be described by the Anderson formalism [9], which is related to the Schulz-Flory polymerization equation [10]. The nature of the product and the product distribution among the carbon numbers will depend upon the catalytic surface, composition (H_2/CO ratio) and the rate of flow of the feed gas, reaction pressure, and the temperature at which the FT synthesis reaction is performed. The above parameters will affect the rate of hydrogen and CO dissociation, hydrogenation, degree of polymerization, and desorption of the product species.

Chain Growth Kinetics: The chain growth probability is designated by the quantity α and represents the probability that an oligomer with $(r-1)$ carbon atoms will grow to an oligomer with r carbon atoms. The product distribution among the carbon numbers follows the polymerization equation

$$W_n = n(1-\alpha)^2 \alpha^{n-1} \quad (4)$$

The above expression, usually known as the Anderson-Schultz-Flory (ASF) polymerization equation, is written

$$\log(W_n/n) = n \log \alpha + \log[(1-\alpha)^2/\alpha] \quad (5)$$

One would then expect a linear relation between $\log(W_n/n)$ and n , with slope $\log \alpha$, as shown in Fig. 1 [4]. The theoretical maxima for various hydrocarbon fractions in the FT product such as gas, naphtha, heavy distillate, and wax have been calculated [11] and can be seen in Fig. 2.

Catalyst Synthesis

Varieties of iron catalysts have been examined for FT synthesis in slurry reactors. These include (1) precipitated iron catalysts [3-5,12,13], (2) fused iron catalysts [14-16], (3) ultrafine-particle catalysts [17-19], and (4) catalysts produced by laser pyrolysis [20,21].

The pioneering work of Kolbel in Germany to develop the Rheinpreussen slurry reactor process after World War II used a precipitated iron catalyst [3]. The results obtained by Kolbel were very favorable, and efforts are ongoing to reproduce the space-time yields or catalyst activities. Koppers [22] of Rheinprussen claimed slurry reactor space-time yields of up to 2800 kg/m³ per day in a laboratory reactor, but all other studies published by his group reported considerably lower values (e.g., 940 kg/m³ per day in a pilot-scale reactor and 740 kg/m³ per day in a laboratory reactor [23]). These investigations and later work by the Mobil group [4,5] using precipitated iron catalysts in a slurry bubble column reactor (see Table 1) have resulted in a sustained interest in this type of catalyst. Accordingly, the effort in the DOE program has been centered on precipitated iron catalysts.

Precipitated Iron Catalysts:

The development of precipitated iron catalysts for slurry-phase synthesis was based on earlier work that was performed with iron catalysts intended for use in fixed-bed processes [1]. The feasibility of the use of precipitated iron catalysts has been demonstrated under relatively mild Arge-type conditions at SASOL [1,24]. Apart from the tests conducted on a limited scale at Rheinpreussen [3] and Mobil [4,5], these catalysts have not been sufficiently demonstrated in a slurry-bubble column reactor representative of commercial operation. The main reason for this is the lack of precise information in the public domain regarding the following factors influencing the activity, selectivity, and stability of the catalysts: (1) pH of precipitation, (2) concentration of Fe and other components such as Cu in the precipitation reactor, (3) temperature of precipitation, (4) residence time of Fe and other components in the precipitation reactor, (5) filtration rate of the hydrated gel, (6) washing rate of the hydrated iron oxide gel, (7) use of binders such as silica to provide mechanical strength, and (8) procedures such as spray drying to obtain uniform size spherical particles with a mean diameter of about 30 microns.

Under the DOE program an iron-based catalyst with the desired properties has been developed [25] for study in the Alternative Fuels Development Unit in LaPorte, Texas. Efforts are underway to scaleup the synthetic procedure in order to make about 2,000 pounds of the catalyst. Some features of the catalyst are (1) spherical particles of average diameter of about 30 microns, (2) FT and WGS activities that are higher than those of the commercial Ruhrchemie Fe catalyst, and (3) favorable suspension behavior in the slurry medium.

Kinetics of the Fischer-Tropsch Synthesis over Fe Catalysts

The CSTR is well-suited for measuring the intrinsic kinetics of the FT reaction as the influence of heat and mass transfer effects in this reactor can be ignored [8]. The kinetic models that have been proposed for the FT reaction will now be examined.

To date, no model can account for the reaction rate under all conditions. Each of the models agrees with the experimental results under certain conditions.

Anderson's rate expression [9]

$$-r_{CO-H_2} = \frac{k P_{H_2}}{1 + a P_{H_2O}/P_{CO}} \quad (6)$$

is applicable when the WGS activity is low. The rate expression is suggestive of a competition between water and CO for the available sites on the catalyst.

Ledakowicz et al. [26] have proposed that the rate expression

$$-r_{CO-H_2} = \frac{k P_{H_2}}{1 + a P_{CO_2}/P_{CO}} \quad (7)$$

could be used at high WGS activity. This rate equation implies that the influence of CO₂ is more important than that of H₂O under these conditions.

Satterfield et al. [27] drew attention to the fact that water inhibits the FT synthesis rate more than does CO₂. It was therefore reasonable to suppose that the concentration of H₂O (or the H₂O/H₂ ratio) is more important than the concentration of CO₂ (or the CO₂/CO ratio) in affecting the oxidation state of the catalyst. It was suggested [28] that the inhibition attributed to CO₂ by Ledakowicz et al. [26] was instead actually caused by H₂O formed by the reverse WGS reaction. Based on these arguments, the following rate equation [29] was favored:

$$-r_{CO-H_2} = \frac{k P_{H_2}}{1 + a P_{H_2O}/(P_{H_2} \cdot P_{CO})} \quad (8)$$

To use equation (8), it is important to have reliable methods for analyzing H₂O and H₂. H₂O tends to tail in some GC columns, but methods to quantitatively determine the H₂O concentration have been established [30]. The kinetics of the FT synthesis has recently been reviewed by Wojciechowski [31].

In addition to fluid dynamic data, the development of reliable kinetic rate expressions for iron catalysts is important for the prediction of the behavior of slurry bubble column reactors. The ongoing research to develop active and stable Fe FT catalysts for the slurry phase will stimulate additional work to develop accurate kinetic rate expressions.

Predicting Catalytic Performance in a Slurry Bubble Column Reactor

From CSTR data obtained on a precipitated iron catalyst, Abrevaya and Shah [12] have predicted the performance in an SBCR. The calculation was based on the CO+H₂ conversion measured in a CSTR at 265°C and 275°C at various feed flowrates (Fig 3). They assumed that the slurry bubble column reactor could be modelled as 11 slurry autoclave reactors-in-series operating at 8%, 16%, 24% ... 88% conversions. Since data were not available below 35% conversion at 265°C and 50% at 275°C (Fig 3), it was assumed that the reaction rate and selectivity at these temperatures did not

Table 1

Comparative Catalyst Performance Data

Reactor Type*	SASOL (Dry, 1981)		Köbel et al. (1955) Rheinpreussen Plant 100Fe/0.1Cu/.05- 0.5% ₀ BCSR	Sakai and Kunugi (1974) [32] 100Fe/0.3Cu/.6- 1.2% ₀ BCSR	MOBIL (Kuo, 1985)	
	Arge Pptd. FB	Synthol Fused CFB			CT 256-3 Low Max	CT 256-13 High Max
Catalyst					Fe/Cu/K ₂ O BCSR	Fe/Cu/K ₂ O BCSR
Conditions						
Temperature, °C	220	325	268	273	260	258
Pressure, atm	25	25	12	10.8	15	15
SV, ML/g-Fe/h	--	--	3.4	12.1	2.6	2.4
H ₂ :CO ratio	1.3-2.0	>2.0	0.67	0.52	0.67	0.67
Activity						
CO+H ₂ conv. (%)	--	--	89.0	78.5 (CO)	86.8	82.2
mol/g-cat/h	--	--	.106	--	.070	.061
Nm ³ /kg-Fe/h	--	--	3.02	--	2.25	1.97
Selectivity, wt%						
C ₁	2.0	10.6	3.2 (CH ₄ +C ₂ H ₆)	2.3	7.8	2.7
C ₂ -C ₄	11.2	35.2	31.3	8.2	24.5	11.1
C ₅ -C ₁₁	18.6	42.5	53.6	4.7 (C ₅ -C ₉)	41.9	18.1
C ₁₂ -C ₁₈	14.5	7.5	10.0	12.8 (C ₁₀ -C ₁₈)	15.4	10.2
C ₁₉ **	53.7	4.2	1.9	71.9	10.8	57.9
C ₁₂ **	68.2	11.7	11.9	84.7 (C ₁₀)	26.2	68.1
Product Yield						
g-HC/Nm ³ converted	--	--	178	151.8	197	206
g-HC/g-Fe/h	--	--	.57	--	.37	.41

* FB - fixed bed, CFB - circulating fluidized bed, BCSR - bubble column slurry reactor

change below 35% and 50% conversion respectively. The calculations made using these assumptions are summarized in Table 2. Subsequent improvements in the catalyst resulted in catalyst performance that was much closer to the target performance.

Table 2

Performance of Precipitated Iron Catalyst [12] in
11 Autoclave Reactors in Series at 21 ATM, 0.7 H₂: CO Feed
(wt-%)

	<u>265° C</u>	<u>275° C</u>	<u>Target</u>
C ₁	4.3	5.8	---
C ₂ (Ethane + Ethylene)	4.6	6.0	---
C ₁ + C ₂	8.9	11.8	7
Sv, nL/h-gFe	1.1	1.6	≥2

Concluding Remarks:

From the survey on Fe FT catalysts for slurry-phase operation, it is evident that additional research is needed for the development of reproducible synthesis of active and stable catalysts. A more complete understanding of the behavior of iron catalysts that can be obtained from modern surface and bulk analytic techniques is required. The correlation of catalyst properties with kinetic data will establish a sound basis for the commercial manufacture of Fe FT catalysts for slurry bubble column reactors.

References:

1. M.E. Dry, in J.R. Anderson and M. Boudart (Eds.), *Catalysis - Science and Technology*, Springer, Berlin, 1981, Vol. 1, pp. 159-255.
2. M. Teper, D.F. Hemming, and J.M. Holmes, *The Cost of Liquid Fuels from Coal, Part 1: Executive Summary*, International Energy Agency Report, November 1984.
3. H. Kolbel and M. Ralek, *Catal. Rev. - Sci. Eng.* **21**, 225 (1980).
4. J.C.W. Kuo, *Slurry Fischer-Tropsch/Mobil Two-Stage Process of Converting Syngas to High Octane Gasoline*, Final Report, DOE/PC/30022-10 (DE84004411), 1983.
5. J.C.W. Kuo, *Two Stage Process for Conversion of Synthesis Gas to High Quality Transportation Fuels*, Final Report, DOE/PC/60019-9, 1985.
6. S.L. Meisel, in "Methane Conversion" (Eds. D.M. Bibby, C.D. Chang, and R.F. Howe), *Studies in Surface Science and Catalysis*, **36**, 17 (1988).
7. P.P. Shah, M.J. Humbach, K.Z. Steigleder, and F.G. Padrta, UOP Des Plaines Technical Center, *Fischer-Tropsch Wax Characterization and Upgrading*, Final Report, DE-AC22-85PC80017, 1988.
8. T.J. Donnelly and C.N. Satterfield, *Appl. Catal.* **56**, 231 (1989).
9. R.B. Anderson, in "Catalysis," Volume 4 (P. H. Emmett, ed.), Reinhold, New York, 1956. See also R.B. Anderson, "The Fischer-Tropsch Synthesis," Academic Press, Orlando (1984).
10. G. Henrici-Olive and S. Olive, *Angew. Chem. Int. Ed.* **15**, 136 (1976).
11. J.H. Gregor, AIChE Spring National Meeting, Orlando, Florida, March 18-20, 1990.
12. H. Abrevaya and P.P. Shah, *Proc. DOE Indirect Liquefaction Contractors' Review Meeting*, Pittsburgh, 1990, p. 203.
13. M.F. Zarochak and M.A. McDonald, *Proc. DOE Indirect Liquefaction Contractors' Review Meeting*, Pittsburgh, 1986, p. 58.
14. G.A. Huff and C.N. Satterfield, *J. Catal.* **85**, 370 (1984).

15. D.M. Bukur and R.F. Brown, *Can. J. Chem. Eng.* **65**, 604 (1987).
16. H. Dabbagh, L.M. Tau, S. Bao, J. Halasz, and B.H. Davis, in "Catalysis Today" (J.W. Ward, Ed), Elsevier, 1988.
17. H. Itoh, H. Hosaka, T. Ono, and E. Kikuchi, *Appl. Catal.* **40**, 53 (1986).
18. E. Kikuchi and H. Itoh, in "Methane Conversion," (D.M. Bibby, C.D. Chang, R.F. Howe, and S. Yurchak, Eds.) Elsevier, 1988.
19. H. Itoh, H. Tanabe, and E. Kikuchi, *Appl. Catal.* **47**, L1 (1989).
20. R.A. Fiato, G.W. Rice, S. Misco, and S.L. Soled, U.S. Patent 4,687,753 (1987).
21. G.W. Rice, R.A. Fiato, and S.L. Soled, U.S. Patent 4,659,681 (1987).
22. H.H. Koppers, *Chem. Age India*, **12**, 7 (1961).
23. D.S. van Vuuren, Assessment of the Techno-economic Potential of Fischer-Tropsch Slurry Reactors, CSIR, South Africa, Report CENG 655 (1987).
24. M.E. Dry, *Catalysis Today*, **6**, 183 (1990).
25. F. Tungate, Private Communication.
26. S. Ledakowicz, H. Nettelhoff, R. Kokuun, and W.-D. Deckwer, *Ind. Eng. Chem. Process Dev.* **24**, 1043 (1985).
27. C.N. Satterfield, R.T. Hanlon, S.E. Tung, Z.-M. Zou, and G.C. Papaefthymiou, *Ind. Eng. Chem. Prod. Res. Dev.* **25**, 407 (1986).
28. I.C. Yates and C.N. Satterfield, *Ind. Eng. Chem. Research* **28**, 9 (1989).
29. G.A. Huff, Jr., and C.N. Satterfield, *Ind. Eng. Chem. Process Des. Dev.* **23**, 696 (1984).
30. G.A. Huff, Jr., C.N. Satterfield, and M.H. Wolf, *Ind. Eng. Chem. Fundam.* **22**, 258 (1983).
31. B. Wojciechowski, *Catal. Rev. - Sci. Eng.* **30**, 629 (1988).
32. T. Sakai and T. Kunugi, *Sekiyu Gakkai Shi*, **17**(10), 863 (1974).

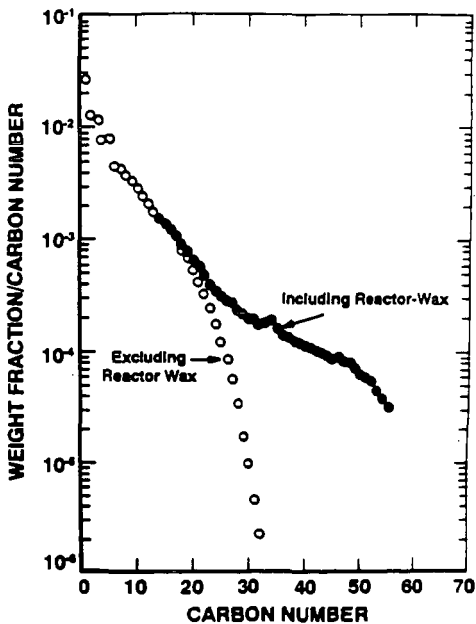


Figure 1. Schulz-Flory distribution for Fischer-Tropsch products from a slurry bubble column-reactor [4].

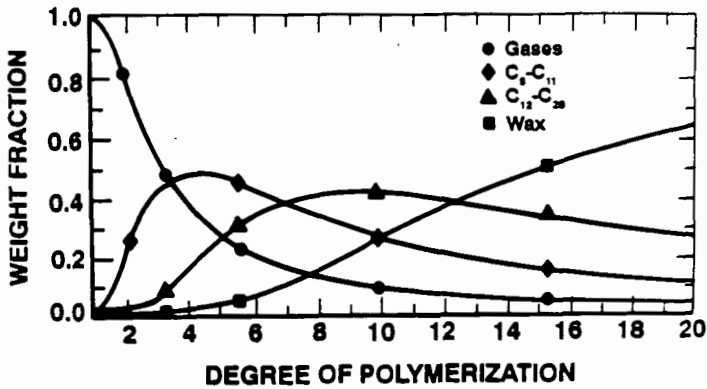


Figure 2. FT product distribution versus degree of polymerization [11].

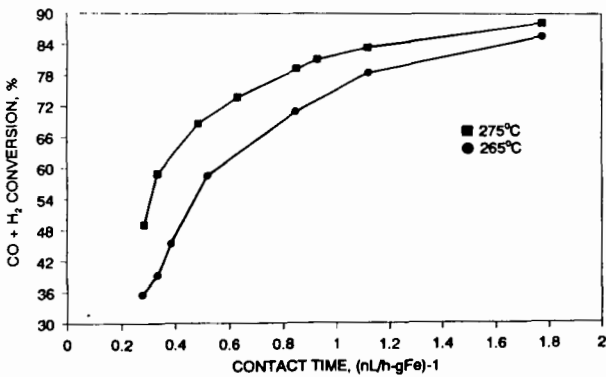


Figure 3. Conversion versus contact time for a precipitated iron catalyst [12] at 21 atm with feed H₂/CO = 0.7.

HYDROGEN AND CARBON MONOXIDE TEMPERATURE PROGRAMMED DESORPTION STUDY OF Mn-Fe CATALYSTS

Y. Soong, V.U.S. Rao, M.F. Zaroachak, and R. J. Gormley
Pittsburgh Energy Technology Center, U.S. Department of Energy,
P.O. Box 10940, Pittsburgh, PA 15236

B. Zhang, Institute of Coal Chemistry, Academia Sinica,
P.O. Box 165, Taiyuan, Shanxi, China

Keywords: manganese-iron, temperature-programmed desorption,

INTRODUCTION

Mn-Fe catalysts have been studied extensively during recent years, primarily because they can enhance the selectivity for low-molecular weight olefins in the Fischer-Tropsch (FT) synthesis (1-9). The reason for the increased selectivity towards light olefins on Mn-Fe catalysts remains controversial. A chemical and/or electronic promoter effect of Mn on the available iron surface has been proposed (4). The change in selectivity upon the addition of Mn to iron catalysts has also been attributed to a MnO species sitting on the Fe surface (1). Moreover, a surface spinel phase (MnFe_2O_4) has been proposed to play an important role in providing high selectivity to light olefins (2,3,5,6). It is still an open question as to whether the spinel phase (MnFe_2O_4) is responsible for the activity and selectivity during the FT synthesis.

In general, Mn-Fe catalysts were prepared by coprecipitation (or impregnation) of the corresponding nitrates. The degradation of a metal complex, a simple method employed in this study, has not been widely utilized. In this study, $\text{MnFe}_2(\text{C}_2\text{O}_4)_3$ was decomposed to prepare the Mn-Fe catalysts. Some of the major advantages of this method are the following: (a) degradation of this complex can lead to the formation of various Mn-Fe oxides by calcination at different temperatures; and (b) pure Mn-Fe spinel can be prepared with the correct stoichiometric metal ratio, $\text{Fe}/\text{Mn}=2$.

Previous studies have reported that hydrogen adsorption on iron catalysts can be activated and dissociative, and carbon monoxide adsorption on iron catalysts includes both associative and dissociative adsorption (4,10,13,14). In an attempt to gain a better understanding of the role that the spinel phase (MnFe_2O_4) plays in Mn-Fe catalysts, a TPD study of Mn-Fe catalysts was conducted.

EXPERIMENTAL

$\text{MnFe}_2(\text{C}_2\text{O}_4)_3$ was prepared as described by Wickhem (15). The catalyst precursor $\text{MnFe}_2(\text{C}_2\text{O}_4)_3$ was calcined in air at different temperatures (1300, 1000, 700, and 500 °C) for 5 hours, followed by quenching in nitrogen. Fe_2O_3 was prepared from the precursor $\text{Fe}(\text{C}_2\text{O}_4)$ by calcining at 500 °C for 5 hours, followed by quenching

in nitrogen.

High purity argon, hydrogen, and carbon monoxide were used in this study. Gas flow rates of 30 ml/min were used for experiments conducted in this study. A temperature-programmed, catalyst characterization system (AMI-1) manufactured by Altamira Instruments, Inc., was used to obtain the TPD spectrum. A ramp of 15°C/min was used for all experiments in this study.

Catalyst samples were first exposed to a stream of argon gas at 120°C for one hour, then they were reduced in hydrogen at 350°C or 450°C for 12 hours. The catalyst was cooled under flowing hydrogen from the reduction temperature to ambient temperature, flushed in argon for one-half hour to remove the weakly held hydrogen, then heated to 650°C and held at 650°C for one-half hour. The TPD spectra obtained from this sequence are referred to as high temperature (HT) H₂-TPD. After being purged with argon at 650°C for about one-half hour, the catalyst samples were then cooled to ambient temperature. The catalysts were exposed to adsorbate gas (H₂ or CO) at ambient temperature for one hour, followed by flushing in argon for one-half hour, and then heated in argon to 650°C and held for one-half hour. The TPD spectra obtained from this sequence are referred to as low temperature (LT) H₂ (or CO)-TPD.

RESULTS AND DISCUSSION

The amount of hydrogen absorbed (or desorbed) was determined from the TPD spectra shown in Figs 1 to 3. The effects of varying calcination and reduction temperatures on hydrogen uptakes are presented in Table 1. For each catalyst, two hydrogen uptakes are measured. One is determined from the HT H₂-TPD, and the other is calculated from the LT H₂-TPD. Three to 50 times as much hydrogen uptake is obtained by comparing the HT H₂-TPD to that of LT H₂-TPD. Based on these two hydrogen uptakes at any reduction temperature, it is apparent that hydrogen adsorption is an activated process over Mn-Fe catalysts. These data are in agreement with previous studies that have shown hydrogen adsorption on iron catalysts can be highly activated (3,13). Noticeably, a high temperature of reduction significantly suppresses the amount of HT-H₂ uptake obtained from the MnFe1300 catalyst (Table 1). This result correlates well with our reaction data that there is a higher syngas conversion of 28% from the MnFe1300 catalyst with a lower reduction temperature, 350°C, versus that of 21% when the catalyst was reduced at 450°C (16). The lower uptakes of hydrogen obtained from higher reduction temperatures may be a result of catalyst sintering and/or MnO encapsulated with iron particles during the higher temperature of reduction. The MnO encapsulated with iron particles has been verified by our XPS observations (16).

XRD results obtained for each of the catalysts are also shown in Table 1. These results show that various phases can be formed by calcination at different temperatures, as anticipated. High calcination temperature (1300°C) favored the formation of a Mn-Fe

spinel before reduction. A mixture of spinel, manganese oxide, and iron oxide was observed when catalysts were calcined at 1000°C. Lower calcination temperatures (700 and 500°C) led to the formation of manganese oxide and iron oxides. Different reduction temperatures can also result in the formation of different phases. In general, two phases, MnO and Fe, were observed when catalysts were reduced at 450 and 350°C. However, the additional spinel phase (MnFe_2O_4) formed when the catalysts were calcined at 1000 or 1300°C and reduced at 350°C. These results are consistent with previous studies on the effects of reduction temperature on spinel phases. Studies on the Mn-Fe catalysts, prepared by the coprecipitation method, indicated that reducing catalysts at a higher temperature than 375°C results in the complete decomposition of the spinel phase to MnO and metallic Fe phases. However, reduction at a lower temperature than 375°C results in a mixture of Fe, MnO, and mixed spinel phases (3,5-7,9). Fe was the only phase observed after the reduction of the Fe500 catalyst prepared using the oxalate precursor.

Figs 1 and 2 illustrate the effects of calcination and reduction temperature on HT H_2 -TPD of Mn-Fe catalysts. Some general observations can be made by comparing the TPD spectra with the XRD results in Table 1. Two desorption peaks (90 to 120°C and 450 to 510°C) can be correlated with the Fe phase (Figs 1a, 2a). As indicated by XRD results, MnO and Fe phases were the only two phases present when catalysts were reduced at 450°C. By correlating TPD spectra in Figs 2b to 2e with XRD results, the MnO-related peaks can be assigned as those peaks with temperatures near 140 to 190°C and 570 to 630°C. These MnO-related peaks were also observed in Figs 1c and 1d. The XRD results also indicate that when catalysts are calcined at 1000 or 1300°C and reduced at 350°C, the spinel phase (MnFe_2O_4) is present along with MnO and Fe phases. The shapes of the TPD spectra for these materials (Figs 1c and 1d) are significantly different from other spectra in Figs 1 and 2, in that they have an additional peak centered at 350°C. This additional peak, centered at 350°C, can be clearly correlated with the spinel phase (MnFe_2O_4). The surface of the Mn-Fe catalyst is probably complex. However, through a systematic series of experiments, the Fe, MnO, and MnFe_2O_4 related TPD spectra can be assigned. Fig. 3 shows the effects of calcination and reduction temperatures on LT H_2 -TPD of Mn-Fe catalysts. Noticeably, the LT H_2 -TPD spectra are much smaller than that in Figs 1 and 2. Combining the TPD spectra on Fig. 3 with the XRD information obtained in Table 1, the following conclusions were reached. The peak centered at 100°C is correlated with the Fe phase (Fig. 3). A broad desorption peak centered at 230°C may be correlated with the MnO phase (Figs 3a, 3b, and 3c). The spinel phase related peak (with peak temperature centered at 350°C in Figs 1c and 1d) was also observed in Figs 3-c and 3-d. Based on the information collected from Figs 1 to 3, the spinel phase does adsorb hydrogen and it is an activated process. Weatherbee et al. indicated that highly activated adsorption of hydrogen on reduced iron could lead to hydrogen-adsorption limiting kinetics and a hydrogen-poor surface resulting in the modification of the product distribution

during hydrogenation (13). Less adsorbed hydrogen that may be available for the hydrogenation on the Mn-Fe catalysts under reaction conditions thus could favor the formation of olefins. Moreover, an additional experiment was conducted to verify the hypothesis that the spinel phase does adsorb hydrogen. The pure spinel, $MnFe_2O_4$, was first heated to $650^\circ C$ in argon to desorb any impurities that remained during the preparation. Then the catalyst was cooled to $280^\circ C$ in argon, followed by exposure to hydrogen for 10 minutes at $280^\circ C$. It was cooled down to ambient temperature in hydrogen, then switched to argon. The TPD spectrum obtained from this experiment showed only one desorption peak, centered at $350^\circ C$, which was identified as the spinel phase related hydrogen desorption peak previously identified.

The LT CO-TPD spectra are shown in Fig. 4. It was found that all the desorption peaks consisted solely of carbon monoxide. Based on the observed peaks, two forms of desorbed CO could be distinguished; one type desorbed at a temperature of about 90 to $110^\circ C$ and the other at about 590 to $630^\circ C$. Both desorption peaks can be correlated with the Fe phase. The lower temperature peak is probably related with the desorption of molecular CO, whereas the higher temperature peak might correlate with the recombination of surface carbon and surface oxygen. The two desorption peaks are consistent with previous studies (4,12). It is interesting to note that the relative ratio of the higher temperature peak versus the lower temperature peak is affected by the reduction temperature (Fig. 4b to 4d and 4e to 4c). A larger ratio is obtained from Fig. 4b and 4e, when the catalyst is reduced at $350^\circ C$, while a smaller ratio is observed from Fig. 4d and 4c, when the catalyst is reduced at $450^\circ C$. This difference in relative ratio correlates well with the reaction results (16). The CO conversion for the MnFe1300,350 catalyst (Fig. 4b) was 23%, while the conversion for the MnFe1300,450 catalyst (Fig. 4d) was 17%. These reaction results indicate that the lower reduction temperature catalyst has a higher CO conversion. The higher relative ratio of the two TPD peaks, obtained from the lower reduction temperature material (Fig. 4b) suggests that the CO dissociation is enhanced at lower reduction temperature. The peak around 230 to $250^\circ C$ may be correlated with the MnO-related phase from Figs. 4c and 4d. No spinel phase related peak could be assigned in Fig. 4b and 4e. From the CO TPD spectra, it can be inferred that the spinel phase does not adsorb CO at room temperature. An additional experiment was also conducted to verify the hypothesis that the spinel phase does not adsorb CO. The pure spinel phase was first heated to $650^\circ C$ in a stream of argon to remove any impurities. Then the catalyst was cooled to $280^\circ C$ and the CO was introduced to the catalyst and held for 10 min followed by cooling to room temperature in CO. The flow was then switched to a stream of argon. The TPD spectrum obtained from this experiment showed no desorption of CO. An attempt was also made to verify whether or not the spinel phase alone is an active phase for syngas conversion. The $MnFe_2O_4$, which had been calcined at $1300^\circ C$ for 5 hours from the spinel precursor, was exposed to synthesis gas at $280^\circ C$ and 21 bar. In the absence of a reduction stage, it exhibited no activity during the 72-hour

testing period. The phase of the catalyst after calcination was shown to be a MnFe_2O_4 spinel (Table 1). After exposing the catalyst to synthesis gas, the phase was still a MnFe_2O_4 spinel, as determined by X-ray diffraction. These results suggest that the MnFe_2O_4 spinel phase is not responsible for syngas conversion when it is present alone. It is speculated that the lower electron density on the catalyst surface is responsible for this effect. It is well known that the MnFe_2O_4 spinel is a near normal spinel in structure. Fe^{+++} ions are distributed on both tetrahedral sites and octahedral sites in a 1:9 ratio. Fe^{+++} differs from Fe^0 mainly in its lower electron density (11). Hence, electron back donation from the Fe^{+++} ions into the 2π orbitals of CO is too weak to involve a metal-carbon bonding. A metal-carbon bonding is a prerequisite for syngas conversion, and therefore, no reaction takes place.

CONCLUSION

In the light of the TPD spectra, XRD results, and our reaction results, we have concluded that MnFe_2O_4 may not be an active phase itself during FT synthesis, because it does not chemisorb CO. The MnFe_2O_4 phase does chemisorb hydrogen in an activated process. The temperature of reduction determines the phases of the Mn-Fe catalyst. The hydrogen adsorption over the Mn-Fe catalysts is an activated process and at least three types of adsorption state may be assigned, namely Fe, MnO, and MnFe_2O_4 related phases.

ACKNOWLEDGMENTS

The authors gratefully acknowledge the technical assistance by Mr. A.G. Blackwell and Mr. N.H. Haden.

REFERENCES

1. I.S.C. Hughes, J.O.H. Newman, *Appl. Catal.* 30,303,1987.
2. U. Lochner, M. Papp, M. Baerns, *Appl. Catal.* 23,339,1986.
3. J. Venter, M. Kaminsky, G.L. Geoffroy, and M.A. Vannice, *J. Catal.* 103,450,1987.
4. K.B. Jensen, and F.E. Massoth, *J. Catal.* 92,98,1985.
5. G.C. Maiti, R. Malessa, M. Baerns, *Appl. Catal.* 5,151,1983.
6. G.C. Maiti, R. Malessa, U. Lochner, H. Papp, M. Baerns, *Appl. Catal.* 16,215,1985.
7. J. Venter, M. Kaminsky, G.L. Geoffroy, M.A. Vannice, *J. Catal.* 105,155,1987.
8. K.M. Kreitman, M. Baerns, J.B. Butt., *J. Catal.* 105,319,1987.
9. R. Malessa, and M. Baerns, *Ind. Eng. Chem. Res.* 27,279,1988.
10. K.H. Huang, X.M. Zerg, J.T. Li, *J. Catal.* 81,259,1983.
11. H. Yoo and H. L. Tuller., *J. Phys. Chem. Solid.*, 49,761,1988.
12. Y. Amenomiya, and G. Pleizier, *J. Catal.* 28,442,1973.
13. G.D. Weatherbee, J.L. Rankin, C.H. Bartholomew, *Appl. Catal.* 11,73,1984.
14. J.L. Rankin, C.H. Bartholomew, *J. Catal.* 100,533,1986.
15. D.G. Wickhem, "Inorganic Synthese"; Vol. 9,152,1967.
16. V.U.S. Rao, R.J. Gormley, S. Pollack, B. Zhong, in preparation

Table 1. Calcination and Reduction Temperature Effects on Catalyst Compositions and Hydrogen Uptakes.

Catalyst	Calcined Temp. °C	XRDC	Reduction Temp. °C	XRDC ^d	HT-H ₂ ^a Uptake ml/g	LT-H ₂ ^b Uptake ml/g
Fe500	500	Fe ₂ O ₃	350	Fe	2.58	0.12
MnFe500	500	Fe ₃ O ₄ Mn ₂ O ₃	350	MnO Fe	3.92	0.49
MnFe700	700	Mn ₂ O ₃	350	MnO Fe	2.13	0.15
MnFe1000	1000	MnFe ₂ O ₄ Mn ₂ O ₃	350	MnFe ₂ O ₄ MnO Fe	2.05	0.21
MnFe1300	1300	MnFe ₂ O ₄	350	MnFe ₂ O ₄ MnO Fe	2.65	0.27
Fe500	500	Fe ₂ O ₃	450	Fe	1.48	0.10
MnFe500	500	Fe ₃ O ₄ Mn ₂ O ₃	450	MnO Fe	3.03	0.95
MnFe700	700	Mn ₂ O ₃	450	MnO Fe	2.23	0.3
MnFe1000	1000	MnFe ₂ O ₄ Mn ₂ O ₃	450	MnO Fe	2.48	0.11
MnFe1300	1300	MnFe ₂ O ₄	450	MnO Fe	1.77	0.29

^aObtained after the temperature-activated adsorption from the stream of hydrogen at reduction temperature and cooling to ambient temperature in the stream of hydrogen (HT H₂-TPD).

^bObtained after adsorption from the stream of hydrogen for one hour at ambient temperature (LT H₂-TPD).

^cObtained after calcination.

^dObtained after the reduced samples were mixed with Dow Corning silicone grease in a glove box for preventing further oxidation.

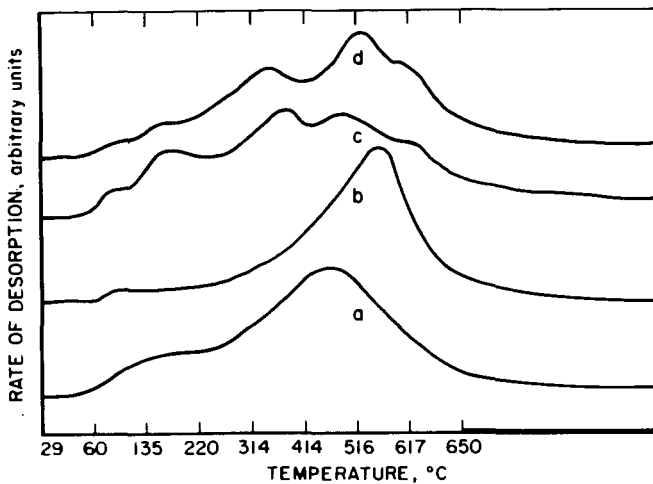


Fig. 1. Temperature-programmed desorption spectra of hydrogen (HT H_2 -TPD) from catalysts as a function of calcination temperatures (catalysts were reduced at 350°C). (a) Fe_2O_3 calcined 500°C; (b) MnFe500 calcined 500°C; (c) MnFe1000 calcined 1000°C; (d) MnFe1300 calcined 1300°C.

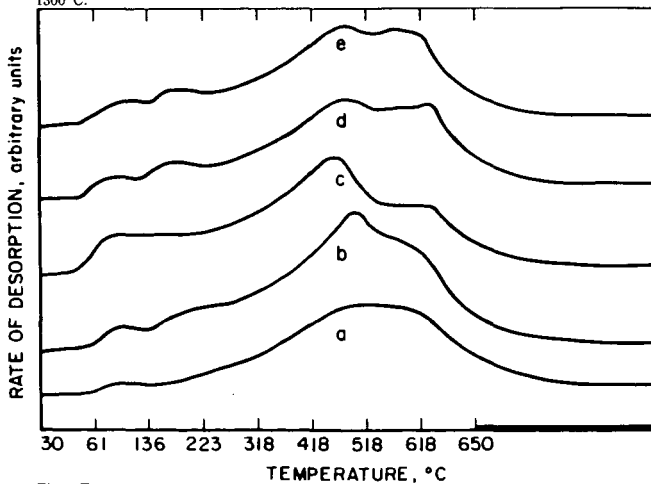


Fig. 2. Temperature-programmed desorption spectra of hydrogen (HT H_2 -TPD) from catalysts as a function of calcination temperatures (catalysts were reduced at 450°C). (a) Fe_2O_3 calcined 500°C; (b) MnFe500 calcined 500°C; (c) MnFe700 calcined 700°C; (d) MnFe1000 calcined 1000°C; (e) MnFe1300 calcined 1300°C.

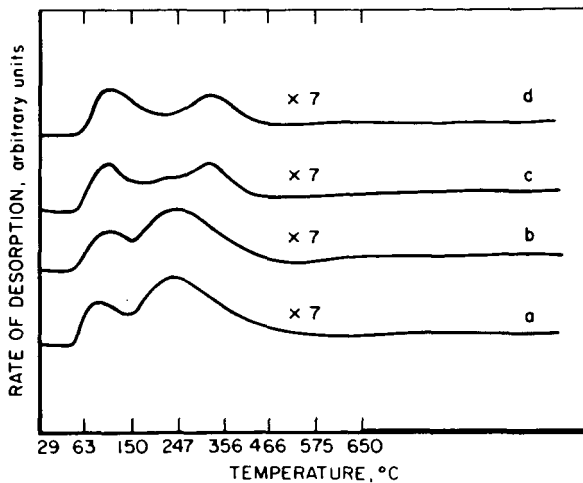


Fig. 3. Temperature-programmed desorption spectra of hydrogen (LT H_2 -TPD) from catalysts as a function of calcination temperatures. (a) MnFe700 calcined 700°C, reduced 450°C; (b) MnFe1300 calcined 1300°C, reduced 450°C; (c) MnFe1000 calcined 1000°C, reduced 350°C; (d) MnFe1300 calcined 1300°C, reduced 350°C.

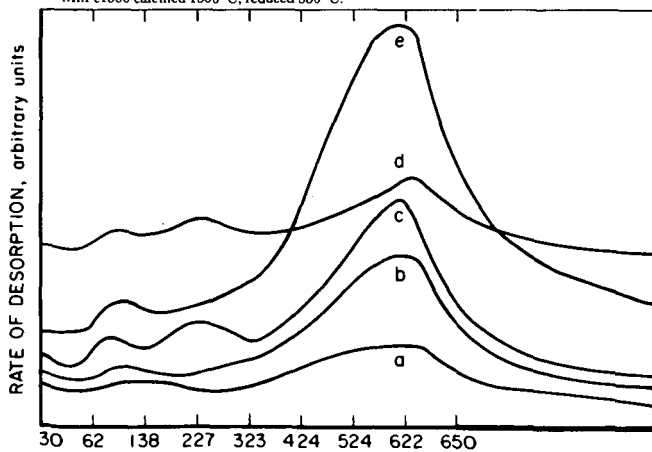


Fig. 4. Temperature-programmed desorption spectra of carbon monoxide (LT CO-TPD) from catalysts as a function of calcination temperatures and reduction temperatures. (a) Fe_2O_3 , 350 calcined 500°C reduced 350°C; (b) MnFe1300, 350 calcined 1300°C reduced 350°C; (c) Mn-Fe1000, 450 calcined 1000°C reduced 450°C; (d) MnFe1300, 450 calcined 1300°C reduced 450°C; (e) MnFe1300, 350 calcined 1300°C reduced 350°C.

RELATIONSHIPS OF COAL STRUCTURE TO MOLYBDENUM CATALYST ACTION IN LIQUEFACTION

Caroline E. Burgess, Levent Artok, and Harold H. Schobert
Fuel Science Program
The Pennsylvania State University
University Park, PA 16802

Keywords: Molybdenum sulfide catalyst, low severity liquefaction, coal structure

INTRODUCTION

Previous work in this laboratory has shown that the addition of ammonium tetrathiomolybdate catalyst precursor (ATTM) to coal at low severity conditions primarily increased the asphaltene yield from subbituminous coals, while for bituminous coals, ATTM primarily increased the oil yield [1]. For coals with higher crosslink density (lower rank coals), the catalyst promoted dissolution, while coals with lower crosslink density did not need catalyst to dissolve, and the catalyst instead mainly participated in the hydrogenation of asphaltenes to oils [1]. Our earlier work has now been extended to several additional coals to include liquefaction data with and without catalyst. This data will be compared with coal aromaticity data determined by ^{13}C NMR and solvent swelling data in pyridine.

EXPERIMENTAL

Two different catalyst precursors were used. Sulfided ammonium molybdate (SAM) was prepared, as described in several publications [1-6], by bubbling H_2S into a solution of ammonium heptamolybdate. Ammonium tetrathiomolybdate (ATTM) was purchased from Aldrich.

The coal was impregnated in the same manner as reported previously [1-8]. Coal was slurried with catalyst precursor solutions for 2 hours and dried to less than 1% moisture. Although several molybdenum sulfide precursors were used, previous data have shown that the predominant active catalyst species is MoS_2 [1-8] and relative comparisons can be made about the effect of molybdenum catalysts on coal liquefaction. However, it should be recognized that the degree of dispersion of the precursors on coal could be different because two different catalyst precursors were used.

A total of eight coals was used. Data on the elemental composition of each coal are contained in Table 1. All reactions were carried out in 25 ml microautoclave (tubing bomb) reactors, and heating was accomplished in a temperature controlled fluidized sandbath. The catalyst loading was 1% expressed as weight of molybdenum (not of molybdenum compound) on a daf basis. The reactor was flushed three times with hydrogen, with the final addition pressurized to 6.9 MPa (cold). The reactor was vertically oscillated 2.5 cm at 200 cycles per minute. The coals PSOC-487, PSOC-831, PSOC-1379, and DECS-12 were reacted in a single stage reaction at 360°C for 1 h (PSOC-1488 for 350°C for 1 h). The solvent used was phenanthrene (naphthalene for PSOC-1488) at a 2/1 solvent-to-coal ratio, and the mass of the coal reacted was 2.5 g. The coal PSOC-1488 was reacted in a temperature-staged reaction (350°C for 1 h followed by 425°C for 10 min). A Texas lignite and a hvB bituminous coal used the following reaction conditions: phenanthrene solvent at a 1/1 solvent-to-coal ratio, with the coal mass 5 g, and the reaction was temperature-staged at 275°C for 30 min and 425°C for 30 min. The Çan (Turkish) coal was reacted in phenanthrene and dihydrophenanthrene (5 g of each of solvent and coal) in temperature-staged reactions of 275°C for 30 min and 425°C for 30 min.

For PSOC-1488, the cooled reactor was vented into a glass expansion bulb, and the contents were analyzed by gas chromatography using a Varian model 3700. The contents of the reactor were then rinsed with tetrahydrofuran (THF) into a dried Soxhlet thimble and extracted for about 12 h under nitrogen. The THF was removed by rotary evaporation. The solid residue was dried at 100°C

for 12 h before weighing. Conversion was calculated by subtracting the weight of the residue from the weight of the coal and dividing by the dmmf weight of the coal. Liquids were further separated into asphaltenes and oils by adding hexane to the THF-soluble portion. This mixture was refluxed for 12 h under nitrogen, followed by filtration into hexane-solubles and insolubles. The hexane was removed by rotary evaporation, and the samples were dried at 100°C for 1 h before weighing. The oil (hexane-soluble) yield was calculated by difference from the conversion percentages of the gas yield, THF solubles, and the THF insolubles.

For the rest of the coals, the work-up procedure was changed slightly. Gas percentages were not determined, so the calculated difference for the oils includes the gas yield as well. Gas yields vary only slightly, so any trend in oil plus gas really reflects changes in oil yield. Once the pressure was vented from the reactor, the contents of the tubing bomb were rinsed with hexane into a dried, weighed ceramic thimble and Soxhlet extracted for about 24 h under nitrogen. The hexane was removed from the extract by rotary evaporation. The hexane-insoluble residue was then Soxhlet extracted with toluene to separate asphaltenes from the residue. Toluene was removed from the extract by rotary evaporation. The toluene-insoluble residue was then Soxhlet extracted with THF to separate preasphaltenes from the residue. THF was removed from the extract by rotary evaporation. Preasphaltenes, asphaltenes, and residue were dried overnight under vacuum at 110°C. Conversion was calculated by subtracting the weight of the residue from the weight of the coal and dividing by the daf weight of the coal.

Solid state ^{13}C NMR was performed using a Chemagnetics NMR Model M100S. The experiment was the standard CPMAS and pulsed Fourier transform (PFT) technique to collect the NMR spectrum. This technique was used for determination of f_a and to characterize the structure of each coal. The conditions used for this were: contact time, 1000 μs ; acquisition count, 10,000; carbon frequency, 25 MHz; the time of the 90° pulse, 5.5 μs ; and a pulse delay of 1 s. Table 2 contains f_a data.

Solvent swelling was performed according to the same procedure as Artok et al. [7] and Davis et al. [8]. About 1 g of coal (-60 mesh) was placed into a graduated centrifuge tube fitted with a screw cap. The coal was centrifuged for 30 min at 3000 rpm (room temperature), and the height of the coal (H_0) was recorded. Pyridine (6-7ml) was added to the coal, and the sample was shaken to ensure that all the coal was wetted with the pyridine. The samples sat for ~24 h. The sample was again centrifuged for 30 min at 3000 rpm, and the new height of the coal (H_s) was recorded. The solvent swelling index, Q , was calculated by H_s/H_0 . Table 2 contains the results of this experiment.

RESULTS AND DISCUSSION

It is important to mention that much of the data discussed in this paper were obtained as part of several different projects. Because each of the projects had somewhat different objectives, different reaction conditions were used to obtain the original data. Therefore it would be impossible to draw quantitative statistical conclusions. However, some useful qualitative comparisons can be discussed. Tables 2 and 3 contain the solvent swelling data, the aromaticity data, and the liquefaction data for all the coals. Table 2 contains single-stage data and Table 3 contains temperature-staged data. The first part of the discussion will focus on the low temperature single-stage data.

For the low temperature single-stage reactions, at every reaction condition, using molybdenum sulfide catalyst shows an increase in the total conversion, even at 275°C. The principal factor of concern in this paper is the change in the light fraction-to-heavy fraction ratio (L/H) compared to the coal rank, the solvent swelling index, and the aromaticity (f_a). The L/H ratio is calculated by dividing the oil plus gas yield by the preasphaltene plus asphaltene yield. For all the subbituminous coals (PSOC-487, -1488, and DECS-1), the L/H ratio decreases when comparing the catalyzed reaction to the uncatalyzed reaction. It appears at low severity that the catalyst functions to depolymerize the coal, not to hydrotreat preasphaltenes and asphaltenes to oils and gas. For the bituminous coals (PSOC-831, PSOC-1379, DECS-6, and DECS-12), the L/H ratio increases when comparing the catalyzed reaction to the uncatalyzed reaction. It appears that the catalyst functions not only to depolymerize the coal, but also to hydrogenate asphaltenes to oils and gas. These data are

similar to data presented in the previous work [1]. It was shown by Burgess et al. [1] that earlier work by Weller and Pelipetz [9] and Garg and Givens [10] fits into this pattern.

There are some other comparisons that can be made for the liquefaction data at 350-360°C. The organic sulfur in the coals can be qualitatively classified as high ($\geq 0.83\%$) or low; the crosslink density can be high (~ 1.7), medium (~ 1.5), or low (~ 1.1); organic oxygen can be high ($\geq 15\%$) or low; and the solvent quality is high (phenanthrene) or low (naphthalene). For the uncatalyzed reactions, the two systems indicating the highest conversions - PSOC-831 and DECS-12 - share the following characteristics: high organic sulfur, a medium crosslink density, and low organic oxygen, while using a relatively good solvent during liquefaction. Organic sulfur is a point of macromolecular decomposition [11] and is important for liquefaction reactivity [12]. It seems odd that a coal with a medium crosslink density would be a better liquefying coal than one with a low crosslink density, but the coal with the medium crosslink density liquefies better than the coal with the high one (the fewer the crosslinks to cut, the easier the liquefaction). High organic oxygen can mean a high percentage of carboxyl groups, and it is thought that carboxyl groups play a role in preventing the hydrogenation of free radicals that can lead to retrogressive crosslinking during liquefaction [13].

For the single stage catalyzed reactions at 350-360°C, liquefaction reactions giving the highest conversions are PSOC-1379 and DECS-12. However, there is no apparent distinction for these coals based on coal properties (at least sulfur, f_a , oxygen, and Q). However, consider the comparison of PSOC-487 and -1379. These coals have comparable Q and oxygen. Note that the higher conversion is obtained with the higher sulfur coal, and furthermore, the higher sulfur coal gives a significant increase in oils. For PSOC-831 and DECS-12, both have comparable Q and oxygen, though lower Q and oxygen values than those of PSOC-487 and -1379. In this case, the coal with higher sulfur gives lower conversion. A possible explanation for these observations is that sulfur is not as important as a reactive site in the higher rank coals (Given found that sulfur was important for lignites [12]). When there is a lower oxygen content, there is less likelihood of retrogressive crosslinking at oxygen sites [13], and hence the intervention of H_2S (generated from hydrogenation of the sulfur compounds) is much less important. For the 487/1379 pair of coals, where sulfur is important, increased conversion comes largely from oils. In the 831/12 pair, where sulfur apparently has no effect, the increased conversion comes largely from asphaltenes and preasphaltenes. It is possible that H_2S facilitates conversion to oils [11, 12].

The discussion will now focus on temperature-staged reactions without catalyst. If PSOC-1488 and DECS-1 are compared, they both have similar oxygen contents, with DECS-1 giving much better liquefaction conversion. Notice the big increase in conversion is due to oils. The better conversion of DECS-1 is consistent with its relatively high organic sulfur content, although the effects of solvent quality and crosslink density must also be considered.

The reaction conditions of temperature-staging plus catalyst give comparable conversions for the three coals (not including the ultra-reactive high organic sulfur coal Çan). However, this is consistent with previous arguments [1], that if a sufficiently severe reaction condition is used (and in the context of the work discussed here catalytic temperature-staging is severe), then the severity of the reaction conditions simply overwhelms effects of coal structure and most coals can be driven to high conversions. The main difference in the reaction for the Çan coal is that the conversion in phenanthrene and catalyst is quite high (96.3% for total conversion and 62.0% for the oil + gas yield) and that the conversion in DHP without catalyst is quite high (93.8% for total conversion and 49.0% for the oil + gas yield). When reacting the Çan coal in DHP and catalyst, there isn't much otherwise reactive coal left to break apart, so the catalyst acts mainly in hydrogenating preasphaltenes and asphaltenes to oil and gas. It is also evident with the Çan coal that even without using catalyst or hydrogen donor solvent, the temperature-staged liquefaction conversion would be very good, hence the coal itself is quite reactive. The Çan coal is also very high in sulfur.

CONCLUSIONS

For the single stage liquefaction experiments, using a catalyst with a subbituminous coal will likely be an asset to help depolymerize the coal, and using a catalyst with a bituminous coal will help

depolymerize the coal and hydrogenate asphaltenes to produce higher oil yields. For the temperature-staged data, there is no correlation for rank. There is no correlation for solvent swelling and aromaticity to the liquefaction data when comparing catalyzed experiments to uncatalyzed experiments. For the low rank coals, coals with higher sulfur content tend to have higher conversions, mainly in the oil fractions. For the bituminous coals, the effect of sulfur is minimal. Future work includes more extensive analysis of the structure of these coals as well some additional coals.

ACKNOWLEDGEMENTS

Various portions of this work have been supported by the U.S. Department of Energy, The Pennsylvania Research Corporation, and The Pennsylvania State University Mining and Mineral Resources Research Institute. The authors are pleased to acknowledge this support.

REFERENCES

1. Burgess, C.E., Artok, L., and Schobert, H.H. *Preprints for Div. Fuel Chem., American Chemical Society*, **36** (2), 462, 1991.
2. Epstein, M.J. M.S. Thesis, The Pennsylvania State University, 1987.
3. Derbyshire, F.J., Davis, A., Lin, R., Stansberry, P.G., and Terrer, M-T. *Fuel Proc. Tech.*, **12**, (7), 127, 1986.
4. Garcia, A.B. and Schobert, H.H. *Fuel*, **68**, 1613, 1989.
5. Burgess, C.E. and Schobert, H.H. *Preprints, Amer. Chem. Soc., Div. Fuel Chem*, **35**, (1), 31, 1990.
6. Burgess, C.E. and Schobert, H.H. *Fuel*, **70**, 372, 1991.
7. Artok, L., Schobert, H.H., Mitchell, G.D., and Davis, A. *Preprints for Div. Fuel Chem., American Chemical Society*, **36** (1), 36, 1991.
8. Davis, A., Schobert, H.H., Mitchell, G.D. and Artok, L. "Catalyst Dispersion and Activity Under Conditions of Temperature-Staged Liquefaction," DOE-PC-898-1-6, Progress Reports, 1989-1991.
9. Weller, S. and Pelipetz, M.G. *Ind. Eng. Chem.*, **43**, (5), 1243, 1951.
10. Garg, D. and Givens, E. *Preprints, Amer. Chem. Soc., Div. Fuel Chem*, **28**, (5), 200, 1983.
11. Garcia, A.B. and Schobert, H.H. In *Coal Science II* (Eds. H.H. Schobert, K.D. Bartle, and L.J. Lynch), American Chemical Society Symposium Series 461, 213, 1991.
12. Yarzab, R.F., Given, P.H., Spackman, W., and Davis, A. *Fuel*, **68**, 1613, 1980.
13. Solomon, P.R., Serio, M.A., Deshpande, G.V., Kroo, E., Schobert, H.H., and Burgess, C. In *Coal Science II* (Eds. H.H. Schobert, K.D. Bartle, and L.J. Lynch), American Chemical Society Symposium Series 461, 193, 1991.
14. Artok, L., Schobert, H.H., Davis, A., and Mitchell, G. Accepted for publication in *Fuel*, 1992.

Table 1: Data for Coal Samples.

Penn State Sample Bank No.	PSOC-487	PSOC-831	PSOC-1379	PSOC-1488	DECS-1	DECS-6	DECS-12	Çan
Scan	Bed # 53	Brazil Block	Colorado F	Deitz	Big Brown	Blind Canyon	Pitt #8	
State	Wyoming	Indiana	Colorado	Montana	Texas	Utah	Penn	
Country	USA	USA	USA	USA	USA	USA	USA	Turkey
ASTM Rank	Sub A	hvC b	hvC b	Sub B	Sub C	hvA b	hvA b	Sub A
Moisture (as received, w%)	11.55	13.02	11.99	23.66	30.00	4.70	2.40	20.20
Mineral Matter (dry, wt%)	6.89	4.16	5.09	6.05	7.62	6.67	11.88	8.80
Elemental Composition								
Carbon	75.91	83.28	76.74	76.57	75.90	81.72	84.75	77.00
Hydrogen	4.78	4.97	4.97	5.20	5.80	6.22	5.66	5.60
Nitrogen	1.21	1.61	1.69	0.95	1.50	1.56	1.39	2.00
Sulfur (organic)	0.42	0.94	0.63	0.51	1.10	0.40	0.83	3.30
Oxygen (by difference)	17.67	8.64	15.96	16.78	15.70	10.10	7.37	12.10
Petrographic Composition								
Virginite	89.60	79.20	92.20	88.60		69.10	83.00	n.d.*
Exinite	2.50	4.90	0.60	3.50		17.00	8.10	n.d.
Inertinite	7.90	15.90	7.20	7.90		13.60	8.90	n.d.

* n.d. = not determined.

Table 2: Data for Solvent Swelling, Aromaticity, and Liquefaction Conversion for Single Stage Reactions.

Coal	Solvent Swelling Q (in pyridine)	f _a	%O Org	%S Rank	Reaction Conditions	Tot Conv wt %	Oils + Gas wt %	Asph wt %	Preasph wt %	L/H ^a
PSOC-487	1.7	0.654	17.67	0.42	Sub A 360°C, phor ^b 360°C, phen, cat ^c	20.4 54.5	0.8 -4.8	7.3 18.6	12.2 40.8	0.04 -0.08
PSOC-831	1.5	0.658	8.64	0.94	hvC b 360°C, phen, cat	29.0 43.2	0.1 4.1	7.0 8.9	21.9 30.2	0.00 0.10
PSOC-1379	1.7	0.634	15.96	0.63	hvC b 360°C, phen, cat	18.1 65.8	3.5 16.2	5.4 19.7	9.3 29.9	0.24 0.32
DECS-12	1.5	0.633	7.37	0.83	hvA b 360°C, phen, cat	38.1 70.6	-0.2 8.1	23.2 18.0	15.3 44.5	-0.01 0.13
PSOC-1488	1.1	0.600	16.78	10.51	Sub B 350°C, naph ^d 350°C, naph, cat	18.3 47.8	11.2 14.0	7.1 33.9	1.58 0.40	
DECS-1 ^e	1.3	0.438	15.70	1.10	Sub C 275°C, phen, cat	6.6 9.0	1.6 1.5	2.2 3.6	2.8 3.9	0.32 0.20
DECS-6 ^e	2.0	0.598	10.10	0.40	hvA b 275°C, phen, cat	17.7 25.0	4.9 6.9	2.1 3.0	10.7 15.1	0.38 0.38

a L/H = Light-to-heavy ratio.

b phen = phenanthrene

c cat = catalyst

d naph = naphthalene

e Referenced data from [1], [7], [14].

Table 3: Data for Solvent Swelling, Aromaticity, and Liquefaction Conversion for Temperature-Staged Reactions.

Coal	Solvent Swelling Q (in pyridine)	f_a	%O	%S Org	Rank	Reaction Conditions	Tot Conv	Olis + Gas	Asph	Preasph	L/H ^a
PSOC-1488	1.1	0.600	16.78	0.51	Sub B	2-stg ^b , naph ^c	30.8	16.9	13.9		1.21
						78.5	21.7	57.7		0.38	
DECS-18	1.3	0.438	15.70	1.10	Sub C	2-stg, phen ^e	53.1	34.0	10.9	8.2	1.78
						78.9	49.0	19.3	10.6	1.63	
DECS-68	2.0	0.598	10.10	0.40	hvA b	2-stg, phen	48.0	27.2	8.5	12.3	1.31
						85.1	38.9	32.5	14.7	0.82	
Çan	1.7	12.10	3.30	Sub A	2-stg, phen, cat	96.3	62.0	27.8	6.5	1.81	
					2-stg, DHP ^f	93.8	49.0	27.8	16.9	1.10	
					2-stg, DHP, cat	98.4	74.1	22.6	1.7	3.05	

a L/H = Light-to-heavy ratio.

b 2-stg = temperature-stage, see text for temperatures and times

c naph = naphthalene

d cat= catalyst

e phen = phenanthrene

f DHP = dihydrophenanthrene

g Referenced data from [1], [7], [14].

REACTANT AND CATALYST STRUCTURE/FUNCTION RELATIONSHIPS IN HYDROCRACKING OF BIPHENYL MOIETIES

Carole J. Read, Stephan Schwarz, and Michael T. Klein
Center for Catalytic Science and Technology
Department of Chemical Engineering, University of Delaware
Newark, Delaware 19716

Keywords: hydrocracking, biphenyl, CoMo-Y-Zeolite

1.0 INTRODUCTION

Catalytic hydrocracking is a flexible refining process that can accommodate a wide range of feedstocks and generate a range of useful products. Part of this flexibility derives from the use of a bifunctional catalyst. A metal function allows for hydrogenation of polynuclear aromatics (PNA's) and dehydrogenation of alkanes to olefin intermediates. An acid function promotes isomerization and cracking. Acting in concert, these functions and the process conditions of temperature, hydrogen pressure, WHSV, etc., combine to lower the molecular weight and increase the H/C ratio of the feedstock.

Clearly the feedstock specifications also play a crucial role. For example, in PNA hydrocracking, the apparently subtle reactant structural feature of six versus five carbon-containing rings can lead to important process implications. The hydrocracking of PNA's containing exclusively six-carbon-membered rings, such as anthracene, phenanthrene and naphthalene, proceeds by the predominant patterns¹⁻³ of: terminal ring hydrogenation, followed by cyclohexyl ring isomerization, ring opening and dealkylation to yield a lower molecular weight aromatic product and light gases (e.g., C₄). On the other hand, the reaction of the five-carbon-membered ring containing PNA fluoranthene (I) involves hydrogenation to tetrahydrofluoranthrene, center ring opening to 5-phenyl tetralin, and biphenyl bond cleavage to tetralin and benzene, as shown in Equation 1.⁴

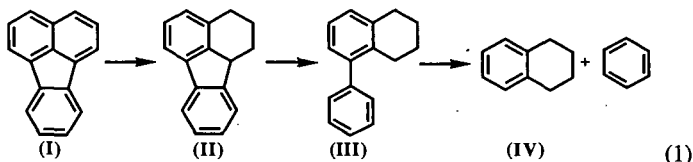


Table 1 summarizes important hydrocracking pathways of fluoranthene⁴, 9-ethyl fluorene, 9-phenyl anthracene, and 2-phenyl naphthalene deduced from reactions with H₂ and an industrial equilibrated NiMo/USY-Zeolite catalyst. These model compounds all generate structures that can undergo the direct biphenyl cleavage. Inspection of Table 1 reveals the minimum structural moiety for direct biphenyl cleavage. Fluoranthene, 2-phenyl naphthalene, and 9-phenyl anthracene, all fully aromatic, require hydrogenation and cracking steps before they have the structure capable of direct biphenyl cleavage which occurs from rows III to IV in Table 1. In contrast, 9-ethyl fluorene has aliphatic character and as a result requires fewer transformations before forming 2-propyl biphenyl, which can be directly cleaved.

It is also instructive to consider the reactions of related compounds that did not follow the efficient bond cleavage pathway. Fluorene, for example, ring opens to 1-phenyl toluene, which contains a benzylic hydride but not the additional β saturated carbon whose deprotonation to an olefin would allow hydrogenation to afford the final alkyl-substituted product⁵. 2-Methyl biphenyl likewise suffers from the same structural deficiency, and undergoes only isomerization reactions. Biphenyl does not directly cleave to form two moles of benzene per mole of biphenyl reacted; rather, it is postulated that cracking occurs via cyclohexyl benzene. Thus the *minimum structure necessary for efficient cleavage* is proposed to be a biphenyl moiety with an alkyl group,

comprising at least two carbons, bonded ortho to the biphenyl bond.

Additional experiments with the NiMo/USY-Z industrial catalyst and 9-ethyl fluorene revealed kinetically significant reactions: cleavage of the center fused cyclopentyl ring, transalkylation, and condensation reactions to form 9-methyl phenanthrene. Comparison of the 5-phenyl tetralin and 2-propyl biphenyl intermediates observed from reaction of fluoranthene and 9-ethyl fluorene, respectively, highlights the causes of these new pathways. The formal [1,5] shift is the only significant pathway for 5-phenyl tetralin. In contrast, the n-propyl group can participate in ring closure and transalkylation. Thus somewhat subtle changes in reactant structure can engender a wide range of available pathways. It is reasonable to expect similar sensitivity with regard to catalyst structure.

The reactions noted above comprise several key molecular transitions: hydrogenation, the net [1,5] biphenyl cleavage, center ring opening of cyclopentyl ring, isomerization, transalkylation, and ring closure. Each of these is influenced by the catalyst properties to a different degree. Herein, we report the preliminary work aimed to determine the catalyst function that influences the kinetics of each.

As a first step, the acidity of the catalyst was probed by varying the sodium content of the zeolite-Y support. The procedure used followed the early work of Ward⁶⁻⁹ and Hansford and Ward^{10,11}. These workers concluded that the concentration of Bronsted acid sites increases linearly with decreasing sodium content of the zeolite until 60-70% of the sodium ions have been replaced. They also found that o-xylene isomerization activity increased with decreasing sodium content. The activity per site also increased with decreasing sodium content.

The foregoing suggests that hydrocracking reactivity can be viewed as a rate functional,¹² which combines structure/function relations $f(S)$ for both the catalyst (S_C) and reactant (S_R). Observed reactivity R is thus a function of both $f(S_C)$ and $f(S_R)$, as in Equation (2).

$$R = R \{ f(S_C), f(S_R) \} \quad (2)$$

The objective of this paper is to report the results of hydrocracking experiments with a standard commercial catalyst and a range of reactant molecules, as a probe of $f(S_R)$, and also experiments involving a probe reactant (9-ethyl fluorene) and a range of carefully prepared catalytic materials that mimic aspects of the industrial catalyst. The goal is to lay a foundation for unraveling more quantitative aspects of R .

2.0 EXPERIMENTAL PROCEDURES

2.1 Material Synthesis

The catalysts prepared for the present work were designed as follows: both commercial (Strem Na-Y zeolite) and synthesized zeolite were used. Sodium zeolite Y was synthesized following an early patent by Breck¹³. Zeolite-Y was synthesized from an aged gel and then washed and filtered. The samples were dried overnight at 110°C and then calcined under a flow of air. The calcination program was heating at 350°C for three hours and then calcining at 500°C for four hours.

A series of acid supports was made by ion exchanging either commercial or synthesized zeolite-Y with ammonium nitrate solutions. The hydrogenation activity was provided by sulfided CoMo. The metal loading and introduction methods are as reported by Cid and co-workers¹⁴⁻¹⁶. The metal function was varied through the use incipient wetness impregnation, ion exchange/impregnation, and rotary vacuum impregnation.

2.1 Zeolite Characterization by XRD and TEM

X-Ray powder diffraction (XRD) of the zeolite samples was accomplished using a Philips XRG 3000 x-ray generator coupled to an APD 3520 controller. The radiation employed was CuK α with a wavelength of 1.540562 Å. All samples were scanned from 6° to 60° 2 θ . The peak heights above the background of the 5

largest peaks of calcined NaY were used to compute % crystallinity according to:

$$\% \text{ Crystallinity} = \frac{(\sum \text{hts. of 5 peaks})_{\text{sample}}}{(\sum \text{hts. of 5 peaks})_{\text{standard}}} \times 100$$

Metal oxide and metal sulfide species in the catalyst samples were identified using Table 2 which lists the characteristic peaks for each of the non-zeolitic phases.

Transmission electron microscopy (TEM) of the samples was accomplished using a Philips EM 400 transmission electron microscope. The sample was prepared for microscopy by dispersing some of the zeolite in n-hexane, transferring a drop of the suspension onto a copper grid and allowing the solvent to evaporate. The average crystal size of the parent zeolite, n , was obtained from micrographs by counting and measuring ~ 200 crystals. Note that $n = \sum(d_i n_i) / \sum n_i$ where d_i is the diameter of the i th particle and n_i is the number of crystals of diameter i .

2.2 Catalytic Hydrocracking Reactions

The hydrocracking pathways and kinetics of 9-ethyl fluorene, 9-phenyl anthracene and 2-phenyl naphthalene in the presence of an equilibrated NiMo/Z-USY were studied at 310-380°C and 153 atm hydrogen. Experimental methods are detailed elsewhere^{4,17}. In brief, hydrocracking experiments were conducted in a batch autoclave or in batch agitated tubing bombs. Experiments conducted in the stirred batch autoclave were in the presence of hexadecane solvent, whereas reactions in the tubing bombs were without.

Additionally, the hydrocracking of 9-ethyl fluorene, 1-phenyl naphthalene, biphenyl, and naphthalene in the presence of the synthesized catalytic materials were studied at 325°C and 153 atm. hydrogen pressure. These experiments were conducted in 12-cm³ SS agitated tubing bombs in the absence of solvent.

For all types of experiments, the catalyst was ground to 80-100 mesh. It was then sulfided with 90% H₂/10% H₂S at flow rate of 30 cm³/min for 2 hours at 400°C. Gas chromatography and gas chromatography/mass spectrometry were used to identify liquid-phase reaction products.

3.0 RESULTS AND DISCUSSION

3.1 Zeolite Characterization

XRD analyses showed that CoMoO₄ was found in all samples whether the cobalt be introduced by impregnation or ion exchange. Co(imp)Mo(imp)NaY also showed evidence of Co₃O₄, but after exchange with NH₄⁺ and subsequent calcination, this oxide could no longer be detected. MoO₃ could not be unambiguously assigned to any of the samples, except for Co(imp)Mo(imp)NaY, since its two strongest lines very nearly coincide with NaY lines¹⁵. The sulfided Co(ex)Mo(imp)NaY did not contain x-ray crystalline Co₉S₈ or MoS₂. Note, however, that since the detection limit of XRD is ~ 2nm, the above results do not necessarily imply that the oxide and sulfide species mentioned were absent.

Table 3 lists the crystallinities of the calcined materials. Clearly impregnation decreased crystallinity. This has also been reported by Cid et al.^{14,15} who observed crystallinities < 40% for high Mo loadings (9% and above). The loss of crystallinity upon impregnation was ascribed to the partial destruction and distortion of the zeolite lattice by the interaction of molybdate anions with framework oxygen. It was noteworthy that impregnation by the rotary evaporation technique yielded slightly more crystalline materials than the incipient wetness technique. When Co was incorporated into the zeolite by aqueous ion exchange prior to Mo impregnation, the reduction in crystallinity was far less pronounced.

The results from the TEM showed an average crystal size of 0.7 μm, with a size range of 0.2 - 1.1 μm.

3.2 Reactant and Catalyst Structure/Function

Preliminary reactions are reported with the following materials: a CoMo impregnated Sirem sodium zeolite-Y (Co(I)Mo(I)/Na-Y), Co ion exchanged Mo impregnated Sirem sodium zeolite-Y (Co(ex)Mo(I)/Na-Y), and a CoMo impregnated onto a twice ammonium exchanged, calcined Sirem sodium zeolite-Y (Co(I)Mo(I)/Sirem 2X ex NaH-Y). All impregnations used the incipient wetness technique. Reactions with biphenyl, naphthalene, 9-ethyl fluorene, and 1-phenyl naphthalene reactants revealed broad trends. Under the reaction conditions of 325°C, 150 atm hydrogen, the main reaction product yield and selectivities are summarized in Table 4.

The first catalyst used was the Co(I)Mo(I)/Na-Y. Naphthalene, 1-phenyl naphthalene, 9-ethyl fluorene, and biphenyl were separately contacted. For naphthalene and 1-phenyl naphthalene, the main reaction was hydrogenation. Naphthalene hydrogenated to tetralin; no decalins were observed. The selectivity to tetralin formation was 54% after 30 minutes reaction time. The naphthalene moiety of 1-phenyl naphthalene was preferentially hydrogenated as the main product was 1-phenyl-1,2,3,4-tetrahydronaphthalene. The hydrogenation kinetics of naphthalene and 1-phenyl naphthalene were of the same order of magnitude. Biphenyl and 9-ethyl fluorene did not react over this catalyst.

The second catalyst examined was a Co(ex)Mo(I)/Sirem Na-Y. Naphthalene, 1-phenyl naphthalene, 9-ethyl fluorene, and biphenyl were individually reacted.

Naphthalene hydrogenated to tetralin with the cobalt exchanged catalyst; some transalkylation reactions occurred to form methyl naphthalenes. The selectivities for tetralin, 2-methyl naphthalene, and 1-methyl naphthalene were 59, 7.4, and 4.2%, respectively, after 25 minutes reaction time. The kinetics of hydrogenation were of the same order of magnitude as with the previous catalyst sample.

1-Phenyl naphthalene preferentially reacted to form 2-phenyl naphthalene (selectivity of 69%, 30 minutes). All four hydrogenation products of 1-phenyl and 2-phenyl naphthalene also formed. The temporal variation of products' yields showed that 1-phenyl and 2-phenyl-1,2,3,4 tetrahydronaphthalenes cleaved to form tetralin and benzene.

Biphenyl underwent predominantly transalkylation reactions to form methyl biphenyls and fluorene with the Co(ex)Mo(I)/Na-Y catalyst. No single ring cleavage products were observed.

Finally, 9-ethyl fluorene was exposed to the Co(ex)Mo(I)/Na-Y catalyst. The center cyclopentyl ring cleaved to form 2-propyl biphenyl (selectivity of 0.75%). No single ring aromatics or naphthenics were observed in the product spectrum. The intermediate 2-propyl biphenyl did undergo ring closure to form 9-methyl-9,10-dihydrophenanthrene and, ultimately, 9-methyl phenanthrene (selectivity of 1.8, 3.8%, respectively, 32 minutes). Transalkylation reactions were dominant, forming methyl, ethyl-fluorenes with a selectivity of 45%, 32 minutes.

The third catalyst was a Co(I)Mo(I)/2x(ex) NaH-Y. The reaction of 9-ethyl fluorene led to center ring cleavage and transalkylation as the predominant reactions. The selectivity to 2-propyl biphenyl was 2.6% (40 minutes). The selectivity for the transalkylation products was 11% after 40 minutes.

Acknowledgement:

We gratefully acknowledge the support of this work by Sun Refining and Marketing Company. Additional acknowledgements are to Mr. Ralph Bertolacini and Dr. Simon Kukes of Amoco Oil and Dr. James Lyons and Mr. Aris Macris of Sun Refining and Marketing Company.

References:

- (1) Lemberton, J.; Guisnet, M. *Applied Catalysis* **1984**, *13*, 181-192.
- (2) Martens, J. A.; Jacobs, P. A.; Weitcamp, J. *Appl. Catal.* **1986**, *20*, 283 - 303.

- (3) Haynes, H. W. J.; Parcher, J. F.; Helmer, N. E. *Ind. Eng. Chem. Proc. Des. Dev.* **1983**, *22*, 401 - 409.
- (4) Lapinas, A. T.; Klein, M. T.; Gates, B. C.; Macris, A.; Lyons, J. E. *Ind. Eng. Chem. Res.* **1987**, *26*, 1026 - 1033.
- (5) Lapinas, A. T.; Klein, M. T.; Gates, B. C.; Macris, A.; Lyons, J. E. *Ind. Eng. Chem. Res.* **1991**, *30*, 42 - 50.
- (6) Ward, J. W. *Journal of Catalysis* **1967**, *9*, 225-236.
- (7) Ward, J. W. *Journal of Catalysis* **1967**, *9*, 396-402.
- (8) Ward, J. W. *Journal of Catalysis* **1968**, *10*, 34-46.
- (9) Ward, J. W. *Journal of Catalysis* **1968**, *11*, 251-258.
- (10) Ward, J. W. and Hansford, R. C. *Journal of Catalysis* **1969**, *13*, 316-320.
- (11) Ward, J. W. and Hansford, R. C. *Journal of Catalysis* **1969**, *13*, 364-372.
- (12) Astarita, G. *Thermodynamics: An Advanced Textbook for Chemical Engineers*; Plenum Press: New York, 1989, pp pp.93-96.
- (13) Breck, D. W. In *Crystalline Zeolite Y*; 1964; U. S. Patent No. 3,130,007
- (14) Cid, R.; F. Orellana *Applied Catalysis* **1987**, *32*, 327-336.
- (15) Cid, R., F. J. Gil Lambias, J. L. G. Fierro, A. L. Agudo and J. Villaseñor *Journal of Catalysis* **1984**, *89*, 478-488.
- (16) Cid, R., J. Villaseñor, F. Orellana, J. L. G. Fierro, and A. L. Agudo *Applied Catalysis* **1985**, *18*, 357-372.
- (17) Lapinas, A. T. PhD Thesis, University of Delaware, 1989.

Table 1. Chemical Motives Susceptible to Efficient Biphenyl Cleavage

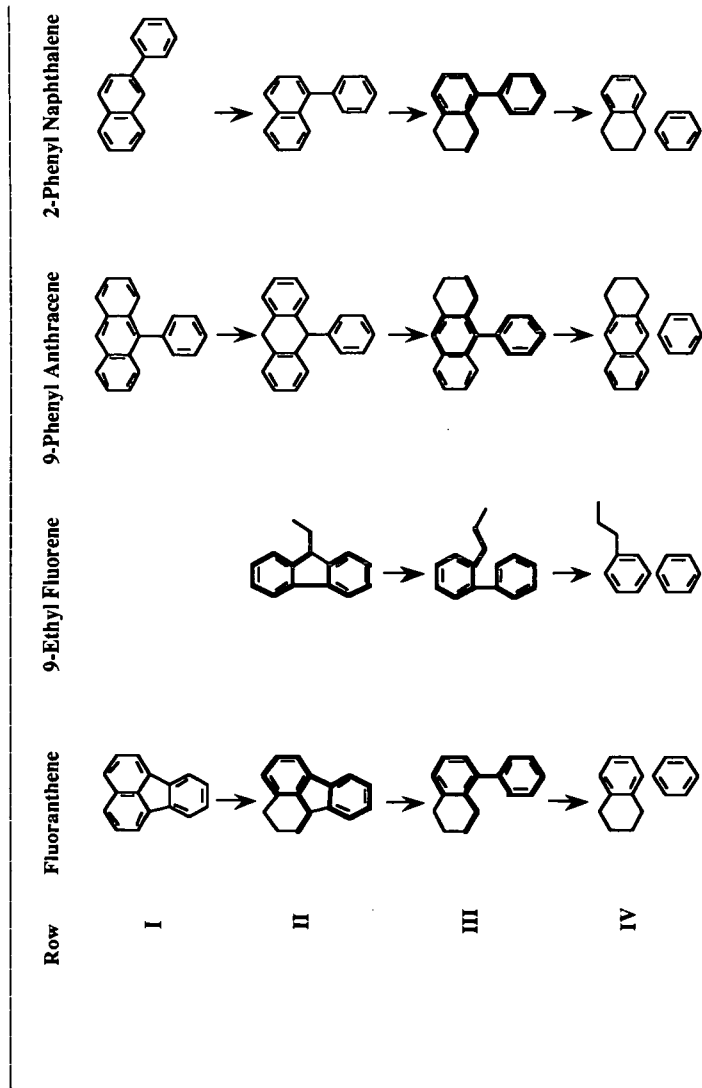


Table 2: Identification of non-zeolitic phases

Species	Largest peak (2 θ)	2nd largest peak (2 θ)
Co ₃ O ₄	36.8°	31.3° (*)
MoO ₃	27.3° (*)	23.3° (*)
CoMoO ₄	26.5°	23.3° (*)
Co ₉ S ₈	52.0°	29.9° (*)
MoS ₂	14.4°	39.5° (*)

(*) : partial overlap with NaY peaks

Table 3: XRD Crystallinities of metal-zeolite Y materials

Catalyst	% Crystallinity
NaY	100
NaHY(2x exch.)	100
Co(imp)Mo(imp)NaY	25
Co(imp)Mo(imp)NaHY(2x exch.)	30
Co(imp)Mo(imp) rot. vap. NaY	45
Co(imp)Mo(imp) rot. vap. NaHY (1x exch.)	40
Co(ex)Mo(imp)NaY	90
Co(ex)Mo(imp)NaY, sulfided	70

Note: rot. vap. = impregnation by rotary evaporation. Other samples impregnated by incipient wetness

Table 4. Hydrocracking reaction selectivities for naphthalene, 1-phenyl naphthalene, 9-ethyl fluorene, and biphenyl

Reactant:	Naph	1-PN	Naph	1-PN	9-et Π	biphenyl	9-et Π
catalyst:	1	1	2	2	2	2	3
T, °C	325	325	325	325	325	325	325
P/atm (at T)	150	150	150	150	150	150	150
t, min	30	21	25	30	32	25	40
conversion of reactant	0.057	0.065	0.634	0.877	0.111	0.035	0.075
Product Selectivities							
benzene				6.71E-02		3.55E-02	
cyclohexyl benzene						2.84E-02	
methyl indans			3.11E-03				
tetralin	5.42E-01	2.79E-02	5.90E-01	7.14E-02			
naphthalene		1.89E-02		8.69E-03			
methyl tetralins			2.82E-02	1.16E-03			
2me naphthalene	1.60E-02		7.39E-02	6.01E-04			
1me naphthalene	5.46E-02		4.18E-02	5.04E-04			
2-methyl biphenyl						3.70E-02	
3-methyl biphenyl						1.35E-01	
4-methyl biphenyl						4.15E-01	
hexahydro fluorenes					2.46E-02		1.37E-01
2propyl biphenyl					7.54E-03		2.59E-02
mw 168's					1.21E-01		1.38E-01
hexahydro-9et-fluorenes					3.54E-02		1.89E-01
fluorene, 38.09					5.94E-03	1.20E-01	6.52E-02
9-me dihydro phenanthrene					1.78E-02		
methyl 9-et fluorenes					4.54E-01		1.10E-01
ethyl 9et fluorene, 53.18					4.50E-02		6.75E-02
9-me phenanthrene, 60.4					3.75E-02		5.99E-03
1-phenyl tetralin		3.51E-01		1.04E-02			
5-phenyl tetralin		9.74E-02		6.97E-03			
2-phenyl naphthalene				6.90E-01			
phenyl tetralins				1.88E-01			
methyl phenyl naphthalenes				1.02E-02			
1 = Co(I)Mo(I)/Na-Y							
2 = Co(E)Mo(I)/Na-Y							
3 = Co(I)Mo(I)2XNaH-Y							

EFFECTS OF PORE STRUCTURE AND SUPPORT TYPE OF CATALYSTS IN HYDROPROCESSING OF HEAVY COAL LIQUIDS

Chunshan SONG*, Kouji HANAOKA+ and Masakatsu NOMURA*

* Fuel Science Program, Department of Materials Science and Engineering, 209 Academic Project Building, The Pennsylvania State University, University Park, PA 16802, USA

+ Department of Applied Chemistry, Faculty of Engineering, Osaka University Yamada-oka 2-1, Suita, Osaka 565, Japan

Keywords: Catalyst; Pore size; Support type; Coal liquids upgrading

INTRODUCTION

Catalyst pore structure determines how easily the reactants can access the interior surface of the catalyst. The pore structure parameters include pore sizes and their distribution, pore volume and surface area. Various classification of pore sizes can be found in literature, but the International Union of Pure and Applied Chemistry (IUPAC) classifies pores of different sizes in the following manner: micropores, < 20 Å; mesopores, 20-500 Å; and macropores, > 500 Å in diameter. The IUPAC classification will be used in this paper. In general, hydrotreating catalysts are prepared by impregnation methods and the catalyst pore structure is determined mainly by the support. Earlier reports by Ho and Weller [1981], Bertolacini et al. [1978], and Shimada et al. [1984] have shown that pore diffusional limitation of reaction rates can be serious in hydroliquefaction of coals over supported catalysts. The catalyst pore structure is also very important for hydroprocessing of heavy coal liquids due to diffusional limitations [Tischer et al., 1985; Yoshimura et al., 1986; Song et al., 1988a, 1989a, 1991a]. However, systematic knowledge of pore size effects is still very limited for hydroprocessing of heavy coal-derived liquids. Reviews of previous work in this area may be found elsewhere [Derbyshire, 1988; Onuma, 1988; Song et al., 1991b].

The present work involves the upgrading of several solvent refined coals (SRC) derived from thermal liquefaction of coals, which contain both asphaltene and preasphaltene. This work attempts to provide a better understanding of the relationship of catalyst pore structure and support type to the conversion of asphaltene and preasphaltene, which in turn could lead to the development of more effective catalyst. This paper will describe 1) the effects of pore size of Ni-Mo/Al₂O₃ catalysts on their performance in hydroprocessing of two different SRCs in terms of oil yields and conversions of heavy fractions, and the interactive chemistry involved in the pore-size dependence for simultaneous conversion of asphaltene and preasphaltene on catalyst surface, 2) the differences in reactivity of heavy fractions in several SRCs and their convertibility in catalytic runs, and 3) comparative examination of alumina- and silica-supported catalysts as well as carbon-coated catalysts.

EXPERIMENTAL

Catalyst Preparation. The four gamma-Al₂O₃ cylindrical extrudates are the same supports that have been in a previous work [Song, 1991a]. The SiO₂ supports were two spherical Cariact-50 and Cariact-10 beads from Fuji-Davison Chemical Company. Table 1 gives their properties provided by the manufacturers. Four Ni-Mo/Al₂O₃ catalysts (NiO: 2.9, MoO₃: 15.8 wt%) were prepared by co-impregnation of (NH₄)₆Mo₇O₂₄·4H₂O and Ni(NO₃)₂·6H₂O from their aqueous solution, followed by calcination and sulfidation [Song et al., 1991a, 1991b]. Two Mo/SiO₂ catalysts containing 15.8 wt% MoO₃ (Cat-SA, Cat-SB) were prepared by using the same procedure. Figure 1 shows the pore size distribution of the prepared Ni-Mo/Al₂O₃ catalysts measured by using a Shimadzu AutoPore-9200 mercury porosimeter. The maximum intrusion pressure was 60,000 psi, which corresponds to pore radius of 18 Å as dictated by Washburn equation with contact angle and surface tension of mercury taken as 140° and 480 dyn/cm, respectively. A commercial catalyst, Akzo Ketjenfine 153S sulfided Ni-Mo/Al₂O₃ [Song et al., 1988, 1991c] was also used in some experiments.

SRC Upgrading. Solvent refined coals (Table 2) derived from Wandoan subbituminous coal (Wan-SRC) and Akabira bituminous coal (Aka-SRC) were used as feedstocks. Aka-SRC was produced from Run 5511 at 420 °C for 34 minutes, and Wan-SRC from Run 5512 at 440 °C for 34 minutes in a 3 ton/day coal liquefaction plant at Sumitomo Coal Mining Co. [Hanaoka et al., 1988]. In some experiments we also used a SCT-SRC sample produced from short contact time pyrolytic liquefaction (SCT-PL) of Wandoan coal at 440-465 °C for 5 minutes in H-donor solvent under N₂ atmosphere [Song et al., 1989b]. The hydroprocessing was carried out in a 60 ml SUS-316 stainless steel rocking

autoclave at 425 °C for 1 h with 4.9 MPa H₂ (5 g SRC : 0.5 g catalyst : 5 g tetralin). The runs of SCT-SRC were carried out under the same conditions, but using 2.5 g SRC, 5 g tetralin, and 1 g catalyst.

Product Separation and Analysis The volume of gaseous products was measured by a continuous flow-type gas volume meter, through which the gases were introduced from the reactor into a plastic gas bag. The gases were analyzed by GC (Shimadzu GC-8A). The liquid and solid products were separated into oil (hexane soluble), asphaltene (hexane-insoluble but benzene-soluble) and BI or preasphaltene (benzene-insoluble). The concentrated oil plus the reaction solvent were analyzed by GC to determine the tetralin/naphthalene ratio. After the solvent has been removed by vacuum distillation (up to 115°C, 8 mmHg), the oil products were subjected to elemental and ¹H NMR analyses [Song et al., 1988c]. The catalysts that have been used once in SRC hydroprocessing were also analyzed (after benzene extraction and drying) by using scanning electron micrograph (SEM, Hitachi S-450) combined with electron probe microanalysis (EPMA, Horiba EMAX-1800E).

RESULTS AND DISCUSSION

Property and Reactivity of SRC. As shown in Table 2, Wan-SRC and Aka-SRC have similar carbon and hydrogen contents, although Wandoan and Akabira coals differ significantly in elemental composition. Both SRCs contain a high proportion of heavy fractions such as asphaltene and preasphaltene. Wan-SRC contains less benzene-insolubles and more asphaltene and oil, as compared to Aka-SRC. Analysis of the fractions from both SRCs showed that the H content and atomic H/C ratio decrease, but N and O contents and the average molecular weights (MW) increase in the order of oil, asphaltene, and BI. The average MW values determined by vapor pressure osmometry are about 590-600 and 270-320 for asphaltene and oil fractions, respectively [Song et al., 1988a]. In addition, relative to the SRCs from long residence time runs in pilot plant, the SCT-SRC from laboratory SCT-PL has higher oil content and H/C ratio, and lower preasphaltene content.

Table 3 gives the data on the thermal runs and some catalytic runs at 425°C. The oil yields from Wan-SRC are generally higher than those from Aka-SRC. Relative to the raw SRCs, thermal runs increased oil yields by 16-18 % and produced 4-5 % gas. The use of a catalyst promoted the production of oil. It appears that the BI fraction of Aka-SRC is more reactive than that of Wan-SRC, and this trend becomes more remarkable when a catalyst was used. Probably this is due in part to the lower severity of conditions used for producing Aka-SRC than that for Wan-SRC. In addition, SCT-SRC of Wandoan coal (see below) appears to be much more reactive than both Wan-SRC and Aka-SRC in terms of higher BI and asphaltene conversions. These results demonstrated that the liquefaction conditions affects the reactivity of the products; the SRC derived from a lower-severity run exhibits a higher reactivity.

Comparison of SiO₂- and Al₂O₃-Supported Catalysts. We examined two Mo/SiO₂ and a number of Ni-Mo/Al₂O₃ catalysts. Since a SiO₂-supported catalyst is less active as compared to a Al₂O₃-supported one for hydrotreating, and since a Ni- or Co-promoted Mo catalyst is more active than a unpromoted catalyst, one would expect a higher activity of Ni-Mo/Al₂O₃ catalyst. As shown in Table 3, KF-153S and Cat-1 did afford higher asphaltene conversion than the SiO₂-supported Cat-SB. However, it is very interesting to note that Cat-SB exhibited considerably higher effectiveness for converting BI fractions of both Wan-SRC and Aka-SRC. It is known that the acidity increases in the order of SiO₂ < Al₂O₃ < SiO₂-Al₂O₃ [Satterfield, 1991]. Because Cariact-50 has much lower surface area than the Al₂O₃ support (78 vs. 203 m²/g) and Cat-SB contains no Ni promoter, the observed superiority of Mo/SiO₂ catalyst over Ni-Mo/Al₂O₃ in BI conversion can be attributed to the large pore diameter (507 Å) and/or lower surface acidity of the silica support.

Table 4 compares the results for runs of Wan-SRC at 400 °C using 20-32 mesh particles of two Mo/SiO₂ and KF-153S Ni-Mo/Al₂O₃ catalysts. The data for Cat-SA and Cat-SB show that a large pore silica (Cariact-50) is better than a small pore silica (Cariact-10) in terms of higher BI conversion. Relative to the two Mo/SiO₂, KF-153S Ni-Mo/Al₂O₃ afforded higher oil yield and higher asphaltene conversion. However, the conversion of BI was substantially higher with Mo/SiO₂ than with KF 153S. Combination of data in Tables 3 and 4 reveals that using silica support is more effective for converting preasphaltene, the BI fraction, while the use of alumina gives higher conversion of asphaltene and in most cases, higher oil yields.

Effect of Particle Size of Ni-Mo/Al₂O₃. Table 5 shows the effects of crushing KF-153S Ni-Mo to <100 mesh particles for hydroprocessing of SCT-SRC. The higher oil yield and conversion with crushed catalyst provide another indication of the intraparticle diffusional limitations occurring during SRC hydroprocessing. In fact, relative to the thermal runs, the cylindrical KF-153S Ni-Mo and its 20-32 mesh (0.84-0.50 mm) particles promoted asphaltene conversion but did not improve BI conversion both for Wan-SRC (Tables 3 and 4) and for SCT-SRC (Table 5). However, the use of <100 mesh (<0.15 mm) KF-153S resulted in significant increase in BI conversion (Table 5).

These results indicate that improving mass transfer has greater impact on conversion of preasphaltene. The superiority of the fine catalyst particles can be attributed to greatly increased external surface area and decreased length of diffusional path, as compared to the 1.5 mm extrudate. In practice, the lowest catalyst sizes permitted in industrial fixed-bed operations are 0.8-1.6 mm. Described in the subsequent sections is SRC conversion using 0.8-1.5 mm cylindrical extrudate Ni-Mo/Al₂O₃.

Effects of Pore Size of Ni-Mo/Al₂O₃ on Product Distribution. In order to examine the pore size effects on a unified basis, one should prepare the catalysts having unimodal and narrow pore size distribution, different median pore diameters, and similar chemical composition. As can be seen from Figure 1, the unimodal pore structure and the significantly different pore sizes of Cat-1 through Cat-4 prepared by using the same procedure, enabled us to evaluate the pore size effects.

Figure 2 presents the results for Wan-SRC hydroprocessing over a series of cylindrical Ni-Mo/Al₂O₃ catalysts with different MPD. Also shown in Figure 2 are the data from the run with KF-153S sulfided Ni-Mo, which has a MPD value (90 Å) similar to that (100 Å) of the well known Shell 324M Ni-Mo [Baker et al., 1987, Lee et al., 1991]. All of these catalysts were used in the form of cylindrical extrudate. It should be noted that Cat-1 though Cat-4 is alumina-supported catalyst, while KF-153S contains 4.5 wt% SiO₂. Relative to thermal run, each of the four prepared catalysts enhanced the production of oil. Figure 3 shows the results for Aka-SRC which originally contained more BI and less asphaltene and oil as compared to Wan-SRC. As can be seen from Figures 2 and 3, both for Wan-SRC and Aka-SRC, the conversion of SRC into benzene soluble products increased in the order of Cat-1 < Cat-2 < Cat-3 ≤ Cat-4. This order is contrary to that of catalyst surface area. The yields of asphaltene, however, decreased with increasing MPD in the small pore size region, but rose with further increase in MPD in the large pore range. The oil yields from catalytic runs of both SRCs with the four prepared Ni-Mo did not vary considerably, but the oil yield from Wan-SRC with KF-153S was lower. The gas yields were nearly constant in the runs of both SRCs.

Pore-Size Effects on Conversion of Heavy Fractions and Interactive Chemistry. Table 6 compares the product distribution and hydrogen consumption for typical runs of Aka-SRC in this work and its isolated asphaltene fraction Aka-Asp reported in previous paper [Song 1991]. The oil yields from thermal runs of Aka-SRC and Aka-Asp are relatively similar to each other, but the catalytic run of Aka-Asp with Cat-1 gave 11% higher, and that with Cat-3 afforded 17% higher oil yield than the corresponding values for runs of Aka-SRC. This is surprising because Aka-SRC originally contained about 32% oil but Aka-Asp contained no oil. The conversions of asphaltene as well as the consumption of gas phase H₂ are considerably higher in the runs of the isolated asphaltene than for the whole SRC. This comparison indicates that catalytic conversion of asphaltene into oil is suppressed during the runs of whole SRC. Probably the presence of preasphaltene inhibits the catalytic reaction of asphaltene.

Table 7 compares the results for hydroprocessing of Wan-SRC and its BI fraction Wan-BI. Apparently, the runs of whole SRC gave better product spectra than those of its BI fraction. This is because Wan-BI is composed of about 85 % preasphaltene and about 15 % quinoline insolubles (Table 2), which are the heaviest fractions in coal liquids. Taking into account the oil content of original Wan-SRC, the oil yields produced from Wan-BI with Cat-3 and Cat-4 are only 2-3% lower, and that with Cat-1 is about 6% lower than the corresponding values for net oil production from Wan-SRC. The net conversion of BI fraction appears to be higher for the runs of isolated Wan-BI than for the whole Wan-SRC. However, such a difference is much smaller as compared to that between the runs of whole SRC and asphaltene. Therefore, the negative impact of asphaltene on preasphaltene conversion is very limited, but preasphaltene materials appear to inhibit the catalytic conversion of asphaltene.

Carbon-Coated Catalysts. Analysis of the benzene-extracted spent catalysts that have been used once in runs of Wan-SRC by using SEM-EPMA showed that the deposition of carbonaceous materials and metal species such as Ca, Fe and Ti took place in the 1 h reaction, being consistent with the findings of Stiegel et al. [1983] and Stohl and Stephens [1987]. These catalysts are denoted as carbon-coated catalysts, in which the amounts of benzene-insoluble materials are estimated to be around 10 wt%. We also conducted the runs of Wan-SRC using the carbon-coated Ni-Mo/Al₂O₃ catalysts. The consumption of gas-phase H₂ decreased and the oxygen content of oil and asphaltene products increased slightly, as compared to the runs with fresh Ni-Mo, which suggest a small decrease in catalytic activity. However, the conversion of BI fraction was substantially higher with the carbon-coated Ni-Mo than with the fresh Ni-Mo, while oil yields with each pair of fresh and carbon-coated Ni-Mo were similar to each other.

Figure 4 shows the relationship between MPD and conversions of BI and asphaltene for runs of Wan-SRC and Aka-SRC over fresh and carbon-coated Ni-Mo catalysts. Increasing catalyst MPD up to about 150 Å increased the conversion of both asphaltene and preasphaltene. Within this range, the BI has relatively less inhibiting effect on asphaltene conversion. Further increasing MPD leads to further increase in conversion of preasphaltene, but this results in decrease in asphaltene conversion. The decrease in the apparent asphaltene conversion is considered to be due

to two different effects: 1) increasing MPD increased conversion of preasphaltene, producing more asphaltene, as suggested by data in Table 7, and 2) diffusion and preferential adsorption of highly polar and polyaromatic BI materials on surface inside pores of large-pore catalysts, which inhibits the adsorption and conversion of asphaltene on catalyst surface, as revealed by the data in Table 6.

It is interesting to note that carbon-coated catalysts gave substantially higher conversion of BI than the fresh catalysts, but the fresh Ni-Mo gave higher asphaltene conversion. We also observed that pure SiO₂-supported catalysts gave higher BI conversion. The KF-153S, which contains 4.5 wt% SiO₂ and is more acidic than pure alumina-supported Ni-Mo, did not improve BI conversion, as compared to the thermal runs. All of these results point to the conclusion that less acidic hydrogenation catalysts are more effective for conversion of BI materials into asphaltene. These observations are consistent with the findings of Derbyshire et al. [1988] and Masuyama et al. [1990] who reported the improved performance of carbon-coated alumina supported Mo catalysts or carbon-supported Mo catalysts and Ca-modified Ni-Mo, respectively, for hydrotreating of coal liquids. Ca addition serves to neutralize or passivate, and carbon coating covers the surface acidic sites. These results, however, are in distinct contrast with those of McCormick et al. [1989] who reported that relative to the other catalysts a Co-Mo/Al₂O₃ catalyst containing 5% SiO₂ exhibits an extremely low coking tendency because of the Bronsted acid sites on the silicated alumina.

A New Concept for Catalyst Design. In industrial practice, a compromise between the need for high activity and for extended life can be achieved by using a bimodal pore size distribution. Some recently developed catalysts such as Shell 317, Amocat 1C and Amocat 1A are Ni-Mo or Co-Mo supported on bimodal Al₂O₃ supports [Lee et al, 1991; McCormick et al., 1989]. Al₂O₃-supported bimodal catalysts have been shown to exhibit better apparent activity for coal liquids upgrading [Tischer, 1985]. However, the present results point to the conclusion that less acidic and larger-pore hydrogenation catalysts are more effective for preasphaltene conversion, but efficient conversion of asphaltene requires mild hydrocracking catalysts. These results suggest a new concept for design of coal liquids upgrading catalyst: two component-bimodal catalyst consisting of a moderately acidic mild hydrocracking component having mostly mesopores and a less acidic hydrogenating component with large mesopores or mostly macropores. This concept needs to be verified by further investigation.

ACKNOWLEDGEMENT

C. Song wish to thank Professor Harold H. Schobert of The Pennsylvania State University for his kind review and helpful comments.

REFERENCES

- Baker, J.R.; McCormick, R.L.; Haynes, H.W., Jr., *Ind. Eng. Chem. Res.* **1987**, *26*, 1895-1901.
Bertolacini, R.J.; Gutberlet, L.C.; Kim, D.K.; Robinson, K.K. *ACS Fuel Chem. Prepr.* **1978**, *23*, 1-10.
Derbyshire, F., *Catalysis in Coal Liquefaction*, IEA/CR, 1988, 66 pp, and references cited therein.
Hanaoka, K.; Song, C.; Nomura, M. *Proc. 24th Coal Sci. Conf.*, Tokyo, **1988**, 222-225.
Ho, P.N.; Weller, S.W. *Fuel Processing. Technol.* **1981**, *4*, 21-29.
Lee, J.M.; Cantrell, C.E.; Gollakota, S.V.; Davies, O.L.; Corser, M.M.; Vimalchand, P., *ACS Fuel Chem. Prepr.* **1991**, *36* (4), 1915-1926.
Masuyama, T.; Kageyama, Y.; Kawai, S. *Fuel* **1990**, *69*, 245-250.
McCormick, R.L.; King, J.A.; King, T.R.; Haynes, H.W., Jr., *Ind. Eng. Chem. Res.* **1989**, *28*, 940-947.
Onuma, K. *Shokubai* **1989**, *31*, 182-187.
Satterfield, C.N. "Heterogeneous Catalysis in Industrial Practice". 2nd Ed., McGraw-Hill, New York, **1991**, Chapter 7., p.211-266.
Shimada, H.; Kurita, M.; Sato, T.; Yoshimura, Y.; Kawakami, T.; Yoshitomi, S.; Nishijima, A., *Bull. Chem. Soc. Japan* **1984**, *57*, 2000-2004.
Song, C.; Nihonmatsu, T.; Nomura, M. *Proc. 24th Japan Coal Sci. Conf.*, Tokyo, **1988a**, 226-228.
Song, C.; Hanaoka, K.; Ono, T.; Nomura, M. *Bull. Chem. Soc. Japan* **1988b**, *61*, 3788-3790.
Song, C.; Hanaoka, K.; Nomura, M. *Energy & Fuels* **1988c**, *2*, 639-644.
Song, C.; Hanaoka, K.; Nihonmatsu, T.; Nomura, M. *Proc. 1989 Int. Conf. Coal Sci.*, Tokyo, **1989a**, 226-228. The median pore radius was erroneously written as median pore diameter in this paper.
Song, C.; Hanaoka, K.; Nomura, M. *Fuel* **1989b**, *68*, 287-292.
Song, C.; Nihonmatsu, T.; Hanaoka, K.; Nomura, M. *ACS Fuel Chem. Prepr.* **1991a**, *36* (2), 542-550
Song, C.; Nihonmatsu, T.; Nomura, M., *Ind. Eng. Chem. Res.* **1991b**, *30*, 1726-1734.
Stiegel, G.J.; Tischer, R.E.; Polinski, L.M. *Ind. Eng. Chem. Prod. Res. Dev.* **1983**, *22*, 411-420.
Stohl, F.V.; Stephens, H.P., *Ind. Eng. Chem. Res.* **1987**, *26*, 2466-2473.
Tischer, R.; Narain, N.K.; Stiegel, G.J.; Cillo, D.L. *J. Catal.* **1985**, *95*, 406-413. 8.
Yoshimura, Y.; Sato, T.; Shimada, H.; Nishijima, A. *Fuel Sci. Technol. Int'l* **1986**, *4*, 621-642.

Table 1. Properties of Al₂O₃ and SiO₂ Supports Used for Preparing the Supported Mo Catalyst

	SiO ₂ Support		Al ₂ O ₃ Support				
	Cariact-10	Cariact-50	S-1	S-2	S-3	S-4	S-C ^a
Median pore diam, Å	90	507	115	120	280	750	90 ^b
Surface area, m ² /g	267	78	203	174			255 ^b
Pore volume, mL/g	1.00	1.05	0.79	0.65	1.05	1.49	0.56 ^b

a) The Kejefine 153S catalyst contains 4.5 wt% SiO₂. b) The values measured for the KF 153S catalyst.

Table 2. Representative Analyses of Samples

Sample	Elemental (wt%, daf)					Atomic H/C	Fractional (wt%, daf)				Ash (wt%)
	C	H	N	S	O ^a		Oil	Asp.	Preasp. ^b	QI or Pyl ^c	
Solvent Refined Coals											
Wan-SRC	85.7	6.1	1.5	0	6.7	0.85	35.7	33.1	26.4	4.8	0.9
Aka-SRC	84.9	6.2	1.8	0.3	6.8	0.87	31.5	27.0	39.9	1.6	0.5
SCT-SRC	86.3	6.7	1.2	0	5.8	0.93	46.0	34.1	19.9	0	—
Raw Coals											
Wandoan	78.3	5.9	1.0	0.1	14.7	0.90	0.9	4.7	1.7	92.7	7.3
Akabira	83.2	6.2	2.1	0.6	7.9	0.89	0.8	0.9	19.5	78.8	8.4

a) By difference; b) Quinoline or pyridine soluble; c) quinoline or pyridine insoluble.

Table 3. Results of Thermal and Catalytic Hydroprocessing of SRC at 425°C

Catalyst		Products (wt%)				Conv (wt%)		H Consum (wt%)	
Name	Composition	Gas	Oil	Asp	BI	Asp	BI	H ₂	Tetralin
Original Wan-SRC		—	35.7	33.1	31.2	0	0	—	—
None	None	4.6	54.4	22.9	18.1	30.8	42.0	0.7	0.6 ^a
KF-153S	Ni-Mo/Al ₂ O ₃	6.2	58.7	14.6	20.6	55.9	34.0	1.4	0.3
Cat-1	Ni-Mo/Al ₂ O ₃	3.6	65.2	15.4	15.8	53.5	49.4	1.6	0.8
Cat-SB	Mo/SiO ₂	3.9	61.5	23.0	11.6	30.5	62.8	1.6	0.3
Original Aka-SRC		—	31.5	27.0	41.5	0	0	—	—
None	None	5.0	48.2	23.7	23.1	12.2	44.3	0.7	0.9
Cat-1	Ni-Mo/Al ₂ O ₃	4.3	59.2	20.7	15.8	23.0	61.9	1.4	0.4
Cat-SB	Mo/SiO ₂	5.4	58.7	25.4	10.5	5.9	74.7	1.3	0.3

a) This value seems to be lower than real value, as compared to the data in Table 4.

Table 4. Hydroprocessing of Wan-SRC over 20-32 mesh SiO₂- and Al₂O₃-Supported Catalysts at 400°C

Catalyst		MPD (Å)	Yields (wt%)		Conv (wt%)		H consum (wt%)	
Name	Composition		Gas	Oil	Asp	BI	H ₂	Tetralin
None	None		1.9	45.9	16.9	20.8	0.7	1.0
Cat-SA	Mo/SiO ₂	90 ^a	1.8	49.7	21.2	28.2	0.9	0.4
Cat-SB	Mo/SiO ₂	507 ^a	1.9	51.3	19.0	35.9	1.1	0.4
KF-153S	Ni-Mo/Al ₂ O ₃	90	1.9	55.5	44.4	22.4	ND	0.3

a) Median pore diameter of SiO₂ supports Cariact-10 and Cariact-50, respectively.

Table 5. Hydroprocessing of SCT-SRC over Cylindrical Extrudate and Finely Crushed KF-153S Ni-Mo/Al₂O₃ Catalysts at 425°C

Catalyst		Gas + Oil (wt%)	Conv (wt%)	
Composition	Size		Asp	BI
Orig. SCT-SRC	—	46.0	0	0
None	—	70.9	40.5	55.8
Ni-Mo/Al ₂ O ₃	1.5 mm cylinder	81.5	72.4	54.8
Ni-Mo/Al ₂ O ₃	<100 mesh powder	87.8	80.6	71.9

Table 6. Comparison of Hydroprocessing of SRC and Its Asphaltene Fraction

Sulfided Ni-Mo/Al ₂ O ₃ MPD (Å)	Aka-SRC			Aka-Asp ^a		
	None	Cat-1 120	Cat-3 290	None	Cat-1 120	Cat-3 290
Products (wt%)						
Gas	5.0	4.3	4.3	5.7	5.2	5.1
Oil	48.2	59.2	62.5	50.7	69.8	80.3
Asphaltene	23.7	20.7	21.7	32.3	22.4	12.8
BI	23.1	15.8	11.5	12.2	2.6	1.8
H Consumed (wt%)						
H ₂	0.7	1.4	1.5	0.5	2.1	2.3
Tetralin	0.8	0.5	0.3	0.4	0.3	0.2

a) Hexane-insoluble but benzene soluble fraction of Aka-SRC.

Table 7. Comparison of Hydroprocessing of SRC and Its Preasphaltene (BI) Fraction

Sulfided Ni-Mo/Al ₂ O ₃ MPD (Å)	Wan-SRC			Wan-BI ^a		
	Cat-1 120	Cat-3 290	Cat-4 730	Cat-1 120	Cat-3 290	Cat-4 730
Products (wt%)						
Gas	3.6	3.7	3.6	10.5	7.6	10.3
Oil	65.2	66.8	66.0	23.5	27.9	27.1
Asphaltene	15.4	18.2	19.6	24.8	30.1	33.1
BI	15.8	11.3	10.8	41.2	34.4	29.5
H Consumed (wt%)						
H ₂	1.6	1.7	1.7	1.7	1.7	1.9
Tetralin	0.8	0.5	0.4	ND	ND	ND

a) Benzene insoluble fraction of Wan-SRC.

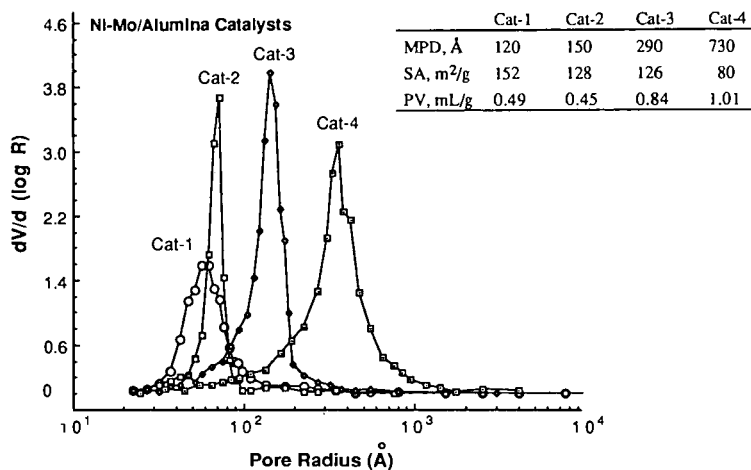


Figure 1. Pore size distribution of prepared Ni-Mo/Al₂O₃ catalysts.

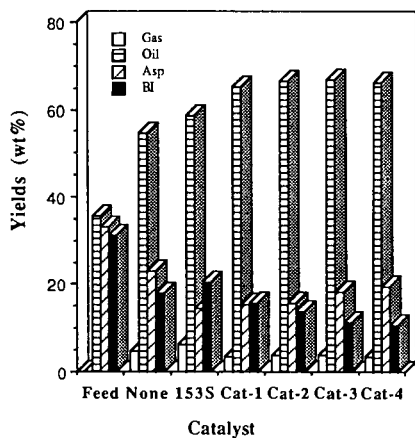


Figure 2. Hydroprocessing of Wan-SRC over unimodal Ni-Mo/Al₂O₃ catalysts with different median pore diameter. See Figure 1 for MPD values.

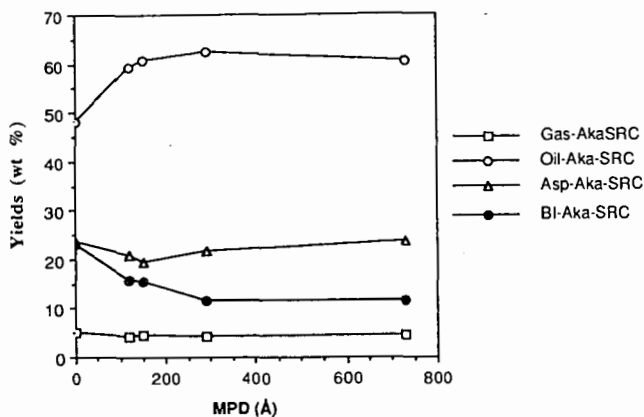


Figure 3. Effects of pore size of Ni-Mo/Al₂O₃ catalysts on product distribution for hydroprocessing of a solvent refined coal (Aka-SRC).

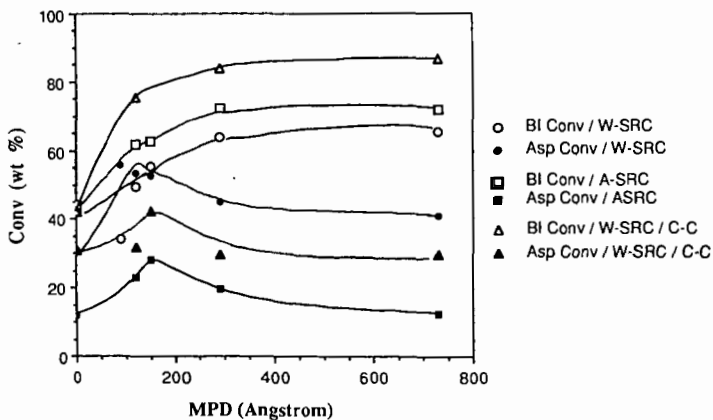


Figure 4. Relation between median pore diameter and conversion of BI and asphaltene with fresh and carbon-coated (C-C) Ni-Mo/Al₂O₃ catalysts for hydroprocessing of Wan-SRC and Aka-SRC. Note that incorporation of the data with KF-153S Ni-Mo containing 4.5 % SiO₂ resulted in some deviation at MPD of 90 Å.

TEMPERATURE-PROGRAMMED CATALYTIC LIQUEFACTION OF LOW RANK COAL USING DISPERSED Mo CATALYST

Lili Huang, Chunshan Song and Harold H. Schobert
Fuel Science Program
Department of Material Science and Engineering
The Pennsylvania State University
University Park, PA 16802

Keywords: temperature-programmed liquefaction, catalysts, conversion

INTRODUCTION

In the presence of catalyst, the specific reaction conditions have a direct effect on conversion in coal liquefaction and on the product distribution [1]. At temperatures lower than 300°C, catalyst precursors such as ammonium tetrathiomolybdate may not be converted to a catalytically active form and thus have no benefit on liquefaction [2]. However, at severe reaction conditions, such as high temperature, retrogressive reactions will take place, and crosslinking or recombination of radicals generated in thermal cracking will reduce the possibility of breaking the coal macromolecule into smaller molecules. In an effort to achieve highest conversion and desired product distribution, low-severity processes have been studied by several research groups. It has been found that temperature-programmed and temperature-staged liquefaction are efficient to maximize the conversion and minimize the retrogressive reactions [3, 4, 5].

The objective of the work reported in this paper is to study the catalytic effect of ammonium tetrathiomolybdate, techniques to disperse this catalyst precursor onto coal, and the optimum reaction conditions for the highest conversion.

EXPERIMENTAL

The coal sample was a Montana subbituminous (DECS-9, PSOC-1546) coal obtained from Penn State Coal Sample Bank. Its composition is summarized as follows: 24.68% moisture, 4.80% ash, 33.46% volatile matter and 37.06% fixed carbon on an as-received basis, 76.11% carbon, 5.14% hydrogen, 0.91% nitrogen, 0.33% organic sulfur and 17.50% oxygen on a dmmf basis. The coal was dried at 95°C in vacuum for two hours before use.

The catalyst precursor, ammonium tetrathiomolybdate (ATTM), was dispersed on coal by incipient wetness method. The loading was 1% of molybdenum on the basis of dmmf coal. Water and a mixture of H₂O/THF (44 : 56) were employed as impregnation solvents. After loading of the catalyst precursor, the coal sample was dried in vacuum for two hours at 105°C, then removed and stored under a nitrogen atmosphere.

Liquefaction experiments were conducted in microautoclave reactors (tubing bombs) in a preheated fluidized sandbath. For each reaction, 4 grams of coal and 4 grams of Wilsonville Middle Distillate (WIMD) as reaction solvent were added to the reactor, following which hydrogen was purged three times, with a final pressure of 7 MPa at room temperature. The reactor was then plunged into the sandbath and agitated at 200 cycles per minute. The tubing bomb reached the reaction temperature in about three minutes. For a single-staged liquefaction (SSL), the tubing bomb was rapidly heated-up to 400°C and held for 30 minutes followed by rapid quench. For a temperature-programmed liquefaction (TPL), the tubing bomb was rapidly heated-up to a relatively low temperature (200°C-300°C) and soaked in sandbath at that temperature for 15 minutes. The

temperature was then gradually increased to a higher temperature level (400°C-450°C) and held for 30 minutes, followed by rapid quench. The rate of temperature increase was 30°C/min to 8.3°C/min, depending on the difference between the lower temperature and the higher temperature. The heat-up period was about 30 minutes, and the total reaction time was about 75 minutes. Temperature-staged liquefaction (TSL) was a different procedure from TPL. A tubing bomb was rapidly heated-up to a low temperature (200°C-300°C), soaked at that temperature for 15 minutes, then it was immediately (without a heating period) transferred to another sandbath of a higher temperature (400°C) and held for 30 minutes followed by rapid quench. Since there was no heating period between two temperature stages, the total reaction time was about 45 minutes, which is different from TPL.

After the reaction, the gaseous product was vented into a gas sample bag and later analyzed by gas chromatography. The liquid and solid products and residue were washed into a tared ceramic thimble using hexane. Then the products were separated under a nitrogen atmosphere by Soxhlet-extraction using hexane, toluene and THF as solvents, the products being classified as oil, asphaltene and preasphaltene respectively. Solvents were removed by rotary evaporation and the products were dried in vacuum at 110°C for about 12 hours, except for the hexane solubles. The solid residue was washed first by acetone and then by pentane several times and dried in the same procedure as the reaction products. The asphaltene, preasphaltene and residue were then weighed, and conversion and product distributions were calculated based on dmmf coal.

RESULTS AND DISCUSSION

The effects of TPL and SSL are compared in Table 1. In the absence of a catalyst, TPL total conversion is 6.4 percentage units higher than SSL. This is mainly due to the gains in asphaltene and preasphaltene yields, while the oil yield remains almost identical in both cases, about 30.2%. In the presence of ATTM as catalyst precursor, total conversion increases again in TPL by 6.6 percentage units, similar to those experiments without catalyst. It is noticed that, different from non-catalytic liquefaction, the oil yield increases drastically by 8.8 percentage units in TPL, while asphaltene decreases by 4.9 percentage units. This may suggest that TPL, with presence of the catalyst, promotes the further cracking or hydrogenation of asphaltene to oil, though the detailed mechanism is not yet clear.

Another comparison is liquefaction with and without catalyst. In SSL runs, total conversion increases 32.2 percentage units by employing ATTM as catalyst. This is mainly due to an oil yield increase (by 12.5 percentage units) and an asphaltene yield increase (by 16.4 percentage units), and to a lesser extent, to a preasphaltene yield increase (by 3.3 percentage units). In TPL runs, catalytic liquefaction achieves 32.4 percentage units higher than non-catalyst run in total conversion. Gas and oil yield increases are the predominant (by 21.2%) contribution to the increase in total conversion. Asphaltene and preasphaltene increase by lesser amounts, 6.7 and 4.4 percentage units respectively. This comparison presents that the addition of ATTM as catalyst efficiently improves both the total conversion of liquefaction and the selectivity of products to the more desirable oils.

As mentioned in previous section, in the procedure of sample preparation, both H₂O and H₂O/THF (44 : 56) were employed as impregnation solvents. The volume of the H₂O/THF mixture required to achieve incipient wetness is about three times of that of pure water. It is apparent that the mixture has higher affinity toward the coal surface than water. This difference in affinity may lead to a different dispersion of the catalyst precursor on coal, which will subsequently result in a difference of catalyst performance. Table 1 provides the conversion data to compare the solvent effect on liquefaction. For SSL runs, samples prepared using H₂O/THF appear a bit more active than samples prepared using H₂O. For TPL runs, the difference is more pronounced. By using H₂O/THF as impregnation solvent, total conversion increases by 10.4 percentage units, which is due to the increase of gas and oil yield (by 10.3 percentage units). The asphaltene and

preasphaltene yields are identical within experimental error. This set of data supports the assumption that by employing H₂O/THF, better catalyst dispersion will be achieved, thus leading to a better catalyst performance.

Temperature-programmed liquefaction may be advantageous over temperature-staged liquefaction because TPL provides a heating period which could slowly generated radicals and allow hydrogenation to take place. Table 2 compares TPL with TSL. For 200/400 runs (the first number indicates the first stage temperature and the second number indicates the second stage temperature), the total conversion increases slightly (1.5 percentage units) in TPL with a remarkable increase in gas and oil yield (7.5 percentage units). In contrast, the asphaltene and preasphaltene yields decrease slightly. For 300/400 runs, the same phenomenon is observed, though in 300/400 runs, both TPL and TSL achieve higher total conversion and gas oil yield. It is apparent that TPL is more favorable to achieve high conversion and better product selectivity. Consistent with the previous observations, the asphaltene yield decreases in TPL experiments. This again reflects the fact TPL promotes the interconversion of asphaltene to oils [6].

Figure 1 shows the conversion as a function of the temperature in the first stage in TPL runs. The curve starts at room temperature, which is in fact the SSL run. The total conversion reaches a maximum at 200°C (91%) and starts to decrease as temperature increases, 86.6% at 250°C and 89.7% at 300°C. The oil yield changes in a very similar way as total conversion, 51.5% at 200°C, 46.8% at 250°C and 50.6% at 300°C. The low temperature stage is used to allow time for the reaction solvent to penetrate into the interior of coal particles [3]. If the temperature of this stage is too high, the reaction solvent may evaporate before penetration. In this case, less solvent will be in the interior of coal and this could result in reduced H-transfer to the coal radicals, which will consequently cause poor liquefaction results. The temperature of the first stage may also affect the activation of catalyst precursor, but how this will subsequently affect the liquefaction is still unknown.

The effect of changing temperature of the second stage in TPL is shown in Figure 2. Although the total conversion, as well as the yields of asphaltenes and preasphaltenes, show a trend of decreasing, the gas and oil yields show a remarkable increase as the temperature increase from 400°C to 450°C (51.5% to 62.4%). This indicates that an increase of second stage temperature may not favor high total conversion of liquefaction, but it has some benefit in achieving high yield of oil and gas. The decrease of total conversion might be caused by retrogressive reactions. At temperatures as high as 450°C, radicals formed in thermal cracking immediately crosslink and recombine with one another to form some very stable compounds that are difficult to liquefy.

CONCLUSIONS

Addition of ATTM as catalyst precursor will increase the total conversion substantially. In the impregnation procedure, using organic compounds in the impregnation solvent appears to lead to a better dispersion of catalyst precursor thus giving a higher conversion. Temperature-programmed liquefaction is advantageous over temperature-staged and single-staged liquefaction regardless of whether a catalyst is used. The change of first and second stage temperature in TPL will influence the conversion, though determining the reasons for these influences relies on future research.

ACKNOWLEDGEMENTS

The authors are pleased to acknowledge the financial support provided by the United States Department of Energy for this work.

REFERENCES

1. B. R. Utz, A. V. Cugini and E. A. Frommell, ACS Sym Ser. **1989**, 473, 289.
2. A. B. Garia and H. H. Schobert, Fuel, **1989**, 68, 1613.
3. C. Song, H. H. Schobert and P. G. Hatcher, ICCS, Sept 1991, Newcastle, United Kingdom.
4. C. E. Burgess and H. H. Schobert, Am. Chem. Soc. Div. Fuel Chem. Prepr., **1990**, 35(1), 31.
5. C. E. Burgess, L. Artok and H. H. Schobert, Am. Chem. Soc. Div. Fuel Chem. Prepr., **1991**, 36(2), 462.
6. F. J. Debyshire, A. Davis, R. Lin, P. G. Stansberry and M.-T. Terry, Fuel Processing Tech., **1986**, 12, 127.

Table 1. Comparison of TPL and SSL Effect on Liquefaction.

Sample	rxn Cond.	Tot Conv.	Gas + Oil	Asph.	Preasph.
Non-cat	SSL	52.22	30.21	12.46	9.55
	TPL	58.57	30.27	17.24	11.06
ATIM THF/H ₂ O	SSL	84.4	42.73	28.86	12.82
	TPL	91	51.49	23.93	15.5
ATIM H ₂ O	SSL	83.24	38.98	19.46	24.8
	TPL	80.57	41.18	23.4	15.42

Oil: hexane soluble.

Asphaltene: toluene soluble but hexane insoluble.

Preasphaltene: THF soluble but toluene insoluble

Table 2. Comparison of TPL with TSL.

Temperature	rxn Cond.	Tot. Conv.	Gas + Oil	Asph.	Preasph.
200/400	TPL	91	51.49	23.93	15.5
	TSL	89.46	43.98	27.62	17.87
300/400	TPL	89.67	50.61	22.67	16.4
	TSL	87.91	42.66	28.37	16.89

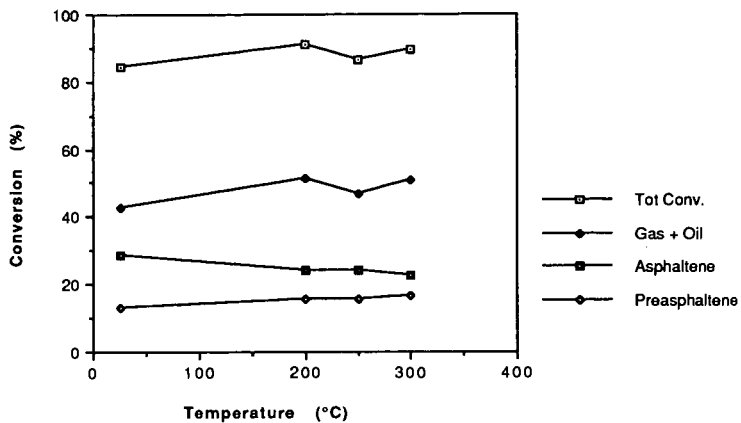


Figure 1. Conversion as a function of first stage temperature in TPL.

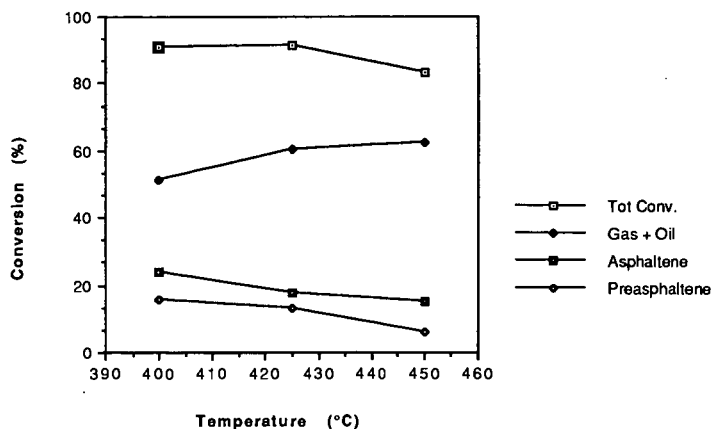


Figure 2. Conversion as a function of second stage temperature in TPL.

EXAFS Studies of Mo, Ni-Y-Zeolite Catalysts

Qiwu Wang and Dale Sayers

Department of Physics, North Carolina State University, Raleigh, NC 27695

Miming Huang, Chunhua Yuan and Shiqiang Wei

Department of Modern Chemistry, University of Science and Technology of China, Hefei, Anhui, P. R. China

Introduction

Bimetallic zeolite catalysts which contain Mo are of great interest as bifunctional catalysts¹⁻⁴. However, there are difficulties in preparing such catalysts since it is difficult to exchange the cations of a zeolite for molybdenum ions directly because high valence cationic molybdenum can only exist in a very acidic solution where ion-exchange equilibria are unfavorable and many zeolites are unstable. Ion exchange with neutral and anionic species results in a large amount of surface loading. In order to overcome the difficulties of aqueous ion exchange, molybdenum is introduced into zeolites by a solid-ion exchange method. A special procedure was developed recently for initiating controlled immigration of $\text{MoO}_2(\text{OH})_2$ into the pores of HY and NiY using MoO_3 in the presence of water vapor.⁵

EXAFS is an effective physical method for determination of the local structure of specific atoms in complex systems such as highly dispersed supported metal catalysts. It has been successfully applied to some metal zeolite catalysts: viz. Pt-Y-zeolite⁶, Cd-Y-zeolite⁷ and Ni, Mo-Y-zeolite⁸ and other bimetallic catalysts⁹⁻¹⁰. In this work, we studied by EXAFS the change of the environment around Mo and Ni as a function of preparation of the Mo, Ni-Y-zeolite to follow the incorporation of Mo and Ni into the framework of the Y-zeolite and to see if there are any Mo-Ni interactions.

Experimental

Samples

The HNaY was prepared by exchange of NaY with a 0.1 N NH_4NO_3 solution at 365K for 1 hour, followed by a direct calcination at 823K for 5.5 hours in a closed vessel. The modified solid ion exchange was performed as following: a mixture of 27 g HNaY and 1.2g MoO_3 was ground in a mortar (hereafter denoted as MoHY), placed in a quartz tube and then calcined at 723K, water vapor at 323K (118 torr) was carried through the mixture using H_2 as vector gas with a flow of 45ml/min. The sample obtained after calcination was then denoted as MoHYR and that after dehydration at 673K as MoHYRD.

The NiY was prepared by ion exchange of HNaY in a 0.5N Ni(NO₃)₂ solution at 318K for 3.5 hours, followed by washing and drying at 393K. To prepare one bimetallic catalyst, MoHYRD was subjected to the same ion exchange process in Ni(NO₃)₂ solution. This sample was denoted as MoNiY (Mo 1.63 wt. %, Ni 2.09 wt. %). A second sample was prepared starting with NiY and using solid ion exchange to incorporate Mo. This sample is denoted NiMoY (Ni 2.07%, Mo 2.5%). After dehydration they are denoted as MoNiYD and NiMoYD respectively. The Mo and Ni contents of the samples were then analyzed by AAS and Na contents were determined by ICP, and X-ray powder diffraction measurements were made using a Cu-target x-ray tube.

X-ray Absorption Measurements

X-ray absorption experiments were performed on beam line X-11A of the National Synchrotron Light Source (NSLS), Brookhaven National Laboratory. The X-ray absorption spectra for Mo and Ni K-edges were recorded with the ring operating at 2.5 GeV beam energy and a beam current of 40-180 mA. The pressed powder samples were mounted on the holder and measured at liquid nitrogen temperature in the transmission mode.

Data analysis was carried out with using standard methods¹¹ and the fitting was done using experimentally determined Mo-O (from ZnMoO₄), Mo-Mo (from metallic Mo) and theoretically calculated Mo-Si, Mo-Ni, Ni-Si, Ni-O and Ni-Ni (using FEFF)¹² phase shifts and backscattering amplitudes. Both single or multiple shell models were assumed for fitting the various filtered Fourier transform (FT) peaks.

Results and Discussion

Mo in Mo,Ni-Y-zeolites

As mentioned above, two different preparations were used: one put Mo into the zeolite first using solid-ion exchange and then introduces Ni cations by aqueous ion exchange. The other incorporates Ni first followed by Mo. Will the different order of incorporating Mo and Ni into Y-zeolite produce different local environments of Mo and Ni in these two catalysts? For these low loading and highly dispersed metal-zeolites, only EXAFS studies of the individual metal elements in them can give the answer to this question.

From Fig.1 it can be seen that the X-ray absorption profile of Mo in NiMoY and NiMoYD in which Mo was introduced into Ni-Y-zeolite are similar to those in MoO₃ and MoHY⁷ having a clear pre-edge peak and the weak structure in the extended absorption region. The spectra of Mo in MoNiY and MoNiYD are virtually the same as those in MoHYR and MoHYRD⁷: no pre-

edge absorption and with a strong oscillation in the extended region which means prominent higher coordination shells.

Fourier transforms of $k^3 \cdot \chi(k)$ for the Mo K-edge EXAFS of figure 1 shows that these differences are in both the first and higher shells (Fig.2). The Mo environment in NiMoY is very similar to MoO₃. The clear decrease of a Mo-Mo feature and a longer Mo-O distance in NiMoYD, in comparison with NiMoY indicates that MoO₃ is further dispersed into the Ni-Y zeolite by the further calcination and dehydration. This is also consistent with the decrease in the higher (Mo-Mo and Mo-O) shells. The fitting results listed in Table 1 quantitatively demonstrate these changes. For both MoNiY and MoNiYD, where Mo was introduced into Y-zeolite by solid-ion exchange, the higher coordination shell structures surrounding Mo are similar and sharper than those in NiMoY and NiMoYD. It is also known that the infrared absorption spectra are nearly same for both MoNiY and MoNiYD.⁷ The long metal oxygen bonds at around 2.6Å in both MoNiY and NiMoY (see Table 2) have been observed before in metal-zeolites.¹³ A Mo-Mo interaction (R~3.63 Å) also was observed by EXAFS in MoO₃/TiO₂ catalysts after calcination.¹⁴ From fitting the experimental $k^3 \chi(k)$ data for MoNiY and MoNiYD isolated from the shells between 2.86 and 3.74Å with Mo-Mo, Mo-Si and Mo-Ni models it can be demonstrated that the Mo has not only Mo and Si which are present in MoHYR and MoHYRD but also a small amount of Ni atoms as its neighbors. An example is shown in Figure 3 for the case of MoNiY. The presence of an interaction between Mo and Ni in Mo,Ni-Y-zeolites may be significant for the catalytic properties of these bimetallic zeolite catalysts.

Ni in Mo,Ni-Y-zeolites

The Ni K-edge absorptions for MoNiY, MoNiYD, NiMoY and NiMoYD all have a strong first X-ray absorption peak which can be related to the oxidation state of Ni (see Fig.4). However, further comparison indicates that there are slight differences in the edge region and a great change in the extended region between MoNiY and NiMoY in both the as-prepared and dehydrated forms. The Fourier transforms of the data in Figure 4 are shown in Figure 5 and clearly show the differences between the MoNi and NiMo forms. The local environment of Ni in MoNiY is very close to that of dispersed NiO (CN=6, R=2.04 Å). After dehydration, the oxygen coordination decreases because of the removal of bound waters, and the Debye-Waller factor decreases. However, the higher shell coordinations still could not be found. Ni²⁺ is still present in a highly dispersed state with a simple oxygen coordination structure only. This is in agreement with other work.¹⁵ The strong interaction between Mo and Ni, as indicated in the previous paragraph, will inhibit the growth of Ni metal particles and results in the

fine Ni particles which would relate to excellent activity and selectivity toward hydrodemethylation of toluene.¹³ In NiMoY and NiMoYD the Ni-O first neighbors have overlapping contributions from higher shells. Multiple shell fitting showed that best fits were obtained for Ni-O, Ni-Si and Ni-Ni coordinations compared with those for Ni-O and Ni-Si or Ni-O and Ni-Ni only. An example of the results with Mo, Ni and O as the neighbors fitted to Fourier filtered data between 2.86-3.74 Å in NiMoY is shown in Figure 6. It indicates that Ni has not only O and Ni but also Mo as its coordination neighbors consistent with the Mo edge results on the same samples.

Summary

From Mo and Ni K-edge EXAFS studies we have studied the difference between the local environments of Mo and Ni in Mo,Ni-Y-zeolites prepared by interchanging the order of introduction of metals into the zeolite. The results clearly indicate that significant differences occur. When Mo is introduced first it seems to be exchanged into the supercages as indicated by the coordination numbers and distances we have found. The subsequent addition of Ni seems to allow Ni to go into nearby cages where it can coordinate to Mo through oxygens. When Ni is added first it seems to go into a smaller cages in an aqueous phase. Subsequent addition of Mo does not affect this environment and the Mo seem to remain essentially as MoO₃. This should not result in an effective interaction between Mo and Ni. These results clearly indicate the importance of the order of exchange of metals onto zeolites in the preparation of bimetallic zeolite catalysts.

References

1. Meszaros-Kis, A. and Valyon, J., in "Zeolites as Catalysts, Sorbents and Detergent Builders" Edited by Karge H. G. and Weitkamp J., Elsevier, Amsterdam, 1989, p.251
2. Laniecki, M., *ibid* P. 259
3. Harris, I. M., Dwyer, J., Garforth, A.A., Mc Ateer, C. H. and Ball, W. J., *ibid* P.271
4. Howe, R. F. and Huang M., Proceeding of 9th International Conference on Catalysis, Canada, 1988, p. 1585
5. Huang, M. and Howe, R. F., *J. Catal.* 108 (1987) 283
6. Wang, Q., Sayers, D., Huang, M., Yuan, C. and Wei, S., abstract in this symposium
7. Moller, K., Eddy, M. M., Stucky, G.D., Herron, N. and Bein, T., *JACS.* 1989, 17, 1564
8. Clozza, A., Bianconi, A., Gareia, J., Corma, A and Burattini, E., *XAFS V*, Ed: Mustre de Leon, J., Stern, E. A., Sayers, D. E., Ma, Y. & Rehr, J.J., North-Holland, 1988, p.162
9. Wang Q. and Wei S., *Kehue Tongbao* 6, 435, (1990)
10. Wang Q. and Wei S., *Chinese J. Chem. Phys.* 3, 49, (1990)
11. Stern, E. A., Sayers, D. E. and Lytle, F. W., *Phys. Rev. B: Solid State II*, 4836-4845, 1975
12. Rehr, J. J., *Physica B* 158 (1989) 1-4 (XAFS V)
13. Huang, M., Yuan, C., Wei, S. and Wang, Q., *in press*
14. Koningsberger, D. C., *XAFS VI*, Ed. S. Hasnain, York, August, 1990, p.28
15. Soeya, T, Kim, D.S., Matsubayashi, N., Shimada, H., Nishijima, A. & Segawa, K., *Photon Factory Activity Report #7* 1989, P.80
16. Clozza, A., Bianconi, A., Garcia, J., *Physica B*, 158, 162, 1989

Table 1 Mo Coordination Shells in Mo,Ni-Y-Zeolites

MoNiY					MoNiYD			
Model	CN	R(Å)	DWF.10 ²	d-E ₀ (eV)	CN	R(Å)	DWF.10 ²	d-E ₀ (eV)
Mo-O	3.2±.2	2.03±.01	0.01±.00	-4.3±.6	2.2±.2	2.00±.01	-0.27±.02	-1.1±.1
Mo-O	1.4±.1	2.62±.01	-0.69±.06	-7.6±.7	0.7±.1	2.61±.01	-0.77±.04	8.4±.6
Mo-Ni	0.9±.2	3.54±.01	0.40±.03	7.1±.6	0.1±.0	3.63±.02	-0.83±.05	7.0±.6
Mo-Mo	3.4±.1	3.70±.02	-0.14±.01	6.1±.4	3.6±.3	3.68±.02	-0.05±.02	6.0±.4
Mo-Si	1.5±.1	4.05±.02	-0.02±.02	-3.0±.3	1.0±.1	4.00±.02	-0.40±.03	3.3±.3
NiMoY					NiMoYD			
Model	CN	R(Å)	DWF.10 ²	d-E ₀ (eV)	CN	R(Å)	DWF.10 ²	d-E ₀ (eV)
Mo=O	0.5±.1;	1.55±.01	-0.03±.01	13.5±3.	0.1±.0	1.53±.01	-0.37±.02	11.7±.9
Mo-O	3.2±.3	1.71±.01	0.04±.01	6.8±.7	2.3±.2	1.72±.01	-0.06±.01	6.8±.6
Mo-O	1.2±.2	1.98±.01	-0.48±.02	-12.6±.8				
Mo-Mo	2.2±.4	3.31±.01	-0.03±.01	3.7±.3				

Table 2 Ni Coordination Shells in Mo,Ni-Y-Zeolites

NiMoY					NiMoYD			
Model	CN	R(Å)	DWF.10 ²	d-E ₀ (eV)	CN	R(Å)	DWF.10 ²	d-E ₀ (eV)
Ni-O	4.3±.2	2.08±.01	0.01±.01	-0.6±.3	4.1±.3	2.07±.01	0.13±.01	2.4±.3
Ni-Si	2.7±.2	2.68±.01	0.22±.01	12.8±.9	1.9±.2	2.66±.01	0.10±.01	14.3±.9
Ni-Ni	2.3±.1	3.03±.01	0.77±.01	-1.2±.5	2.9±.2	2.98±.01	0.72±.04	5.5±.5
Ni-Ni	1.8±.1	3.94±.01	0.42±.01	8.2±.7	2.1±.2	3.96±.01	0.40±.01	3.9±.4
Ni-Mo	4.0±.4	4.51±.02	0.72±.01	14.2±.1.	4.0±.3.	4.53±.02	0.70±.08	15.0±1.2
Ni-O	2.1±.2	4.95±.02	-0.91±.01	-9.6±.3	2.9±.4	4.97±.02	-0.78±.0	-11.3±.4
MoNiY					MoNiYD			
Model	CN	R(Å)	DWF.10 ²	d-E ₀ (eV)	CN	R(Å)	DWF.10 ²	d-E ₀ (eV)
Ni-O	4.9±.2	2.04±.01	0.36±.01	6.5±.4.	3.2±.3	2.05±.01	-0.13±.01	9.3±.4

Note: The experimental standard data are used for fitting: Mo-O(CN=4,R=1.78) from ZnMoO₄ and Mo-Mo (CN=12,R=2.73Å) from Mo metal foil; FEFF program was used to calculate the standard data for Mo-Si(CN=12, R=2.69Å), Mo-Ni(CN=12, R=2.61Å), Ni-O(CN=6,R=2.09Å), Ni-Si(CN=12,R=2.69Å), Ni-Ni(CN=12,R=2.96Å) and Ni-Mo(CN=12, R=2.61Å).

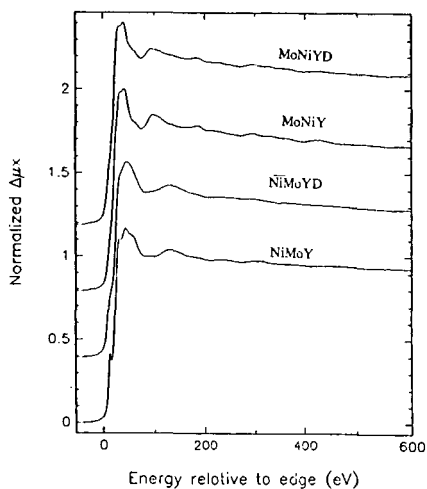


Fig.1 The normalized X-ray absorption spectrum versus energy for Mo in MoNiYD and MoNiY in which Mo were introduced first and in NiMoYD and NiMoY where Ni first. The energy scale is relative to the binding energy of the Mo 1s state (20,000 eV).

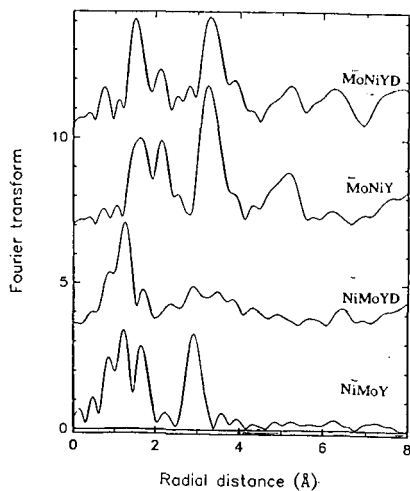


Fig.2 A comparison of the magnitudes of the Fourier transforms of the weighted Mo EXAFS for MoNiYD, MoNiY, NiMoYD and NiMoY zeolites versus R. The transforms are all of $k^3X(k)$ and taken over a k-space range of $3-14 \text{ \AA}^{-1}$.

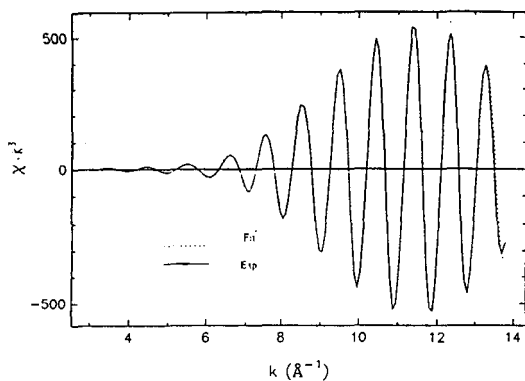


Fig.3 An overplot of the Fourier filtered $k^3X(k)$ data of Mo in MoNiY and the best fitting results (see Table 1) versus R. The fitting range was from 2.86 to 3.74 \AA . The fit included Mo-Mo, Mo-Ni and Mo-Si contributions.

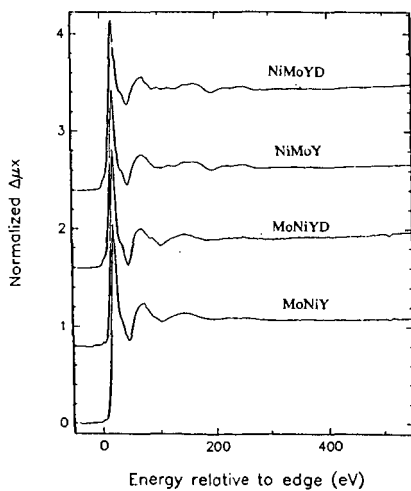


Fig. 4 The normalized X-ray absorption spectrum versus energy for Ni in NiMoYD and NiMoY in which Ni were introduced first and in MoNiYD and MoNiY where Mo first. The energy scale is relative to the binding energy of the Ni 1s state.

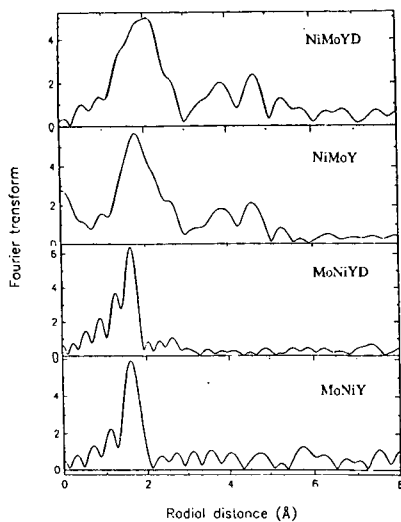


Fig.5 A comparison of the magnitudes of the Fourier transforms of the weighted Ni EXAFS for NiMoYD, NiMoY, MoNiYD and MoNiY zeolites versus R. The transforms are all of $k^3X(k)$ and taken over a k-space range of $3-14 \text{ \AA}^{-1}$.

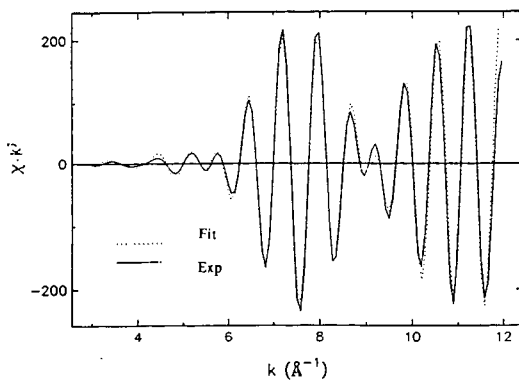


Fig.6 An overplot of the Fourier filtered $k^3X(k)$ data of Ni in NiMoY and the best fitting results (see Table 2) versus R. The fitting range was from 3.0 to 5.1Å. The fit included Ni-Ni, Ni-Mo and Ni-O contributions.

**SYNTHESIS OF C₅ ETHERS FROM METHANOL AND 2-METHYL-1-PROPANOL
(ISOBUTANOL)**

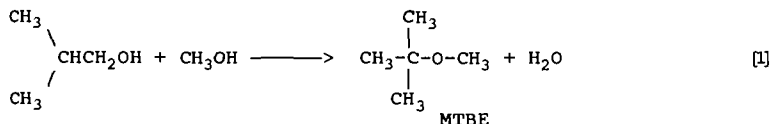
K. Klier, R.G. Herman, M.A. Johansson, and O.C. Feeley
Department of Chemistry, S.G. Mudd #6
Lehigh University, Bethlehem, PA 18015

Keywords: Alcohol dehydration, Ether synthesis

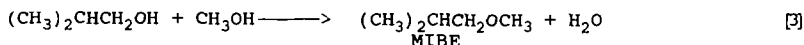
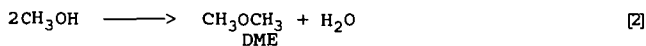
Introduction

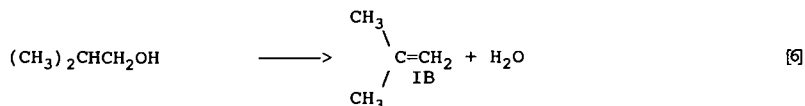
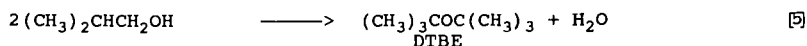
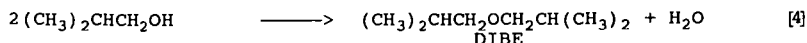
Methyl-tertbutyl ether (MTBE) and tertamyl-methyl ether (TAME) technology is well established with methanol and a branched olefin (iso-butene or 2-methyl-butene) as source feedstock (1,2). The recently announced engineering innovation of reaction with distillation led to a new process, ETHERMAX, by Dow-Hülse-Kohl (3), in which the thermodynamic equilibrium is shifted in favor of MTBE by the product removal directly in the catalytic reactor. Despite the very fast growth of the MTBE and TAME production capacity worldwide, there is a potential shortage of the feedstock olefins (4) and by some accounts of methanol (5), should MTBE/TAME be used as the principal oxygen additive and octane booster for partial replacement of aromatics in gasolines (3).

As isobutene can be obtained by dehydration of 2-methyl-1-propanol (isobutanol) and isobutanol can be directly synthesized from the syngas CO/H₂ (6,7), there is an alternative route to MTBE via the syngas-derived isobutanol. Still a more attractive route to MTBE would be via the direct coupling of alcohols,



if the selectivity of the process could be controlled so that reaction [1] is the dominant route. There are several other reactions that can occur in a system that couples isobutanol with methanol: coupling of two methanol molecules to dimethyl ether (DME) [2], of methanol and isobutanol to methyl-isobutyl ether (MIBE) [3] which is a low octane isomer of MTBE, of two isobutanol molecules to di-isobutyl ether (DIBE) [4] or di-tertbutyl ether (DTBE) [5], dehydration of isobutanol to isobutene (IB) [6], and oligomerization of isobutene to C₈, C₁₂, etc. hydrocarbons.

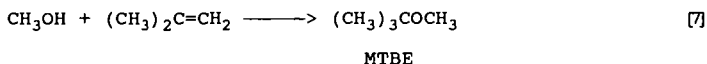




All of the above reactions [1] - [6] are acid-catalyzed, and the use of solid acids is preferred to that of acid solutions. The factors influencing selectivity are thermodynamic constraints, the concentration and strength of the catalyst acid sites, and mass transfer related phenomena such as shape- or diffusion controlled selectivity in zeolites. In this work we report on the selectivities of isobutanol-methanol coupling over two classes of catalysts, organic polymeric sulfonic acids and inorganic acids based on silica-alumina, mordenite, montmorillonite, and sulfate-modified zirconia.

Thermodynamic Considerations

The standard free energies for the key reactions involved in the set [1] - [6] are represented in Figure 1 for two temperatures, 298 and 400K. It is evident that at 400K and above, the synthesis of MTBE from methanol and isobutene [7]



becomes a thermodynamically uphill process while if the two alcohols are the reactants in reaction [1], the path to MTBE is exoenergetic. Further, the mixed ether isomer of MTBE, MIBE, that is readily formed over Nafion H (8), is a thermodynamically less favorable product than MTBE. Elevated pressure will favor the ether-forming reactions [1] - [5] over the dehydration of isobutanol [6] in which the molar volume increases when going from the left to the right.

Kinetic Considerations

Although kinetics of reactions [1] - [6] and related processes have been studied in detail only over Nafion H (9), it is important to summarize the main features of that kinetic behavior here, because the kinetic patterns provide guidelines for testing protocol over a wide range of catalysts. The results of kinetic studies of coupling methanol with isobutanol over Nafion H yield the following conclusions:

- (i) Dehydration of isobutanol to IB, reaction [6], requires two acid sites, one of which binds isobutanol and one that supplies an acid catalyzing function for the isobutanol dehydration. The consequence of this kinetic behavior is that at high pressures, isobutanol poisons its own

dehydration and the kinetic order becomes negative with isobutanol concentration. Methanol also exhibits a retarding effect on isobutanol dehydration by competitive adsorption and blocking of the acid sites.

- (ii) The formation of DME, reaction [2], and DIBE, reaction [4], requires two sites occupied by the respective alcohol, methanol for DME and isobutanol for DIBE. The consequence of this behavior is that at high pressures, the kinetics become "saturated" and the rates of DME or DIBE reach constant values.
- (iii) The formation of MIBE, reaction [3], requires two sites occupied by the two different alcohols. The consequence of this behavior is that there is a maximum rate at an optimum ratio of partial pressures of the two alcohols. Quantitative evaluation of the observed rates shows that isobutanol is approximately two times more strongly held by the acid sites of Nafion H than methanol.
- (iv) The conversion of MIBE to the thermodynamically more stable MTBE or isobutene and methanol is kinetically strongly hindered.

The dual site character of all catalyzed reactions involved imposes a requirement that the acid sites be highly concentrated on the surface of any prospective heterogeneous catalyst. Further, pressure is recognized as an important variable controlling the selectivity to ethers (high pressures) or isobutene (low pressures).

Organic Polymeric Catalysts

In this section, we compare the outcome of isobutanol-methanol coupling under standard test conditions developed in this laboratory. Reaction conditions were similar to those described in Nunan et al (8). The test reaction used 5 g of catalyst at 90°C under a total pressure of 1 atm. The flow rate of each alcohol was 1.72 mol/kg cat/hr and was achieved by pumping an equimolar mixture of isobutanol and methanol. The flow rate of He and N₂ is 16 mol/kg cat/hr. The catalyst bed was diluted to 20 cm³ with Pyrex beads. The organic polymers were all sulfonic derivatives in their hydrogen form, and they are listed in Table I.

Steady state conversions were obtained within the first hour of the reaction. Data were collected for several hours time-on-stream during which no catalyst deactivation was detected. The results of the standard test over these polymers are summarized in Table II. The major products, excluding water, of the reaction of the two alcohols are given in this table. In addition, minor amounts of C₆ and C₁₂ hydrocarbons, formed from the di- and trimerization of isobutene, were detected. The order of activity of the catalyst was found to be Amberlyst ≈ Purolite > BioRad > Nafion.

Product selectivities for the different catalysts are illustrated by Figure 2. Water, which is, of course, the major product of these dehydration reactions, is not included in the selectivity analysis. Under the standard reaction conditions, Nafion-H appears to be the best catalyst for MIBE production. The other catalysts produce significant amounts of MTBE, along with other ethers, viz. DTBE, DIBE, and DME. The higher selectivity of Nafion towards MIBE formation may be due to the distinctly different nature

of the acid sites of Nafion. The sulfonic acid groups of perfluorinated Nafion contrast with the sulfonic acid groups of the other hydrocarbon based resins tested in this study.

Inorganic Solid Acid Catalysts

The following inorganic acid catalysts were tested: H-Mordenite (Norton), $\text{SiO}_2/\text{Al}_2\text{O}_3$ (Davison), Montmorillonite K-10 (Aldrich), and ZrO_2 treated with sulfuric acid, which will be designated as ZrO_2/SO_4 .

The preparation of ZrO_2/SO_4 was according to the work of Hino and Arata (10). $\text{ZrOCl}_2 \cdot 8\text{H}_2\text{O}$ was added to aqueous ammonia to precipitate $\text{Zr}(\text{OH})_4$ which was washed and dried at 100 °C overnight. The dried $\text{Zr}(\text{OH})_4$ weighing 10 g was placed on a folded filter paper and 150 ml of 1N H_2SO_4 was poured through it. The wet powder was dried at 110°C overnight and then calcined at 620 °C for 3 hr. Pretreatment of other catalysts consisted of calcination of Mordenite and $\text{SiO}_2/\text{Al}_2\text{O}_3$ at 400°C, the Montmorillonite catalysts being used as received.

The reaction conditions and catalyst weight used for the inorganic catalysts were identical to those used for the organic catalysts mentioned above. In addition, in light of their much higher temperature stability, the inorganic catalysts were studied at reaction temperatures of 125°C, 150°C, 175°C, as well as 90°C.

The results of the standard test over these inorganic catalysts are summarized in Table IV.

The product selectivities of these catalysts are shown in Figures 3-6. Water, the coproduct of all the dehydration reactions, is not included in the selectivity calculations.

The patterns that emerge are the following:

- (i) H-mordenite is a selective catalyst for dehydration of methanol to DME. Isobutanol is not converted to any ethers or dehydrated significantly to isobutene over H-mordenite under the conditions used. Evidently the pore size or shape of H-mordenite restricts reactions of isobutanol; even though the isobutanol molecule is small enough to enter the larger channel pores of mordenite, its conversion is suppressed by one or all of the following three classic mechanisms of zeolite shape selectivity: (a) inaccessibility of acid centers that possibly reside primarily in the narrow side channels of the mordenite structure; this type of size exclusion in alcohol dehydration was first studied by Weisz et al. (11), however it should be noted that acid sites in mordenite are accessible to molecules as large as 1-methyl-2-ethylbenzene at higher temperatures (12) (b) retardation of isobutanol transport by preferential diffusion of methanol, diffusive selectivity was studied by Chen and Weisz (13) (c) size restrictions on the transition states involving isobutanol, isobutyl esters, and isobutyl oxonium ions. Csicsery first proposed the concept of restricted transition state selectivity in zeolites (12).

- (ii) Sulfate-modified zirconia is an efficient and highly selective catalyst for the dehydration of isobutanol to isobutene, with methanol dehydration to DME suppressed. The reasons for this selectivity pattern have not been established but it is tentatively suggested that isobutanol is more strongly bonded than methanol to the sulfate groups on the zirconia surface so that methanol activation is suppressed. The relative bonding strength of isobutanol and methanol to the sulfate-modified zirconia would have to be more markedly different than that on Nafion H because DME and MIBE are co-products with isobutene over Nafion H but not over the sulfate-modified zirconia.
- (iii) There is an overall order of activities for the dehydration reactions over the inorganic acids used,
 $\text{ZrO}_2/\text{SO}_4^{2-} > \text{H-mordenite} > \text{SiO}_2/\text{Al}_2\text{O}_3 > \text{H-Montmorillonite}$
- (iv) The inorganic catalysts are generally less active than the organic polymeric catalysts at 90°C except for H-mordenite which is active and selective for methanol dehydration to DME. Higher temperatures are needed for significant alcohol dehydration with inorganic catalysts. In general, the organic polymeric catalysts are unstable at these higher temperatures.

Conclusions

Acid-catalyzed reactions of an equimolar mixture of methanol and 2-methyl-1-propanol (isobutanol) gave rise to homo- and heteroethers, as well as to isobutene, depending on the catalyst used. The organic polymeric acids were selective towards MIBE which is a low octane isomer of MTBE. A particularly high selectivity to DME was displayed by H-mordenite, evidently due to a combination of factors that are summarily termed "shape selectivity". The sulfate-modified zirconia proved to be a selective catalyst for isobutanol dehydration to isobutene, with ether formation suppressed. The inorganic catalysts displayed a lower activity than sulfonated organic resins and thus higher temperatures were needed, but the sulfate-modified ZrO_2 has proven to be promising when isobutene is a desirable product of alcohol isobutanol dehydration in the mixture with methanol. The significant advantages of inorganic catalysts are their applicability at high temperatures and ease of regeneration.

Acknowledgements

This work was supported by the U.S. Department of Energy Grant No. DE-AC22-90PC90044.

References

1. Chase, J. D. and Galvez, B. B., *Hydrocarbon Process.*, 60(3) (1981) 89.
2. Chase, J. C., in "Catalytic Conversions of Synthesis Gas and Alcohols to Chemicals," ed. by R. G. Herman, Plenum Press, New York (1984) 307.
3. Ainsworth, S.J., *Chem. & Eng. News*, (June 10, 1991) 13.
4. Shearman, J., *Chem. Eng.*, (July 1991) 44v.
5. *Oil & Gas Journal*, (Aug. 19, 1991) 28.

6. Nunan, J. G.; Bogdan, C. E.; Klier, K.; Smith, K. J.; Young, C.-W.; and Herman, R. G., *J. Catal.*, 116 (1989) 195.
7. Nunan, J. G.; Herman, R. G.; and Klier, K., *J. Catal.*, 116 (1989) 222.
8. Nunan, J. G.; Klier, K.; and Herman, R. G., *J. Chem. Soc., Chem. Comm.*, (1985) 676.
9. Nunan, J. G.; Klier, K.; and Herman, R. G., to be submitted.
10. Hino, M. and Arata, K., *J. Chem. Soc., Chem. Commun.*, (1980) 851.
11. Weisz, P.B.; Frilette, V.J.; Maatman, R.W.; and Mower, E.B., *J. Catal.*, 1, (1962) 307.
12. Csicsery, S.M., *J. Catal.*, 19, (1970) 394.
13. Chen, N.Y.; Mazuik, J.; Schwartz, A.B.; and Weisz, P.B., *Oil & Gas Journal*, (Nov. 18, 1968) 154.

TABLE I
Organic Catalysts

	Polymer base	Resin type	Decomposition Temperature
Amberlyst-15	Polystyrene	Macroreticular	≈120 °C
Purolite 150	Polystyrene	Macroreticular	≈120 °C
BioRad AG50WX2	Polystyrene	Gel	≈120 °C
Nafion-H	Fluorocarbon	Gel	>200 °C

TABLE II
Yields over Organic Catalysts
(mol/kg cat/hr)

	DME	Butenes	MIBE	MTBE	C8 ether
Amberlyst-15	0.042	0.041	0.053	0.013	0.014
Purolite 150	0.034	0.048	0.062	0.011	0.015
BioRad AG50WX2	0.015	0.011	0.040	0.004	0.008
Nafion-H	0.004	0.002	0.014	0.0003	0.003

TABLE III

Yields over Inorganic Catalysts
(mol/kg cat/hr)

	T _{Reaction}	DME	Butenes	MIBE	MTBE	C8 ether
H-Mordenite	90°C	0.060	-----	-----	-----	-----
	125°C	0.6599	-----	-----	-----	-----
	150°C	0.83	0.068	-----	-----	0.004
ZrO ₂ /SO ₄ ⁼	90°C	-----	-----	0.003	-----	-----
	125°C	0.006	0.067	0.02	0.003	0.008
	150°C	0.027	0.696	0.068	0.009	0.017
	175°C	0.103	1.29	0.049	0.007	-----
SiO ₂ /Al ₂ O ₃	90°C	-----	-----	-----	-----	-----
	125°C	0.007	0.028	0.011	0.001	0.003
	150°C	0.021	0.225	0.032	0.005	0.014
	175°C	0.039	0.943	0.049	0.007	0.016
Montmorillonite	90°C	----	-----	-----	----	-----
	125°C	0.008	0.008	0.008	----	0.004
	150°C	0.019	0.071	0.019	0.004	0.014
	175°C	0.034	0.378	0.029	0.014	0.031

Fig. 1 Free energy of ether synthesis reaction pathways

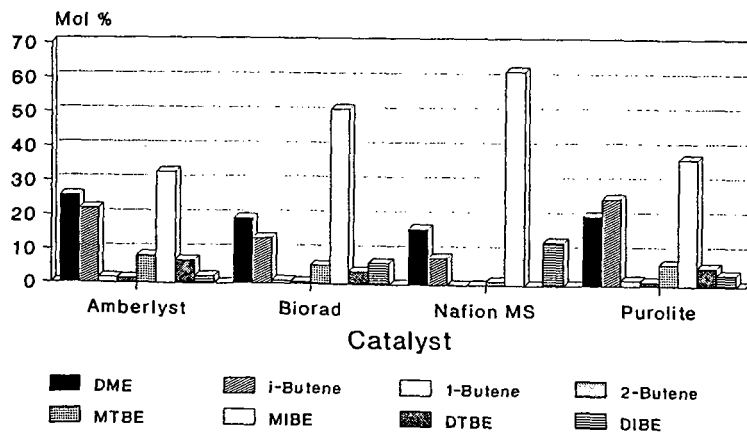
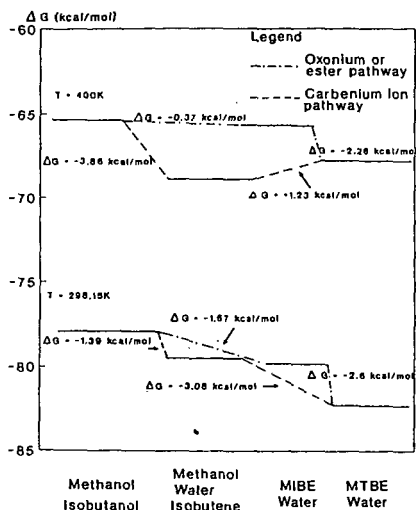


Fig. 2 Selectivity over organic catalysts for the methanol + isobutanol reaction at 90 °C.

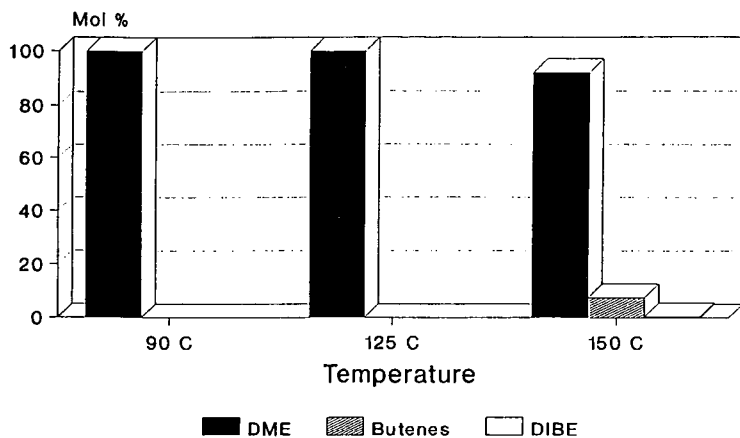


Fig. 3 Selectivity over H-mordenite for the methanol + isobutanol reaction at various temperatures.

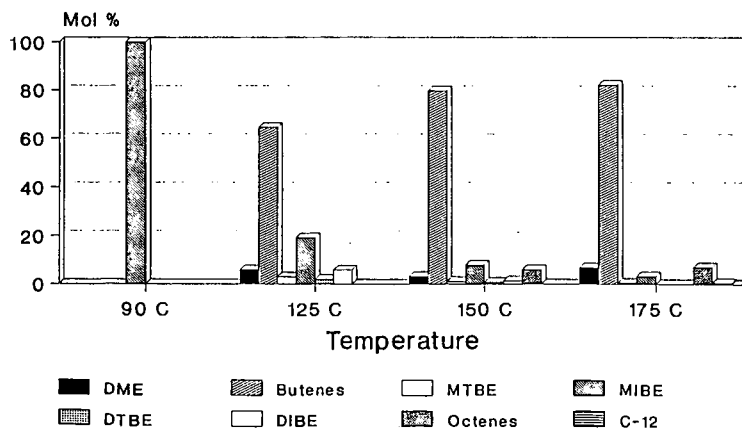


Fig. 4 Selectivity over ZrO₂/SO₄ for the methanol + isobutanol reaction at various temperatures.

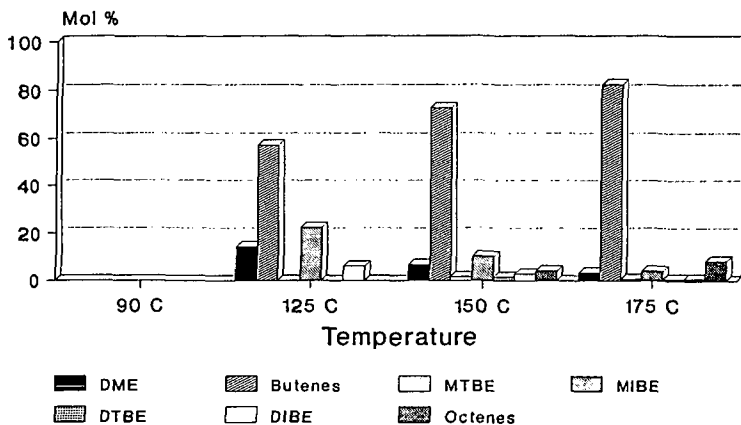


Fig. 5 Selectivity over $\text{SiO}_2/\text{Al}_2\text{O}_3$ for the methanol + isobutanol reaction at various temperatures.

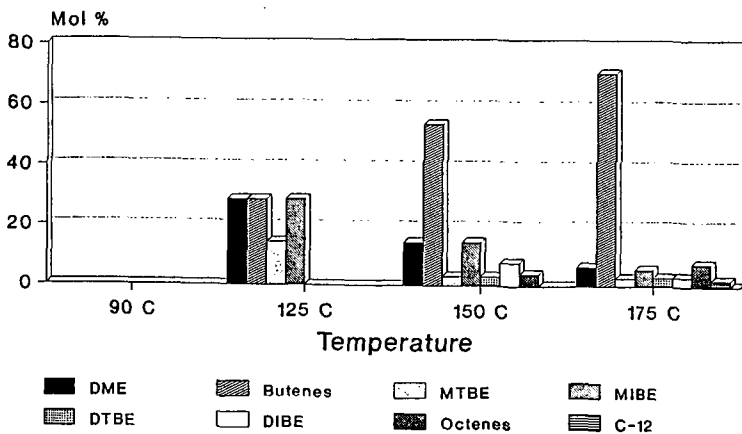


Fig. 6 Selectivity over Montmorillonite for the methanol + isobutanol reaction at various temperatures.

ISOBUTYLENE SYNTHESIS OVER ZIRCONIA AND MODIFIED ZIRCONIA USING HYDROGEN LEAN SYNTHESIS GAS

by

Rayford G. Anthony, Walter Postula, Zhentao Feng, C. V. Philip, and Aydin Akgerman
Kinetics, Catalysis and Reaction Engineering Laboratory
Department of Chemical Engineering
Texas A&M University
College Station, TX 77843-3122

INTRODUCTION

Early work on isobutylene and isobutane synthesis employed thoria based catalysts. Later isoalkenes were produced when zirconia was used at lower pressures and temperatures of 623 to 773 K. The difficultly reducible oxide catalysts such as ThO_2 (1,2) and Dy_2O_3 , (3) were used under very severe conditions. A CdO catalyst combined with acid supports was used under mild conditions. Recently, Maruya, et al.(4) and Onishi et al. (5) reported the use of ZrO_2 at mild conditions, and methoxide species and formate ions have been observed on the surface of the ZrO_2 catalysts. Maruya, et al. (6) also produced a C_4 fraction with 99% isobutylene with carbon C_4 selectivities in the range of 77 to 85%. The latter value was obtained when zirconia was impregnated with NaOH . The mechanism for formation of the branched alkanes has been postulated to be different than the mechanism for formation of linear alkanes.

Vedage et al. (7) postulated that linear products are produced by CO insertion into an alkoxide instead of an aldol-like condensation scheme in which a formyl species reacts with an enolate ($\text{RCH}_2\text{-HCHO}$) at the carbon next to the carbonyl carbon. Mazanec (8) proposed a CO insertion scheme involving a bound aldehyde to produce a cyclic acyl which has two valence structures and the carbonyl carbon in one has carbenic character. Subsequent 1,2 shifts of hydrogen or R can lead to linear or branched products. Condensations reactions between eta-enolates and alkoxides were proposed to account for deviations from the Schulz-Flory distribution. Tseng et al. (9) and Jackson and Ekerdt (10) present the results of a comprehensive study and discuss proposed mechanisms on isosynthesis using zirconia. The formation of C_4s is postulated to be by addition and condensation reactions (4,6,9,10).

This manuscript reports data on isobutylene synthesis using zirconia prepared by coprecipitation and modified sol gel procedures.

CATALYSTS SYNTHESIS AND CHARACTERIZATION

Synthesis: The two procedures used for synthesizing the catalysts presented herein were as follows: [1] Reaction of zirconyl nitrate with ammonium hydroxide which precipitates as zirconium hydroxide and is then dried and calcined at 500 °C for 2.5 hours. This catalyst is labelled Cat 1. [2] The sol gel procedures developed by Dosch et al. (11) were used to produce a sodium hydrous zirconium oxide, which was ion exchanged with HCl to remove the sodium, washed with acetone, dried and calcined at 500 °C for 4 hours. This catalyst is referred to as Cat 2.

Characterization: Differentiation between cubic zirconia and tetragonal zirconia by use of XRD has been reported to be very difficult to impossible. Cubic zirconia is normally formed at temperatures above 1200 °C except in the presence of alkali or alkaline salts. The cubic form can then be stabilized at lower temperatures. Inspection of XRD powder patterns suggests that one should be able to distinguish between the cubic and tetragonal forms. However, this is very difficult to accomplish except for highly crystalline zirconia. Catalysts prepared by procedure 1 could be made as tetragonal or monoclinic depending on the procedure used in calcination. Only the zirconia which had a monoclinic structure as indicated by an XRD powder pattern was used in this study.

The hydrous sodium zirconium oxide prepared by Dosch's method had an ion exchange capacity of approximately 4.5 meq/g. For the catalytic evaluations the sodium content was decreased to less than 0.3% using HCl exchange and then calcined at 500 °C for 4 hours. After calcination Catalyst #2 appeared to be monoclinic. Zirconia formed by this method should be more acidic than the zirconia prepared according to procedure #1.

CATALYSTS EVALUATION

Two reactor systems, one constructed by us referred to as BR1 and an AE MSBTR 900 purchased from Autoclave Engineers, were used in the evaluation of the catalysts. For both systems the catalysts were loaded and purged with nitrogen at 400 °C for 4 hours prior to conducting the activity studies. Catalytic activity data reported herein for the precipitated catalysts, Cat. #1 batches 3 and 4, were obtained in the BR1 and AE MSBTR 900, and catalytic activity data reported for Cat. #2 were obtained using the AE MSBTR 900, only. Methanol and higher alcohols were detected as product from Cat. 1 when using the AE MSBTR 900, which had on-line analysis of the products. The analysis of the product for BR1 was off-line, and no alcohols were detected in the product stream. Figure 1 illustrates the activity and effect of pressure on CO conversion for zirconia using catalysts CAT 1&2. The space time, τ , is defined as the bulk volume of the catalysts divided by the volumetric feed rate calculated at reaction conditions. The actual residence time is greater than the space time because of the decrease in the number of moles with reaction. However, at low conversions space time is a close approximation to residence time, which is dependent on the extent of reaction. Figure 1 shows that pressure does not have a significant effect on conversion at equal space times for a 1:3 or a 1:1 CO:H₂ ratio. Similarly results were obtained by Pichler and Ziesecke (1,2) for thoria catalysts. The data also indicate that Cat. #2 is not as active as Cat. #1. Figure 2 illustrates the expected trend for change in conversion with space time at 95 atm. and 400 °C and 50 atm and 425 °C. A space time of 90 seconds is required to obtain 20% CO conversion. Figure 3 illustrates the expected increase in conversion with increasing temperature for the two catalysts. The trends are the same indicating essentially the same reaction mechanism and activation energy.

In order to gain some insight into the type of reactions occurring several ratios were calculated, and are presented in Table 1. Table 1 illustrates the average values obtained for the isosynthesis profile, the branched to linear C₄s and the isobutylene selectivity within the C₄ fraction. The isosynthesis profile was defined by Jackson and Ekerdt (10) as the ratio of C₄s to (C₂s + C₃s), and is a measure of the relative importance of the condensation reactions. Ratios obtained in this study are comparable with the values reported by Jackson and Ekerdt (10).

Figures 4, 5, and 6 illustrate the effect of pressure, space time, and CO:H₂ ratio on the molar ratio of isobutylene to methane and the weight ratio of isobutylene to C₂* for Cat. #1. Figure 4 shows that for a 1:3 CO:H₂ ratio and low CO conversions (<5%) the isobutylene to

C_5^+ decreases as the pressure is increased, but the molar ratio of isobutylene to methane is essentially constant at 0.3. However, Figure 5 shows that for 95 atm and a 2:1 CO:H₂ ratio, the isobutylene to methane molar ratio varies from 0.5 to 0.75 as the CO conversion is increased with an increase in residence time. Figure 6 shows the effect of temperature and pressure on the ratio of isobutylene to C_5^+ . Low pressures and high temperatures increases the ratio.

CONCLUSIONS

The bench scale reactor systems have been successfully operated for a period of approximately one month with the collection of a substantial amount of data. The data reported above are for batches 3 and 4, Cat. 1. Data were also obtained on a catalyst prepared by catalyst preparation #2. Batches 3 and 4 for preparation of Cat. 1 were chosen because the XRD patterns and Raman spectra indicated they were predominately monoclinic, unlike the result obtained for other batches. Cat 2 was used to study the effect of acidity, and the effect of using a the modified sol gel method for preparing the catalyst. Experiments on Cat #1 in both reactor systems demonstrated the reproducibility of our experimental techniques. The activity of the zirconia catalysts are low and long residence times are required to obtain high CO conversions.

ACKNOWLEDGEMENT

This work was done as a part of the U.S. Department of Energy on "Catalysts and Process Development for Synthesis Gas Conversion to Isobutylene," Contract No. DE-AC22-90PC90045, Texas A&M Research Foundation Project No. 6722

LITERATURE CITED

1. Pichler, H., and Ziesecke, K-H., "Über die bei der Isosynthese entstehenden sauerstoffhaltigen Verbindungen, unter besonderer Berücksichtigung der Alkole," *Brennst. Chem.*, **31**, 360 (1950a).
2. Pichler, H., and Ziesecke, K-H., "The Isosynthesis," *Bur. Mines Bull.*, 488 (1950b).
3. Kieffer, R., G. Cherry, and R. E. Bacha, "Carbon Monoxide-Hydrogen Reactions. Mechanism of Isobutane Formation in Isosynthesis," *Mol. Chem.*, **2**(1), 11- 23 (1983).
4. Maruya, K., T. Maehashi, T. Haraoka, S. Narui, Y. Asakawa, K. Domen, and T. Onishi, "The CO-H₂ Reaction over ZrO₂ to Form Isobutene Selectively," *Bull. Chem. Soc. Jpn.*, **61**, 667-671 (1988).
5. Onishi, T., Maruya, K-I, Domen, K., Abe, H., and Kondo, J., "The Mechanism of CO Hydrogenation Over Zirconium Oxide Studied by FT-IR," *Catalysis: Theory to Practice*, Vol. 2 (M. J. Phillips and M. Ternan, Editors), Proceedings of the 9th International Congress on Catalysis, Calgary, (1988).
6. Maruya, K., T. Fujisawa, A. Takasawa, K. Domen and T. Onishi, "Effect of Additives on Selective Formation of Isobutene from the CO-H₂ Reaction over ZrO₂," *Bull. Chem. Soc. Jpn.*, **62**, 11-16 (1989).
7. Vedage, G. A., P. G. Himerfarb, G. W. Simmons, and K. Klier, in "Solid State Chemistry in Catalysis" Eds. R. K. Grasselli and J. F. Bradzil, ACS Symposium Series No. 279 (1985).
8. Mazanec, T. J., "On the Mechanism of Higher Alcohol Formation Over Metal Oxide Catalysts" *J. Catal.* **98**, 115 (1986).

9. Tseng, S. C., N. Jackson, and J. G. Ekerdt, "Isosynthesis Reactions of Carbon Monoxide/Hydrogen Over Zirconium Dioxide," J. Catal. 109(2), 284-297 (1988),
10. Jackson, N. B. and Ekerdt, J. G., "The Surface Characteristics Required for Isosynthesis over Zirconium Dioxide and Modified Zirconium Dioxide," J. of Catal. 126, 31-45 (1990).
11. Dosch, R.G., Stephens, H. P., and Stohl, F. V., SAND89-2400, Sandia National Laboratories, 1990.

Table 1. Isothesis Characteristics of Catalyst 1 and Catalyst 2

Weight Ratios	Catalyst 1	Catalyst 2	Jackson & Ekerdt(10)
Isosynthesis Profile ¹	4.55 ± 1.28	2.29 ± 0.79	2.30
Branched C ₄ /Linear C ₄	2.71 ± 0.67	2.97 ± 0.33	5.67
i-C ₄ H ₉ /All C ₄ s	0.63 ± 0.06	0.37 ± 0.15	0.84

¹ Defined as (total weight of C₄ hydrocarbons)/(total weight of C₂s and C₃s).

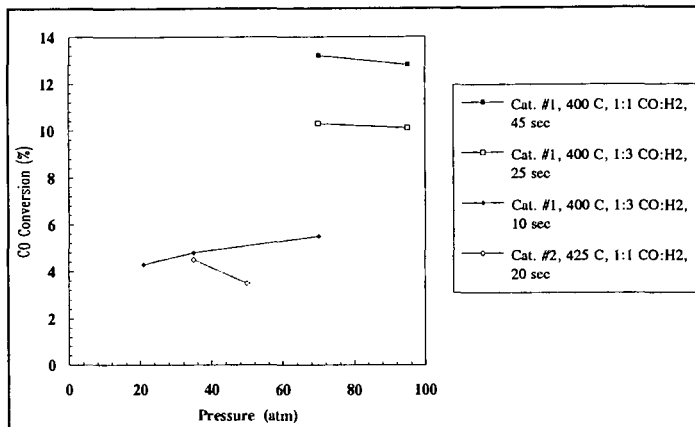


Figure 1. Effect of Pressure on Activity for Catalysts #1 and #2.

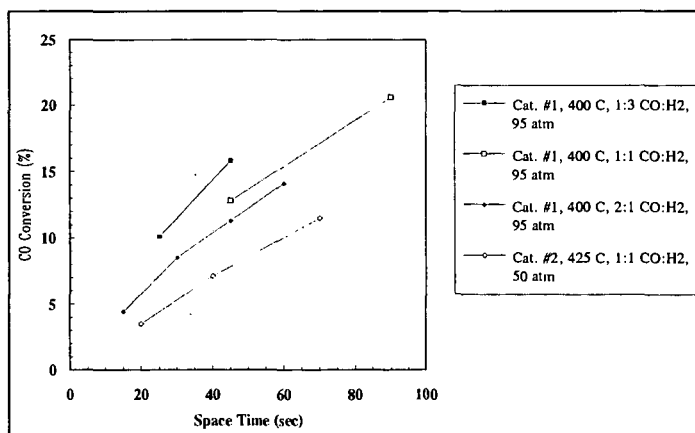


Figure 2. Effect of Space Time on Activity for Catalysts #1 and #2.

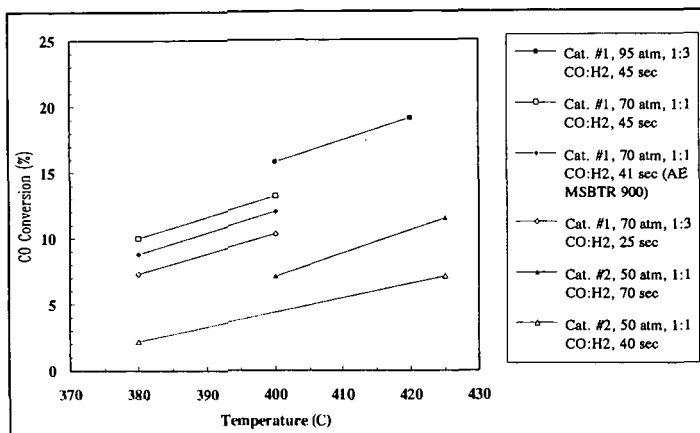


Figure 3. Effect of Temperature on Activity for Catalysts #1 and #2.

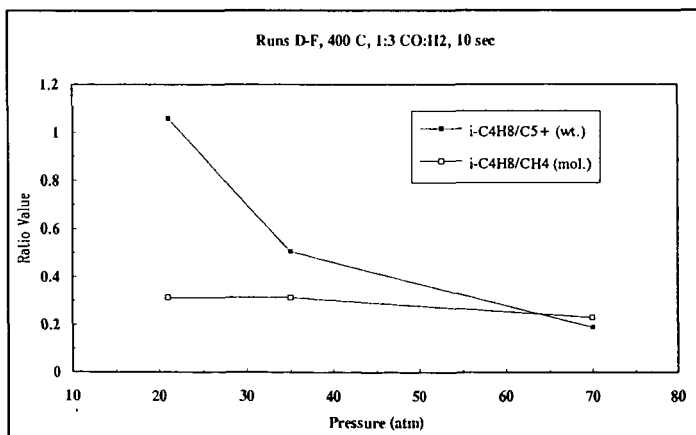


Figure 4. Effect of Pressure on Selectivities for Catalyst #1.

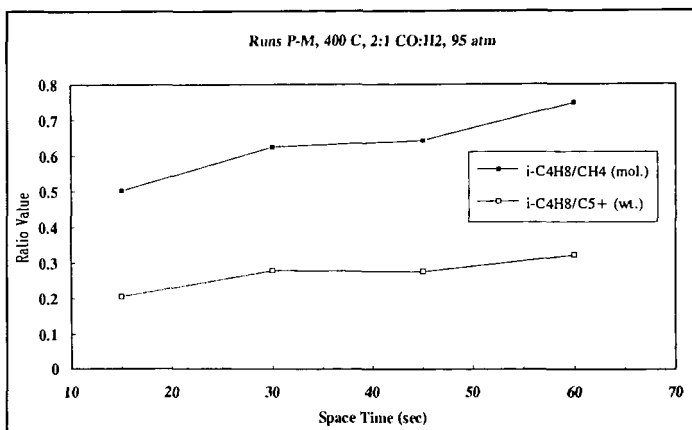


Figure 5. Effect of Space Time on Selectivities for Catalyst #1.

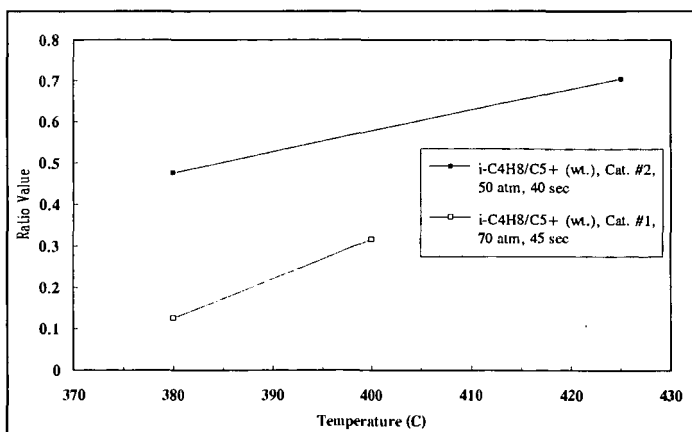


Figure 6. Wt. ratio of isobutylene/C₅+ increases with temperature for Cat. #1 and #2.

ACTIVITY, CHARACTERIZATION, AND SINTERING BEHAVIOR OF SULFATED IRON OXIDES IN LIQUEFACTION OF LOW PYRITE COALS.

V.R.Pradhan, J.W.Tierney, and I.Wender,
Chemical and Petroleum Engineering Department,
University of Pittsburgh, Pittsburgh, PA 15261.

Keywords: Highly dispersed catalysts, Direct coal liquefaction.

Abstract

The activity of small amounts of iron and molybdenum added as finely divided sulfated oxide/oxyhydroxide catalysts (FeOOH/SO_4 , $\text{Fe}_2\text{O}_3/\text{SO}_4$ and $\text{Mo}/\text{Fe}_2\text{O}_3/\text{SO}_4$) for the direct liquefaction of low pyrite bituminous (Blind Canyon) and subbituminous coals (Wyodak) is reported in this paper. The quantification of dispersion and the composition of sulfated iron oxide/oxyhydroxide catalysts before and after coal liquefaction reactions is also reported. Catalytic dispersions (such as surface area and particulate size) were determined for the oxides and oxyhydroxides of iron containing 3-4 wt% of sulfate anion as such and after their transformation from the oxide phase to the sulfides during the course of coal liquefaction. The rates of these transformations were studied at 400°C and information on the size and composition of the resulting sulfide particles was obtained. It was found that the initially added sulfated iron oxides were completely converted to pyrrhotite, Fe_{1-x}S , after only five minutes of reaction at 400°C. Fe_7S_8 , prepared by treating sulfated iron oxide with sulfur in the presence of tetralin, was also used as a catalyst for coal liquefaction and was found almost as effective as the initial sulfated iron oxide. 1000-5000 ppm of iron and 20-100 ppm of molybdenum were used in our catalytic systems with respect to coal. Molybdenum, used in small amounts, was more effective when used with the calcined form of the sulfated iron oxide than with its uncalcined form, FeOOH/SO_4 .

Introduction

Catalysis for direct coal liquefaction (especially for coal dissolution) by highly dispersed catalysts is a topic of considerable interest among researchers in this field^[1]. Application of finely divided and chemically modified powdered solid catalysts, especially those based on cheap and environmentally benign iron, is very promising^[2,4,5]. The objective of our research has been to develop novel catalytic systems based on the sulfate and molybdate anion-promoted oxides/oxyhydroxides of iron which can provide high dispersions and activity for coal liquefaction.

We have synthesized and characterized a number of sulfate-promoted oxides of metals such as Fe, Sn, Zr, Ti, and Hf.^[3] We recently reported on the use of sulfate-promoted iron and tin oxides for the direct liquefaction and coprocessing of Argonne Illinois No.6 coal with tetralin and with Maya ATB heavy oil respectively^[6,7]. The sulfate anion treatment of iron(III)oxides was found to enhance their acidic character and bring about a decrease in the particulate size. Sulfated iron oxides were also found to be active as catalysts at low iron concentrations (3500 ppm with respect to coal) for coal liquefaction. The sulfated iron oxide catalysts were completely converted to highly dispersed (average size = 15 nm) pyrrhotites (Fe_{1-x}S) under coal liquefaction conditions in the presence of enough sulfur.

In this paper, we discuss the properties and activities of a new class of sulfated catalysts. These are based on sulfated oxyhydroxides of iron, FeOOH/SO_4 and $\text{Mo}/\text{FeOOH}/\text{SO}_4$. A comparison is made between the activities of different sulfated iron oxyhydroxides promoted with molybdenum. The effects of small catalyst concentrations (20-100 ppm Mo and 1000-5000 ppm Fe) on conversion levels of a low-pyrite Blind Canyon coal were studied. An attempt was made to characterize the composition and the extent of dispersion of the sulfided catalysts obtained during coal liquefaction reactions. This includes study of the rate at which the initial sulfated metal oxide is converted to the corresponding sulfide under coal liquefaction conditions and also determination of the extent of catalyst particle agglomeration with time at reaction temperature.

Experimental

Catalyst Preparation and Characterization: The sulfated oxides and oxyhydroxides of iron were prepared from either the sulfate, chloride, or nitrate salts precipitated with either ammonia water or urea depending on whether heterogeneous or homogeneous coprecipitation routes were followed. Small amounts of molybdenum (0.5-2 wt% of the iron oxyhydroxides) were introduced into the catalysts by the incipient wetness impregnation technique from an aqueous solution of ammonium heptamolybdate. The catalysts were characterized by BET-surface area analysis, sulfur analysis, thermogravimetry (TGA), acidity measurements, thermal stability measurements, X-ray diffraction, and electron microscopy. The residues of coal liquefaction experiments were also analyzed using X-ray diffraction and a JEOL 2000 FX STEM (100 kV beam) with an energy dispersive X-ray spectrometer (EDX) to determine composition and dispersion information about the catalytic phases formed under liquefaction conditions.

Reaction Studies: The low-pyrite Blind Canyon obtained from the Penn State Coal Research Bank and Wyodak (subbituminous) obtained from the Argonne Premium Coal Sample Bank were used for these studies. Elemental analyses of the two coals are shown in Table 1. Tetralin was used as the reaction solvent (3:1 by weight to coal) and elemental sulfur (2:1 by weight to catalyst) was used for catalyst sulfidation. Coal liquefaction reactions were carried out in both a 300 cc stainless steel autoclave reactor and a 27 cc tubing bomb microreactor. Elemental sulfur was used in excess for sulfiding catalysts in situ. Soxhlet extraction with methylene chloride was used to determine coal conversion. Soluble products were recovered by rotary evaporation at 45°C under vacuum. Pentane solubles (oils) were determined by adding 40 volumes of n-pentane to the methylene chloride solubles and using Soxhlet extraction with n-pentane. Pentane-insoluble but methylene chloride soluble material was referred to as asphaltenes.

Results and Discussion

Catalyst Characterization: Specific surface areas of the sulfated iron oxyhydroxides and oxides, modified with small amounts of molybdenum, were determined by the BET method. In going from the unsulfated oxyhydroxides to the sulfated ones, surface areas increased from about 40 m^2/g to 127 m^2/g . Nitrogen adsorption porosimetry measurements indicated a bimodal distribution of the pores (essentially the void spaces between the primary crystallites). X-ray diffraction line broadening measurements and transmission electron microscopy indicated the particle size of the oxyhydroxides to be between 15-20 nm. The particles were elongated and needle-shaped. Differential thermal analysis studies of the sulfated oxyhydroxides indicated that crystallization to

the oxides occurred above 450°C. The presence of small amounts of the sulfate group in the oxyhydroxides, thus, delayed the crystallization (and therefore crystal growth) by about 150°C. Sulfated oxyhydroxides also exhibited a significant chemisorption of pyridine at high temperatures indicating a strong surface acidic character. A summary of catalyst properties is given in Table 2; the uncalcined sulfated iron oxyhydroxide has a specific surface area higher than its calcined form, sulfated iron oxide. The molybdate anion (MoO_4^{2-}), added in small amounts (3 wt% of the oxide), exhibits a similar influence on the catalyst properties as does the sulfate anion.

Reaction Studies:

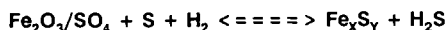
1. Effect of Reaction Temperature : The following three catalytic systems were used for the liquefaction of Argonne Wyodak coal (0.17 % pyrite) at different temperatures to determine the qualitative effect of reaction temperatures on the activities of these catalysts for coal conversion: $\text{Fe}_2\text{O}_3 + \text{S}$, $\text{Fe}_2\text{O}_3/\text{SO}_4 + \text{S}$, and $\text{Mo}/\text{Fe}_2\text{O}_3/\text{SO}_4 + \text{S}$. As shown in Figure 1, the activities of sulfated catalysts for the production of oils (n-pentane solubles) from coal increased proportionately in going from 375 to 425°C.

2. Sulfated Iron Oxyhydroxides and Molybdated Iron Oxide : The FeOOH/SO_4 and $\text{Fe}_2\text{O}_3/\text{MoO}_4$ catalysts resulted in comparable levels of coal conversion to n-pentane solubles as did the sulfated iron oxide for the liquefaction of Wyodak coal (Figure 2) under similar reaction conditions. From these results we see that the effect of anions in modifying the catalytic properties of transition metal oxides is not anion-specific so long as the modifying anion is held by the oxide surface strongly even at high temperatures. The effect of adding sulfuric acid separately with the unsulfated iron oxide was not the same as that of previously sulfated iron oxide. The combination of pure iron oxide and dilute sulfuric acid resulted in a slightly higher conversion values than the iron oxide alone, but these conversions were lower than those obtained with presulfated iron oxide.

3. Effect of Iron and Molybdenum Catalysts Loadings on Liquefaction of Low-Pyrite Blind Canyon Coal : In order to study the effect of small catalyst loadings on coal conversion levels, it was necessary to use a coal containing as low an amount of pyritic iron as possible. For this reason, Blind Canyon coal was chosen for these studies. Sulfated iron oxyhydroxide, which was found as active as the sulfated iron oxide catalyst, was employed as catalyst for the runs carried out to determine the effect of small loadings of iron on coal conversion (1000-5000 ppm with respect to coal). The results are shown in Figure 3. It can be noted from Figure 3 that the catalytic effect of added iron (as 15 nm size FeOOH/SO_4 catalyst) becomes significant only above 2500 ppm of iron with respect to coal. The incorporation of small amounts of molybdenum into this sulfated oxyhydroxide ($\text{Mo}/\text{FeOOH}/\text{SO}_4$) was not as effective for coal conversion as that in the sulfated iron oxide ($\text{Mo}/\text{Fe}_2\text{O}_3/\text{SO}_4$). The lack of high molybdenum dispersion due to the absence of a calcination treatment for the earlier catalyst might be part of the reason for its lower activity as compared with the calcined catalyst, $\text{Mo}/\text{Fe}_2\text{O}_3/\text{SO}_4$. The effect of molybdenum loadings between 20-200 ppm (with respect to coal) added with 2500 ppm Fe as $\text{Mo}/\text{Fe}_2\text{O}_3/\text{SO}_4$ is shown in Figure 4. Additional amounts of molybdenum in an already active sulfated iron oxide do not bring about significant enhancement in total coal conversions (conversions increase from about 75 % in the absence of Mo to about 80 % in its presence), but the yield of light oil (n-pentane soluble products) is significantly enhanced in the presence of small amounts of Mo. This suggests that

molybdenum, due to its strong hydrogenation function (in the form of MoS_2), helps to produce more oil at the expense of the asphaltenes.

Catalyst Transformation and Sintering Studies: It is well understood now that any iron-based catalyst precursor added at the beginning of coal liquefaction is converted to iron sulfides in the presence of enough sulfur under liquefaction conditions. The quantification of sulfided phases, thought to be catalytic, is essential for the understanding of the mode of action of the iron-based catalysts. We have made an attempt to investigate the rate of transformation (i.e. compositions of sulfides formed at different reaction times) and the extent of catalyst sintering (i.e. the degree of catalyst dispersion) of the iron-containing phases that result from addition of sulfated iron oxides during coal liquefaction. In general, the stoichiometry (or composition) of the iron phases formed during liquefaction is controlled by the following equation:



The objective here is to determine the atomic ratio (Fe/S) and the grain sizes of the iron-phases in the coal liquefaction residues using analytical tools such as X-ray diffraction and electron microscopy. The composition of the catalysts (sulfated and sulfided phases) and their sizes have been studied at different reaction times using the following model systems:

- (I) Active carbon + tetralin + $\text{Fe}_2\text{O}_3/\text{SO}_4$ catalyst
- (II) Tetralin + S + $\text{Fe}_2\text{O}_3/\text{SO}_4$ (Presulfidation)
- (III) Low-pyrite Blind Canyon coal + S + finely divided iron catalysts + tetralin

Active carbon was used instead of coal to avoid interference due to the mineral matter from coal. The reactions were carried out under identical conditions as coal liquefaction with the addition of elemental sulfur for metal sulfidation. When the reactions were carried out with a sulfated iron oxide catalyst for different reaction times, it was found that the initial sulfated iron oxide takes about five minutes at reaction temperature to convert completely to the sulfided iron phases, i.e., pyrite and finally pyrrhotites. The grain size changes occur primarily during this transformation. No further changes (increases) in the grain size of iron-containing phases was observed even when the reaction was carried out for two hours. The initially added sulfated iron oxide catalyst (particle size = 20 nm) were converted completely to pyrrhotite after five minutes of reaction (particle size = 10-50 nm). A similar transformation picture was seen when a soluble precursor of iron, $\text{Fe}(\text{CO})_5$ was used. Figure 6 shows the transmission electron micrographs of the sulfated iron oxide before and after reaction treatment as in the model system (II) indicated earlier. As shown in Figure 5, all of the initial sulfated iron oxide had been converted to pyrrhotites, primarily, Fe_7S_8 . There was no apparent increase in the grain size during this high temperature transformation. Figure 6 compares the particle sizes of the sulfided iron catalysts derived *in situ* from FeOOH/SO_4 and $\text{Fe}(\text{CO})_5$ precursors during direct liquefaction of Blind Canyon coal. The results of catalyst size and composition studies obtained using the model system (I) followed by examination of the residues by XRD, TEM, and EDX, are summarized in Table 3. Complete transformation of the initially added sulfated iron oxide catalyst to pyrrhotite occurred after five minutes at reaction temperature. The grain size change associated with this phase change was observed by electron microscopy, while particle sizes of the sulfided phases essentially remained the same without much further agglomeration or sintering for two hours of reaction time.

Conclusions

The increase in total conversion as well as the increase in conversion to oils obtained with sulfated oxides is attributed primarily to enhanced "dispersion" (surface area/gm) with possibly a small contribution, made early on, from the high surface acidity of these oxides. Due to increase in the specific surface area and decrease in the average particle size of the oxides upon addition of small amounts of the sulfate group, conversion of the oxides to active catalytic sulfide phases, especially to non-stoichiometric sulfides of iron, is facilitated. More of the active catalyst surface of these sulfides becomes available for reaction and catalyst agglomeration is decreased. Sulfated iron-based finely divided catalysts result in better catalytic dispersion than soluble precursors such as $\text{Fe}(\text{CO})_5$. Addition of small amounts of molybdenum to the sulfated iron oxides increases its activity, especially for the production of oils.

References

1. Derbyshire, F.J., Energy & Fuels, **1989**, 3, 273-277.
2. Suzuki, T., Yamada, H., Sears, P., Watanabe, Y., Energy & Fuels, **1989**, 3, 707-713.
3. Pradhan, V.R., Tierney, J.W., Wender, I., Prep. Pap., Am. Chem. Soc., Div. Fuel Chem., Vol. 35, No. 2, **1990**.
4. Cugini, A.V., Utz, B.R., Krastman, D., Hickey, R.F., Balsone, V., Prep. Pap., Am. Chem. Soc., Div. Fuel Chem., Vol. 36, No. 1, **1991**.
5. Herrick, D.E., Tierney, J.W., Wender, I., Huffman, G.P., Energy & Fuels, **1990**, 4, 231-235.
6. Pradhan, V.R., Huffman, G.P., Tierney, J.W., Wender, I., Energy & Fuels, **1991**, 5, 497-507.
7. Pradhan, V.R., Herrick, D.E., Tierney, J.W., Wender, I., Energy & Fuels, **1991**, 5, 712-720.

Table 1. Elemental Analyses of Coals (All in weight percents)

Coal	Carbon	Hydrogen	Nitrogen	Oxygen	Sulfur	Pyritic Sulfur
Wyodak	75.0	5.4	1.1	18.0	0.5	0.17
Blind Canyon	81.6	6.2	1.4	10.3	0.5	0.02

Table 2. Summary of Catalyst Characterization Before Reaction

Catalyst	Wt % SO ₄	Surface Area, m ² /g	Average Size, nm (XRD)	Average Size, nm (TEM)
Fe ₂ O ₃	0.0	26.8	46	65
Fe ₂ O ₃ /SO ₄	3.4	81.7	12	20
Mo/Fe ₂ O ₃ /SO ₄	3.1	81.5	12	20
FeOOH/SO ₄	10.2	127.0	12	25
Fe ₂ O ₃ /MoO ₄	0.0	88.0	09	15

Table 3. Results of Catalyst Transformation and Sintering Studies on Model System (I)

Reaction Time	Iron-Phases Detected	Average Particle Size (XRD)	(Fe/S) Atomic Ratio
0 min.	Fe ₂ O ₃ , Fe ₃ O ₄ , FeS ₂ , Fe _{1-x} S	14 nm	1.4
30 min.	Fe ⁰ , FeS ₂ , Fe _{1-x} S	16 nm	1.0
120 min.	Fe _{1-x} S	16 nm	0.9

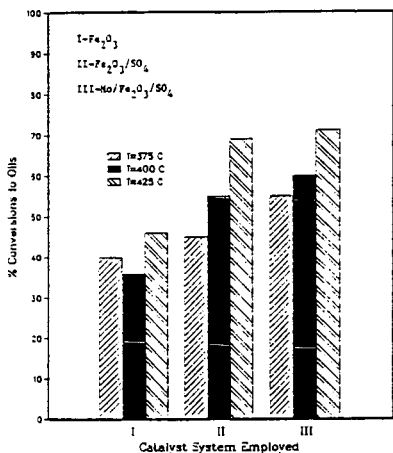


Figure 1. Activity of Sulfated Catalysts for Direct Liquefaction of Wyodak Coal at Three Reaction Temperatures

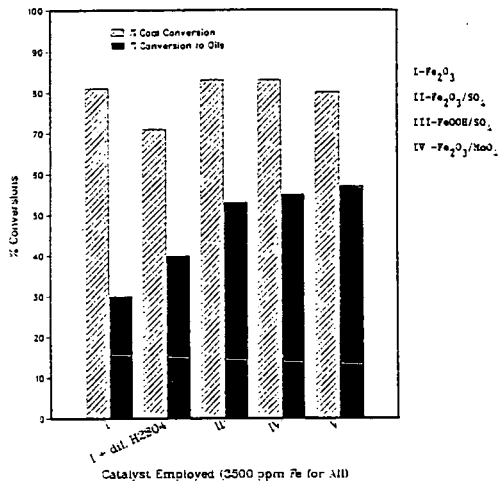


Figure 2. Activity of Oxyhydroxide and a New Molybdated Catalyst for Liquefaction of Wyodak at 400°C

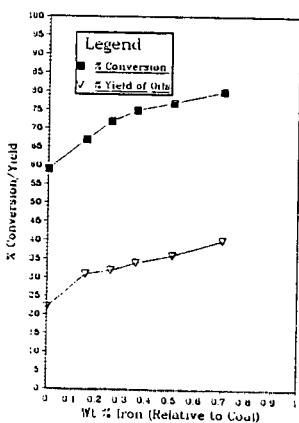


Figure 3. Conversion of Blind Canyon vs. Iron Concentration at 400°C

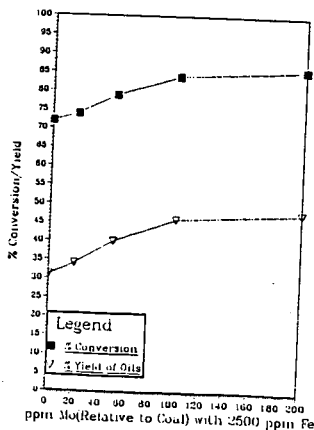


Figure 4. Conversion of Blind Canyon vs. Molybdenum Concentration at 400°C

Before Reaction-

Size = 20 nm



After Reaction-

Size = 20 nm

Fe_7S_8

$Fe_{11}S_{12}$



From $FeOOH/SO_4$

size = 10-25 nm



From $Fe(CO)_5$

size = 20-50 nm

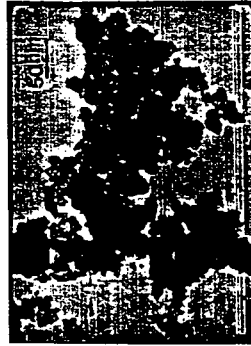


Figure 5. Sulfated Iron Oxide Catalyst: Before and After Sulfidation Reaction.

Figure 6. Dispersion of Fe-Containing Particles after Coal Liquefaction Reaction using Two Different Precursors.

CATALYTIC REACTIONS OF SULFIDED IRON- AND MIXED METAL-PILLARED CLAYS

Edwin S. Olson and Mary L. Yagelowich
Universal Fuel Development Associates, Inc.
Grand Forks, ND 58201

and

Ramesh K. Sharma
University of North Dakota Energy and Environmental Research Center
Grand Forks, ND 58202

Key words: catalysts, pillared clays, coal liquefaction

ABSTRACT

Iron-pillared montmorillonites were prepared by several methods and tested in hydrocracking and hydrogenation reactions. Rapid collection of the iron-intercalated clays was necessary for maximum activities, as was removal of residual sodium ions by exchange with ammonium ions. Calcination and sulfidation of the iron-pillared clays resulted in the formation of pyrrhotite, much of it in particles large enough to exhibit sharp XRD peaks. Thus the iron tends to migrate from its originally dispersed state, and surface area decreases with collapse of the layers. Alumina-pillaring prior to, or simultaneously with, intercalation of the iron resulted in more stable catalysts. The combined effects of clay acidity and hydrogen activation by the pyrrhotite resulted in high conversions in hydrocracking and hydrogenation tests. The presence of pyrrhotite resulted in minimal coking and condensation reactions.

INTRODUCTION

The goal of the UFDA catalyst research program is the development of disposable, highly dispersed, high surface area catalysts for the direct liquefaction of coal. These catalysts consist of sulfided iron clusters intercalated into smectite clays. The smectite clays are swelling phyllosilicate minerals, commonly found as components of soils and sediments and often found as large, mineralogically pure deposits (1). These materials are highly useful in many chemical applications because of their small particle size ($<2 \mu$), appreciable surface area for adsorption of organic molecules, and unique intercalating capabilities. Hence, they are utilized for supporting microcrystalline or metal cluster catalytic sites. Acid-modified smectites were used for a number of years as petroleum-cracking catalysts in the Houdry process, giving gasoline in high yields (1). In the mid 1960s they were replaced by more thermally stable and selective zeolite catalysts.

The use of large stable cations to pillar the aluminosilicate layers of clays results in the formation of porous networks analogous to zeolites. In these pillared clays, intercalation of hydroxylated or complexed metal cations maintains the clay layer structure after loss of water and generates a large micropore dimension. These structures are stable up to 450° to 500°C in contrast to the nonpillared clays which dehydrate and collapse at temperatures over 200°C. Acid zeolites are more stable at high temperatures; however, their pores are too narrow to be useful for coal macromolecules. The advantage of the pillared clay catalyst over the zeolites is that pore size can be controlled and made larger

than that of most of the zeolites. Therefore, these pillared clay catalysts may be more effective in cracking the large coal macromolecules than the conventional catalysts. The intent of this work is to discover how to obtain finely dispersed iron sulfide (pyrrhotite) catalytic sites in the pillared clay structure that will be useful for coal liquefaction.

RESULTS AND DISCUSSION

Initial work was concerned with preparation methods for iron-pillared montmorillonites. The sodium form of this clay disperses to an extremely fine particle size in an aqueous medium with low concentrations of base. This form was preferred for metal ion exchange reactions that give the intercalated clays, since the clay layers are highly separated in this state and mass transfer is rapid. Iron in the form of a polyoxytriiron (III) complex (heptaacetatohydroxytriiron nitrate) was exchanged for the interlayer cations of the dispersed sodium montmorillonite (2). The iron-exchanged clays were subsequently calcined to form the stable polyoxyiron cation-pillared clays. For creation of catalytic sites for activation of hydrogen, the oxyiron species were converted to sulfide forms by treatment with hydrogen sulfide or carbon disulfide.

Intercalation of polyoxytriiron resulted in a change in particle-size distribution, with a substantial portion of larger particles (78%) being formed by agglomeration of the very fine particles. A fine particle fraction was also isolated by high-speed centrifugation. Calcination of the two fractions gave materials consisting of larger particles. X-ray diffraction studies of both calcined catalyst precursor fractions showed that hematite and maghemite (both Fe_2O_3) had formed. The material from the fine clay particles contained hematite in greater abundance than that from the larger particles. The formation of these different compositions during the calcination of the iron-exchanged clays may be attributed to partial hydrolysis of the triiron clusters during washing and collection procedures. The fine particles were exposed to water for a much greater period of time. These data appear to be similar to those obtained by Lee and others (3) for pillaring with hydrolyzed ferric chloride, which indicated that hematite particles had formed. The d_{001} peak corresponding to the interlayer spacing was quite broad in the 2θ plot for both samples, indicating that spacings are irregular in the calcined products.

The difference in iron oxide composition between the calcined fine and larger particles of intercalated clay was further investigated by using a more rapid method in collection of the fine particles. X-ray diffraction of the calcined clays from the fine particles had a much smaller amount of hematite than the clay prepared by the former method. Thus the 2θ plots of catalyst precursors obtained from both the fine and larger particles in this preparation were very similar.

Methods for conversion of the oxyiron-intercalated clays to active sulfide forms were compared. Sulfidation was carried out either by heating the calcined precursor with a mixture of H_2S (100 psi) and H_2 (900 psi) in the rocking heater at 400°C for 2 hr or by in situ reaction with 40 mg of carbon disulfide that was added with the test compound, decalin solvent, or coal, depending on the reaction being carried out. The catalysts prepared by treatment with H_2S exhibited major peaks corresponding to pyrrhotite. The pyrrhotite peaks were relatively narrow, indicating that the particle size of the iron sulfide in the catalyst may be larger than desired for high catalyst activity. Sulfidation under these conditions may have mobilized the iron in the pillars so that some larger iron sulfide particle formed, as described by Lee and others (3). In contrast, the

catalysts activated by in situ treatment with CS_2 did not show significant peaks for pyrrhotite or pyrite. Since sulfidation did occur, the iron sulfide species in these catalysts must be very minute. As described below, these catalysts had superior hydrocracking activities.

When sulfidation was carried out with larger amounts of H_2S , x-ray diffraction showed that much of the iron was converted to pyrite rather than pyrrhotite. The pyrite-containing catalyst was easily converted back to the pyrrhotite form by further treatment with hydrogen at 400°C .

Surface areas of the fine particle and large particle iron-pillared clay catalysts were 156 and $181 \text{ m}^2/\text{g}$, respectively. However, on sulfiding the fine particle iron-pillared clay catalyst in H_2S and H_2 at 400°C for 2 hours, the surface area dropped to $17 \text{ m}^2/\text{g}$. The reduction in surface indicates an undesired collapse of the interlayer structure or formation of iron sulfide agglomerates.

Hydrocracking activities of iron-pillared clay catalysts were determined by reacting with bibenzyl as the test compound. Reactions were carried out at 350°C for 3 hours in the presence of 1000 psi of molecular hydrogen in a 10-ml rocking autoclave reactor. The catalysts were recovered in quantitative amounts, and no retrograde reactions or coke were observed during reactions.

Comparison of the bibenzyl hydrocracking results for the initial sulfided catalysts prepared from the fine and larger iron-pillared clay particles showed that the catalyst from the hematite-containing fines had a much lower activity (62% conversion) than the catalyst from the large particles (80% conversion). The lower activity of the catalyst from the fines was attributed to hydrolysis reactions that occurred prior to calcining. For the second batch of pillared clays that were rapidly collected, the bibenzyl hydrocracking activities of the sulfided catalysts were essentially identical for the fine and larger particles (79 and 80% conversion, respectively). This observation was consistent with the low hematite content of both precursors as demonstrated by the similar 2θ plots described above.

Examination of the products obtained from the reactions of bibenzyl with sulfided iron-pillared clays provided information on the nature of the hydrocracking activity for the catalysts. The major products were benzene, toluene, and ethylbenzene. Benzene and ethylbenzene were the largest products, and the amount of benzene was considerably more than ethylbenzene, indicating the further cracking of the ethylbenzene to benzene. These products are indicative of the Brönsted acid catalysis mechanism. The mechanism involves the ipso protonation of an aromatic ring of bibenzyl, followed by aryl-methylene bond cleavage to form benzene and phenylethyl carbonium ion. The phenylethyl carbonium ion is reduced to ethylbenzene by hydride transfer or hydrogenation, or it could undergo a variety of reactions to give other products. This reaction mechanism is common in reactions catalyzed by clays and clay-supported catalysts. The formation of toluene probably occurs via a Lewis acid catalyzed mechanism, since the temperature is too low for homolytic cleavage of the central bond in bibenzyl. Reduction of carbonium ion intermediates in the reaction may or may not involve the iron sites.

The bibenzyl cracking products included many hundreds of other components, indicative of rearrangements and hydrogen addition as well as hydrocracking. Part of the single-ring aromatics was hydrogenated to give cycloalkanes in the reactions with sulfided catalysts. A substantial amount of methylcyclohexane was formed, probably from cleavage of the tertiary carbonium ion derived from

phenylethylcyclohexane or hydrogenation of the ring-protonated bibenzyl. Minor components formed as a result of hydrocracking were propylbenzene, butylbenzene, tetralin, ethylbibenzyl, and phenylethylbibenzyl, etc. The alkylbenzene products resulted from hydrogenation of bibenzyl followed by cracking reactions, probably involving Lewis acid sites.

A second factor in determining the activity of the catalysts was the concentration of iron introduced into the clay. Use of a smaller amount of iron might result in a lower number of pillars and, consequently, result in a larger micropore volume. Exchange of one-third of the total equivalents of sodium by the triiron acetate cation rather than using an excess of the triiron gave a catalyst, after calcination and sulfidation of the large particle fraction, that was as active in hydrocracking reactions (79% conversion) as the catalyst prepared previously with excess triiron complex. The fine particle fraction had a lower activity (33% conversion).

The presence of excess sodium in the catalyst brings up a question regarding the possible loss of Brönsted acid sites due to the presence of sodium cations. The sodium ions were exchanged out of one of the clays (from the fine particles) with ammonium ions following the iron-exchange. Calcination of this precursor to drive off ammonia gave a more active catalyst (64% conversion compared with 33%), because of regeneration of the Brönsted acid sites.

A comparison of the sulfided versus nonsulfided forms of the iron-pillared clays showed that the nonsulfided forms had a much lower hydrocracking activity (36 and 40% conversions for fine and large particles, respectively). These values are consistent with those obtained for other clay supports. Major products from nonsulfided catalysts were the same as those obtained with sulfided catalysts. The major difference in activity for the nonsulfided clays was the lower conversion, lower amounts of cyclohexanes, and lower proportion of ethylbenzene. Some of the reaction products were addition products of bibenzyl that may be regarded as Friedel Crafts addition products. However, extensive condensation and coke formation were not observed in the reaction. In comparison, acidic clay catalysts gave larger amounts of condensation products. Our results indicate that iron-pillared clays are effective in cleaving aryl-methylene and other C-C bonds at lower (350°C) temperature.

A general problem with the iron-pillared clays is that the calcination and/or sulfidation treatments appear to mobilize the iron and generate particles of the iron oxide and sulfide that are larger than desired for maximum utilization of the iron. Surface areas are also substantially decreased, owing to collapse of the layer structure. The use of discrete mixed alumina/iron-pillared clays or of alumina-pillared clays as supports for pyrrhotite active sites may give a more effective particle size for the iron sites and more stable pillared structures. The aluminum pillars are stable to calcining and sulfidation treatments.

Aluminum pillars were introduced by treatment of sodium montmorillonite dispersions with the oxaluminum cation, and various methods were investigated for intercalation of the iron. Several pillared clay catalysts with discrete pillars composed of alumina and of iron oxide were prepared by intercalation of sodium montmorillonite first with oxaluminum cations and then with oxiron cations (sequential pillaring). These materials differed in the amounts of alumina and iron oxide introduced. After calcining and sulfiding with hydrogen sulfide/hydrogen mixture, these catalysts exhibited high activities, with conversions of 85 to 88% in hydrocracking tests with bibenzyl. Neither the

concentration of alumina or iron had a significant effect on the activities, and a relatively low iron concentration (500 ppm) was quite active in the tests.

A second method for preparation of the discrete pillars was utilized. In this method, the oxyaluminum cations and the oxyiron cations were added simultaneously to the sodium montmorillonite in large excess. The catalyst obtained by calcining and sulfiding as above was nearly equally effective in hydrocracking tests with bibenzyl (83% conversion). Thus either the simultaneously or sequentially mixed pillared clays gave stable clays containing effective concentrations of pyrrhotite and acidic sites for catalysis.

The third method for preparing mixed pillared clays utilized a mixed oxymetal cation complex composed mainly of aluminum with a small amount of iron. This alloy-pillaring gave a catalyst with lower activity in hydrocracking tests (72% conversion). X-ray diffraction showed that iron from the alloy pillar had been converted to pyrrhotite by the sulfidation; hence, the lower activity is probably due to some collapse of the pillared structure during this transformation of the iron.

Since the presence of sodium ions was found to exert a significant negative effect on hydrocracking conversion, one of the sequentially pillared catalysts was treated with ammonium nitrate in order to exchange out any remaining sodium ions. After calcination to volatilize the ammonia and sulfidation, the catalyst gave a slightly better conversion in the bibenzyl hydrocracking test (89%).

The method of sulfiding the iron in the mixed metal-pillared catalyst was also varied. By adding a small amount of carbon disulfide to the reaction rather than presulfiding the catalyst with hydrogen sulfide/hydrogen, a significantly higher conversion of bibenzyl was obtained (94%). The reason for higher activity is suspected to be that the pyrrhotite particle size is smaller with this method of sulfiding (see discussion above).

In addition to effective catalysis of hydrocracking reactions at moderate temperatures, the iron-pillared clays were effective catalysts for catalyzing the hydrogenation of pyrene. Hydrogenation of pyrene with a sulfided (H_2S/H_2) iron-pillared clay catalyst at 350°C for 3 hr gave an 88% conversion to hydrogenated pyrenes. The hydropyrene yields were better than those obtained with sulfided nickel molybdenum under identical conditions (69%). Conversion to the hexahydropyrenes had not proceeded very far in the latter case. A mixed metal-pillared catalyst was tested with pyrene at 400°C in the rocking microreactor with 1000 psi of hydrogen (measured at room temperature). A 68% conversion of the pyrene was obtained. The lower yield is consistent with the smaller equilibrium constant for hydrogenation at the higher temperature. Importantly, hydrocracking of the hydrogenated pyrenes was observed (20%) at the higher temperature. At 440°C, the conversion of pyrene dropped to 50%, and the yield of hydrocracked products increased slightly (23%).

Preliminary liquefaction testing with Wyodak subbituminous coal in tetralin solvent was performed using the discreet alumina/iron-pillared catalyst. The liquefaction reaction was carried out at 425°C for 1 hr in a 71-ml reactor with 1000 psi hydrogen (measured at ambient temperature). The catalyst was sulfided by adding a small amount of carbon disulfide. THF insolubles, THF solubles, and toluene solubles were measured by weighing. The pentane solubles consisted of coal-derived oil as well as tetralin solvent; therefore, the oil yield was determined by the difference between the isolatable products described above and the maf coal weight (thus the amount includes gases and reaction product water). For this reaction, yields of THF solubles were 19%, toluene solubles were 25%,

and oils/gases were 46%, with a total conversion to soluble products of 90%. The composition of the oil product was determined by gas chromatography of the pentane/tetralin solution. This analysis showed that the coal-derived oil product consisted of 9% phenolics and 25% hydrocarbons, based on maf coal. This product quality is better than previously attained with this coal in a 1-hr single-stage run. Further coal liquefaction tests are in progress.

ACKNOWLEDGEMENT

The support of the US Department of Energy is gratefully acknowledged.

REFERENCES

1. Ryland, L.B.; Tamale, M.W.; Wilson, J.N. Catalysis; Emmett, P.H. Ed.; Reinhold: New York, 1960, Vol. 7, Chap. 1.
2. Yamanaka, S.; Doi, T.; Sako, S.; Hattori, M. Mat. Res. Bull. 1984, 19, 161-168.
3. Lee, W.Y.; Raythatha, R.H; Tatarchuk, B.J. J. Catal. 1989, 115, 159-179.

Crystalline sodium or potassium silicon titanates prepared at temperatures of 200 °C or less as catalysts supports

R. G. Anthony^a, C. V. Philip^a, and R. G. Dosch^b

^aKinetics, Catalysis and Reaction Engineering Laboratory, Department of Chemical Engineering, Texas A&M University, College Station, TX 77843-3122, United States

^bSandia National Laboratories, Div. 6212, Box 5800, Albuquerque, NM 87185, United States

1. INTRODUCTION

Hydrous sodium or potassium titanium and hydrous titanium/silicon oxides have been shown to be excellent precursors in the preparation of active hydrogenation catalysts (1,2,3,4). Anthony and Dosch (5) and Anthony et al. (6) recently reported the synthesis of six new layered crystalline titanates, and the catalytic activity of Pd and sulfided NiMo supported on these titanates. TS-1, a titanium-silicalite, is a mild oxidation catalyst for epoxidation of olefins and hydroxylation of phenols and aromatics when using hydrogen peroxide as the oxidant. Zorite, a natural molecular sieve with a Si/Ti ratio of 2.6, has been synthesized by Kuznicki, USP 4,853,202. He has also synthesized molecular sieves with Si/Ti ratios in the range of 2 to 10. Young, USP 3,329,481 synthesized a Si/Ti compound (TS 26), which he called a molecular sieve, but the XRD pattern is characteristic of a layered material.

This manuscript reports the synthesis and catalytic activity of sodium and potassium silicon titanates when used as precursors in preparation of sulfided NiMo catalysts. Catalytic activity is determined by using the model reactions, hydrogenation of pyrene at 300 °C and hydrodesulfurization of dibenzothiophene at 350 °C. Stephens et al. (7,8,9) have shown that rate constants for pyrene hydrogenation correlate with ultimate catalytic activity for coal liquefaction.

2. EXPERIMENTAL

The chemicals used in the preparation of a sodium silicon titanate (TAM-1) and a potassium silicon titanate (TAM-4) were tetraisopropyl orthotitanate, tetraethyl orthosilicate, an aqueous solution of sodium hydroxide, an aqueous solution of potassium hydroxide, a solution of tetramethylammonium hydroxide (TMAOH) in methanol, and tetraalkylammonium bromide (TRAB), where the alkyl group, R, was propyl, butyl or pentyl. The synthesis procedure was in two parts. First, an aqueous mixture containing all the reagents except the alkoxides was prepared. Second, the alkoxides were mixed and then added to the aqueous mixture while stirring and a gel formed. These ingredients were transferred to a reactor, which was placed in an oven preset to the appropriate temperature. Reaction times were 90 to 96 hours. The sodium silicon titanate was recovered by filtration and washing the precipitate with water and acetone. Typical molar ratios of Na or K:TMAOH:H₂O:MeOH:TPAB:Si:Ti were 1:1.58:200:13:3:1:1 for TAM-1 and 2:0:175:0:2:1:1 for TAM-4. The procedure for preparing the sulfided nickel catalyst was the same as for the T2CT as reported by Anthony et al (6).

Activity experiments were conducted in minibatch reactors at 300 °C and 350 °C for pyrene hydrogenation and for hydrodesulfurization (HDS), respectively. The reactors were charged with 10 mg of catalysts, a solution containing 10% pyrene in hexadecane, and hydrogen pressure of 1000 psi at room temperature. The minibatch reactors were immersed in a constant temperature fluidized sand bath for a period of 15 minutes. After reaction the reactors were quenched, and the products were analyzed by gas chromatography. A similar procedure was followed for the HDS experiments, except dibenzothiophene was used instead of pyrene.

3. RESULTS AND DISCUSSION

3.1 Catalyst Characterization

The XRD patterns for TAM-1 and TAM-4 are presented in Figures 1 and 2. TAM-1 had the following properties: The first peak of the XRD was at d_0 -spacings of 1.47-1.5 nm. Other properties were surface areas of 150 to 170 m²/g, pore volumes of 0.9 to 1.0 cc/g, and a weight loss of 18 to 20% on heating for 10 hours in a vacuum at 170 °C. Weight loss on heating to 500 °C varied from 15 to 20% as compared to the 35 to 40% observed for TAM-4 and T2CT (6,7). The peaks at d_0 -spacings of 5.4, 5.2, 3.71 and 3.60 nm disappeared after evacuation for 10 hours at 170 °C. The FTIR spectra shown in Figure 3 for TAM-1 has distinct peaks, a doublet or W shaped peaks in the range of 830 to 1020 cm⁻¹. The relative intensities of the peaks at 1490 cm⁻¹ and 1640 cm⁻¹ are greater when tetrabutyl ammonium bromide is used in the synthesis compared to those when tetrapropyl ammonium bromide is used. The triplet at 4250 cm⁻¹ characteristic of quaternary ammonium compounds is present, but the absorption bands due to the primary C-H stretches are absent except when tetrapentyl ammonium bromide is used as the template. The average C:N ratio of 6 ± 1.2 obtained for TAM-1 indicates incorporation of mostly TMAOH even though the TP₃AB, TBAB, or TP₂AB was used in the synthesis. When heating TAM-1 from 100 to 500 °C, the differential scanning calorimeter (DSC) recorded exothermic regions with peaks at 260 °C (376 mw/g) and 325 °C (543 mw/g). After heating TAM-1 for four hours at 500 °C or a shorter time at 700 °C, two phases as determined by XRD and electron microscopy characteristic of titania and silica were present.

The ion exchange capacity of TAM-1 was determined by using the following procedure. A 0.1 N HCl solution was to added to a slurry of 50 mg TAM-1 in 50 ml of distilled, deionized water to maintain a pH of 3 for a period of 4 hours. Then it was filtered and rinsed with water and acetone and air dried. This procedure was repeated for the solids a second time. Eighty two percent of the sodium was removed in the first exchange and 86% of the remaining sodium was removed in the second exchange for a total sodium removal of 97.5 %. Hence, the ion exchange capacity was 4.1 meq/g, which is approximately equal to the initial sodium content (7.9 wt%).

TAM-4 had a d_0 -spacing of 0.78 nm and a distinctly different XRD pattern from TAM-1. The quaternary ammonium compounds were not incorporated into the structure as indicated by the absence of the IR peak at 1490 cm⁻¹ in the FTIR spectra (Figure 4), and the low nitrogen content (<0.09%) from the CHN analysis. When heated to 500 °C for four hours or more the samples were converted to anatase titania and silica, and the percent volatiles was 40 to 45% (based on room temperature drying). If a sample was dried at 100 °C prior to calcination the volatiles were approximately 20%. TAM-4 was prepared with KOH/Ti ratios of 1.5 to 2.7, and variation of the concentration of the quaternary compounds appeared to have little effect on the XRD patterns of the final material. The DSC for TAM-4 was endothermic over the complete temperature range with a peak at 160 °C (-545 mw/g). Surface area of the as prepared TAM-4 was 194 m²/g

Analysis for titanium and silicon were determined by AA and ICP on selected TAM-1 and TAM-4 samples. The Si/Ti atomic ratios in the products were within 5% of the Si/Ti ratio in the charge solution.

Two U. S. patents (4,938,939, July 3, 1990, and 7,853,202, August 1, 1989) were issued in 1989 and 1990 to S. Kuznicki on the synthesis of small pore and large pore crystalline titanium/silica molecular sieves. These molecular sieves represent new structures with titanium in octahedral coordination and silicon in tetrahedral coordination. The Si/Ti ratios are in the range of 2 to 10 and preferably 5. The XRD patterns and compositions of these molecular sieves are significantly different than the titanates prepared in this study. However, work by Young, USP 3,329,481, claims the synthesis of a titanium silicate molecular sieve, TS-26. Examples presented by Kuznicki on Young's

work are a TS-26/ETS-1 are more fully characterized than the samples synthesized by Young. The bar spectra in Figure 2 is the XRD spectra for ETS-1/TS-26. TAM-4 appears to be a different material than ETS-1/TS-26 since the TAM-4 contains several new peaks, and not all of the remaining peaks match the bar spectra.

A material labelled ETS-2 was also synthesized by Kuznicki, but not claimed in the patent. The same procedure was used as in preparing TS-26, but no potassium was used in the synthesis. Even though the starting mixture contained approximately 1:1 Ti:Si, the material synthesized was "almost devoid of silica," and had significant peaks at 0.875, 0.370 and 0.316 nm with relative intensities of 85, 40, and 100, respectively. Obviously, this material is different than TAM-1 or TAM-4.

3.2 Catalytic Activity

A comparison of catalytic activity for hydrogenating pyrene to dihydropyrene using sulfided Ni/Mo supported on T2CT (6), TAM-1, TAM-4, hydrous titanium oxide, and hydrous silicon titanium oxide with the commercial catalysts, Shell 324 and Amocat 1C, is shown in Table 1. The data illustrate that sulfided Ni/Mo supported on T2CT (6), TAM-1, and TAM-4 have comparable activity on an active metal basis as the commercial catalysts and the Ni/Mo-Na_{0.5}Ti amorphous catalyst, but the sulfided Ni/Mo Na_{0.5}TiSi_{0.25} amorphous catalyst has a much higher activity. For the amorphous Ti catalysts, as well as, T2CT(6), the majority (>98%) of the sodium was removed prior to loading with Mo and Ni by using 0.1 N HCl. However, TAM-1 and TAM-4 had sodium and potassium levels of 2.27% and 3.61%, respectively, prior to the loading even though ion exchange had been performed. Initial sodium and potassium levels of TAM-1 and TAM-4 varied from 8 to 12%. The ion exchange procedure used to determine the extent of exchange and the procedure used in the catalysts preparation were different. Aqueous mixtures of approximately 10% solids were used when preparing the catalysts instead of the 0.1% solids used in determining ion exchange capacity. Table 1 also illustrates the significant resistance to pore diffusion exhibited by the commercial catalysts.

The HDS activity of the TAM catalysts is shown in Table 1. The catalytic activity of TAM-1 and TAM-4 on a per gram of catalysts is considerably less than that of Shell 324. This difference is probably due to the low molybdenum loading since the activity of the TAM catalysts on a per gram of Mo basis is substantially greater than that for Shell 324. A significant difference occurs in the ratio of biphenyl to cyclohexyl benzene, which is much greater for the TAM catalysts than Shell 324 or the Sandia amorphous catalysts. The ratio also varies significantly for the TAM catalysts depending on the method of preparation.

4.0 CONCLUSION

Two new alkali silicon titanates have been synthesized which show high hydrogenation activities when used as precursors for sulfided NiMo catalysts. Based on the XRD patterns these are new materials. Even though the first reflection of TAM-4 and TS-26 and ETS-1 are the same, the remaining portion of the spectra indicates that TAM-4 is a different material. A characteristic of TAM-1 is the doublet that occurs between 830 and 1010 cm⁻¹ on the FTIR. Incorporation of template appears to be indicated by the peak at 1490 cm⁻¹ and the overtone bands at 4250 cm⁻¹.

5. ACKNOWLEDGMENTS

This work was supported by the US Department of Energy at Sandia National Laboratories under contract DE-AC04-76DP000789 and by the Sandia National Laboratories for Texas A&M Research Foundation projects 6571 and 6806.

Table 1. Comparison of Catalysts Activities for Hydrogenation of Pyrene (pyr) and Hydrodesulfurization (HDS) of Dibenzothiophene

Catalyst	Form	Mo, % ^a	Ni, % ^a	SA, m ² /g	k_{pyr} (g cat g) ⁻¹	k_{pyr} (g Mo g) ⁻¹	η pyr. hyno.	k_{HDS} (g cat g) ⁻¹	k_{HDS} (g Mo g) ⁻¹	BP/CHB
Shell 324	1/32" Extrud.	13.2	2.7	152	0.041	0.31	0.24	0.016	0.121	1.6
Shell 324	-100 Mesh	13.2	2.7	152	0.120	0.91	0.72	ND	ND	ND
Shell 324	-200 Mesh	13.2	2.7	152	0.158	1.20	0.92	0.028	0.158	1.9
Amocat 1C	1/16" Extrud.	10.7	2.4	177	0.038	0.36	0.24	ND	ND	ND
Amocat 1C	-100 Mesh	10.7	2.4	177	0.059	0.55	0.38	ND	ND	ND
Amocat 1C	-200 Mesh	10.7	2.4	177	0.155	1.45	1.0	ND	ND	ND
NiMo-Type 2 CT (Batch #50)	-100 Mesh Sulfided @ 425 °C	5.35	1.76	160 ^c	0.065	1.22	0.8 ^d	ND	ND	ND
TAM-1, SV/T = 1.1	-100 Mesh/leached @ 500 °C/sulfided @ 425 °C	2.85	0.97	160 ^c	0.027	0.94	ND	0.0085	0.30	11.9
TAM-1, SV/T = 1.1	-100 Mesh/sulfided @ 425 °C	2.85	0.97	160 ^c	0.024	0.83	ND	0.0073	0.26	3.16
TAM-4, SV/T = 1.0	-100 Mesh/leached @ 500 °C/sulfided @ 425 °C	1.93	0.65	194 ^c	0.025	1.30	ND	0.0010	0.513	12.3
TAM-4, SV/T = 1.0	-100 Mesh/sulfided @ 425 °C	1.93	0.65	194 ^c	0.026	1.36	ND	0.0084	0.43	8.3
NiMo-N ₂ O ₂ IT ^b	-100 Mesh	11.2	3.7	130	0.186	1.66	ND	0.0302	0.302	2.8
NiMo-N ₂ O ₂ ITS ₁₃₂ ^b	-100 Mesh	8.7	3.0	166	0.268	3.08	ND	0.0132	0.985	2.8

^aComposition and surface areas of as-received Amocat 1C and Shell 324. Composition of HTO and CT-based Catalysts after calcination @ 500°C. ^b These are the latest and best of the HTO-Based NiMo Catalysts. ^cPrior to ion exchange and after degassing at 150 °C for 12 hours. ^d Effectiveness Factor; Effective Diffusivities based on pyrene for Shell 324 and Amocat 1C are 6.5 (10)⁻¹² and 3.2 (10)⁻¹¹ m²/s. The effectiveness factors were calculated assuming a pseudo first order rate equation and spherical particles. ^eCalculated based on an estimate of the effective diffusivity of pyrene. ND Not determined. BP/CHB Moles of biphenyl divided by the moles of cyclohexyl benzene. A high ratio indicates efficient utilization of hydrogen.

6. LITERATURE CITED

1. Dosch, R. G., H. P. Stephens, and F. V. Stohl, U.S. Patent No. 4,511,455 (April 16, 1985).
2. Dosch, R. G., H. P. Stephens, F. V. Stohl, B. C. Bunker and C. H. F. Peden, Hydrous Metal Oxide-Supported Catalysts: Part I. A Review of Preparation Chemistry and Physical and Chemical Properties, SAND89-2399, National Laboratories, 1990.
3. Dosch, R. G., H. P. Stephens and F. V. Stohl, Hydrous Metal Oxide-Supported Catalysts: Part II. A Review of Catalytic Properties and Applications, SAND89-2400, Sandia National Laboratories, 1990.
4. Stephens, H. P., R. G. Dosch and F. V. Stohl, *Ind. & Engr. Chem. Prod. Res. Dev.*, 24, (1985) 15.
5. Anthony, R. G. and R. G. Dosch, R. G., Pages 637-646, in *Preparation of Catalysts V* Ed. G. Poncelet, P.A. Jacobs, P. Grange and B. Delmon, Elsevier Science Publishers B. V., Amsterdam (1991).6
6. Anthony, R. G., C. V. Philip and R. G. Dosch, *Catalysis Today*, In press (Originally presented at the ACS meeting in NY in August, 1991).
7. Stephens, H.P. and R. N. Chapman, *PREPRINTS, Fuel Div.*, 28(5), (1983) 161.
8. Stephens, H.P. and F. V. Stohl, *PREPRINTS, Fuel Div., ACS*, 29(6), (1984) 79.
9. Stephens, H. P. and R. J. Kottenstette, *PREPRINTS, Fuel Div., ACS*, 30(2), (1985) 345.

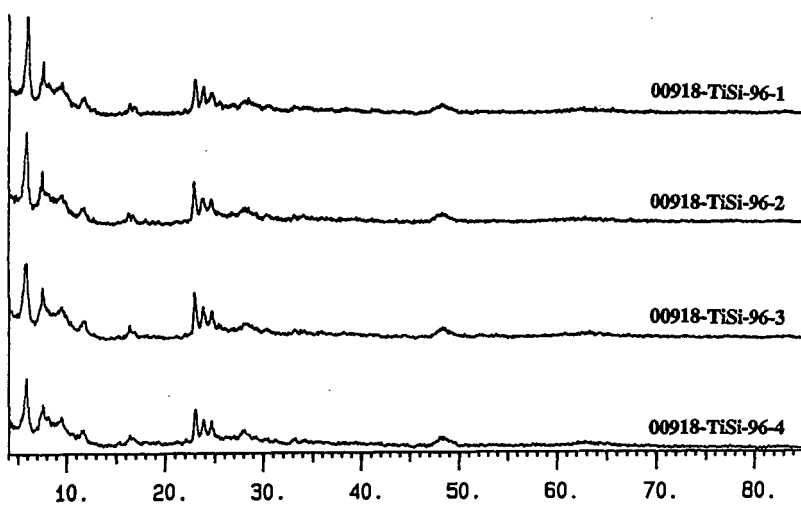


Figure 1. Comparison of XRD Patterns for TAM-1 Prepared with Different Charge Compositions.

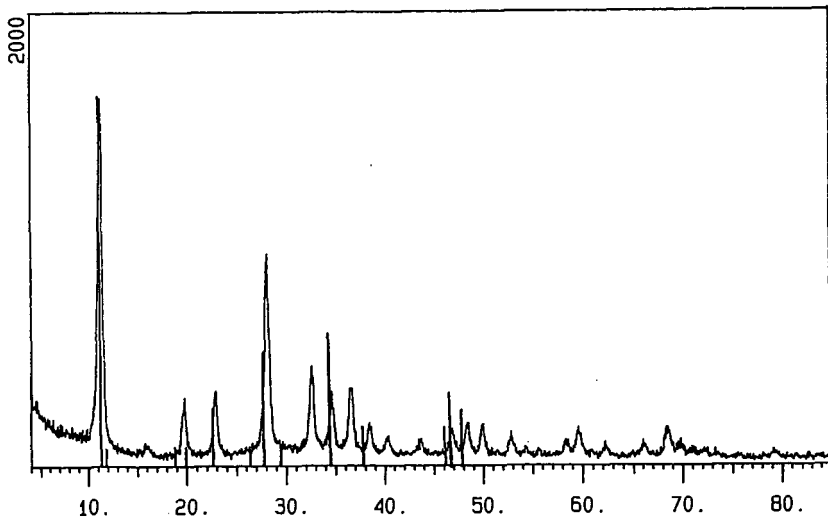


Figure 2. Comparison of XRD Powder Patterns for TAM-4 and ETS-1/TS-26 (Bars).

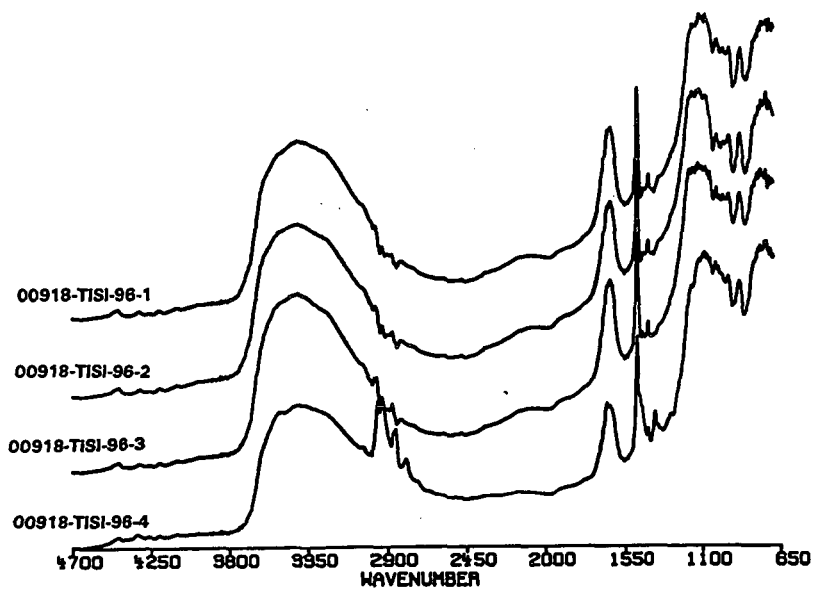


Figure 3. Comparison of FT-IR Spectra for TAM-1 Prepared Using TP₃AB and TP₅AB.

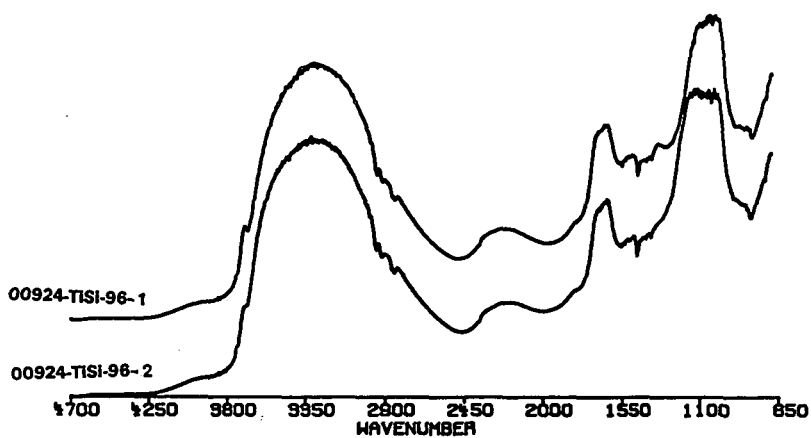


Figure 4. Comparison of FT-IR Spectra for Different Batches of TAM-4.

ETHYLATION OF TETRAHYDROQUINOLINE USING Ru/Mo BIMETALLIC CATALYST PRECURSORS SYSTEM.

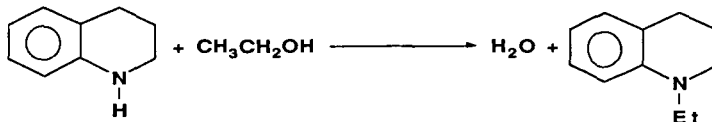
Sang-Man Koo, D. Ryan, and R. M. Laine
The Department of Materials Science and Engineering and
the Department of Chemistry, University of Michigan,
Ann Arbor, MI. 48109-2136

Keywords: Ethylation ; Tetrahydroquinoline ; Bimetallic Catalyst Precursors.

Heteropolyanions (HPAs) offer the opportunity to develop soluble forms of surface confined catalysts. HPAs are inexpensive, well-characterized, water soluble metal oxide clusters, e.g. $[EM_{12}O_{40}]^{4-}$ where E = Si or P and M = Mo or W.¹ They are easily modified to contain other transition metals such as Co, Ni or Ru and, can be made soluble in organic solvents.¹⁻³ The protic forms exhibit extremely high acidities with pK_a 's \approx 0-2.¹ In addition, selectively modified HPAs can function as low temperature hydrogenation catalysts that exhibit microporosity.⁴ HPAs are multi-functional catalysts that could be used to promote both hydroliquefaction and hydrotreating. The overall goal of the work reported here concerns our efforts to evaluate HPAs as soluble liquefaction and hydrotreating catalysts, with the goal of developing soluble analogs of surface confined catalysts.^{5,6}

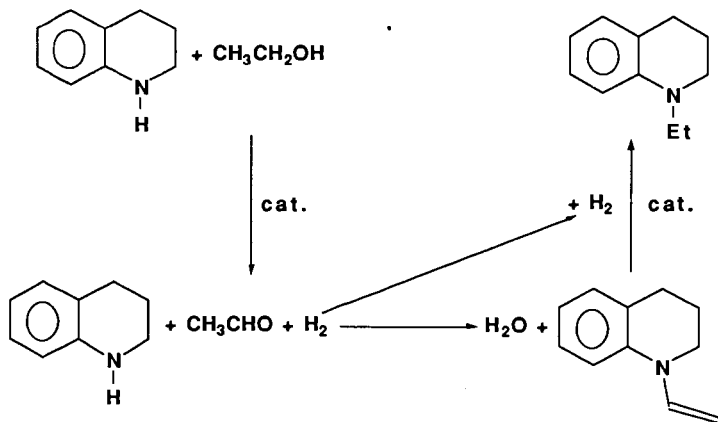
The primary purpose of the work reported here is to carefully delineate the reactivity patterns of RuMo bimetallic precatalysts. In particular, efforts were made to understand the reactivity of tetrahydroquinoline (THQ) at moderate temperatures. We have previously shown that bimetallic RuMo and trimetallic RuCoMo organometallic derived, supported catalysts will promote HDN of THQ at temperatures of 350°C.^{5,6} Thus, we were interested to determine whether or not our recently developed, unsupported RuMo catalysts would have sufficient activity to work at temperatures below 250°C.

The preliminary results of this study are quite surprising and warrant further, more detailed studies. First, we find that THQ does not undergo HDN to products such as propylaniline, propylbenzene, propylcyclohexane, nor is it hydrogenated to decahydroquinoline. However, it does undergo a surprising reaction with the ethanol solvent wherein the nitrogen is ethylated according to the following reaction:



At 220°C, this reaction goes to 40% completion in 25 h at 1000 psig H₂ using a standard bimetallic precatalyst system [4 mL EtOH stock solution, 4.39 x 10⁻⁴ M in Mo-HPA:1 mL stock solution, 5.74 x 10⁻⁴ M in RuCl₃/1.96 x 10⁻⁴ M Ru₃(CO)₁₂, 50 μL CS₂] as shown in Figures 1 and 3. What is extremely surprising about this reaction is that when it is run either with 4 mL of Mo-HPA stock solution or only 1 mL of RuCl₃ [or Ru₃(CO)₁₂] stock solution, where no synergistic effects are possible, almost no product is observed. In baseline tests, the Mo-HPA derived catalyst appears to function slightly better than the RuCl₃ derived catalyst [or nearly the same as Ru₃(CO)₁₂]. Apparently, it is necessary to have the bimetallic catalyst form in order to observe ethylation.

Another unexpected result comes from the observation that, for RuCl₃/Mo-HPA catalyst precursor system, dropping the initial H₂ pressure from 1000 psig to 400 psig does not affect the rate of reaction at all (Figure 2). At least under the two pressures measured, it appears that H₂ pressure plays no role in the rate limiting step. Based on our previous work in this area, we can suggest a mechanism that explains this observation:⁷



In this reaction scheme, the first step involves dehydrogenation of ethanol to form acetaldehyde which condenses with THQ to form the enamine, shown in the lower right hand

corner. The enamine is then readily hydrogenated to **N-Et-THQ**.

In contrast to the RuCl₃/Mo-HPA precatalyst system, the Ru₃(CO)₁₂/Mo-HPA system exhibits significant H₂ pressure dependence (Figure 4). The percent conversion rate (also TF value) reaches a maximum at 600 psig H₂ (~296 for TF and 32 for TF') as shown in Figure 4 and Table 1). The inhibition in catalyst activity observed above 600 psig H₂ is somewhat unexpected and further study will be needed.

Figure 5 and Table 2 show the effects of relative concentrations of bimetallic precatalyst on catalyst activity for **THQ** ethylation. Except at the lowest value of [Ru₃(CO)₁₂]/[Mo-HPA], increasing the relative concentration of Ru₃(CO)₁₂ results in a decrease in percent conversion and lower TF (and TF') values. Maximum TF (or TF') values are obtained when a 1 mL/4 mL(Ru/Mo) precatalyst stock solution mixture is used.

Initial rates of reaction were determined for each temperature from 220 to 250°C with initial H₂ pressures of 600 psig. Raw reaction rate data are used to calculate initial TFs which are used as k_{obs}.⁸ These data allow us to calculate the energy of activation, E_a = 27 ± 3 kcal/mole. When the reaction temperature was below 210°C, the percent conversion on to **N-Et-THQ** is much less than 1 %, even after 24 hours.

One possible conclusion as to why the bimetallic system is so much better than the individual metals is that one metal does one of the above catalytic operations well and the other poorly. The second metal then does the reverse. If this is the case, then from our hydrogenation studies, we would conclude that Mo catalyst sites are responsible for dehydrogenation and the Ru catalyst sites are responsible for hydrogenation.

In hydrotreating crude oil, oil shale and coal liquids; it is certain that primary and secondary alcohols will form during the process. Given that standard HDN catalysts contain sulfided Mo sites and Co sites, it is likely that these intermediate alcohols will alkylate any amine sources produced coincidentally. Although, Co is not as good a hydrogenation catalyst as Ru, at the elevated temperatures currently used for hydrotreating, it is possible that alkylation will occur quite readily.

Acknowledgements

We wish to thank the Department of Energy and the Pittsburgh Energy and Technology Center for generous support of this work through contract no. DE-FG22-90PC90313.

References

1. Heteropoly and Isopoly Oxometalates, M. T. Pope, Springer-Verlag Pub., Berlin, GDR,

1983.

2. R. F. Renneke and C. L. Hill, *J. Am. Chem. Soc.*, (1988) **110**, 5461.
3. R. K.C. Ho, W. G. Klemperer, *J. Am. Chem. Soc.*, (1978) **100**, 6774.
4. A. R. Siedle, R. A. Newmark, M. R. V. Sahyun, P. A. Lyon, S. L. Hunt, and R. P. Skarjune, *JACS* (1989) **111**, 8346.
5. "Bulk Ruthenium as an HDN Catalyst", A. S. Hirschon and R. M. Laine, *J. Energy and Fuels* (1988) **2**, 292-295.
6. "Use of Promoters to Enhance Hydrodenitrogenation and Hydrodeoxygenation Catalysis", A. S. Hirschon, L. L. Ackerman, R. M. Laine, and R. B. Wilson, Jr. *Proc. of the 1989 Internat. Conf. on Coal Science, Tokyo.* Vol. **II**, p. 923.
7. "Homogeneous Catalytic Cleavage of Saturated Carbon-Nitrogen Bonds." Y. Shvo, M. Abed, Y. Blum, and R. M. Laine, *Isr. J. Chem.* (1986) **27**, 267-275.
8. k_{obs} at each temperature is obtained from the slope of the equation, $d[N-Et-THQ]/dt = k_{obs}[Q]^0$, assuming zero order reaction from data obtained. The activation energy, E_a , is calculated from the expression $k_{obs} = A e^{(-E_a/RT)}$.

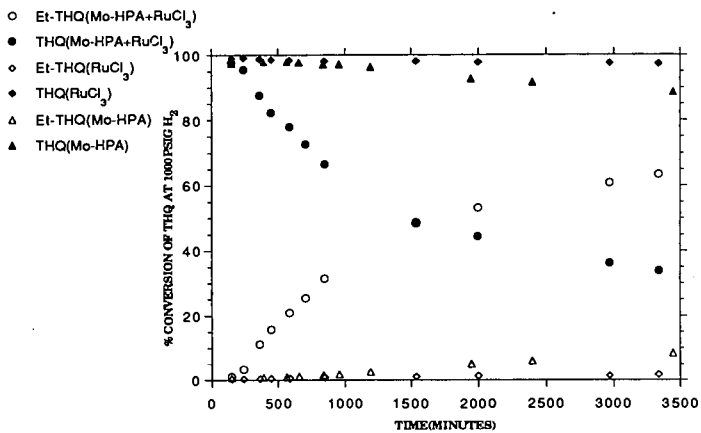


Figure 1. Percent Conversion of THQ to N-Et-THQ for Individual and Mixed Bimetallic Catalyst Precursors at 1000 Psig H₂ and 220 °C.

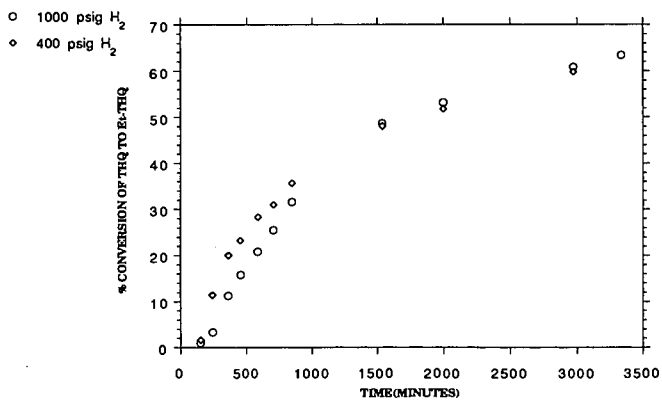


Figure 2. Percent Conversion of THQ to N-Et-THQ for Mo-HPA/RuCl₃ Bimetallic Catalyst Precursors in two different H₂ pressure at 220 °C.

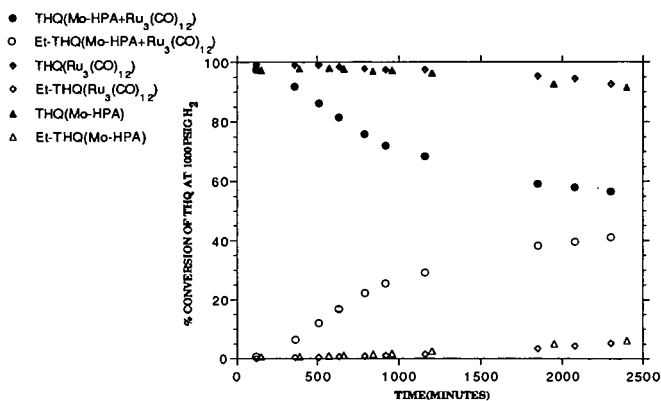


Figure 3. Percent Conversion of THQ to N-Et-THQ for Individual and Mixed Bimetallic Catalyst Precursors at 1000 Psig H₂ and 220 °C.

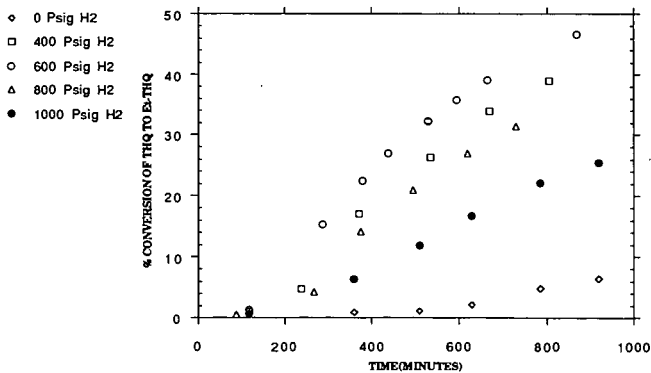


Figure 4. Percent Conversion of THQ to C₂H₅-THQ for Bimetallic Mo-HPA/Ru₃(CO)₁₂ Precatalyst at Various Pressures.

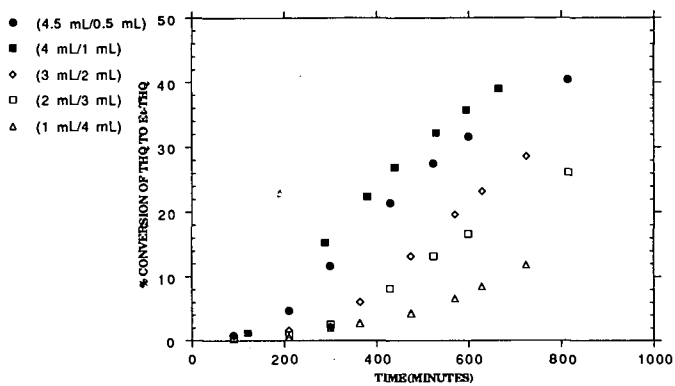


Figure 5. Percent Conversion of C_6H_8 -THQ at Different Relative Concentration of Bimetallic Catalyst Precursors.

(Mo-HIPA/Ru₃(CO)₁₂)/v, 1 mL Mo-HIPA=1.1 × 10⁻⁴ M and 1 mL Ru₃(CO)₁₂=1.98 × 10⁻⁴ M)

Table 1. Turnover Frequencies of Mixed Bimetallic Catalyst Precursors at different H₂ Pressure and 220 °C.

H ₂ Pressure	TF(Total no. of moles of catalyst precursor)	TF(Total no. of moles of Metal atoms)
0 psig	61 ± 17	7 ± 2
400 psig	221 ± 20	24 ± 2
600 psig	296 ± 14	32 ± 2
800 psig	190 ± 20	21 ± 2
1000 psig	140 ± 10	15 ± 1

*TF(TF) = no. of moles of product, N-Et-THQ/no. of moles of catalyst (or metal atoms)/h

*The total no. of moles of catalyst precursor is 6.34 x 10⁻⁶ moles [Mo-HPA/Ru₃(CO)₁₂=4.38 x 10⁻⁶/1.96 x 10⁻⁶].

*The total no. of moles of metal atoms is 5.85 x 10⁻⁵ moles (Mo/Ru=5.26 x 10⁻⁶/5.87 x 10⁻⁶).

Table 2. Turnover Frequencies of Mixed Bimetallic Catalyst Precursors at different Relative Concentration. (600 psig H₂ and 220 °C)

Relative volume (Ru/Mo) of catalyst precursor soln	Concentration	no. of moles of Ru ₃ (CO) ₁₂ catalyst precursor (x 10 ⁻⁶ moles)	no. of moles of Mo-HPA catalyst precursors (x 10 ⁻⁶ moles)	Total no. of moles of metal atoms (x 10 ⁻⁵ moles)	TF(Catalyst)	TF(Metal)
0.5 mL/4.5 mL	0.98/4.93	5.91	6.21	273 ± 38	26 ± 3	
1 mL/4 mL	1.95/4.38	6.34	5.85	236 ± 14	32 ± 2	
2 mL/3 mL	3.91/3.29	7.19	5.12	214 ± 24	30 ± 3	
3 mL/2 mL	5.87/2.19	8.06	4.39	144 ± 19	27 ± 3	
4 mL/1 mL	7.82/1.1	8.92	3.66	81 ± 15	20 ± 4	

*TF and TF's are defined as in table 1.

EXAFS Studies of Mo-Y-Zeolite Catalysts

Qiwu Wang and Dale Sayers

Department of Physics, North Carolina State University, Raleigh, NC 27695

Miming Huang, Chunhua Yuan and Shiqiang Wei

Department of Modern Chemistry, University of Science and Technology of
China, Hefei, Anhui, P. R. China

Introduction

In recent years there has been an increasing interest in molybdenum containing zeolite catalysts as effective bifunctional catalysts.¹⁻⁴ Different techniques have been used to prepare and characterize the Mo-zeolites. It is difficult to exchange the cations of a zeolite for molybdenum ions directly because high valence cationic molybdenum can only exist in very acidic solution where ion-exchange equilibria are unfavourable and many zeolites are unstable. Ion exchange with neutral and anionic species results in a large amount of surface loading. In order to overcome the difficulties of aqueous ion exchange, molybdenum is introduced into zeolites by the solid-ion exchange method. A special procedure was developed recently for initiating controlled immigration of $\text{MoO}_2(\text{OH})_2$ into the zeolite pore of HY with MoO_3 in the presence of water vapor.⁵

EXAFS is an effective physical method for determination of the local structure of specific atoms in complex systems such as highly dispersed supported metal catalysts. It has been successfully applied to some metal zeolite catalysts: viz. Pt-Y-zeolite⁶, Cd-Y-zeolite⁷ and Ni, Mo-Y-zeolite⁸ and other bimetallic catalysts⁹⁻¹⁰. However, an EXAFS study of Mo-zeolite prepared with solid-ion exchange method has not been published. In this work, we studied by EXAFS the change of the local environment around Mo in the preparation of Mo-Y-zeolite directly to see if Mo incorporated into the framework of Y-zeolites. As prepared, reduced and dehydrated samples were studied.

Experimental

Samples

The HNaY zeolite was prepared by exchange of NaY with 0.1 N NH_4NO_3 solution at 365K for 1 hour, followed by a direct calcination at 823K for 5.5 hours in a closed vessel. The modified solid ion exchange was performed as following: a mixture of 27 g HNaY and 1.2g MoO_3 was ground in a mortar

(hereafter denoted as MoHY), placed in a quartz tube and then calcined at 723K, water vapor at 323K (118 torr) was carried through the mixture using H₂ as the vector gas with a flow of 45ml/min. The sample obtained after calcination was then denoted as MoHYR. This sample then underwent dehydration at 673K (MoHYRD). The contents of the samples were then analyzed by AAS, Na contents were determined by ICP, and X-ray powder diffraction measurements were made using a Cu-target x-ray tube.

X-ray absorption measurement

X-ray absorption experiments were performed on beam line X-11A of the National Synchrotron Light Source (NSLS), Brookhaven National Laboratory. The X-ray absorption spectra for Mo K-edge were recorded with the ring operating at 2.5 GeV beam energy and a beam current of 40-180 mA. The pressed powder samples were mounted on the holder and measured at liquid nitrogen temperature in the transmission mode.

Data analysis was carried out with using standard methods¹¹ and the fitting was done using experimentally determined Mo-O (from ZnMoO₄), Mo-Mo (from metallic Mo) and theoretically calculated Mo-Si (using FEFF)¹² phase shifts and backscattering amplitudes. Both single or multiple shell models were assumed for fitting the various filtered Fourier transform (FT) peaks.

Results and Discussion

1. XAS of Mo-Y-zeolites

The normalized X-ray absorption curves of MoO₃, MoHY, MoHYR, MoHYRD and Mo metal are shown in Fig.1. The high pre-edge peak on the MoHY curve provides strong evidence for the presence of a short M=O bond characterizing MoO₃ in the mixture of MoO₃ and HY.¹³ This feature of MoO₃ almost disappears after calcination of the mixture at 723K in the presence of water vapour which means that the incorporation of Mo from MoO₃ into zeolite has taken place. XRD measurement also showed that MoO₃ diffraction peaks located at $d=6.907, 3.801$ and 3.255\AA were absent in these samples.¹⁴ Further changes of the spectrum occurred when the sample was calcined in H₂ (MoHYR) and then dehydrated (MoHYRD). The comparison between $k^3\chi(k)$ of MoO₃ and MoHYRD (see Fig.2) indicates that a great change of the environment around Mo in them clearly takes place because of the solid-ion exchange process. Further comparison of the Fourier transforms as shown in Figure 3 also show significant changes but no strong evidence for the formation of the metallic phase. From these comparisons

we assume that there is no significant change of the oxidation state of Mo after incorporation of MoO₃ into the zeolite.

2. Fitting results

Fitting to the Fourier isolated shells in each sample was done using the reference compounds cited above. A summary of the results are listed in Table 1 for the three catalysts studied as well as MoO₃. For the first three shells in MoHY, a good fit was only obtained with a short Mo=O bond along with two Mo-O bonds. Any other combination of Mo oxygen bonds had variances at least a factor of two greater than the resulted shown here. It is also consistent with the observation of the absorption profiles (Fig.1) and Fourier transforms (Fig.3) where the first Mo=O peak changed.

When Mo is incorporated into the supercages of the zeolite, fitting shows that two new longer Mo-O bonds, 2.03-2.05 Å and 2.66-2.67 Å, are formed instead of 1.70 and 1.96Å bonds in MoO₃. For the first two peaks in the FT of MoHYRD, the isolated $k^3\chi(k)$ and the fitting curve with two longer Mo-O models are overplotted in Fig.4. The agreement is excellent. It was observed previously that the longer metal-oxygen bond around 2.6 Å can be present in metal-Y-zeolites.¹⁵ The Mo-Mo interaction fitting results (see CN and R for Mo-Mo in Table 1) show that initially when Mo has been exchanged with the cationic ions in zeolite the Mo-Mo coordination is relatively large with an average Mo-Mo bond about 3.40Å but that this is significantly changed after reduction and dehydration. The Mo coordination number decreases from 6 (MoHY) to 1 (MoHYRD). This means that Mo was dispersed into the supercages of Y-zeolite, probably in octahedral clusters as [-Si-MoO₄-MoO₄-Si-]. Also a new third coordination shell around Mo in MoHYR and MoHYRD develops which is a combination of both Mo and Si(or possibly Al). The fitting of the third Fourier transform peaks in MoHYR and MoHYRD with both Mo-Mo and Mo-Si models greatly reduces the fitting variation between the experimental and calculated EXAFS data by up to 10-15 times compared to those with Mo or Si only as the neighbor. From Fig. 5 and 6, it can be seen that the two shell fitting gives the best results. The presence of Si around Mo from the zeolite framework, the decrease of the Mo-Mo coordination and the appearance of a long Mo-O bond all support the hypothesis that the solid-ion exchange method produces a Mo-substituted zeolite.

References

1. Meszaros-Kis, A. and Valyon, J., in "Zeolites as Catalysts, Sorbents and Detergent Builders" Edited by Karge H. G. and Weitkamp J., Elsevier, 1989, p.251
2. Laniecki, M., *ibid* P. 259

3. Harris, I. M., Dwyer, J., Garforth, A.A., Mc Ateer, C. H. and Ball, W. J., *ibid* P.271
4. Howe, R. F. and Huang M., *Proceeding of 9th International Conference on Catalysis, Canada, 1988*, p. 1585
5. Huang, M. and Howe, R. F., *J. Catal.* 108 (1987) 283
6. Yokoyama, T., Kosugi, N., Asakura, K., Iwasawa, Y. and Kuroda, H., *J. Physique* 47, C8-273, 1986
7. Moller, K., Eddy, M. M., Stucky, G.D., Herron, N. and Bein, T., *J. Am. Chem. Soc.*, 1989, 117, 1564
8. Clozza, A., Bianconi, A., Garcia, J., Corma, A and Buratini, E., *XAFS V* edited by Mustre de Leon, J., Stern, E. A., Sayers, D. E., Ma, Y. & Rehr, J.J., North-Holland, 1988, p.162
9. Wang Q. and Wei S., *Kehue Tongbao* 6, 435, (1990)
10. Wang Q. and Wei S., *Chinese J. Chem. Phys.* 3, 49, (1990)
11. Stern, E. A., Sayers, D. E. and Lytle, F. W., *Phys. Rev. B: Solid State* 11, 4836-4845, 1975
12. Rehr, J. J., *Physica B* 158 (1989) 1-4 (XAFS V)
13. Garner, C. D., *EXAFS and Near Edge Structure IV*, *J de Physique* 47, C8-1111, 1986
14. Huang, M., Yuan, C., Wei, S. and Wang, Q., *in press*
15. Koningsberger, D. C., *XAFS VI*, 6th International Conference on XAFS, York, 5-11 August, 1990, p.28

Table 1. Mo Coordination Shells in Mo-Y-Zeolites and Mo Trioxide

MoHY					MoO3			
Model	CN	R(Å)	DWF.10 ²	d-E ₀ (eV)	CN	R(Å)	DWF.10 ²	d-E ₀ (eV)
Mo=O	1.1±.1	1.58±.01	-0.59±.03	12.8±.5	1.0±.1	1.63±.01	-0.35±.03	12.0±1.0
Mo-O	3.4±.3	1.77±.01	-0.24±.06	-2.1±.2	2.5±.2	1.78±.01	0.27±.02	-7.0±.7
Mo-O	2.4±.2	1.98±.01	-0.56±.09	-2.1±.2	1.5±.1	1.97±.01	-0.68±.06	-2.0±.2
Mo-Mo	5.7±.2	3.36±.02	0.73±.01	3.2±.3	8.9±.8	3.48±.02	0.18±.02	-7.7±.8
Mo-O	2.5±.2	3.92±.02	-0.84±.08	-8.9±.8	7.6±.5	3.90±.02	-0.57±.05	-8.9±.9
MoHYR					MoHYRD			
Model	CN	R(Å)	DWF.10 ²	d-E ₀ (eV)	CN	R(Å)	DWF.10 ²	d-E ₀ (eV)
Mo-O	2.5±.2	2.03±.01	-0.27±.02	-7.9±.6	2.7±.2	2.05±.01	-0.23±.01	-6.7±.7
Mo-O	1.3±.1	2.67±.01	-0.52±.05	2.0±.2	1.3±.1	2.65±.01	-0.72±.01	6.6±1.0
Mo-Si	1.6±.1	3.45±.02	-0.27±.01	-10.7±.8	0.7±.1	3.45±.01	1.10±.01	-7.7±1.0
Mo-Mo	1.8±.1	3.75±.02	-0.28±.02	-5.6±.5	1.1±.1	3.75±.01	-0.22±.01	0.9±.1

Note: The experimental standard data are used for fitting: Mo-O (CN=4, R=1.78Å) from ZnMoO₄ and Mo-Mo (12, 2.73Å) from metal Mo foil.

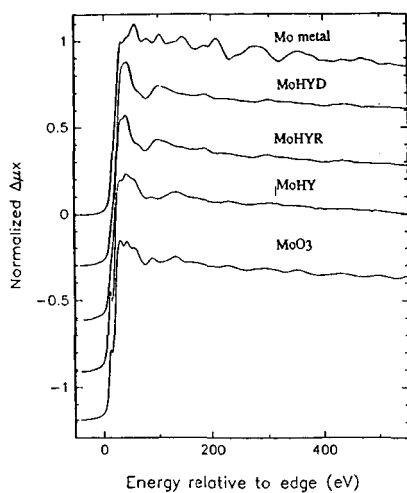


Figure 1. The normalized x-ray absorption spectrum versus energy for Mo metal, Mo in Y-zeolite which has been reduced and dehydrated as described (MoHYRD), Mo in Y-zeolite which has been reduced (MoHYR), Mo in Y-zeolite as prepared (MoHY) and MoO₃. The energy scale is relative to the binding energy of the Mo 1s state (20,000 eV).

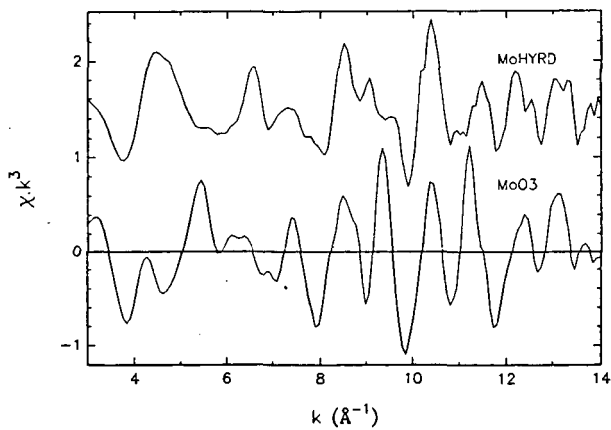


Figure 2. A comparison of the weighted spectra $k^3\chi(k)$ versus k of MoHYRD and MoO₃.

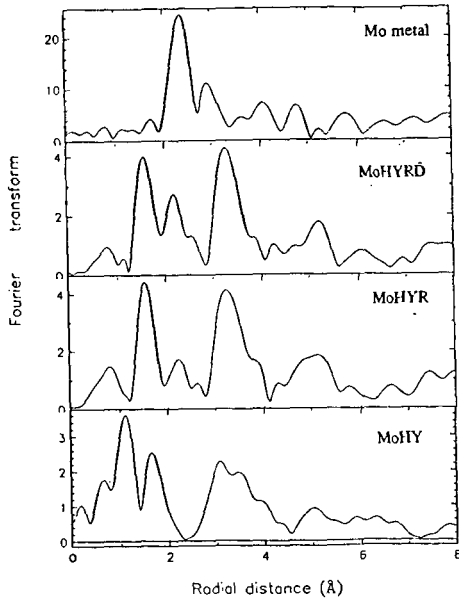


Figure 3. A comparison of the magnitudes of the Fourier transforms of the weighted EXAFS for Mo metal, MoHYRD, MoHYR, and MoHY versus R . The transforms are all of $k^3\chi(k)$ and taken over a k -space range of 3-14 \AA^{-1} .

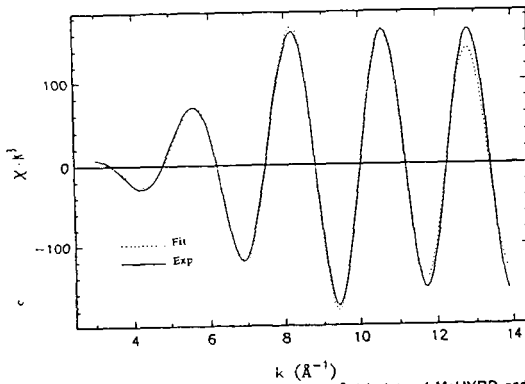


Figure 4. An overplot of the Fourier filtered $k^3\chi(k)$ data of MoHYRD and the best fitting results (see Table 1) versus r . The filtering range was from 1 to 2.8 \AA^{-1} . The fitting included two Mo-O bonds only.

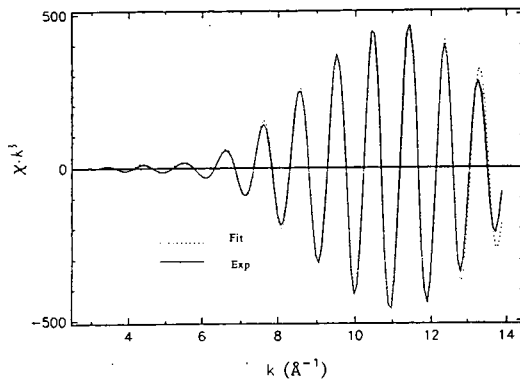


Figure 5. An overplot of the Fourier filtered $k^3\chi(k)$ third shell data of MoHYR and the best fitting results (see Table 1) versus R . The filtering range was from 2.8 to 4.1 \AA^{-1} . The fit included both Mo-Mo and Mo-Si contributions.

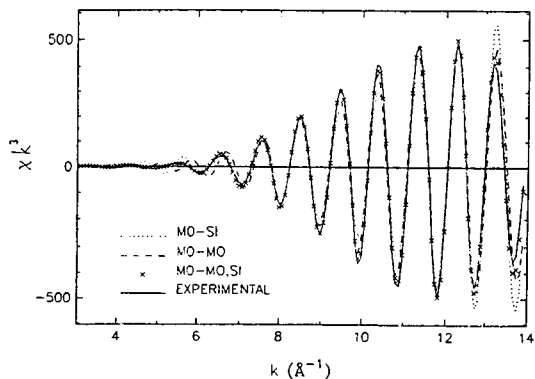


Figure 6. A comparison of the Fourier filtered $k^3\chi(k)$ third shell data of MoHYR and fits containing Mo-Mo only (---), Mo-Si only (···), and Mo-Mo and Mo-Si (xxx) versus R . The filtering range was from 2.8 to 4.1 \AA^{-1} .

HETEROPOLYANIONS, SOLUBLE PRECATALYSTS FOR QUINOLINE HYDROGENATION.

Sang-Man Koo, M.L. Hoppe, and R. M. Laine
The Department of Materials Science and Engineering and
the Department of Chemistry, University of Michigan,
Ann Arbor, MI. 48109-2136

Keywords: Heteropolyanions ; Quinoline Hydrogenation ; Bimetallic Catalyst Precursors.

Within the past two decades, inorganic chemists have developed a growing fascination for metal cluster chemistry, especially metal cluster catalysis chemistry. The sources of this fascination are the potential benefits cluster catalysis can provide to: (1) further the development and understanding of heterogeneous catalysis through modeling studies; (2) advance the development of new, industrially important, homogeneous catalysis chemistry, and (3) provide a sound basis for the development of "surface confined" metal cluster catalysis chemistry. The latter area being the translation of metal cluster catalysis chemistry to the development of new heterogeneous catalysts.

In this study, we describe initial efforts to evaluate a set of heteropolyanions (HPAs, $[EM_{12}O_{40}]^{4-}$ where E = P and M = Mo or W, Mo-HPA, W-HPA) as potential liquefaction and hydrotreating catalysts. We develop a standard set of reaction parameters for quinoline (Q) hydrogenation to tetrahydroquinoline (THQ) by delineating the effects of variations in temperature, H_2 pressure, catalyst and Q concentrations on the catalytic activity of a set of precatalysts. These standard parameters are then used to survey other potentially useful catalysts.

At the outset, it was anticipated that soluble HPAs would serve as precatalysts to the true, active species. It was also recognized that under the reaction conditions employed, the soluble HPAs might be transformed to heterogeneous species. We find that under the reaction conditions employed; the precatalysts described here, decompose to give heterogeneous catalyst particles that actively catalyze hydrogenation of Q to THQ. The following studies establish the parameters of the process leading to formation of active catalyst and define conditions used to survey of other potential catalysts.

The effects of variations in H_2 pressure (P_{H_2}) on catalyst activity are shown in Figure 1. There appears to be an almost linear relationship between H_2 pressure and catalyst activity (turnover frequency, TF).¹ Under the conditions studied, it was not possible to ascertain the P_{H_2} required to reach the falloff region, where the relationship TF/P_{H_2} is no longer linear.

Figure 2 shows the effect of total metal concentration on catalyst activity for Mo-HPA.

The highest catalyst concentration used in this study (5.5×10^{-4} M) is less than 0.02 mole percent of the Q concentration used. Within the range of catalyst concentrations studied, except at very low concentrations, there appears to be a linear relationship between catalyst concentration and TF. These results are extremely valuable because, as discussed below, the active catalyst is heterogeneous. At low metal concentrations, the linearity of the conc./TF relationship is lost because of errors in reproducibility at very low conversions.

The Figure 3 results indicate that under the reaction conditions studied, the rate of Q hydrogenation to THQ is not linearly dependent on initial Q concentration. The turnover frequency reaches its maximum (TF = 20) at [Q] = 4.23 M at [Mo-HPA] = 5.5×10^{-4} M. Considering the extremely high Q concentrations used, there are three likely explanations for the observed falloff. One is that above [Q] = 4.23 M, the reaction conditions are pseudo first order, with H₂ pressure being the only variable and the falloff above these concentrations resulting from experimental error. Alternately, at these high concentrations, Q competes successfully with H₂ for active catalyst sites thereby slowing the rate of hydrogenation. A third explanation is that at these high Q concentrations, the reaction solution composition is quite different--there is much less EtOH. Consequently, the solvation of the precatalyst changes or the decomposition mechanism and therefore the surface area of the active catalyst produced is diminished.

Initial rates of reaction were determined for each temperature from 150 to 225°C with initial H₂ pressures of 400 psig. Raw reaction rate data are used to calculate initial TFs which are used as k_{obs} .¹ These data allow us to calculate an activation energy of $E_a = 16 \pm 3$ kcal/mole.

Figure 4 indicates that the bimetallic Mo-HPA/RuCl₃·xH₂O precatalyst system offers the highest catalytic activity (TF ~ 10) of the precatalysts surveyed. The absence of catalytic activity for W-HPA and (NH₄)VO₃ were somewhat unexpected considering the modest activities of the polyoxomolybdate catalysts.

The baseline studies presented above were conducted to: (1) develop a set of standard conditions for testing HPA precatalyst systems; (2) identify promising precatalysts for further study at higher temperatures, and (3) establish hydrogenation reactivity patterns of the prospective catalyst systems. These studies were designed to answer several important questions concerning the utility of HPAs as hydrotreating and hydroliquefaction precatalysts. The questions include: (1) Do HPA derived catalysts function as heterogeneous or homogeneous catalysts?; (2) What advantages do HPAs offer over conventional catalysts?; and (3) Are polymetallic HPA derived catalysts better than conventional or monometallic HPA catalysts?

How Do HPA Derived Catalysts Function: As noted above, the HPA systems function as heterogeneous catalysts rather than homogeneous catalysts. Proof of heterogeneity comes from the fact that catalyst activation requires: (1) hydrogen reduction; (2) CS₂, and (3) an induction period (10-15 min at 200°C) prior to onset of catalyst activity. All of these components are necessary to obtain catalytic activity. In addition, once the heterogeneous catalyst has been formed, removal of all of the reaction solution (by decantation in air) followed by readdition of more Q and EtOH (but not CS₂) and repressurization to the initial H₂ pressure, gives the same catalyst activity as obtained initially--without an induction period. Thus, the heterogeneous particles formed by reduction, sulfidation and degradation of the HPAs is the true, active catalyst. One important observation is that there is a linear correlation between precatalyst concentration and catalyst activity (Figure 2). This linear relationship occurs despite the fact that catalysis occurs after conversion of the homogeneous precatalyst to the active, heterogeneous form.

It can be argued that increases in precatalyst concentration should lead to lower, relative catalyst surface areas (leading to lower TF/mole metal) as initially nucleated catalyst particles serve as growth sites for the decomposition of additional HPA molecules. Given that the correlation is linear, we presume that nucleation is a solution phase rather than a surface phenomena. Thus, all of the catalyst particles may be expected to be of approximately the same dimensions. Scanning electron microscopy supports this idea, given that the fresh catalyst particles, seen at highest magnification, are all submicron and therefore offer very high surface areas.

What Advantages Do HPAs Offer Over Conventional Catalysts: Several potential advantages are offered by HPAs relative to conventional catalysts. First, HPAs are soluble in a variety of polar and slightly polar solvents including water, MeOH, EtOH, and acetonitrile. Consequently, under liquefaction conditions, it should be possible to tailor the HPA/solvent system to optimize coal swelling and coincidentally catalyst dispersion. By comparison, conventional soluble catalysts such as ammonium heptamolybdate; which exhibits essentially the same activity as Mo-HPA (see Figure 4), is soluble only in water.

Bimetallic HPAs were also examined. Surprisingly, studies with the bimetallic precatalyst,² (NH₄)₆[Co₂Mo₁₀O₃₈H₄]·7H₂O, reveal catalytic activities somewhat less than exhibited by Mo-HPA and the heptamolybdate on a per-mol of metal basis. The most likely explanation is that the effectiveness of "CoMo" and NiMo bimetallic catalysts derives from their ability to promote C-N bond hydrogenolysis rather than hydrogenation of Q to THQ. Indeed, one could argue from our data on Mo-HPA, (NH₄)₆[Co₂Mo₁₀O₃₈H₄]·7H₂O, and the heptamolybdate that hydrogenation of Q must occur almost entirely on sulfided molybdenum sites. The bimetallic compound, (NH₄)₆[Co₂Mo₁₀O₃₈H₄]·7H₂O,² with some cobalt should

generate catalyst particles with some portion of the surface "protected" by cobalt. Consequently, if sulfided molybdenum sites are indeed responsible for hydrogenation and surface areas are comparable, one would expect the $(\text{NH}_4)_6[\text{Co}_2\text{Mo}_{10}\text{O}_{38}\text{H}_4] \cdot 7\text{H}_2\text{O}$ derived catalyst to exhibit lower TFs for Q hydrogenation, as observed.

Polymetallic HPA Precatalysts vs Conventional or Monometallic HPA Precatalysts: We have conducted one set of tests based on our previous discovery that RuMo bimetallic systems were exceptionally active HDN systems.³ Our previous studies were conducted with the objective of optimizing Ru/CoMo/ α -alumina catalysts for the HDN of Q to propylbenzene.³ It was assumed that the major function of Ru in this trimetallic system is to promote C-N bond cleavage at low temperatures. Limited efforts were made to determine the effects of ruthenium on the individual metals (Co and Mo) with the finding that a RuMo organometallic surface confined catalyst exhibits the same synergistic activity for production of propylbenzene as the trimetallic catalyst. However, no effort was made to explore the effects of Ru on Q hydrogenation activity in this catalyst system.

Figures 5 and 6 show Q to THQ conversions as a function of time for typical reactions run using Ru/Mo-HPAs bimetallic systems where Ru is introduced either as RuCl_3 or $\text{Ru}_3(\text{CO})_{12}$, and for the individual precatalysts. These Figures also show the simple sums of the conversion percentages of the individual catalysts for comparison with the true bimetallic catalysts. In both instances, the actual bimetallic catalyst offers activities some 20% higher than the sums of the two metals used individually. The results clearly point to a synergistic system. However, it is too early to speculate on the reasons for these results.

Hydrogenation Modeling Studies vs HDN Activity vs. Coal Liquefaction Behavior. The RuMo precatalyst system, which shows good Q to THQ conversion activity, was studied based on the exceptional abilities of a supported RuMo material to promote THQ HDN catalysis as previously reported from these laboratories.³⁻⁸ Although it is tempting to claim that the hydrogenation activities parallel the previously observed C-N bond hydrogenolysis activities, we believe that the parallel is coincidental. For example, both Rh and Pd catalysts are quite effective hydrogenation catalysts but exhibit only moderate HDN activity.^{9,10}

The current studies with a Ru/Mo-HPA precatalyst system works well and will be explored extensively in the future. However, this system can only serve as a baseline for liquefaction studies because the precatalyst system consists of a mixture of soluble forms of both Ru and Mo. In direct liquefaction studies, a major concern will be our ability to create the same bimetallic catalyst properties in single particles following impregnation of coal with the two independent, soluble species. We view this as unlikely with the current set of precatalysts.

Acknowledgements

We wish to thank the Department of Energy and the Pittsburgh Energy and Technology Center for generous support of this work through contract no. DE-FG22-90PC90313. We would also like to thank Dr. A. Hirschon of SRI International for helpful discussions.

References

1. k_{obs} at each temperature is obtained from the slope of the equation, $d[\text{THQ}]/dt = k_{\text{obs}}[\text{Q}]^0$, assuming zero order reaction from data obtained. The activation energy, E_a , is calculated from the expression $k_{\text{obs}} = Ae^{(-E_a/RT)}$.
2. G. Tsigdinos, Dissertation Abstract, University of Michigan, B22, 732 (1961)
3. "Modeling the Hydrodenitrogenation Reaction Using Homogeneous Catalyst Model Systems." A. S. Hirschon, R. B. Wilson, Jr.; and R. M. Laine, *New J. Chem.*, **11**, 543-547 (1987).
4. "New Catalysts for Hydrotreating Coal Liquids." A. S. Hirschon, R. B. Wilson Jr., and R. M. Laine, *Am. Chem. Soc. Div. Fuel. Prepr.* **31**, 310-317 (1986).
5. "New Approaches to Enhance Hydrodenitrogenation of Coal Liquids" A. S. Hirschon, R. B. Wilson, Jr., R. M. Laine, in Adv. in Coal Chemistry, Theophrastus Publ, Athens 1988, p 351.
6. "Ruthenium Promoted Hydrodenitrogenation Catalysts." A. S. Hirschon, R. B. Wilson Jr., and R. M. Laine, *J. Appl. Cat.* **34**, 311-316 (1987).
7. "Bulk Ruthenium as an HDN Catalyst", A. S. Hirschon and R. M. Laine, *J. Energy and Fuels* **2**, 292-295 (1988).
8. "Use of Promoters to Enhance Hydrodenitrogenation and Hydrodeoxygenation Catalysis", A. S. Hirschon, L. L. Ackerman, R. M. Laine, and R. B. Wilson, Jr. *Proc. of the 1989 Internat. Conf. on Coal Science, Tokyo.*, Vol. **II**, p. 923.
9. S-I Murahashi, Y. Imada, and Y. Hirai, "Rhodium Catalyst Hydrogenation of Quinolines and Isoquinolines under Water-Gas Shift Conditions", *Bull. Chem. Soc. Jpn.* **62**, 2968 (1989).
10. M. J. Guttieri and W. F. Maier, *J. Org. Chem.* **49**, 2875 (1984).

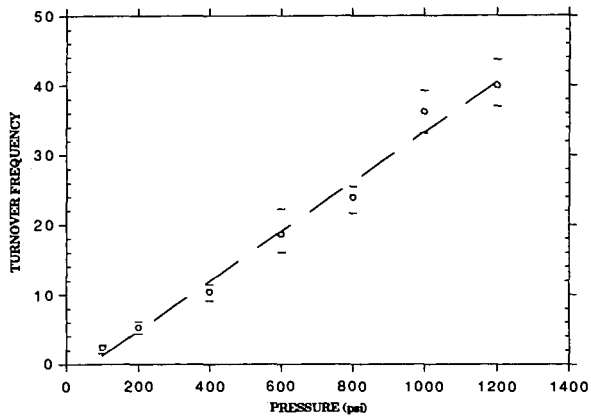


Figure 1. Turnover Frequency as a Function of Initial H_2 Pressure.
Pressures shown are measured at room temperature.

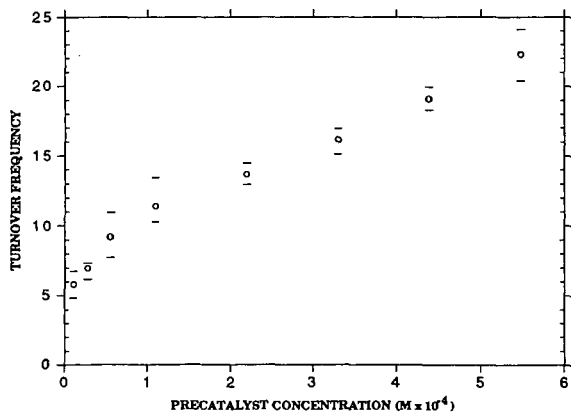


Figure 2. Turnover Frequency as a Function of $[Mo-HPA]$
Activities were determined based on less than
25% conversion of Q to THQ

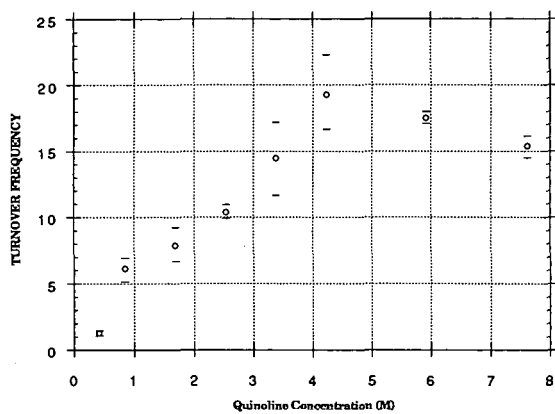


Figure 3. Turnover Frequency as a Function of Changes in [Quinoline]

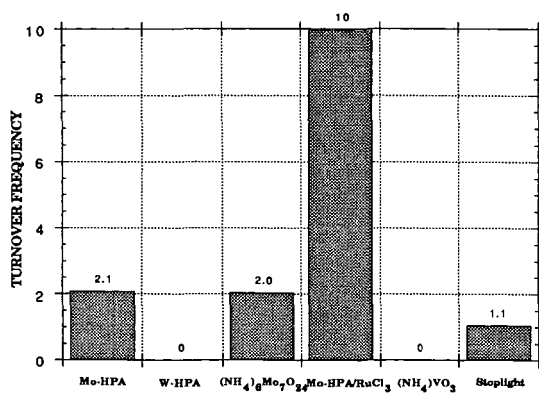


Figure 4. Initial Turnover Frequencies at 175 °C, 400 psig H₂ for Selected Precatalysts. TFs calculated based on total moles of metal. Error limits are +6%.

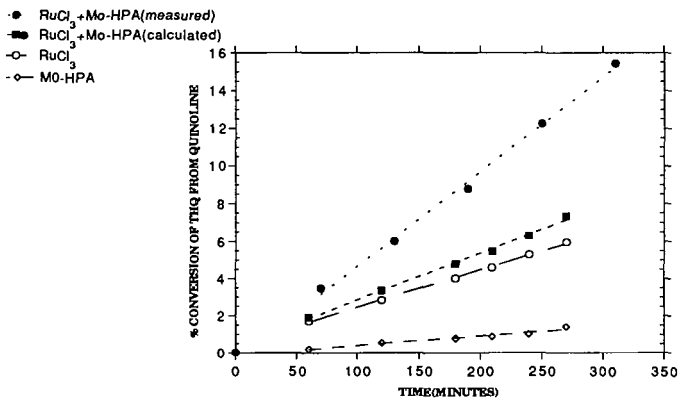


Figure 5. Percent Conversion of THQ from Quinoline for Bimetallic Precatalyst Systems (Mo-HPA, Mo-HPA/RuCl₃·3H₂O, and RuCl₃·3H₂O). Reactions run at at 175 °C, 400 psiiH₂.

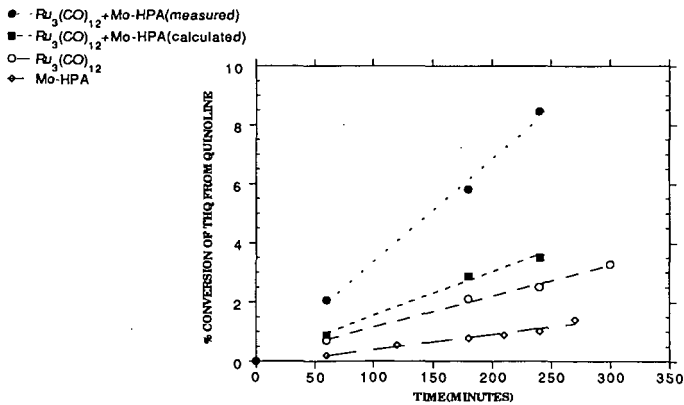


Figure 6. Percent Conversion of THQ from Quinoline for Bimetallic Precatalyst Systems (Mo-HPA, Mo-HPA/Ru₃(CO)₁₂ and Ru₃(CO)₁₂). Reactions run at 175 °C, 400 psiiH₂.

MICROEMULSION-MEDIATED SYNTHESIS OF NANOSIZE MOLYBDENUM SULFIDE COAL LIQUEFACTION CATALYSTS

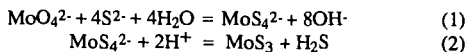
E. Boakye, N. Vaidyanathan, L.R. Radovic and K. Osseo-Asare
Department of Materials Science and Engineering
The Pennsylvania State University, University Park, PA 16802

INTRODUCTION

In heterogeneous catalysis, the size of the catalyst is of considerable importance in that the extent of reaction is often inversely proportional to the particle size of the catalyst. As a consequence, various methods have been used to synthesize particles of large specific surface area for catalysis applications (1-3). Most of these methods are based on hydrocolloids (1) and aerosols (2). Recently microemulsion-based synthesis is also attracting attention (3). Haruta et al. (1) prepared molybdenum sulfide particles in the micrometer size range by reacting ammonium molybdate and thioacetamide. Different particle sizes were obtained by varying the pH. In the preparation of iron sulfide catalysts for coal liquefaction, Andres et al. (2) used an aerosol-based method to synthesize iron oxide particles which were used *in situ* with carbon disulfide to liquefy coal. The liquefaction yield was found to be inversely proportional to the particle size. The synthesis of nanosize particles using inverse microemulsions has been reported for a variety of materials (4,5), among which are the hydrogenation catalysts nickel and cobalt borides (3), and platinum-group metals (6,7). Others worth noting are cadmium sulfide (4,8-10), copper, lead, and indium sulfides (9,11), cadmium selenide (12), silica (5), and silver halide (13,14). In this communication a microemulsion-based method for the synthesis of molybdenum sulfide nanosize particles is reported for the first time. This material is currently under active investigation as a potential coal liquefaction catalyst (15).

An inverse microemulsion is a thermodynamically stable, optically isotropic dispersion of microdrops of water in an external oil phase stabilized by a surfactant (16-18). The microemulsion systems used in this study are: polyoxyethylene(5)nonylphenylether (NP-5)/cyclohexane/water and NP-5/tetralin/benzyl alcohol/water. The latter system was used previously in this laboratory as a medium for the synthesis of silica nanoparticles (5). In these systems the water molecules interact with the hydrophilic portion of the surfactant molecules via hydrogen bonding to form inverse micelles. The addition of more water molecules results in the formation of swollen inverse micelles, often referred to as inverse microemulsions. The water pools inside the inverse micelles vary in size depending on the water-to-surfactant molar ratio (R) and are in the size range of 3-30 nm (16-18). Due to the cage-like nature of the water pools, particle growth is limited when particle precipitation is effected in them. Advantage has been taken of this unique property of inverse microemulsions to synthesize nanosize molybdenum sulfide particles in the size range 10-150 nm. The large surface area available on these nanoparticles results in a high yield of hexane-soluble oils when coal is liquefied (15).

The chemistry pertaining to the formation of molybdenum sulfide is summarized below:



The following thiomolybdate species are formed when ammonium molybdate is reacted with the sulfide ligand at a pH of 3-11: $\text{MoO}_3\text{S}^{2-}$, $\text{MoO}_2\text{S}_2^{2-}$, MoOS_3^{2-} and MoS_4^{2-} . Extensive formation of the tetrathiomolybdate ion depends on the sulfur-to-molybdenum ratio and on solution pH (19-22). As can be seen from Equation 2, molybdenum sulfide forms when an acid is added to tetrathiomolybdate species.

EXPERIMENTAL SECTION

The following chemicals were obtained from Aldrich: the non-ionic surfactant polyoxyethylene(5)nonylphenylether (NP-5), ammonium tetrathiomolybdate (99.97%), cyclohexane (99%) and 1,2,3,4-tetrahydronaphthalene (tetralin). Before use cyclohexane and tetralin were dried with molecular sieves. The inverse microemulsions NP-5/cyclohexane/water and NP-5/tetralin/benzyl alcohol/water were prepared at room temperature by adding 10% sulfuric acid to a solution of 0.134 M NP-5/cyclohexane and 0.4 M NP-5/tetralin/benzyl alcohol, respectively. The acid-solubilized microemulsion was deoxygenated by bubbling nitrogen gas through it for 20 min. This procedure was followed by adding 1×10^{-3} M and 1×10^{-2} M ammonium tetrathiomolybdate to the 0.134 M NP-5/cyclohexane and 0.4 M NP-5/tetralin/benzyl alcohol, respectively. Nitrogen was further bubbled while the molybdenum sulfide was being precipitated according to Equation 2. For the NP-5/cyclohexane/water microemulsion the concentration of the reactant species was constant with respect to the total microemulsion. On the other hand, in the case of the NP-5/tetralin/benzyl alcohol/water microemulsion, the concentration of the reactant species was maintained at a constant value with respect to the water pools.

Ultraviolet/visible spectra were obtained with a Hewlett Packard 84151A diode array spectrophotometer. Samples for transmission electron microscopy were prepared by directly dropping a very small amount of molybdenum sulfide dispersion on carbon-coated copper grids and drying at room temperature. Prior to sample extraction, each sample bottle was sonicated for 1 min. Particle sizes were determined with a Philips 420 transmission electron microscope operating at 120 kV with a resolution of about 0.6 nm. The diameters of at least 300 particles were measured for each sample to obtain an average particle diameter and standard deviation.

RESULTS AND DISCUSSION

Molybdenum sulfide nanoparticles have been synthesized successfully in the following microemulsion systems: NP-5/cyclohexane/water and NP-5/tetralin/benzyl alcohol/water. Figures 1 and 2, respectively, refer to the ultraviolet/visible absorption spectra of ammonium tetrathiomolybdate and molybdenum sulfide particles in a 0.1 M NP-5/cyclohexane microemulsion system. The microemulsions represented in these two figures contained equal amounts of 1.0×10^{-3} M ammonium tetrathiomolybdate, except that the microemulsion in Figure 2 contained 10% sulfuric acid. These two figures are different in that the absorption peaks for MoS_4^{2-} and $\text{MoO}_2\text{S}_2^{2-}$ (23) are absent in Figure 2 while a peak with an onset wavelength of about 350 nm appears. The disappearance of the peaks for the thiomolybdate species suggests that conversion (i.e., Equations 2 and 3) took place in the inverse microemulsion when the thiomolybdate species found themselves in the same inverse micelle with protons:



NP-5/Cyclohexane/Water. Figures 3 and 4, respectively, present TEM micrographs of molybdenum sulfide particles in the 0.134 M NP-5/cyclohexane/water microemulsion system and a plot of water-to-surfactant molar ratio (R) versus the average particle diameter. The average particle diameter decreases with R to a value of 2 and then increases with R. This trend may be rationalized in terms of nucleation and growth phenomena (3,4,14). The process of particle formation from dissolved ions can be represented in the following order: Ions \rightarrow Monomer \rightarrow Nuclei \rightarrow Particles (24). After a stable nucleus is formed, it can grow by the following growth processes: (a) Incorporation of ions and monomers in solution into already formed nuclei (3), and (b) aggregation of primary particles or nuclei to form bigger particles (4,14).

The nucleation and initial growth of particles takes place in the inverse micelles through collision, fusion and splitting of inverse micelles. In order to form a stable nucleus, a cluster containing a critical number of monomers (N_c) must form. A useful

parameter in this connection is that of the ion occupancy number, i.e., the number of reactant species in an inverse micelle. A nucleus is formed if the ion occupancy number is greater than N_c . As the water-to-surfactant molar ratio is decreased, the surfactant aggregation number decreases (25,26) and the micellar concentration increases. This corresponds to a decrease in the ion occupancy number because the concentrations of the reactant species (MoS_4^{2-} and H^+) in the microemulsion are constant. For low R values, relatively fewer water cores will therefore contain the minimum number of ions required to form a nucleus. As a result, the ions left over after the nucleation process are relatively large. These ions will be incorporated into the already formed nuclei via inter- and intramicellar communication and will contribute to growth, leading to large particles, as demonstrated by the top left side of Figure 4.

As R increases, the aggregation number increases, the micellar concentration decreases, and therefore the ion occupancy number increases. The observed decrease in particle size with increase in R below $R=2$ can be attributed to the increase in ion occupancy number with R. From nucleation theory, the greater the number of nuclei in the inverse microemulsion, the smaller the particle size. This is because there will be relatively few ions left over after the nucleation process, i.e., almost all the ions are used up in the nucleation process.

At $R>2$ the proportion of water in the microemulsion is relatively large, hence the aggregation number is large and the concentration of swollen inverse micelles (water pools) is significantly reduced. As a first approximation, if only one nucleus forms in a water pool, then the decrease in the number of water pools corresponds to a decrease in the number of nuclei that transform into primary particles; hence, there is an increase in the concentration of excess ions which are not utilized in the nuclei formation and are therefore available for particle growth.

NP-5/Tetralin/Benzyl Alcohol/Water. The microemulsion system consisting of NP-5/tetralin/benzyl alcohol has an inherent advantage for coal liquefaction in that tetralin is an excellent process solvent and hence the need to harvest the particles from the synthetic medium can be avoided. Figures 5 and 6 represent respectively the TEM micrograph and a plot of the average particle size versus the water-to-surfactant molar ratio (R) in the 0.4 M NP-5/tetralin/benzyl alcohol/water microemulsion. The particle size decreases with increasing R to a value of 2, and then increases with R. The trend in Figure 6 can be explained in an analogous manner to that observed in Figure 4. In this system two factors, i.e., the water-to-surfactant molar ratio (R) and reactant concentration, increased the ion occupancy number simultaneously.

CONCLUSIONS

Nanosize molybdenum sulfide particles have been synthesized in 0.134 M NP-5/cyclohexane/water and 0.4 M NP-5/tetralin/benzyl alcohol/water microemulsions. The particle size varies with the water-to-surfactant molar ratio. The synthesis of molybdenum sulfide using tetralin as a solvent has potentially important technological applications since catalyst preparation does not involve particle harvesting. Advantage can be taken of the variation of particle size with the water-to-surfactant molar ratio (R) to make particles of desired sizes for coal liquefaction. It should be mentioned that liquefaction tests conducted so far have given high yields of hexane-soluble oils and the yield of oils has been found to be inversely proportional to particle size (15).

ACKNOWLEDGEMENT

This work is being supported by the Department of Energy, Contract No. DE-AC22-90PC90054.

REFERENCES

1. M. Haruta, J. Lemaitre, F. Delannay and B. Delmon, *J. Coll. Interf. Sci.* **101**, 59 (1984).
2. M. Andres, H. Charcosset, P. Chiche, L. Davignon, G. Djega-Mariadassou, J.P. Joly and S. Pregermain, *Fuel* **62**, 69 (1983).
3. I. Ravet, J.B. Nagy and E.G. Derouane, in "Preparation of Catalysts IV," Elsevier (B. Delmon, P. Grange, P.A. Jacobs and G. Poncelet, Eds.), 1987, p. 505.
4. T.I. Towey, A. Khan-Lodhi and B.H. Robinson, *J. Chem Soc. Faraday Trans.* **86**, 3757 (1990).
5. K. Osseo-Asare and F.J. Arriagada, *Coll. Surf.* **50**, 321 (1990).
6. M. Boutonnet, J. Kizling and P. Stenius, *Coll. Surf.* **5**, 209 (1982).
7. A. Claerbout and J.B. Nagy, in "Preparation of Catalysts V," Elsevier (G. Poncelet, P.A. Jacobs, P. Grange and B. Delmon, Eds.), 1991, p. 705.
8. C. Petit and M.P. Pileni, *J. Phys. Chem.* **98**, 2282 (1988).
9. P. Lianos and J.K. Thomas, *Mater. Sci. Forum* **25-26**, 369 (1988).
10. S. Modes and P. Lianos, *J. Phys. Chem.* **93**, 5854 (1989).
11. T. Dannhausser, M. O'Neil, K. Johansson, D. Whitten and G. McLendon, *J. Phys. Chem.* **90**, 6074 (1986).
12. M.L. Steingerwald, A.P. Alivisatos, J.M. Gibson, T.D. Harris, R. Kortan, A.J. Muller, A.M. Thayer, T.M. Duncan, D.C. Douglas and L.E. Brus, *J. Am. Chem. Soc.* **110**, 3046 (1988).
13. M. Dvolaitzky, R. Ober, C. Taupin, R. Anthore, X. Auvray, C. Petipas and C. Williams, *J. Dispers. Sci. Technol.* **4**, 29 (1988).
14. M.I. Hou and D.O. Shah, in "Interfacial Phenomena in Biotechnology and Materials Processing" (Y. Attia, B.M. Moudhil and S. Chander, Eds.), Elsevier, 1988, p. 443.
15. N. Vaidyanathan, E. Boakye, K. Osseo-Asare and L.R. Radovic, *ACS Preprints, Fuel Chem. Div.* (San Francisco, 1992), in press.
16. J.H. Fendler, *Chem. Rev.* **87**, 877 (1987).
17. B. Lindman, P. Stilbs and M.E. Moseley, *J. Coll. Interf. Sci.* **83**, 569 (1981).
18. S.E. Friberg and P. Bothorel (Eds.), *Microemulsions: Structure and Dynamics*, CRC Press (Boca Raton, FL), 1987.
19. J. Prasilova and J. Burclova, *Radiochem. Radioanal. Lett.* **11**, 351 (1972).
20. V. Yatirajam, U. Ahuja and L.R. Kakkur, *Talanta* **23**, 819 (1976).
21. N.J. Clarke and S.H. Laurie, *J. Inorg. Biochem.* **12**, 37 (1980).
22. M.A. Hammer and A.G. Sykes, *Inorg. Chem.* **19**, 2881 (1980).
23. P.J. Aymonino, A.C. Ranade, E. Diemann and A. Muller, *Z. Anorg. Allgem. Chem.* **371**, 300 (1969).
24. A.E. Nielson, *Kinetics of Precipitation*, MacMillan, New York, 1964.
25. A. Veerbek, E. Gelade and F.C. De Schryver, *Langmuir* **2**, 448 (1986).
26. J.C. Railey and M. Buzier, *J. Coll. Interf. Sci.* **116**, 30 (1987).
27. J.B. Nagy, A. Gourgue and E.G. Derouane, *Stud. Surf. Sci. Catal.* **16**, 93 (1983).

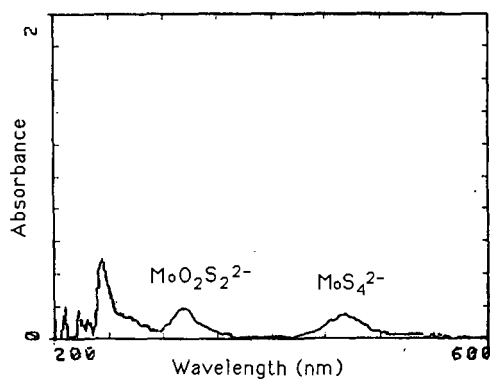


Figure 1. Absorption spectrum of 1×10^{-3} M thiomolybdate species in 0.1 M NP-5/cyclohexane/water microemulsion, $R=3$. (The concentration of the thiomolybdate species is with respect to the water pool volume.)

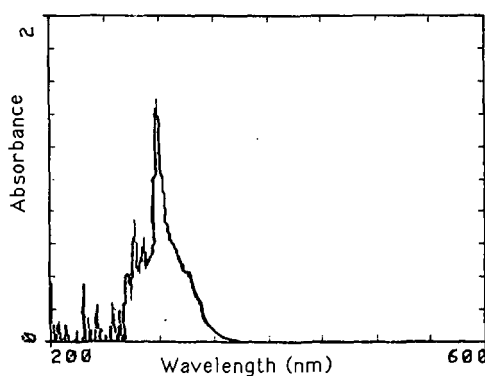


Figure 2. Absorption spectrum of molybdenum sulfide in 0.1 M NP-5/cyclohexane/water microemulsion, $R=6$, $[\text{MoS}_4^{2-}] = 1 \times 10^{-3}$ M. (The concentration of thiomolybdate species is with respect to the water pool volume.)

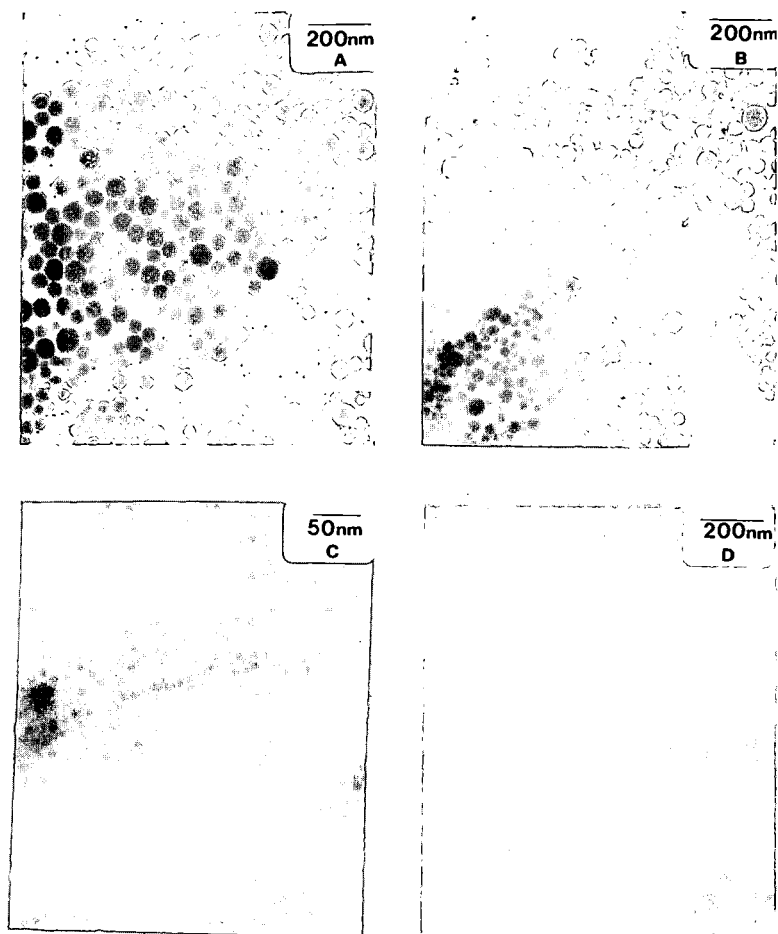


Figure 3. TEM micrographs of molybdenum sulfide particles prepared in 0.134 M NP-5/cyclohexane/water microemulsions: (A) R=1; (B) R=1.5; (C) R=2; (D) R=3.

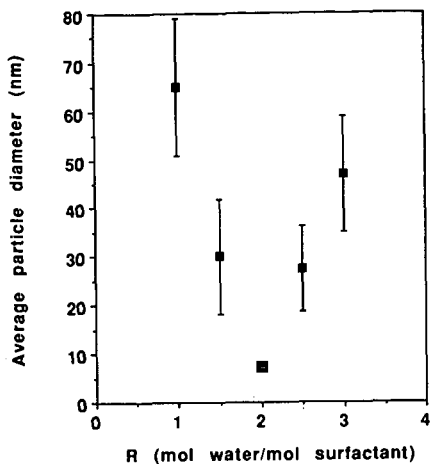


Figure 4. Effect of water-to-surfactant molar ratio (R) on average particle size for the 0.134 M NP-5/cyclohexane/water microemulsion. (The concentration of reactant species is constant with respect to the microemulsion.)

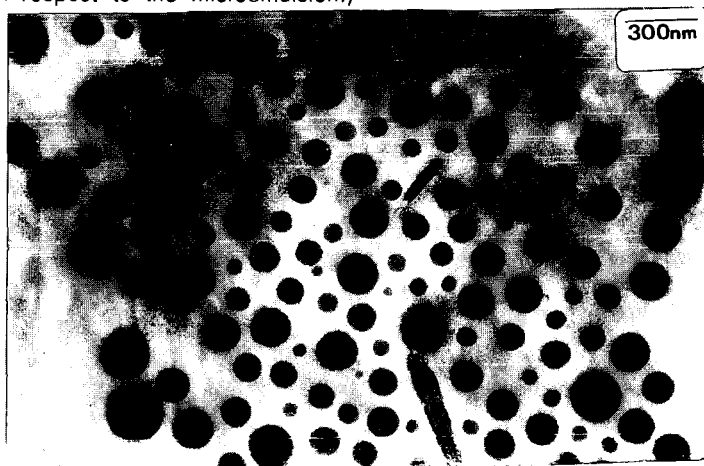


Figure 5. TEM micrograph of molybdenum sulfide prepared in 0.4 M NP-5/tetralin/benzyl alcohol microemulsion.

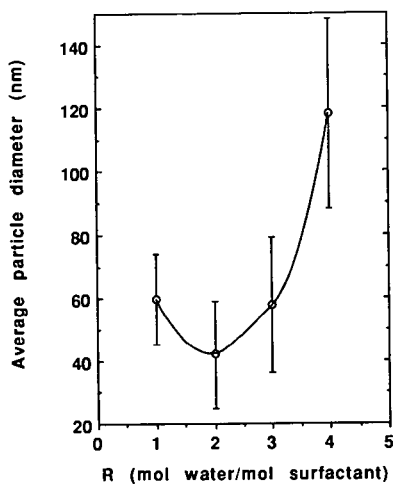


Figure 6. A plot of average particle diameter versus water-to-surfactant molar ratio (R) for the 0.4M NP-5/tetralin/benzyl alcohol microemulsion. The concentration of reactant species is constant with respect to the water pools.

IN-SITU MODEL STUDIES OF METAL SULFIDE CATALYSTS

N.M. Rodriguez, and R.T.K. Baker
Chemical Engineering Department,
Auburn University
Auburn, AL 36849

Keywords: In-situ Electron Microscopy, catalytic hydrogenation of graphite, metal sulfide-hydrogen interactions

ABSTRACT

In-situ electron microscopy studies of the dynamic behavior of certain metal sulfides supported on single crystal graphite showed that when such specimens were treated in 0.2 Torr hydrogen, pitting of the carbonaceous support at edges, steps and defect regions of the basal plane occurred. In the absence of a catalyst attack of graphite by molecular hydrogen was not observed until the temperature was raised to above 1000°C. In contrast, when a metal sulfide was present gasification of the graphite took place at very low temperatures. We believe that this unusual behavior, which is quite different to that observed in the presence of metal catalysts, is the result of attack by atomic hydrogen which is produced from the interaction of molecular hydrogen with the metal sulfide particles. These observations are consistent with those of other workers who have studied the interaction of microwave generated atomic hydrogen species with graphite.

INTRODUCTION

Over recent years a considerable wealth of knowledge has been amassed on the manner by which catalysts can modify both the rate and selectivity of various reactions involving the conversion of petroleum feedstocks into a variety of fuel fractions and chemicals. There are tremendous opportunities available if one can learn how to exploit the potential of these petroleum-related catalyst systems to manipulate the decomposition of coal to produce a similar spectrum of speciality chemicals. Of particular importance with regard to the conversion of carbonaceous solids such as coal to high molecular weight hydrocarbons are the catalytic reactions involving hydrogen. In this context, it is well worth considering the phenomenon of migration or "spillover" of adsorbed species which is known to occur with certain supported metal catalyst systems. Perhaps the most widely known example of spillover behavior is that associated with dissociation of molecular hydrogen over certain metal catalysts.

The phenomenon of hydrogen spillover was first suggested from the observations that the rate of decomposition of GeH₄ to Ge was accelerated in the presence of platinum¹. The effect was also demonstrated by very elegant experiments in which the transformation of WO₃ to H_xWO₃ during treatment in hydrogen in the presence of Pt/Al₂O₃ induced a color change from yellow to blue². Hydrogen spillover also appears to play an important role in the extent of reduction of a titanium oxide support when platinum was introduced onto this material and the system heated in hydrogen^{3,4}. Early work by Boudart and coworkers⁵ showed that hydrogen spillover from platinum to carbon occurred at 350°C and subsequently it has been demonstrated that this behavior can lead to methanation of the solid carbon⁶⁻⁸. Although the nature of the diffusing species is not yet established, it does appear that atomic hydrogen could be involved in the reaction mechanism.

The concept of using atomic hydrogen to convert carbonaceous solids to an assortment of hydrocarbon products has been reported by a number of workers⁹⁻¹⁸. In these studies hydrogen atoms were generated either in low pressure microwave discharge systems or by dissociation of molecular hydrogen over a hot tungsten filament. There is general agreement that the interaction of atomic hydrogen with carbonaceous solids can take place at a relatively rapid rate even at room temperature. On the other hand, a wide variation in the hydrocarbon product distribution and composition has been reported from such reactions, which appears to be related to the type of discharge system used to produce atomic hydrogen, the hydrogen pressure and the time of exposure. Vastola and coworkers¹¹ and later Gesser and Czubyrt¹⁸ found that acetylene and methane were the major products with minor amounts of ethane, methylacetylene and pentane arising from the reaction of atomic hydrogen with graphite. In another study, Gill and coworkers¹⁰ produced hydrogen atoms by dissociation of H₂ over a tungsten filament and allowed these atoms to react with a carbon solid at 77K. At low pressure conditions methane, ethane, propane and butene along with an identified higher molecular weight compound were produced from the reaction with graphite. In contrast only methane and ethane were formed at higher pressures when helium was added to the hydrogen.

From this brief overview of the interaction of atomic hydrogen species with coals and carbons it is clear that this approach holds a great deal of potential for the conversion of such solids into a variety of extremely useful precursor hydrocarbon molecules. The notion of producing atomic hydrogen via various discharge techniques is extremely interesting and offers the opportunity of controlling the energy of the atomic species, however, this experimental approach is fraught with technical difficulties when one attempts to scale up such a reactor system. The question which arises is can we perform such reactions by generating atomic hydrogen species from a somewhat simpler route, i.e. by catalytic dissociation of molecular hydrogen.

The characteristics of a suitable candidate for this operation would be one which has the capacity to dissociate molecular hydrogen in a reversible manner at relatively low temperatures. Examination of the literature shows that while the majority of metals are capable of dissociating molecular hydrogen, they do not readily release the atomic species. In contrast, it appears that certain metal sulfides and in particular molybdenum disulfide may well possess the desired characteristics¹⁹.

In the current study we have used the technique of controlled atmosphere electron microscopy to directly observe the behavior of hydrogen on two types of model catalyst systems:

- (a) cobalt supported on graphite, and,
- (b) molybdenum disulfide on graphite.

These two catalyst systems were found to exhibit dramatic differences in their behavior towards hydrogen and reasons for these observations are discussed.

EXPERIMENTAL

The experiments reported here were performed using a modified JEOL 200CX TEM electron microscope. This instrument is equipped with a custom designed environmental cell, which accommodates a heating stage. Specimens can be heated

up to a temperature of 1000°C while at the same time being exposed to a gas environment at pressures up to 3.0 Torr. The resolution of this instrument when used in conjunction with a closed-circuit television system is of the order of 0.4 nm.

Transmission specimens of single crystal graphite and molybdenum disulfide were prepared by a standard cleaving technique. Two procedures were used to prepare molybdenum disulfide/graphite specimens. In the first method, the sulfide was introduced onto the graphite in the form of particles from an ultrasonic dispersion of the powder in iso-butanol. In a second approach, transmission sections of both materials were mounted side by side on nickel grids. Cobalt was deposited onto the graphite substrates by evaporation of spectrographically pure wire from a tungsten filament at a residual pressure of 10^{-6} Torr. The conditions were selected so as to produce a film of metal at least one atom on average thickness. The reactant gas, hydrogen, was 99.999 % pure and used without further purification.

RESULTS AND DISCUSSION

(a) Cobalt/Graphite - Hydrogen

When cobalt/graphite specimens were heated in the presence of 0.2 Torr hydrogen, the deposited metal film was observed to nucleate into discreet particles at 350°C. On continued heating particles located on the graphite edge and steps sites were seen to exhibit dramatic changes in their wetting characteristics with the substrate and this behavior was reflected in a change in the mode by which they operated during the subsequent hydro-gasification reaction. This sequence of events is depicted schematically in Figure 1. At 400°C, particles were found to undergo a wetting and spreading action along the graphite prismatic faces. This behavior preceded the onset of catalytic attack at 450°C, which took place by the edge recession mode. It was interesting to find that the receding edges were aligned in particular directions, being parallel to the $\langle 11\bar{2}0 \rangle$ crystallographic orientations of graphite.

At 650°C, the catalyst exhibited a modification in its wetting properties with the graphite, which resulted in the re-formation of particles. This transformation was accompanied by a change in the mode of catalytic attack from edge recession to channeling. During channeling the active particles maintain contact with the graphite interface and as a consequence during propagation across the basal plane, always remain at the leading face of the channel. Quantitative kinetic measurements of a number of channeling sequences showed that the typical propagation rates exhibited by 25 nm diameter particles at 840°C was of the order of 10 nm/sec. A survey of many regions of the specimen revealed that the majority of channels were straight and oriented parallel to the $\langle 11\bar{2}0 \rangle$ graphite crystallographic directions.

It is possible that the observed a change in wetting characteristics of the metal particles on the graphite which takes place at 650°C is a result of carbon being dissolved in the metal particles, and this event is known to induce changes in the interfacial energy of such particles²⁰. Previous studies with other metals have shown that although this behavior appears to be a general phenomenon²¹, the temperature where such transformations occur vary with each system. Finally, it is clear that in this type of catalyzed hydro-gasification reaction the removal of carbon atoms to form methane only occurs at the catalyst/graphite interface, there being no evidence for loss of carbon from regions devoid of catalyst material at temperatures below 1000°C.

(b) Molybdenum Disulfide/Graphite - Hydrogen

Treatment of graphite specimens containing particulates of molybdenum disulfide, in 0.2 Torr hydrogen produced some very unusual effects. Inspection of the graphite surface showed that even at room temperature erosion of certain regions of the basal plane was taking place. This took the form of the creation of very tiny pits (~ 3 nm width), which initially tended to form as discreet clusters. On continued reaction at the same temperature these pits expanded along certain directions and developed into single larger pits, about 10 nm in width, which adopted an hexagonal outline with an internal island of carbon. This sequence of events is shown in the schematic diagram, Figure 2. As the reaction proceeded it became apparent that the formation of pits was not restricted to regions in the immediate vicinity of the sulfide particles. Indeed, they tended to preferentially occur at surface imperfections on the graphite basal plane such as vacancies, steps and along twin bands. Other workers^{22,23} have used the gold decoration technique to demonstrate that atomic hydrogen species can attack the basal plane regions of graphite to produce monolayer pits. Such features would not be observed in the present experiment since the contrast difference afforded by conventional TEM does not allow one to distinguish differences in thickness down to this level.

It is difficult to rationalize these extraordinary observations without invoking the participation of very reactive species such as atomic hydrogen which is produced by dissociation of molecular hydrogen on the sulfide catalyst. The pattern of behavior found in this work is consistent with that reported by other workers who have studied the interaction of microwave generated atomic hydrogen species with graphite. The finding that attack of the graphite surface could take place at regions remote from the catalyst particles suggests that the active entities have the ability to migrate across the graphite surface to active sites via a "spillover" mechanism. Initial concern that the electron beam might be exerting some influence on the reaction was dispelled in subsequent experiments by performing blank experiments in which specimens were reacted in hydrogen in the absence of the beam for periods of up to 2 hours. When such specimens were eventually examined it was clear that there had been extensive reaction prior to exposure to the beam.

On raising the temperature to 100°C the attack became indiscriminate in nature so that the whole surface gradually acquired a textured appearance. Also at this time, it was evident that the initially formed pits were tending to lose their faceted outline and become more circular in shape reaching diameters of 40 nm. In many cases, as pits expanded they merged into adjacent ones with a result that vast areas of the graphite surface were progressively removed.

The intensity of the reaction increased perceptibly at 200°C and it was significant to find that over prolonged periods at this temperature a carbonaceous deposit started to accumulate on the surface with the result that in some cases it was difficult to resolve the presence of shallow pits that had been previously apparent at lower temperatures. This observation suggests the possibility that some of the graphite is undergoing hydrogasification to produce hydrocarbons other than methane, which are susceptible to decomposition in the presence of the electron beam. At 350°C the reaction became so extensive that under these conditions the surface acquired a holey structure and experiments were normally terminated as the graphite specimens gradually lost their integrity.

In a further series of experiments the form of the specimen was changed to that where the molybdenum disulfide and graphite components were physically separated from one another. When this combination was reacted in 0.2 Torr hydrogen then attack of the pristine graphite surface was once again observed at room temperature. The subsequent behavior of these specimens was identical to that described above. The finding that it is not necessary for the catalyst to be in direct contact with the carbonaceous solid in order to promote hydro-gasification suggests that at the gas pressures used in these experiments it is possible for the active species to be transported through the gas phase in addition to the surface migration route.

ACKNOWLEDGMENTS

Financial work for this research was provided by the United States Department of Energy, Basic Energy Sciences, Grant DE-FG05-89ER14076 and CFFLS program Contract No DE-FC22-90-PC90029

REFERENCES

1. Taylor, H. S., *Ann. Rev. Phys. Chem.*, **5**, 646 (1967).
2. Khoobiar, S., *J. Phys. Chem.* **68**, 411 (1964).
3. Baker, R. T. K., Prestridge, E. B., and Murrel, L. L., *J. Catal.* **79**, 348 (1983).
4. Dumesic, J. A., Stevenson, S. A., Sherwood, R. D., and Baker, R. T. K., *J. Catal.* **99**, 79 (1986).
5. Boudart, M., Aldag, A. W., and Vannice, M. A., *J. Catal.* **18**, 46 (1970).
6. Tomita, A., and Tamai, Y., *J. Catal.* **27**, 293 (1972).
7. Olander, D. R. and Balooch, M., *J. Catal.* **60**, 41 (1979).
8. Chang, T. S., Rodriguez, N. M., and Baker, R. T. K., *J. Catal.* **123**, 486 (1990).
9. Blackwood, J. D., and McTaggart, F. K., *Aust. J. Chem.*, **12**, 533 (1959).
10. Gill, P. S., Toomey, R. E., and Moser, H. C., *Carbon* **5**, 43 (1967).
11. Vastola, F. J., Walker, Jr., P. L. and Wightman, J. P., *Carbon* **1**, 11 (1963)
12. Wood, B. J., and Wise, H., *J. Phys. Chem.* **73**, 1348 (1969)
13. McCarroll, B., and McKee, D. W., *Carbon*, **9**, 301 (1971)
14. Sanada, Y., and Berkowitz, N., *Fuel*, **48**, 375 (1969).
15. Amano, A., Yamada, M., Shindo, T., and Akakura, T., *Fuel* **63**, 718 (1984).
16. Amano, A., Yamada, M., Shindo, T., and Akakura, T., *Fuel* **64**, 123 (1985).
17. Wong, C.-L. Chen, C.-W. and Timmons, R. B., *Fuel* **65**, 1483 (1986).
18. Gesser, H. D., and Czubryt, J. J., *Fuel* **67**, 375 (1988).
19. Wright, C. J., Sampson, C., Fraser, D., Moyes, R. B., Wells, P. B. and Riekel, C., *J.C.S. Faraday I* **76**, 1585 (1980).
20. Weisweiler, W., and Mahadevan, V., *High Temp.-High Pressures* **4**, 27 (1972).
21. Baker, R. T. K., in "Carbon and Coal Gasification" (Eds. Figueiredo, J. L., and Mouljn, J. A.) Martinus Nijhoff Publishers, The Netherlands, 231 (1986).
22. Chen, J. P. and Yang, R. T., *Surf. Sci.* **216**, 481 (1989).
23. Pan, Z. J., and Yang, R. T., *J. Catal.* **123**, 206 (1990).

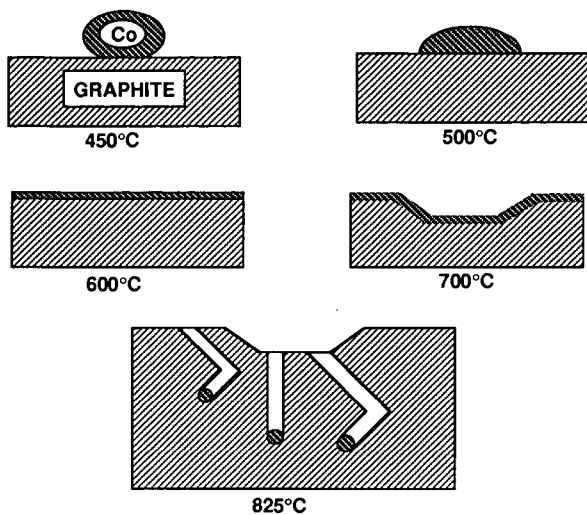


FIGURE 1. Change in wetting properties of a particle on graphite and the concomitant modification in catalytic action.

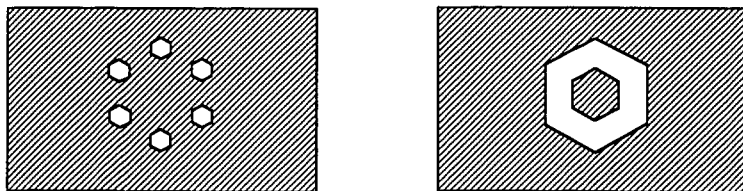


FIGURE 2. Development of pits in graphite from interaction with atomic hydrogen

Dispersed Catalysts for Coal Dissolution

Frank Derbyshire and Todd Hager

University of Kentucky Center for Applied Energy Research
3572 Iron Works Pike, Lexington, KY 40511-8433

Introduction

In 1988, one of the authors conducted a review of the status of catalysis in direct coal liquefaction.[1] The objectives were to assess the current state of knowledge and to identify new directions for research. The application of catalysts was addressed with respect to the two-stage processing concept, distinguishing the processes of primary coal dissolution and coal liquids upgrading.

Supported catalysts are quite adequate to the task of hydroprocessing distillate coal liquids. However, in the presence of high-boiling and non-distillable liquids, they are rapidly deactivated by the deposition of carbonaceous materials and metals. Furthermore, since large molecules cannot access the active catalyst surface, supported catalysts can only indirectly influence the processes of coal dissolution and residual coal liquids upgrading.

To surmount these problems, there are several possible approaches to developing new supported catalysts that are less prone to deactivation. However, it is also considered that there is considerable potential for improving liquefaction processing and economics through the development and appropriate application of highly dispersed catalysts. The principle objectives are to promote the process of primary coal dissolution and produce a solubilized product that can be upgraded with greater facility in a second stage over supported catalysts. Dispersed catalysts may also help to realize the potential of using cheap, low-rank coals as feedstocks by increasing the low rates and extent of conversion that are normally attained. Additionally, they may help to lower constraints on solvent quality, facilitating greater flexibility in the selection of recycle solvent fractions and the coprocessing of coals with petroleum residua.

This paper will address the use and development of coal dissolution catalysts. Emphasis will be given to iron-based catalysts because of cost considerations, and to their applicability to the liquefaction of low-rank coals.

Liquefaction of Low-Rank Coals

Before entering a discussion of dispersed catalysts, *per se*, some comments will be addressed to the liquefaction of low-rank coals. The present interest in these coals as liquefaction feedstocks relates to their lower cost, and to their ability to produce higher yields of low molecular weight products than bituminous coals.[2-4] It has been shown by comparative studies of processing bituminous and subbituminous coals that, in the latter case, the rate of deactivation of the second stage supported catalyst is lower and the resid is more reactive.[5] Against this, low-rank coals tend to convert more slowly and to lower ultimate conversions. Pilot plant experience has also shown that these coals can cause severe operating problems through the formation of deposits.[6]

The thermal liquefaction of low-rank coals proceeds with difficulty, due to their normally low content of catalytically active mineral matter and to the high reactivity of the organic structure. The latter allows crosslinking reactions to proceed at moderate temperatures, rendering the coal more difficult to dissolve. However, in the presence of a suitable catalyst, these phenomena can be suppressed and the potential for producing high distillate yields can be realized (Figure 1). [2]

Research by Keogh and Davis [7] has shown that the liquefaction pathways for bituminous coals and subbituminous coals are quite different. The triangular plot in Figure 2 shows the conversion routes followed by these coals from insoluble organic matter, to preasphaltenes and asphaltenes, to oil and gas. These data were developed from microautoclave experiments using a large number of coal samples, donor and nondonor solvents, and various supported and unsupported catalysts. What is found is that the two ranks of coal fall into different bands, and, as discussed above, oils are produced more directly from subbituminous coals, indicative of their being composed of smaller structural units. A second relevant finding is that, for a given coal, none of the variables affects the conversion pathway or conversion selectivity, and the only measurable effect is to increase the conversion kinetics. Thus it seems that selectivity can only be influenced by choice of feedstock, but that appropriate catalysts can improve the rate of conversion.

Dissolution Catalysts

The activity of dissolution catalysts is considered to depend on their composition and the extent of their dispersion and intimate contact with the coal-solvent slurry. These are interrelated factors, since the composition of the catalyst precursor will determine the methods that can be used for its addition and dispersion, and the efficacy of its conversion to an active form.

The extent of dispersion over, and in, the solid coal, and in the coal-solvent slurry, is directly related to the catalyst effectiveness. Until the coal is dissolved, there is no available mechanism by which reactants can be transported to the catalyst, and hence the basic requirement is to transport the catalyst to the reacting species. Overwhelming evidence has accumulated to demonstrate that catalyst activity is enhanced by introducing the precursor in a form more conducive to attaining high dispersion. [8]

There are no really satisfactory techniques for measuring high levels of dispersion. Its attainment and maintenance is inferred from the results of liquefaction experiments, and it is not usually possible to distinguish unequivocally the influence of other factors. For example, the rate of conversion of the precursor to a sufficiently active form may be too slow to influence the process of coal dissolution. The active form of catalysts such as Fe and Mo is generally believed to be a sulfide. In many cases, the attainment of this phase relies upon in-situ sulfiding, and there is scant information on the relative kinetics of dissolution and sulfiding reactions.

While direct comparisons are difficult, it is apparent that, all other things being equal, molybdenum is a much more active catalyst than iron. However, in the absence of suitable methods for catalyst recovery and/or recycle, the cost of Mo is considered prohibitive.

In the developments in Germany in the 1920s and 1930s, finely ground Mo catalysts were first used for the liquid phase hydrogenation of brown coal tar, initially at concentrations as high as 25%. [9] Effective results were subsequently obtained with much lower concentrations of Mo impregnated as ammonium molybdate solution onto brown coal char. Without the ability to separate and recover catalyst, attention was ultimately directed to using lower catalyst concentrations or lower cost catalysts. The impregnation of brown coal with ammonium molybdate allowed a concentration of 0.02% wt. of coal to be used. To reduce cost, iron ores were introduced at higher concentrations (2% wt of coal and higher). Iron compounds supplanted Mo on the brown coal char supports, and the effectiveness of the iron ores was later improved through their partial replacement by impregnating ferrous sulfate directly on the coal, which presumably aided dispersion.

For the same reasons, iron-based catalysts are preferred now, and there are considerable efforts to find means to enhance their activity. Much of this work is of a fundamental

nature and therefore it is not entirely reasonable to require economic justification. Nevertheless, it must be taken into account that the more exotic the preparation, the higher will be the cost, and that this could negate the basis for using iron as a starting point.

Directionally, the main approach to increasing catalytic activity is towards increasing the dispersion of the catalyst precursor and to maintaining this high dispersion after transformation to the active phase. Several techniques have been used to this end including the use of oil soluble organometallics, the synthesis of ultrafine particles, and the application of impregnation techniques to add the iron directly into the coal matrix.

High activities are reportedly favored by catalysts introduced as oil-soluble organometallic precursors such as naphthenates and carbonyls [10-15]. The work of Yamada et al. [13] showed that the catalytic effect of the cyclopentadienyliron dicarbonyl dimer $[(\text{FeCp}(\text{CO})_2)_2]$ is of the same order of magnitude as that of iron pentacarbonyl. The dicarbonyl dimer at a catalyst loading of 1 wt% Fe of resulted in an increase in conversion to THF solubles from 57% to 93% for an Illinois #6 bituminous coal at 425° C and 711 psig H_2 (cold) for 60 min. This compares favorably to the 92% conversion obtained for the same catalyst loading with the precursor molybdenum hexacarbonyl $(\text{Mo}(\text{CO})_6)$. The iron pentacarbonyl also showed the same high catalytic activity for a subbituminous Wandoan coal in the presence of added sulfur, resulting in a total conversion of 94%. Other iron carbonyls, $\text{Fe}_2(\text{CO})_9$ and $\text{Fe}_3(\text{CO})_{12}$, resulted in similar high conversions.[14] This indication that the iron carbonyls are effective catalyst precursors is supported by more recent experiments by Herrick et al. who used the iron pentacarbonyl precursor in coprocessing Illinois #6 bituminous coal with a Maya resid and found an increase in conversion to methylene chloride solubles from 39% to 82% at similar conditions to those used in the liquefaction studies but with an initial H_2 pressure of 1000 psig and a catalyst loading of 0.5 wt% Fe.

The addition of sulfur to the catalyst precursor can have a significant effect on the activity of some catalysts, particularly in the liquefaction of low sulfur coals. In the case of iron pentacarbonyl, the addition of elemental sulfur resulted in an increase of both the total conversion (~10%) and oils (~13%) for a low sulfur Wandoan coal.[13] For $\text{W}(\text{CO})_6$, the addition of sulfur increased the conversion from 52% to 94% and the oils from 14% to 57%. At a catalyst loading of 0.4 wt% Mo the total conversion for the precursor $\text{Mo}(\text{CO})_6$ increased by 17% while the oil yield increased by 13%. This indicates that while most of the organometallic precursors require sufficient sulfur for transformation to the active phase, the activity of iron is improved less by added sulfur than molybdenum or tungsten based precursors.

The results of some studies indicate that, even with soluble precursors, quite large crystallites or agglomerates can be formed during liquefaction and hence the potentially high dispersion is not realized or maintained. There is some evidence to indicate that, if the precursor is introduced as particulates, there is less tendency for agglomeration. Fine iron particles (50 nm mean diameter) synthesized by a flame pyrolysis technique appeared to have retained their particle size and shape during presulfiding and coal liquefaction.[16,17]

In this same context, efforts have been directed towards improving the dispersion of iron based catalyst precursors through the synthesis of ultrafine particles (UFPs) with diameters that can be significantly less than 100 nm. The increase in catalytic activity that is expected with decreasing particle size may be due to a combination of effects: an increase in exterior surface and an associated enhancement of sulfiding kinetics; a radical departure from bulk properties, especially with regard to surface energetics as the particle size is reduced below about 10 nm. The synthesis of ultrafine catalyst particles could therefore provide a means

to enhance the activity of dispersed iron (or other metal) catalysts. Several techniques have been used to produce this type of precursor, including pyrolysis in a flame or by laser.

The laser pyrolysis technique has been used to produce iron carbide UFPs from a mixture of iron pentacarbonyl and ethylene.[18] Particles of Fe_3C and Fe_7C_3 have been produced with average particle diameters of 4-20 nm. In this research, the synthesis of carbides was primarily intended as a starting point from which to establish procedures for the synthesis of oxide, sulfide, and mixed-metal phases. Although it is generally considered that the active phase of Fe and Mo is a sulfide form, recent studies by Oyama and co-workers have shown that supported and unsupported Mo carbides and nitrides exhibit high activity for hydrodenitrogenation and hydrodesulfurization reactions [19-21], raising the possibility that the carbides and nitrides of Mo and other metals may be active liquefaction catalysts.

Liquefaction studies were conducted with the Fe_3C and Fe_7C_3 UFPs using a subbituminous Wyodak coal at 385 °C, 800 psig H_2 (cold) for 15 minutes in the presence of sulfur added as dimethyldisulfide. The results of these experiments demonstrated that, under these conditions, the particles exert only a moderate catalytic effect that is slightly less than that of the oil soluble precursor iron naphthenate. At 400°C the particles increase the total conversion by ~10% above the thermal baseline. Mössbauer studies of the liquefaction residues show that, unlike the Mo carbides mentioned above, the particles are sulfided and transformed to pyrrhotite. The different response of Fe and Mo carbides to sulfiding may well relate to the much higher stability of the latter.

The moderate performance of the iron carbide UFPs may be attributable to a number of causes relating to the unusual properties of nanometer size particles, and may not be an accurate reflection of their intrinsic activity. The particles, as synthesized, are pyrophoric and the present procedure involves slow stabilization in an O_2/He mixture to allow handling in air. The method produces a surface oxide coating. Trapping the particles directly in a solvent or coal-solvent slurry may obviate this problem. The particles also tend to agglomerate, possibly aided by magnetic effects, and techniques must be developed to ensure their efficient dispersion. Thermal stability is another factor: in-situ X-ray diffraction studies have shown that sintering starts in the region of 300°C; experiments conducted under liquefaction conditions, and in the absence of coal, show that the particles are very susceptible to sintering but, in the presence of added sulfur, this tendency is reduced. Neither are there, as yet, data on the comparative kinetics of sulfiding and coal dissolution, and the prospect exists catalyst may not be present in an active form while critical reactions are taking place in the coal.

A second example of UFP synthesis is the formation of aerosol oxides formed by the combustion of metal chlorides in a hydrogen-oxygen flame.[22,23] These particles have diameters around 50 nm and surface areas between 20 and 50 m^2/g . The iron oxide aerosols have demonstrated a high catalytic activity in the presence of added sulfur at a catalyst loading of 2% for the liquefaction of a bituminous coal at 350 °C and 2000 psig H_2 (cold) for 60 minutes. The results show a doubling of the total conversion from 25% to 52%. This was only slightly less than that produced by a molybdenum aerosol generated by the same technique. This catalytic effect is reduced at higher temperatures. Again, as with the other iron based catalysts, XRD of the liquefaction residues indicate the transformation of the Fe_2O_3 aerosol to pyrrhotite in the presence of sulfur.

The use of an incipient wetness technique to impregnate the coal with Fe^{3+} from an aqueous solution has been shown to give high dispersion of the catalyst precursor on a coal substrate [24]. The coal matrix also aids in maintaining the high dispersion subsequent to activation. At a catalyst loading of 2500 ppm the precipitated FeOOH yielded the same

catalytic activity as 1500 ppm molybdenum, added as ammonium heptamolybdate, for the liquefaction of an Illinois #6 coal at 425 °C and 2500 psig H₂ for 1 hour. The addition of sulfur was necessary to cause the transformation to the active form. The transition of amorphous iron to crystalline pyrrhotite occurred between 300° C and 350° C, although pyrrhotite is probably present below 350° C in particles with diameters less than 10 nm.

The application of Mössbauer and EXAFS spectroscopies to the study of iron based catalysts has been very informative. Studies conducted by Huffman et al. [25] used a variety of catalyst precursors including Fe₂O₃ on carbon black, Fe₂O₃/SO₄²⁻, iron added by cation exchange, and chemical impregnation by FeCl₃. The primary form of the as-dispersed iron catalyst was shown to be either an oxide or oxyhydroxide. The introduction of catalyst by ion exchange techniques showed that the iron formed small crystallites of superparamagnetic FeOOH.

Modified Iron Catalysts

Another route to improving the activity of iron catalysts is to modify their composition. One approach has been to change the surface properties of hematite particles by treating a precipitated FeOOH with H₂SO₄. [26,30] Studies of these particles after calcining indicate the formation of Fe₂O₃/SO₄²⁻. This notation denotes SO₃ chemisorbed on the surface of Fe₂O₃ in a nonstoichiometric relation. The sulfate group is believed to be responsible for the superacidity displayed by these particles. The addition of the sulfate group also leads to a decrease in the average crystallite size, which is believed to be the primary reason for their enhanced activity. Liquefaction studies using an Illinois #6 coal at 400 °C and 1000 psig H₂ (cold) for 1 hour showed an increase in the total conversion from 65 % to 90 %, in the presence of added sulfur, for a catalyst loading of 0.35 wt. %. Similar enhanced activity was seen for the liquefaction of a subbituminous Wyodak coal. Analysis of the liquefaction residues indicate that the majority of the catalyst had been transformed to pyrrhotite with only traces of oxide phases remaining.

There are a number of instances in the literature which show that metals in combination can be more effective catalysts than they are individually. The presence of titanium in the German "red mud" catalyst has been suggested to promote the activity of iron. Other research has shown that titanium can promote the activity of molybdenum, leading to significant increases in distillate production, as shown in Figure 3. [27]

It has been found that the effectiveness of an iron catalyst can be greatly improved by the addition of small concentrations of molybdenum, such that the combination has the same activity or higher than much higher concentrations of Mo alone. [28,29] The addition of 20 - 100 ppm Mo to the Fe₂O₃/SO₄²⁻ was found to increase the oil yields as well as the total conversion in the coprocessing of an Illinois # 6 coal. [30] The incorporation of 2% Mo to the iron oxide aerosol particles formed by flame pyrolysis showed a significant increase in conversion for both a bituminous and a subbituminous coal. [31] The activity of the Mo doped aerosol particles was higher than that of a supported Ni-Mo catalysts despite the higher concentration of Mo present in the supported catalyst.

These studies have shown that by the addition of low concentrations of promoter metals, the activity of iron catalysts can be enhanced either to provide increased performance at the same concentration or equivalent performance at reduced concentrations. In either case, gains could be made at marginal extra catalyst cost which retains the "disposability" of the catalyst while effecting process economies which more than compensate.

Intermetallic hydrides have also been the subject of investigations. These alloys form reversible metal hydrides that can store molecular hydrogen within the metal matrix at

densities greater than that of liquid hydrogen. Several of these alloys have shown some activity as liquefaction catalysts.[32,33] In studies using a hvA bituminous coal, the activity of these intermetallic hydrides was shown to follow the trend $\text{CaNi}_5 = \text{LaNi}_5 > \text{FeTi} > \text{Mg}_2\text{Cu} > \text{Mg}_2\text{Ni}$, although the variation between the higher three is less than 5%. The highest activity resulted in a doubling of the total conversion over a noncatalytic baseline at temperatures between 370 °C and 427 °C. There has also been speculation that the enhanced activity of iron aerosols in the presence of added tin aerosols is due to the transitory formation of an intermetallic hydride that is unstable at room temperature.[34]

References

- 1) Derbyshire, F. J., IEACR/08, London, UK, IEA Coal Research, 69 pp (1988)
- 2) Wu W R K, Storch H H, 1968, Hydrogenation of Coal and Tar. Bulletin 633, Washington, DC, USA, US Department of the Interior, Bureau of Mines, 195pp.
- 3) Derbyshire F J, Stansberry P G, 1987, *Fuel*, **66**, 1741-2
- 4) Tomlinson G C, Gray D, Neuworth M B, Talib A, Report SAND85-7238, Albuquerque, NM, USA, Sandia National Laboratories, 105pp.
- 5) El Sawy A, Gray D, Talib A, Tomlinson G, 1986, Report SAND86-7103, Albuquerque, NM, USA, Sandia National Laboratories, 198pp.
- 6) Nakako, Y.; Ohzawa, T.; Narita, H., 1991 ICCS Proceedings, Oxford, UK, Butterworth-Heinemann, 652-5 (1991).
- 7) Keogh, R. A.; Davis, B. H., *ACS Div. of Fuel Chem. Preprints*, **36**(2) 438-44 (1991).
- 8) Weller, S.; Pelipetz, M. G., *I&EC Eng. & Proc. Dev.* **43**(5) 1243-6 (1951).
- 9) Donath, E. E.; Hoering, M., *Fuel Proc. Tech.*, **1** 3-20 (1977).
- 10) Watanabe, Y.; Yamada, O.; Fujita, K.; Takegami, Y.; Suzuki, T., *Fuel*, **63** 752-5 (1984).
- 11) Suzuki, T.; Yamada, O.; Then, J. H.; Ando, T.; Wantanabe, Y., Proceedings- 1985 ICCS, Sydney, NSW, Australia, Pergamon Press, 205-8 (1985).
- 12) Hirschon, A. S.; Wilson, R. B., "Designed Coal Liquefaction Catalysts", *ACS Div. of Fuel Chem. Preprints*, **36**(1) 103-7 (1991).
- 13) Yamada, O.; Suzuki, T.; Then, J. H.; Ando, T.; Wantanabe, Y., *Fuel Proc. Tech.*, **11** 297-311 (1985).
- 14) Suzuki, T.; Yamada, O.; Takahashi, Y.; Wantanabe, Y., *Fuel Proc. Tech.*, **10** 33-43 (1985).
- 15) Herrick, D. E.; Tierney, J. W.; Wender, I.; Huffman, G. P.; Huggins, F. E., *Energy and Fuels*, **4**(3) 231-6 (1990).
- 16) Andres, M.; Charcosset, H.; Chiche, P.; Djega-Mariadassou, G.; Joly, J-P.; Pregermain, S., Preparation of Catalysts III (eds. G. Poncelet and P. Grange), Elsevier, 675-82 (1983).
- 17) Andres, M.; Charcosset, H.; Chiche, P.; Davignon, L.; Djega-Mariadassou, G.; Joly, J-P.; Pregermain, S., *Fuel* **62** 69-72 (1983).
- 18) Hager, G. T.; Bi, X. X.; Derbyshire, F. J.; Eklund, P. C.; Stencel, J. M., *ACS Div. of Fuel Chem. Preprints*, **36** (4) 1900-8 (1991).
- 19) Oyama, S. T.; Schlatter, J. C.; Metcalfe, J. E.; Lambert, J. M., *I&EC Research*, **27**, 1639-48 (1988).
- 20) Schlatter, J. C.; Oyama, S. T.; Metcalfe, J. E.; Lambert, J. M., *I&EC Research*, **27**, 1648-53 (1988).
- 21) Sajkowski, D. J.; Oyama, S. T., *ACS Div. of Fuel Chem. Preprints*, **35** (2) 233-36 (1990).
- 22) Bacaud, R., *Applied Catalysis*, **75** 105-17 (1991).
- 23) Cebolla, V. L.; Diack, M.; Oberson, M.; Bacaud, R.; Cagniant, D.; Nickel-Pepin-Donat, B., *Fuel Proc. Tech.*, **28**(2) 183-201 (1991).

- 24) Cugini, A. V.; Utz, B. R.; Krastman, D.; Hickey, R. F.; Balsone, V., *ACS Div. of Fuel Chem. Preprints*, **36** (1) 91-102 (1991).
- 25) Huffman, G. P.; Ganguly, B.; Taghiei, M.; Huggins, F. E.; Shah, N., *ACS Div. of Fuel Chem. Preprints*, **36**(2) 561-9 (1991).
- 26) Pradhan, V. R.; Tierney, J. W.; Wender, I.; Huffman, G. P., "Catalysis in Direct Coal Liquefaction by Sulfated Metal Oxides", *Energy & Fuels*, **5** 497-507 (1991).
- 27) Wilson, T. P.; Hurley, G. F., Technical Report 84002-1-4950, Union Carbide Olefins Company, South Charleston, WV, USA, 125pp, (1960)
- 28) Derbyshire, F. J.; Davis, A.; Schobert, H. H.; Stansberry, P. G., *ACS Div. of Fuel Chem. Preprints*, **35**(1) 51-60 (1990).
- 29) Garg, D.; Givens, E. N., *ACS Div. of Fuel Chem. Preprints*, **28**(5) 200-9 (1983).
- 30) Pradhan, V. R.; Herrick, D. E.; Tierney, J. W.; Wender, I., *Energy & Fuels*, **5**(5) 712-20 (1991).
- 31) Bacaud, R.; Charcosset, H.; Jamond, M., *Fuel Proc. Tech.*, **24** 163-9 (1990).
- 32) Johnson, S. D.; Smith, J. E. Jr., *Applied Catalysis*, **44**(1-2) 53-71 (1988).
- 33) Smith, J. E. Jr.; Johnson, S. D., *ACS Div. of Fuel Chem. Preprints*, **35**(1) 823-30 (1990).
- 34) Besson, M.; Bacaud, R.; Brodski, D.; Bussiere, P.; Charcosset, H.; Djega-Mariadassou, G.; Oberson, M.; Sharma, B. K., *Fuel*, **69** 35-43 (1990).

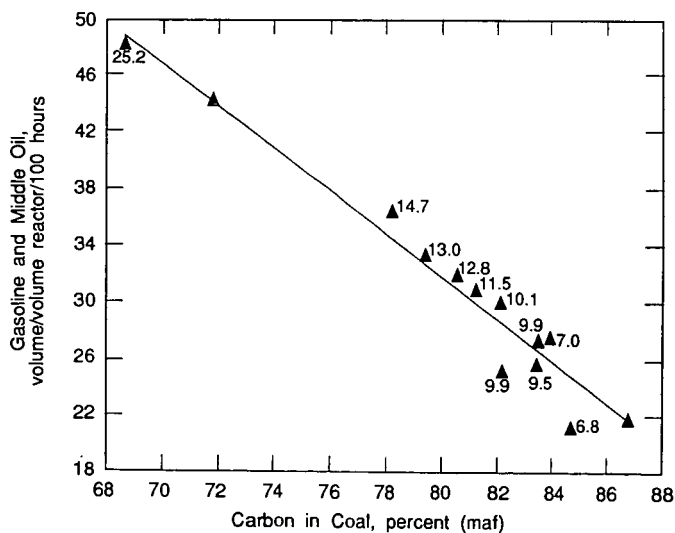


Figure 1. Yield of Gasoline Plus Middle Oil in Relation to Coal Rank
(Numbers Indicate Oxygen Content)

(Adapted from Wu and Storch, [2])

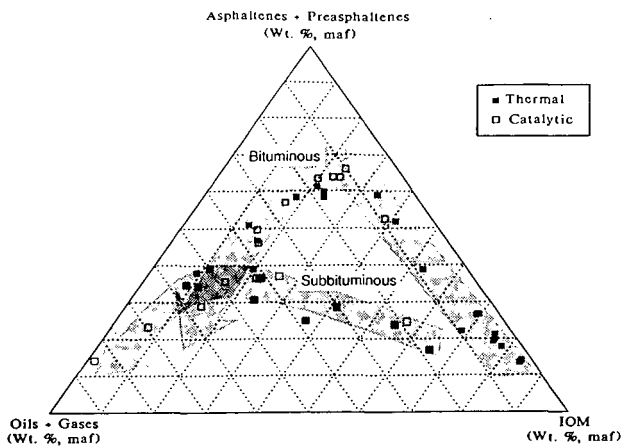


Figure 2. Liquefaction Pathways for Bituminous and Subbituminous Coals. (from Keogh and Davis[7])

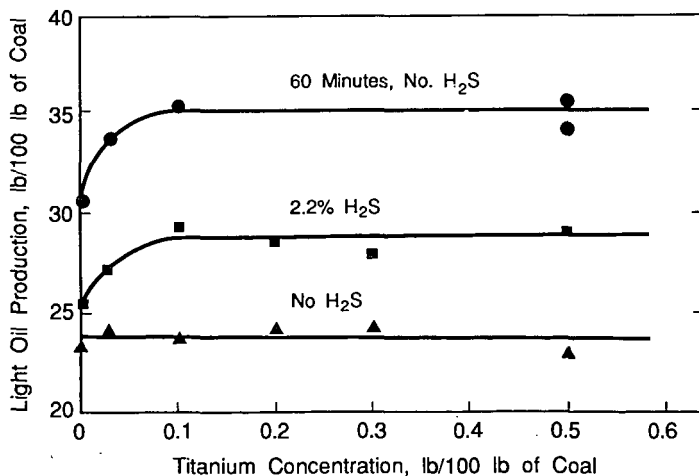


Figure 3. The Promotional Effect of Titanium on Molybdenum for Light Oil Production (0.2% Molybdenum; 480°C; 4400 psi H₂)

(From Wilson and Hurley [27])

ADVANCES IN THE MODELLING OF LIGAND-ACCELERATED HETEROGENEOUS REACTIONS

M. Garland^a, H.P. Jalett,^b H.U. Blaser^b

(a) Department of Chemical Engineering,
Swiss Federal Institute of Technology,
Universitätsstrasse 6, CH-8092 Zürich,
Switzerland (b) Central Research Services,
CIBA-GEIGY AG, R1055.6, CH-4002
Basel, Switzerland

INTRODUCTION

The term ligand-accelerated catalysis first appeared in conjunction with the osmium catalyzed dihydroxylation of alkenes.¹ In this reaction, a chiral auxiliary, normally a natural occurring cinchona alkaloid, is added to a solution containing OsO₄ and alkene. The resulting homogeneous system, leads to both the enantiomeric excess of one diol as well as a marked increase in reaction rate.

In addition to a dramatic 1-2 orders of magnitude increase in reaction rate, a remarkable interdependence between the optical yield (ee) and rate at low concentrations of chiral modifier is observed.² This interdependence can be easily recognized by examining simultaneous plots of ee and rate versus modifier concentration. Such plots exhibited a strong increase in rate, but an even more spectacular increase in ee, as a function of modifier. Indeed, such characteristic plots give the impression that a maximum ee is reached long before the maximum rate for the system is attained.

The heterogeneous and enantioselective hydrogenation of α -keto esters, catalyzed by cinchona modified Pt/Al₂O₃ was first reported by Orito et al.^{3,4} Initial studies with both the unmodified (racemic) and

fully modified (enantioselective) Pt/Al₂O₃ systems showed that the rate of hydrogenation for the latter was roughly 1 order of magnitude higher.⁵ Indeed, at 20°C and 10.0 MPa hydrogen the measured turnover frequency for the fully modified system approaches 50 s⁻¹.⁶ However, mass transfer control can be avoided by using a powdered catalyst, low loadings and a proper level of agitation.⁶

Subsequent studies were carried out with trace quantities of cinchona (modifier/Pt_T \leq 1).⁷ These experiments confirmed that both ee and rate were continuous functions of the cinchona concentration. Moreover, these functions yielded the characteristic types of curves indicative of a ligand accelerated reaction. With a modifier to Pt_T concentration as low as 0.25 in toluene,⁷ or less than 0.10 in acetic acid,⁸ maximum optical yields can be obtained.

The interdependence of ee and rate for the cinchona modified Pt/Al₂O₃ systems, were successfully analyzed in the context of a two-cycle mechanistic scheme. After imposing a mass balance constraint on the total platinum in the system, a simple relationship between ee and rate arises (Eq 1). This slope-intercept form correctly describes the interdependence of ee and rate for experiments conducted in toluene and ethanol as solvents.⁷

$$ee_{obs} = a + b/r_{obs} \quad 1$$

$$a = 100(2s-1)k_m/(k_m - k_u)$$

$$b = 100(2s-1)k_u k_m Pt_T / (k_m - k_u)$$

In the following, Eq 1 is modified to include a stoichiometry for the modified platinum sites. The data from toluene experiments are then re-examined. Emphasis is given to (i) the turnover frequency based on the number of modified sites and (ii) the form of the adsorption isotherm.

EXPERIMENTAL

The 5% Pt/Al₂O₃ catalyst used in this study (Engelhard 4759) had a mean particle size of 55 μm, a BET surface area of 140 m²/g, a mean pore radius of 50 Å, a real density of 5.0 g/ml, and a dispersion of 0.28.⁶

A 50 ml batch reactor, with cooling jacket, baffles, a 3 cm magnetic stirring bar, a thermocouple, and a capillary sampling line, was used for all kinetic experiments. A 45 ml reservoir, pressure regulators, pressure transducers and a cryostat were connected to the reactor. The reactor could be maintained isothermal ΔT = 0.3°C, and isobaric ΔP = 0.1 MPa for the duration of an experiment.

Typically, 100 mg catalyst (pretreated 2 hours in H₂ at 400°C), 0.2 mg 10,11-dihydrocinchonidine (HCD), 10 ml ethyl pyruvate and 20 ml solvent were charged to the reactor. The system was then purged 5 times with argon under stirring.

In the absence of stirring, the reservoir and reactor were pressurized with hydrogen. After 2-3 minutes, both the stirrer and data acquisition were started. Initial rate data was analyzed after the 30 second saturation period. Optical yields were determined after derivatization followed by glc.⁶

RESULTS AND DISCUSSION

Basic Derivation for EE and Rate First, consider a mass balance for the total platinum surface atoms Pt_T in an experiment, in terms of unmodified and modified platinum atoms and also the degree of surface modification x_m.

$$Pt_T = Pt_u + Pt_m \quad 2$$

$$x_m = Pt_m/Pt_T \quad 3$$

The observed rate of product formation can then be written (i) in terms of the modified and unmodified rates (ii) by including pseudo first order rate constants k_u and k_m (iii) by including the variable x_m.

$$r_{obs} = r_u + r_m \quad 4$$

$$r_{obs} = k_u Pt_u + k_m Pt_m \quad 5$$

$$r_{obs} = [(1-x_m)k_u + x_mk_m]Pt_T \quad 6$$

By introducing an intrinsic selectivity s for the modified sites, expressions can be written for the rate of formation of the R and S enantiomers as well.

$$r_R = 0.5k_u Pt_u + sk_mk_m Pt_m \quad 7$$

$$r_S = 0.5k_u Pt_u + (1-s)k_mk_m Pt_m \quad 8$$

Using only the variables defined above, and the definition of ee, two new expressions can be written for the observed optical yields ee_{obs}.

$$ee_{obs} = 100(r_R - r_S)/(r_R + r_S) \quad 9$$

$$ee_{obs} = 100(r_R - r_S)/r_{obs} \quad 10$$

$$ee_{obs} = [100(2s-1)x_mk_m Pt]/r_{obs} \quad 11$$

Further, rearranging Eq 6 gives:

$$x_m = [(r_{obs}/Pt_T) - k_u]/(k_m - k_u) \quad 12$$

Finally, elimination of x_m from Eq 11 leads to the interdependence between ee and rate (or TOF).

$$ee_{obs} = a + b/TOF \quad 13$$

$$a = 100(2s-1)k_m/(k_m - k_u)$$

$$b = 100(2s-1)k_u k_m/(k_m - k_u)$$

Comment I. For data which conforms to the slope-intercept form of Eq 13, the condition m < 0 represents a ligand

accelerated reaction, whereas the condition $m > 0$ represents a ligand decelerated reaction.

The numerical value of k_u can always be obtained from an unmodified experiment or from the relationship $k_u = b/a$. Further, if the system is entirely modifiable, or if one explicitly assumes $(x_m)_{\max} = 1$, then it is possible to solve for k_m and s . Otherwise k_m and s remain undetermined.

Comment II. The above derivation avoids a number of potential problems. Foremost, the exact relationship between the quantity of modifier and the number of modified platinum sites is unknown, and may well differ from system to system. For example, we don't know if the system obeys a simple Langmuir adsorption isotherm, and there may well be some adsorption on the support. (See Comment IV)

The final expression for a two-cycle system Eq 13, involving just e and rate, and free from both $[HCd]$ and x_m , was tested on the toluene system.⁷ A very good linear correlation was obtained, namely, $s = 0.93 \pm 0.02$, $k_u = 1.03 \pm 0.07 \text{ s}^{-1}$ and $k_m = 10.0 \pm 0.7 \text{ s}^{-1}$.

Inclusion of Stoichiometries. Clearly, it is an oversimplification to assume that each platinum atom is a site. This is particularly true for modified sites Pt_m , where adsorption of modifier ($MW \approx 300$) certainly requires an ensemble of platinum atoms. Accordingly, we define a modified site Pt^* in terms of a stoichiometry ν_m of modified atoms. Additionally, a new consistent rate constant k^* for a modified site can be defined.

$$Pt^* = Pt_m / \nu_m \quad 14$$

$$k^* = \nu_m k_m \quad 15$$

$$r_m = k^* Pt^* \quad 16$$

Next, let us assume that a modified site consists of a single cinchona molecule and an ensemble of platinum atoms. The quantity of adsorbed modifier $[HCd]_{ad}$ can be defined in terms of the number of modified sites, and in terms of an appropriate equilibrium constant.

$$[HCd]_{ad} = Pt^* \quad 17$$

$$[HCd]_{ad} = K_{eq} [HCd]_{soln} Pt_u \quad 18$$

Finally, there is the implicit assumption that all platinum atoms are modifiable. This is almost certainly not the general case. As a very simple example, consider platinum crystallites in very narrow pores ($< 10 \text{ \AA}$). Such atoms are almost certainly inaccessible to the modifier.

Accordingly, the total number of surface platinum atoms which are potentially modifiable, is considerably less than the number of surface platinum atoms i.e. $Pt_T \leq Pt_{surf}$, and we can write:

$$Pt_T = \xi Pt_{surf} \quad 19$$

$$0 \leq \xi \leq 1 \quad 20$$

Comment III. If the adsorption of a cinchona molecule is very strong, i.e. the equilibrium constant is very large, then the number of modified platinum atoms and the fraction modification are simply:

$$Pt_m = \nu_m [HCd]_T \quad 21$$

$$x_m = \nu_m [HCd]_T / Pt_T \quad 22$$

At this point, the rate of reaction can be rearranged, and its derivative with respect to $[HCd]_T$ can be taken. This provides a very good estimate of the magnitude of the pseudo first order rate constant k^* for a modified site when the condition $k_u \ll k_m$ is fulfilled.

$$r_{obs} = [k_u + x_m(k_m - k_u)] Pt_T \quad 23$$

$$r_{\text{obs}} = (k_v/Pt_T) + v_m[\text{HCd}]_T(k_m - k_u)$$

$$dr_{\text{obs}}/d[\text{HCd}]_T = v_m(k_m - k_u) \quad 25$$

$$dr_{\text{obs}}/d[\text{HCd}]_T \approx k^* \quad 26$$

The minimum value of the rate constant k^* for experiments conducted in toluene as solvent at 20°C is $k^* \approx 130 \text{ s}^{-1}$. If the above assumptions concerning strong adsorption and stoichiometry are correct, then k^* is the effective turnover frequency per molecule of dihydrocinchonidine!

Comment IV. The product of ee and TOF is a very interesting function because it serves as a measure for the fraction modification x_m . Such a measure can suggest an appropriate form for an adsorption isotherm between dihydrocinchonidine molecules and the platinum surface.

$$ee \cdot \text{TOF} = 100(2s-1)k_m x_m \quad 27$$

A plot of (ee•TOF) versus $[\text{HCd}]_T/Pt_{\text{surf}}$ is shown in Figure 1. Clearly, the results for the cinchona and $\text{Pt}/\text{Al}_2\text{O}_3$ system are in agreement with a simple Langmuir adsorption isotherm, with no further complication or qualifications.

The above result is interesting because it has been suggested that enantioselection in the cinchona system arises due to a *well ordered array* of adsorbed modifier.^{9,10} The results presented in Figure 1 strongly argue against such a suggestion. Indeed, the formation of a well ordered array or even the statistically random aggregation of 3 or 4 modifier molecules, as the source of enantioselection, would not lead to the simple, continuous and asymptotically increasing form shown in Figure 1.

This latter result strongly suggests that an enantioselective site consists of *one cinchona alkaloid molecule and an ensemble of platinum atoms*.

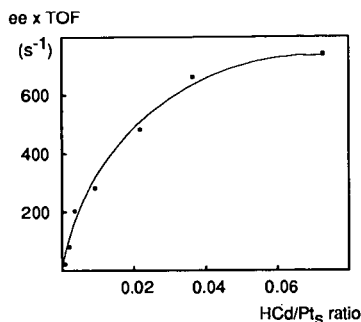


Figure 1. The function (ee•TOF) versus $[\text{HCd}]_T/Pt_{\text{surf}}$ for data taken in ethanol as solvent. (See Eq 27)

A considerably more complex relationship exists between ee and rate at yet higher loadings of chiral modifier in both toluene and ethanol as solvent and at high loadings in acetic acid.

REFERENCES

- [1] Jacobsen, E.N.; Marko, I.; Mungall, W.S.; Schröder, G.; Sharpless, K.B. *J. Am. Chem. Soc.* **1988**, *110*, 1968.
- [2] Jacobsen, E.N.; Marko, I.; France, M.B.; Svendsen, J.S.; Sharpless, K.B. *J. Am. Chem. Soc.* **1989**, *111*, 737.
- [3] Orito, Y.; Imai, S.; Niwa, S. *J. Chem. Soc. Jpn.* **1979**, 1118.
- [4] Orito, Y.; Imai, S.; Niwa, S. *J. Chem. Soc. Jpn.* **1980**, 670.
- [5] Blaser, H.U.; Jalett, H.P.; Monti, D.M.; Reber, J.F.; Wehrli, J.T. *Stud. Surf. Sci. Catal.* **1988**, *41*, 153.
- [6] Garland, M.; Blaser, H.U. *J. Am. Chem. Soc.* **1990**, *112*, 7048.
- [7] Garland, M.; Jalett, H.P.; Blaser, H.U. *Stud. Surf. Sci. Catal.* **1991**, *58*, 177.
- [8] Blaser, H.U.; Jalett, H.P.; Wiehl, J.J. *Mol. Cat.* **1991**, *68*, 215.
- [9] Thomas, J. *Angew. Chem. Adv. Mater.* **1989**, *101*, 1105.
- [10] Wells, P.B. *Faraday Discuss. Chem. Soc.* **1989**, *87*, 1.

Fuel Chemistry Division Invited Paper
Spring ACS Meeting April 5-10, 1992, San Francisco, CA
last revision: January 9, 1992

COMPUTATIONAL APPROACH TO THE PREDICTION OF BIMETALLIC CLUSTERS

PREPRINTS OF THE FUEL CHEMISTRY DIVISION, ACS

Liqiu Yang, Todd J. Raeker, Ann M. Schoeb, Xi Wu,
Terry King and Andrew E. DePristo
Ames Laboratory, USDOE
Iowa State University, Ames, IA 50011

Keywords

structure of bimetallics; corrected effective medium theory; partial bond energies

Abstract

The catalytic properties of bimetallic clusters will be influenced by the detailed structure of the cluster surface. Enrichment of one metal at the surface is one feature of obvious importance. Other, less obvious, features are preferential population of edge and corner binding sites on the surface and micromixing that influences ensemble size on the surface planes.

We review the range of methods developed to treat this problem, from the computationally demanding corrected effective medium (CEM) theory (a semi-empirical density functional based method) to the computationally simple method of partial bond energies. Parametrization of the latter is shown to be feasible using the former.

Comparisons of theoretical predictions with experimental data will be made for heats of formation in selected alloys and for surface segregation behavior in $\text{Rh}_{0.9}\text{Pt}_{0.1}(111)$. Detailed results on the shape, site composition and surface micromixing will be shown for selected systems chosen from $\text{Rh}_x\text{Pd}_{1-x}$, $\text{Ni}_x\text{Pd}_{1-x}$, and $\text{Rh}_x\text{Ni}_{1-x}$, $\text{Rh}_x\text{Pt}_{1-x}$ and $\text{Pt}_x\text{Cu}_{1-x}$ with $x=[0,1]$ for sizes between 200 and 1200 total atoms.

Introduction

The prediction of structure and energies of bimetallic clusters in the range of 200-2000 atoms provides an important technological problem for fundamental descriptions of metal-metal bonding. These systems are relevant to the performance of bimetallic catalysts¹ and also small enough to be treated by reasonably accurate theoretical density functional theory methods.²⁻⁴ They are also large enough to be treatable by empirical bonding models.⁵⁻⁷ Thus, such systems can provide an excellent testing ground for theoretical methods as well as demonstrate the utility of new theoretical methods in conjunction with rapidly advancing computer technology.

Theory

A hierarchy of theories have been used to describe bimetallics. We give a brief overview of each here. The reader interested in more details should consult the references, especially ref.(2d) for CEM, ref.(2c) for MD/MC-CEM and ref.(4) for construction of embedding functions in either theory. Applications to bimetallic

surfaces can be found in ref.(3). For the method of partial bond energies, the reader should consult refs.(5-7) for an overview.

For a set of N-atoms, $\{A_i, i=1, \dots, N\}$, the CEM theory utilizes the following equations to calculate the interaction energy:

$$\Delta E(\{A_i\}) = \sum_{i=1}^N \Delta E_{LMTO}(A_i; n_i) + \frac{1}{2} \sum_{i=1}^N \sum_{j=1}^N V_c(i, j) + \Delta G(\{A_i\}) \quad (1)$$

$$n_i = \frac{1}{2Z_i} \sum_{j=1}^N \int n(\vec{r} - \vec{R}_i) n(\vec{r} - \vec{R}_j) d\vec{r} \quad (2)$$

$n(\vec{r} - \vec{R}_i)$ is the unpolarized atomic electron density distribution (from Hartree-Fock calculations) while Z_i and \vec{R}_i are the atomic number and nuclear position, respectively. This equation is valid under the assumption that the total system electron density can be approximated as the superposition of atomic electron densities.

The first term is the sum of the embedding energy for each atom, *each term of which is solely a function of the average electron density environment of that particular type of atom*. The subscript 'LMTO' indicates that these are provided by forcing the CEM method to duplicate the results of self-consistent Linearized Muffin Tin Orbital density functional calculations on the cohesive energy of the homogeneous bulk solid at lattice constants from 30% expansion to 10% contraction.^{4a} Since these embedding energies are a major component of the system interaction energy, it is important to determine them accurately and this procedure does so, at least for coordinations approaching that of the bulk. For very low coordinations, it is necessary to supplement the LMTO calculated values with experimental data from the diatomic binding curve.^{4b}

The second term consists of pairwise additive coulombic energies. $V_c(i, j)$ is the sum of electron-electron, electron-nuclear and nuclear-nuclear coulomb interactions between atoms A_i and A_j . These are determined from the electron densities of each atom and are not adjustable.

The last term, ΔG , is the difference in kinetic-exchange-correlation energies of the N-atom and atom-in-jellium systems. It is a true many body term which is extremely time consuming computationally since it involves computation of a three dimensional multicenter integral of complicated functions of both the electron density and its gradient with respect to electronic coordinates.

To lower the computational effort, a simpler theory has been developed with acronym MD/MC-CEM since it is fast enough to use in direct MD and MC simulations of large systems. In this method, the ΔG term is approximated as a function of n_i and incorporated into new effective embedding terms. This yields the working equation as:

$$\Delta E(\{A_i\}) = \sum_{i=1}^N \Delta F_{LMTO}(A_i; n_i) + \frac{1}{2} \sum_{i=1}^N \sum_{j=1}^N V_c(i, j) \quad (3)$$

The effective embedding functions, ΔF_{LMTO} are determined again from LMTO calculations on the homogeneous bulk system.

The above two methods involve continuous change in interaction energies with separations between atoms. Neither is pairwise additive, and thus describes the delocalized bonding in metals. The CEM method can be derived from the fundamental density functional theory under the assumption of additive atomic densities. The MD/MC-CEM method is more empirical, depending upon a rather uncontrolled approximation to the kinetic-exchange-correlation energy difference energy. This method is very similar to the EAM method which simply postulates a form like Eq.(3) and replaces all terms by empirical forms. (e.g. Morse potentials or shielded coulomb like terms for the two body interactions).^{8,9} The EAM approach also utilizes the density at the nucleus of atom A_i instead of the average in Eq.(2), to identify a jellium density.

We have also utilized a much simpler formulation than either CEM theory. This calculates the energy of an atom by counting the bond energies with each of its nearest neighbors, adjusting the strength of each bond according to the number of neighbors. This is the method of partial bond energies and leads to the working equation for a system of one atom type:

$$\Delta E ([A_i]) = \sum N_i \epsilon (A_i ; N_i) \quad (4)$$

where $\epsilon(A_i;N_i)$ is the bond energy of atom A_i with N_i nearest neighbors. This equation must be supplemented with the interchange energy when there are different types of atoms.⁵ Note that bond lengths are not required in the application of this method because the interatomic potential is a function of coordination rather than distance. However, this approach does require the assumption that the metal particle maintains a fixed lattice type during the simulation. In the results reported below the simulations are fixed in an fcc lattice.

The connection between these methods is that the CEM theory can be used to provide the partial bond energies by using selected calculations on various metal surfaces and metal vacancy formation.¹⁰

Results and Discussion

First, consider the Rh_xPt_{1-x} system. The surface energies (in J/m^2) predicted by CEM (MD/MC-CEM) are 2.37 (2.73), 2.52(2.88) and 2.71 (3.12) for Rh(111), Rh(100), Rh(110), respectively.^{4a} Experimental data on surface free energies of polycrystalline samples¹¹ at the metal's melting point and at 298 K can be used to extrapolate to 0 K with the result being 2.94 J/m^2 . The agreement is excellent as it is for other fcc metals.^{4a} The CEM predictions of the alloy formation energy are -2.4, -2.2 and -1.7 kJ/mole for $x=0.75$, 0.5 and 0.25 respectively. Since Pt and Rh alloy even at low temperatures, this small negative alloy formation energy is very reasonable. The MD/MC-CEM method predicts 42.0, 53.3 and 39.1 kJ/mole, respectively, and is thus inaccurate for this system. Indeed, we have found that MD/MC-CEM is inaccurate for all mixtures of Ir, Pt and Au with all other metals, except Ir,Pt and Au.

Using CEM calculations of the various Pt and Rh systems yields the partial bond energies shown in Fig.(1). For comparison, partial bond energies using a quadratic fit to limited experimental data are also shown. The agreement is quite good except at very low coordinations where the previous approach involves extrapolation.

Predictions of the surface fraction of Rh in Rh_xPt_{1-x} bimetallics cluster with 201 total atoms is shown in Fig.(2) based upon Monte-Carlo simulations at 973 K. These

are calculated using the partial bond energies assuming that the cluster retains a fcc lattice arrangement of atoms. Even though these simulations allow the structure of the particle to deviate from the initial cubo-octahedral shape, no such morphology change occurs due to the thermodynamic stability of that arrangement. The one point from the CEM results is also shown. Since the latter allows for continuous deformation of all atomic positions, it provides confidence that the use of the partial bond energy/Monte-Carlo simulation with an fcc lattice is adequate for this system.

Next, consider the Rh_xPd_{1-x} system. The surface energies (in J/m^2) predicted by CEM (MD/MC-CEM) are 1.63 (1.89), 1.74(2.00) and 1.87 (2.18) for Pd(111), Pd(100), Pd(110), respectively.^{4a} Experimental data on surface free energies of polycrystalline samples¹¹ at the metal's melting point and at 298 K can be used to extrapolate to 0 K with the result being $2.17 J/m^2$. The agreement is again excellent. The CEM predictions of the alloy formation energy are 1.5, 1.9 and 1.5 kJ/mole for $x=0.75$, 0.5 and 0.25 respectively. The experimental value¹² at 1575 K is 10 kJ/mole with the difference from 0 K easily made up by variation in heat capacity. The MD/MC-CEM method predicts 2.2, 2.9 and 2.2 kJ/mole, respectively, and is thus quite acceptably accurate.

Results for 201 and 1289 atom clusters are shown in Figs.(3) and (4), respectively. The clusters exhibit increased enrichment of Pd on the surface and a substantial favoring of edge-corner sites at the surface. Thus Pd atoms occupy low coordination sites on the surface. There is only a slight temperature dependence of the enrichment between 600 K and 1000 K.

In the Ni_xPd_{1-x} and Rh_xNi_{1-x} clusters (not shown), the metal segregating to the surface is Pd for the former and Ni for the latter. From these and other systems, a few general statements can be made: 1/ the metal with the smallest surface energy segregates to the lowest coordination sites first, then to other low coordination sites; 2/ an increase in temperature drives the mixing and thus decreases the degree of segregation; and, 3/ as the size of the cluster increases, the surface-segregating metal populates the entire surface at lower total concentration.

Experimental verification of these predictions is problematic. Only surface composition measurements have been attempted leaving site population and micromixing properties to speculation. The standard surface science tools such as Auger electron spectroscopy (AES) are not feasible due to the very nature of the particles. In addition, traditional methods of estimating surface composition using selective chemisorption are known to significantly perturb these bimetallic systems.⁵ In certain simple systems a combination of 1H NMR and hydrogen chemisorption have indicated the predictions give reasonable results.¹³ We can apply the predictions to low-index plane simulations that are more easily verified experimentally, however. The fcc(111) surface of $Rh_{0.9}Pt_{0.1}$ was simulated with the partial bond energy/Monte Carlo method in the same manner as the 201 atom particle discussed above yielding the results in Fig.(5). Recently, Fisher and co-workers have used AES and ion scattering spectroscopy to determine that the surface composition of this system is $\approx 70\%$ Rh in the 1200 K temperature range,¹⁴ which is in good agreement with our predictions.

Acknowledgement

This work was supported by the Advanced Industrial Concepts Division of the U.S. Department of Energy through the Ames Laboratory, which is operated for the U.S. DOE by Iowa State University under Contract No. W-7405-Eng-82. The more extensive CEM calculations were performed on the nCUBE 2 hypercube at two different sites: 1) the Scalable Computing Laboratory, Ames Laboratory; 2) the Massively Parallel Computational Research Laboratory, Sandia National Laboratory at Albuquerque.

References

1. J. H. Sinfelt, Bimetallic Catalysts: Discoveries, Concepts and Applications, John Wiley & Sons, (1983).
2. a) J. D. Kress and A. E. DePristo, *J. Chem. Phys.* **88**, 2596 (1988);
b) J. D. Kress, M. S. Stave and A. E. DePristo, *J. Phys. Chem.* **93**, 1556 (1989);
c) M. S. Stave, D. E. Sanders, T. J. Raeker and A. E. DePristo, *J. Chem. Phys.* **93**, 4413 (1990);
d) T. J. Raeker and A.E. DePristo, *Int. Rev. Phys. Chem.* **10**, 1 (1991).
3. a) T. J. Raeker, D. E. Sanders and A. E. DePristo, *J. Vac. Sci. Tech.* **A8**, 3531 (1990);
b) T. J. Raeker and A. E. DePristo, *Surf. Sci.* **248**, 134 (1991);
c) T. J. Raeker and A. E. DePristo, "Alloy formation energetics and dynamics in the Ni/Cu(100) and Ni/Cu(111) systems," *J. Vac. Sci. Tech.* **A** (in press, 11/91).
4. a) S. B. Sinnott, M. S. Stave, T. J. Raeker and A. E. DePristo, *Phys. Rev. B* **44**, 8927 (1991);
b) D. E. Sanders, D. M. Halstead and A. E. DePristo, "Metal/metal homo-epitaxy on FCC(111) and FCC(001) surfaces: deposition and scattering from small islands," *J. Vac. Sci. Tech.* **A** (in press, 12/91).
5. T. S. King, "Bond Breaking and Chemical Thermodynamic Models of Surface Segregation," in Surface Segregation Phenomena, eds. P. A. Dowben and A. Miller, CRC Press (1990).
6. X. Wu, S. Bhatia and T. S. King, "Characterization of Small Metal Particles," *J. Vac. Sci. Tech.* **A** (in press).
7. J. K. Strohl and T. S. King, *J. Catal.* **118**, 53 (1989).
8. C. L. Liu, J. M. Cohen, J. B. Adams and A. F. Voter, *Surf. Sci.* **253**,334 (1991).
9. a) M. S. Daw and M. I. Baskes, *Phys. Rev. B* **29**, 6443 (1984);
b) S. M. Foiles, M. I. Baskes and M. S. Daw, *Phys. Rev. B* **33**, 7983 (1986);
c) T. Ning, Q. Yu and Y. Ye, *Surf. Sci.* **206**, L857 (1988);
d) M. S. Daw, *Phys. Rev. B* **39**, 7441 (1989).
10. T. J. Raeker, L. Yang, A. M. Schoeb, X. Wu, T. S. King and A. E. DePristo, (to be submitted).
11. L. Z. Mezey and J. Giber, *Jap. J. App. Phys.* **21**, 1569 (1982).
12. R. Hultgren, P. D. Desai, D. T. Hawkins, M. Gleiser, and K. K. Kelley, Selected Values of the Thermodynamic Properties of Binary Alloys (American Society for Metals, Metals Park, OH, 1973).
13. X. Wu, B. C. Gerstein and T. S. King, *J. Catal.* **121**, 271 (1990).
14. a) G. B. Fisher and C. L. DiMaggio, *Surf. Sci.* (submitted);
b) D. D. Beck, C. L. DiMaggio and G. B. Fisher (personal communication).

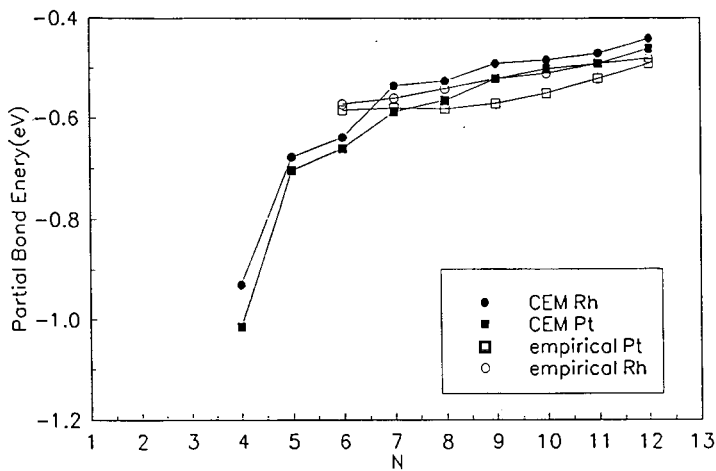


Fig. 1 Partial bond energies for Pt and Rh as determined from CEM calculations and also from previous work using a quadratic form (in N) fit to surface energies.

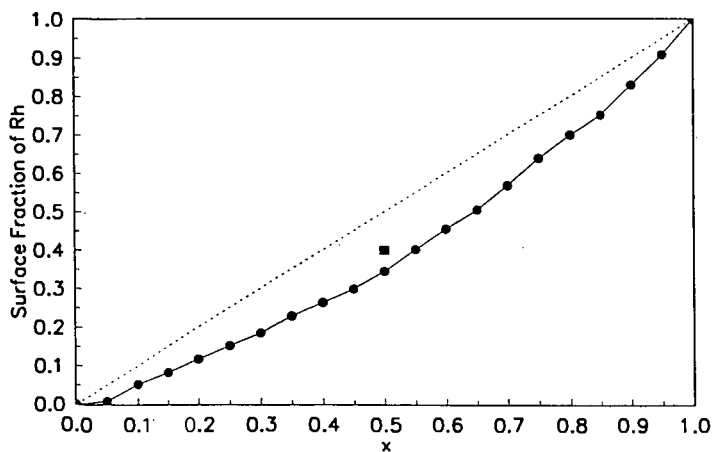


Fig. 2 Surface fraction of Rh in $\text{Rh}_x\text{Pt}_{1-x}$ clusters with 201 total atoms as predicted by the partial bond energy model at 973 K. A single point for $x=0.5$ (■) is shown based upon a full CEM simulation at 600 K. The dotted line separates enrichment (above) and depletion (below) regions.

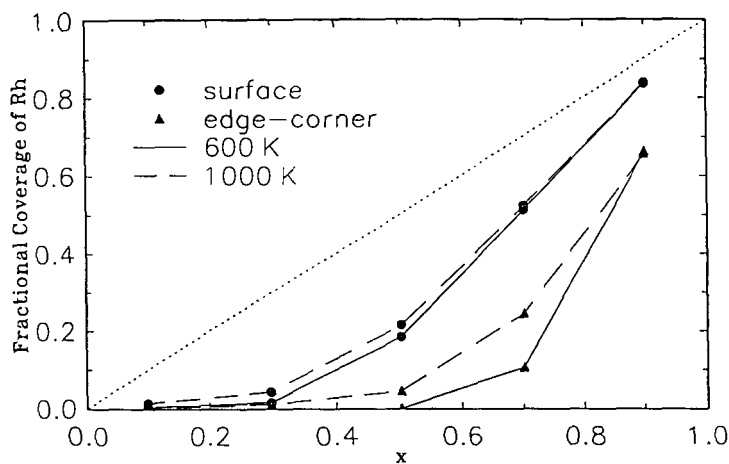


Fig. 3 Fractional coverage of Rh at surface and edge-corner sites in $\text{Rh}_x\text{Pd}_{1-x}$ clusters with 201 total atoms as predicted by the MD/MC-CEM model.

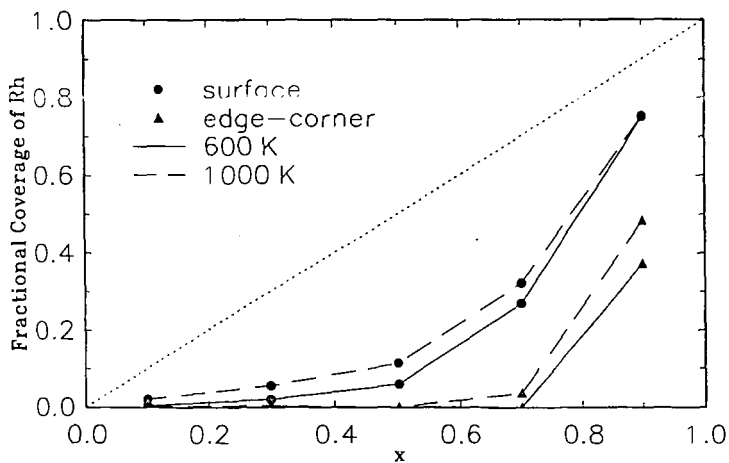


Fig. 4 Same as Fig.(3) but for 1289 total atoms.

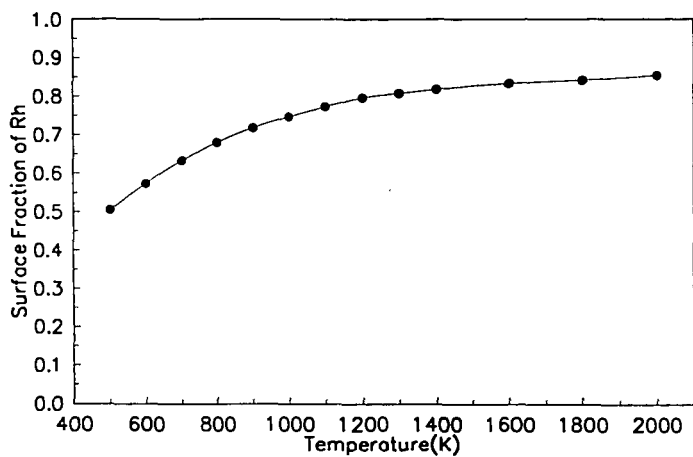


Fig. 5 Surface fraction of Rh in $\text{Rh}_{0.9}\text{Pt}_{0.1}$ (111) as predicted by the partial bond energy model.

MOLECULAR DESIGN OF SUBSTRATE BINDING SITES

John A. Shelnut, J. David Hobbs

Fuel Science Division 6211
Sandia National Laboratories
Albuquerque, NM 87185

Keywords: Molecular modeling, catalysis, porphyrin

ABSTRACT

Computer-aided molecular design methods were used to tailor binding sites for small substrate molecules, including CO₂ and methane. The goal is to design a cavity, adjacent to a catalytic metal center, into which the substrate will selectively bind through only non-bonding interactions with the groups lining the binding pocket. Porphyrins are used as a basic molecular structure, with various substituents added to construct the binding pocket. The conformations of these highly-substituted porphyrins are predicted using molecular mechanics calculations with a force field that gives accurate predictions for metalloporphyrins (Shelnutt, *et al.*, *J. Am. Chem. Soc.* **1991**, *113*, 4077). Dynamics and energy-minimization calculations of substrate molecules bound to the cavity indicate high substrate binding affinity. The size, shape, and charge-distribution of groups surrounding the cavity provide molecular selectivity. Specifically, calculated binding energies of methane, benzene, dichloromethane, CO₂, and chloroform vary by about 10 kcal/mol for metal octaethyl-tetraphenylporphyrins (OETPPs) with chloroform, dichloromethane, and CO₂ having the highest affinities and with methane and benzene having the lowest. Significantly, a solvent molecule is found in the cavity in the X-ray structures of Co- and CuOETPP crystals obtained from dichloromethane.

INTRODUCTION

We have set for ourselves the ambitious goal of designing and synthesizing molecules with a high affinity binding site for a given substrate molecule. Preferably, the molecule containing the substrate binding cavity would also possess some additional chemical functionality, such as a catalytic center at which the substrate would be converted to a useful product. Because over 70 metals in various oxidation states can be incorporated into the porphyrin macrocycle and because of the high degree of variability in the peripheral substituents, we have chosen the metalloporphyrins as a foundation for construction of the required binding site. By using the porphyrin ligand, we gain considerable freedom both in the choice of catalytic metal at its center and in the selection of peripheral substituents used to construct the binding cavity of the chosen substrate molecule.

Our initial goal is to construct a porphyrin with a substrate binding pocket for which only non-bonding forces contribute to the selective binding of the substrate to the active site. The inclusion of such a cavity gives several potential benefits. These benefits include (1) increased affinity for the substrate and decreased product affinity, (2) enhanced selectivity for a particular substrate molecule, (3) enhanced regioselectivity of the reaction, (4) lower catalyst self-destruction rates and increased catalyst stability, (5) product slate selectivity resulting from trapping of radical intermediates for recombination, and (6) enhanced reactivity from molecular orientational and conformational lowering of transition states, to name a few. All of these benefits of a substrate binding pocket are realized to one degree or another in naturally occurring biological catalysts called enzymes, particularly for the metalloporphyrin-containing enzymes. These enzymes, for example cytochrome P₄₅₀, methylreductase, and the photosynthetic reaction center, catalyze many important energy-related chemical or photochemical reactions. Thus, computer-modeling studies of these enzymes give many important clues to the structural features that might be engineered into our designed catalyst. These features include (1) a catalytic metal ion, (2) appropriate electronic properties for the ligands of the metal, (3) complementary size and shape for the substrate binding pocket, (4) suitable properties like hydrophobicity and charge distribution for the groups lining the pocket, and (5) molecular rigidity of the cavity.

The molecular rigidity of the cavity results in enhanced substrate binding affinity, an

especially important asset for catalytic conversion of small gaseous substrate molecules like CO₂ and methane. Because the rigid binding pocket is present even in the absence of the substrate molecule, enzyme studies show that the 'hole' in the catalyst contributes (about 2 kcal/mol) to the binding energy (for each methylene-group-sized unit) of the substrate molecule through the dispersion energy contribution to the interaction with the bound substrate. In the example of an enzyme and its alkane substrate in water, two unfavorable hydrophobic interfaces result, one from the water molecules filling the hydrophobic pocket and another from the alkane dissolved in the solvent; these unfavorable hydrophobic interactions are removed when the substrate binds to the preformed pocket, accounting for about 3 kcal/mol for a methylene-sized molecular unit. Electrostatic forces also enhance the binding energy. After the rigidity of the cavity is insured, energy contributions to the binding energy of the substrate molecule can be optimized by careful design of the binding cavity of our tailored enzyme analog.

The molecular rigidity of the binding pocket possessed by the enzymes has been one of the most difficult structural features to mimic in our metalloporphyrin-based enzyme analogs. However, by using so-called highly substituted porphyrins we have been able to engineer the required molecular rigidity into our designed catalysts. Using a molecular model based on a porphyrin normal coordinate analysis, we found that the porphyrin ring, when maximally substituted at the periphery with non-hydrogen substituent groups, was rigidly distorted into a saddle shaped conformation. Furthermore, in this distorted geometry the substituents at the β -pyrrole carbons form a binding pocket of a size and shape suitable for binding small molecules like CO₂ and light alkanes. And, by lining the pocket with groups with properties complementary to the substrate, we could promote substrate binding to the pocket for times on the order of nanoseconds (in molecular dynamics calculations at 300 °K in vacuum).

Many of the designed catalysts have been synthesized and subjected to experimental structural studies. The calculated conformations of the designed catalysts have been verified by X-ray crystallography, NMR spectroscopy, UV-visible absorption spectroscopy, and resonance Raman spectroscopy.¹⁻³

Evidence of substrate binding is found in the X-ray crystal structures of the cobalt and copper derivatives of octaethyl-tetraphenylporphyrin. As described below, small solvent molecules are observed in the substrate binding cavity in X-ray crystal structures of this highly-substituted metalloporphyrin.

MATERIALS AND METHODS

Cobalt(II) and copper(II) octaethyltetraphenylporphyrin (OETPP) were synthesized as described previously.² The X-ray crystal structures were reported previously,² however the location of solvent molecules in the crystals was not discussed. Views of the packing of porphyrin molecules in the crystal are shown in Figures and were generated on an Evans&Sutherland PS390 graphics workstation. One of two crystallographically distinct solvent molecules is located in the cavity as shown (Figures 2 and 3).

Molecular modeling calculations were performed on a Personal Iris 4D35 workstation using BIOGRAF software from Molecular Simulations, Inc. The calculations were carried out as described previously for a series of nickel porphyrins.² The force field is the same as that reported earlier for nickel(II) porphyrins,² but extended to include other metal ions including Co(II) and Cu(II).³ This force field has been successful in predicting porphyrin conformations that agree well with X-ray crystal structures.^{2,3} Parameters for the oxygen atoms in CO₂ and for the Cl atoms in the halogenated methanes were taken from the DREIDING force field.⁴ Partial atomic charges were assigned to the porphyrin and solvent molecules by the method of charge equilibration.^{4,5} Minimizations were carried out for several initial orientations of the substrate molecule, because of the many local minima resulting from different substrate orientations in the binding pocket.

RESULTS AND DISCUSSION

Figure 1 shows the energy-minimized structure of nickel(II) octapropyl-tetraphenylporphyrin (NiOPTPP) with CO₂ bound in one of the grooves generated by four of the quasi-axial β -pyrrole ethyl substituents. Clearly, CO₂ fits nicely in the elongated cavity of the catalyst, so we decided to evaluate the selectivity of the cavity for a variety of small substrate molecules.

Tables I-III summarize the results of molecular mechanics calculations for the binding of various small molecules, including CO₂, methane, benzene, dichloromethane, and chloroform, to the elongated cavity. The relative binding energies are seen to vary over several kcal/mole, depending

primarily on the size of the substrate and distribution of charge in the substrate molecule. In the model, van der Waals interactions and electrostatic interactions between the substrate molecule and the designed porphyrin catalyst are the only forces that contribute to the binding energy. Benzene binds most weakly because the partial charges on the atoms are small. The chlorinated methanes bind most strongly because the highly electronegative chlorine atoms result in large partial charges on the substrate atoms which interact strongly with complementary charges on the catalyst. In particular, the interactions between the electronegative oxygen (or chlorine) atoms of the substrate and the nearby hydrogen atoms of the ethyl groups of the catalyst are important. In our calculation the electrostatic energy falls off as $1/r^2$, making the interactions with the closest atoms most significant. The $1/r^2$ -dependence is used to mimic the presence of a solvent in a crude way. The dielectric constant of the solvent is assumed to be 1, represents an organic solvent.

Examination of Tables I and II, for catalysts with well defined cavities (NiOETPP and CuOETPP), shows that the order of binding energies is: $\text{CHCl}_3 > \text{CO}_2 \approx \text{CH}_2\text{Cl}_2 > \text{benzene} > \text{methane}$. The van der Waals contribution to the binding energy varies over the range from 6 to 13 kcal/mole for all substrates, lowest values being for the smallest substrates of the group. The electrostatic contribution is large (2-6 kcal/mole) for the substrates with electronegative atoms and small for the hydrocarbons. The internal energies (bond stretch, angle bend, etc.) adjust to some extent upon substrate binding, particularly the torsions. The cavity is slightly larger for CuOETPP (Table II) than for NiOETPP (Table I), and the larger cavity results in weaker binding of each substrate. This effect is even more in evidence when the ethyl groups are replaced by methyl groups (NiOMTPP, Table III), and the cavity is lost altogether. Then, the binding energies of all substrates (except benzene) decrease.

Clearly, the results in Tables I and II indicate that dichloromethane is expected to have one of the highest affinities for the cavity. Therefore, it is not surprising to find a dichloromethane molecule in the cavity in the X-ray crystal structure of the Co and Cu derivatives of OETPP. Figures 2 and 3 show orthogonal views of two of the CuOETPP molecules in the crystal. Also shown are two equivalent dichloromethane molecules that are located in the cavity. The dichloromethane molecules are not coordinated to the copper(II) ion. Copper is usually four-coordinate, square planar with the porphyrin occupying all four ligand sites. The lack of coordination of the dichloromethane is also clear from the greater than 3-Å distance between the metal and the heavy atoms of the substrate.

The binding site apparently does not have a strong preference for a particular orientation of the bound substrate molecule. We conclude this from the many orientations of the substrate molecule that give rise to structures with energies close to the lowest listed for each substrate in Table I. Two such structures are given for dichloromethane and CO_2 in the Tables. Here too, the X-ray data support a similar conclusion based on the thermal parameters for atoms of the dichloromethane located in the cavity. The isotropic displacement coefficient for the carbon atom of the dichloromethane molecule in the pocket is approximately twice as large as for the average carbon atom of the porphyrin. The isotropic parameters for the chlorines are about four times as large as the average carbon atom. This points to a disordered orientation of the dichloromethane molecule in the cavity. The second crystallographically distinct dichloromethane molecule, which is not located in the pocket, is even more disordered.

Efforts are in progress to measure $^{13}\text{CO}_2$ binding to the iron(III) derivatives of the designed catalysts using ^{13}C -NMR spectroscopy. On the basis of the molecular modeling results we have chosen to carry out the experiments in the solvent benzene, which is less likely to spend time in the cavity. We wish to measure the decrease in the ^{13}C relaxation time (T_1) due to the interaction with the paramagnetic Fe(III) center in FeOETPP, when the porphyrin is added to a solution of benzene saturated with $^{13}\text{CO}_2$. The relaxation time decreases depending on how much time the $^{13}\text{CO}_2$ stays in the vicinity of the paramagnetic center and how close to the center the CO_2 comes. Thus, we expect to find a much larger decrease for FeOETPP, which has a binding cavity for CO_2 , than for Fe octamethyl-tetraphenylporphyrin (FeOMTPP), which is structurally very similar to FeOETPP but lacks a cavity in which CO_2 can bind. From Table III, note that the ordering of substrate binding energies is different when the cavity is lost for CuOMTPP. In particular, the benzene solvent binds more strongly than CO_2 for OMTTPs. Preliminary experiments in collaboration with R. A. Assink support these conclusions.

ACKNOWLEDGEMENTS

This work supported by U. S. Department of Energy Advanced Industrial Concepts Catalysis/Biocatalysis Program and Pittsburgh Energy Technology Center under Contract DE-AC04-76DF00789. We express thanks to C. J. Medforth at the University of California at Davis and R. A. Assink at Sandia National Laboratories for helpful discussions.

REFERENCES

1. Medforth, C. J.; Berber, M. D.; Smith, K. M.; Shelnut, J. A., *Tetrahedron Letts.* **1990**, 31, 3719.
2. Shelnut, J. A.; Medforth, C. J.; Berber, M. D.; Barkigia, K. M.; Smith, K. M., *J. Am. Chem. Soc.* **1991**, 113, 4077.
3. Sparks, L. D.; Medforth, C. J.; Park, M.-S.; Chamberlain, J. R.; Ondrias, M. R.; Senge, M. O.; Smith, K. M.; Shelnut, J. A., *J. Am. Chem. Soc.*, 1992, submitted.
4. Mayo, S. L.; Olafson, B. D.; Goddard III, W. A., *J. Phys. Chem.* **1990**, 94, 8897.
5. Rappe, A. K.; Goddard III, W. A., *J. Phys. Chem.*, to be submitted.

TABLE I. Relative Substrate Binding Energies (kcal/mole) and Distance from Metal to Nearest Substrate Atom (Å) for Ni Octaethyl-Tetraphenylporphyrin.

Substrate	Total E	VDW	ES	Torsion	Angle	Bond	Invers.	Dist.*
methane	7.4	5.8	2.3	-1.9	0.3	0.7	0.0	3.88 C
benzene	10.4	9.6	0.0	0.5	0.2	0.0	0.0	3.37 C
CH ₂ Cl ₂	14.0	12.1	2.8	-2.1	0.0	1.2	0.0	3.17Cl
	12.7	9.7	4.4	-1.3	-0.5	0.4	0.0	3.73 C
CO ₂	14.3	8.9	5.7	-0.9	0.0	0.4	0.3	3.43 C
	13.9	9.1	6.1	-1.6	-0.1	0.4	0.0	3.20 C
CHCl ₃	17.1	13.0	5.1	-1.9	-0.2	1.2	0.0	3.23Cl

*Distance between the metal and the nearest heavy atom.

TABLE II. Relative Substrate Binding Energies (kcal/mole) and Distance from Metal to Nearest Substrate Atom (Å) for Cu Octaethyl-Tetraphenylporphyrin.

Substrate	Total E	VDW	ES	Torsion	Angle	Bond	Invers.	Dist.*
methane	5.5	4.6	2.0	-1.5	-0.2	0.7	-0.1	3.56 C
benzene	10.0	0.7	10.6	-1.6	-0.1	0.4	0.0	3.56 C
CH ₂ Cl ₂	12.5	7.0	3.8	1.6	-0.2	-0.2	0.4	3.65 C
	11.6	10.7	2.3	-1.3	-0.3	0.2	0.0	3.54Cl
CO ₂	12.8	6.7	5.4	-0.3	0.2	0.7	0.0	3.19 C
	12.7	9.8	7.2	-3.7	-0.8	0.5	-0.5	3.39 C
CHCl ₃	15.2	12.3	5.5	-2.6	-0.3	0.9	-0.6	3.29Cl

*Distance between the metal and the nearest heavy atom.

TABLE III. Relative Substrate Binding Energies (kcal/mole) and Distance from Metal to Nearest Substrate Atom (Å) for Ni Octamethyl-Tetraphenylporphyrin.

Substrate	Total E	VDW	ES	Torsion	Angle	Bond	Invers.	Dist.*
methane	4.4	3.2	1.0	0.1	0.3	-0.1	-0.1	3.48 C
benzene	10.9	10.2	0.1	0.1	0.4	0.2	-0.1	3.85 C
CH ₂ Cl ₂	10.1	8.5	2.2	-0.7	-0.3	0.5	-0.1	3.46 C
	10.1	8.6	2.5	-1.7	0.1	0.7	-0.1	3.57Cl
CO ₂	9.6	7.0	2.9	-0.2	-0.1	0.0	-0.1	3.13 O
	6.8	6.5	0.2	-0.9	-0.1	1.1	-0.1	3.24 C
CHCl ₃	11.9	9.2	3.8	-1.2	-0.4	0.5	-0.1	3.60Cl

*Distance between the metal and the nearest heavy atom.

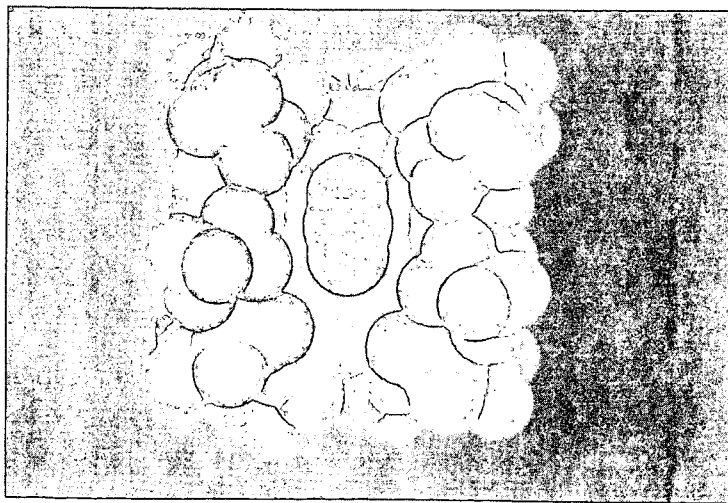
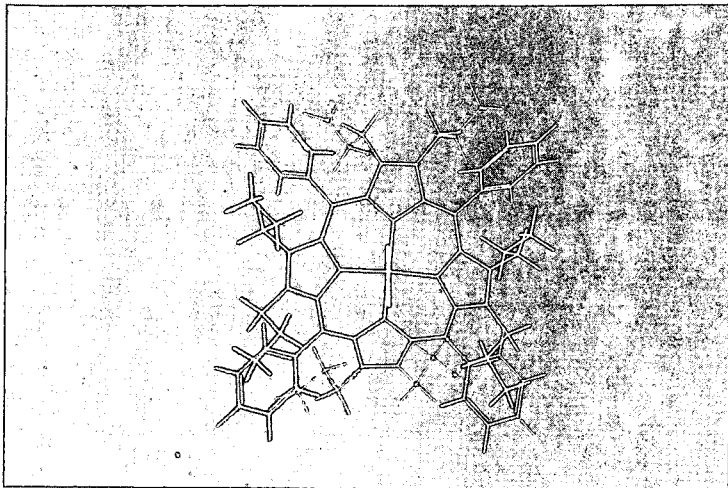
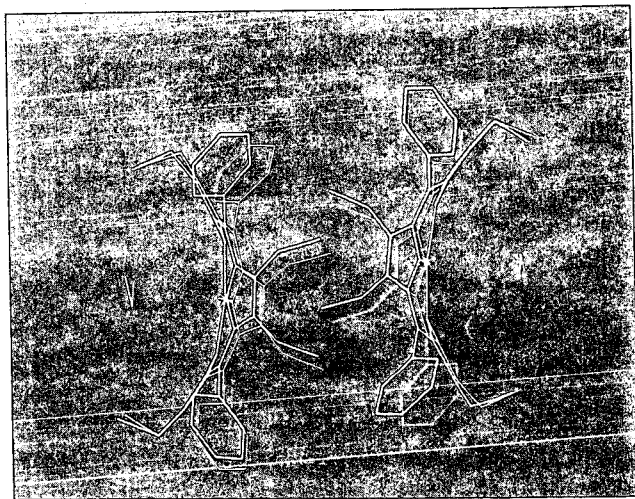
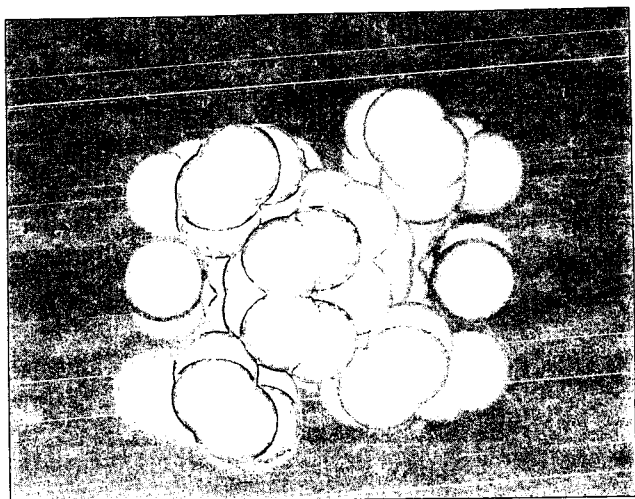


Figure 1. Energy-minimized structure of nickel(II) octapropyl-tetraphenylporphyrin (NiOPTP) showing CO₂ bound in the cavity formed by the porphyrin macrocycle and the quasi-axial ethyl groups. View looking down into the substrate binding cavity of NiOPTP where CO₂ is bound (center).



View of the X-ray crystal structure of copper(II) octaethyl-tetraethylporphyrin (CuOETTP) showing two molecules of CuOETTP and two dichloromethane molecules (top and bottom) in the binding cavity.

Figure 2.

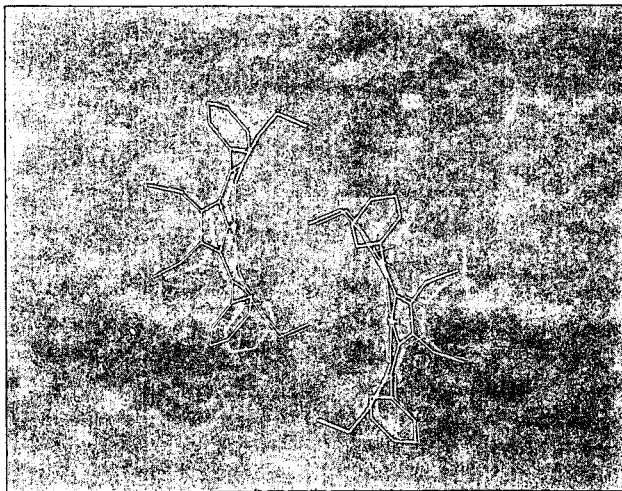
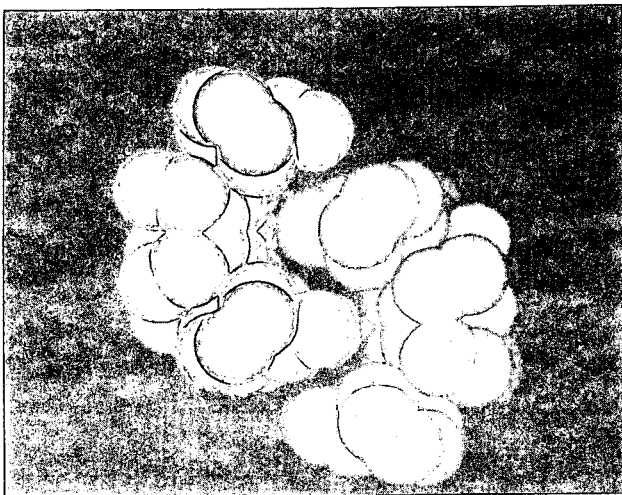


Figure 3. View of the X-ray crystal structure of copper(II) octaethyl-tetraphenylporphyrin (CuOETPP) showing two molecules of CuOETPP and two dichloromethane molecules (top and bottom) in the binding cavity. View is orthogonal to that of Figure 2.

**THE SYNTHESIS AND CHARACTERIZATION OF NEW COPPER
COORDINATION COMPLEXES CONTAINING AN ASYMMETRIC
COORDINATING CHELATE LIGAND: APPLICATION TO ENZYME ACTIVE
SITE MODELING ***

M.W. Droege,¹ J.H. Satcher, Jr.,¹ R.A. Reibold,¹ T.J.R. Weakely²

¹Lawrence Livermore National Laboratory, PO Box 808, Livermore, Ca., 94550

²Dept of Chemistry-University of Oregon, Eugene, OR., 97403

Keywords: *Asymmetric coordination, binuclear complex, methane monooxygenase*

ABSTRACT

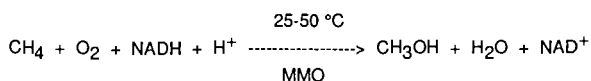
A new class of ligand which produces a binuclear metal complex with coordination asymmetry has been designed and synthesized. A binuclear copper complex has been prepared and characterized including a single crystal x-ray structure analysis. The structure reveals that one copper is 5-coordinate (distorted square pyramidal) while the other copper is only 4-coordinate (distorted square planar) and are separated by an endogenous μ -alkoxo oxygen and a bridging acetate. Although this structural type of chelator has been found in biological systems, it has not been previously described for inorganic coordination complexes prepared by design. It is anticipated that this ligand and derivatives of it will play an important role in mimicking chemical reactivity of enzyme active sites that function by substrate interaction at only one metal of a multimetal active site.

INTRODUCTION

The catalytic oxidation of light hydrocarbons, especially methane derived from natural gas, is an important research area attracting considerable attention. The potential for natural gas (methane) processing will depend on the development of catalyzed routes directly converting methane to higher valued products (heavier hydrocarbons, olefins, and alcohols). However, methane is chemically quite inert and has not proved easy to convert to liquid hydrocarbons. As a result, no technologies are currently available to process methane economically. It is well-known that a select group of aerobic soil/water bacteria called methanotrophs can efficiently and

*Work performed under the auspices of the U.S. Department of Energy by the Lawrence Livermore National laboratory under Contract No. W-7405-ENG-48.

selectively utilize methane as the sole source of their energy and carbon for cellular growth.¹ The first reaction in this metabolic pathway is catalyzed by the enzyme methane monooxygenase (MMO) forming methanol:



Methanol is a technologically important product from this partial oxidation of methane since it can be easily converted to liquid hydrocarbon transportation fuels, used directly as a liquid fuel itself, or serve as a feedstock for fine chemicals production.

Microorganisms can produce MMO in two distinct forms: a membrane-bound particulate form or a discrete soluble form. The soluble form consist of three main proteins: A, B, and C. Protein A is an iron-containing oxygenase that reacts with methane, producing methanol,² and is therefore the focus of our work. Spectroscopic and thermodynamic studies have postulated that the metals in Protein A occur in a binuclear iron center and function as the active site for methane oxidation.^{3,4,5} Although some of the details vary, the general description of the iron site in Protein A is a binuclear cluster containing some type of μ -oxo ligand between the iron atoms. The remaining ligands (derived from adjacent amino acid residues) coordinate to the metals through nitrogen or oxygen and the Fe-Fe distance is between 3.0-3.5 Å. Compared to the soluble form of MMO the particulate form is poorly characterized and is thought to contain copper ions at the active site. This form is also active in methane oxidation in the biological system.⁶

Our work centers on the synthesis and characterization of inorganic/organic chemical models of the active site of MMO (both particulate and soluble). We have focused on the synthesis of an unsymmetrical, binuclear chelating ligand possessing an alkoxy group that can serve as a bridging μ -oxo ligand. The advantage of such a ligand system is twofold: (a) metal complexes of an asymmetric binucleating ligand will provide coordinative unsaturation at only one metal resulting in focused substrate reactivity at that site and (b) a single ligand with binuclear coordination provides a more robust environment for metal oxidation state changes and accompanying chemical reactivity.

We report here the synthesis of a prototype asymmetrical binuclear chelating ligand, its reactivity with copper ion, and characterization of two new copper chelate complexes. This work provides the first proof-of-concept for the formation of a binuclear complex with different coordination at each metal ion. Such complexes are relevant to the development of model systems for the active site of MMO.

EXPERIMENTAL

The synthesis of the chelating ligand HMeL obtained by a five step procedure in ~35% overall yield is outlined in scheme 1. The synthesis of copper complexes of this ligand are described below.

(N,N,N'-tris-((N-methyl)-2-benzoimidazolylmethyl)-N'-methyl-1,3-diamino-2-propionato) copper(II) perchlorate [CuHMeL(ClO₄)₂·CH₃CN (1). A solution of 1.00g (1.86 mmol) of HMeL in 15 mL methanol was treated with a solution of 0.688g Cu(ClO₄)₂·xH₂O (17.2% Cu, 1.86 mmol Cu²⁺) in 15 mL methanol with stirring. A blue precipitate forms immediately on addition of copper solution and the mixture was allowed to stir at room temperature for 10 minutes. The resulting mixture was cooled at -20°C for ~1 hr, the blue solid collected on a glass frit (pale green filtrate), washed with 10-15 ml cold methanol and dried under vacuum at 25°C. Crude yield was 1.3256g of blue-green solid. The dried solid was dissolved in 75 mL hot acetonitrile, filtered hot, and cooled. X-ray quality crystals were obtained by vapor diffusion of ether into this solution. The blue-green crystals were collected on a frit and vacuum dried (83% yield). Anal. Calcd. for C₃₃H₃₉Cl₂CuN₉O₉: C, 47.18; H, 4.68; N, 15.00. Found: C, 47.07; H, 4.85; N, 14.73.

(μ-O,O'-acetato)(N,N,N'-tris-((N-methyl)-2-benzoimidazolylmethyl)-N'-methyl-1,3-diamino-2-propionato)dicationicopper(II,II) bisperchlorate [Cu₂MeL(OAc)(ClO₄)₂·2H₂O (2).

(a) A solution of 1.00g of HMeL (1.86 mmol) and 0.507g sodium acetate trihydrate (3.72 mmol) in 15 mL of methanol was treated with 1.377g Cu(ClO₄)₂·xH₂O (17.2% Cu, 3.72 mmol Cu²⁺) in 15 mL methanol with stirring. A light blue precipitate forms initially and is quickly replaced (~30 sec) by a deep blue solid. The mixture was stirred for 30 min. at room temperature and then cooled at -20°C overnight. The solid was collected on a glass frit, washed with 10mL of cold methanol, and air dried to yield 1.703g of sky-blue powder. Further purification was achieved by vapor diffusion of ether into 50 mL of an acetonitrile solution of this solid to yield dark blue crystals (90.3% yield). Anal. Calcd. for C₃₃H₄₂Cl₂Cu₂N₈O₁₃: C, 41.43; H, 4.64; N, 11.71. Found: C, 41.34; H, 4.64; N, 11.13. (b) A 0.1036g (0.125 mmol) sample of (1) was placed in 10 mL of methanol to produce a pale blue-green solution and solid. To this suspension 0.046g of Cu(ClO₄)₂·xH₂O (0.125 mmol) followed by 0.034g sodium acetate trihydrate (0.25 mmol) were added sequentially as solids. The mixture was warmed to 50°C and stirred for 30 minutes. The solid was collected and washed with cold methanol, and recrystallized by vapor diffusion of ether in acetonitrile to yield dark blue crystals of (2).

RESULTS AND DISCUSSION

Scheme 1 shows the synthetic route for the prototype binuclear chelating ligand, HMeL. Elemental analysis and NMR studies confirm the composition and structure of the ligand. It possesses a hydroxy functionality that could serve as a bridging alkoxo group and aliphatic and

aromatic nitrogen coordination groups (benzimidazole). Using the C-OH bond as a bisecting line in this molecule, it is clear that the ligand has the potential to coordinate two metal ions in different environments. One half of the ligand provides three coordination sites (2 nitrogens and 1 bridging oxygen) while the other half provides four coordination sites (3 nitrogens and 1 bridging oxygen).

Reactions with copper ion demonstrate that the ligand is a potent chelating agent. Blue or blue-green colored complexes are formed rapidly in the presence of copper(II). The complexes are synthesized by stoichiometric reactions in methanol using hydrated metal salts. Characterization by elemental analysis and single crystal x-ray crystallography show that either mononuclear or binuclear complexes are obtained. For a metal-to-ligand ratio of 1:1 a mononuclear complex is obtained (Figure 1). The structure of the complex shows a distorted, trigonal bipyramidal coordination environment around Cu with five Cu-N bonds (average Cu-N distance $\sim 2 \text{ \AA}$). In this case, the hydroxo functionality does not coordinate to the metal and in the structure is located remote from the metal. On the other hand, with a metal-to-ligand ratio of 2:1 and in the presence of 2 equivalents of sodium acetate, a binuclear complex is formed (Figure 2). The structure shows that the ligand has chelated two copper ions, that the copper ions share the alkoxo oxygen (bridging μ -oxo), and that a coordinated acetate ion bridges the two metals. As a result, one Cu ion is coordinatively saturated (5-coordinate distorted trigonal pyramidal) while the other Cu is only four coordinate (distorted square pyramid). The mixed oxygen, nitrogen ligation have average Cu-N(O) distances of $\sim 2 \text{ \AA}$ typical of Cu(II) coordination complexes. The role of acetate in this reaction is both to serve as a coordinating bridge between the two copper sites and as a general base that assists in deprotonation of the organic hydroxo group forming the charged alkoxo bridging species. Interestingly, the crystal structure shows that in the solid-state an oxygen from one of the ClO_4^- counterions is weakly bound to the 4-coordinate Cu ion (about 2.6 \AA away) suggesting that this Cu is coordinatively unsaturated and that there is a potential 5th site for binding. Initial attempts to demonstrate this binding site have been successful and an azido bridged binuclear Cu complex has been prepared and isolated.⁷ It appears that complexes of this type can show selective reactivity at one metal site. Such behavior is a key requirement for bioinorganic mimics of the MMO active site.

CONCLUSIONS

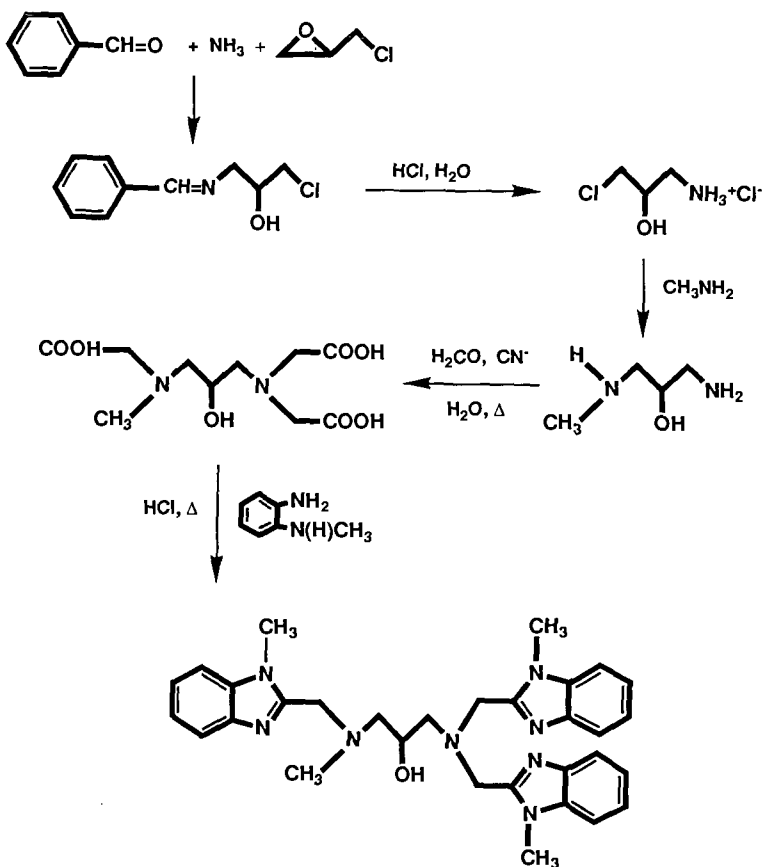
A binuclear, unsymmetric coordinating ligand that is an effective metal chelator has been designed and prepared. The new ligand has been shown to react rapidly with copper(II) forming a variety of copper coordination complexes. The binuclear complex is of significant interest since it represents proof-of-principle for the development of coordinatively asymmetric, binuclear metal chelate complexes. Although this structural type of chelator now appears to be common in biological systems, it has not been previously described for inorganic coordination chemistry. It is

expected that this ligand and derivatives of it will play an important role in the development of bioinorganic complexes that aim to mimic enzyme active sites that function by substrate interaction at only one metal site of a multimetal active site.

Work performed under the auspices of the US Department of Energy by the Lawrence Livermore National Laboratory under contract No. W-7405-ENG-48

REFERENCES

1. Dalton, H. *Adv. Appl. Microbiol.* **1980**, *26*, 71-87.
2. (a) Woodland, M.P.; Dalton, H. *J. Biol. Chem.* **1984**, *259*, 53-59. (b) Green, J.; Dalton, H. *J. Biol. Chem.* **1985**, *260*, 15795-15801. (c) Fox, B.G.; Froland, W.A.; Dege, J.E.; Lipscomb, J.D. *J. Biol. Chem.* **1989**, *264*, 10023-10033.
3. (a) Woodland, M.P.; Patil, D.S.; Cammack, R.; Dalton, H. *Biochim. Biophys. Acta* **1986**, *873*, 237-242. (b) Fox, B.G.; Surerus, K.K.; Munck, E.; Lipscomb, J.D. *J. Biol. Chem.* **1988**, *263*, 10553-10556.
4. Prince, R.C.; George, G.N.; Savas, J.C.; Cramer, S.P.; Patel, R.N. *Biochim. Biophys. Acta* **1988**, *952*, 220-229.
5. Ericson, A.; Hedman, B.; Hodgson, K.O.; Green, J.; Dalton, H.; Bentsen, J.G.; Beer, R.H.; Lippard, S.J. *J. Am. Chem. Soc.* **1988**, *110*, 2330-2332.
6. (a) Stanley, S.H.; Prior, S.D.; Leak, D.J.; Dalton, J. *Biotechnol. Lett.* **1983**, *5*, 487. (b) Park, S., Hanna, M.L., Taylor, R.T., Droege, M.W. *Biotechnology and Bioengineering* **1991**, *38*, 423-433.
7. Droege, M.W.; Satcher, J.H., Jr.; Weakley, T.J.R. Unpublished results.



Scheme 1. Reaction pathway producing chelating ligand [HMeL].

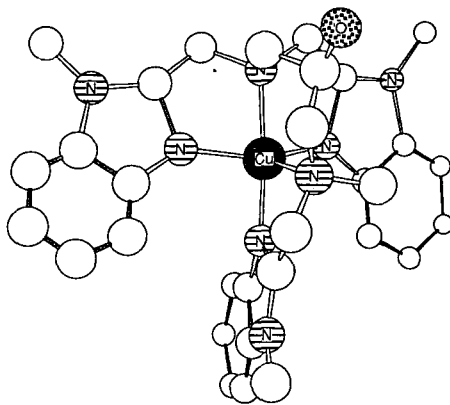


Figure 1. Structure of mononuclear Cu(II) complex (1). Open circles represent carbon atoms. Hydrogen atoms not shown for clarity.

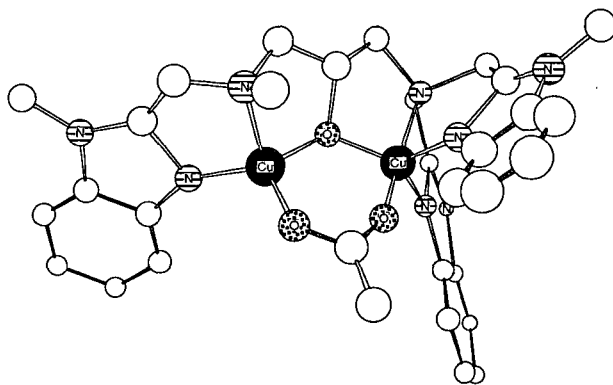


Figure 2. Structure of binuclear Cu(II) complex (2). Open circles represent carbon atoms. Hydrogen atoms not shown for clarity.

SUPPORT EFFECTS ON PALLADIUM CATALYSTS FOR METHANOL FUEL APPLICATIONS

Todd F. Brewer and Martin A. Abraham
Department of Chemical Engineering
The University of Tulsa
Tulsa, OK 74104

Ronald G. Silver
Allied Signal, Inc.
P.O. Box 580970
Tulsa, OK 74158

ABSTRACT

Methanol, formaldehyde, carbon monoxide, and propylene conversion were examined in a laboratory flow reactor over three base-metal containing alumina-supported palladium (Pd) catalysts in addition to Pd on γ -alumina catalyst. The base metals were cerium, barium, and a combination of the two. Experiments were performed to determine the effect of air to fuel ratio on lightoff temperatures of various feed components for the base-metal catalysts as compared to Pd on γ -alumina. For a vehicle operating at fuel-rich or stoichiometric conditions, the cerium containing catalyst gave the best overall performance among those tested. However, at lean conditions, all the catalysts had similar performance.

Keywords: Methanol Oxidation, Palladium Catalyst, Base Metals

INTRODUCTION

Methanol is a strong candidate as an alternative fuel to gasoline. Since methanol is essentially free of contaminants such as lead and sulfur, it has an advantage over gasoline in minimizing the poisoning of catalysts used for emissions control. In addition, methanol exhaust does not contain many of the hydrocarbon species present in gasoline exhaust. Methanol exhaust is composed primarily of unburned methanol, formaldehyde, carbon dioxide, and small amounts of hydrocarbons generated when methanol is used as a mixture with gasoline. The major components that are cause for concern are the photochemically active formaldehyde and the unburned methanol.

Unburned methanol is of particular importance during cold-start conditions where a vehicle

usually operates under fuel-rich conditions to improve driveability. Methanol levels in the exhaust during cold-start conditions can be as high as 0.9 volume percent as compared to 0.04 volume percent during normal operation (McCabe, et al., 1990). With the passage of the Clean Air Act, further tightened restrictions on exhaust emissions have resulted in extensive research on the design of catalysts that will reduce emissions from a methanol-fueled vehicle.

McCabe and coworkers (McCabe, et al., 1986) investigated the effect of feed stream composition and reactor temperature on methanol oxidation. Among the catalysts tested, rhodium (Rh), silver (Ag), and copper (Cu) were found to be much less active than either platinum (Pt) or palladium (Pd) (McCabe, et al., 1986). However, the presence of carbon monoxide had

little effect on the oxidation of methanol over these catalysts, while significantly affecting the Pt and Pd catalysts and raising the lightoff temperature for methanol over both catalysts. As a consequence, low temperature methanol oxidation activities of the Ag and Cu catalysts were as good or better than those of Pt or Pd in the presence of carbon monoxide (CO). This is consistent with weak chemisorption of CO compared to methanol on Ag and Cu surfaces, as observed in previous work (Ryberg, 1982; Madix, 1980). Also, the Ag displayed a high selectivity to complete oxidation; in particular, the Ag catalyst provided the lowest formaldehyde yield of all catalysts (McCabe, et al., 1986).

Additional studies by McCabe, et al., (1986) have investigated the kinetics of methanol oxidation on a Pt wire in a flow reactor at low ($3e-4$ atm) pressure. The proposed mechanism involves a major pathway responsible for approximately 99 percent of methanol oxidation and a minor pathway that accounts for the remaining 1 percent. The proposed mechanism is illustrated in Figure 1.

Automotive catalysts for gasoline powered vehicles generally include palladium or platinum. Palladium, which is less expensive than platinum, is subject to poisoning by the sulfur present in gasoline (Kummer, 1986). Methanol fuels generally have very little sulfur, thus Pd only catalysts may be a viable option for alternative-fuel vehicles. In addition, recent experiments have shown extended durability for Pd-only catalysts in engine-aging studies (Summers, et al., 1989). Pd, which is the least expensive noble metal, is also the preferred noble metal for C_1 and C_2 hydrocarbon conversions. Palladium's viability as an option for a methanol-fuel vehicle exhaust catalyst provides the impetus to investigate methanol oxidation over palladium-only catalyst formulations.

This paper presents the results of our experimental evaluation of the performance of two base-metals when incorporated into the washcoat of a palladium monolith catalyst. All results are compared to a palladium-only (Pd) catalyst with an alumina washcoat and no base-metal present. Experiments were conducted in a laboratory flow reactor with a feed gas chosen to simulate exhaust from a

methanol-fuel vehicle. All catalysts were tested fresh as supplied by the manufacturer. The effect of oxygen to fuel ratio on the lightoff temperatures of methanol, formaldehyde, carbon monoxide, and propylene was examined. Within this paper, we report on the performance of each catalyst at varying oxygen and methanol concentration. The effects of variation in the washcoat formulation were determined and analyzed in terms of an appropriate reaction description.

EXPERIMENTAL

Laboratory catalyst evaluations were carried out in a stainless steel flow reactor system shown in Figure 2. Catalyst samples were 1 inch in diameter by 0.5 inch long cylindrical sections of ceramic monolith wrapped with an inert fiberglass paper to eliminate void space between the catalyst and reactor wall. The reactor and process lines were heated with Thermolyne heating tapes, and the reactor temperature was monitored with a type J thermocouple placed against the center of the effluent side of the catalyst. Control of the reactor temperature was achieved with a solid state power controller.

Feed gases were supplied via gas cylinders fitted with pressure regulators and individual gas flow rates were controlled with rotameters. Methanol, formaldehyde, and water were introduced into the feed as liquid and vaporized upon mixing with the heated gas feed. Liquid flow rates were controlled with the combination of a metering valve and a rotameter. The liquid feed was injected into the process stream through a septum port just after the pre-heater of the process gases (Figure 2) and the feed stream passed upward through the catalyst. The pre-heater served to increase the temperature of the feed stream gases sufficiently to insure vaporization of the liquid feed. Temperature at the point of injection of the liquid was measured with a type J thermocouple.

Feed samples were taken at the reactor effluent at low temperature with very little or no conversion (as determined by the partial pressure of CO_2). Conversion of the feed components was measured via off-gas analysis of the effluent stream with a Dycor M200 Series Quadrupole

Gas Analyzer. Data was first taken in analog mode which allowed scanning of a wide (0-100 AMU) mass range to insure there were no unforeseen products, and then in tabular mode, which scans a maximum of twelve pre-selected AMU. Data was recorded in the form of partial pressures and conversion to molar flow rates was accomplished by calibration of each component's response factor with standard gas mixtures. Response factors of the individual gases were measured relative to a standard gas. Deconvolution of the mass spectral data was accomplished using the spectral library supplied by the manufacturer.

Experiments were performed over the range 100-400 °C at varying oxygen and methanol concentration. Data points were taken every 6-7 °C to insure identification of the lightoff temperature within a narrow range. Space velocities in all cases were approximately 13,000 h⁻¹ (volume basis; standard conditions). The Oxygen:Fuel ratio was calculated as :

$$\lambda = \frac{F_{O_2}}{\left(\frac{1}{2}F_{MeOH} + \frac{1}{2}F_{CO} + \frac{1}{2}F_{(C_2H_6)}\right)}$$

where F_i is the molar flow rate of component (i). The oxygen to fuel ratio was manipulated by altering the oxygen content in the feed.

Four different Pd-only catalysts supported on a γ-alumina washcoat on a ceramic monolith were evaluated fresh: 1) Pd-alumina with no base-metal, 2) Pd-alumina with barium, 3) Pd-alumina with cerium, and 4) Pd-alumina with both barium and cerium. All catalysts were supplied by Allied Signal, Inc. Each catalyst sample was preconditioned in a rich (λ<1) feed at 350°C for one hour to eliminate any oxide coatings from the surface of the catalyst. All samples were evaluated at 3 different feed compositions : 1) rich feed, λ=0.75-0.80, 2) stoichiometric feed, λ=1, and 3) lean feed, λ=1.15-1.20.

RESULTS

The results are presented as plots of conversion versus reactor temperature, hereafter referred to as lightoff plots. Within this paper, the lightoff temperature is considered the temperature at which 50 percent conversion occurs. The extent of conversion depends on the stoichiometry of the feed stream. All results presented are lightoff plots comparing the performance of the four catalysts tested at one stoichiometry. Methanol conversion is presented at rich, stoichiometric, and lean conditions, while the stoichiometric cases are presented for the other exhaust components; formaldehyde, carbon monoxide, and propylene.

Methanol Conversion

Methanol conversion under rich conditions is indicated as a function of temperature in Figure 3.a. For the palladium-alumina catalyst, conversion increased to approximately 0.2 at 150 °C, then decreased as the temperature increased to 200 °C. At that point, methanol conversion increased dramatically, achieving greater than 0.8 conversion at 250 °C. The addition of cerium led to a substantial decrease in lightoff temperature, and eliminated the low temperature peak in conversion. With cerium present, conversion increased steadily over the temperature range 120 to 200 °C. With barium in place of cerium, a similar effect was noticed, however, the lightoff temperature was shifted nearly 80 °C to higher temperatures compared to Pd on bare alumina. The addition of cerium to the barium containing catalyst had essentially no effect on the lightoff behavior for methanol.

Similar results were observed for stoichiometric feed conditions. As illustrated in Figure 3.b, the palladium-alumina catalyst exhibited slight conversion at approximately 140 °C, prior to increasing sharply at 200 °C. The addition of cerium provided a small decrease in the observed lightoff temperature to 190 °C and again eliminated the low temperature peak in conversion. In this case, the presence of barium increased the low temperature conversion to 0.2 at approximately 140 °C, but increased the lightoff temperature relative to the Pd-alumina

catalyst. Cerium addition to the barium-containing catalyst eliminated the low temperature conversion and decreased the lightoff temperature to approximately 175 °C.

Results for the lean case, indicated in Figure 3.c, illustrate a narrowing of the lightoff temperature range between the four catalysts. The palladium-alumina catalyst displayed a steady increase in conversion to 0.40 as the temperature increased to 190 °C; the low temperature peak phenomenon was not evident in this case. The addition of cerium did not dramatically affect the lightoff temperature, however, the low temperature conversion was diminished compared to the palladium-alumina case. The addition of barium increased the lightoff temperature by approximately 25 °C relative to all other catalysts, and gave the poorest conversion at low temperature. The addition of cerium to the barium-containing catalyst improved the low temperature conversion from 0.05 at approximately 150 °C for the barium-only case to 0.2 for the combined catalyst. In addition, the combined catalyst provided a lower lightoff temperature by about 20 °C than the barium catalyst.

Comparison of methanol conversion as a function of stoichiometry indicates: 1) Under rich conditions, the catalysts containing cerium or cerium and barium exhibited the lowest lightoff temperatures for methanol, 2) In all three cases the barium catalyst gave the highest lightoff temperature, and 3) The combined cerium-barium catalyst exhibited the lowest lightoff temperature under stoichiometric and lean conditions.

Other Exhaust Components

Formaldehyde conversion under stoichiometric conditions is presented as a function of temperature in Figure 4. For the palladium-alumina catalyst, a steady increase in conversion was observed over the temperature range 100-180 °C, followed by a sharper increase to 0.8 conversion at approximately 225 °C. The cerium catalyst exhibited the low temperature conversion peak observed previously with the palladium-alumina catalyst during methanol conversion, yet provided a lightoff temperature that was essentially the same as the alumina catalyst. The barium catalyst again exhibited the

poorest performance, exhibiting lightoff at approximately 250 °C, or 30 °C higher than the other catalysts. Cerium addition to the barium-containing catalyst lowered the lightoff temperature to approximately the same as the palladium-alumina and the cerium catalysts. Formaldehyde conversion did not exceed 90 percent for any of the catalysts.

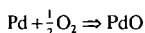
Carbon monoxide (CO) conversion under stoichiometric conditions, shown in Figure 5, was very similar over all four catalysts. Also, the lightoff temperature remained approximately constant between 210 °C and 240 °C, regardless of washcoat composition. Lightoff for CO was much more rapid than was previously noted for methanol, with CO going from near 0% conversion to near 100% conversion in approximately 20 °C. Under stoichiometric conditions complete CO conversion was observed in all catalysts. The combined cerium-barium catalyst yielded the highest lightoff temperature, approximately 25 °C higher than the other catalysts, which all exhibited essentially the same lightoff behavior.

Propylene conversion (Figure 6) displayed many of the same patterns as did the conversion of CO. For this component, as well as CO, the lightoff range narrowed as oxygen content increased. Lightoff temperatures also consistently decreased with increasing oxygen. Propylene exhibited a very narrow temperature range for lightoff, similar to that observed for CO. Conversion increased from essentially 0% to approximately 100% in about 20 °C. Again, the combined cerium-barium catalyst exhibited the highest lightoff temperature of the four catalysts, with 0.5 conversion occurring at approximately 250 °C, as opposed to approximately 220 °C for the palladium-alumina catalyst.

DISCUSSION

The low temperature conversion peak can be interpreted according to previous theory put forth by McCabe, et. al. (1988), for oxidation of formaldehyde over palladium catalyst. In that analysis, it is assumed that the palladium surface is in a reduced state at low temperature conditions but in the oxidized state at higher temperatures. Kinetic analysis of methanol

oxidation over a palladium monolith catalyst has been performed previously (Brewer, and Abraham, 1991) that would seem to support this theory. It may be that the reaction



occurs between 140 and 150 °C. The lower activity of the oxidized surface for oxidation reactions would possibly explain the decrease in catalyst activity in this temperature range. Another explanation could be the presence of two pathways, similar to the mechanism illustrated in Figure 1, where one pathway is favored over a select temperature range and upon passage to sufficiently high temperature a shift back to the major pathway occurs.

The barium catalyst gave the worst performance for methanol oxidation under all conditions. Conversely, catalysts containing cerium consistently were amongst the best-performing catalysts for methanol oxidation. In general, for all catalysts tested in these experiments, an effect of increasing the oxygen concentration was to decrease the lightoff temperature (the exceptions being the lightoff temperatures of 160 °C and 190 °C observed for the cerium-barium and the cerium catalyst under stoichiometric conditions). These observations suggest that cerium enhances the availability of oxygen for the methanol oxidation reaction, whereas barium decreases oxygen availability. As oxygen concentration in the feed increased, and thus its availability for reaction, the influence of cerium was diminished; the inhibition by barium was apparently secondary relative to the enhancement due to cerium.

CONCLUSIONS

Methanol conversion is one of the major topics of concern in methanol-fueled vehicle emissions. Conversions under rich conditions are of particular interest because the vehicles run under rich conditions when they are first started, which is also when catalyst temperatures are low. The cerium catalyst and the combined cerium-barium catalyst displayed the best performance in the conversion of methanol under

rich conditions, the combined Ce-Ba catalyst was best under stoichiometric conditions, and all four catalysts were roughly equal under lean conditions. The barium catalyst generally provided the highest lightoff temperatures of the catalysts tested, although barium did not seem to hinder the performance of the combined cerium-barium catalyst appreciably.

REFERENCES

- Brewer, T.F.; Abraham, M.A. "Methanol Oxidation over Palladium Monolith Catalyst", submitted for publication, (1991).
- Kummer, J.T., *J. Phys. Chem.*, **90**, 4747, (1986).
- Madix, R.J., in "Advances in Catalysis", Academic Press: New York, (1980).
- McCabe, R.W.; Mitchell, P.J., *J. Phys. Chem.*, **90**, 1428, (1986).
- McCabe, R.W.; Mitchell, P.J., *Applied Catalysis*, **27**, 83, (1986).
- McCabe, R.W.; Mitchell, P.J., *Applied Catalysis*, **44**, 73, (1988).
- Ryberg, C.R., *Phys. Rev. Lett.*, **49**, 1579, (1982).
- Summers, J.C.; White, J.J.; and Williamson; W.B., *SAE Paper #890794*, presented at International Congress and Exposition, (1989).

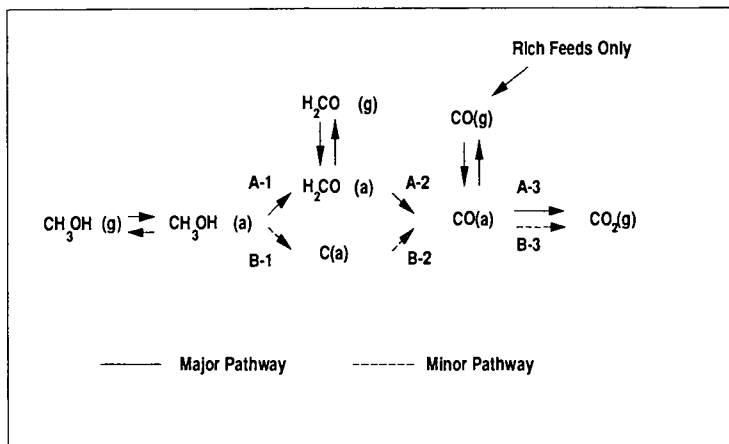


Figure 1: Proposed methanol oxidation pathways (McCabe, et al., 1986). Pathways are simplified. Only carbon-containing species are shown; (a) denotes adsorbed species.

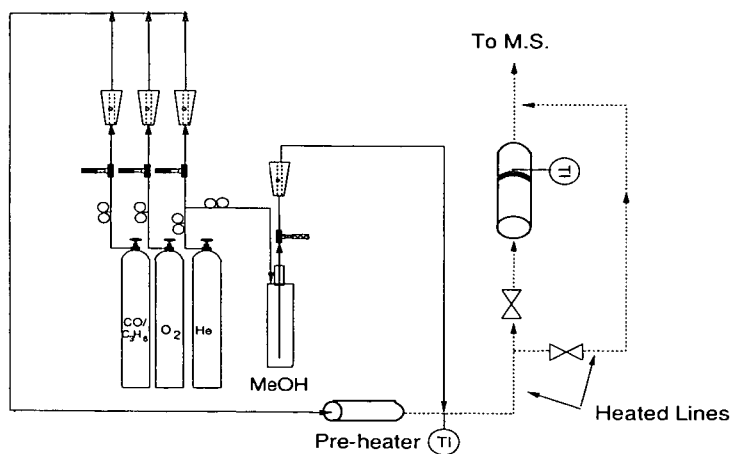


Figure 2: Detailed schematic of experimental apparatus.

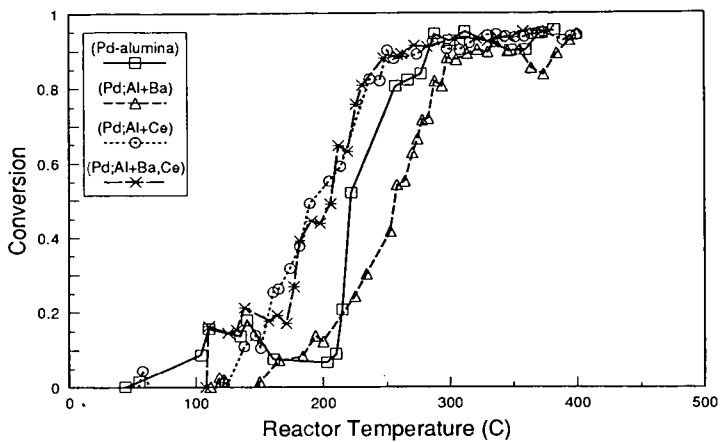


Figure 3.a: Effect of base metal additives on methanol conversion under rich feed conditions ($\lambda < 1$).

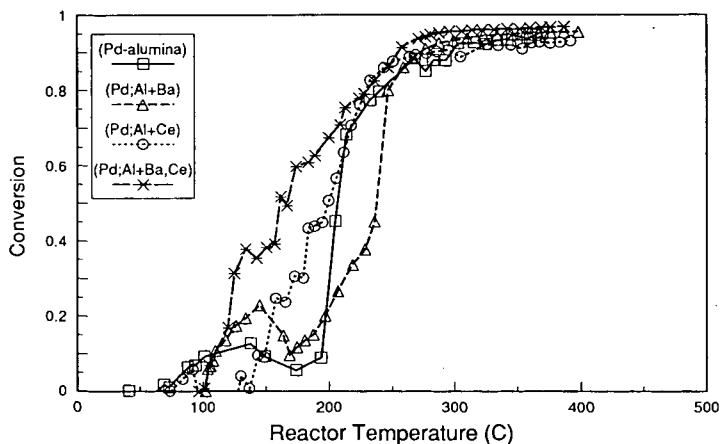


Figure 3.b: Effect of base metal additives on methanol conversion under stoichiometric feed conditions ($\lambda = 1$).

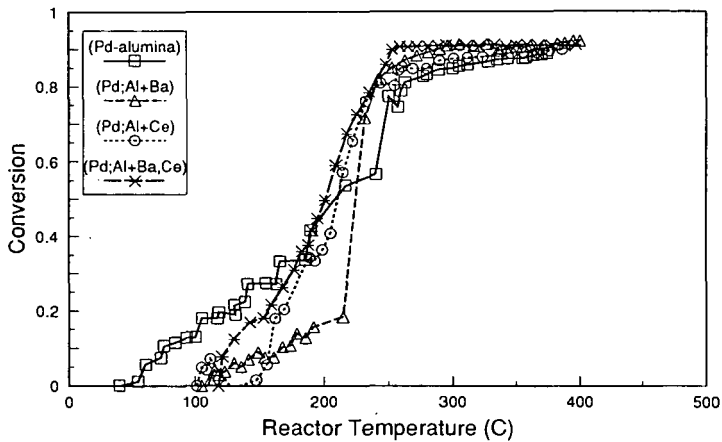


Figure 3.c: Effect of base metal additives on methanol conversion under lean feed conditions ($\lambda > 1$).

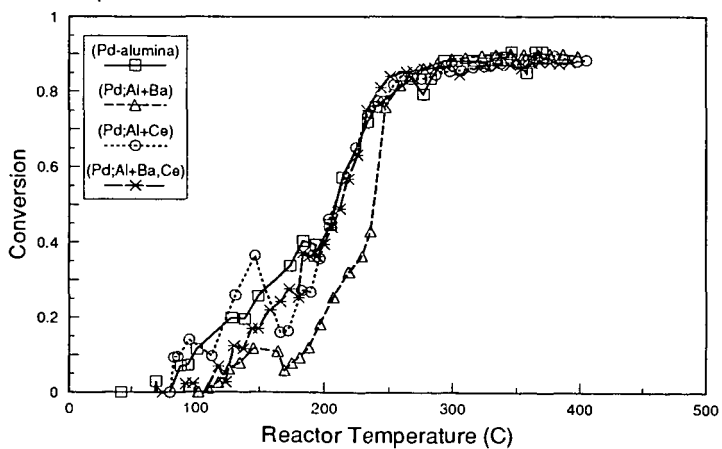


Figure 4: Effect of base metal additives on formaldehyde conversion under stoichiometric feed conditions ($\lambda = 1$).

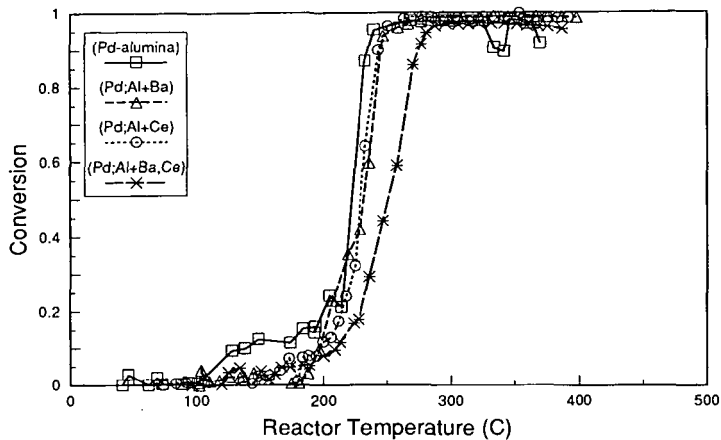


Figure 5: Effect of base metal additives on carbon monoxide conversion under stoichiometric conditions ($\lambda=1$).

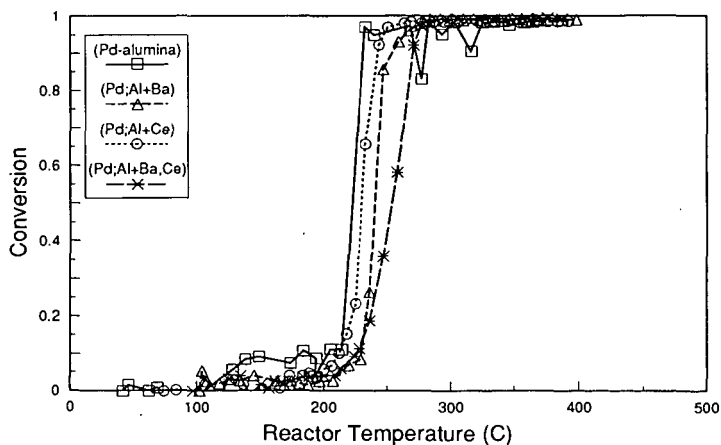


Figure 6: Effect of base metal additives on propylene conversion under stoichiometric conditions ($\lambda=1$).

OXIDATIVE COUPLING OF METHANE OVER
RARE-EARTH-BASED NONREDUCIBLE COMPOSITE-METAL-OXIDES CATALYSTS¹

Yuda Liu, Guodong Lin, Hongbin Zhang, Junxiu Cai,
Hiulin Wan, and K. R. Tsai
Department of Chemistry
Institute of Physical Chemistry
Xiamen University
Xiamen 361005, China

ABSTRACT

Nonreducible composite metal-oxides catalysts of the host-dopant type can be very effective catalysts for methane oxidative coupling (MOC) reaction(s) and for oxidative dehydrogenation of ethane to ethene. A systematic study of the relative efficacies of the alkali and alkaline-earth dopants used as selectivity promoters for lanthania-based MOC catalysts in relation to the cationic polarizabilities, and of the behavior of a CsOH-coated lanthania catalyst towards treatment with CO₂ plus O₂ near the MOC reaction temperature and toward CO₂-containing feeds has been made, together with laser Raman spectroscopic detection of superoxide ions in the freshly activated catalyst. The results strongly indicate that O₂⁻ adspecies is an active oxygen species responsible for the initial alkane-hydrogen-abstraction reactions.

INTRODUCTION

Methane oxidative coupling (MOC) over solid catalysts is of great current interest because of its potential importance in the utilization of the world's abundant natural gas resource for the production of ethylene or liquid fuels, and of its fundamental significance in the catalytic activation and selective conversion of the first and the most inert member of paraffin hydrocarbons. Much attention has been focused on the development of better catalysts for the MOC reaction(s) and on mechanistic studies of O₂ activation and methane conversion; and important advances have been made since the pioneering work of Keller & Bhasin [1], as shown by many recent reviews [2].

The great number of MOC catalysts reported in the literature may be roughly classified into three main categories (1) nonreducible composite metal-oxides with stable cationic valency; (2) basic-oxide-supported catalysts of reducible oxides of certain IVA, VA metals, e.g., PbO_x, Bi₂O_x, or oxides of certain IIb-elements (Zn and Cd); and (3) alkali-oxides (or phosphates or sulfates or chlorides)-promoted complex catalysts containing oxides of certain transition metals, e.g., MnO_x, TiO_x, MoO_x, and the recently reported CaO-NiO-K⁺ [3].

MOC catalysts of the first category are the most extensively investigated. These are usually of the host-dopant type, each consisting of a host oxide of a higher-valent cationic metal from the IIA or IIIB or IVB group doped with one or more basic oxides with lower and stable cationic valency from the IA, or IIA or IIIB group so as to generate or increase lattice anionic vacancies, which appear to be requisite for dioxygen chemisorption and activation. However, the IIA-IA

¹ Work supported by the National Natural Science Foundation of China and by a grant for spectroscopic characterization from the State Key Laboratory for Physical Chemistry of The Solid Surface, Xiamen University.

catalyst systems all suffer from the serious drawback of high volatilization loss of the alkali promoters and significant sintering at the MOC reaction temperature [2,3a]. The use of high-melting trivalent or quadri-valent metal oxides with stable cationic valency, such as alkaline-earth oxides (AEO) and/or oxides of IIIB metals, especially the M_2O_3 -type rare-earth-oxides (REO), many of which are known [4] to exist in the cubic C-type structure, a defective fluorite structure with regular disposition of anionic vacancies (e.g., Sm_2O_3). As pointed out in references [5-6], these REO with the C-type structure or layer-type structure (e.g., La_2O_3) are extremely open to oxygen chemisorption. These REO, especially Sm_2O_3 , have been found to show very high oxygen conversion efficiency and fairly good MOC activity and selectivity [2,7,8], but Sm_2O_3 appears to have only marginal C-type structural stability at the MOC reaction temperature [3a]. Doping La_2O_3 and Sm_2O_3 catalysts with small amounts of alkali or AEO has been found to enhance C_2 selectivity [2,3a,6-8], but the results from different investigators are not very consistent. It is known [9] that metal oxides with the fluorite structure (notably ThO_2) can form wide ranges of solid solutions with many M_2O_3 -type REO, and can also dissolve AEO to some extent, especially when the host-dopant cationic sizes are comparable. Thus defective-fluorite-structure (DFS) with high concentration of anionic vacancies can be created by proper doping of the fluorite-type host-oxides with metal-oxides of lower cationic valency. As recently shown by Cameron et al. [10], such dopings can radically change the low-activity ThO_2 host-oxide into very active and selective MOC catalysts for the co-feed operation. For the nonreducible composite metal-oxides, the active site for the initial alkane-hydrogen-abstraction reaction is most probably certain chemisorbed oxygen species, the very nature of which is still not clear, and remains a matter of controversy [2,6,10-12]. The mechanism of promoter action of the alkali and AEO dopants also remains to be clarified.

In this paper, further experimental evidence for the catalyst activities and selectivities in relation to structural types and anionic vacancies for this category of MOC catalysts is first presented; this is followed by presentation and discussion of the results of a systematic study of the relative efficacies of the alkali and AEO promoter in relation to the cationic polarizabilities, and of the behavior of a CsOH-coated La_2O_3 catalyst towards treatment by CO_2 plus O_2 , as well as towards CO_2 -containing feeds, together with detection of anionic-dioxygen species in the freshly activated catalyst, with the aim of shedding some light on the nature of the active oxygen species and the mechanism of the promoter action.

EXPERIMENTAL

Catalyst Preparation, Evaluation, and Characterization

Undoped La_2O_3 , Y_2O_3 , ZrO_2 , and ThO_2 , as well as the $[Y_2O_3]ZrO_2$ (35 mol.% Y:65 mol.% Zr), $[La_2O_3]ThO_2$ (30 mol.% La:70 mol.% Th), and $pSm_2O_3]ThO_2$ (30 mol.% Sm:70 mol.% Th) host-dopant pairs, the Bi_2O_3 -doped $[La_2O_3]ThO_2$ catalyst (10 mol.% Bi:20 mol.% La:70 mol.% Th), and the AEO-doped (5 mol.% M^{2+} in each case) La_2O_3 catalysts were prepared by drying and ignition (830-900°C, 1 hr) of freshly precipitated, or co-precipitated hydroxides, or carbonates in the case of the AEO-doped La_2O_3 catalysts, while the alkali-sulfates-doped La_2O_3 catalysts (5 mol.% M in each case) and the CsOH-coated lanthania catalyst (10 mol.% Cs:90 mol.% La) by impregnation of ignited lanthania with the aqueous metal sulfates and CsOH, respectively, followed by drying and ignition (700°C).

Catalyst evaluation was carried out in a quartz microreactor (6.0 mm i.d. with concentric quartz tubing serving as thermal-couple well)-G.C. (TCD) outfit, 0.20 mL of catalyst sample (30-60 mesh) being used in each case. The feed ($CH_4:O_2:N_2 = 24.6:5.6:69.8$ vol.% being used throughout this work) and the reactor effluents were analyzed with a gas chromatograph

(Shanghai Fenxi, Model #103) equipped with thermal conductivity detector, a molecular-sieve-5A column, as well as a Porapak-Q column, being used to separate O₂, N₂, CH₄, and CO, as well as CO₂, C₂H₄, and C₂H₆ (C₃₊ and H₂O being neglected), respectively, and N₂ as the internal reference for the quantitation of each gaseous component from its G.C. peak. The selectivity for each C-containing product and the ΣC₂ yield were expressed in terms of the carbon-efficiency (%) of methane conversion to the respective product. In each case, a 95 ± 2% carbon material balance was obtained. Laser Raman spectra for freshly activated sample of the CsOH-coated La₂O₃ catalyst and for partially deactivated sample, as well as for freshly prepared sample (ignited at 700°C for 1 hour in ambient air) before the activation treatment, were taken at room temperature with a Spex Ramalog-6 spectrometer with argon laser (5145 Å) as the excitation source.

RESULTS AND DISCUSSION

Catalyst Performance in Relation to Compositions and Structural Peculiarities

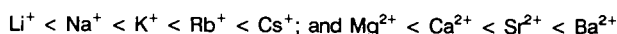
The experimental results show that doping ThO₂ with a trivalent-lanthanide oxide (La₂O₃ and Sm₂O₃ appeared to be equally effective), or ZrO₂ with Y₂O₃, to produce a composite metal oxide with defective fluorite structure (DFS) can be very effective in changing a poor MOC catalyst with no intrinsic anionic activity and, especially selectivity (Table 1), in accordance with observations by previous workers [10]. Note that these DFS metal-oxides are known to be solid electrolytes with high anionic conductivities, especially the zirconia-yttria system [9]. It is interesting to note that the 10 mol.% Bi₂O₃-doped [La₂O₃]ThO₂ catalyst appeared to be a highly efficient methane-combustion catalyst, rather than a MOC catalyst. Conceivably, the presence of the redox-active Bi (III/IV) in the DFS lattice of [La₂O₃]ThO₂ can promote the reductive dissociation of O₂ (O=O bond energy: 118 kcal) chemisorbed at an anionic vacancy into 2O⁻, most probably via the formation of O₂²⁻ (ionic 'O-O' bond energy: 34 kcal) as precursor; and high concentration and mobility of O⁻ in the catalyst may be conducive to deep oxidation of CH₄ (C₂H₆ and C₂H₄), and detrimental to MOC selectivity. Incidentally, doping a [25 mol.% LaO_{1.5}]ThO₂ with 5 mol.% PbO was also found to promote CO₂ formation (64% CO₂, 36% C₂).

Table 1
Catalyst Activity and Selectivity in Relation to Structural Peculiarities

Catalyst System Composition	Structure Type	Reaction Temp.(°C)	GHSV (h ⁻¹)	Conversion		Selectivity C ₂ (%)
				CH ₄ (%)	O ₂ (%)	
ThO ₂	Fluorite	760	12x10 ⁴	11	34	42
30 mol.% SmO _{1.5} -ThO ₂	DFS	760	12x10 ⁴	27	95	57
30 mol.% LaO _{1.5} -ThO ₂	DFS	760	12x10 ⁴	28	94	55
BiO _{1.5} -LaO _{1.5} -ThO ₂ (10 : 20 : 70)	DFS	700	12x10 ⁴	13	98	0 (100% CO ₂)
ZrO ₂	Monoclinic	760	3x10 ⁴	19	98	7
Y ₂ O ₃	C-type	760	3x10 ⁴	26	98	38
35 mol.% YO _{1.5} -ZrO ₂	DFS	760	3x10 ⁴	26	92	46

Promoter Effects of Alkali Sulfates and Alkaline-Earth Oxides on La₂O₃ Catalyst

The promoter effects were found to increase with increasing cationic sizes:



This may be correlated to the increasing tendencies towards the formation of the corresponding metal-superoxides [13-14], which, in turn, may be correlated to the increasing cationic polarizabilities [15]. Conceivably, by acquiring an electron trapped at an anionic vacancy, or from an O^{2-} ion, an O_2^- adspecies may be formed from a chemisorbed O_2 ; likewise, O_2^{2-} adspecies may then be formed by acquiring a second electron. The O_2^{2-} adspecies may dissociate reversibly into $2 O^-$, which may readily diffuse into the bulk. The half-life of anionic dioxygen adspecies, especially O_2^- , may be prolonged by side-on coordination [14] to a highly polarizable dopant cation (e.g., Cs^+ , Rb^+ , or K^+) known to have a strong tendency to form metal superoxide [12-13], which, however, is very sensitive to inhibition by moisture [14], due to conversion into the highly soluble and thermally very stable alkali hydroxide (with the exception of $LiOH$, which is barely soluble in water, and dehydrates to Li_2O at $850^\circ C$ [4b]). Note that the promoter effects of the alkali sulfates, with the notable exception of Li_2SO_4 , all appeared to decrease rapidly with time on stream. However, the promoter effect of Na_2SO_4 , taken in the first 30 minutes to an hour was reproducibly found to be slightly better than that of Li_2SO_4 (Table 2).

Table 2
Promoter Effects of Alkali Sulfates and AEO on La_2O_3 -Based Catalysts

Catalyst (mol.%)	Temp. ($^\circ C$)	GHSV (h^{-1})	Conversion (%)		Selectivity (% Efficiency)		
			CH_4	O_2	C_2H_6	C_2H_4	ΣC_2
5% Li^+/La_2O_3	700	1.5×10^4	29.4	85.8	29.5	31.0	60.5
5% Na^+/La_2O_3	700	1.5×10^4	28	83	29	33	62
5% K^+/La_2O_3	700	1.5×10^4	29	80	30	35	65
5% Rb^+/La_2O_3	700	1.5×10^4	30	89	33	35	68
5% Cs^+/La_2O_3	700	1.5×10^4	29	80	34	36	70
La_2O_3	700	3.0×10^4	28.1	99.0	24.6	25.3	49.9
5% Mg^{2+}/La_2O_3	700	3.0×10^4	28.6	97.8	26.2	25.6	51.8
5% Ca^{2+}/La_2O_3	700	3.0×10^4	27.9	98.0	27.1	25.6	52.7
5% Sr^{2+}/La_2O_3	700	3.0×10^4	28.0	98.1	30.4	24.8	55.2
5% Ba^{2+}/La_2O_3	700	3.0×10^4	28.9	98.1	32.6	26.5	59.1

Effects of CO_2 Treatment and of CO_2 in Feed on $CsOH$ -Coated Lanthania Catalyst

The 10 mol.% $CsOH/La_2O_3$ catalyst was found to behave like molten $CsOH$ (ca. 25-30 Å thick) supported on La_2O_3 ($4 m^2/g$). The MOC activity and selectivity were again found to decline rapidly with time on stream (Table 3), most probably also due to inhibition by H_2O coproduced in the MOC reactions; but the ΣC_2 selectivity was increased with the addition of 4-5 vol.% of CO_2 into the feed, though with a slight depression in the CH_4 conversion. Moreover, the catalyst could be reactivated by treatment with CO_2 plus a few percents of O_2 . Laser Raman spectrum of the freshly activated sample taken at room temperature indicated the presence of a large amount of carbonate ($1086 cm^{-1}$ st, $700 cm^{-1}$ w), a small amount of CsO_2 ($1128 cm^{-1}$ w, plus some weak, unresolved and unidentified peaks around $980-1000 cm^{-1}$), the assignments of the Raman peaks being made with reference to [15-16]. After 3 hours on stream, only the large carbonate-peak at $1086 cm^{-1}$ remained; the peak assignable to CsO_2 being no longer visible. The spectroscopic characterization will be communicated in more details later. Conceivably, molten $CsOH$ can readily absorb CO_2 to form Cs_2CO_3 (d. $610^\circ C$ [4b]), which is readily decarbonated at $700^\circ C$ to form Cs_2O , which in turn can readily absorb O_2 to form, predominantly, CsO_2 [13], plus a small amount of Cs_2O_2 ; both of these may dissolve in the molten $CsOH$, and appear to be not so active and selective as compared with the previous case

of 5 mol.% Cs₂SO₄/La₂O₃ where O₂⁻ adspecies was probably partially stabilized by Cs⁺ dopant cations incorporated into the surface lattice of La₂O₃ during the impregnation and heat treatment.

Table 3
Effects of CO₂-O₂ Treatment and of CO₂ in the Feed on 10 mol.% CsOH/La₂O₃ Catalyst

Time (min.) on Stream	Feed or Reagent	Temp. (°C)	Conversion (%) ^a		Selectivity (%) ^a			YΣC ₂ ^a (%)
			CH ₄	O ₂	C ₂ H ₆	C ₂ H ₄	ΣC ₂	
0-30	Feed	700	27.8	94.7	30.1	23.9	54.0	15.0
30-150	Same	700	27.4	94.7	27.2	22.5	49.7	13.6
150-250	Same	700	26.4	95.8	26.5	21.9	48.4	12.8
250-310	CO ₂ +2% O ₂	700						
310-335	Feed	700	28.5	95.9	28.5	25.2	53.7	15.3
335-400	Feed+5% CO ₂	700	27.5	99.0	90.8	38.5	55.0	15.1
400-430	Feed	700	28.9	93.8	26.6	23.8	50.0	14.6
430-460	Feed+4% CO ₂	700	27.8	93.6	27.8	25.2	53.0	14.7

Feed: CH₄:O₂:N₂ = 24.6:5.6:69.8 (vol.%). GHSV: 2x10⁴h⁻¹. ^aData taken at the end of the time interval.

Thus the results of the last two sections strongly indicate that O₂⁻ adspecies, is an active-oxygen species responsible for the initial alkane-hydrogen-abstraction in the MOC reactions (and in oxidative dehydrogenation of ethane). This is in line with the known experimental fact that this step requires a fairly large activation energy [2.12a], and that significant amounts of O₂⁻ adspecies, rather than O⁻ and O₂²⁻ species, are present in the great majority of efficient MOC co-feed catalysts. These findings have important bearings on the design of MOC catalysts and operating conditions.

REFERENCES

- G. E. Keller and M. M. Bhasin, *J. Catal.*, **73** (1982) 9.
- (a) J. S. Lee and S. T. Oyama, *Catal. Rev.*, **30** (1988) 249; (b) G. J. Hutchings, M. S. Scurrill, and J. W. Woodhouse, *Chem. Soc. Rev.*, **18** (1989) 251; (c) Y. Amenomiya et al., *Catal. Rev.*, **32** (1990) 163; (d) J. H. Lunsford, *Catal. Today*, **6** (1990) 235; (e) J. H. Lunsford in "Natural Gas Conversion" (B. Delmon and J. T. Yates, eds.) p. 3, Elsevier, Amsterdam, 1991.
- P. Pereira, S. H. Lee, G. A. Somorjai, and H. Heinemann, *Catal. Lett.*, **6** (1990) 255.
- S. J. Korf, J. A. Ross, J. M. Diphooom, R. H. J. Veehof, J. G. van Ommen, and J. R. H. Ross, *Catal. Today*, **4** (1989) 27.
- (a) A. F. WElls, "Structural Inorganic Chemistry" (Oxford University Press, Oxford, 1984); (b) "CRC Handbook of Chemistry & Physics", 66th Ed., 91985).
- A. G. Anshits, E. N. Voskresenskaya, and L. I. Kurteeva, *Catal. Lett.*, **6** (1990) 67.
- J.-L. Dubois and C. J. Cameron, *Appl. Catal.*, **67** (1990) 49.
- K. Otsuka, q. Liu, M. Hatano, and A. Morikawa, *Chem. Lett.*, (1987) 1835.
- J. M. DeBoy and R. F. Hicks, *J. Chem. Soc., Chem. Commun.*, (1988) 982.
- E. C. Subbarao (ed.), "Solid Electrolytes", pp 35-46) Plenum Press, 1980).
- J.-L. Dubois, B. Rebours, and C. J. Cameron, *Appl. Catal.*, **67** (1990) 73.
- Otsuka et al., *Chem. Lett.*, (1987) 77; *Inorg. Chim. Acta*, **121** (1986) 237.
- (a) E. Morales and J. H. Lunsford, *J. Catal.*, **118** (1989) 255; (b) Y. Osada et al., *Appl. Catal.*, **59** (1990) 59.

13. R. E. Hall in "Encyclopedia of Chemical Technology" (Kirk & Othmer, eds), 3rd Ed., vol. 17, pg 1, Wiley Interscience Press Inc., 1982.
14. V. H. Lux, R. Kuhn and T. Niedermaier, *Z. anorg. alleg. Chem.*, **298** (1959) 285.
15. L. Andrews, J.-T. Hwang and C. Trindle, *J. Phys. Chem.*, **77** (1973) 1065.
16. H. H. Eysel and S. Thym, *Z. anorg. alleg. Chem.*, **411** (1975) 97.

SOME PROBLEMS IN THE MODELING OF COMPLEX CHEMICAL PROCESSES

SIDNEY W. BENSON
Distinguished Professor of Chemistry and
Scientific Director, Emeritus
Loker Hydrocarbon Research Institute
University of Southern California
Los Angeles, California 90089-1661

Keywords: acetylene, pyrolysis, surface reactions, C-1 Chemistry

INTRODUCTION

In the last decade, the "mature" science of chemical kinetics has entered what may be termed the "Computer Age". Thirty years ago, the goal of chemical engineers working with a chemical process would be to obtain an explicit rate expression describing the rate dependence on experimental parameters. For diverse reasons, this is no longer a sufficient result. The availability of high speed computers together with relevant kinetic and thermochemical data have today made possible the description of a complex chemical process in terms of the elementary kinetic steps comprising it. Explicitness is no longer necessary

This evolution has been accelerated by a need to satisfy increasingly stringent environmental requirements as well as the need to reduce the cost of optimization of chemical processes. Experiments, particularly in larger scale equipment can become prohibitively expensive and time consuming. Computer experiments, on the contrary are inexpensive and can be adapted, in combination with the appropriate fluid mechanics, to rapid and inexpensive scaling. Laboratory experiments in 1 cm diameter tubing are relatively cheap and easy to do but may not represent the results of an industrial flow process carried out in 10 cm to 20 cm pipes.

Fuel chemistry has been one of the pioneers in adapting computer kinetics to its various needs. In doing so it has brought together the chemical engineer, the academic kineticist and the fluid dynamicist in what is truly today, a multi-disciplinary effort. Despite the considerable reluctance of each of these specialists to interact with each other, there is no alternative to a directed and active dialogue. This "social" barrier has been little discussed but has been as much a challenge as the technical problems themselves. From my own experience as an academic kineticist who has done much industrial consulting, I would estimate that the usual mode of arms length interaction between kineticist and engineers has generated a 10 to 20 year lag in the utilization of basic science. A good part of this lag arises from difficulties in the basic kinetic science itself and this is the subject I would like to discuss here.

Kinetic modeling of a complex chemical process requires the following:

- 1.) A complete knowledge of the elementary kinetic steps--the mechanism.
- 2.) Accurate thermochemical data on all of the species involved.
- 3.) Accurate kinetic data for each step.
- 4.) An understanding of surface processes which may be of importance.

Historically, the first attempt to model a complex system was the Rice-Herzfeld analysis of the thermal cracking of hydrocarbons almost 60 years ago.¹ While enormously simplified compared to our current understanding this work provided the prototype for all subsequent efforts. The problems, then as now remain the same, namely, the four requirements outlined above.

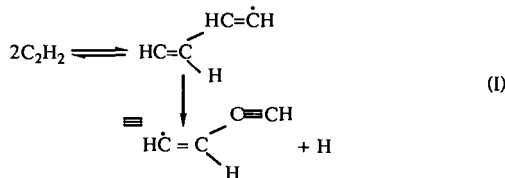
Mechanism

It is impossible to prove that any given mechanism is correct or complete. Its operational test is that it reproduces quantitatively all available data on any chemical process. An interesting example is provided by the pyrolysis of acetylene. While early work on acetylene had been interpreted in terms of a free radical mechanism² recent workers have tried to interpret this chemistry in terms of an active carbene isomer of acetylene, vinylidene:^{3,4}

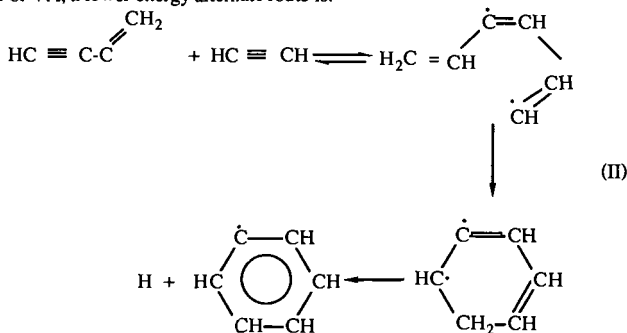


The reason for invoking such a species was that the conventional free radical mechanism could not account for the observed rate of pyrolysis of acetylene by as much as a factor of 100 at 1000°K. However, a recently proposed mechanism invoking a different radical initiation process has been shown to account for all the features of C_2H_2 pyrolysis.⁵

This most recent free radical mechanism makes use of vinyl acetylene (VA), the first product of acetylene pyrolysis, as an autocatalytic agent which provides a fast low energy path to free radical initiation. In the absence of VA free radicals are provided by a bimolecular process:



In the presence of VA, a lower energy alternate route is:



This second path (II) has an activation energy of 30 kcal whereas the first path (I) has $E = 67$ kcal. Using estimated rate constants consistent with the data on VA-acetylene copyrolysis⁶ it turns out that at a $[\text{VA}]/[\text{C}_2\text{H}_2]$ ratio of 10^{-7} at 800°K the two paths are equal in rate. The well documented induction period in acetylene pyrolysis is then the time required via slow initiation path (I) to produce the small amounts of VA needed to permit path (II) to take over as the initiation source.

Surface Processes

Surface chemistry still represents the very gray area of modeling. We have very little detailed knowledge of the thermochemistry or kinetics of surface reactions. Anyone who has worked with high temperature pyrolysis reactions is familiar with "coking" in hydrocarbon systems and the importance of surface generated reactions. In the past two years the discovery of important reactions on the surfaces of nitric acid ice crystals in the Antarctic stratosphere has provided an unexpected jolt to the atmospheric kineticists. Recent work on diamond formation from CH_4 at high temperature has given an enormous stimulus to the study and understanding of radical reactions of surfaces.¹⁰ Hopefully, this will produce some quantitative kinetic and thermochemical data from which we can build a systematic base. For the moment, surface reactions will continue to be treated empirically.

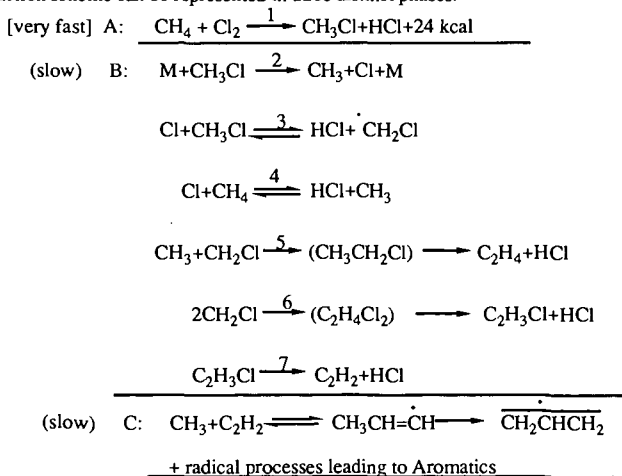
It is well however to note that for radical-molecule reactions at surfaces, these are essentially members of the gas phase family subject only to non-bonded interactions due to steric crowding.

Metals and metal oxides may differ basically from hydrocarbon surfaces in that they present very polar environments and their reactions may resemble ionic or ion-pair reactions rather than the mildly polar reactions of hydrocarbons and their radicals.

Equally of note is the fact that there is a large loss in entropy for a gas phase species on chemisorbing at a surface site. We can estimate entropies of chemisorbed species to an accuracy of about 1-2 cal/mole^oK so that with a knowledge of the surface concentration we can estimate heats of chemisorption to 1 kcal.

The High Temperature Reaction of $\text{Cl}_2 + \text{CH}_4$

A recent example of modeling with importance in C-1 chemistry has just been done in my laboratories at USC.¹¹ We have modeled the reactions of $\text{Cl}_2 + \text{CH}_4$ mixed hot at 700 to 900°K. It is an extremely rapid, exothermic reaction capable of reaching peak temperatures of 1400-1500°K. The reaction scheme can be represented in three distinct phases:



Modeling has shown that the gas phase reaction will produce up to 70 and 80% of useful products per mole Cl_2 with about 78% conversion of CH_4 per pass. Useful products are predominantly $\text{C}_2\text{H}_2 + \text{C}_6\text{H}_6$ with lesser amounts of ethylene, butadiene, vinyl chloride, and styrene. Only trace amounts of naphthalene or higher species are formed.

Comparison with laboratory data in high surface reactors suggest that only surface reactions can account for the carbon formation observed at longer residence times. This system which represents an economically attractive methane convertor presents some very interesting engineering problems; rapid mixing of hypergolic species, hot $\text{Cl}_2 + \text{CH}_4$ and rapid quenching (100 msec) of the reaction stream before significant surface reactions have occurred.

REFERENCES

1. Rice, F. O.; Herzfeld, K. F. J. Am. Chem. Soc. **1934**, 56, 284.
2. Cullis, C. F.; Franklin, N. H. Proc. Royal Soc. (London), **1964**, A280, 139.
3. Duran, R. P.; Amorebieta, V. T.; Colussi, A. J. J. Amer. Chem. Soc. **1987**, 109, 3154.
4. Kiefer, J. H.; Von Drasek, W. A. Int. J. Chem. Kinet. **1990**, 22, 747.
5. Benson, S. W. Int. J. Chem. Kinet. **1992**, 24, 000.
6. Chanmugathas, C; Heicklen J. Int. J. Chem. Kinet. **1986**, 18, 701.
7. Benson, S. W. "Thermochemical Kinetics", 1976, 2nd Ed., John Wiley and Sons, NY
8. Benson, S. W.; Cohen, N. Chapter in The Chemistry of Alkanes and Cycloalkanes, J. Wiley and Sons, accepted, 1992.
9. Benson, S. W.; Garland, L. J. Phys. Chem. **1991**, 95, 4915.
10. Harris, S. J.; Bolton, D. N.; Blint, R. J. J. Appl. Phys. **1991**, 70, 2654.
11. Mitchell, T; Benson, S. W.; et al "A Kinetic Model for the Homogeneous Formation of Unsaturated Hydrocarbons", Symposium on Natural Gas Upgrading. This meeting.

KINETIC STABILITY OF UNSATURATED ORGANICS AT HIGH TEMPERATURES

Wing Tsang
Chemical Kinetics and Thermodynamics Division
National Institute of Standards and Technology
Gaithersburg, Maryland 20899

Introduction

Key words: unsaturated organics, kinetics, decomposition

Chemical processes involving organic compounds at high temperatures are controlled largely by the chemical and thermal stability of the unsaturated compounds that are formed during the decomposition process. This report reviews recent quantitative work dealing with these questions in the context of the thermal kinetics of reactions of such molecules in purely pyrolytic systems. It will also seek to highlight some of the important uncertainties in the understanding of the kinetics of such systems. The paper will begin with a summary of the present state of knowledge on the strength of the bonds (bond dissociation energies) that hold an unsaturated compound together. This will be followed by discussions on unimolecular reactions of molecules and radicals. For the former, bond dissociation and molecular processes will be considered. In the case of radicals, interest is on dissociation and isomerization. Bimolecular processes to be covered include metathesis and radical addition to stable compounds and radical combination with other radicals. Many of these processes are relatable to each other through the equilibrium constants. Thus the correct thermochemistry for reaction intermediates will be an underlying theme throughout this paper.

Bond Energies

The addition of unsaturation to an alkane leads to drastic changes in the strength of the bonds in the molecule. The general situation in terms of a number of typical cases is summarized in Figure 1¹⁻⁴. It can be seen that the bonds immediately adjacent to the site of unsaturation are strengthened, while those beta to that site are weakened. Thus the smallest unsaturates such as ethylene and acetylene, in terms of bond breaking through unimolecular decomposition, are rendered more stable. Indeed, for these compounds, unimolecular bond cleavage is probably not an important initiation reaction in comparison to radical induced decomposition processes under the conditions of most practical systems. For larger species, unsaturation leads to destabilization. This is a direct manifestation of the resonance energy of the new radicals that are formed.

There are still considerable uncertainties on the exact values of the bond energies given above. This may not be too serious for many high temperature applications, since the dependence on the activation energies decrease with temperature. It is however less satisfactory in cases where accurate branching ratios are required. As will be surmised from the subsequent discussion, there is now good capability for extrapolation and interpolation. Predictions can still be subject to large errors.

Unimolecular Decomposition Processes

Table 1 contains rate expressions for bond breaking processes involving olefins², aromatics⁴, alkynes² and a representative alkane². All the reactions of the unsaturated compounds lead to the formation of resonance stabilized radicals and represent important dissociation channels. It can be seen that the differences in the activation energy from the alkane can be accounted quite accurately by the resonance energy. There is also a consistent decrease in the A-factor for the decomposition of the unsaturated compounds. It is possible to account for this by the more "tightened" structure of the resonance stabilized radical in comparison to that of the alkyl radicals formed during the decomposition of the alkanes. Of particular interest are the three dienes, 1,7-octadiene⁵, 1-7 octadiyne⁷ and 1,5 hexadiene^{8,6}. In the first case, the results are consistent with the assumption that substitution gamma to the bond being broken will have negligible effects. There is a factor of 2 divergence from this correlation for 1,6octdiyne. The data for 1,5 hexadiene are derived from the results on the allyl combination process. Although the A-factor appears to be slightly smaller than what would have been expected on the basis of the general trends, the discrepancies are not particularly large. Thus given the rate expression for an alkane it is quite straightforward to derive a similar expression for an unsaturated compound.

The resulting rate expressions leads to rate constants that are consistently larger than that for the comparable alkanes. This is especially true at the lower temperatures where the activation energies have larger effects on the rate constants. Unlike the alkanes, the larger unsaturated compounds can also decompose through a molecular "retro-ene" channel. This involves passage through a six centered transition state². Some experimentally determined rate expressions can be found in Table 3.¹ Figure 2 contains Arrhenius plots for decomposition of 1-hexene and 1-hexyne through bond breaking and retro-ene channels. The larger rate constants for C-C bond cleavage in 1-hexene compared to that for 1-hexyne are entirely due to the change in the resonance energy of the two radicals formed during decomposition. However, the ordering is reversed for the molecular decomposition channel. From purely geometric considerations one would have thought that the preference would have been for 1-hexene since the 120° C-C-C bond angle in this compound should have resulted in less strain in the transition state than the linear C-C-C structure in 1-hexyne. The consequence is that the molecular process is more likely to be important for the decomposition of the latter. Interestingly, for the alkylbenzenes the retro-ene process appears to be much less important. At 1100 K it has not been possible to detect any contribution from this source in the decomposition of n-pentylbenzene⁴. In general, molecular channels becomes increasingly important with greater unsaturation. Thus, the predominant modes of 1,5 hexadiyne decomposition is to benzene and fulvene^{8,9}.

Where there are no C-C bonds for which cleavage leads to resonance stabilized radicals, then the weakest bonds are the resonance destabilized C-H bonds. This however only moves these values to the upper end of the numbers for C-C bond cleavage in alkanes. Furthermore, the A-factor for C-H bond break can be expected to be somewhat smaller than that for C-C bond cleavage. An interesting situation arises for compounds such as propene and toluene where there the breaking of the C-C bond next to the site of

unsaturation may become competitive with that for C-H bond cleavage. In the case of toluene the experimental data are controversial¹⁰⁻¹¹. The situation is made more uncertain by the fact that at the high temperatures required for these decompositions, the reactions are into the pressure dependent region. Thus it is not only necessary to have accurate high pressure rate expressions but also the energy exchange parameter. A satisfactory fit of the data pertaining to propene decomposition have been published recently¹².

The stability of the small unsaturated compounds also brings into play the possibility of other modes of decomposition. Thus in the case of ethylene¹³, there is considerable evidence for a reaction channel involving vinylidene. For butadiene decomposition the data is suggestive of an analogous process¹⁴. In the case of cis-butene-2 the decomposition data have been interpreted in terms of the direct formation of butadiene¹⁵. In the case of benzene however, C-H bond cleavage appears to be the predominant decomposition mode under all conditions¹⁶. Another initiation process that is unique to unsaturated compounds is the possibility of radical formation through bimolecular reaction or the reverse of radical disproportionation reactions¹⁷. Rate expressions for these processes can be readily derived through the equilibrium constant and well established rate constants for the latter on the assumption that the temperature dependence of the disproportionation process is small.

There are very little data on the kinetics of the decomposition of unsaturated radicals. For the vinyl radical, one can calculate a high pressure rate expression on the basis of the reverse reaction and the thermodynamics¹³. However, under practically all high temperature conditions the process is well into the fall-off region. Thus it is necessary to determine a collision efficiency. Unfortunately, the lower temperature measurements on the pressure dependence cannot be fitted within the framework of RRRM theory. This leaves predictions of high temperature behavior very uncertain. The situation with respect to phenyl and benzyl radical is not completely clear¹⁸. They may be so stable that in most systems decomposition may not be an important destruction channel. This is probably the case for propargyl. The rate expression for the decomposition of allyl radical to form allene and hydrogen atom⁵ have recently been determined. The rate expression consistent with the low temperature rates for the reverse reaction is $5 \times 10^{13} \exp(-29500/T) \text{ s}^{-1}$. This can be compared with a rate expression of $4 \times 10^{13} \exp(-19000/T) \text{ s}^{-1}$ ¹⁹ for the comparable decomposition of isopropyl radical. There is thus over 20 kcal/mol difference in activation energy and is in fact much larger than the difference in that for C-H bonds in ethylene and ethane. On a per hydrogen basis the A-factor is somewhat larger and is consistent with the "stiffer" allyl as compared to alkyl radicals. In the case of butenyl-2, from the reaction of hydrogen with butadiene it is possible to derive the rate expression $4 \times 10^{13} \exp(-24200/T) \text{ s}^{-1}$. It would appear that the resonance energy is almost fully expressed in the activation energy of the decomposing species. Butenyl-3 contains a beta C-C bond that is adjacent to the double bond and a beta C-H bond that is also allylic. For alkyl radicals beta C-C bond cleavage is always the preferred decomposition mode. There is need for data on this and related unsaturated systems such as a butadienyl. The branching ratio for C-C and C-H bond cleavage have important consequences on models for the building of the larger unsaturated structures during hydrocarbon decomposition.

Larger alkyl radicals can readily isomerize through hydrogen migration. Transfer between the 1,4 and 1,5 appear to be more facile than the 1,2 and 1,3 reactions. At 1100 K contributions from the latter have been noted. Similar processes can occur for the unsaturated counterparts. In addition the latter can also cyclize. Thus 4-pentenyl-1 can cyclize to form the cyclopentyl radical⁵. There are large uncertainties in the rate expressions for such processes. Activation energies are expected to be low or in the 20 kcal/mol range and A-factor should reflect a "tight" transition state. This leads to major uncertainties in the nature of the breakdown products of the larger unsaturated molecules and is an important barrier in tracing the breakdown pathways of hydrocarbons in high temperature systems.

For high temperature unimolecular processes, it is necessary to consider at all times the effect of fall-off. In general, existing data can be fitted within the framework of RRKM calculations. The problem with vinyl mentioned earlier is probably the only exception. The requirements for making correct predictions are accurate high pressure rate expressions and the average energy transferred per collision and is particularly important for the estimation of branching ratios. This has been discussed earlier for propene decomposition. Low activation energy decomposition processes may have additional complications at high temperatures since a steady state distribution may not be achieved. Thus the standard treatment is not adequate and the solution of non-steady state master equation is required. Programs to carry out such calculations are now beginning to appear. It would be interesting to test such procedures with careful experiments.

Radical Attack

The weakness of the allylic and benzylic C-H bonds leads naturally to the assumption that rate constants for abstraction processes resulting in the formation of resonance stabilized species will be vastly enhanced over that for alkyl radicals. This is not the case and is demonstrated in Figures 2 and 3 where the comparison is for the abstraction of benzylic and allylic hydrogens by hydrogen and methyl and the corresponding alkane, propane. It will be noted that the 10-11 kcal/mol difference in the bond being broken if directly manifested in the activation energy would have led to differences of 2 orders of magnitude at 1100 K and 4 orders of magnitude at 550 K. Instead, in the case of abstraction by methyl it is apparent that the rate constants on a per hydrogen basis are commensurate with that from an secondary hydrogen. For abstraction by hydrogen atoms, rate constants on a per hydrogen basis are only a factor of 2 larger than that for the normal hydrogens and not even as large as that for a secondary hydrogen. It will be recalled that the difference in bond energies between primary and secondary hydrogens in alkanes is about 2 kcal/mol. These results are consistent with a transition state that is similar to the reactants and contrasts with the situation for unimolecular decomposition where the resonance energy is fully manifested. Consistent with the former is the relative constancy in the rate constant for the abstraction of benzylic and allylic hydrogens. These observations also can serve as a basis for prediction of abstraction rate constants for other reactions that lead to resonance stabilized products.

Through detailed balance one can then calculate the rate constant for

abstraction by resonance stabilized species. Due to the resonance destabilization of the bond this is an endothermic process. Since this is not made up by a faster abstraction rate constant in the forward direction, abstraction by resonance stabilized radicals must be quite slow. The consequence is that such species can cause chain termination through combination with other radical processes present in the system.

In the case of a vinylic C-H bond, the increase in bond strength appears to be manifested in the form of a smaller rate constant for the abstraction process. This can be seen in Figure 3, where the recent data for methyl abstraction²⁰ of a vinylic hydrogen from ethylene can be compared with the molecules discussed earlier. There are virtually no other reliable data on the rate constants of abstraction by vinylic or phenyl radicals. Since such processes are all more exothermic than comparable processes by methyl, it is very tempting to use the results from methyl as a lower limit.

Radicals can add to a site of unsaturation. In many instances this is a reaction that has no effect. For example terminal addition of H-atom to propene will lead to the formation of isopropyl radical which will readily go back to propene in high temperature systems. Terminal addition is the observed addition mode at room temperature. It has recently been found that the preference for terminal addition is mainly an enthalpic effect and is related to the stability of the radical that is formed²¹. Thus as the temperature is increased non-terminal addition becomes increasingly important. Non-terminal addition by hydrogen to a compound such as propene will lead to the formation of n-propyl radical which will decompose to form propene and methyl. The effect is that of a displacement reaction. Should the general trend hold then terminal addition to butadiene will be overwhelmingly favored and the induced decomposition by hydrogen atom to form vinyl and ethylene cannot be an important process. Addition processes, even at the non-terminal position have lower activation energies than the competitive abstraction processes. The A-factors are however lower. It is thus important at lower temperatures. Figure 4 summarizes data on hydrogen attack on isobutene and toluene²²⁻²³. It is clear that hydrogen addition to the olefin is favored over that for the aromatic. The overall effect of these processes is to remove the side chains from the unsaturated structure.

Resonance stabilization renders organic radicals much less thermally and chemically reactive. Thus it is expected that their steady state concentrations will be much larger. Reaction with itself and other organic radicals will then become important. The rate constants for such process are not much different than that of the non-resonance stabilized species. These radicals will also add to unsaturated compounds. As the temperature is increased the reaction will be reversed. The newly formed radical can also isomerize or cyclize. As a result one has a chemical activation system involving low activation energy process. There has been considerable recent work involving vinyl and phenyl addition to unsaturates²⁴. As in the case for the resonance stabilized case these may be reversible. Alternatively the addition may be followed by ejection of a fragment of the original molecule. The results must then be treated in terms of a chemical activation process. Such treatment is handicapped by the fact that the experimental results are really a combination of several elementary single step processes. Without the rate expressions for the true elementary steps extrapolations and predictions may be unreliable.

References

1. MacMillen, D. F. and Golden, D. M., *Annu. Rev. Phys. Chem.*, 33, 439, 1982
2. Tsang, W., "Comparative Rate Single Pulse Shock Tube in the Thermal Stability of Polyatomic Molecules," *Shock Tubes in Chemistry*, A. Lifshitz ed., Marcel Dekker, pg. 59, 1981.
3. Tsang, W., *J. Am. Chem. Soc.*, 107, 2873, 1985
4. Tsang, W., *J. Phys. Chem.*, 94, 3324, 1990
5. Tsang, W. and Walker, J. A., *J. Phys. Chem.* submitted
6. Tsang, W. and Walker, J. A.; "The Thermal Decomposition of Octadiyne as a Source of Propargyl Radicals" in preparation
7. Tulloch, J. M., Macpherson, M. T., Morgan, C. A. and Pilling, M. J., *J. Phys. Chem.*, 86, 3812, 1982
8. Stein, S. E., Walker, J. A., Suryan, M. M. and Fahr, A., 24th Sym. (Int.) on Combustion, (The Combustion Institute, Pittsburgh, Pa.), 1990, 85
9. Brown, R. F. C., *Pyrolytic Methods in Organic Chemistry*", Academic Press pg. 324
10. Pamidimukkala, E. M., Kern, R. D., Patel, M. R., Wei, H. C., and Kiefer, J. H., *J. Phys. Chem.*, 91, 2148, 1987
11. Muller-Markgraf, W. and Troe, J., 21st Symp. on Comb., 1988, 815
12. Tsang, W., *J. Phys. Chem. Ref. Data*, 20, 221, 1991
13. Tsang, W. *J. Phys. Chem. Ref. Data*, 15, 1087, 1986
14. Tsang, W. and C. Y. Lin, in preparation
15. Alfassi, Z. B., Golden, D. M., Benson, S. W., *Int. J. Chem. Kin.*, 5, 991, 1973
16. Hsu, D. S. Y., Lin, C. Y., Lin, M. C., 21st Symp. (Int.) on Comb. (The Combustion Institute, Pittsburgh, 1984, pg 623
17. Stein, S. E., "Free Radicals in Coal Conversion" in "Chemistry of Coal Conversion" (Schlosberg, R., ed.) Plenum Publishing, 1985, pg. 13
18. Kern, R. D., Wu, C. H., Skinner, G. S., Rao, V. S., Kiefer, J. H., Towers, J. A., and Mizerka, L. J., 20th Symp. (Int.) on Comb. (The Combustion Institute, Pittsburgh, Pa.) 1984 pg 789
19. Tsang, W. *J. Phys. Chem. Ref. Data.*, 17, 887, 1988
20. Zhang, H. X., and Back, M. H.; *Int. J. Chem. Kin.*, 22, 21, 35
21. Slagle, I. R., Batt, L., Gmurczyk, G. W., Gutman, D. and Tsang, W., *J. Phys. Chem.*, 95, 7732, 1991
22. Fahr, A. and Stein, S. E., *J. Phys. Chem.*, 92, 4951, 1988
23. Tsang, W. and Walker, J. A., 22nd Symp. (Int.) on Comb. (The Combustion Institute, Pittsburgh, Pa.), 1988, 101
24. Robaugh, D. and Tsang, W., *J. Phys. Chem.* 90, 4159, 1986.

Table 1: Rate expressions for various bond breaking processes(1100K).

$k(\text{hexane} \rightarrow 2\text{propyl}) \rightarrow 2.5 \times 10^{16} \exp(-41000/T) \text{s}^{-1}$
 $k(\text{hexene-1} \rightarrow \text{allyl} + \text{propyl}) \rightarrow 8 \times 10^{15} \exp(-35600/T) \text{s}^{-1}$
 $k(\text{hexyne-1} \rightarrow \text{propargyl} + \text{npropyl}) \rightarrow 8 \times 10^{15} \exp(-36300/T) \text{s}^{-1}$
 $k(1,7\text{octadiene} \rightarrow 4\text{-pentenyl} + \text{allyl}) = 1.2 \times 10^{16} \exp(-35700/T) \text{s}^{-1}$
 $k(1,7\text{octadiene} \rightarrow 4\text{-pentynyl} + \text{propargyl}) = 1.6 \times 10^{16} \exp(-35760/T) \text{s}^{-1}$
 $k(1,5\text{hexadiene} \rightarrow 2\text{ allyl}) = 7 \times 10^{14} \exp(-29500/T) \text{s}^{-1}$
 $k(\text{n-phenylbenzene} \rightarrow \text{benzyl} + \text{nbutyl}) = 1 \times 10^{16} \exp(-36500/T) \text{s}^{-1}$
 $k(1\text{-phenyl-1-pentene} \rightarrow 3\text{-phenyl-2-propenyl} + \text{ethyl}) = 3 \times 10^{15} \exp(-33800/T) \text{s}^{-1}$

Table 2. Rate expressions for the decomposition of unsaturated compounds into molecular entities

$$\begin{aligned}
 k(\text{hexene-1} \rightarrow 2\text{propene}) &= 4 \times 10^{12} \exp(-28900/T) \text{ s}^{-1} \\
 k(1,7\text{-octadiene} \rightarrow 1,4, \text{pentadiene} + \text{propene}) &= 3 \times 10^{12} \exp(-27900/T) \text{ s}^{-1} \\
 k(1\text{-hexyne} \rightarrow \text{allene} + \text{propene}) &= 5 \times 10^{12} \exp(-28400/T) \text{ s}^{-1} \\
 k(6\text{-methylheptyne-2} \rightarrow 1,2\text{butadiene} + \text{isobutene}) &= 2 \times 10^{12} \exp(-28700/T) \text{ s}^{-1} \\
 k(1,7\text{octadiyne} \rightarrow \text{allene} + \text{pent-1-ene-4-yne}) &= 5.6 \times 10^{12} \exp(-27860/T) \text{ s}^{-1}
 \end{aligned}$$

Figure 1. Typical Bond Dissociation Energies for alkanes, alkylbenzenes, alkenes and alkynes.

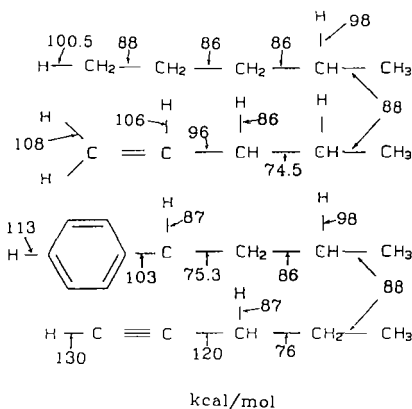


Figure 2. Rate constants for 1-hexene and 1-hexyne decomposition through bond breaking and retro-ene reactions.

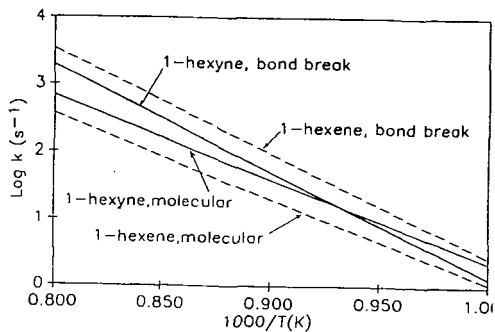


Figure 3. Rate constants for abstraction of hydrogen by hydrogen leading to benzyl, allyl, n-propyl and isopropyl radicals. [per hydrogen basis]

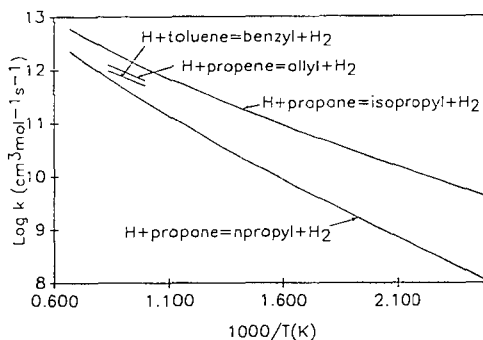


Figure 4. Rate constants for abstraction of hydrogen by methyl leading to benzyl, allyl, vinyl, isopropyl and n-propyl radicals. [per hydrogen basis]

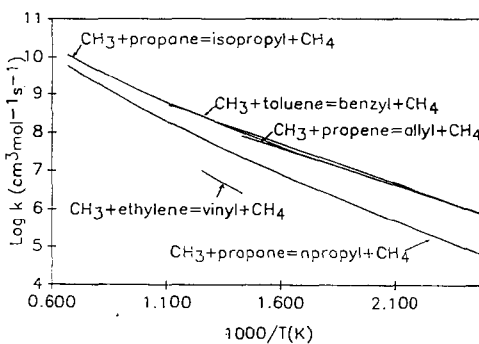
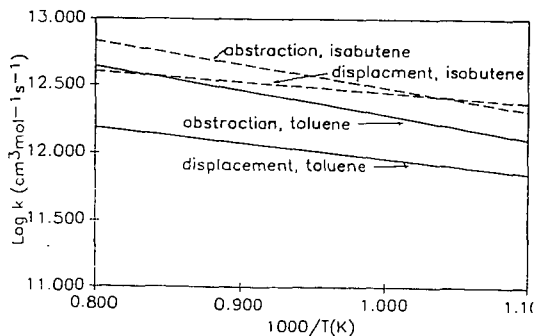


Figure 5. Rate constants for hydrogen atom attack on isobutene and toluene.



AUTORADIOGRAPHIC AND HYDROTHERMAL PROBES OF INTERFACIAL CHEMISTRY IN OIL SHALE AND COAL

David S. Ross
SRI International
Menlo Park, CA 94025

Keywords: hydrous pyrolysis, autoradiography, maturation

INTRODUCTION

The chemistry leading to the formation of petroleum hydrocarbons is an area of considerable interest, and major progress in our understanding has evolved in widely ranging studies over the past 25-30 years. The advances are due in large part to a broadening interest in the problem, encompassing large portions of the geochemistry, coal chemistry, and chemical kinetics communities, and to the development and application of new and sophisticated instrumentation.

However despite these advances, it is clear that there are still sizeable gaps in our perceptions of the processes, extending down to a very fundamental level. Thus for example, while the formation of petroleum is normally thought to be a geologically lengthy process involving the diagenetic breakdown and maturation of accumulated organic matter, it has been recently shown that petroleum hydrocarbons can be formed in much shorter periods of time in sedimented, submarine rift basins at 280°-350°C (Simoneit, 1985; Simoneit, et al., 1987). The products include an *n*-alkane distribution typical of petroleum, and highly condensed polynuclear aromatic hydrocarbons (PAHs) including phenanthrene, pyrene, benzpyrenes and coronene. The alkane origins are unclear, as are those of the PAHs, which are commonly observed as products of hydrocarbon pyrolysis only at temperatures above 550°C, while coronene itself is not generated at temperatures below 650°C (Commins, 1969). These temperatures are obviously far greater than those in the vent region, and the observations reflect the operation of largely unexplored but significant chemical processes.

One of the tools widely used in maturation studies is hydrous pyrolysis, or the heating of immature sediment in liquid water at pyrolytic conditions at 290-360°C (Lewan et al., 1979; 1981). (The critical temperature of water is 374°C.) The process is thought to accelerate maturation so that hydrocarbon development can be examined in a laboratory setting, although the claim that the procedure exactly mimics the natural process has been questioned (Monthieux et al., 1985; Tannenbaum and Kaplan, 1985; Comet et al., 1986).

Whatever the case, the chemistry of very hot water at the organic-mineral boundary is central to question of hydrocarbon production. Specific key issues are the nature of bonding at the interface, and effects of water in the hydrothermal regime on the chemistry. The discussion here offers some thoughts on those questions, drawing upon both our interpretation of hydrous pyrolysis data by Hoering (1984), and our work on organic/mineral interfacial interactions.

BACKGROUND

In studies of maturation it has been shown that the presence of liquid water increases the pyrolysate yield (Comet et al., 1986) and minimizes or eliminates the high olefin yields seen in dry pyrolysis (Hoering, 1984). It is often suggested that the key role of water in

hydrous pyrolysis is to cap pyrolytically formed organic free radicals (Monthioux et al., 1985; Hoering, 1984; Comet et al., 1986).



However this reaction is endothermic by 25-30 kcal/mol, and cannot be significant at hydrous pyrolysis temperatures. We have recently pointed out that if free radical chemistry is significant in hydrous pyrolysis, a more likely route is rapid, initial ionic deuterium-protium exchange between D_2O and a phenol, a thiol, or H_2S , followed by deuterium atom transfer to organic free radical sites (Ross, 1992).



On the other hand there is no compelling evidence at present supporting any specific mechanistic route.

Nonetheless some sense of the sequence for hydrocarbon production can be developed with attention to the hydrous pyrolysis work by Hoering (1984). He reported on the treatment of finely divided samples of Messel shale with D_2O at 330°C/3 days, under which conditions about 8% of the organic carbon was recovered as a mixture resembling petroleum hydrocarbons. The recovered products included a series of *n*-alkanes over the range C_{14} - C_{30} , with each alkane itself comprised of a broad distribution of isotope isomers containing 0 to more than 14 deuterium atoms. The D-isomer distributions were all very similar, with the maxima spanning D_3 - D_6 for the various alkanes, and with no apparent trend. Preexisting alkanes and olefins were ruled out as the source of the products by using source rock that had been previously extracted. The possibility that trapped alkanes surviving prior extraction were sources was eliminated in control experiments in which the source material was spiked with *n*-octadecane, which which then recovered after treatment with a considerably lower deuterium content than had been noted for the kerogen-derived material.

A particularly meaningful result was from work in which the starting shale was spiked with the olefin *n*-octadecene. Fully 60% of the olefin was recovered as the corresponding *n*-alkane, a result demonstrating the significant reduction potential available at hydrous pyrolysis conditions. Indeed, hydrogen is a common gaseous product in hydrous pyrolysis experiments (Lewan et al., 1979; 1981). The recovered alkane in this case contained deuterium, although the distribution was different from that found in the kerogen-derived alkanes. These results are discussed more fully below.

RESULTS AND DISCUSSION

Hydrous Pyrolysis and Deuterium Distribution

In considering Hoering's results, we seek to reconcile the data with a simple reaction model.* The development here is primarily qualitative, and our goal is the simple compari-

* A preliminary version of this work has recently appeared (Ross, 1992).

son of calculated and observed isotope isomer distributions. Detailed, quantitative reaction kinetics will be considered in a later development.

The basis of the process is the output from an integration routine based on the Gear algorithm (Moore and Pearson, 1981) and operated on a VAX 11/750 computer. The operation numerically simulates the sequential exchange in (1), presuming identical



rate constants for each step. (The kinetic isotope effects at these temperatures should be insignificant.) The output is a series of D-isomer profiles, with the major isomer moving to increasing substitution with time.

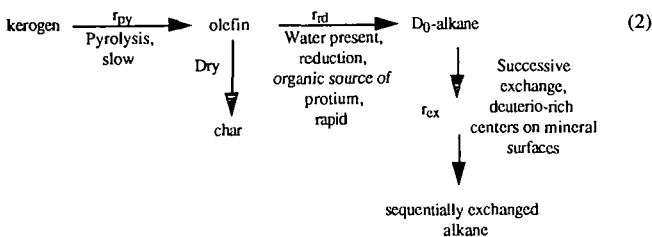
The deuterium contents in the alkanes recovered by Hoering in the alkane-added, the olefin-added, and the straightforward hydrous pyrolysis experiments are shown in Table 1. The table shows first that while the isotope substitution in the alkane-added experiment is small, there is nonetheless almost 30% exchange. Thus the *n*-alkane is not unreactive toward exchange in the system. In addition, in the face of a large excess of D₂O, 9% and 4-6% of the olefin- and kerogen-derived alkane are D₀ respectively. These values are not insignificant and suggest that reduction of olefin from a strictly protio source precedes exchange, which then operates on the D₀ alkane.

Next, the D/H ratios show that despite their similar %-D values, the kerogen-derived alkane has experienced far more exchange than has the alkane recovered from the olefin-added study. This difference is displayed in Figure 1a which shows the isomer data for the kerogen-derived *n*-heptadecane, and in 1b which presents the distribution for the *n*-octadecane from added *n*-octadecene. In the former the distribution peaks at D₃ and extends to isomers beyond D₁₄. In contrast the in 1b peaks at D₂, and no D-isomer is reported beyond D₁₀.

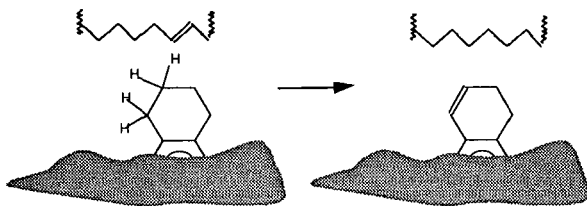
Also presented in the figures are the predicted distributions based on eq (1), starting with the D₀-isomer, and adjusted to peak respectively at D₃ and D₂. Clearly in 1a the observed distribution is far broader than the calculated one; there is both far more D₀ and significant isotope substitution beyond D₈ in the recovered product than predicted in the simple statistical model. A similar lack of fit is observed for the other *n*-alkanes recovered in the work.

The match in 1b on the other hand is very good. The added olefin obviously behaves differently from thermally generated, kerogen-derived alkane precursors. It must be quickly reduced to the protio alkane, which then exchanges as in eq (1).

Accordingly, to explain the generation of alkane from kerogen, the thermal generation of olefin must be included in our considerations, as shown in the scheme in (2). The scheme includes separate pyrolysis, reduction, and exchange steps, and a branching step for dry pyrolysis to be discussed below. Since the olefin reduction is rapid, $r_{rd} \gg r_{py}$, the rate of alkane production is essentially the pyrolysis rate. We presume the reduction step to proceed necessarily by way of reaction with the nonexchangeable protium in the organic



phase, i.e.



while exchange must take place on the mineral surfaces which have been equilibrated with D_2O .

We can next consider a selection of scenarios in which the ratios $r_{\text{py}}/r_{\text{ex}}$ are varied over a range of values (Figure 2). The *n*-heptadecane profile is also shown in the figures. They show that for a fixed exchange rate a relatively high alkane production rate provides a distribution shown in 2a like that in 1a except in this case the peak is at D_6 . Reducing the ratio by an order of magnitude rolls the peak down to lower D-values, and provides a satisfactory fit to the observed profile as shown in 2b. Decreasing the ratio still further in 2c yields a profile favoring the low-D side, as would be expected as the conditions shift toward what is effectively a large reservoir and a steady-state supply of precursor.

The match in 2b supports the sense of the scheme in eq (2) that alkane precursor supply is not instantaneous, but with a rate comparable to that for exchange. Thus for the Hoering work, $r_{\text{rd}} \gg r_{\text{py}} = r_{\text{ex}}$. A key aspect of this exercise is the comparison of figures 1b and 2b, for which the ratio of exchange rates necessary for the observed fits, $r(2b)_{\text{ex}}/r(1b)_{\text{ex}}$, is about 3. This result is in line with the difference in the H/D ratios for the olefin-added and kerogen-derived alkanes in Table 1. Since the exchange is mineral surface promoted, these data reflect an extensive association of the kerogen with the mineral surface in the source rock, and extensive chemistry specific to the interface.

Autoradiological Probe of the Mineral/Organic Boundary

It is recognized that silica surfaces bind hydrocarbons in what must be donor-acceptor complexes (Iler, 1979). Similarly, oxygen-containing compounds including benzoates, phthalates, salicylates, phenols, and catechols complex with aluminum oxides and hydrox-

ides (Davis and Hem, 1989). However little is known about the interactions at the phase boundary and the nature of the bridging structures.

In recent studies directed at the formation and durability of asphalt-aggregate bonds in highways we have developed some relevant data using tritium-tagged organics and autoradiographic techniques as sketched in Figure 3 (Ross, et al., 1991). Clean surfaces of several aggregate samples were exposed to very dilute solutions of the compounds 4-HO₂C-C₆H₅(CHT)₂(CH₂)₁₀CH₃ (I) and C₆H₅(CHT)₂(CH₂)₁₀CH₃ (II) in refluxing toluene (111°C/~30 min).^{*} The samples were then extracted with toluene in a Soxhlet (20 hr), and the flat surface was mated to fast photographic film. Following 8-day exposures the samples were extracted with water in a Soxhlet (100°C/2 hr), and photographed again.

The results for a rock sample containing primarily silica and K-feldspar (potassium aluminosilicate) treated with the carboxylic acid (I) are presented in Figure 4. The images in 4a and 4b show the results following the toluene and water extractions, respectively, and both show remaining organic material in a mosaic of distinct bonding and nonbonding zones. 4b is less intense than 4a, a significant result demonstrating the removal of some but not all of the material.

This result cannot be reconciled with simple acid-base association between (I) and the surface since such complexing would be fully destroyed by water. It is recognized that benzene yields a carbonaceous film on clean platinum surfaces at around 100°C (Davis and Somorjai, 1980), and aluminosilicates engage in similar activity (Somorjai, 1991). However the phenomenon has received little study, and little is known about the nature of the films nor of their bonding to the mineral surface. We surmise that the tritium-containing substances bound to the mineral surface are residues from surface promoted decomposition, and are very strongly bound to the surface.

The character of the sites associated with the films is revealed in SEM/EDAX studies of the same rock surface presented in Figure 5. 5a is an enlarged portion of 4b (top, left of center), and 5b is the SEM image of that region at about 50 x magnification. K and Si maps of the same region are shown in Figures 5c and 5d, respectively; Ca, Al, and Fe maps were also prepared but are not shown. The figure shows the Si distribution to be uniform over the region, as are the Ca and Fe distributions although they show a lower density of spots. The K and Al maps, however, shows distinct patterns of K-rich and -poor regions, which are, respectively, feldspar, a potassium aluminosilicate, and silica.

Comparison of the image in Figure 5a and the K map in Figure 5c shows an unmistakable similarity in patterns. This match demonstrates a preferential reactivity of, and bonding to, the feldspar regions of the rock. Examination of the SEM image of the surface in 5b shows a faint pattern also matching the K map. Such patterns are not visible in aggregate that has not been treated, and reflect the deposition of the film in the active regions.

Subsequently the unsubstituted arene II was studied with aggregate samples that were virtually fully silica, and provided faint but well defined images faithful to the exposed silica surface following the toluene-stripping (not shown). Water-stripping in this case eliminated all trace of the signal. There is little doubt that the silica surfaces in the studies with I show some signal; however it is difficult to be observed because of the much stronger response in the feldspar regions. This result, a carbonaceous film surviving 20 hr of toluene extraction derived from an organic compound with not polar functionality on a relatively unreactive surface, demonstrates the likely ubiquity of these films, and their possible significance in source rock and the maturation process.

^{*} The solutions also contained asphalt, an aspect of the work not important to the discussion here.

CONCLUSIONS

The action of water at the organic-mineral interface is apparent from the diminishing signal in Figures 4a and 4b. The water in some manner strips some of the organic material from the surface. It is conceivable that the stripping involves hydrolysis of the mineral phase supporting the organic film rather than action at the bonds bridging the two phases. Whatever the specific mode of action, the process should be important in hydrous pyrolysis in separating the two phases.

This activity goes hand in hand with the moderation of the acidity of mineral sites by water, as recognized by Tannenbaum and Kaplan (1985). Acidic sites on clay surfaces have been invoked as a significant feature of maturation (Alexander, et al., 1982, 1984), and water must therefore be significant to the degree and direction of that chemistry. We have utilized these views in eq (2), suggesting that in the absence of water the high surface acidity irreversibly reincorporates the pyrolytic products into the organic phase as char.

Thus since aromatization is a major driving force during maturation (Hayatsu et al., 1987), and therefore a source of hydrogen (or reduction potential), we can envision a system which in the absence of water the organic phase remains associated with the mineral phase, and thermolytically releases hydrogen and relatively small quantities of olefin. The major product is an H-poor char on the surface. In contrast when water is present, the phases are separated, the moderated surface acidity reduces char formation, and the olefins are available for reduction to alkanes. The alkanes then engage in hydrogen exchange with other appropriate sites on the mineral surface before escaping into the aqueous medium, which at near critical temperatures is a good alkane solvent (Skripka, 1979).

ACKNOWLEDGEMENT

It is a pleasure to acknowledge very useful discussions of hydrous pyrolysis with my colleagues Dr. Donald McMillen and Dr. Ripudaman Malhotra. Dr. McMillen was helpful in clarifying the important issue of a mixed ionic/free radical sequence for protium/deuterium exchange, and Dr. Malhotra emphasized the point that slow kerogen thermolysis could be significant in the product isomer patterns.

REFERENCES

- Alexander, R., Kagi, R. I., and Larcher, A. V., 1982. *Geochemica et Cosmochimica Acta*, **46**, 219-222.
- Alexander, R., Kagi, R. I., and Larcher, A. V., 1984. *Organic Geochemistry*, **6**, 755-760.
- Comer, P. A., McEvoy, J., Giger, W., and Douglas, A. G., 1986. *Organic Geochemistry*, **9**, 171-182.
- Commins, B. T., 1969. *Atm. Env.*, **3**, 565-572.
- Davis, J. and Hem, J., 1989. *The Environmental Chemistry of Aluminum*, G. Sposito, Ed., CRC Press, Inc., Boca Raton, FL, pp 186-218.
- Davis, S., and Somorjai, G., 1980. *J. Catalysis*, **65**, 78-83.
- Hayatsu, R., Botto, R. E., Scott, R. G., McBeth, R. L., and Winans, R. E., 1987. *Organic Geochemistry*, **11**, 245-250.
- Hoering, T. C., 1984. *Org. Geochem.*, **5**, 267-278.

- Iler, R., 1979. *The Chemistry of Silica*. John Wiley and Sons, New York, pp. 652-653 and 656-657.
- Lewan, M. D., Winters, J. C., and McDonald, J. H., 1979. *Science*, **203**, 897-899.
- Lewan, M. D., Winters, J. C., and Williams, J. A., 1981. *Adv. in Organic Geochemistry 1979*, M. Bjorøy et al., eds., John Wiley and Sons, Ltd., Chichester, p. 524-533
- Monthieux, M., Landais, P., and Monin, J.-C., 1985. *Organic Geochemistry*, **8**, 275-292.
- Moore, J., and Pearson, R., 1981. *Kinetics and Mechanism*, Third Edition, John Wiley and Sons, New York, 318-324.
- Ross, D. S., Loo, B., and Mirsalis, J., 1991. *Fundamentals of the Asphalt-Aggregate Bond*, Report prepared for the Strategic Highway Research Program, Contract No. SHRP-87-AIIR-11.
- Ross, D. S., 1992. *Organic Geochemistry*, **18**, 79-81.
- Simoneit, B.R.T., 1985. *Can. J. Earth Sci.*, **22**, 1919-1929.
- Simoneit, B.R.T., Grimalt, J. O., Hayes, J. M. and Hartman, H., 1987. *Geochim. Cosmochim. Acta*, **51**, 879-894.
- Skripka, V. G., 1979. *Chemistry and Technology of Fuels and Oils*, **15**, 88-90.
- Somorjai, G., 1991. Personal communication.
- Tannenbaum, E. and Kaplan, I. R., 1985. *Nature*, **317**, 708-709.

Table I

D-Introduction into Recovered Alkane^a

	From added <i>n</i> - octadecane	<i>n</i> -Octadecane from added octadecane	Kerogen-derived <i>n</i> - C ₁₇ - C ₂₉
<u>%-D-containing^b</u>	28	91	94-96
<u>D/H</u>	0.02	0.09	>0.20 ^c

a. From Hoering, 1984

b. Fraction of recovered alkane with at least one deuterium atom.

c. The D-quantities were not presented beyond D₁₄, but the exchange pattern suggests significant contribution by more highly exchanged isomers. The D/H value is thus a lower limit.

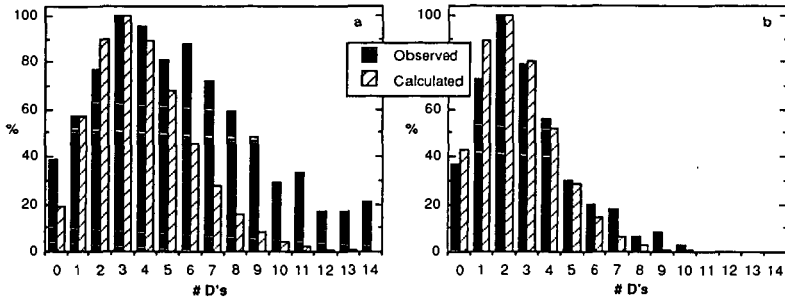


Figure 1. a) D-distribution for kerogen-derived heptadecane and calculated profile.
 b) D-distribution for octadecene-derived octadecane and calculated profile. In both cases the calculation is for simple exchange via eq. 1.

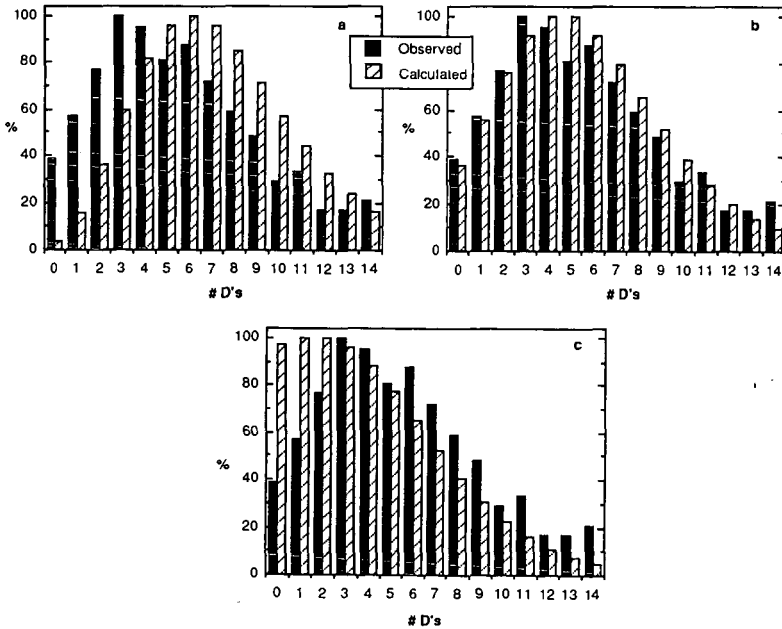
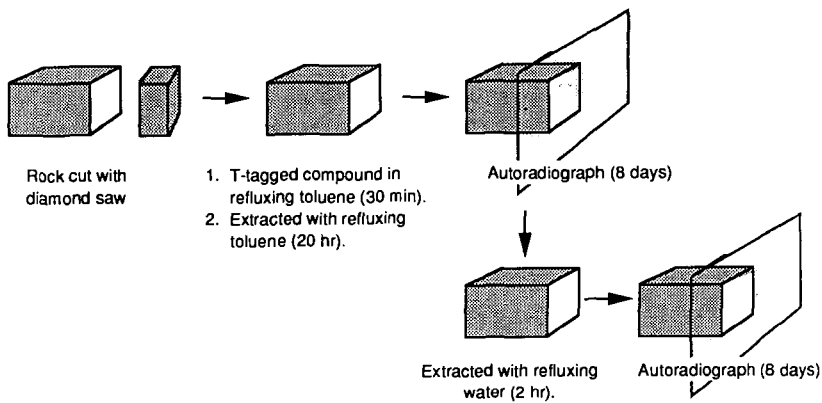
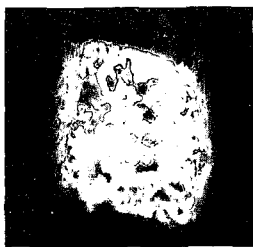


Figure 2. D-profile for kerogen-derived heptadecane and calculated profiles via eq. 2.
 a) $r_{py}/r_{ex} = 4.60$ b) $r_{py}/r_{ex} = 0.46$ c) $r_{py}/r_{ex} = 4.6 \times 10^{-2}$



CAM-2847-2

Figure 3. Sequence for autoradiographic study.



(a) AR image after toluene-stripping



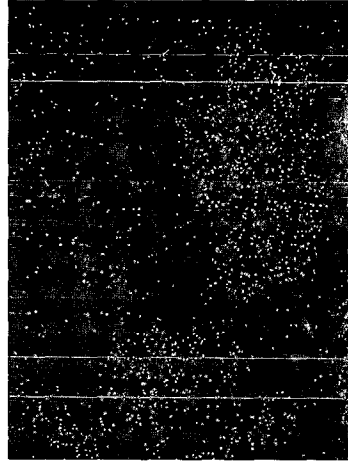
(b) AR image after water-stripping

CPM-2847-1

Figure 4. Autoradiograph images following treatment with $\text{HO}_2\text{C-Ar(CHO)}_2(\text{CH}_2)_{10}\text{CH}_3$.



(a) AR Image

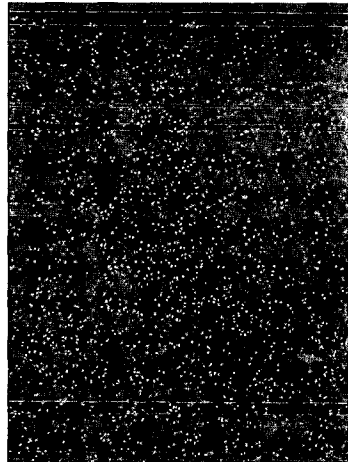


(c) K Map



(b) SEM Image

A



(d) Si Map

RP-8674-8A

Figure 5. SEM/EDAX studies of test piece with carboxylic acid.

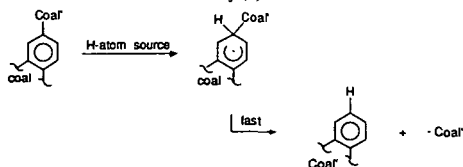
HYDROGEN-TRANSFER IN RETROGRADE REACTION -- THE HERO AND THE VILLAIN

Donald F. McMillen and Ripudaman Malhotra
SRI International
333 Ravenswood Ave., Menlo Park, Calif. 94025

Keywords: Liquefaction Mechanism, Hydrogen-Transfer, Bond-Cleavage, Retrograde Reaction.

INTRODUCTION

Much attention has been focused over the years on the nature of the bond cleavage that takes place during coal liquefaction, pyrolysis, and combustion. Owing to the essential impossibility of determining the "critical" linkages between clusters in the organic structure of coals, much of what we now "know" has only been inferred from comparisons between coal behavior and that of model compounds or probe molecules. Nevertheless, it is now generally recognized that a picture of this bond cleavage that involves only the spontaneous thermal scission of weak bonds is, at best, incomplete and that the cleavage of strong bonds as a result of hydrogen-transfer should be included in our picture of coal conversion chemistry (1).



Scheme 1. Cleavage of strong bonds engendered by H-transfer to ipso position.

Recognition of the fact that hydrogen-transfer is a *prerequisite* to strong bond cleavage (rather than merely a subsequent step necessary to limit recombination) leads, via consideration of microscopic reversibility, to the conclusion that hydrogen-transfer is also a prerequisite to the *formation* of strong bonds, or retrograde reaction. Tracing Scheme 1 backwards, for instance, the link between Coal and Coal' is not "locked" into place until some agent removes the ipso H-atom in what amounts to the reverse of the first step. Thus, the task of increasing coal liquefaction yields may in some cases involve the dilemma that introduction of a particular H-transfer agent will increase bond *formation* as well as bond cleavage. It follows then that the relative utility of various H-transfer agents in liquefaction cannot be truly understood unless we know their proclivity for promoting both bond-cleavage and bond-formation. This paper is an attempt to assess the various categories of coupling reactions that may constitute the retrograde processes limiting coal conversion yields and their sensitivity to changing reaction conditions.

Although the importance of retrogressive reactions has become more obvious through careful studies of liquefaction kinetics and products, the fundamental chemical reactions and their kinetics have remained obscure. For instance, researchers such as Neavel recognized some time ago that soluble products could be generated *and consumed* very rapidly under coal liquefaction conditions (2). Similar observations have been made for pyridine solubles under pyrolysis conditions, where there is no added solvent (3). In a sense the whole technology of heavy oil conversion is bound up with retrograde reactions, in that thermal treatment of petroleum asphaltene under a variety of conditions can produce *similar amounts of distillate, but the amount of retrograde product (coke) generated in conjunction with these volatiles is critically dependent on conditions of catalyst, medium, and hydrogen pressure (4-5)*. Thus the impact of retrograde processes can be quite obvious, but the detailed nature of the responsible bond forming reactions is unclear.

In order to provide a background for better addressing retrograde reactions, we have examined the literature for evidence of retrograde reactions not only in actual coal conversions, but in studies of model compounds, probe molecules, and grafted-probes, and have tried to extend our understanding of the bond-forming chemistry in some of these circumstances by mechanistic numerical modeling. This model was chemically detailed, but structurally limited -- not intended in any way to actually model the conversion of a real coal, but to ascertain how chemical factors influence certain classes of reactions under different circumstances.

This modeling incorporates the most basic of the bond cleavage types now thought to be important in coal liquefaction, and its validity is dependent of course on the appropriateness of the reactions considered. In this paper we summarize some of the results of this literature scrutiny and modeling effort.

RESULTS AND DISCUSSION

Pyrolysis of Grafted Coals. Zabransky and Stock have covalently grafted various groups to an Illinois No. 6 coal through various C-O and C-C linkages and pyrolyzed these coals using a resistively heated wire grid reactor (6-12). Through isotopic labeling of various carbons and hydrogens in the grafted groups, followed by mass spectrometric analysis of the gaseous products, identifiable portions of the grafted structures were tracked with a degree of certainty that is not achievable with unmodified coals. These studies have allowed the authors to reach a number of interesting conclusions regarding the nature of bond cleavages in structures typified by the grafted groups. Here we wish to focus instead on what limits this cleavage, specifically on how retrograde reactions compete with the bond scission processes.

Some indication of the severity of retrogression can be seen from the products reported by Zabransky and Stock (6-12) for pyrolysis of deuterium- and ^{13}C -labeled- O-n-propyl, O-n $\text{C}_{18}\text{H}_{37}$, O- $\text{CH}_2\text{CH}_2\text{Ph}$, and O- CH_2Ph Illinois No. 6 coals. Selected results are shown in Table 1, derived from their data.

The authors have discussed the extent to which the results reveal that the cleavage of strong bonds by β -scission, following either H-abstraction from an alkyl group or H-transfer to an aromatic group, are important routes for fragmentation of the grafted structures. They conclude, for instance, that the abstraction route for the aliphatic portion of alkyaromatic structures tends to be more facile than the ipso-addition route; at least when the aromatic is a single phenyl ring. These pathways account for cleavage of 2 to 40% of the grafted groups (6,9). Just as important as determination of the modes of cleavage, however, is comparison of the yields of cleaved products with the inferred yields of uncleaved, or retrograde, products. Table 1 shows the percents of the grafted portions that are converted to various cleavage products, as determined by isotopic labeling. Though the heavier products were not fully analyzed, and high precision was difficult to achieve on the scale of the experiments, the general trend is clear: substantially less than half of the grafted groups were evolved, via either weak bond thermolysis or induced scission of strong bonds, during pyrolysis to final temperatures generally in the 750 to 850°C range. This observation becomes still more striking when the rate of thermolysis of the O-C linkages in the various graftings are considered.

Table 2 shows estimated rates of cleavage for various final pyrolysis temperatures, and also the fractions of the linkage expected to be still intact by the time a particular temperature is reached (at the 1000°C/s heating rate used in the pyrolysis experiments). To take into account cage recombination, the last three columns in Table 2 are estimated by assuming that 99% of the radicals produced by thermolysis recombine before they can escape the cage, in effect extending the life of the weakly bonded species by a factor of 100 [SSD85].

The slowest homolysis is of course expected for the O-alkyl grafts, in which the O-C bonds are about 10 kcal/mol stronger than any of the O-arylmethyl cases (14). Even for this most strongly bound group, pyrolysis to a final temperature of 750°C (with zero hold-time), would leave an unconverted fraction of less than 1%, were there no recombination. However, if 99% recombination occurred in the cage, the fraction unconverted by 750°C would increase to 97%. Thus, for the O-alkyl grafted coals, the expected homolytic conversion of the graft to volatiles would critically depend on the extent of cage recombination. In contrast, the O-benzyl-type graftings have estimated homolysis rates that are higher by at least two orders of magnitude, and the fractions unconverted by 750°C would be no more than 4%, even assuming 99% cage recombination. Given this difference, it is striking that, in spite of having the slowest homolysis rates, the O-alkyl graftings are seen in Table 3-1 to have the highest fractional conversions to the corresponding alkane and its degradation products (~40%). For comparison, row 4 in Table 1 shows that only 8% of the weakly bound benzyl group of O-benzyl coal was detected as toluene. Clearly, the ease of conversion to volatile products in the case of alkyl structures is not dependent primarily on the ease of homolysis.

If the primary determinant of the extent of conversion of these weakly bound grafts is not the homolysis rate, then it must be either the rate of retrogression of these structures (including the fate of initially formed radicals), or the rate of the induced bond scission. For the case of O-nPr coal, Zabransky and Stock have shown (by examination of alkane/alkene ratios) that facile volatiles production with the O-nPr coal is not due to bond-scission induced by H-abstraction, but does indeed arise from homolysis (11,12). Thus, the conversion of O-propyl coal to aliphatic fragments is more complete than the conversion of O-benzyl coal to toluene, *in spite of* the fact that the former conversion occurs via a much slower homolysis. The successful homolysis of aliphatic linkages that are significantly stronger than the weak bond in the O-benzyl coal thus fixes the cause for the low yields of toluene on the proclivity of aromatic structures for undergoing retrograde reactions.

Pyrolysis of Polymeric Coal Models. More detail about the structural factors that facilitate retrograde reaction (other than the simple presence of aromatic groups) can be obtained from polymeric coal model studies. Several years ago, Solomon and Squire studied 27 polymers containing aromatic, hydroaromatic, and heteroaromatic groups linked together by ethylene, methylene, propylene, oxymethylene, ether, aryl-aryl, sulfide, and ester bridges (15,16), using the same heated-grid technique for the pyrolysis of the polymer models as was used by Zabransky and Stock used for their grafted coals. Because of limitations of space, we will merely summarize some of the conclusions that can be drawn from this study.

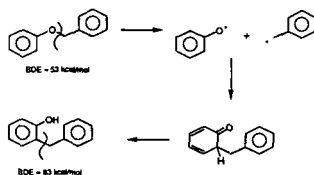
The primary focus of Solomon was on two-atom, i.e., weak linkages, for the reason that the traditional picture of thermal coal conversion chemistry then held that coal conversion resulted from spontaneous thermal cleavage (i.e., homolysis) of such weak linkages. However, precisely because most of the polymers consisted of low molecular weight clusters linked in linear chains by weak bonds, we find that the results offer a clearer view of the impact of retrograde reactions than they would with models containing some strongly linked clusters. These results reiterate some of the conclusions drawn from the grafted coal studies of Zabransky and Stock (6-12) and allow new ones to be drawn regarding the factors that limit the conversion of the polymers to volatiles. Among the most important of these conclusions are the following.

- Retrograde reactions profoundly limit volatile (or liquid) yields, which are controlled more by these coupling reactions than by the weakness of connecting bridges.
- Polymers or coal grafts containing aromatic components undergo retrograde reaction much more readily than aliphatic components.
- Increasing size of the aromatic clusters increases char yield, even under conditions where oligomer volatility limitations are unlikely to play a large role.
- As expected, the presence of hydroaromatic structure within the polymeric network decreases the retrograde reaction.
- Retrograde reactions tend to be worse for oxymethylene bridged polymers (particularly if in quinonoidal structures), notwithstanding an ~10 kcal/mol lowering of bond strength;
- Strengthening of weak ethylene bridges by removal of aliphatic hydrogen when there is no better source available contributes to char formation, but perhaps more importantly induces other crosslinking reactions to take place.

Nature of the Retrograde Reactions. From the studies highlighted above, together with related studies of coals and polymeric models and the work of Stein on the coupling of aromatics (17-21), we arrive at the following conclusions about the potential classes of retrograde reaction involving uncharged species in coal structures.

1. Radical Recombination

- Resonance stabilized radicals -- Two resonance stabilized radicals can result only in the formation of weak bonds, providing only temporary retrograde products, *except* in the case of ring recombination of phenoxy radicals. The latter case can result in successful retrograde reaction because the highly unstable initial adduct is able to rapidly rearrange through facile inter-molecular *proton* transfer reactions that are known (22) to be accessible to phenolic structures at coal liquefaction temperatures *even* in hydrocarbon solvents.



Scheme 2. Formation of strong retrograde linkages by ring recombination of aryloxy radicals.

- Aryl radicals -- Recombination of two aryl radicals would produce a biaryl linkage, at ca. 115 kcal/mol the strongest C-C single bond possible in hydrocarbons; however, the reactivity of aryl radicals necessarily means their concentrations will normally be far too low to participate in cross-recombination reactions, let alone self-recombination reactions.
2. Radical Addition to Unsaturated Systems
- Aryl radicals -- Aryl radicals, if formed, are known to add readily to any other aromatic system. The strength of the new bond formed means that hydrogen is readily displaced, even in the gas phase (18,21), where the primary loss process available is direct unimolecular loss of H-atoms. In the condensed phase, where H-atom loss by radical disproportionation and radical hydrogen-transfer will be relatively much more favored, we would expect aryl radical addition to be essentially irreversible. That is, during coal liquefaction effective H-atom removal would be no problem and the principal factor limiting aryl radical addition will be the rate of aryl radical generation.
 - Resonance stabilized radicals -- The addition of resonance stabilized radicals to aromatic systems constitutes the opposite extreme: the carbon-carbon bond formed will be at least 20 kcal/mol weaker than the C-H bond that needs to be displaced (13,14), i.e., direct addition-elimination or displacement of H atoms by resonance-stabilized radicals are much less favored. Such coupling requires "special" circumstance that are nonetheless present during much of the liquefaction process. These circumstances are either high concentrations of displacing radicals, the presence good leaving groups on these aromatic systems, extremely effective H-atom acceptors in the reaction mixture, or multiple opportunities for radical addition. In other words, coupling reactions of this type will be highly dependent on the nature of the H-atom removal agents.
 - Molecular coupling -- Stein found it necessary to invoke direct bimolecular coupling of closed-shell aromatics to form biradicals in order to account for the coupling of anthracene (20). This reaction can be thought of as the addition of a highly unstable biradical; no bimolecular H-transfer process is fast enough to compete with the β -scission of the resulting biradical adduct to re-generate the two closed-shell aromatics. Adducts formed by such additions can evidently be stabilized only when geometrical factors favor very rapid *intra*-molecular H-atom transfer reactions.

ASSESSMENT OF RETROGRADE REACTION BY MECHANISTIC MODELING.

In this section we summarize some results from use of a numerical reaction model (23) employing a surrogate coal structure to help address the factors controlling competing bond scission and retrograde reaction pathways during the initial stages of coal liquefaction. The addition of stabilized radicals was chosen as the retrograde reaction type, not because we believe it to necessarily be always the most important class of retrograde reaction, but because it is the class of bond-making reaction whose outcome is most likely to be sensitive to changing hydrogen-transfer conditions. The addition of resonance-stabilized radicals is highly reversible, such that if it results in successful formation of strong bonds between aromatic clusters, it will be because a very small fraction of a large number of original additions ultimately go on to stable products. For simplicity, we have limited the model to a pure hydrocarbon system, though the same general considerations will also apply to systems containing phenolics, where the presence of the -OH groups will in all likelihood further promote radical addition.

The model we have used is very detailed; it incorporates all relevant fundamental chemical reactions (non-ionic) of essentially all species, both closed shell and free radical, in the reaction system. Because of this detail, the model, of necessity, includes only a very limited set of starting structures. All models is homogeneous; it consists of relatively low molecular weight species assumed to be miscible in all proportions. We have made the simplifying assumptions that the system is free of concentration gradients and requires no mass- or heat-transport. The activity of H₂ in solution is taken to equal that provided by presumed equilibrium with the gas-phase H₂ pressure. This model was not intended in any way to actually simulate the conversion of a real coal, but to ascertain how chemical factors influence certain classes of reactions under different circumstances. There has been absolutely no attempt to force the model results to correspond to the phenomenology of coal liquefaction or pyrolysis.

Space prevents a full description of the model and results here; these details will be presented elsewhere (24). Given below is a brief summary of the results of the modeling as they apply to the prevention of retrograde

reaction. In some cases these results are a quantitative illustration of what could be qualitatively anticipated from thermochemical considerations. In other cases the results were qualitatively surprising.

- All scavengers that operate via a radical capping process have a dual role—they also act as initiators.
- "Scavengers" typically found to best aid coal conversion to volatiles or liquids appear to perform better because they are superior in some aspect other than scavenging.
- At short reaction times, where there is a large generation of fragment radicals from homolysis of the weakly bonded coal surrogate, modeling indicates that dihydroanthracene, as the better scavenger, indeed maximizes the yield of capped fragment radicals, and minimizes the yield of recombination products and radical displacement retrograde products.
- However, at long reaction times, the "better" scavenger actually *enhances* the yield of retrograde product. This is because, at longer reaction times when the burst of radicals from the decomposing coal has largely died away, the principal source of fragment radicals is abstraction of hydrogen atoms from the previously capped fragment species by the pool of scavenger radicals generated by the scavenger itself. Thus, the model elaborates a trend which has been noted previously (25), namely that coal conversion tends to be better in the presence of hydroaromatics that are *not* the best scavengers, and is evidently better because these latter scavengers tend to be better hydrogenolysis reagents, while being poorer radical initiators.
- Higher temperatures provide more reaction, but if there is not something to mitigate retrograde reactions, higher temperatures tend to cause the retrograde reactions to increase as fast or faster than the bond-cleavage reactions. This modeling result appears to be completely in accord with the common observation that increasing liquefaction temperature beyond about 440°C tends to lower coal conversion, and similarly in pyrolysis, that higher heating rates tend to decrease char yields, *primarily* when the higher heating rates are associated with more rapid removal of volatile products, (26).
- Under the conditions modeled, displacement of carbon-centered radicals from aromatic rings accounted for roughly four times as many retrograde products as did displacement of H-atoms
- The presence of H₂ does *not* inhibit retrograde product formation as much as it hydrogenolyzes retrograde products faster after they are formed. In fact, modeling indicates that H₂ can, at certain reactions times, *increase* the yield of retrograde products.
- The impact of added H₂ on hydrogenolysis (at least in the short term) does *not* come primarily through its maintenance of a useful hydroaromatic content, as has often been postulated in coal liquefaction, but through a higher steady state concentration of H• that is established long before the hydroaromatic content can be substantially affected.

Summary and Conclusions

Our examination of literature data, together with thermochemical considerations and the associated numerical modeling of simplified reaction systems leads us to the following summary picture of retrograde reaction during coal conversion.

Recombination with Phenoxy Radicals. The major case where where radical recombination can lead to a true retrograde product is ring-recombination of a phenoxy radical with resonance-stabilized carbon-centered radicals. Studies with the model compound benzyl phenyl ether have shown that the presence of scavengers can decrease but cannot easily eliminate the formation of diarylmethane linkages through this route. We suggest that facile intramolecular proton-transfer efficiently converts the initially formed and unstable keto-form to the strongly bonded phenolic form. No such isomerization pathway is available for ring-recombination of two benzylic radicals.

Dual Function of Radical Scavengers. Modeling has illustrated the apparent paradox that the best scavengers may do the worst job of preventing radical addition. Hydroaromatic structures such as 9,10-dihydroanthracene that have very weak benzylic C-H bonds will also tend to have high steady state concentrations

of the ArH• radicals generated in the scavenging act. Thus, the "better" scavengers may result in a lower steady state concentrations of candidate retrograde radicals *only* when the principal source of such radicals is something other than these abstractions, such as a rapid homolysis or β -scission. Accordingly, the concentration of resonance-stabilized radicals like benzyl and phenoxy can sometimes be decreased by scavengers, but they cannot be lowered below a minimum corresponding to the level that is generated by the hydroaromatic scavenger system functioning as an initiator.

Modeling also reveals that in many instances, the donor solvent content or H₂ pressure do not serve so much to decrease the rate of retrograde product formation as to cleave such products after they have been formed. In fact, the presence of these reagents may actually *increase* the rate of retrograde product formation at certain times. Thus, the major impact of H₂ lies not in its scavenging ability, which is very modest, but in the fact that whatever scavenging does take place produces free H-atoms, which are highly active hydrogenolysis agents. This "direct" hydrogenolysis activity of free H-atoms is seen to be a much more important effect of H₂, at least at short reaction times, than the indirect effect of maintenance of donor level.

Aryl Radical Addition. Since aryl-aryl bonds are so strong, displacement of H-atoms by addition of aryl radicals is prevented primarily by minimizing formation of these radicals in the first place. Literature results suggest the somewhat counterintuitive observation that aryl radicals are generated principally by the much larger pool of (individually much less reactive) resonance stabilized radicals.

Resonance Stabilized Radical Addition. The displacement of C-H bonds by resonance stabilized radicals (whether acyclic and therefore leading to diarylmethane linkages, or cyclic and leading ultimately to biaryl linkages) will usually be dependent not only on the concentration of potential displacing radicals, but also on the facility with which the reaction system stabilizes the intermediate adduct by removing the hydrogen atom that is being substituted. For example, modeling indicates that retrograde products from homolytically generated benzylic radicals are lower when dihydroanthracene (rather than dihydrophenanthrene) is the hydroaromatic scavenger. However, at long reaction times, when the main source of benzylic attacking radicals is the radical soup itself, the higher radical concentration provided by the "better" scavenger acts to *generate* more attacking radicals and also to more readily stabilize the adducts through radical disproportionation. In addition, the very good H-atom accepting capability of anthracene itself also increases the fraction of the initial adducts that are successfully stabilized as retrograde products.

ACKNOWLEDGEMENT

The authors wish to acknowledge the Support of the U.S. Department of Energy in various projects whose goals have included an improved understanding of the chemistry responsible for coal liquefaction.

REFERENCES

1. McMillen, D. F.; Malhotra, R.; Nigenda, S. E. *Fuel*, **1989**, *68*, 380.
2. Neavel, R. C. *Fuel*, **1976**, *55*, 237.
3. Fong, W. S.; Peters, W. A.; Howard, J. B. *Fuel*, **1986**, *65*, 251.
4. Savage, P. E.; Klein, M. T.; Kukes, S. G. *Fuel*, **1988**, *2*, 619.
5. Khorasheh, F.; Rangwala, H. A.; Gray, M. R.; Dalla Lana, I. G. *Energy & Fuels*, **1989**, *3*, 716.
6. Rose, G. R.; Zabransky, R. F.; Stock, L. M.; Huang, C.; Srinivas, V. R.; Tse, K. *Fuel* **1984**, *63*(10), 133.
7. Mahasay, S. R.; Nardin, R.; Stock, L. M.; Zabransky, R. F. *Energy & Fuels* **1987**, 65.
8. Ettinger, M. D.; Mahasay, S. R.; Stock, L. M.; Zabransky, R. F., *Energy & Fuels* **1987**, 274.
9. Ofosu-Asante, K.; Stock, L. M.; Zabransky, R. F. *Fuel* **1989**, *68*, 567.
10. Ofosu-Asante, K.; Stock, L. M.; Zabransky, R. F. *Energy & Fuels* **1988**, *2*, 511.
11. Chatterjee, K.; Stock, L.M.; Zabransky, R. F. *Fuel* **1989**, *68*, 1349.

12. Zabransky, R. F.; Stock, L. M., "Thermally Initiated Carbon-Carbon Bond Cleavage Reactions Occurring During Coal Gasification, Final Report, Gas Research Institute, GRI-88/0272, December 1988.
13. Benson, S. W. *Thermochemical Kinetics*, 2nd ed; John Wiley and Sons: New York, 1976.
14. McMillen, D. F.; Golden, D. M., "Hydrocarbon Bond Dissociation Energies," *Ann. Rev. Phys. Chem.* **198** 493.
15. Squire, K. R.; Solomon, P. R.; Carangelo, R. M.; DiTaranto, M. B. *Fuel* **1986**, *65*, 833.
16. Squire, D. R.; Solomon, P. R.; DiTaranto, M. B., "Synthesis and Study of Polymer Models Representative of Structure - Phase II", Final Report, Gas Research Institute, August, 1985.
17. Fahr, A.; Mallard, W. G.; Stein, S. E. *21st Symposium International On Combustion: The Combustion Institute* **1988**, 825.
18. Fahr, A.; Stein, S. E. *J. Phys. Chem.* **1988**, *92*, 4951.
19. Mechanisms of Condensation of Biaryl Hydrocarbons, Senthilnathan, V. P.; Stein, S. E. *J. Org. Chem.* **198** 3000.
20. Stein, S. E.; Griffith, L. L.; Billmers, R.; Chen, R. H. *J. Org. Chem.* **1987**, *52*, 1582.
21. Chen, R. H.; Kafafi, S. A.; Stein, S. E., *Am. Chem. Soc.* **1989**, *111*, 1418.
22. McMillen, D. F.; Ogier, W. C.; Ross, D. S., *J. Org. Chem.* **1981**, *46*, 3322.
23. Malhotra, R.; McMillen, D. F. *Energy Fuels* **1990**, *4*, 184.
24. McMillen, D.F.; Malhotra, R., to be submitted to Energy and Fuels.
25. McMillen, D. F.; Malhotra, R.; Hum, G. P.; Chang, S. -J., *Energy Fuels* **1987**, *1*, 193.
26. Howard, J. B., "Fundamentals of Coal Pyrolysis and Hydroxyrolysis," in *Chemistry of Coal Utilization*, Sec Suppl. Vol., ed. M. A. Elliot, Wiley-Interscience, New York, 1981, Chapter 12.

TABLE 1
FATE OF STRUCTURES GRAFTED TO COAL VIA PHENOLIC OXYGEN:
PYROLYSIS IN A HEATED WIRE GRID^a

Grafted Structure	% of Graft Converted to		
	C ₁ -C ₃	PhH	PhCH ₃
-nC ₃ H ₇	1.7 C ₁ 9.1 C ₂ 28 C ₃	NA	NA
-nC ₁₈ H ₃₇	7.2	NA	NA
-CH ₂ CH ₂ Ph	4.5 C ₁ ≤ 10 C ₂	≤ 1	≤ 2
-CH ₂ Ph	-	1.2	8.0
-CH ₂ PhCH ₂ CH ₃	5.3 C ₂	NR	NR
			Unaccounted ^b
			61
			≥ 83
			91

^aHeating rate approximately 1000°C/s to a maximum temperature of about 800°C

^bUnaccounted for and presumably added to the coal. Where the analysis of major fragment pieces was not reported ("NR"), this column was left blank.

TABLE 2
ESTIMATED RATES OF HOMOLYSIS AND ANTICIPATED FRACTIONAL REACTION FOR GRAFTED LINKAGES

Coal Structure	Grafted Structure	BDE ^a	k _{homolysis} (s ⁻¹) ^b				Unconverted Fraction Remaining at T ^c				Unconverted Fraction Remaining at T ^d with 99% Recombination			
			650	700	750	800	700	750	800	800	700	750	800	
Coal-O-	-nC ₃ H ₇	61	8.4	4.9 × 10 ⁻¹	2.3 × 10 ²	0.65	0.09	9.9 × 10 ⁻⁶	1 × 10 ⁻⁵	.996	.97	.89		
Coal-O-	-CH ₂ Ph	52	1.5 × 10 ³	6.6 × 10 ³	2.5 × 10 ⁴	0	0	0	0	0.5	0.04	5 × 10 ⁻⁶		
Coal-O-	-CH ₂ - 	47	2.3 × 10 ⁴	8.7 × 10 ⁴	2.9 × 10 ⁵	0	0	0	0	1 × 10 ⁻⁵	1 × 10 ⁻¹⁹	0		

^aEstimated from values given in References 13 and 14. The assumption is made that coal structure bearing the oxygen atom is a single, unsubstituted phenyl ring. Inasmuch as this phenyl ring must have at least one other "substituent" to be a part of a polymeric coal matrix, this assumption provides an upper limit to the strength of the grafted linkage. Based on an E₀ = BDE + RT; A = 10^{13.5} s⁻¹.

^bUnreacted Fraction = e^{-(k_T t)^{0.05}}, where 0.05 is the time for the sample to heat from (T-50)°C to T_{final} at 1000°C/s, the heating rate used by Zabransky and Stock. Because k_{T-50} is a lower limit to the rate constant during the last 50°C, the calculated value over-estimates the unreacted fraction.

^dUnreacted fraction assuming 99% recombination is given by e^{-(k_{T-50} t)(0.05)(0.01)}, again an over-estimate of the unreacted fraction.

FROM ONE EXTREME TO THE OTHER: USING FUNDAMENTAL CHEMISTRY TO
UNDERSTAND COAL BEHAVIOR OVER WIDE RANGES OF CONDITIONS

Stephen E. Stein
Chemical Kinetics and Thermodynamics Division
NIST
Gaithersburg, MD 20899

Key Words: Kinetics, Polycyclic Aromatic Compounds, Model
Compounds

Efforts to understand coal chemistry at a fundamental level face a good deal of complexity and uncertainty, but can also lead to major simplifications. Certain fundamental ideas have very broad applicability and can unify seemingly divergent aspects of coal behavior. Three such cases will be discussed. 1) With increasing coal rank and coal processing severity, increasingly strong bonds are broken. An overview of the "scissile" (weak) bonds present in coal and the conditions under which they cleave will be discussed, covering conditions from geothermal processing to fast coal pyrolysis. 2) While the chemical details of condensation reactions of polyhydroxy-benzenes are not entirely clear, these reactions cannot be avoided and it is probable that they determine the chemical properties of higher rank coals and underlie char-forming reactions in coal processing. A discussion of some of the implications of these reactions for coal chemistry will be presented. 3) Theoretical results suggest remarkably little dependence of the thermochemistry and free radical kinetics of polycyclic aromatic hydrocarbons (PAHs) on molecular size. This can lead to a considerable simplification in the analysis of coal char chemistry.

1) Simple Bond Breaking

Chemical bond dissociation follows a first-order rate law with the rate constant:

$$k_{\text{break}}/\text{s}^{-1} = 10^{15.0\pm 1} \exp(-\text{Bond Dissociation Energy}/RT)$$

Given a characteristic time, t , for which the temperature T , has remained constant, bonds weaker than some bond strength $\text{BDE}(T, t)$ will be unstable towards dissociation. For coal, characteristic times range from geologic ages (10^8 years or 10^{15} sec) to fast coal pyrolysis (10^{-3} sec) and temperatures from ambient to over 600 C. The types of bonds in coal with these characteristics will be pinpointed and discussed. They span the rather narrow range of bond strengths from 50 - 65 kcal/mol and include most varieties of alkyl-aryl ethers and 1,2-diarylethane linkages. The most significant scissile bonds in the thermal processing of coal are those just strong enough to have resisted dissociation under geothermal conditions.

2) Polyhydroxy aromatics

Studies of the reactions of dihydroxy-aromatic compounds by McMillen [1] and ourselves [2] demonstrate that at under conditions characteristic of coal liquefaction, these substances are almost entirely transformed into polymeric materials. Since the ortho hydroxy/alkoxy structure is the characteristic reactive unit in lignin and, presumably, in low rank coals and since these will ultimately form dihydroxybenzenes through dissociation pathways under coalification and coal processing conditions, these reactions are probably may be of central importance in the formation of high rank coals and char. A discussion of features of these reactions that are known and unknown will be presented.

3) Polycyclic Aromatic Hydrocarbons

These are characteristic products in the pyrolysis of virtually all hydrocarbons and are predominant in char and probably in anthracite coal. Theoretical studies [3] indicate that the edges of very large PAH clusters have chemical properties very similar to those of conventional and well-studied PAHs. Even at the edges of a layer of graphite properties of chemical structures depend very little on the long-range network of pi-electrons- instead individual sites behave in a manner similar to similar sites on convention PAHs. These "active sites" are the centers of reactions in both combustion and gasification.

References:

- 1) D.F. McMillen, S.J. Chang, S.E. Nigenda and R. Malhotra, Prepr. Div. Fuel Chem., Am. Chem. Soc. 4, 414 (1985).
- 2) S.E. Stein, Accounts of Chemical Research, 24(11), 250 (1991).
- 3) F.M. Wang, V.P. Senthilnathan and S.E. Stein, Proceedings of 1989 International Conference on Coal Science, Tokyo, Japan, 1989, 165-168.

ASH DEPOSITION BEHAVIOR OF A COAL, A CLEAN COAL, AND A CHAR IN A DROP TUBE FURNACE

M. Rostam-Abadi, J.A. DeBarr, and R.D. Harvey

Illinois State Geological Survey
615 E. Peabody Drive
Champaign, IL 61820

Keywords: ash deposition, mild gasification char, drop tube furnace

INTRODUCTION

This work was undertaken as part of a larger study to evaluate the combustion characteristics of chars derived from Illinois coals under mild gasification (MG) conditions. The principle product (60 to 70 percent by weight) of MG processes is a char that must be effectively utilized to improve the overall economics of the process. During the past several years, one of the major research activities at the Illinois State Geological Survey has been to examine the suitability of using MG char as a fuel, alone or as coal-char blend, in typical industrial pulverized-coal (PC) boilers. The physical and chemical characteristics and reactivity of laboratory- and pilot plant-prepared MG chars have been reported (1-4).

In this paper preliminary results of a study to evaluate the ash deposition behavior of an MG char under conditions representative of PC boilers are presented. The results are compared to those obtained with the raw coal and a physically cleaned coal. Ash deposition tests were performed in a laminar flow (drop tube) furnace.

EXPERIMENTAL

Sample Preparation - The clean coal and the char were made from an original sample of the Herrin coal seam (IL No. 6) that was provided by the Illinois Basin Coal Sample Program, identified as IBC-101 (5). The parent sample represented the product from the mines preparation plant. The analysis of the coal is given in table 1.

The clean coal was prepared from a 200x400 mesh size fraction of the original coal in a Denver model D-2 batch flotation system. Approximately 150 grams of coal was combined with four liters of water in the flotation cell. A flotation agent (2-ethyl hexanol) was added at an equivalence of 6 lbs/ton. Additional ash was removed by repeating the procedure using the clean coal as the starting material. The clean coal was vacuum filtered, dried in a vacuum oven at 80 °C, and stored under nitrogen to prevent oxidation. The analysis of the product sample is given in table 1. The amount of ash in the clean coal is 6.4% which corresponds to a 34% decrease compared to the parent (200x400 mesh) coal. However, the clean coal retains almost 87% of the sulfur present in the original coal. This is because 72% of the sulfur in the parent coal is in the form of organic sulfur which is not removed by flotation methods.

A 5.1 cm ID batch fluidized-bed reactor system was used for the production of the char. The sample used for char production was a 28x100 mesh size fraction of the coal. In each run, about 200 grams of the coal was fluidized by nitrogen flowing at 6 l/min and heated according to a multi-step heating procedure to minimize agglomeration of coal particles in the reactor. The final temperature and final soak time were adjusted to produce three chars with volatile matter contents of about 7, 12, and 15%. The 7% volatile char was selected for ash deposition studies because it had higher ash content (14.1%, see table 1) than the other chars. The final temperatures and soak times for the char were 600 °C and 60 mins. After the final soak, the samples were cooled under

nitrogen purge and stored under nitrogen.

Ash Characteristics - The ash compositions (major and minor oxides) were determined by routine methods, and the ash fusability temperatures of the coal, clean coal, and char were determined by the ASTM D1857 method. These data were used to calculate silica ratio, base/acid ratio, T_c (temperature at critical viscosity), T_{250} (temperature at which the slag has a viscosity of 250 poise), the viscosity of slag at 2600 °F and the slugging index and fouling index.

Ash Deposition Studies - Ash deposition tests were conducted in a drop tube furnace (DTF) located at the University of North Dakota's Energy and Environmental Research Center (UNDEERC). The DTF is described elsewhere (6). A brief description of the ash deposition probe follows.

The water-cooled ash deposition probe, shown in figure 1, consists of a 2.2 cm OD stainless steel tube with a 3.8 cm OD diameter cap. A machined, boiler-steel substrate plate (3.8 cm diameter by 0.64 cm thick) prepared from 1040 carbon steel, supplied by the Babcock and Wilcox Company, is attached to the top of the probe. The substrate plate temperature can be maintained between 350 to 540 °C to simulate a boiler heat transfer surface, by adjusting cooling water and the tightness of the screws that hold the substrate to the probe. The temperature is monitored by a Type K thermocouple in contact with the plate. The substrate plates were polished with SiC polishing discs starting at 120 grit and proceeding to 600 grit. The substrates were oxidized at 400 °C for 20 hours in air to produce an oxide layer on the steel.

In each test, the drop tube furnace was stabilized at 1500 °C and the nominal gas flow rates of 1 l/min primary gas flow and 3 l/min secondary gas flow. The sample feeder was loaded with the desired sample, and the feed rate adjusted to give approximately 0.2 g/min. After the test run, the probe was allowed to cool and the substrate with the ash deposit removed and stored pending strength tests on the ash deposit. The strength of the deposits formed in the DTF were measured using a strength testing apparatus. The strength testing apparatus is described elsewhere (6).

RESULTS

Ash Characteristics - Analyses of the ash from these samples showed only small differences between the coals and char (table 2). The cleaning process removed soluble sulfate minerals, and about half the calcite. The clay minerals and quartz were retained in the clean coal. The temperature for which the ash achieves the desired viscosity of 250 poise (T_{250} , table 3) ranged from 2030 °F (clean coal) to 2115 °F (char). Experience indicates values below 2600 °F are desirable (7).

Slugging indices for the three samples fell in the medium range, according to Attig and Duzy (8), while the fouling index was high for the feed coal and char samples and medium for the clean coal (table 3).

Ash deposition studies - The results of the ash deposition tests are shown in table 4. The ash weight was normalized to a feed rate of 0.13 g/min. This gave a basis to compare the different tests. Clean coal produced about 50% more deposit than the parent coal (figure 2). However, the parent coal and clean coal gave deposit weight curves with similar slopes. Ash deposit weights of the char were substantially higher than either coal or clean coal.

The deposit weight for the clean coal increased faster than that of the parent coal in spite of the fact that it contains about two-thirds the ash of coal (9.7% vs. 6.4%). Without a detailed mineral analysis of the deposits, it is difficult to determine the cause of this behavior. Because the cleaning process removed a portion of the original

mineral matter (particularly calcite, see table 2), altering the composition of the remaining ash, the new composition may have resulted in a "stickier" ash with a higher melting point than the original ash. The ash deposition behavior of the char is consistent with its high ash content (14.1%).

The deposit growth rate curves were used to calculate sticking coefficients. The sticking coefficient (SC) is defined as:

$$SC = \text{rate of ash deposition/rate of firing of ASTM ash}$$

where "ASTM ash" is the ash yield of the fuel as determined by the standard ASTM proximate analysis procedure, or in this study, by TGA analysis of the fuel. The sticking coefficient is a normalized measure of how much ash in the fuel is sticking to the substrate plate of the ash deposition probe, and has a value between zero and one. A value of zero indicates that none of the ash is sticking; a value of one indicates that all of the ash is sticking. The higher the value of the sticking coefficient, the more slagging and fouling are likely to occur.

The deposit rates were calculated from best-fit curves that were determined using the deposit weight and time (table 4). For the parent coal and clean coal, a quadratic equation was fitted to the deposit weight data. It was not possible to obtain a meaningful quadratic equation to fit the data for the char. The instantaneous deposit rates were divided by the ASTM ash firing rate to give the sticking coefficients. The data indicate that the clean coal deposits grew at a faster rate than the parent coal (figure 3). While it was not possible to determine a numerical sticking coefficient for char, the normalized deposit weight data presented in table 4 show that the sticking coefficient for char is high, indicating that the deposits from the char grew much faster than those of the coal samples.

The differences observed in the sticking coefficients for the parent coal and clean coal are likely related to the association of the inorganic constituents in the coal. The inorganic components in the clean coal occur within and/or with carbonaceous particles because the cleaning process removes much of the extraneous (or carbon free) mineral grains. During combustion, the inorganic components associated with coal particles are subjected to higher temperatures than extraneous mineral grains. As a result of the higher temperatures, more of the particles melt and are sticky when they reach the deposition probe, producing a higher sticking coefficient. It is also possible that the included minerals are collected on the surface of the extraneous mineral particles (those deposited on the probe) and carry off the probe by the extraneous mineral particles.

The deposit strength curves are shown in figure 4. Clean coal has a gradual slope to the deposit strength curve and is lower in strength than the coal. The parent coal has an initial slope similar to that of clean coal, but the strength increases rapidly near the top of the deposit. The deposit strength of char exceeded the maximum capacity of the test apparatus (100 psi) and was not included in figure 4.

The difference in the strength of the deposits produced from the parent and cleaned coals is probably due to the types of ash particles in deposits. The strength of the clean coal deposits was lower than the other samples because some of the reactive, liquid producing ash components were removed by cleaning. For example, during the cleaning process a significant amount of pyrite is removed. The iron in pyrite, when combined with aluminosilicates in a combustion environment, produces low melting-temperature phases that are responsible for greater deposit strengths. The greater amount of iron present in the parent coal probably caused the parent coal's stronger deposits. The deposits produced from the clean coal most likely did not contain sufficient fluxing agents such as iron to develop high strength.

Physically, the deposits left by the clean coal were not molten whereas the deposits left by the coal were molten near the top. The deposits left by the char were molten not only at the top but also down the center of the deposit. Melting of deposits increases their strength; this explains the high strength of the char deposits.

CONCLUSIONS

The ash deposition behavior of an Illinois Herrin (No. 6) coal, and of a clean coal product, and a char derived from the parent coal was evaluated. The deposits were collected on a water-cooled stainless steel probe located inside an entrained flow reactor operating at 1500 °C and 20% oxygen. Standard ASTM analyses showed only small differences between the composition of the coal and char ashes; however, the clean coal had substantially lower soluble sulfate minerals and calcite than the coal. Ash deposition studies in a DTF showed that although the clean coal produced a larger deposit that grew at a faster rate than that of the original coal, the clean coal deposits were weaker than those of the coal and showed evidence of partial melting. The deposits from the char grew much faster than that of either the coal or clean coal. Due to extensive melting, the deposits formed by the char were much stronger than those of either the parent coal or clean coal.

ACKNOWLEDGEMENTS

This work was sponsored by The Illinois Department of Energy and Natural Resources through its Coal Development Board and Center for Research on Sulfur in Coal. We thank Dr. S. A. Benson, Mr. D. L. Toman, and Dr. D. P. McCollor for coordinating DTF tests at EERC.

REFERENCES

1. Rostam-Abadi, M., J.A. DeBarr, and W.T. Chen, 1989. ACS, Div. Fuel Chem., prep., 35 (4), pg. 1264-71.
2. Rostam-Abadi, M., J.A. DeBarr, and W.T. Chen, 1990. Thermochemica Acta, 116, pg. 351-356.
3. Rostam-Abadi, M., J.A. DeBarr, and W.T. Chen, 1992. To be published in Thermochemica Acta.
4. DeBarr, J.A., M. Rostam-Abadi, and C.W. Kruse, 1992. ACS Div. Fuel Chem., prep, General Papers, San Francisco, CA, April 5-10.
5. Harvey, R.D. and C.W. Kruse, 1988. J. of Coal Quality, 7 (4), pg. 109-112.
6. Toman, D.L., D.P. McCollor, and S.A. Benson, 1991. Annual Technical Progress Report submitted to ISGS and U.S. DOE.(PETC), EERC, University of North Dakota.
7. Babcock & Wilcox, 1972. Steam - its generation and use. Babcock & Wilcox, New York, NY, pg. 4-15.
8. Attig, R.C. and A.F. Dazy, 1969. Proceedings, Am. Power Conference, 31, pg. 290-300.

Table 1. Proximate and ultimate analysis for samples (dry basis)

Particle Size Mesh	270x400 Parent Coal	200x400 Clean Coal	270x400 Char
Moisture	2.9	1.6	0.9
<u>Proximate, wt%^a</u>			
Volatile Matter	41.8	41.5	7.3
Fixed Carbon	48.5	52.2	78.9
H-T Ash	9.7	6.3	13.8
<u>Ultimate, wt%^b</u>			
Hydrogen	5.2	5.5	2.2
Carbon	69.5	73.3	78.2
Nitrogen	1.5	1.8	2.2
Oxygen ^c	9.5	9.8	1.1
Sulfur	4.6	4.0	2.9
BTU/lb	12674	13293	12791
lb SO ₂ /MMBTU	7.2	6.0	4.6

^a TGA analysis, ^b LECO CHN 600 analyzer, ^c determined by difference

Table 2. Ash composition

Oxide	Parent Coal*	Clean Coal	Char
<u>Ash Analyses (% of ash)</u>			
SiO ₂	48.60	49.30	48.20
Al ₂ O ₃	17.49	17.81	17.36
Fe ₂ O ₃	18.22	19.53	18.08
CaO	4.89	2.20	4.76
MgO	0.99	1.31	0.98
K ₂ O	2.22	2.37	2.22
Na ₂ O	1.47	1.11	1.50
TiO ₂	0.89	1.34	0.90
P ₂ O ₅	0.27	0.14	0.26
MnO ₂	0.05	0.04	0.06
SrO	0.04	0.05	0.04
BaO	0.04	0.05	0.04
SO ₃	4.19	1.94	4.29
Silica ratio	68.85	68.15	66.93
Base/acid	0.41	0.39	0.41

*Mineral matter in IBC-101: 2.6% quartz, 0.5% calcite, 2.1% pyrite and Marcasite, 3.3% kaolinite, 2.4% illite, and 2.1% expandable clay.

Table 3. Ash fusability temperatures

	Parent Coal	Clean Coal	Char
<u>Ash Fusion ('F, reducing)</u>			
Initial def.	2055	2030	2115
Softening	2140	2140	2185
Hemispheric	2225	2245	2260
Fluid	2310	2350	2330
<u>Empirical ash properties</u>			
T ₂₅₀ , 'F	2425	2480	2460
T _{cv} , 'F	2584	2558	2584
Slag viscosity (poise) @2600 'F	105	125	106
Slagging index	1.75	1.53	1.20
type	med.	med.	med.
Fouling index	0.60	0.43	0.62
type	high	medium	high

Table 4. Ash deposition weights

Sample	Time (min)	Coal fed (g)	Ash (g)	Normalized ash (g)
Char	10	0.78	0.0619	0.1032
	20	2.70	0.2669	0.2570
	30	3.68	0.2618	0.2775
Parent coal	10	1.48	0.0488	0.0429
	20	2.24	0.0650	0.0754
	30	3.52	0.1029	0.1140
Clean coal	10	0.90	0.0463	0.0669
	20	3.81	0.1438	0.0981
	30	2.83	0.1070	0.1475

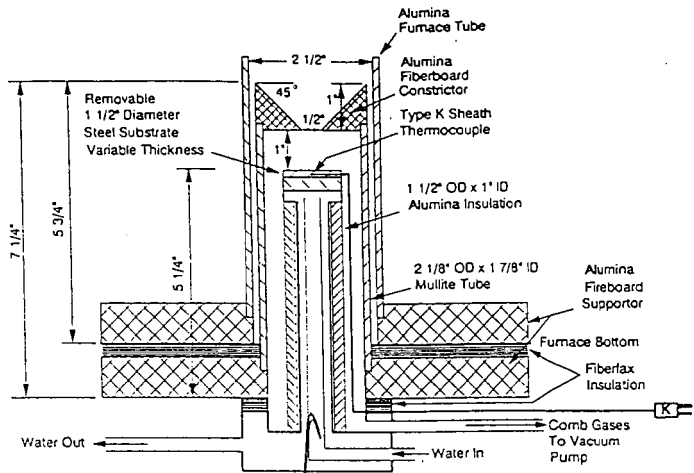


Figure 1. Ash deposition probe.

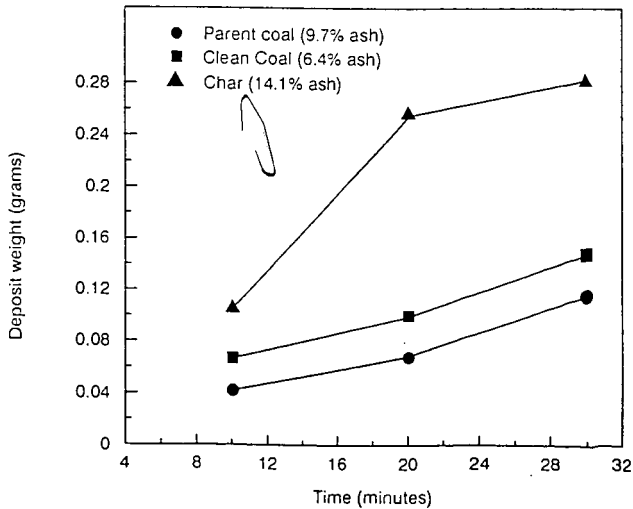


Figure 2. Deposit growth rates for fuels ($T = 1500^{\circ}\text{C}$)

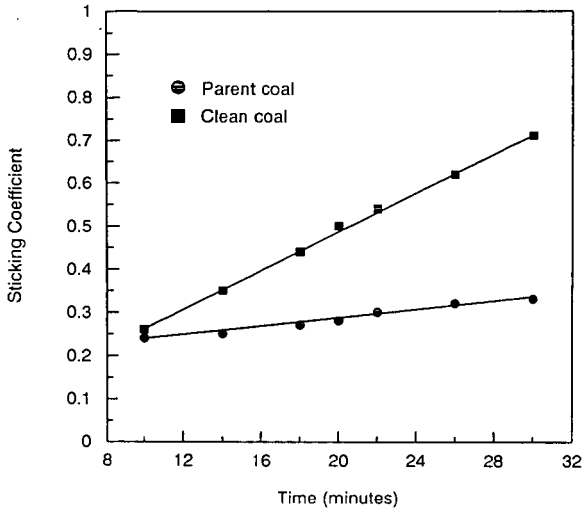


Figure 3. Sticking coefficients for coal samples.

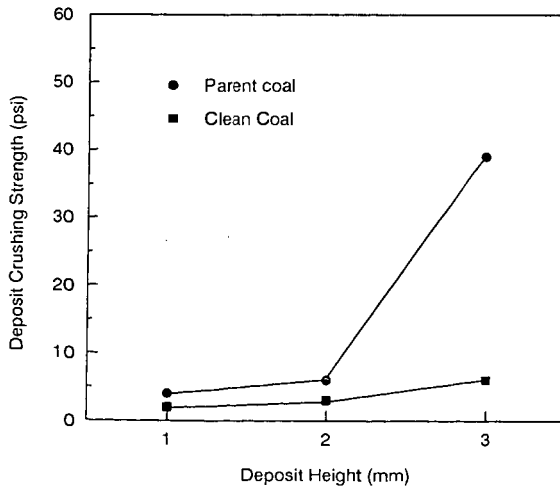


Figure 4. Deposit crushing strength for coal samples.

PROPERTIES OF MILD GASIFICATION CHARs: A COMPARISON OF PILOT PLANT- AND LABORATORY-PREPARED SAMPLES

J. A. DeBarr, M. Rostam-Abadi, R. D. Harvey and C. W. Kruse,
Illinois State Geological Survey, Champaign, IL

Keywords: mild gasification, pyrolysis, coal-char blend

INTRODUCTION

Mild gasification (MG) of high volatile bituminous coal to produce high quality liquid, solid and gaseous products has been a major coal research activity at the Illinois State Geological Survey (ISGS) since 1986. Three major foci of the program have been to 1) evaluate conditions for producing the highest quality liquids; 2) characterize the char; and 3) develop a market for char. The feasibility of using MG chars, alone or as a coal-char blend, in typical industrial pulverized-coal boilers has been examined as one avenue for char use. In the ISGS studies, MG chars of various volatile matter (VM) content have been prepared both in laboratory and pilot plant facilities. In this paper, the effect of char preparation conditions on the physical and chemical properties of MG chars is discussed.

EXPERIMENTAL

Pilot plant-prepared samples - Chars were prepared from sample number 3 of the Illinois Basin Coal Sample Program (IBC-103) (1). This sample is a mine-washed coal (rank HvBb) and consists of a blend of 80% Herrin (No. 6) and 20% Springfield (No. 5) coals. The chars were produced in the Mild Gasification Unit at The United Company (formerly United Coal Company Research Corporation) in Bristol, Virginia (2). The chars were prepared by heating the coal (<2000 μm) under a slight vacuum in an 8-inch i.d., 8-foot fixed-bed reactor. The reactor was located inside a natural gas-fired furnace maintained at 760°C during the production runs. Three partially devolatilized (PD) samples (herein referred to as PD chars) designated as PD-1, PD-2 and PD-3 were prepared using residence times of 1.70, 2.90 and 3.17 hours. For each sample, 38-53, 53-75, 75-105, 105-150 and 150-212 μm particle size fractions were prepared. Further details of sample preparation are given elsewhere (3). All samples were stored under nitrogen prior to use.

Laboratory-prepared samples - Chars were derived from sample number 1 of the Illinois Basin Coal Sample Program (IBC-101). This sample was obtained from the Herrin (Illinois No. 6, HvCb) seam and was a mine-washed coal. Three PD coals (herein referred to as PD-89 chars) were prepared from 150-600 μm IBC-101 coal in a 2-inch i.d. batch fluidized-bed reactor system. A multi-step heating procedure was used to minimize agglomeration of coal particles in the reactor. The final temperature and final soak time were adjusted to produce the desired level of VM in the char. Final temperatures and soak times for laboratory chars were 475°C, 10 mins for the high-volatile char (PD-1-89); 505°C, 30 mins for the medium-volatile char (PD-2-89); and 600°C, 60 mins for the low volatile char (PD-3-89). All samples were ground and sieved in a step wise manner to prepare 38-53, 53-75 and 105-150 μm size fractions. Other details of sample preparation are given elsewhere (4).

Devolatilization behaviors of the coal and chars were determined using a thermogravimetric analyzer (TGA). Each sample was heated in flowing nitrogen (200 cc/min) to 900°C at a constant heating rate of 20°C/min. The weight of sample remaining, the rate of weight loss and the gas temperature in the vicinity of the sample were monitored by a computer as a function of time. The proximate and ultimate analyses and total sulfur contents of the samples were measured using LECO MAC 400, CHN 600, and SC32 analyzers. Internal surface areas of the samples were obtained from nitrogen and carbon dioxide absorption at -196° and -77°C, respectively. Ash

composition and ash fusion temperatures of the samples were determined according to method ASTM D1857.

Reactivities of chars were measured in air using the TGA system. A sample mass of 2-4 mg was heated at 50°C/min under nitrogen flow (200 cc/min) to between 400 and 480°C for these experiments. A modified TGA quartz furnace tube was used to allow the reactant gas (200 cc/min) to enter the quartz reactor tube directly (3). The objective was to achieve, as quickly as possible, a uniform concentration when the reactant gas was introduced into the furnace tube to obtain reliable rate data in the initial stage of reaction. The percent weight of the char remaining, the rate of weight loss and gas temperature in the vicinity of the sample were monitored.

RESULTS AND DISCUSSION

The results of the proximate and ultimate analyses for 105-150 μm IBC-101, IBC-103, PD chars and PD-89 chars are given in table 1. The VM contents (dry basis) of pilot plant chars were 22.1% (PD-1), 14.1% (PD-2) and 10.3% (PD-3). The laboratory chars had VM contents (dry basis) of 18.5% (PD-1-89), 15.4% (PD-2-89) and 9.8% (PD-3-89). Coal IBC-101 has a higher VM and sulfur content, and lower carbon content, than IBC-103. The laboratory chars had projected SO_2 emissions 27% less than IBC-101 while pilot plant chars had projected SO_2 emissions 14% less than IBC-103 coal. The differences in projected emissions could be that only half the sulfur present in IBC-103 is organic sulfur, while nearly 75% of the sulfur in IBC-101 is present in the organic form. It has been shown that at pyrolysis temperatures below 600°C, organic sulfur is more easily removed than pyritic sulfur (5).

The TGA devolatilization profiles of 105-150 μm IBC-103 and pilot plant chars are shown in figure 1. The devolatilization process for coal can be divided into three stages: stage I, below 380°C, the loss of "free" moisture and the release of trapped gases and low molecular weight materials; stage II, 380°C to 550°C, the release of major amounts of tar and gas; and stage III, the thermal decomposition and/or reactions of pyrite impurities in the coal and secondary pyrolysis of the char (6).

Devolatilization profiles obtained for pilot plant chars (figure 1) exhibit weight loss in the three stages described for the coal. The weight loss (about 2.2%) in stage I could have been due to oil and tars that were trapped within the particles during preparation of these chars. TGA analysis to determine boiling point curves for coal oil and tars have indicated that these materials devolatilize below 400°C (7). Weight losses for stage II were about 14% for PD-1, 7.5% for PD-2, and 5% for PD-3. This stage of reaction should be absent for chars that have already been processed at temperatures above 550°C. The weight loss for IBC-103 coal was about 25% between 380 and 550°C. The fact that pilot plant chars lose weight in stage II indicates varying amounts of "coal-like" material remaining in these chars. Devolatilization data for a 15% VM coal-char blend prepared by mixing a char made in a microbalance reactor at 800°C with IBC-103 are shown in figure 1. It is seen that between 350-550°C, the shape of the weight loss curve for the coal-char blend is similar to that of PD-2; confirming the notion that the pilot plant chars contain coal-like material.

Because the pilot plant reactor was heated externally, it is expected that, due to heat transfer limitations, coal particles in the center of the 8-inch reactor were subjected to temperatures lower than those near the wall of the reactor. Unsteady-state one-dimensional heat transfer calculations revealed that the temperature near the center of the reactor was less than 400°C, temperatures at which the rate of pyrolysis is appreciable, even after 3 hours. This implies that there was a radial temperature profile at least within a portion of the reactor. As a result, coal particles were subjected to various thermal histories producing mixtures of highly devolatilized coal and "raw" coal.

The weight percent of coal-like material in each char was calculated using the relationship given below.

$$p = \frac{W_{PD}/(W_{PD} + FC_{PD})}{W_c/(W_c + FC_c)} \times 100\%$$

where: W_c = percent weight loss in stage II for coal; W_{PD} = percent weight loss in stage II for chars; FC_c = percent fixed carbon (dry-ash-free basis) in coal; and FC_{PD} = percent fixed carbon (dry-ash-free basis) in chars. The values of FC_c and FC_{PD} were obtained from table 1. A value of 25.6% was used for W_c (see figure 1). These calculations show that for 105-150 μm chars, the amount of coal-like material present in PD-1, PD-2 and PD-3 was 49%, 24% and 14%, respectively.

The devolatilization profiles of 105-150 μm IBC-101 coal and laboratory chars are shown in figure 2. Coal IBC-101 exhibits a volatile release profile similar to that of IBC-103. The weight loss below 150°C amounted to 6.5% for IBC-101, and less than 1.0% for the laboratory chars. The weight loss between 150 and 380°C was about 2% for the coal, and less than 1% for the laboratory chars. For these chars a noticeable weight loss begins about 460°C for PD-1-89, 520°C for PD-2-89 and 615°C for PD-3-89. These temperatures are consistent with the maximum heat treatment temperatures used during laboratory char preparation. This indicates that laboratory chars were homogeneous and not mixtures of highly devolatilized coal and raw coal.

Internal surface areas for 53-75 μm samples are presented in table 2. The two coals have comparable CO_2 surface areas, but IBC-101 had a substantially higher N_2 surface area than IBC-103. The CO_2 surface areas for the coals ranged from 216 to 239 m^2/g and were typical of HvC bituminous coals. Chars had lower N_2 -BET surface areas than their parent coal, indicating perhaps that the incomplete removal of volatile matter resulted in partial plugging of a large fraction of the pores in the coal that were previously accessible to N_2 at -196°C. The extent of devolatilization had little influence on development of CO_2 surface area. The pilot plant chars had lower CO_2 surface areas than IBC-103, whereas the laboratory chars had higher CO_2 surface areas than IBC-101. The laboratory chars (PD-3-89) had about twice the surface area of the pilot plant chars (PD-3). It has been found previously that chars prepared from IBC-101 and IBC-103 under identical conditions in laboratory-scale reactors had identical surface areas (5). This suggests that different char preparation conditions, not different parent coals, are responsible for differences in surface areas of the chars. During laboratory char preparation, special precautions were taken to minimize agglomeration of IBC-101, while no such precautions were used for pilot plant char production using IBC-103. This could explain the differences in the surface areas of the chars, but without further study, no definite conclusions can be inferred.

Apparent rates [$R = (1/m)dm/dt$; m = mass (ash-free) of sample] from TGA reactivity tests, calculated at 50% burn-off, indicate virtually no dependence on particle size in the temperature range used for oxidation studies (400-480°C) (2,3). This suggests that oxidation rates were sufficiently low such that pore diffusion had no rate-limiting effect and the reaction proceeded under kinetically controlled conditions.

Arrhenius plots (apparent rates vs $1/T$) for PD-3 and PD-3-89 chars are presented in figure 3. The activation energies calculated are approximately 33 kcal/mol for both chars. Laboratory chars are about an order of magnitude more reactive than pilot plant chars. A comparison of reactivities of these chars, with those reported previously for chars prepared from Illinois No. 6 coal (3,8,9), is also shown in figure 3. The reactivity of PD-3-89 (laboratory-prepared char) is comparable with those of chars prepared in similar laboratory-scale reactors (3,8). A 15% VM char prepared in the TGA from IBC-103 (the same coal used to prepare PD-3) exhibited similar reactivity to that of PD-3-89. PD-3 has reactivity comparable to the reactivity which has been reported

for a pilot-scale char (9). These results confirm that char preparation conditions and reactor size and type influence the reactivity of the resultant char.

Ash composition and ash fusion temperature data were used to calculate a number of empirical parameters (10). The results of these tests and other ash characterization data for IBC-101, IBC-103, PD-3 and PD-3-89 are compiled in table 3. The two coals exhibit differences in ash composition which can affect the empirical parameters derived. Coal IBC-101 has a higher concentration of CaO, Na₂O and SO₃, and a lower concentration of Al₂O₃ than IBC-103. The higher Na₂O content translates into a significantly higher fouling index for IBC-101 (high fouling type) than IBC-103 (low fouling type) (10). The slagging index (10) for IBC-101 is significantly higher than that of IBC-103 due to the higher sulfur content of IBC-101. Both coals, however, fall in the range consistent with medium-slagging coals.

A direct comparison of the ash properties of PD-3 and PD-3-89 is not appropriate since the ash properties of the parent coals are different. However, the ash composition and ash characteristic values for PD-3 and PD-3-89 are nearly identical to those of their parent coals. MG processes did not significantly alter the composition of the ash, and there is no evidence that chars have different slagging or fouling indices than those of their parent coals.

SUMMARY AND CONCLUSIONS

Chars with about 10, 15 and 20 percent VM were prepared from Illinois coals under mild gasification conditions both in pilot- and laboratory-scale reactors. The method of char preparation influenced the physical and chemical properties of the chars. Pilot-scale chars were mixtures of highly devolatilized coal and relatively unreacted coal, and had devolatilization characteristics similar to a blend prepared by mixing the parent coal and char. Pilot-scale chars were an order of magnitude less reactive than laboratory-scale chars. Measured CO₂ surface areas of laboratory-scale chars were about two times greater than those of pilot-scale chars. MG processes did not significantly alter the composition of the ash, and there was no evidence that chars have different slagging or fouling indices than their parent coals.

ACKNOWLEDGEMENTS

This work has been sponsored by the Illinois Department of Energy and Natural Resources through its Coal Development Board and Center for Research on Sulfur in Coal.

REFERENCES

1. Harvey, R. D. and C. W. Kruse, 1988. *J. Coal Qual.*, 7(4), pp. 109-112.
2. Rostam-Abadi, M., J. A. DeBarr, C. W. Kruse, D. L. Moran, R. D. Harvey and R. R. Frost, 1987. Final Technical Report, CRSC, Champaign, IL.
3. Rostam-Abadi, M., J. A. DeBarr and W. T. Chen, 1988. "Combustion Characteristics of Coal-derived Solid Fuels". Final Technical Report, CRSC, Champaign, IL.
4. Rostam-Abadi, M., J. A. DeBarr, R. D. Harvey, S. A. Benson, D. P. McCollor, 1989. "Reactivity and Combustion Properties of Coal-derived Solid Fuels". Final Technical Report, CRSC, Champaign, IL.
5. Hackley, K. C., R. R. Frost, C-L. Liu, S.J. Hawk and D. D. Coleman, 1990. *Illinois State Geol. Survey Circ.* #545.
6. Rostam-Abadi, M. and C. W. Kruse, 1983. *Proc. of the 12th Annual North Amer. Thermal Analysis Society Conf.*, paper #175.
7. Kruse, C. W., A. D. Williams and F. D. Guffey, 1989. Final Technical Report, CRSC, Champaign, IL.
8. Khan, M. R., 1987. *Fuel*, 66(12), pp. 1626-1634.
9. Dutta, S. and C. Y. Wen, 1977. *Ind. Eng. Chem. Process Des. Dev.*, 16(1), pp.31-37
10. Attig, R. C. and A. F. Duzy, 1969. *Proc. Amer. Power Conf.*, 31, pp. 290-300.

Table 1. Proximate and ultimate analyses for 105-150 μm fuels (dry basis).

	IBC-101	PD-1-89	PD-2-89	PD-3-89	IBC-103	PD-1	PD-2	PD-3
Moisture	6.6	1.3	1.3	0.6	2.0	2.1	1.9	1.8
<u>Proximate</u>								
Volatile Matter	42.0	18.5	15.4	9.8	36.7	22.1	14.1	10.3
Fixed Carbon	48.4	68.4	71.8	76.6	54.3	67.5	74.2	78.0
<u>Ultimate</u>								
Hydrogen	5.04	3.47	3.08	2.16	5.13	3.47	2.39	1.64
Carbon	69.68	72.55	75.66	77.99	75.06	77.85	79.71	80.58
Nitrogen	1.44	1.70	1.82	1.87	1.67	1.95	1.92	1.78
Oxygen	9.96	5.83	3.74	1.48	6.89	4.43	2.46	2.46
Sulfur	4.28	3.35	2.96	2.93	2.24	1.95	1.81	1.79
Ash	9.6	13.1	12.7	13.6	9.01	10.34	11.71	11.74
Btu/lb	12790	12504	12716	12706	13490	13245	13010	12828
lbs SO ₂ /MM Btu	6.7	5.4	4.7	4.6	3.3	2.9	2.8	2.8

Table 2. Surface areas for 53-75 μm fuels.

	IBC-101	PD-1-89	PD-2-89	PD-3-89	IBC-103	PD-1	PD-2	PD-3
BET(CO ₂)	239	249	305	354	216	194	175	165
BET(N ₂)	61.3	2.0	3.8	9.5	3.8	1.2	1.0	0.8

Table 3. Ash characterization of coals and chars.

Character	IBC-101	PD-3-89	IBC-103	PD-3
<u>Ash analyses (% of ash)</u>				
SiO ₂	48.60	48.20	49.63	47.77
Al ₂ O ₃	17.49	17.36	22.13	21.82
Fe ₂ O ₃	18.22	18.08	18.16	21.82
CaO	4.89	4.76	1.59	1.58
MgO	0.99	0.98	0.92	0.90
K ₂ O	2.22	2.22	2.44	2.35
Na ₂ O	1.47	1.50	0.33	0.30
TiO ₂	0.89	0.90	1.30	1.20
P ₂ O ₅	0.27	0.26	0.33	0.37
MnO	0.05	0.06	0.02	0.03
SrO	0.04	0.04	0.06	0.03
BaO	0.04	0.04	0.06	0.05
SO ₃	4.19	4.29	1.43	1.22
Silica ratio	68.85	66.93	70.6	69.0
Base/acid	0.41	0.41	0.32	0.34
<u>Ash fusion temp., °F, reducing</u>				
Initial deformation	2055	2115	2000	2050
Softening	2140	2185	2160	2220
Hemispheric	2225	2260	2310	2335
Fluid	2310	2330	2465	2460
<u>Empirical ash properties</u>				
T ₂₅₀ , °F	2425	2460	2490	2510
T _{cv} , °F	2584	2584	2305	2310
Slag viscosity (poise @2600°F)	105	106	175	140
Slagging				
index	1.75	1.20	0.71	0.61
type	medium	medium	medium	medium
Fouling				
index	0.60	0.62	0.11	0.11
type	high	high	low	low

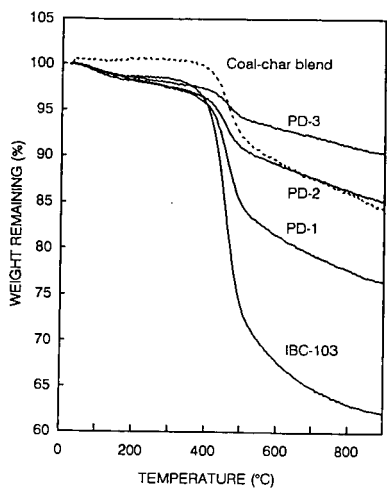


Figure 1. TGA devolatilization profiles for IBC-103, PD chars and a coal-char blend.

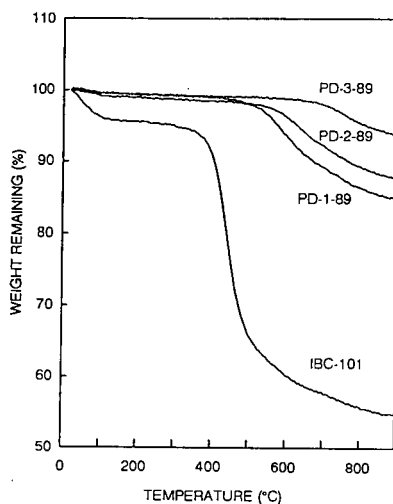


Figure 2. TGA devolatilization profiles for IBC-101 and PD-89 chars.

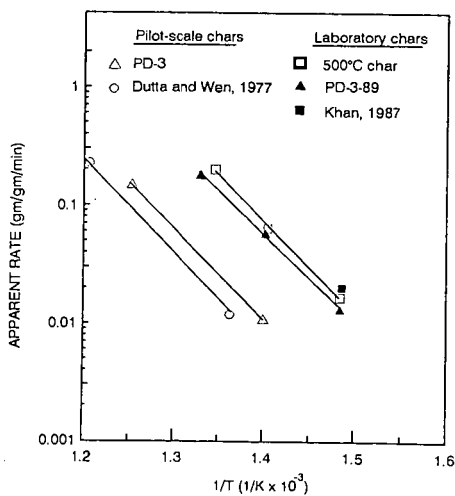


Figure 3. Arrhenius plot for fuels in 1 atm air

PREDICTING THE TRANSIENT DEVOLATILIZATION OF VARIOUS COALS WITH FLASHCHAIN

Stephen Niksa
High Temperature Gasdynamics Laboratory
Mechanical Engineering Department
Stanford University, Stanford, CA 94305

Alan R. Kerstein
Combustion Research Facility
Sandia National Laboratories
Livermore, CA 94550

Keywords: Modeling; Coal Rank Effects; Transient Devolatilization

INTRODUCTION

In coal-fired utility boilers, devolatilization generates the gaseous fuel compounds which ignite and stabilize the flame. Precursors to noxious gases are also released as the coal thermally decomposes. Pulverized coal injected into hot gases devolatilizes while it heats at $10^4 - 10^5$ K/s. The process takes only several milliseconds, and is completed before the fuel reaches its ultimate temperature. The rank of coal largely determines the total amount of volatiles as well as the proportions of heavy aromatic tar compounds and noncondensable gases. Coal rank is also an influence on the reaction rate, albeit a poorly characterized one. Until very recently no reliable transient data were available for boiler conditions, although laboratory studies at slower heating rates indicated that low rank coals devolatilize significantly faster than bituminous coals.¹

This study uses FLASHCHAIN²⁻⁴ to demonstrate that continuous variations of only a handful of structural features in the coal and one rate constant underlie the transient devolatilization of coals across the rank spectrum. It shows that the ultimate analysis is the only sample-specific data needed for accurate predictions of ultimate tar and total yields with this theory, consistent with a previous parametric sensitivity study.⁴ Lignites and low volatility coals are featured in this evaluation, to complement the emphasis on subbituminous and high volatile (hv) bituminous samples in the first evaluation.⁴ This study extends earlier work further by identifying the parametric basis for reliable transient predictions for rapid atmospheric devolatilization of any coal type.

GUIDELINES FOR THE DATA CORRELATIONS AND MODEL PARAMETERS

Taken together, the two laboratory studies⁵⁻⁶ selected for the model evaluation depict the behavior throughout the entire range of coal types, for wide ranges of temperature and heating rate at atmospheric pressure. Freihaut and Proscia used a wire-grid heater in which the sample was dispersed in a layer only a few particles deep, and assigned process temperatures after very extensively characterizing the vagaries of fine-wire thermocouples in such systems.⁷ Their ultimate weight loss values and tar yields are based on heatup at 725 K/s, followed by 10s at the stated reaction temperatures. Transient weight loss is available for a heating rate of 800 K/s. Even though forced quenching was not implemented, their samples cooled at rates from 1500 to 2000 K/s, which is fast enough to virtually eliminate decomposition during cooling. However, their transient tar yields are too scattered to be used for model evaluations.

Chen and Niksa⁷ used a novel radiant coal flow reactor to impart heating rates exceeding 10^4 K/s. Their calculated thermal histories, described elsewhere,⁸ indicate a nominal heating rate of 15,000 K/s for the long-residence-time-cases considered here. The corresponding model predictions are based on transient heatup at this rate to 1300 K. Predicted tar yields are compared to the sum of the measured yields of tars and oils, consistent with the product recovery scheme in their study.

Collectively 14 different coal samples are represented. As seen in Table I, they represent nominal ranks from lignite to anthracite, and 40% of them are low volatility samples. Note also that in three cases, virtually identical samples were used in both laboratory studies. The atomic H/C and O/C ratios are based on the reported ultimate analyses. The additional structural and characterization data in Table I are needed to define FLASHCHAIN's input parameters. All values are based on regressions of literature values reported elsewhere.^{2,4} So the only coal-specific input for these simulations is the ultimate analyses. Thus, this study will determine if samples having the same nominal rank but different O/C and H/C ratios can be distinguished with this theory, as suggested by a previous study of parametric sensitivity.⁴

All parameters in the constitution submodel are collected in Table II. Four are based on molecular weights: that of the aromatic nucleus, MW_A , is used to normalize those of labile bridges (MW_B/MW_A), char links (MW_C/MW_A), and peripheral groups (MW_P/MW_A). The tabulated values show that nuclei become more massive in coals of higher rank, and both the labile and refractory connections among them become smaller. The proportion of intact links in the whole coal, $p(0)$, follows the tendency in the pyridine extract yields (in Table I) to remain constant for ranks through hv bituminous. It then rises precipitously for coals of higher ranks, consistent with their smaller extract yields because structures which are more tightly interconnected have fewer smaller fragments to be extracted. The fraction of labile bridges among intact links, $F^b(0)$, decreases from its value of unity for lignites in proportion to the carbon content. The values in Table II for carbon contents below 85% are based on the regression reported previously.⁴ However, the sample population for that regression had few low volatility samples, whose total and tar yields were badly scattered. Based on the yields for the 4 samples in Chen and Niksa's study, the last 6 entries in Table II are given by $F^b(0) = 0.096 - 0.031(\%C, \text{daf})$. In the future, this regression will be used for all carbon contents over 86%.

The selectivity coefficient between scission and spontaneous char condensation, v_B , also varies with rank. Since crosslink formation has been clearly related to CO_2 evolution,⁹ the values of v_B are proportional to O/C ratios, but only for values below 0.2 or for carbon contents less than 83%. The latter restriction is consistent with the fact that precursors to CO_2 are either carboxylic acid or ketone functionalities, which are present only in coals having lower carbon contents. The former restriction is based on data correlations for the low carbon-content samples in this study. (Our previous evaluation included no coals with such low carbon contents.)

Regarding the reaction rate parameters, those for recombination and peripheral group elimination and the expression for the saturated vapor pressure of tar precursors, P^{SAT} , are identical to values reported previously, and fixed for all coal types. The mean activation energy for bridge decomposition is also at its former value. But the frequency factor, A_B , and std. dev. in the bridge energy rate, σ , have been generalized in correlations with the carbon content, based on the correlations of transient weight loss presented below. Whereas these parameter correlations assign the same values reported previously for hv bituminous coals,³ they prescribe significantly faster reaction rates at low temperatures for coals of lower rank. However, for ranks above hv bituminous, the bridge decomposition rates vary very little.

In the simulations reported below, the operating conditions of temperature, heating rate, and/or time were varied to match those in the experiments, while all coal properties and rate constants were specified according to Table II. A simulation of each thermal history requires from 2 to 5 minutes on a 386 personal microcomputer operating at 20 MHz, with an 8-Bit Fortran compiler.

RESULTS

Figures 1 and 2 present comparisons among the predicted and measured values of ultimate weight loss and tar yields, respectively. The measurements at 725K/s were taken for a 10 s reaction period at temperatures from 900 to 1100K. Simulations are based on the same heating rate and 5 s at 1000K, which is long enough to simulate complete devolatilization. The predictions are within experimental uncertainty for coals across the rank spectrum, except for the 1520 lignite and the 1516 low volatile bituminous. The latter discrepancy is especially difficult to rationalize because the prediction for 15,000 K/s with a virtually identical sample in Chen and Niksa's data is nearly exact.

Similarly, the significant enhancements in weight loss due to the 20-fold increase in heating rate in this data set are predicted within experimental uncertainty for all coal types.

Predicted tar yields in Fig. 2 are also quantitatively accurate, and there are no systematic deviations with coal rank. FLASHCHAIN also predicts that tar yields are substantially enhanced with faster heating, in accord with the observed behavior of all bituminous samples. Considering that 70% of the predictions in Figs. 1 and 2 (denoted by circles) are based on the parameters identified with an independent data base, these results also demonstrate that the ultimate analysis is the only coal-specific input required for accurate ultimate yields with FLASHCHAIN. The additional data on low volatility samples and the extended correlation for $F^*(0)$ appear to expand the range of rank which can be accurately simulated.

In addition to transient weight loss, this model accurately predicts the temperature dependence of ultimate yields, as seen in Figs. 3 and 4. Simulated transient weight loss is based on heatup at 800 K/s, whereas ultimate yields are based on heatup at 725 K/s, followed by 10 s isothermal reaction periods at the indicated temperatures. In Fig. 3 for the lignite (1443), these three quantities are correlated within experimental uncertainty at all temperatures. In Fig. 4, ultimate weight loss for an hvA bituminous sample (1499) is reliably correlated, but calculated tar yields are high by 4 wt%. Data from this coal also validates the calculated transient weight loss through 1000K. Unfortunately, the current data base can only be used to evaluate transient predictions for ranks through hv bituminous.

DISCUSSION

Predicting the ultimate weight loss and tar yields from any coal type is treated here as a matter of distinguishing aliphatic, heteroatomic, and aromatic constituents, rendering functional groups superfluous. In its submodel for coal constitution, FLASHCHAIN introduces the segregation of all oxygen and aliphatics into labile bridges and peripheral groups, and all aromatics and nitrogen into char links and aromatic nuclei. This crucial partitioning is implemented with balances based on the ultimate analysis, carbon aromaticity, and aromatic carbon number per monomeric unit. (Proton aromaticity is also included but found to be inconsequential.) The predictions reported here demonstrate that the ultimate analysis is the only coal-specific input needed with this theory. Regression values of all other inputs are the basis for accurate predictions, for reasons identified in our previous sensitivity study.⁴ Now that the population for these regressions has been expanded by the addition of a few lignites and several low volatility coals, predictions can be generated for virtually any coal sample. This extension paves the way for examinations of extensive literature data for coal rank effects, now underway.

Regarding transient behavior, FLASHCHAIN reveals a new basis for interpreting and understanding the factors underlying the transient devolatilization of any coal type. FLASHCHAIN now incorporates this tendency through newly-identified correlations of the frequency factor and variance in the energy distribution for bridge decomposition with carbon content. From a practical standpoint, this approach yields reliable predictions for ranks from lignites through hv bituminous, but extensions to low volatility samples must await additional transient data.

From a mechanistic standpoint, inferences based on the trends in these rate constants should be closely circumscribed. Neither FLASHCHAIN nor any other current model includes the types of reaction mechanisms which can associate specific functionalities and reaction channels with the observed tendencies. There is, nevertheless, one obvious implication. In so far as oxygen content diminishes with increasing coal rank, the variations suggest that oxygenated species accelerate reaction rates during the early stages, as expected for any free-radical chain mechanism among hydrocarbons. Indeed, CO_2 and H_2O are major products during the initial stages.⁵ Oxygenated species are also implicated in the broadening of the temperature range for devolatilization with decreasing rank, in that CO is always a major product of the latest stages of devolatilization.⁶

ACKNOWLEDGEMENT

Partial support for S. Niksa was provided by EPRI through their Exploratory Research Program. Partial support for A. R. Kerstein was provided by the Division of Engineering and Geosciences, Office of Basic Energy Sciences., U. S. Department of Energy.

REFERENCES

- Howard, J. B., in *Chemistry of Coal Utilization*, 2nd Suppl. Vol.; Elliot, M.A., Ed.; Wiley-Interscience: New York, 1981; Chapter 12.
- Niksa, S. and Kerstein, A. R., *Energy Fuels* 5(5): 647-664 (1991).
- Niksa, S., *Energy Fuels* 5(5): 665-672 (1991).
- Niksa, S., *Energy Fuels* 5(5): 673-683 (1991).
- Freihaut, J. D. and Proscia, W. M., Final Report to U. S. DOE/Pittsburgh Energy Technology Center for Contract No. DE-AC22-89PC89759, August 1991.
- Chen, J. and Niksa, S., "Coal Devolatilization During Rapid Transient Heating. Part 1: Primary Devolatilization," *Energy Fuels*, to appear, 1992.
- Freihaut, J. D., Proscia, W. M., and Seery, D. J., *Energy & Fuels* 3:692 (1989).
- Chen, J. and Niksa, S., "A Radiant Flow Reactor for High-Temperature Reactivity Studies of Pulverized Solids," *Rev. Sci. Instrum.*, to appear, 1992.
- Suuberg, E. M, Lee, D., and Larsen, J. W., *Fuel* 64:1668 (1985).

Table I. Coal Properties

Sample	%C, daf	H/C	(O+S)/C	f_a'	AC/CI	MW _{MON}	Y _{PYR}	MW _G
1443	66.5	.931	.306	.493	9.7	356	26	26.5
1520	69.0	.877	.271	.533	10.6	348	26	26.5
1488C	69.5	.863	.260	.541	10.8	345	26	26.5
1493C	74.1	.858	.136	.614	12.5	329	26	26.3
1493	75.5	.798	.179	.637	13.1	326	26	25.6
1499	79.9	.825	.122	.706	14.7	312	26	23.7
1451C	82.5	.815	.077	.748	15.7	305	26	22.5
1451	84.0	.803	.079	.772	16.2	300	26	21.8
1516	87.4	.614	.055	.826	17.5	291	26	20.3
CBMC	87.5	.759	.021	.827	17.5	290	26	20.2
1516C	88.7	.676	.018	.846	18.0	288	21.6	19.7
1521C	89.6	.643	.019	.861	18.3	285	14.8	19.3
1508C	89.9	.614	.035	.865	18.4	284	12.5	19.2
1468	94.3	.237	.024	.935	20.1	276	0	17.2

*The suffix "C" denotes samples of Chen and Niksa;⁶ all others are Freihaut and Proscia's.⁵

Table II. Structural Model Parameters

Sample	MW _A	C _A	MW _B /MW _A	MW _C /MW _A	MW _G /MW _A	p(0)	F ^B (0)	v _B	v _E
1443	125	9.7	1.859	.836	.511	.911	1.000	.150	2.40
1520	134	10.6	1.602	.721	.442	.911	1.000	.150	2.23
1488C	135	10.7	1.563	.704	.430	.911	0.983	.150	2.19
1493C	148	11.6	1.307	.588	.359	.911	0.858	.329	2.03
1493	152	11.9	1.258	.566	.347	.911	0.821	.202	2.05
1499	165	12.9	1.044	.470	.288	.911	0.702	.370	2.00
1451C	176	13.7	0.901	.406	.247	.911	0.632	.500	1.93
1451	180	14.1	0.838	.377	.230	.911	0.591	.500	1.90
1516	169	13.4	1.079	.485	.297	.911	0.329	.500	2.48
CBMC	182	14.2	0.886	.399	.243	.911	0.366	.500	2.19
1516C	183	14.4	0.866	.390	.239	.920	0.329	.500	2.21
1521	186	14.6	0.836	.376	.230	.937	0.301	.500	2.21
1508C	181	14.4	0.897	.404	.247	.943	0.291	.500	2.33
1468	178	14.5	1.005	.452	.097	1.000	0.154	.500	2.86

Evaluation of Predicted Ultimate Weight Loss

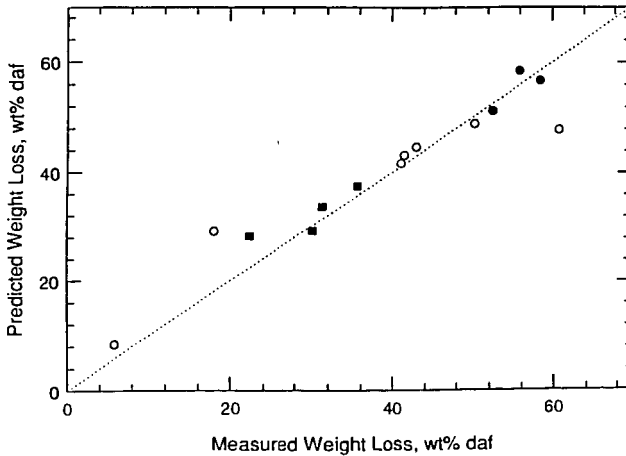


Figure 1. An evaluation of predicted weight loss for the coals in Table I versus measured values. Measured values were reported by Freihaut and Proscia² for atmospheric devolatilization for a heating rate of 725 K/s and 10 s at temperatures from 900 to 1100 K (open symbols); and by Chen and Niksa³ for a heating rate of 15,000 K/s to a temperature high enough to achieve complete primary devolatilization (filled symbols). Predicted values are based on the parameters in Tables II and III and heatup at 725 K/s with 5 s at 1100 K and at 15000 K/s to 1300K. All cases denoted by circles are based solely on parameter values assigned for an independent data base.

Evaluation of Predicted Ultimate Tar Yields

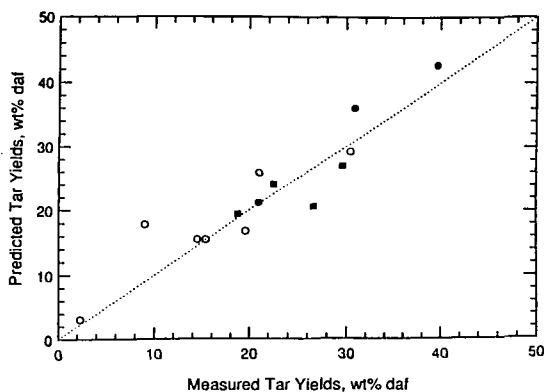


Figure 2. An evaluation of predicted ultimate tar yields for the coals in Table I versus measured values. Measured values were reported by Freihaut and Proscia⁵ for atmospheric devolatilization for a heating rate of 725 K/s and 10 s at temperatures from 900 to 1100 K (open symbols); and by Chen and Niksa⁶ for a heating rate of 15,000 K/s to a temperature high enough to achieve complete primary devolatilization (filled symbols). Predicted values are based on the parameters in Tables II and III and heatup at 725 K/s with 5 s at 1100 K and at 15000 K/s to 1300K. All cases denoted by circles are based solely on parameter values assigned for an independent data base.

Transient and Ultimate Yields for 1443

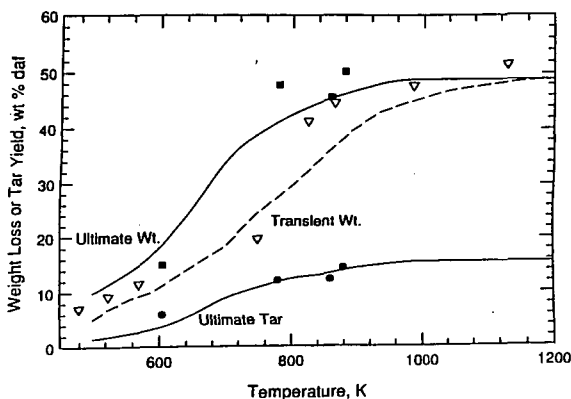


Figure 3. Comparisons between measured and predicted ultimate weight loss and tar yields and weight loss during transient heatup for a lignite (1443). Data were reported by Freihaut and Proscia⁵ for a heating rate of 725 K/s and 10 s at the indicated temperatures, for ultimate values, and rates from 650 to 1250 K/s and nominal cooling rates from 1500 to 2000 K/s for the transient data. The respective simulations are based on identical conditions for the ultimate yields, and a heating rate of 800 K/s to the indicated temperatures without allowing for decomposition during cooling, which is negligible at such fast cooling rates.

Transient and Ultimate Yields for 1499

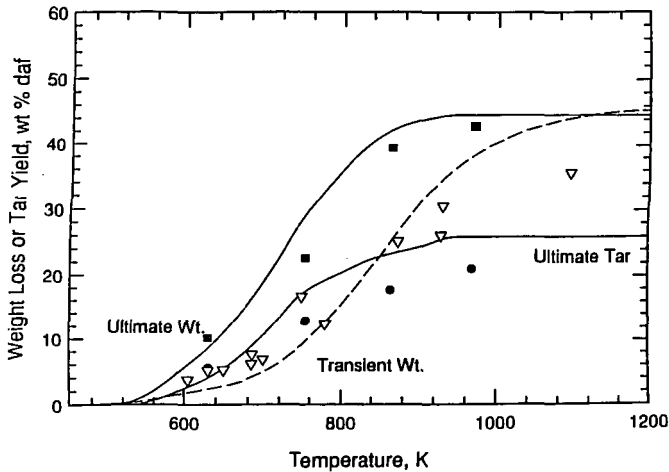


Figure 4. Comparisons between measured and predicted ultimate weight loss and tar yields and weight loss during transient heatup for an hvA bituminous coal (1443). Data were reported by Freihaut and Proscia⁵ for a heating rate of 725 K/s and 10 s at the indicated temperatures, for ultimate values, and rates from 650 to 1250 K/s and nominal cooling rates from 1500 to 2000 K/s for the transient data. The respective simulations are based on identical conditions for the ultimate yields, and a heating rate of 800 K/s to the indicated temperatures without allowing for decomposition during cooling, which is negligible at such fast cooling rates.

IMPROVED DIFFERENTIATION OF SULFUR FORMS IN COALS BY
SELECTIVE DEGRADATION WITH PERCHLORIC ACID MIXTURES

R. Markuszewski^a, X. Zhou, and C. D. Chriswell
Fossil Energy Program, Ames Laboratory, Iowa State University
Ames, Iowa 50011

and

^aInstitute of Gas Technology, Chicago, IL 60616

Keywords: sulfur forms in coal; coal analysis for sulfur;
perchloric acid dissolution of coal

INTRODUCTION

Recent work at the Ames Laboratory has resulted in proposing a promising new technique for determining sulfur forms in coal based upon the step-wise oxidation of coal with perchloric acid (1). Initial results on determination of sulfur forms by selective oxidation with perchloric acid have been very encouraging (2). Relatively sharp and reproducible delineations have been observed for sulfide, sulfate, pyritic, and organic sulfur in some cases. Other preliminary studies on model organosulfur compounds have shown it to be possible to differentiate between at least two groups of organic sulfur compounds by this technique (3). In more recent work, the reproducibility of these results has been confirmed, more detailed conditions for extracting selectively the various sulfur species have been specified, and more coal samples with higher organic sulfur content have been tested.

EXPERIMENTAL PROCEDURES

Based upon earlier observations of the behavior of coal, pyrite, and sulfate salts with boiling HClO_4 at various temperatures (1), a reaction scheme was developed for the direct determination of sulfur forms in coal which uses the variable oxidizing power of HClO_4 to dissolve selectively sulfur-containing components and convert them to sulfate for turbidimetric measurement. In the original procedure for the consecutive determination of sulfur forms in a single sample of coal (2), sulfate was extracted with a HClO_4 solution boiling at 120°C, pyrite with a HClO_4 solution boiling at 155°C, and organic sulfur with a solution of 9:1 HClO_4 - H_3PO_4 boiling at 205°C. In all 3 steps, sulfur-containing gases were trapped in 15% H_2O_2 , and sulfate was determined in the trap and in the aqueous filtrate. If any sulfide was present, it was captured and measured in the H_2O_2 -filled gas trap during the extraction of sulfate. For some coals, however, total sulfur recovered was slightly less than total sulfur in the coal (0.2-0.4% abs.). The low recovery could be due to: 1) incomplete absorption of sulfur-containing gases by the neutral H_2O_2 solution in the trap, 2) dissolution of some organosulfur compounds at 155°C without total conversion to sulfate, and 3) analytical factors, such as incomplete precipitation of BaSO_4 due to high acidity. For other coal samples, the discrepancy between pyritic and organic sulfur forms determined by the ASTM and the HClO_4 procedures was significant. Some of these possibilities have been tested experimentally in previous work (4-6).

RESULTS AND DISCUSSION

Determination of Sulfur Forms in Coal

Using the original procedure, the following results were obtained for sulfur forms in Illinois, Pittsburgh, and New Zealand coals (minus 60 mesh) and in another Illinois No. 6 coal (minus 200 mesh), as shown in Table 1. While for the minus 60-mesh coal samples the agreement between the HClO_4 and ASTM procedures for pyritic and organic sulfur forms is reasonable, it is quite divergent for the minus 200-mesh sample. Therefore, further tests were conducted to test the conditions for selective extraction of sulfur forms.

Table 1. Sulfur Form (in %) Determined by HClO_4 and ASTM Procedures

	Sulfate	Sulfide	Pyritic	Organic	Total
<u>Illinois No. 6 (-60 mesh)</u>					
HClO_4 (avg. of 4 detns.)	0.74	0.02	1.79	1.64	4.19
ASTM (1 detn.)	0.75	n.d.	1.69	1.77	4.21
<u>Pittsburgh No. 8 (-60 mesh)</u>					
HClO_4 (avg. of 2 detns.)	0.48	0.01	1.13	1.32	2.94
ASTM (1 detn.)	0.49	n.d.	1.18	1.47	3.14
<u>Charming Creek N.Z. (-60 mesh)</u>					
HClO_4 (1 detn.)	0.04	0.01	0.11	5.02	5.18
ASTM (1 detn.)	0.04	n.d.	0.02	5.38	5.44
<u>Illinois No. 6 (-200 mesh)</u>					
HClO_4 (avg. of 2 detns.)	0.24	0.04	3.27	1.38	4.93
ASTM (1 detn.)	0.20	n.d.	2.87	1.85	4.92

Dissolution of Sulfur from Coal as a Function of Temperature

The original procedure, based on extracting -60 mesh coal using the boiling point of the pure HClO_4 solution as the temperature guide, resulted in typical S-shaped dissolution curves, as shown previously (1) for an Illinois No. 6 coal sample containing 4.85% total sulfur (0.26% sulfate, 2.42% pyritic, and 2.17% organic sulfur). Although there was a lot of scatter for that -60 mesh coal, it was on the basis of such curves, as well as the behavior of pure pyrite and mineral sulfate, that the HClO_4 b.p. of 120, 155, and 203°C were selected for the extraction of sulfate, pyritic, and organic sulfur, respectively.

When the extraction procedure was repeated for another Illinois No. 6 coal, -200 mesh and containing 4.98% total sulfur (0.04% sulfate, 3.04% pyritic, and 1.90% organic sulfur), the much smoother curve depicted in Figure 1 was obtained. In this and all subsequent figures, the temperature of the reaction mixture (HClO_4 plus coal) is plotted. The curve shows a definite break at ~140-145°C, showing a clear delineation between pyritic and organic sulfur.

Analysis of Coal Residues After HClO_4 Extraction

In order to get additional information about the possible dissolution of organic sulfur and the oxidation of organic matter in the coal, the undissolved materials from HClO_4 extractions at several temperatures, as well as a sample of the raw coal, have been further analyzed for organically associated S, Cl, and O using our SEM-EDX procedure described earlier (7).

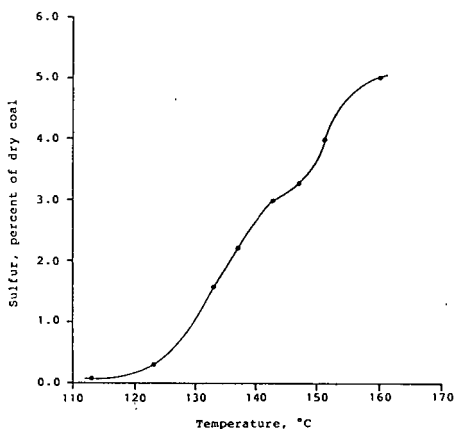


Figure 1. Total sulfur recovered (as percent of dry coal) as a function of reaction temperature for Illinois No. 6 coal (~200 mesh)

Because this technique measures organically bound elements on a dry, mineral matter-free (dmmf) basis, the results could not be directly compared to those obtained by the ASTM or HClO_4 procedures (the coal contained 28.8% ash). However, there were several interesting trends. First of all, it was evident that the organic sulfur content was fairly constant, within the experimental errors of this technique, until a temperature of about 147°C. At the same time, there was a significant increase in organic oxygen and chlorine as the temperature increased. This was not unexpected since the coal was being oxidized, and chlorination is known to occur during the perchloric acid degradation of organic compounds (3). When corrected for O and Cl content, the organic S content appeared to be fairly constant almost up to 151°C.

Dissolution of Iron During Extraction of Sulfur from Coal

The solutions from Illinois coal samples extracted for sulfur at different temperatures (Figure 1) were also analyzed for iron by atomic absorption spectrophotometry. The results are presented in Figure 2, and the amount of undissolved material is presented in Figure 3. It is evident that the amount of dissolved iron increases up to ~143°C and then becomes constant, indicating that all the pyrite has been dissolved before the coal matrix starts to be dissolved. Also, at 113°C, where only sulfate is extracted, pyrite is not dissolved.

Dissolution of Coal During Extraction of Sulfur

Figure 3 represents the weight loss for the same Illinois coal sample depicted in Figure 1. It is evident that the amount of undissolved material does not decrease until temperatures of ~143°C are reached, indicating that the organic matrix and the associated organic sulfur have not been leached out at a temperature at which pyrite has been dissolved. This is also corroborated by the color of the extracts, which are colorless or pale yellow until ~143°C

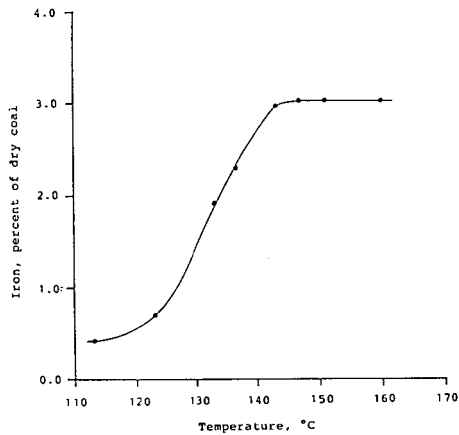


Figure 2. Dissolved iron (as percent of dry coal) as a function of reaction temperature for Illinois No. 6 coal (-200 mesh)

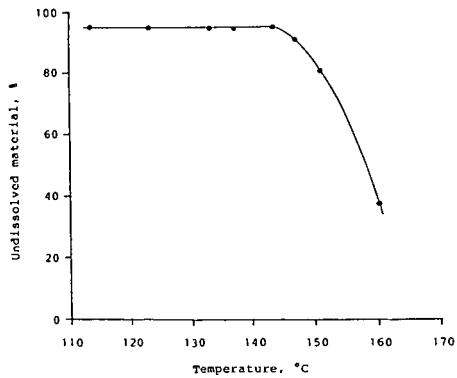


Figure 3. Undissolved material as a function of reaction temperature for Illinois No. 6 coal (-200 mesh)

and then become orange to deep-brown at higher temperatures at which coal begins to dissolve. Further details of these observations are described elsewhere (8).

New Procedure for Determination of Sulfur Forms

Based upon the results above, it was concluded that better delineation of sulfur forms could be obtained by employing lower temperatures for the dissolution steps, i.e., 110°C for sulfate and 143°C for pyrite sulfur. Applying this modified procedure to another sample of Illinois No. 6 coal gave the results presented in Table 2. It is evident that the agreement between these results and those from ASTM procedures is very good.

Table 2. Sulfur forms (percent of dry coal) in Illinois No. 6 (bottle 7) by HClO₄ procedure using new step-wise oxidation conditions.

S form	Mixture Temp. (°C)	% S (dry basis)				% S by ASTM (dry basis)
		Expt.1	Expt.2 ^a	Expt.3 ^a	Average	
Sulfate	110	0.07	0.07	0.07	0.07	0.04
Pyritic	143	2.99	2.91	2.98	2.96	3.04
Organic	180-200	1.71	1.79	1.76	1.75	1.88
Totals		4.77	4.77	4.81	4.78	4.96

^aHClO₄-H₃PO₄(9:1) mixture.

Dissolution of Coal in HClO₄ With Admixtures

In order to obtain even more selectivity, several admixtures were tested with HClO₄ to alter its oxidizing power. One was the addition of H₃PO₄ to promote the dissolution of pyrite and thus extract all pyritic sulfur at a lower temperature without affecting the organic sulfur. In practice, the results were not useful. While the temperature of dissolution was lowered by a few degrees, no further enhancement of differentiation was observed.

The addition of iron salts, however, was more useful. It was anticipated the ferric salts would promote the dissolution of pyrite, as demonstrated by the Meyers process. Catalytic amounts (50-100 mg) of FeCl₃ or Fe(ClO₄)₃ showed no activity. But when a series of extractions was performed at a lower temperature, at which it is known that HClO₄ by itself does not extract all the pyrite, with increasing amounts of Fe(ClO₄)₃ added to the mixture and boiled for 1.5 or 2.5 h, the curve depicted in Figure 4 was obtained.

For the extraction of coal with varying amounts of added Fe(ClO₄)₃ for 1.5 or 2.5 h at 134.5°C, the amount of S removed increased rapidly from 0 to 0.05M Fe(ClO₄)₃. From 0.05 to 0.7M Fe(ClO₄)₃, the amount of S removed continued to increase less rapidly, and above 0.7M Fe(ClO₄)₃ it was fairly constant. These data imply that all the inorganic S could be removed at 134.5°C in the presence of as little as 0.05M Fe(ClO₄)₃, compared to 143°C required in its absence. They also imply that some organic S form (~0.9%) is labile and can be removed in the presence of <0.7M Fe(ClO₄)₃ at a temperature of only 134.5°C.

Dissolution of Coals With High Organic Sulfur in HClO₄

For a Spanish lignite (9.63% tot. S, 0.05% sulf. S, 1.06% pyr. S, and 8.52% org. S, as determined by ASTM), a break occurred at ~140°C, corresponding to ~2.5% S; this compares with 1.1% inorganic S by ASTM. Thus, it is very likely that

~1.4% additional (and therefore "organic" sulfur) was dissolved at this temperature. The form of this "organic" sulfur is unknown; it could be noncarbon-bonded sulfur. But the fact is that some form of sulfur that is classified as organic sulfur by ASTM dissolved under these mild conditions. Another break occurred at about 160-167°C corresponding to about 6-7% S, and the remainder of the sulfur dissolved at about 200°C. This would imply that the lignite might contain about 1.1% inorganic S, 1.4% very easily oxidized "organic" S, about 3.5-4.5% organic S that is comparable to that in Illinois No. 6 coal, and about 3-4% organic S which is more difficult to remove. For a specially prepared Bevier seam coal (containing ~3% total S of which ~2.5% is organic S), the results are less easily interpreted. Additional experiments are being carried out to characterize the S forms in more detail.

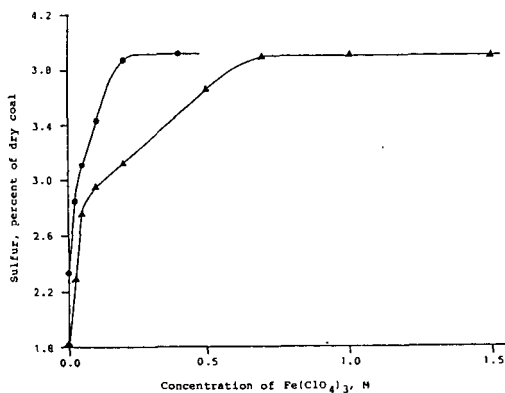


Figure 4. Total sulfur recovered (as percent of dry Illinois No. 6 coal) as a function of $\text{Fe}(\text{ClO}_4)_3$ concentration at 134.5°C

▲ extraction time 1.5 h; ● extraction time 2.5 h

CONCLUSIONS

The delineation of S forms in coal is possible by selective oxidative degradation with boiling HClO_4 . In the plot of total sulfur extracted by boiling HClO_4 of various concentrations, there is a clear delineation between sulfate and pyritic S and between pyritic and organic S. The temperatures at which such differentiations can be made are somewhat lower than previously expected and thus provide better conditions for a more accurate measurement of the various S forms in coal.

The extraction of pyritic S is also directly related to the amount of extracted iron. Organic S is extracted only when oxidative degradation of coal becomes significant, signalling the dissolution of coal, as shown by the deepening color of the extracts and the analyses of the residues.

The presence of $\text{Fe}(\text{ClO}_4)_3$ enhanced the selectivity of HClO_4 in the extraction of sulfur from coal, especially at lower temperatures. Increasing the

$\text{Fe}(\text{ClO}_4)_3$ concentration up to 0.05M allowed the removal of all inorganic sulfur at 134.5°C. Increasing the $\text{Fe}(\text{ClO}_4)_3$ concentration further, up to 0.7M but still at 134.5°C, removed a significant portion of what has to be labile organic S. Further increases in $\text{Fe}(\text{ClO}_4)_3$ concentration did not remove additional organic S. This has to be termed intractable organic S and could be related to the thiophenic-type S.

The HClO_4 dissolution procedure applied to a Spanish lignite with high organic S, showed 4 different forms of S. But specific assignment of functionality to all 4 classes is not as yet possible. Further tests are continuing on this Spanish lignite and on Bevier coal, both containing mostly organic S.

ACKNOWLEDGEMENT

The experimental work was done at Ames Laboratory which is operated for the Department of Energy by Iowa State University under Contract No. W-7405-Eng-82. Most of this work was supported by the Assistant Secretary for Fossil Energy, through the Pittsburgh Energy Technology Center.

REFERENCES

1. C. W. McGowan and R. Markuszewski, "Fate of Sulfur Compounds in Coal During Oxidative Dissolution in Perchloric Acid," Fuel Processing Technology, 17(1), 29-41 (1987).
2. C. W. McGowan and R. Markuszewski, "Direct Determination of Sulfate, Sulfide, Pyritic, and Organic Sulfur in a Single Sample of Coal by Selective, Step-Wise Oxidation with Perchloric Acid," Fuel, 67(8), 1091-1095 (1988).
3. C. W. McGowan, K. Qualls Cates, and R. Markuszewski, "The Conversion of Organic Sulfur in Coal to Sulfate Using Perchloric Acid," Am. Chem. Soc. Div. Fuel Chem. Preprints, 33(1), 225-231 (1988).
4. K. S. Ailey Trent, C. W. McGowan, and R. Markuszewski, "Analysis for Organosulfur Compounds in Perchloric Acid Solutions Resulting from the Oxidation of Coal for the Determination of Pyrite," presented at ACS meeting, Atlanta, GA, April 14-19, 1991.
5. X. Zhou and R. Markuszewski, "Characterization of Sulfur Forms in Coal by Oxidative Degradation," presented at Iowa Academy of Science Annual Meeting, Dubuque, IA, April 19-20, 1991.
6. K. S. Ailey Trent, C. W. McGowan, E. Lachowicz, and R. Markuszewski, "A Standard Addition Method for the Measurement of Sulfate Produced During the Determination of Sulfur Forms in Coal Using Perchloric Acid," Am. Chem. Soc. Div. Fuel Chem. Preprints, 36(3), 1198-1203 (1991).
7. W. E. Straszheim, R. T. Greer, and R. Markuszewski, "Direct Determination of Organic Sulphur in Raw and Chemically Desulphurized Coals," Fuel, 62(9), 1070-1075 (1983).
8. R. Markuszewski, X. Zhou, and W. E. Straszheim, "Characterization of Sulfur Forms in Coal by Oxidative Degradation," in Processing and Utilization of High-Sulfur Coals IV, P. R. Dugan, D. R. Quigley, and Y. A. Attia, eds., Amsterdam, Netherlands, 1991, pp. 43-54.

DETERMINING MOLECULAR WEIGHT DISTRIBUTIONS OF POLAR COAL DERIVED LIQUIDS BY MEANS OF COMBINED GC/MS AND VACUUM TG TECHNIQUES

Huaying Huai and Henk L.C. Meuzelaar
Center for Micro Analysis & Reaction Chemistry
University of Utah, Salt Lake City, UT 84112.

Keywords: molecular weight distribution of coal liquids, gas chromatography/chemical ionization mass spectrometry, vacuum thermogravimetry

BACKGROUND

A novel, low temperature (<300 C) coal liquefaction method described by Shabtai et al. [1], consisting of a mild hydrotreatment (HT) step followed by base-catalyzed depolymerization (BCD) is thought to proceed by selective scission of C-C and C-O type bonds in the bridges connecting the aromatic and hydroaromatic clusters making up the bulk of the coal matrix, while minimizing secondary condensation reactions. Consequently, the resulting liquid products are expected to consist primarily of "monomeric" building blocks of the type and size inferred from solid state NMR measurements [2], i.e., corresponding to (hydro)aromatic structures with 10-15 aromatic carbons, 2-3 aliphatic carbons and 1-2 substituted oxygens (in addition to more sporadic sulfur, nitrogen or metal substituents) depending on coal rank, maceral composition, depositional environment and weathering status. In agreement with these expectations, the cyclohexane soluble "oil" fractions of the HT-BCD product, comprising up to 70% of the daf coal, were found to be completely vacuum distillable and to contain significant quantities of volatile, low MW components when analyzed by combined gas chromatography/mass spectrometry (GC/MS).

In order to further verify the mechanistic assumptions underlying the HT-BCD method as well as to obtain valuable information regarding type and size of the monomeric building blocks in coals, we decided to determine the precise molecular weight distribution (MWD) of HT-BCD oil fractions. The term MWD will be used interchangeably here with MMD (molecular or molar mass distribution). In view of the relatively low molecular weight and high polarity of the HT-BCD oil fractions, the use of gel permeation chromatography (GPC), also referred to as size exclusion chromatography [3], techniques was rejected in favor of mass spectrometry (MS) using "soft ionization" methods, such as field ionization (FI) and chemical ionization (CI), which tend to produce little or no fragmentation of molecular ions. Direct probe FIMS measurements were performed by Dr. H.R. Schulten (Fresenius Institute, Wiesbaden, GFR) whereas CIMS analyses were carried out in our laboratory using on-line prepreparation by short column capillary gas chromatography (GC) and sample injection by means of Curie-point flash evaporation. Well-known shortcomings of MS techniques include: possible loss of volatile components during sample introduction (in particular during direct probe MS); incomplete transport of low volatile components into the ion source (especially when using GC/MS); compound dependent response differences; and inability to analyze nonvolatile residues. Therefore, vacuum thermogravimetry (VTG) was selected as a tool for quantitative calibration, similar to its well established use for calibrating simulated distillation (SIMDIS) methods [4]. The results of these DP-FIMS, GC/CIMS and VTG experiments with a mixture of coal liquid like model compounds as well as with HT-BCD oil fractions from three ANL-PCSP (Argonne National Laboratory - Premium Coal Sample Program) coals, viz. Beulah Zap lignite, Illinois #6 hvCb and Blind Canyon hvBb coals, will be reported here.

RESULTS AND DISCUSSION

Since VTG showed each of the three HT-BCD oil samples to be completely vacuum distillable below 300 C without signs of degradation (Figure 1) we first attempted to determine the respective molecular weight distributions by means of DP-FIMS. As shown in Figure 2, MWD profiles obtained by DP-FIMS indicated apparent number average MW (MW_n) values in the 370-400 Dalton range. Considering the expected size of the molecular building blocks, e.g., 200-300 Daltons, these MW_n values were thought to be rather high.

Since direct probe introduction methods in MS are prone to loss of volatile components, a short capillary GC column operating at high linear flow velocities was used as a sample introduction device instead. Due to the unavailability of a GC/FIMS system, CIMS became the method of choice at this point. The advantages of using short capillary GC columns at high linear flow velocities over more conventional GC conditions are illustrated in Figure 3. Also note the effectiveness of isobutane Cl in minimizing fragmentation of molecular ions in comparison with the standard electron ionization technique. GC/CIMS data were obtained with a Finnigan MAT ion trap detector (ITD) type MS system. Comparison of the summed DP-FIMS and GC/CIMS spectra of Illinois #6 HT-BCD oil in Figures 2b and 3c, respectively, shows marked differences in observed ion distribution profiles. Obviously, the FIMS spectra suffer from a relative lack of low mass signals, presumably due to evaporation losses, whereas the GC/CIMS profiles lack some of the higher MW signals shown by FIMS, apparently due to a minor loss of heavy ends unable to pass through the short GC column.

Notwithstanding the discrepancies between the DP-FIMS and CIMS profiles, both types of profiles display a highly similar temperature dependence of avg. MW values (see Figure 4) except in the low MW part of the FIMS profile. However, as can be seen in Figure 2, the low MW part of the FIMS profile is entirely made up of low intensity mass peaks, apparently representing small quantities of residual oil remaining after evaporative loss of the lower ends. Consequently, the low MW part of the DP-FIMS curve is less reliable. Figure 5 demonstrates the temperature windowing technique used to calculate average MW values from temperature resolved MS data.

Considering the obvious differences in experimental conditions between the direct probe FIMS and the Curie-point vaporization GC/CIMS techniques the observed high degree of similarity in MW_n /Temp relationships merits some discussion. Because partial vapor pressures of individual compounds are independent of total pressure any apparent differences in temperature dependent behavior between the two systems must be due to intermolecular interactions and/or to transport limitations. Since high vacuum FIMS conditions resemble those of molecular distillation processes both effects are minimized and molecular size (as defined by the so-called "exclusion volume" [5]) becomes the dominant factor. Similarly, the Curie-point flash evaporation method used in GC/CIMS analysis effectively reduces the effect of intermolecular interactions by briefly elevating the sample to relatively high temperatures. Furthermore, the low effective sample concentrations in the gas and liquid phase, the chemical inertness of the fused silica capillary GC columns, the nonpolar poly(dimethyl/silicone) coating, the high linear carrier gas flow velocities and the short residence times combine to reduce intermolecular interactions and minimize transport limitations in the GC/CIMS system. Experimental support for these arguments can be found in the observation that capillary GC elution temperatures of petroleum crudes closely resemble vacuum distillation temperatures at 10 mm Hg [6]. Naturally, since kinetic considerations predict a strong heating rate dependence for apparent distillation and elution temperatures, it is important to use comparable heating rates in both experiments. Fortunately, heating rate is one of the most readily adjustable experimental parameters. Therefore, remaining temperature differences between desorptions, distillation or elution techniques may effectively be minimized by small adjustments in heating rate.

In order to transform the established MWn/Temp relationship into a molecular weight distribution, i.e., MWn/Weight Fraction relationship, we need to determine a reliable Weight Fraction/Temp relationship. In other words: what fraction of the sample (whether expressed as number of molecules or fraction of weight) is distilled, desorbed or eluted over each temperature interval?. This was measured by synthesizing a standard mixture consisting of known quantities of 87 coal-liquid like model compounds. In view of the unavailability of many possible coal liquid components any such mixture constitutes at best an approximation of a true coal liquid. Nevertheless, as shown in Figure 6, the observed MWn/Temp relationship (using GC/CIMS) is closely similar to that seen in Figure 4 (maximum avg. MW difference in 100-300 C range ≤ 10 Daltons). This encourages the further use of this model mixture to establish a Distillation Weight Fraction/Temp relationship by means of VTG (Fig. 7). As shown in Figure 7 the VTG curve (at approx. 5 mm Hg) closely follows the response corrected GC elution curve obtained at similar heating rate. By contrast, the ambient pressure ("transport limited") TG curve differs substantially from the vacuum TG profile.

Combination of the MW/Temp relationship (Figure 6) with the Weight Fraction/Temp relationship (Figure 7) produces the calculated Weight Fraction/MW relationship (=Molecular Weight Distribution) shown in Figure 8. Comparison with the known MWD of the model compound mixture in Figure 8 appears to confirm the validity of the combined GC/CIMS annex VTG approach.

In order to perform a more detailed analysis of the underlying relationships between average MWs and GC elution temperatures and to compare these with the atmospheric boiling point (ABP)/Elution Temp relationship used in SIMDIS [6] a smaller subset of 28 model compounds was selected for which ABP data are available in the literature. As shown in Figure 9, both correlations are of comparable strength ($r=0.990$ for ABP vs. temp., Figure 9a, with $r=0.985$ for MW vs. temp. Figure 9b), provided that n-alkanes are excluded from the model compound set in both cases. The anomalous behavior of n-alkanes in SIMDIS has been documented before [6]. As might be expected, the weakest correlation is found between ABP and MW (Figure 9c, $r = 0.971$). Intermolecular forces play a major role in determining ABP's without affecting MW values [7]. The fact that GC elution temperatures and MW values do not exhibit a perfect correlation does not necessarily argue against our prior assumption that under the special GC conditions used in our experiments (flash evaporation, high linear flow velocities, and short capillary column with inert walls and nonpolar coating) molecular exclusion volume may be the rate determining parameter. Exclusion volumes, although directly related to MW, are obviously influenced by other molecular properties as well. Unfortunately, exclusion volume values for the model compounds used were not available at the time of writing.

Application of the above described combined approach to the HT-BCD oils of the three ANL coals produces the three MW/Elution Temp. relationships shown in Figure 10. In agreement with the model data, all three coal liquids produced highly similar profiles in spite of significant differences in chemical composition. Most importantly, the calculated linear regression fit for the average slope and offset of the MW/Elution Temp relationship obtained for the model compounds shows an excellent fit with the coal liquid data as well. Finally, calibration of the relationship in Figure 10 with the measured vacuum TG profiles in Figure 1 results in the calculated MWD profiles shown in Figure 11. Note that the calculated average MW values, as well as the small but significant shift between the three coal liquids appear to be in line with the previously discussed assumptions regarding the type and size of key building blocks in coals of low to medium rank.

CONCLUSIONS

1. Short capillary GC columns operating at high linear flow velocities (facilitated by keeping the column outlet at vacuum pressure) produce elution temperature data which correlate closely with molecular weight for a broad selection of alkyl- and/or heteroatom substituted aromatic and hydroaromatic compounds. Correlation with vacuum TG data on fractional weight loss as a function of distillation/desorption temperature enables calculation of mass corrected MWD profiles. Based on the strength of the observed correlations, the error of the calculated MW values is expected to be well within $\pm 5\%$, which compares favorably with the reported accuracy of GPC based techniques for polar coal liquids [8].

2. For more or less strongly related coal-derived liquids, e.g. produced by the same liquefaction procedure, the observed relationship between avg. MW and elution temp. appears to be stable enough to eliminate the need for frequent recalibration by GC/CIMS (or GC/FIMS) techniques. Thus, a single vacuum TG determination under standardized conditions appears to be the method of choice for calculating reliable MWD profiles (provided that any significant quantities of n-alkanes are separated out before the measurement). For vacuum distillable coal liquids of unknown overall composition development of an on-line TG/MS technique (using FI or CI) may well provide the most direct approach to quantitative determination of MWD profiles (as long as excessive losses of volatile components are avoided).

3. Cyclohexane soluble "oil" fractions obtained from ANL coals of low to medium rank by means of low temperature HT-BCD were found to consist of molecular building blocks of a size and type which closely agree with solid state NMR data. Presumably, coal-derived liquids showing much larger average MW values (such as commonly seen in the coal liquefaction literature) must represent either: (a) high MW subfractions; (b) incompletely depolymerized fractions; (c) secondary recombination products; (d) retrograde reaction products; or (e) biased analytical procedures.

4. Arguably, MWD profiles provide a better yardstick for measuring the conversion efficiency of a given coal liquefaction process than solubility based parameters since the latter correlate poorly with molecular size and, thus, with the degree of depolymerization achieved.

ACKNOWLEDGEMENTS

The authors wish to thank H.R. Schulten, K. Holbrook, M. Statheropoulos and J.S. Shabtai for their highly valuable advice and kind help. This work was supported by the Consortium for Fossil Fuel Liquefaction Science (U.S. DOE) and by the Advanced Combustion Engineering Research Center NSF, State of Utah, 23 industrial participants and U.S. funded by DOE.

REFERENCES

1. Shabtai, J.S.; Saito, I. U.S. Patent 4,728,418, issued Mar. 1, 1988.
2. Solum, M.S.; Pugmire, R.J.; Grant, D.M. *Energy & Fuels*, 1989, 3, 187.
3. Evans, N.; Haley, T.M.; Mulligan, M.J.; Thomas, K.M. *Fuel*, 1986, 65, 694.
4. Southern, T.G.; Iacchelli, A.; Cuthiell, D.; Selucky, M.L. *Anal. Chem.*, 1985, 57, 303-308.
5. Perry, E.S. "Distillation under High Vacuum", in: *Distillation*, E.S. Perry and A. Weissberger (eds.), Interscience Publishers, Chapter V, 1965, pp. 535-551.
6. Annual Book of ASTM Standards, 1988, Vol. 05.02, pp. 506-513.
7. Boduszynski, M.M. "Limitations of Average Structure Determination for Heavy Ends in Fossil Fuels" in: *Liquid Fuels Technology*, 1984, 2(3) pp. 211-232.
8. Bartle, K.D. "Chromatographic Techniques" in: *Spectroscopic Analysis of Coal Liquids*, J.R. Kershaw (ed.), 1989, pp. 13-40.

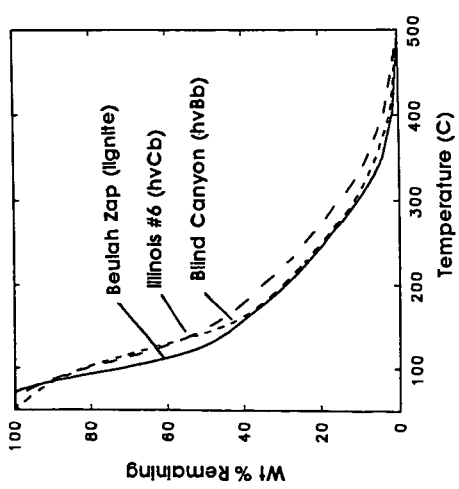
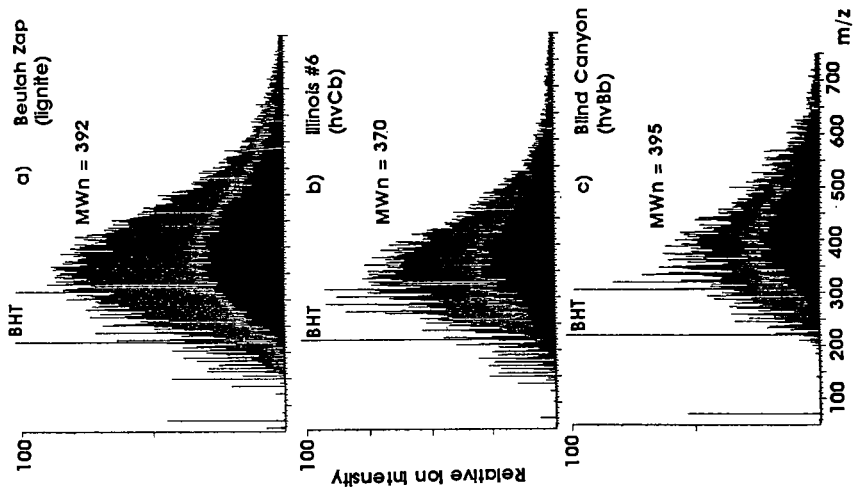


Figure 1. Vacuum TG curves for three HT-BCD oils.

Figure 2. Direct probe field ionization MS profiles for three HT-BCD oils. Note BHT (dibutylhydroxytoluene stabilizer residue from THF extraction) at m/z 220.

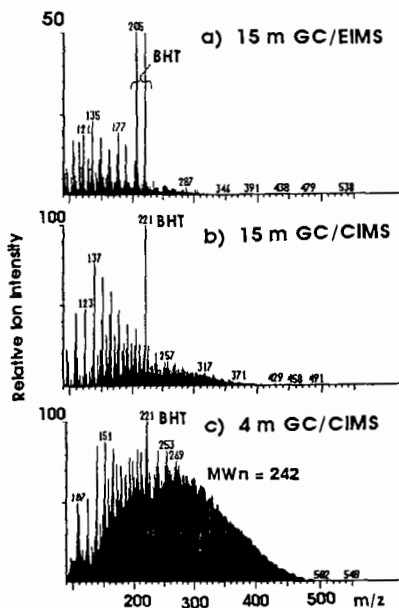


Figure 3. Effect of column length (15 m vs. 4 m) and ionization method (EI vs. CI) on ion distribution profiles of Illinois #6 HT-BCD oil.

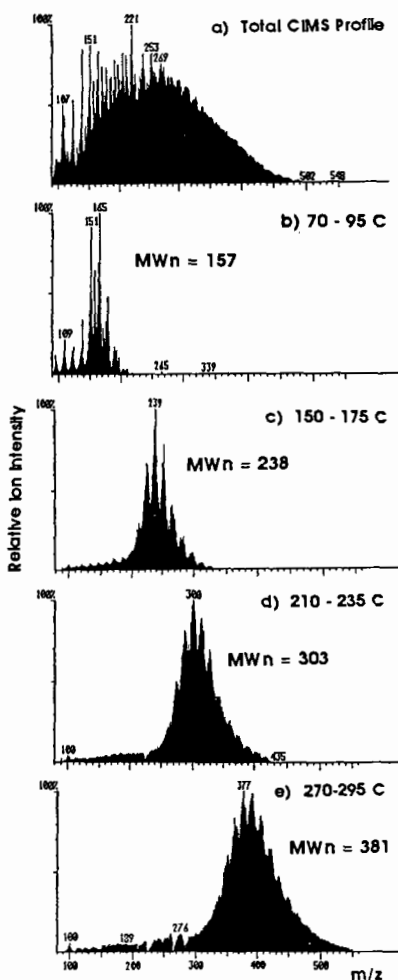


Figure 5. Temperature window (25 C) technique used to calculate avg. MW/Temp relationship data illustrated for GC/CIMS profile of Illinois #6 HT-BCD oil.

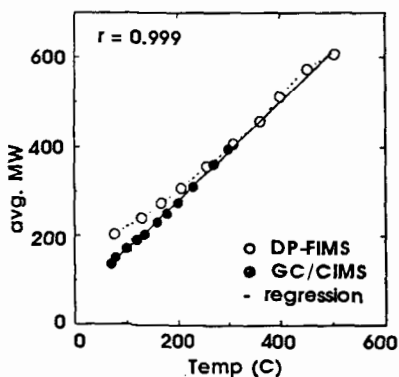


Figure 4. Comparison of avg. MW/Temp relationships observed by DP-FIMS and GC/CIMS analysis of Illinois #6 HT-BCD oil.

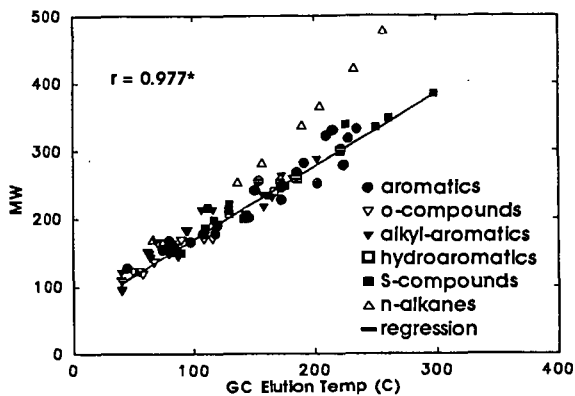


Figure 6. Observed MW/GC elution temperature relationship for a mixture of 87 model compounds. *n-alkanes removed from regression calculation.

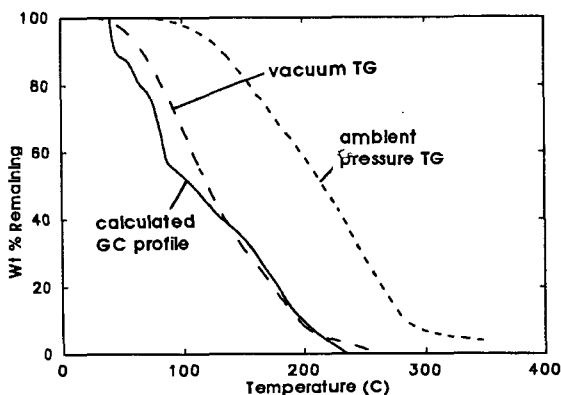


Figure 7. Comparison between Temperature/Fraction Weight loss relationships obtained by vacuum TG and ambient pressure TG of a mixture of 87 model compounds, as well as by weight corrected, integrated GC elution profiles.

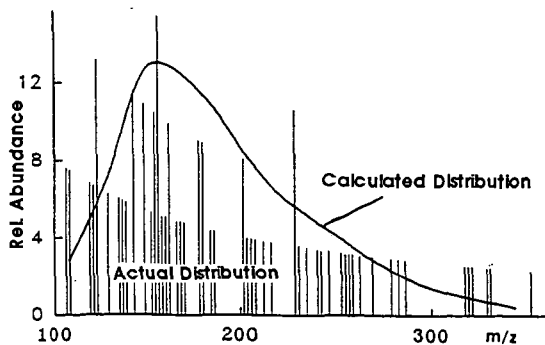


Figure 8. Comparison between calculated MWD and actual MWD of model compound mixture.

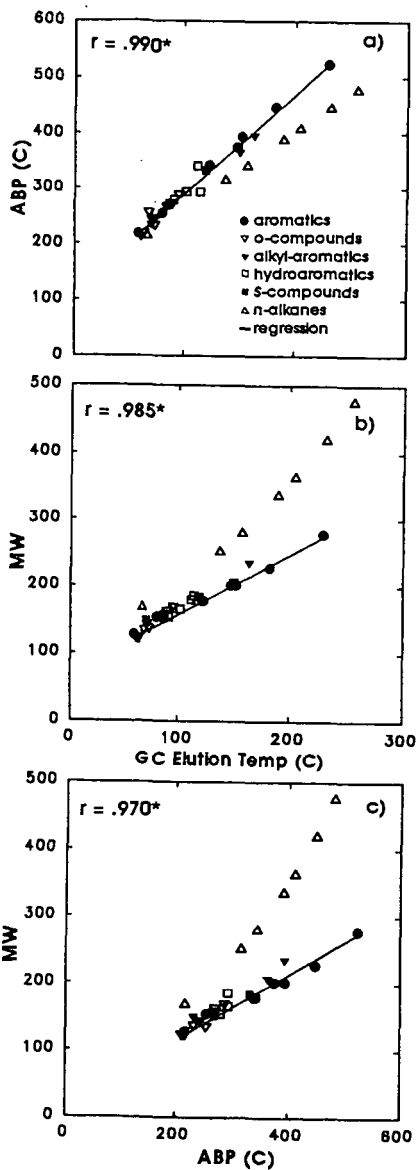


Figure 9. Observed correlations between ABP (Atmospheric Pressure Boiling Point), MW and GC elution temperature for a subset of 28 selected model compounds. n-alkanes removed.

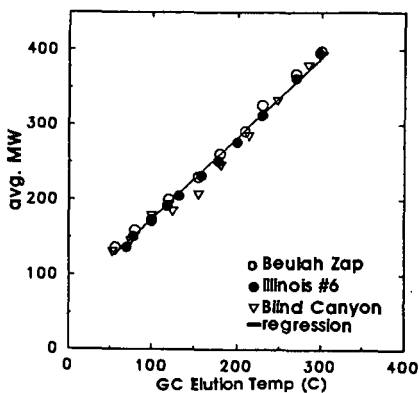


Figure 10. Comparison between observed avg. MW/GC elution temp relationships for three HT-BCD oils and the predicted regression line obtained from the 87 model compound mixture.

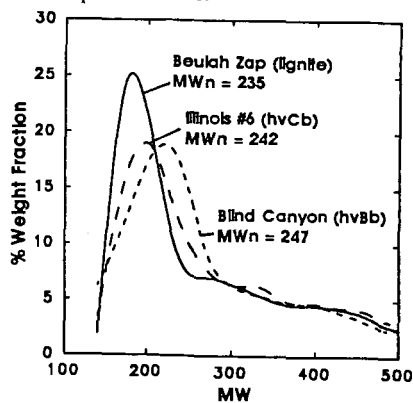


Figure 11. Calculated MWD curves for the three HT-BCD oils. Note slight increase in MW_n as a function of rank.

LIQUEFACTION OF WATER PRETREATED COALS

Michael A. Serio, Erik Kroo and Peter R. Solomon

Advanced Fuel Research, Inc.
87 Church Street
East Hartford, CT 06108

Keywords: Pretreatment, Water, Coal, Liquefaction, Pyrolysis

INTRODUCTION

Water pretreatment of coal has been studied previously as a means to increase the yields of liquid products from extraction (1-5), pyrolysis (3-6), or liquefaction (7,8) of coal. However, the mechanisms of this process and the applications to coals of a wide range of ranks are still a subject of considerable debate. The benefit of water pretreatment on increasing yields from direct liquefaction of coal has not been clearly demonstrated, although effects on the composition and molecular weight distribution have been observed (7,8). The goals of this study are to gain an understanding of the chemistry of water or steam coal pretreatments and to assess the importance of such pretreatments on subsequent coal liquefaction.

EXPERIMENTAL

Sample Selection - The selection of coal samples was made from the Argonne Premium Sample Bank. Since pretreatment is potentially most useful for lower rank coals which are subject to retrograde reactions, the coals used were the Zap Lignite, the Wyodak subbituminous and the Illinois No. 6 bituminous. Selected experiments were also done with the Pittsburgh Seam bituminous coal from the same sample bank.

Steam/Water Pretreatment Experiments - A new reactor system was designed to carry out high pressure (up to 6000 psig), high temperature (up to ~ 400°C) steam or water pretreatment of coal in a closed bomb (20 ml) reactor. After 1-3 g coal is fed into the bomb and the reactor head is screwed on to get a gas tight seal, the system is purged with N₂ or evacuated, the high temperature, high pressure valve on the reactor base is closed, and the water is injected directly into the coal through the capillary tube with a ~ 0.1-1.0 ml/min rate. Deaerated and deionized water is used throughout the reaction.

Simultaneously with the water injection, the reactor is immersed into the fluidized sand bath held at the required temperature. The pressure is measured in the water feed capillary tubing directly after the pump. The amount of water pumped in and the temperature determines whether steam and/or water pretreatment is done. The results described in the current paper are for pretreatment with subcritical water at 350°C, 4000 psig and pretreatment times from 10 to 1000 minutes.

After the reaction, the bomb is quickly quenched with water, flooded with up to 300-600 psig N₂ and depressurized with a 0.8 liter previously evacuated sampling tank. The yields of product gases, e.g., H₂, CO₂, CO, CH₄, C₂H₆, C₂H₄, C₂H₂, and H₂S are determined by GC. After opening

the reactor, the pretreated coal is taken out of the reactor by washing it with deionized water and filtering under an N_2 atmosphere. N_2 is passed through the coal sample for about an hour to obtain a sample with approximately the same moisture content as the starting coal sample. In addition to the reactor, an N_2 purged glove box was also constructed to facilitate all the product work up in an oxygen-free environment.

Product Analyses - The residues from the water pretreatment experiments with the four coals were subjected to analysis by programmed pyrolysis (TG-FTIR), solvent extraction, FT-IR, SEM/x-ray analysis and liquefaction experiments in a donor solvent. The liquefaction experiments were done with 0.5 g of coal residue and 3 g of solvent (dihydrophenanthrene) in a 20 ml agitated bomb reactor for 30 min. at 400°C.

RESULTS

Experiments with a Range of Coals - Selected results for the characterization of the residues by TG-FTIR, solvent extraction with pyridine, and liquefaction experiments in a donor solvent are summarized in Figs. 1-3. The results for pyrolysis tar yields (Figs. 1a, 2a, 3a) show a sharp increase at short pretreatment times with a gradual decrease at longer times when compared to the raw coal. The oxygenated gases, CO, CO_2 and H_2O (data not shown) decline with increasing pretreatment time, except for an initial increase in CO. Conversely, the amount of CH_4 from pyrolysis has the opposite trend.

The set of data on pyridine extractables is less complete but indicates that, for the three coals, the yield increases at relatively short pretreatment times (by as much as a factor of two) and gradually declines at longer pretreatment times (see Figs. 1e, 2e, 3e), thus following the same general trend as the tar yield. The larger set of data for the Illinois coal is quite clear with regard to this trend. In the case of the Illinois coal, pretreatment for 20 minutes resulted in a more than doubling of the % DAF pyridine extractables (81 vs. 36%). The results were generally lower when an ampoule of Illinois coal was used which was not freshly opened (compare open circles and solid circles in Figure 3). The results to date indicate that of the four coals examined (Zap, Wyodak, Illinois, Pittsburgh), the Illinois coal is the most sensitive to coal freshness. For the Pittsburgh coal, the pyridine extractables increase slowly with increasing pretreatment time.

The liquefaction results for the two low rank coals (Zap, Wyodak) indicated significant reductions at short pretreatment times, particularly for the Zap lignite, in the yields of toluene and pyridine solubles (see Figs. 1f and 2f). The liquefaction yields for the low rank coals improved at longer pretreatment times but were generally not as high as for the untreated coal. Conversely, improved or similar yields of oils and toluene solubles are observed for selected pretreatment experiments with Illinois coal. However, these results could not be reproduced consistently with Illinois coal. It appeared that the results were sensitive to the "freshness" of the coal. For ampoules which were just opened, the yields of soluble products from the pretreated coals were lower than for samples which had been opened days or weeks earlier and stored in a nitrogen purged glove box. A likely explanation is that the solvent is forming adducts with the water pretreated samples. This conclusion is supported by the observation of negative oil yields, since the oil yields are determined by difference. The very fresh Illinois samples appear to be the most reactive toward solvent adduction. The differences between the fresh and "aged" Illinois samples is also evident by comparing the yields of pyrolysis gases and pyridine extractables in Fig. 3. This same phenomenon may explain why the liquefaction yields for the pretreated Zap and Wyodak coals go through a minimum at short pretreatment times, and are generally less than for the raw coals.

This hypothesis was tested by doing mild oxidation experiments on raw and pretreated Illinois and Zap coals, as discussed below.

Mild Oxidation Experiments - The samples generated in the mild oxidation studies were subjected to characterization by liquefaction in donor solvent (30 min., 400°C in dihydrophenanthrene). The results for toluene solubles and oils for the mild oxidation experiments and reference experiments are summarized in Table 1. This table only includes data for freshly opened ampoules in the case of Illinois coal. Experiment #80 indicates that mild oxidation of a

TABLE I - SUMMARY OF LIQUEFACTION EXPERIMENTS ON ILLINOIS AND ZAP COALS

Coal Type	Run No.	Treatment	Liquefaction Yields DAF %	
			Toluene Solubles	Oils
Ill. #6		---	42 to 48	14 to 17
		pretr.	11 to 40	(-12) to 40
	80	pretr. + H ₂ O ₂ ^(b)	64	19
	84	H ₂ O ₂ ^(a) + pretr.	48	7
	88	H ₂ O ₂ ^(b) + pretr.	62	19
	91	Fe ⁶⁺ ^(c)	49	7
	85	H ₂ O ₂ ^(b)	53	12
	93	H ₂ O ₂ ^(b) + H ₂ S*	90	34
Zap		---	26 to 36	12 to 14
		pretr.	18 to 21	12 to 15
	82	pret. + H ₂ O ₂ ^(b)	30	14

Notes: 150 ML solution, 5 gr. coal: (a) 0.003 M (b) 0.5 M (c) 1 M

All water pretreatments were done at 350°C, 4000 psig for either 20 minutes (#80, #82) or 60 minutes (#84, #88) pretreatment time.

* Liquefaction was done in the presence of 80 psig H₂S.

water pretreated Illinois coal gives an increased yield of toluene solubles and oils from liquefaction of the residue and that the values are generally higher than from liquefaction of the raw coal. Similar results are observed for mild oxidation of a water pretreatment residue from Zap lignite (see experiment #82 in Table 1). These results are consistent with the hypothesis that ortho dihydroxy functionalities created by water pretreatment are responsible for the retrogressive solvent incorporation reactions which artificially reduce the liquefaction yields. This conclusion is based on the assumption that the mild oxidation will remove the dihydroxy functionalities. Additional experiments were done with Illinois coal (#84, #88) where the coal was oxidized prior to water pretreatment. This would serve to remove dihydroxy functionalities which are already

present in the coal and the phenolic groups that are precursors to the dihydroxy functionalities that are formed during water pretreatment. In this case, the toluene solubles and oil yields are also higher than for the coal that was only subjected to water pretreatment. It was also found that mild oxidation by itself (#85) or mild oxidation followed by liquefaction in the presence of H_2S (to restore catalytic activity of pyrite) also gave results that were equal or superior to the raw coal.

FT-IR Analyses of Water Pretreated Coals - Residues from water pretreatment of all four coals were subjected to analysis by quantitative FT-IR functional group analysis. The samples were chosen from a range of pretreatment times (20, 180, 300, 1080, 1200 minutes) at $350^\circ C$, 4000 psig. The quantitative results for aromatic hydrogen (H_{ar}), aliphatic hydrogen (H_{al}), hydroxyl hydrogen (H_{OH}) and ether oxygen (O_{ether}) are given in Fig. 4. For all of the coals, except Pittsburgh, pretreatment led to a monotonic decline in the oxygen content. This is consistent with previous work on water pretreatment (6-9) and with the idea that the process is similar to an accelerated aging of the coal.

A lot of attention has been paid to the effect of water or steam pretreatment on hydroxyl groups. For all four coals, the concentration of hydroxyl OH declined with increasing pretreatment time, except for a small initial increase with Zap. This is in agreement with the results of Khan et al. (9) but not with Brandes et al. (6). Brandes et al. (6) concluded that steam pretreatment significantly increased the number of hydroxyl groups. This conclusion was primarily based on the fact that mild O-alkylation of steam pretreated coal with labeled methyl iodide introduced twice the enrichment of ^{13}C when compared to the raw coal. Some IR data was also used to support this conclusion, using a diffuse reflectance technique which measures surface concentrations. It is possible that the loosening of the structure resulting from steam pretreatment makes the coal more reactive toward the O-alkylation procedure, and that the actual number of hydroxyl groups does not increase significantly. It is also possible that the concentration of OH groups increases on the surface of the water pretreated coals but not in the bulk. Of course, any comparison with previous work must consider the fact that the results in Fig. 4 are for samples produced in subcritical water and over a wide range of pretreatment times. Most of the previous studies (3-6,9) were done in subcritical steam at lower pressures (~1000 psig) and for relatively short times. Some additional work on resolving the -OH region of the spectrum indicated that the concentration of ortho dihydroxy functions does initially increase for all of the coals following water pretreatment.

The trends for hydrogen functional groups appeared to vary with coal type. For the two low rank coals (Zap, Wyodak), pretreatment increased the fraction of aromatic hydrogen, while for the two higher rank coals (Illinois, Pittsburgh), this fraction was decreased. The contrast between the behavior of the Zap and Illinois coals is especially striking in this regard. For the two low rank coals, the amount of aliphatic hydrogen (H_{al}) goes through a maximum with increasing pretreatment time, while for the two higher rank coals, H_{al} declines steadily.

DISCUSSION

The increase in pyridine extractables and tar yields is consistent with literature observations (4,6,9). The tar yields and pyridine solubles yields show a maximum with increasing pretreatment time (except for the Pittsburgh coal) which indicates the onset of retrograde reactions as pretreatment proceeds (10). Conversely, the yields of toluene solubles (TS) from liquefaction are

at a minimum where pyrolysis tar yields are at maximum, which is contrary to previous studies on liquefaction (11) and expectations. However, the individual experimental data around the minimum toluene solubles values were very dispersed, especially for the Illinois No. 6 coal.

Table 1 shows the liquefaction results of experiments with Illinois No. 6 coal in somewhat more detail. Since the oil fraction is measured by weight difference, the only explanation for negative values is that there was solvent incorporation into the toluene insoluble part of the coal matrix and that this depends on how fresh the coal was. In the case of the Illinois coal, an exposure of this particular coal to even very low oxygen concentrations prior to pretreatment apparently causes a very significant change in the pretreatment and subsequent liquefaction behavior. There are reports in the literature of the sensitivity of Illinois No. 6 coal to rapid oxidation at ambient temperatures (12,13). The problem of measuring the incorporated solvent calls for a proper separation of the solvent and solvent derivatives which is very difficult to do on a quantitative basis given the complex nature of the coal liquid.

A second approach, which we have taken, is to hypothesize a reaction scheme for that particular behavior which is in harmony with the experimental data and then to test it. Our hypothesis is that it is the phenoxy radical which reacts with water to form dihydroxy products, as illustrated in Fig. 5, and that the recombination of the dihydroxy and solvent radicals leads to solvent incorporation into the coal matrix, as illustrated in Fig. 6. However, dihydroxy compounds are not stable at such high temperatures and must therefore appear only as intermediate products leading to the "recovery" of the toluene solubles yields after prolonged pretreatment. An example of two decomposition routes for ortho dihydroxy benzenes is shown in Fig. 7.

Phenols are the most widespread components of coals and literature data show a decrease of total phenolic OH in the coal as well as increase of low molecular weight dihydroxy benzenes during water pretreatments (7,14). Our own FT-IR results support this picture as does the initial increase in pyrolytic CO formation (see below). Since phenoxy radicals are relatively stable due to resonance stabilization, they represent a high steady state concentration at elevated temperatures. As the number of condensed aromatic rings adjacent to the phenoxy radical increases, the stability increases and the reactivity decreases. This might be an explanation as to why the Pittsburgh coal behaves differently during water pretreatment than the lower rank coals.

Dihydroxy benzenes are prone to retrograde reactions (15) or decomposition. One type of decomposition may lead to CO evolution from the residue as shown in Fig. 7. Our experimental data show an initial increase in the pyrolytic CO evolution with a maximum in time corresponding to the minimum in the toluene solubles yield and the maximum in the tar yield (see Figs. 1-3). This is in contrast to a general decline in pyrolytic CO₂ and H₂O with increased pretreatment time and a corresponding reduction in organic oxygen content for the water pretreatment residues. There is a small amount of CO formation during pretreatment, but it is an intermediate product only.

McMillen and coworkers (15) found that, under liquefaction conditions, dihydroxy compounds readily couple with themselves or with the solvent (in their case, tetrahydroquinoline) and also form high molecular weight products, the amount of which increases in the presence of coal. The self coupling produces a diaryl cyclic ether molecule. This is consistent with our FT-IR data, (see Fig. 4) which show the ether group concentration reaching a maximum or declining slowly after relatively short hydrothermal treatment times, while the concentration of hydroxyl decreases steadily.

Our suggestion is that one of the principal reactions to cause solvent incorporation into the coal matrix under liquefaction conditions is the reaction of surface ortho dihydroxy functionalities with the solvent. A short hydrothermal treatment will enhance solvent incorporation due to the increased surface concentration of dihydroxies. Prolonged pretreatment will destroy these functionalities, as shown by Ross et al. (12), thus reducing solvent additions but introducing strong crosslinks and resulting in a decrease in liquefaction yields. A parallel process of depolymerization of the coal during hydrothermal treatment is compensating for this new crosslink formation, the final result being a slight increase or no increase of liquefaction yields relative to the untreated coal at long pretreatment times. The proposed mechanism is summarized in Fig. 8.

Since higher yields of toluene solubles and oils were obtained from samples of Illinois coal that were not freshly opened, or were treated with solutions of H_2O_2 our suggestion is that a mild oxidation substantially decreased solvent incorporation by removal of ortho dihydroxy functionalities or their precursors. This result suggests a possible way to avoid the detrimental effect of solvent incorporation and thus significantly increase liquefaction yields from water pretreated coals. Future work will involve additional experiments and literature work to test the hypothesis. The results will also be considered in light of the recent model compound studies of Siskin and Katritsky (16).

CONCLUSIONS

The conclusions can be summarized as follows:

1. The analysis of pyrolysis and pyridine extractables data from water pretreated Zap lignite and Wyodak subbituminous coal (reduction in CO_2 yield, maximum in tar yield, maximum in extractables, increase in CH_4 yield) shows a strong similarity of water pretreatment to an accelerated geological aging process. The results for the Illinois and Pittsburgh bituminous coals were similar, though less dramatic, except for the extractables yields.
2. The geological aging analogy is also consistent with results that were obtained in the literature on steam or water pretreatment, since it explains why the treatment is effective in increasing pyrolysis yields for low rank coals and is ineffective or reduces pyrolysis yields for high rank coals. However, there are certain trends, such as the fact that the CO yield appears to follow the tar yield (goes through a maximum along with the tar) which do not agree completely with this analogy.
3. The FT-IR data indicate a general reduction of oxygen groups during water pretreatment, including hydroxyl groups, although there is an initial increase in dihydroxy functionalities.
4. The results from liquefaction experiments on samples produced to date indicate only modest benefits in the best cases. The worst results are obtained at short pretreatment times where solvent incorporation into the coal is apparently reducing the observed yields of soluble products. For Illinois coal, the best results are obtained from "aged" samples, which appear to be less prone to the solvent adduction reactions.

5. The data are consistent with a mechanism in which water pretreatment increases the concentration of ortho dihydroxy species in the coal at short pretreatment times. Support is provided by FT-IR results and an initial increase in pyrolytic CO formation from the residue. These functions are believed to be responsible for the solvent incorporation reactions. They can be removed by increasing the pretreatment time or mild oxidation of the coal using H₂O₂ after water pretreatment.

ACKNOWLEDGEMENTS

The support of this work by the U.S. DOE Pittsburgh Energy Technology Center under Contract No. DE-AC22-89PC89878 is gratefully acknowledged.

REFERENCES

1. Bienkowski, P.R., Narayan, R., Greenkorn, R.A., Choa, K.W., IEC Res., **26**, 202, (1987).
2. Bienkowski, P.R., Narayan, R., Greenkorn, R.A., and Choa, K.C., Ind. Eng. Chem. Res. **26**, 206, (1987).
3. Graff, R.A. and Brandes, S.D., Proceed. of the New Fuel Forms Workshop, U.S. DOE Fossil Energy, p. 35, (1986).
4. Graff, R.A. and Brandes, S.D., Energy & Fuels, **1**, 84, (1987).
5. Zhou, P. and Brandes, S.P., "Steam Conditioning of Coal for Synfuels Production", 7th Annual Gsaification Contractors Review Meeting, (June 16-19, 1987).
6. Brandes, S.D., Graff, R.A., Gorbaty, M.L., and Siskin, M., Energy & Fuels, **3**, 494, (1989).
7. Ross, D.S. and Hirschon, A., ACS Div. of Fuel Chem. Prepr., **35**(1), 37, (1990).
8. Ross, D.S., Hirschon, A., Tse, D.S., and Loo, B.H., ACS Div. of Fuel Chem. Prepr., **35**(2), 352, (1990).
9. Khan, M.R., Chen, W.-Y., and Suuberg, E.M., Energy & Fuels, **3**, 223, (1989).
10. Serio, M.A., Solomon, P.R., Kroo, E., and Charpenay, S., ACS Div. of Fuel Chem. Preprints, **36**(1), 7, (1991).
11. Serio, M.A., Solomon, P.R., Kroo, E., Bassilakis, R., Malhotra, R., and McMillen, D., ACS Div. of Fuel Chem. Preprints, **35**, (1), 61, (1990).
12. Gethner, J.S., Fuel, **66**, 1091, (1987).
13. Kelemen, S.R., Freund, H., Energy & Fuels, **3**, 498-505, (1989).
14. Ross, D.S., Hirschon, A., Tse, D.S., and Loo, B.H., Fuel, **70**, 289 (1991).
15. McMillen, D.F., Chang, S.J., Nigenda, S.E. and Malhotra, R., ACS Div. of Fuel Chem. Prepr., **30** (4), 414, (1985).
16. Siskin, M., and Katritzky, A.R., "Reactivity of Organic Compounds in Hot Water: Geochemical and Technological Implications", Science **254**, 231 (1991).

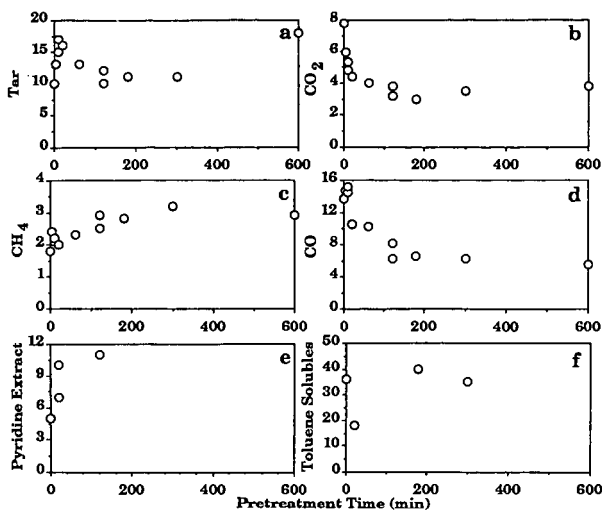


Figure 1. Results from Analysis of Zap Residues Produced by Water Pretreatment at 350°C, 4000 psig for a Range of Pretreatment Times. (a-d) Data on Pyrolysis Gas Yields from TG-FTIR Analysis; (e) Data for Extractables Yield Using Pyridine at Room Temperature; (f) Data for Toluene Solubles Yield from Donor Solvent Liquefaction. All Results are Given on a DAF Basis.

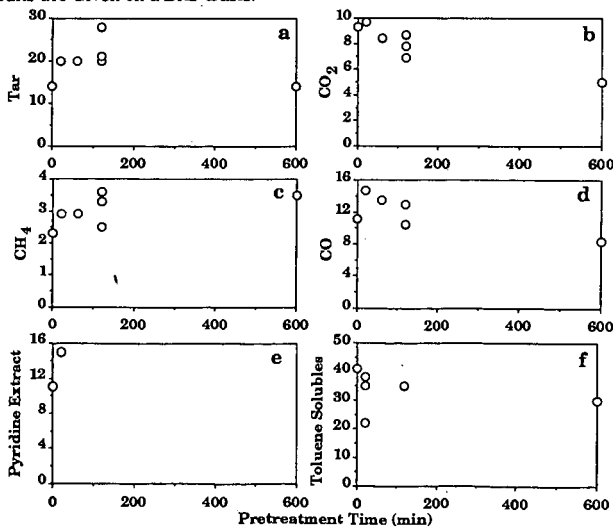


Figure 2. Results from Analysis of Wyodak Residues Produced by Water Pretreatment at 350°C, 4000 psig for a Range of Pretreatment Times. (a-d) Data on Pyrolysis Gas Yields from TG-FTIR Analysis; (e) Data for Extractables Yield Using Pyridine at Room Temperature; (f) Data for Toluene Solubles Yield from Donor Solvent Liquefaction. All Results are Given on a DAF Basis.

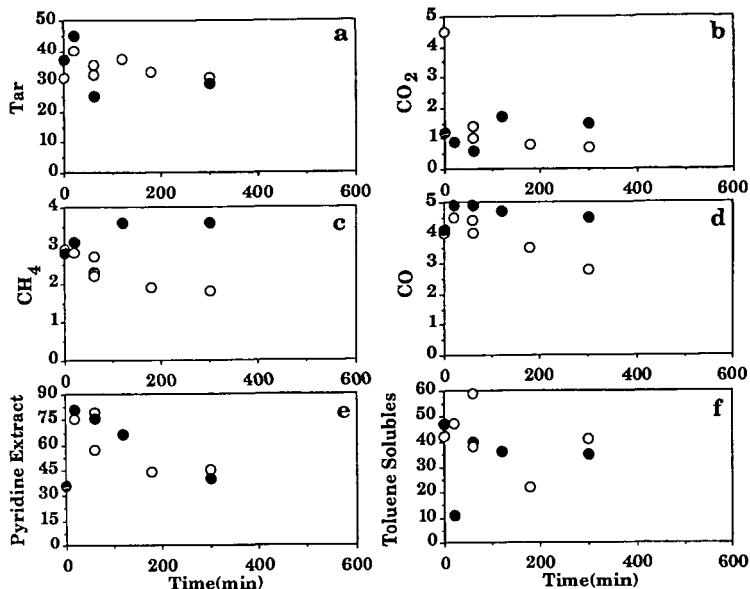


Figure 3. Results from Analysis of Illinois Residues Produced by Water Pretreatment at 350°C, 4000 psig for a Range of Pretreatment Times. (a-d) Data on Pyrolysis Gas Yields from TG-FTIR Analysis; (e) Data for Extractables Yield Using Pyridine at Room Temperature; (f) Data for Toluene Solubles Yield from Donor Solvent Liquefaction. All Results are Given on a DAF Basis. Solid Circles are for Freshly Opened Samples. Open Circles are for Samples which had been Previously Open.

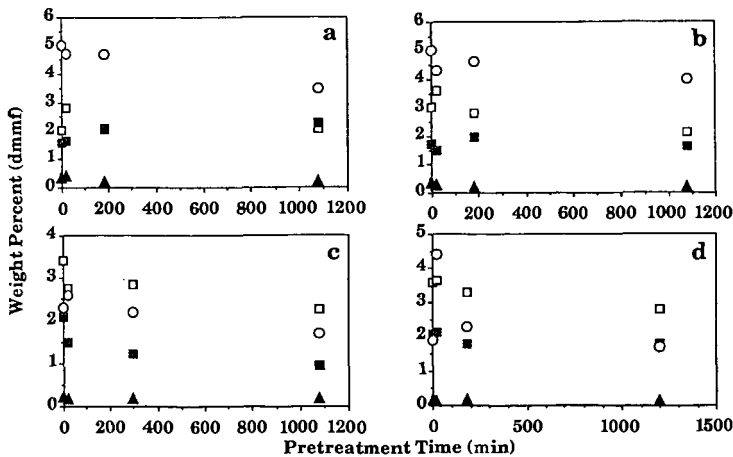
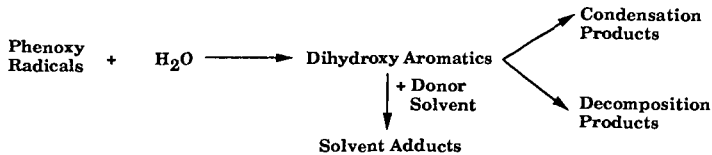
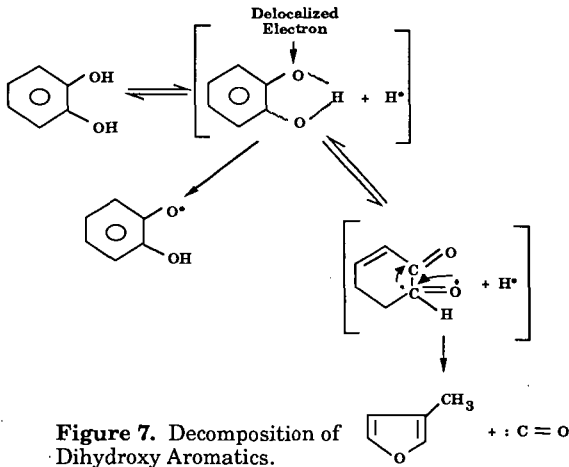
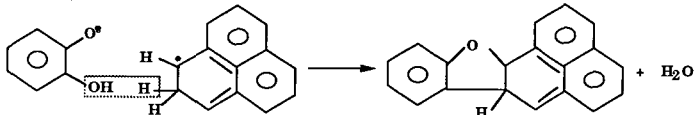
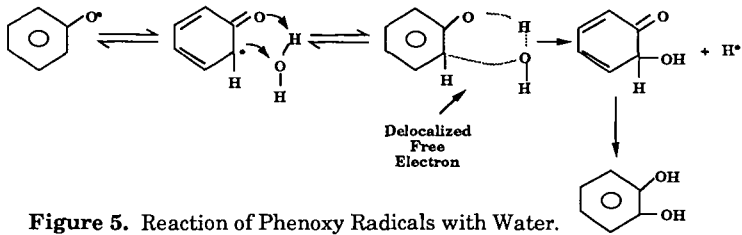


Figure 4. Results from FT-IR Analysis of Residues from Four Coals Produced by Water Pretreatment at 350°C, 4000 psig for a Range of Pretreatment Times. a) Zap; b) Wyodak; c) Illinois; d) Pittsburgh. □ - H_{al}; ■ - H_{ar}; ▲ - H_{OH}; ○ - O_{ether}.



OPTIMIZATION OF REACTOR CONFIGURATION IN COAL LIQUEFACTION

Alfred G. Comolli
Edward S. Johanson
L.K. (Theo) Lee
R. H. Stalzer

Hydrocarbon Research, Inc.
100 Overlook Center, Suite 400
Princeton, New Jersey 08540

Key Words: Liquefaction
CSTR - Continuous Stirred Tank Reactor
Fixed Bed Reactor

Introduction

The Department of Energy is sponsoring several Advanced Liquefaction Programs which taken together have the potential to reduce product costs from direct liquefaction to a level of \$25 per barrel. HRI has been selected to study the optimization of reactor configurations with a goal of developing a feasible cost-effective processing scheme that will result in an increased overall yield of higher quality distillates. HRI will evaluate combined ebullated-bed and fixed-bed processing, three ebullated-bed stages and interstage feed concentration following the primary reactor. Since the high pressure temperature reactors and associated equipment can comprise 15 to 20% of the capital costs of a grass roots plant, significant savings can result from improved reactor configurations and a decrease in required reactor volume. Further cost reductions will result from expected improvements in product selectivity (gaseous vs liquid) lower hydrogen consumption and better product quality by reduction of heteroatom content and increases in hydrogen content.

The configurations to be studied are :

- Incorporation of a fixed-bed, plug flow reactor after partial conversion and micronization of coal in an upstream CSTR (Continuous Stirred Tank) reactor.
- Comparison of three CSTR reactors with a two-stage system.
- Reconcentration of unreacted solids and residues between stages for improved kinetics in two stage CSTR systems.

An assessment of the preferred temperatures and volumes for multiple stages will also be conducted.

Background

The HRI CTSL⁽¹⁾ Process uses a relatively low temperature first-stage (750-775°F) and a higher second-stage temperature (815-825°F)⁽¹⁾. The first stage, with more favorable hydrogenation conditions, regenerates the hydrogen-donor capacity of the recycle solvent, while accomplishing a significant degree of coal liquefaction (conversion) and production of distillable liquids. The second stage completes the conversion of the coal and produces additional distillable liquids. This process offers a large improvement over earlier processes. With Illinois No. 6 coal over 95% liquefaction of MAF coal has been attained, with a yield of distillate oils (C₄750°F) of 78 W% of MAF coal. The CTSL Process employs an ebullated bed of catalyst, which maintains an expanded condition for catalyst and permits passage of large solid particles and avoids problems in dealing with highly viscous liquefied material especially in the first stages of the coal liquefaction reactions.

A principal debit of the ebullated bed reflects the fact that it is a relatively well mixed system with the reactive phase composition (and reaction potential) throughout the reactor corresponding to the product stream composition, in effect a CSTR (Continuous Stirred Tank Reactor) configuration. Such a mode has a kinetic disadvantage relative to that of a plug flow (fixed bed or packed bed) mode where the reaction potential declines progressively throughout the reactor only reaching that of product stream composition at the outlet of the reactor. This disadvantage of ebullated bed reactors is mitigated to a degree by staging, but even the two stage system requires greater reactor volumes especially when targeting very high conversion levels, in excess of 90%.

The first order (for coal concentration) modelling, using CSTR (Continuous Stirred Tank Reactor) reaction equations, has evolved from analysis of coal conversion results from CTSL and various modes of coal liquefaction experience at the HRI R&D center. Application of such a model requires identification of several species of coal types of different reactivity, more or less corresponding to various maceral types identified by petrographic analyses, although the correlating proportions have been developed from the actual two-stage CTSL, or single stage H-Coal, liquefaction results. Classification into three species (one unreactive) has proven adequate to rationalize CTSL experimental results giving coal conversion between 30% and 97% of MAF coal.

Hydrogen-transfer reactions from donor-solvent constituents in the liquid phase are a factor in coal conversion; however, in the correlation of CTSL results where the donor-solvent is generated in situ including this parameter has not been necessary, even though donor quality changes with catalyst deactivation. The overriding factor is that only small changes in conversion have occurred as the catalyst age in CTSL Bench Experiments.

These CTSL correlations are being tested in the current program and will be modified to fit the integrated reaction performance prior to projecting performance of the new reactor configurations.

Using first order kinetic modelling the various reactor configurations can be compared relative to two-stage CSTR performance. *Figure 1* compares reactor volumes to achieve certain coal conversions with Illinois #6 coal. For example as shown, a system following first-order kinetics at 95% conversion would require 130% greater reactor volume as a two-stage than as a plug-flow fixed bed system, all other kinetic factors being equal.

Fixed Bed Reactor

The application of fixed-bed reactors for direct coal conversions was extensively tested in the Synthoil[®] process as a first stage. Problems occurred with plugging, coking and rapid catalytic deactivation. HRI is testing fixed-bed hydrocracking in a second or third stage application where the unconverted coal and ash concentration averages from 10-20% and the particle size is generally less than 325 mesh (44 microns) compared to a typical feed concentration of 35 to 50% and a size of 50 mesh (300 microns). HRI's application as a finishing reactor at low temperature using trilobe catalyst for low pressure drop along with the lower concentration and smaller size should reduce plugging problems and will provide data for modelling.

A simple first-order model with identical rate constants and at a conversions of 95% in two-stages indicates that the CSTR Fixed-Bed would require only 55% of the reactor volume as the CSTR-CSTR configuration.

In modelling the CSTR-Fixed Bed and CSTR-CSTR systems on Black Thunder sub-bituminous, the plug flow option with an isothermal second stage could raise coal conversion by about 3.4% and lower the bottoms plus gas yield by 3.9% of dry coal, with 0.3 W% low hydrogen consumption. The indicated yield of distillates would be 4% higher than in the conventional arrangement, and this yield per unit of hydrogen consumption would be 9% higher.

Three Stage CSTR Systems

The addition of a third ebullated bed in series to the CTSL configuration would assuredly result in closer approach to plug flow-fixed bed potential and involves virtually no processing uncertainties.

The ebullated bed configuration in series differs from previous three stage concepts in control of stage temperatures to obtain an optimum interrelation of hydrogenation and cracking functions. A large part of previous efforts included a high temperature-short contact time pre-reaction of the coal slurry to maximize the degree of coal conversion. Apparently, such a pattern did not promote hydrogenation functions to the degree that would assure the best selectivity to light liquid products, which can be obtained from coupled multistage catalytic system.

It is recognized that three stage testing does not represent a radical innovation, since from the inception of the ebullated bed development it was recognized that the "stirred-tank" effect of the ebullated system has a kinetic disadvantage which could be mitigated in part by staged systems, two, three or more reactors.

However, the effort involves the three ebullated bed configuration largely as a reference for other essential innovations of this program, the use of a fixed bed as the third stage, or the incorporation of a practical method of reconcentration of heavy reactants before entering further staging.

A simple first order kinetic model, with equal temperatures in the stages, indicates that a three-stage system would require 25% less total reactor volume than the two-stage system at a conversion level of 95%.

The three-stage concept can be improved further through interstage product separation and reactant concentration and/or incorporation of a fixed-bed upgrading stage.

Product Stream Concentration

The concentration of primary reactants declines progressively in a plug-flow system and is lower stage-by-stage in a close-coupled, multistage CSTR system. More effective use of reaction space for the conversion of liquid and solid phase reactants can be promoted if their concentrations in the liquid phase could be maintained at higher levels and the hydrogen partial pressure increased. For example, in a three-stage CSTR system with simple first-order kinetics, attaining 95% conversion, the primary reactant concentration being fed to the third stage is about 15% of that in the feed to the first stage. Nominally, if the third stage feed concentration were raised to that of the original feed the proportion of reaction in the third stage could be correspondingly increased. Calculations based on the simple first-order model indicate that a three-stage system of CSTR reactors with reconcentration of the second stage product going to the third stage to obtain the same content of the reacting components as in the first stage feed would require only 43% as much total reactor volume to attain 95% conversion as would be needed in a conventional two-stage system with no interstage feed concentrations. Use of an interstage vapor/liquid separator offers the opportunity to increase the reactant (650 F° slurry) concentration, increasing subsequent stage hydrogen partial pressure (through fresh hydrogen addition), and decreasing the production of by-product light hydrocarbon gases (C_1-C_3) produced from further cracking of the 650 F liquid products.

Experimental

The feedstocks for this program are being obtained from interstage and product samples from HRI's CTSL Bench-Scale and PDU programs on Wyoming Black Thunder sub-bituminous and Illinois #6 bituminous coals.

The principal experimental systems that are being used are:

- A fixed bed microreactor with continuous liquid (slurry) and gaseous feeds.
- A 300 cc fixed bed reactor. This system represents a closer prototype to large scale equipment.
- A rapidly agitated microautoclave, 20 cc in volume, with very rapid heating and cooling. This apparatus used as a batch operation with and without catalysts is in a kinetic regime similar to a fixed bed plug flow reactor. Earlier experimental work has demonstrated kinetic effects of a pattern similar to those of prototype bench unit CTSL operations.
- A Robinson-Mahoney agitated reactor, containing a rotating catalyst basket, with a 1000 cc reaction volume. This system as a continuous flow operation corresponds to a catalytic CSTR configuration of the CTSL system with somewhat greater flexibility and simplicity of operation.

Plans

The program covers two years of activity, starting in October 1991 through September 1993. Experimental work is currently underway. Successful results from this program may be scaled to larger development units in a succeeding optional two year program.

References

1. A. G. Comolli, E. J. Johanson, "Evaluation of the Catalytic Two-Stage Liquefaction (CTSL) Process", Direct Liquefaction Contractors Conference, Pittsburgh, Pa., October, 1988.
2. P. M. Yavorsky, Sakhtar and S. Friedman, "Process Developments" Fixed Bed Catalysis of Coal to Fuel Oil". American Institute of Chemical Engineers Symposium Series Vol. 70 No. 137, 1974 pp.101-105.

FIGURE 1

REACTOR CONFIGURATION AND REACTOR VOLUME

First Order Kinetics

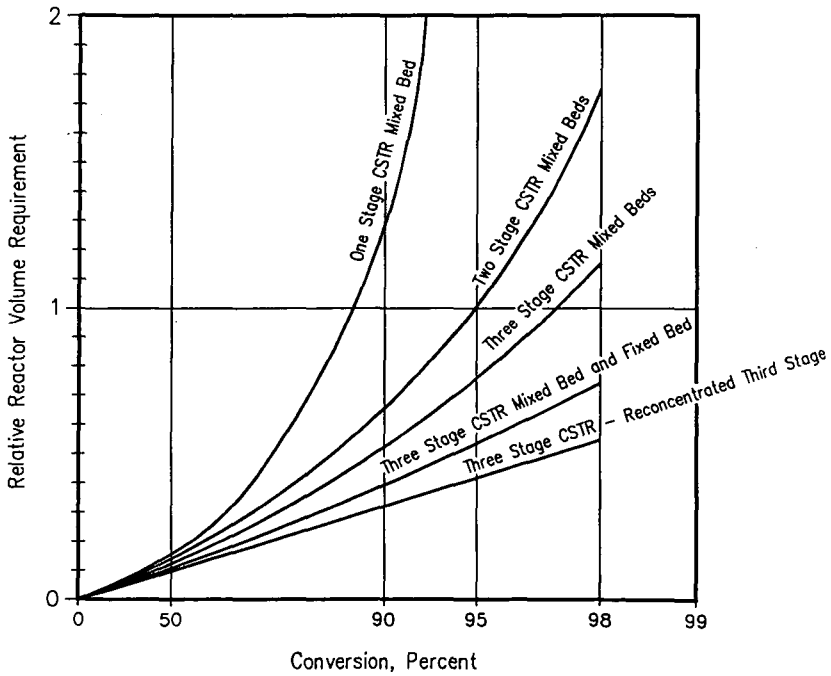


Figure 1. DT coal hydrogenation process, simplified flowsheet.
R, reactor. HS, IS, CS, hot-, intermediate-, cold separator.
VF, vacuum flash unit

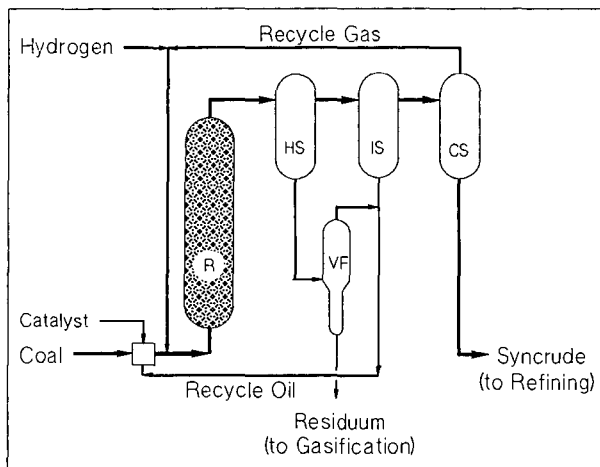


Figure 2. ASTM D-2887 boiling analyses of product and recycle oil from IGOR⁺ coal hydrogenation (dotted lines) and DT coal hydrogenation (solid lines).

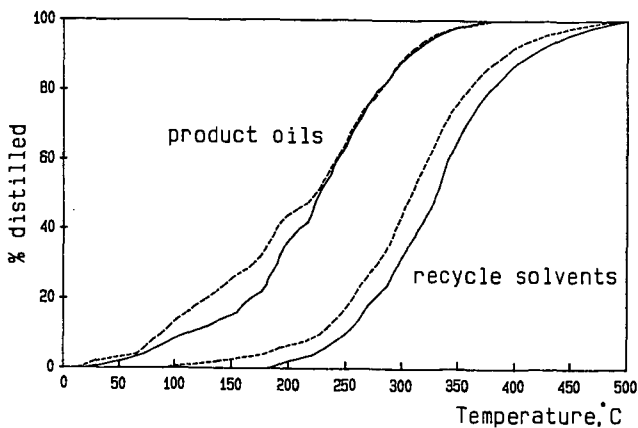


Figure 3. IGOR process, simplified flowsheet.

FB, fixed-bed catalyst. Other symbols, see Fig. 1.

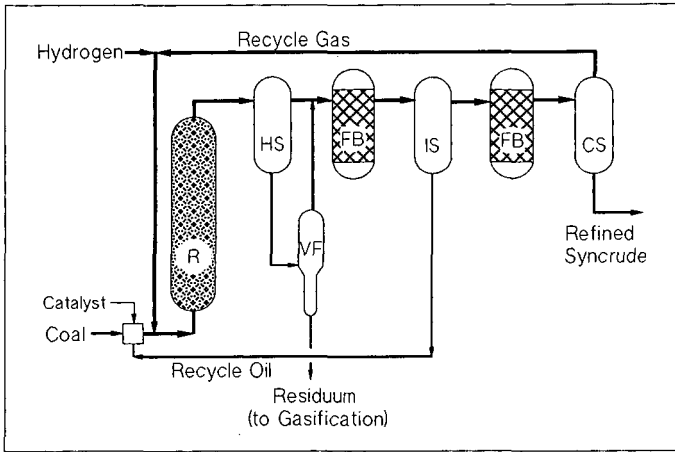
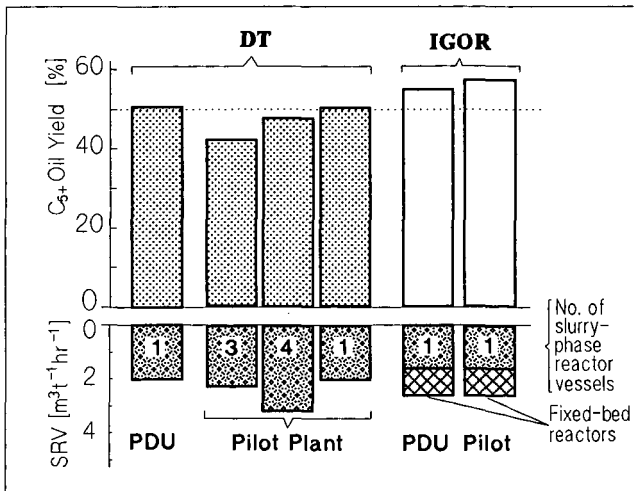


Figure 4. DT and IGOR process scale-up history.

SRV, specific reactor volume, d.a.f. coal basis.



IGOR - TAKING THE SHORT CUT IN COAL HYDROGENATION

B. O. Strobel
DMT Forschung und Prüfung, IKK 3
D-4300 Essen 13, Germany

R. Löring
RAG Oel und Gas, Gleiwitzer Platz 3
D-4250 Bottrop, Germany

Keywords: coal hydrogenation, upgrading, integrated refining, IGOR process

ABSTRACT

The primary liquids obtained from conventional coal hydroconversion processes all require extensive downstream hydrotreating. With a hydrotreating reactor appropriately integrated into a coal hydrogenation scheme, reformer/hydrocracker feed quality specifications can directly be attained, with only one process unit. A further modified arrangement even leads to significantly increased hydrocarbon oil yields from coal. The developing of the novel process, integrated gross oil refining (IGOR), is described. Results and experiences from PDU and from pilot plant operation are discussed.

INTRODUCTION

Several coal hydrogenation processes have been developed to technical maturity since coal-to-oil technologies were given a chance again. A good number of novel features have been successfully incorporated, but the competing schemes can all still be seen as mere modifications of the conventional high-pressure hydrogenation process: Apart from the processing steps they have all in common (slurry preparation, solvent recycle, indirect pre-heating, asphaltenes & solids separation, etc.), there is another joint feature. The primary coal-derived distillates ("syncrudes") are unacceptably high in oxygen and nitrogen contents and require extensive further refining prior to hydrocracking, reforming, or use as a marketable fuel whatsoever. (e.g.¹) Particularly in view of the black sediments that form even during short-term storage, and which are severely poisonous to upgrading catalysts, these syncrudes should only be taken with some reservations as the clean distillates they seem to be.

A further aspect which requires attention is, that the raw syncrudes have biological implications and are perceived as a potential health hazard at least in the working field. In syncrudes, primarily polynuclear aromatics, aromatic nitrogen bases, benzene, and phenols as well are of relevance to health considerations. It has therefore been recommended that the available coal hydrogenation processes be operated or modified such as to yield lower boiling and preferably saturated coal oils.² Developing an entirely different hydrogenation scheme might be another option, yet some way of integration of refining and saturation should already help to improve the technical, environmental, and probably also the economical preconditions for a future coal hydrogenation industry.

EXPERIMENTS AND RESULTS

A 0.2 t/d PDU and a 200 t/d pilot plant have been operated within the development work presented in this paper. All runs referred to in the following were carried out under 30 MPa total pressure, with a German HVBA feed coal and red mud as the catalyst in coal conversion. Commercial Ni-Mo-alumina catalysts were used in the fixed-bed reactors.

As for PDU operation, normally one week runs with the conditions maintained unchanged made a good basis for reliable data. With any mode of integrated refining, the runs were typically extended to last one month or more, primarily in order to make possible catalyst deactivation visible. For the same reason, these runs were repeated after several months.

DT Process Operation.

In order to explain the procedures and equipment used, we will firstly refer to the - earlier - DT process configuration (*Figure 1*), as this process provided the basis for the further developments.

A coal slurry is prepared from dried, ground coal, some powdered once-through catalyst, and a distillate-type process recycle oil. After treat gas addition (high-pressure recycle gas plus hydrogen make-up), the slurry is passed through heat exchangers and pre-heated to 420 °C. The upflow tubular reactor is operated as a rule at 475 °C. Still under process pressure, the reaction products are separated with a series of coolers/heat exchangers and stripper volumes: At about 450 °C minerals, unconverted coal, and little- and nonvolatile organic liquids are removed from the vapors and gases and let down from the hot separator. In a vacuum flash unit, some high-boiling overhead oil is recovered from the hot slurry, and a hot liquid underflow that contains around 50 % solids. The overhead oil is used as a recycle oil component, the underflow residuum as a liquid gasifier feed for hydrogen production.

The oil fraction condensed through appropriate temperature reduction (to around 300 °C) of the hot separator overhead vapors, is obtained as the intermediate separator letdown in just the amount required for coal slurry preparation. By further cooling of the high-pressure vapors and gases, the net syncrude yield condenses, along with process water which separates readily from the organic phase. - The high-pressure gases that leave the cold separator are oil-scrubbed for hydrocarbon gas reduction, and recycled to the hydrogenation unit.

DT Process Modification: Integrated Net Oil Refining.

Much as with practically any proven coal hydrogenation process, the syncrudes recovered from DT coal conversion will require extensive refining. With respect to their eventual utilization as motor fuels and possibly jet fuels, DT syncrudes have favorable boiling ranges (end points lie around 330 °C). But in order to meet the existing specifications for marketable fuels and hydro-conversion feed oils, respectively, the high concentrations of oxygen and nitrogen containing compounds as well as fused-ring aromatics need be radically reduced. Because of the essentially cyclic nature of coal-derived oils, comparatively severe conditions are required in the hydro-refining of such feed.

We found that it is not only viable but even advantageous to integrate a hydrorefining and saturation stage into a coal hydrogenation plant rather than running the units separately.³ With a fixed-bed catalytic reactor arranged downstream the intermediate separator, the product oil vapors are hydrotreated still before they are condensed and let down. Thus, by taking advantage of both the high-pressure, hydrogen-rich gas as well as the sensible heat of the separator overhead stream, appreciable savings in investment and energy costs can be realized.

Extended PDU runs established that the product oil qualities obtained with separate refining are attained with integrated refining as well. The total heteroatoms concentration - nitrogen, oxygen, and sulfur - can be kept well below 10 mg/kg. Oil yields from separate and from integrated refining, respectively, are naturally about the same: With the little reactive German bituminous feed coal, the yields of refined C₄+ oil amount to 54 % w/w on dry, ash-free coal in both cases.

Integrated Gross Oil Refining.

Further coal hydrogenation tests included a modified integrated refining scheme in which the fixed-bed reactor was arranged such as to hydrotreat not only the net product but also the oil continually recycled for coal slurry preparation ("gross oil refining"). The heavy distillate fraction - vacuum flash overhead oil - was injected before the reactor. With a liquid hourly space velocity four times the previous one and with the feed boiling range much higher at that, several hundred mg/kg hetero atoms were left in the net product oil. Net oil yield, however, had surprisingly soared to more than 60 %. Tracer and other investigations have made clear that the yield improvement is brought about thanks to a much extended liquid/solid residence time in the coal conversion reactor.⁴ The "driving force" is enhanced oil stripping which in turn is due to the more readily volatile recycle oil, see the boiling curves plotted in *Figure 2*.

With nitrogen contents between 80 and 100 mg/kg and even higher oxygen levels, the product oil fails to meet minimum feed specifications for further processing over bifunctional catalysts. In other words, the extra oil yield is obtained at the expense of quality, which additional hydrotreatment indispensable.

The process recycle oil, once equilibrated through continual recycling, will - simply speaking - behave as an inert diluent that does not undergo further hydrogenation reactions. Seen from this point of view, the fixed-bed reactor is merely treating the net product oil, though at an unfavorably high space velocity. Therefore, it seemed promising to apportion the catalyst filling into two separate but smaller reactor volumes, with the first one employed for gross-oil- and the second one for net-oil-treatment only (see *Figure 3*).⁵ The results received with this mode of operation fully answered the expectations, as both high oil yield and perfect quality were obtained now at the same time. This process mode was named IGOR⁺. It compares favorably with other processes as can be concluded from *Table 1* - in particular when considering the rather low reactivity of German bituminous coal. A synopsis of PDU results obtained with the various process modes discussed above is shown in *Table 2*.

DISCUSSION

Process operation experiences.

Even if quite obvious, it should be noted that IGOR⁺ product oil, thoroughly different from any syncrude, is water-white, stable in storage, and completely free of "that certain coal-oil smell". Less obvious, most of the process internal oil streams, particularly the recycle solvent inventory, have a merely faint, "clean" odor and separate easily from water. Moreover thanks to IGOR⁺, any biotoxic potential suspected in the previous process liquids has in all probability been removed. The improvement of the environmental conditions, in particular at the PDU with its frequently opened containers and its occasional leaks and spills, is unmistakable.

With the IGOR modes of operation, a new situation was encountered in coal slurry handling: Density and viscosity of the recycle oil had become too low to keep the solids suspended so that settling, pump failures, and other problems emerged. As a countermeasure, the earlier slurry viscosity was re-adjusted to its previous value by simply raising solids concentration from 42 to 51 % (coal-to-oil ratios, 1:1.4 and 1:1, resp.). As the slurry feed rate was not correspondingly reduced, this meant an increase in specific coal feed rate by 20 %. It turned out that, different from the DT process, oil yield suffered only little from the elevated specific coal feed rate. At the same time, apparently due to the reduced liquid feed load to the first fixed-bed reactor, product analyses showed no sign of oil quality reduction. Thus, a slurry solids concentration of more than 50 %, and a specific feed rate of 0.6 kg m.a.f coal per hour and per liter of reactor volume, became features of IGOR "standard" operation conditions.

Coal conversion temperatures in the IGOR process are somewhat lower than in the DT process which results in a reduced gas make and thus, in a comparatively lower hydrogen demand. Some extra hydrogen, on the other hand, is consumed in the methanation of the carbon oxides which takes inevitably place at the highly active refining catalysts. The coals that are typically fed to the process form only little carbon oxides (roughly 1 % on coal under DT process conditions) so this is certainly not too great a drawback. But a great advantage was found as well:

In any conventional coal hydrogenation process, continuous purge water injection is mandatory in order to prevent plugging of high-pressure gas lines with carbon dioxide derived salts, essentially ammonium carbamates. Hence sour water output is much higher than would be brought about from only hydrodeoxygenation and the coal moisture. With integrated refining there are no carbon oxides left, so purge water is no longer necessary. At the same time, refining has completely removed the phenols. Accordingly there is not only much less waste water to be treated but it does also no longer contain phenols that had to be dealt with. Total Organic Carbon had averaged 10,000 mg/kg in the conventional process (DT); with IGOR⁺, TOC values never exceeded 50 mg/kg.

Scale-up Experiences and Results.⁷

In most if not all direct coal liquefaction projects that were continued to pilot scale, the syncrude yields obtained in the PDUs could not be reproduced on a hundred-tons-per-day level [LIT X]. Initially, this was also true for the DT process. A single volume (11 l) made the PDU coal conversion reactor while a tanks-in-series reactor system was used on pilot plant scale, much as with the I.G. technology development. At identical specific coal feed rates, three tubular reactors (5 m³ each) gave significantly less oil yield on coal than had been obtained with the PDU. Even with a much lower specific feed rate - a fourth 5 m³ cylinder added - and with the reaction temperature elevated by 10 K in addition, oil yield still remained slightly below the PDU results. Contrary to all expectations, this changed when the cascade was replaced by a 15-m³ capacity, cheaper-to-fabricate "large-volume reactor". Now the results were exactly the same as those in the 1,400 times smaller unit.

The process was tested on pilot scale directly with the large-volume reactor; as the fixed-bed catalytic reactors, the 5-m³ cylinders were used. The results obtained were even somewhat more favorable than in the small-scale tests. In *Figure 4*, the above development history is illustrated and reviewed.

With the large KOHLEÖL pilot plant at Bottrop, still another benefit of the IGOR process could be demonstrated. It has been possible to bring the coal slurry up to reaction starting temperature exclusively through heat exchange with reaction product streams and preheating of the treat gas. In other words the slurry preheater, always an expensive and delicate component of the plant, was no longer necessary.

CONCLUSION

More recently in the PDU, a different bituminous coal - much more reactive yet higher in minerals at the same time (11 % ash, dry) - was processed under "standard" IGOR⁺ operation conditions. In the product oil, a total hetero atoms content of less than 5 mg/kg was achieved, and the C₄⁺ yield came as high as 66 % on d.a.f.coal.

Thus far in IGOR process testing, with totalized operation periods of up to 330 days, in neither of the two fixed-bed reactors were observed signs of serious catalyst deactivation. Presently, the only limitation foreseen is with feed coals that have too high an oxygen content and thus excessive carbon oxides formation, so that uneconomically much hydrogen might be spent in methanation.

The most apparent advantages of the process over its predecessors can be summarized as follows. IGOR⁺ means:

Reduced

- equipment needs
- recycle oil flow
- hydrocarbon gas formation
- waste water treatment requirements

Eliminated

- purge water injection
- carbon oxides
- phenols
- polynuclear aromatics & aromatic amines
- slurry preheater

Increased

- oil from coal yields
- specific coal feed rate
- coal concentration in the slurry feed

Improved

- product quality
 - naphtha cut ready for reforming,
 - gas oil cut ready for hydrocracking
 - or blending with diesel fuel
- working place environment
- overall plant operation
- process efficiency and economy

Rather than by splitting apart coal-to-oil conversion into discrete stages that can be individually optimized but will also suffer from individual idiosyncrasies, good yields of clean hydrocarbon liquids are also accessible in a more straightforward method using a relatively simple, integrated hydrogenation process.

ACKNOWLEDGMENT

Funding of the KOHLEÖL development program by the Minister für Wirtschaft, Mittelstand und Technologie des Landes Nordrhein-Westfalen is gratefully acknowledged.

REFERENCES

- 1 Döhler W., Graeser U., Hallensleben J., Jankowski A. (1983), *Erdöl und Kohle* **38**, 370-372.
- 2 Wilson B.W., Mahlum D.D., Pelroy R.A. (1986), *Fuel Processing Technol.* **13**, 1-16.
- 3 Ruhrkohle AG: US 4,602,992.
- 4 Strobel B.O., Schubert H., Clark K.N. (1991), Proceedings, *1991 Int. Conf. Coal Science*, Newcastle-upon-Tyne, UK, 823-826.
- 5 Ruhrkohle AG: US 4,602,992.
- 6 Peluso M., Schiffer A.N., Schindler H.D. (1981), Symp. Paper, *Coal Technology 81*, Houston, Tx.
- 7 Anon. (1988), *Kohleölanlage Bottrop, Abschlußbericht*. Ruhrkohle AG, Veba Oel AG. Essen, Gelsenkirchen.

Table 1. Syncrude yields and properties from different coal hydrogenation processes.
[Data partly after Peluso et al.⁶]

PROCESS:	EDS	H-Coal	ITSL	SRC II	DT	IGOR ⁷
Feed coal	Illinois # 6	Indiana # 5	Kentucky # 9	Ruhr Gasflamm, Prosper		
- Carbon	% d.a.f. 77	78	78	79.5	85	
C ₄₊ Oil yield	% on d.a.f. coal 39	50	56	43	55	60
Oil Inspection:						
- Boiling end	ASTM D86, °C 520	520	450	480	330	331
- Hydrogen	% 11.2	10.7	10.7	9.6	10.0	13.7
- Oxygen	mg/kg 15,000	15,000	7,000	35,000	27,000	< 5
- Nitrogen	mg/kg 3,000	3,000	4,000	1,400	9,000	< 2
- Sulfur	mg/kg 800	800	800	2,000	800	< 1

Table 2. Feed and product characterization for DT and IGOR process modes.

		PROCESS:	DT	IGOR	IGOR ⁺
Feed Coal		Ruhr Gasflamm, Prosper (HVBA)			
Proximate analysis					
Ash				5.1	
Volatile matter	% dry			36.5	
Elemental analysis					
Carbon	% d.a.f.			84.8	
Hydrogen	"			5.6	
Oxygen	"			7.2	
Nitrogen	"			1.5	
Sulfur	% dry			1.0	
PDU Operation Conditions:					
Specif. d.a.f. coal feed rate	kg ltr ⁻¹ hr ⁻¹		0.5	0.5	0.6
Coal/oil ratio in slurry feed	kg kg ⁻¹		1 : 1.4	1 : 1	1 : 1
Total pressure	MPa		30	30	30
Reaction temperature	°C		475	470	470
Catalyst in coal conversion	(dispersed)	red mud	red mud	red mud	red mud
Catalyst in hydrotreating	(fixed bed)	—	Ni—Mo	Ni—Mo	Ni—Mo
Hydrogen consumption	% on d.a.f. coal		6.7	9.3	9.0
Product Yields:					
C ₄₊ Net product oil	% on d.a.f. coal		55	61	60.5
Flash residuum [a.f. basis]	"		24	20	21
C ₁ —C ₃ Hydrocarbon gases	"		20	18	17
Reaction water & inorg. gases	"		7.5	10	10
C ₅₊ Oil Inspection:					
Density @ 20°C	g cm ⁻³		0.930	0.844	0.833
Boiling analysis, ASTM D86					
I.B.P.	°C		96	87	80
10 %	"		144	127	115
30 %	"		196	183	175
50 %	"		222	226	220
70 %	"		250	252	251
90 %	"		290	289	289
F.B.P.	"		330	331	331
Elements					
Hydrogen	%		10.0	13.0	13.7
Oxygen	mg/kg		9,000	85	< 5
Nitrogen	mg/kg		27,000	160	< 2

HIGH CONVERSION IN COAL LIQUEFACTION WITH LOW HC GAS PRODUCTION

W. H. Wiser, J. Shabtai, Q. Yang and Z. Yang

Department of Fuels Engineering
University of Utah
Salt Lake City, Utah 84112

INTRODUCTION

For the past 30 years or more the projected cost of producing a synthetic crude from coal has been from 50% to 100% (sometimes more) higher than the cost of crude petroleum at the time of comparison. The work in this research program addresses that fact, and represents an attempt to significantly reduce the cost of producing liquids from coal. Inasmuch as hydrogen is an expensive reactant, a principal objective in this research is to avoid large-scale use of hydrogen, to be achieved by minimizing the production of hydrocarbon gases in the conversion process. It is noted that one can exercise much greater control over the chemistry intended to occur in a system if the reactions can be carried out in a fluid phase, liquid or gaseous, compared with reactions in the solid phase. This is particularly true when coal is the solid-phase reactant. An objective in this work, therefore, is to proceed from solid coal to a liquid as inexpensively as possible.

A process for direct conversion of coal to liquids usually begins by slurring the coal in a liquid. Inasmuch as there does not exist a reliable technology for introducing dry solids into a region in which pressures of 1500 psig or higher must exist, slurring the coal in a liquid is used to permit pumping the coal into the pressurized region. The presence of a liquid phase surrounding the coal particles after introduction into the reactor, as well as inside of the pores and channels of the coal, inhibits heat transfer into the particle by any means one may choose to use to heat the coal particles to reaction temperature (generally above 400 °C), resulting in residence times in the hot zone of many minutes, characteristically between 15 minutes and one hour. One loses control over most of the chemistry of the process. Specifically, when the coal and its primary conversion products are exposed to temperatures above 375 °C for such long periods of time, many thermal degradation reactions occur, most of them undesirable. These reactions lead to high yields of hydrocarbon gases, hence high hydrogen consumption. They also lead to asphaltene production, making the downstream processing of the liquids more difficult.

The experiments being conducted in this work were designed to examine the chemistry which may occur when the coal particle

is heated to reaction temperature in times of one or two seconds, and the liquefaction process to form primary liquids is completed in times measured in seconds rather than minutes. It was expected, and is now observed, that conversions greater than 70% by weight of the coal, accompanied by ratios of liquids/HC gases of 10/1 or greater, can be achieved. The question of how coal may be introduced into a system to achieve these results, a question probably in the mind of the reader, is not an objective of this research program. However this question is now being addressed in a proposal now in preparation. The theoretical considerations which underlie that concept indicate a reasonable promise of success experimentally.

EXPERIMENTAL

Two reactor systems have been designed and constructed, namely a batch micro-reactor and a continuous-flow tubular reactor.

A sketch of the micro-reactor is shown in Figure 1. The reactor has an internal volume of 107 cc, and is constructed of stainless steel. It is designed to accommodate pressures up to 3000 psig at temperatures up to 600 °C. The coal sample is supported on a stainless steel gauze, attached to two electrodes to provide for electrical heating. A thermocouple is mounted immediately above the wire gauze, not touching the gauze but such that it will be embedded in the coal sample. A second thermocouple is placed to read temperatures in the gas space between the coal sample and the wall of the reactor. Cooling coils are located in the walls of the reactor, but they have not been required for experiments at the short times of these experiments. A special temperature controller was constructed which provides for rapid heat-up to the required temperature, while avoiding temperature over-shoot of more than a few degrees.

In a typical experiment, coal is crushed to pass through a 200 mesh Tyler Series screen (coal particles -74 microns). The soluble acid catalyst (see Table I) is impregnated into the pores of the dry coal, and the solvent evaporated. Two hundred grams of coal are placed on the wire gauze, exercising care to ensure that the coal particles completely surround the tip of the thermocouple. The reactor is closed, and pressurized with hydrogen to a calculated pressure such that the pressure at operating temperature will be about 1500 psig. At the completion of the experiment at a predetermined time, the reactor system is quenched. The gases are passed to a gas sampler, then to a wet-test meter. Gas samples are analyzed by gas chromatograph (GC). From the GC analysis and wet-test meter measurements, quantities of individual hydrocarbon gases are calculated. The liquids collected from the vessel are combined with liquids removed from the solids by extraction, and weighed. The solids are weighed.

The continuous flow reactor consists of a straight stainless steel tube, 5/16 inch inside diameter, heated by a series of electrical heating jackets, each operated from a temperature controller. The length of the reactor is increased by adding tube sections. Coal is prepared as described above, and fed to the reactor from a lock hopper utilizing a star feeder. Hot hydrogen gas is injected into the reactor with the coal. Residence times in the reactor are established by changes in gas flow rates, coupled with changes in coal feed rates by the star feeder, and by changes in reactor tube length. The products from the reactor pass through a solids separation vessel, maintained at the temperature of the reactor, then through two cooled vessels for liquids removal. The gases pass to a gas sampler, then to a wet-test meter. Determinations of product quantities and analyses are as described above.

RESULTS AND DISCUSSION

Representative experimental data from the microreactor are presented in Table I. The coal sample consisted of 200 mg of a Wyodak sub-bituminous coal. The experiment was conducted as described above. After 20 seconds, the system was quenched, and products removed and analyzed as described above. Fifty percent by weight of the coal was converted to liquids and gases in this experiment, with a ratio of liquids/HC gases of 10.6/1.0. The extracted char was then used as the solid feed for a second pass of 20 seconds duration. An additional 58% of the char (representing 29% of the original coal), was converted in this second pass, resulting in a total conversion of 79% by weight of the coal. In the second pass the ratio of liquids/HC gases was extremely high, namely about 23/1. When the results of the two passes are combined, the overall ratio liquids/HC gases is 15/1. Duplicate experiments revealed very good reproducibility of the data.

The data of Table I reveal important information relative to the potential for conversion of coal to high liquid yields with low yields of hydrocarbon gases. In the microreactor the coal sample sits on the heating mantle, with the thermocouple buried inside of the coal sample. The thermocouple indicated achieving reaction temperature in the coal sample in about 2-3 seconds. A second thermocouple located midway between the coal sample and the wall of the reactor indicated a maximum temperature at that location in the gas phase of 80 °C. During the experiment of 20 seconds (per pass) as the coal structure is depolymerized and molecules formed, made possible in large yields by the catalyst, much of the liquid-size molecules with sufficient vapor pressure at 500 °C distill from the residual coal mass to be almost instantly quenched in the surrounding gas phase, which is at a temperature well below that required for extensive cracking of these molecules, thus leading to very low gas yields. Under

these conditions, in the first pass those easily-released units in the coal, which upon release yield HC gases, together with any HC gases formed by thermal cracking, constitute not more than about 8% by weight of the total products evolving from the residual coal in that pass (approximately 4% of the weight of the original coal). The additional gases formed following the first pass constitute an extremely small portion of the products evolving during the second pass (about an additional 1% of the weight of the original coal). Thus the results in Table I reveal a liquid yield of about 74% by weight of the coal, while limiting hydrocarbon gases to about 5% by weight of the coal.

A sample of the data obtained from experiments conducted in the continuous-flow tubular reactor are presented in Table II. The coal utilized in this experiment was also a Wyodak sub-bituminous coal. Gas-flow rates in this experiment indicated a solids (and products) residence time in the reactor of about 17 seconds. In the first pass of the solids through the reactor, about 56% of the coal, by weight, was converted to liquids and gases, with a ratio of liquids/HC gases of 8.3/1.0. Following removal of the liquids from the solids by extraction, these solids were fed to the tubular reactor for a second pass, under reactor conditions identical to the first pass. In the second pass, 37% of those solids (representing about 16% by weight of the original coal fed in the first pass) was converted, for a total combined conversion in the two passes of 72%. The ratio of liquids/HC gases in the second pass was about 14/1, and the overall ratio liquids/HC gases for the two passes was 9.5/1.0.

The mechanics of the liquids and solids in the continuous-flow system utilized in these experiments are different from those which obtain in the microreactor, leading to lower ratios of liquids to HC gases. However one can visualize a continuous-flow system which may give yields and product ratios approaching those observed in the microreactor system. It may be difficult to operate such a system configuration at a bench scale.

The liquid products obtained from reactions of the Wyodak coal in the microreactor in the presence of MoS_2 or $\text{FeCl}_3 \cdot 6\text{H}_2\text{O}$ catalyst were subjected to GC and FTIR analysis.

Gas chromatography on a 12-ft x 1/8-in column packed with 8% OV-17 on 100-120 mesh Chromosorb HP indicated that essentially all of the product components are distillable between ca 100-300 °C. The chromatogram consisted of well-resolved peaks corresponding to low-molecular weight cleavage products. The chemical compound types present were clarified by FTIR analysis of product films, using a Perkin-Elmer, 1600 Series FTIR Spectrometer. Figure 2 provides an example of FTIR spectra for the liquid products.

The spectrum indicates the presence of several types of functional groups and characteristic aromatic ring substitution patterns in components of the liquid product, as follows: phenolic (and possibly alcoholic and carboxylic acid) groups, (O-H stretching bands between $3200-3650\text{ cm}^{-1}$; non-associated OH groups, sharp band near 3640 cm^{-1} ; associated OH groups, broad band between $3250-3450\text{ cm}^{-1}$); CH_3 , CH_2 and CH groups in alkyl substituents (or paraffins) and CH_2 and CH groups in naphthenic rings (at least three C-H stretching bands in the $2830-2980\text{ cm}^{-1}$ region); carbonyl groups in esters and possibly carboxylic acids ($\text{C}=\text{O}$ stretching bands near 1731 and 1767 cm^{-1} , due to aromatic and saturated esters, correspondingly); aromatic rings (breathing band near 1602 cm^{-1}); CH_3 , CH_2 and CH groups (C-H bending maxima between $1340-1470\text{ cm}^{-1}$); phenolic and aryl etheric groups (C-O stretching bands in the $1150-1310\text{ cm}^{-1}$ region); penta-substituted aromatic rings, viz., a single non-substituted aromatic hydrogen (weak C-H out-of-plane bending band at 885 cm^{-1} ; low concentration); tetra- and penta-substituted aromatic rings, viz., 1 or 2 adjacent non-substituted aromatic hydrogens (C-H out-of-plane bending band near 861 cm^{-1}); tri- and tetra-substituted aromatic rings, viz., 2 or 3 adjacent non-substituted aromatic rings (C-H out-of-plane bending band at 811 cm^{-1}); ortho-disubstituted aromatic rings, viz., 4 adjacent non-substituted aromatic hydrogens (C-H out-of-plane medium-intensity bending band near 767 cm^{-1} and a strong bending band at 745 cm^{-1} , indicating relatively high concentration of this ring-substitution type); and monosubstituted aromatic rings, viz., 5 adjacent aromatic hydrogens (very weak band at 697 cm^{-1} ; very low concentration of this ring-substitution type).

The molecular weight distribution of product components and more precise structural information are presently being sought by GC/MS.

TABLE I

Experimental Data from the Microreactor

Coal feed: Wyodak sub-bituminous, -200 mesh

Reactor temperature: 500 °C

Reactor pressure: 1500 psig

Time at reactor temperature: 20 seconds per pass

Catalyst: $\text{FeCl}_3 \cdot 6\text{H}_2\text{O}$, impregnated from acetone solution

<u>Run No.</u>	<u>Pass</u>	<u>Pass % Conv. Liquids + HC gases</u>	<u>Cum. Conv. Liquids + HC gases</u>	<u>Pass ratio Liq/HC gases</u>	<u>Cumulative ratio Liq./HC gases</u>
23-1	1st	50.0	50.0	10.6	10.6
23-2	2nd	58.0	79.0	22.6	15.0

TABLE II

Experimental Data from the Continuous Reactor

Coal feed: Wyodak sub-bituminous, -65, +100 mesh

Reactor temperature: 450 °C

Reactor pressure: 1500 psig

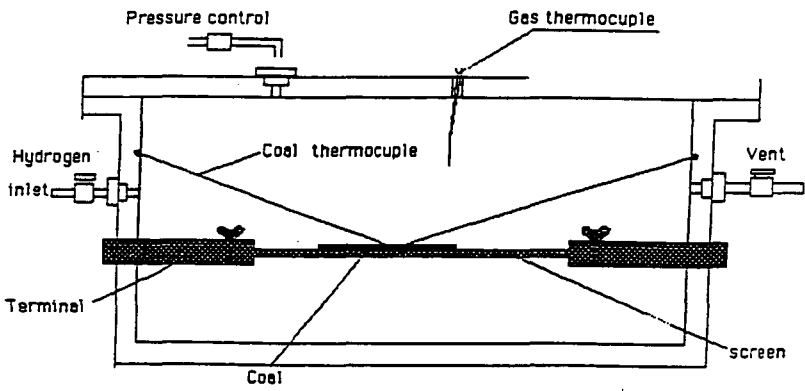
Gas flow velocity: 0.8 feet/sec

Catalyst: $\text{FeCl}_3 \cdot 6\text{H}_2\text{O}$, impregnated from acetone solution

Material balance: 93%, based upon dmmf coal

<u>Pass</u>	<u>Pass % Conversion Liq. + HC gases</u>	<u>Cumulative % Con. Liquids + gases</u>	<u>Pass ratio Liq/HC gases</u>	<u>Cumulative ratio Liq./HC gases</u>
1st	55.6 %	55.6 %	8.3	8.3
2nd	37.2 %	72.7 %	13.7	9.5

FIGURE 1
The Micro-reactor



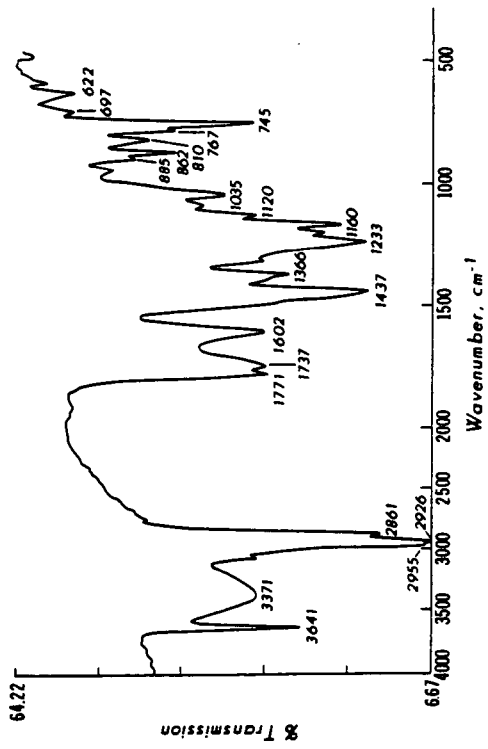


Fig. 2. FTIR Spectrum of Liquids from the Short Residence Time Procedure.

BIOLIQUEFACTION OF COAL SYNTHESIS GAS

K. T. Klasson, M. D. Ackerson, E. C. Clausen, J. L. Gaddy
Department of Chemical Engineering
University of Arkansas
Fayetteville, AR 72701

Keywords: synthesis gas, ethanol, coal bioliquefaction

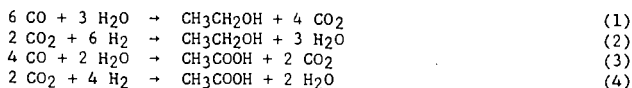
INTRODUCTION

Synthesis gas, a mixture of primarily CO, H₂ and CO₂, is a major building block in the production of fuels and chemicals. The gas may be produced from several sources, including coal, oil shale, tar sands, heavy residues, biomass or natural gas. Most synthesis gas is produced today by catalytic reforming of natural gas, although the partial oxidation of heavy liquids is also practiced (Graboski, 1984). Only a small percentage of the synthesis gas currently produced is by gasification of solid fuel. However, because of the large reserves of coal in the United States (300 year supply at the current consumption rate (Specks and Klussman, 1982)), synthesis gas production from coal will become an important technology in the future.

Coal gasification, which is a combination of pyrolysis and combustion reactions (Simbeck *et al.* 1982), produces a gas consisting of more than 50 percent H₂ and CO, the balance being a mixture of CO₂, CH₄, H₂S, COS and nitrogen compounds. The actual composition depends upon process conditions and the coal that is employed. The raw gas has a low to medium Btu content, with a heating value of 160-450 Btu/SCF, depending on whether air or oxygen is used during gasification (Coffin, 1984). Following quenching and purification, the synthesis gas contains 25-35 percent H₂, 40-65 percent CO, 1-20 percent CO₂, 0-7 percent CH₄ and other compounds in small quantities.

Catalytic processes may be used to convert syngas into a variety of fuels and chemicals, such as, methane, methanol, formaldehyde, acetic acid, etc. (Courty and Chaumette, 1987). Microorganisms may also be used to convert synthesis gas components into fuels and chemicals. Biological processes, although generally slower than chemical reactions, have several advantages over catalytic processes, such as higher specificity, higher yields, lower energy costs and generally greater resistance to poisoning. Furthermore, the irreversible character of biological reactions allows complete conversion and avoids thermodynamic equilibrium relationships.

Clostridium ljungdahlii, Strain PETC, was originally isolated from animal waste in the University of Arkansas laboratories, and is the only known organism capable of producing ethanol from CO, CO₂, and H₂ in synthesis gas (Barik *et al.* 1988). The overall stoichiometry for the formation of ethanol and acetate from CO and H₂/CO₂ has been established as (Vega *et al.* 1989a):



However, under optimal growth conditions, the organism produces acetate in favor of ethanol, with acetate:ethanol product ratios as high as 20:1 (Vega *et al.* 1989a). Research has concentrated on improving the product ratio in favor of ethanol using techniques found to be successful in boosting solvent production by other clostridial species. Improvements in solvent formation over acid production by clostridia have been obtained by utilizing nutrient limitation (Bahl *et al.*, 1986), reducing agent addition (Rao *et al.* 1987; Rao and Mutharasan, 1988), pH shift (Holt *et al.*, 1984; Huang *et al.*, 1986), hydrogen addition (Su *et al.*, 1981) and alternate medium constituents.

The purpose of this paper is to present results of batch and continuous laboratory studies with *C. ljungdahlii* in converting CO, CO₂ and H₂ in synthesis gas to ethanol. In addition, the effects of the sulfur gases H₂S and COS on growth, substrate uptake and product formation are presented and discussed.

MATERIALS AND METHODS

Organism and Medium. *Clostridium ljungdahlii*; Strain PETC, was originally isolated from chicken waste in the University of Arkansas laboratories, and later identified and characterized by Dr. R. S. Tanner, University of Oklahoma, Department of Botany and Microbiology. The culture was stored in a non-shaking incubator (Precision Scientific, Chicago, IL) at pH 5 and 37°C on a basal medium and synthesis gas (65% CO, 24% H₂ and 11% CO₂), and transferred every two weeks.

Equipment and Procedures. Medium preparation was carried in an atmosphere of 80% N₂ and 20% CO₂, as described by Hungate (1969) and Ljungdahl and Wiegel (1986). The initial pH was adjusted to 4.0-4.5 with HCl. Batch experiments were carried out in serum stoppered bottles with working volumes of 158 mL (Wheaton Scientific, Millville, NJ) or 1218 mL (Bellco Glass, Inc., Vineland, NJ). Continuous experiments were performed in Bioflo fermenters (New Brunswick Scientific, New Brunswick, NJ), modified for anaerobic operation. The medium used in the fermentations for the kinetic analyses contained yeast extract, vitamins, and minerals. The medium in continuous reactor studies and sulfur tolerance studies contained no yeast extract and minimal B-vitamins.

Analytical Procedures. Cell concentrations (in mg/L) were determined by comparing optical density readings at 580 nm in a Bausch and Lomb (Milton Roy Company, Rochester, NY) Spectronic 21 spectrophotometer with a standard calibration curve. Gas compositions were obtained by gas chromatography with a 180 cm Carbosphere, 60/80 mesh, column. Liquid analyses were performed by gas chromatography on previously acidified samples in a 60 cm column packed with Porapak QS at 180°C. 1-Propanol was used as the internal standard during liquid phase analysis after first verifying that 1-propanol was not present as a product.

RESULTS AND DISCUSSION

Development of a Kinetic Model. Figures 1 and 2 show cell concentration and substrate (CO) profiles for the conversion of CO to ethanol and acetate by *C. ljungdahlii* in batch culture. Initial CO partial pressures ranging from 1.0-1.6 atm in synthesis gas were used in order to study the effects of CO on cell growth and substrate uptake. A medium containing 0.01% yeast extract was used in this study.

Figure 1 shows that cell growth was essentially the same at each CO partial pressure up to a batch fermentation time of 100 h. At this time, the cell concentration increased with increasing CO partial pressure. The cell yield on CO, $Y_{X/S}$, was found to be 0.79 g cells/mol CO. The time for complete CO utilization was essentially constant with CO partial pressure (Figure 2). Also, the rate of CO utilization, as obtained from the slopes of the plots, was essentially constant with initial CO partial pressure. Product profiles (data not shown) showed ethanol to acetate molar product ratios of approximately 1:10 regardless of CO partial pressure due to the presence of yeast extract.

A kinetic analysis was performed on the data to determine kinetic parameters for growth and CO uptake utilizing a modified Monod model to include substrate inhibition (Andrews, 1969):

$$\mu = \frac{\mu_m P_{CO}^L}{K_p + P_{CO}^L + (P_{CO}^L)^2/W} \quad (5)$$

and

$$q_{CO} = \frac{q_m P_{CO}^L}{K'_p + P_{CO}^L + (P_{CO}^L)^2/W'} \quad (6)$$

The parameters μ_m , q_m , K_p , K'_p , W , and W' are kinetic parameters to be determined. A similar set of equations may be written for the uptake of H_2 , if desired.

The procedure for finding the kinetic parameters involves first finding the mass transfer coefficient, K_{La} , via material balance on the mass transfer-controlled gas-liquid system. The estimation of K_{La} involves finding the volumetric CO disappearance in the closed system, $-(1/V_L) dN_{CO}/dt$, and plotting it as a function of the partial pressure of CO in the gas phase. If part of the data fall on a straight line, mass transfer limiting conditions may be assumed. This generally occurs at low CO partial pressures or at high cell concentrations. The procedure is demonstrated in Figure 3. As noted in the figure, K_{La}/H equals 8.55 mmol CO/atm·L·h.

Once K_{La}/H is determined, the dissolved CO tension, P_{CO}^L (analogous to the dissolved CO concentration in the liquid phase), is found for situations where mass transfer is not controlling. The parameters in Equations (5) and (6) may then be found by rearranging the equations and performing a quadratic regression as illustrated in Figures 4 and 5 for the specific growth rate and specific uptake rate, respectively. A detailed presentation of this procedure has been shown previously for the bacterium *Peptostreptococcus productus* (Vega et al. 1989b).

Straight lines are obtained in plotting either P_{CO}^L/μ or P_{CO}^L/q as a function of P_{CO}^L (Figures 4 and 5), indicating that substrate inhibition was unimportant at least for $P_{CO}^L \leq 1.1$ atm. Furthermore, the intercepts on the

ordinates in both figures were essentially zero, indicating that K_p and K_p were negligible in comparison to P_{CO} . Thus, Equations (5) and (6) reduce to zero-order equations for *C. ljungdahlii* grown on CO, with $P_{CO} \leq 1.1$ atm.

and

$$\mu = \mu_m = 0.04 \text{ h}^{-1}$$
$$q = q_m = 42.7 \text{ mmol CO/g cell}\cdot\text{h}$$

If the specific uptake rate of CO is converted to a carbon mass basis, a value of 0.22 g C/g cell·h is obtained for q_m , which is comparable to the rate of glucose uptake by *Saccharomyces cerevisiae* with a q_m of 0.27 g C/g cell·h (Vega, 1985). This rate indicates that *C. ljungdahlii* has reaction rates equivalent to other organisms that are used for commercial fermentations.

THE USE OF CELL RECYCLE IN THE CSTR

A cell recycle apparatus was used in conjunction with a standard CSTR as a method to increase the cell concentration inside the reactor. This is particularly important since total product formation with *C. ljungdahlii* has been shown to be proportional to the cell concentration inside the reactor.

Fermentations were carried out in a 1.6 L CSTR with cell recycle. The total liquid volume in the reactor was 1.0 L, consisting of basal medium without yeast extract and one-half B-vitamins. Ammonium phosphate dibasic was used to enhance cell growth. The temperature of the reactor was held constant at 37°C and the agitation rate was 400 rpm. The gas flow rate was 16.5 mL/min and the liquid flow rate was 300 mL/d.

Figures 6 and 7 show cell concentration and product concentration profiles for the CSTR with cell recycle. In these experiments, the CO conversion was rather low. As is shown in Figure 6, the maximum cell concentration reached was 1300 mg/L at 800 h, increasing significantly from the 200 mg/L concentration after 300 h. The product concentrations, shown in Figure 16, changed significantly with time. At a time of 300 h, the ethanol concentration was about 4 g/L and the acetate concentration was nearly 2 g/L. At a later fermentation time of 800 h, the ethanol concentration reached 15 g/L with an acetate concentration of 4 g/L. Other cell recycle studies have shown a 6 g/L ethanol concentration with a corresponding zero acetate concentration.

SULFUR GAS TOLERANCE OF *C. LJUNGDAHLII*

Many bacterial cultures capable of converting CO to products have been found to be quite tolerant of the sulfur gases H₂S and COS (Vega et al., 1990; Smith et al., 1991). *Peptostreptococcus productus*, for example, which converts CO to acetate, is able to successfully convert CO to acetate in the presence of 19.7 percent H₂S or COS after culture acclimation. The methanogen *Methanobacterium formicicum*, on the other hand, is able to tolerate only 6.6 percent H₂S or COS. However, even this latter result is encouraging, since typical coal-derived synthesis gas contains only 1-2 percent sulfur gases, mainly as H₂S.

C. ljungdahlii, grown in the presence of Na₂S in place of cysteine-HCl as the reducing agent for several weeks, was evaluated for its tolerance to H₂S and COS in batch bottle experiments. The 155 mL bottles containing 50 mL of liquid medium devoid of yeast extract and adjusted to pH 4.3, were first gassed with synthesis gas to a pressure of 10.7 psig. The desired amount of H₂S or COS (2.5 mL-20mL) at 1 atm was then added. This batch system was allowed to equilibrate overnight. As a final step 10 mL of *C. ljungdahlii* were added prior to incubation at 34°C.

The effects of H₂S on growth and substrate uptake by *C. ljungdahlii* are shown in Figures 8 and 9, respectively. As is noted in Figure 8, growth was not significantly slowed at H₂S concentrations below 5.2 percent. Upon the addition of 9.9 percent H₂S, however, growth essentially stopped. Similar results are noted with substrate uptake in the presence of H₂S (see Figure 9). The presence of H₂S slowed the rates of substrate uptake only slightly up to an H₂S concentration at 5.2 mole percent. Similar results were obtained with concentrations of COS up to 5.2 percent.

These concentrations are for in excess of maximum sulfur gas concentrations possible in coal synthesis gas. It should also be realized that dramatic effects can be obtained with prolonged sulfur gas acclimation. *P. productus*, for example, was only marginally tolerant of H₂S and COS in initial studies. Concentrations up to 20 percent were tolerated after a period of acclimation to the sulfur gases.

CONCLUSIONS

The anaerobic bacterium *Clostridium ljungdahlii* has been shown to be effective in converting CO, CO₂ and H₂ to ethanol. Rates of carbon uptake by *C. ljungdahlii* comparable to the rate of carbon uptake by the yeast *Saccharomyces cerevisiae* have been obtained. A CSTR cell recycle system has been shown to be effective in permitting the cell concentrations necessary for high concentrations of ethanol. An ethanol concentration of 13 g/L with a corresponding acetate concentration of 4 g/L has been attained. Alternatively, an ethanol concentration of 6 g/L without the presence of acetate has been reported. Finally, *C. ljungdahlii* has been shown to be tolerant of H₂S or COS in concentrations exceeding typical levels in synthesis gas.

LIST OF REFERENCES

- Andrews, J. F. (1969), *Biotechnol. Bioeng.* 10, 707.
Bahl, H., Gottwald, M., Kuhn, A., Rale, V., Andersch, W., and Gottschalk, G. (1986), *Appl. Environ. Microbiol.*, 52, 167.
Barik, S., Prieto, S., Harrison, S. B., Clausen, E. C., and Gaddy, J. L. (1988), *Appl. Biochem. Biotechnol.*, 18, 363.
Coffin, J. M., (1984), *Energy Progress*, 4, 131-137.
Courty, Ph. and Chaumette, P. (1987), *Energy Progress*, 7, 23.
Graboski, M. S., (1984) In Catalytic Conversion of Synthesis Gas and Alcohols to Chemicals, R. G. Herman (ed.) Plenum Press, New York, pp. 37-50.
Holt, R. A., Stephens G. M., Morris, J. G. (1984), *Appl. Environ. Microbiol.*, 48, 1166.
Huang, L., Forsberg, C. W., and Gibbons, L. N. (1986), *Appl. Environ. Microbiol.* 51, 1230.

- Hungate, R.E. (1969), *Meth. Microbiol.* **3B**, 117.
- Ljungdahl, L. G., and Wiegel, J. (1986), Manual of Industrial Microbiology and Biotechnology (Demain, A. L., and Solomon, N. A., eds.), American Society for Microbiology, pp 84-96.
- Rao, G. Ward, P. J. and Mutharasan, R. (1987), *Annals N. Y. Acad. Sci.* **506**, 76.
- Rao, G. and Mutharasan, R. (1988), *Biotechnol. Letters*, **10**, 129.
- Simbeck, D. R., Dickenson, R. L., Moll, A. J. (1982), *Energy Progress*, **2**, 42.
- Smith, K. D., Klasson, K. T., Ackerson, M. D., Clausen E. C. and Gaddy, J. L. (1991) *Appl. Biochem. Biotechnol.*, **28/29**, 797.
- Specks, R. and Klussmann, A. (1982) *Energy Progress*, **2**, 60-65.
- Su, T. M., Lamed, R., and Lobos, J. H. (1981), "Effect of Stirring and H₂ on Ethanol Production by Thermophilic Fermentation," Proceedings of the Second World Congress of Chemical Engineering and World Chemical Exposition, Montreal, p. 356.
- Vega, J. L. (1985), M. S. Thesis, University of Arkansas.
- Vega, J. L., Prieto, S., Elmore, B. B., Clausen, E. C., and Gaddy, J. L. (1989a), *Appl. Biochem. Biotechnol.* **20/20**, 781.
- Vega, J. L., Clausen, E. C., and Gaddy, J. L. (1989b), *Biotechnol. Bioeng.* **34**, 774.
- Vega, J. L., Klasson, K. T., Kimmel, D. E., Clausen E. C. and Gaddy, J. L. (1990) *Appl. Biochem. Biotechnol.*, **24/25**, 329

ACKNOWLEDGMENT

The work presented in this paper was made possible through the financial support of the U. S. Department of Energy, Pittsburgh Energy Technology Center, under contract numbers DE-AC22-88PC79813 and DE-AC22-89PC89876.

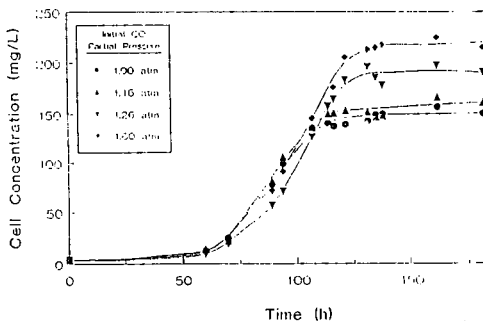


Figure 1. Cell Concentration Profile for the Fermentation of CO by *G. Ljungdahlii*

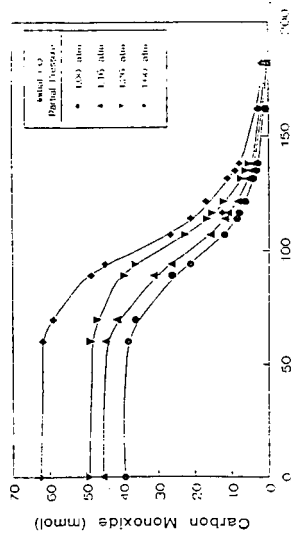


Figure 2. CO Profile for the Fermentation of CO by *S. limosus*.

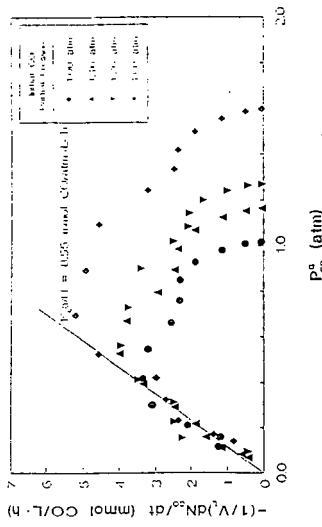


Figure 3. Determination of the Mass Transfer Coefficient for the Fermentation of CO by *S. limosus*.

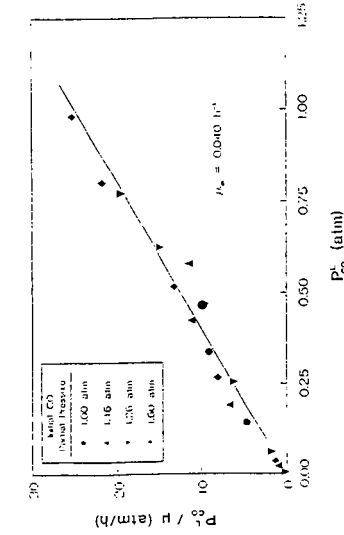


Figure 4. Determination of Monod Model Kinetics for the Rate of Cell Growth by *S. limosus*.

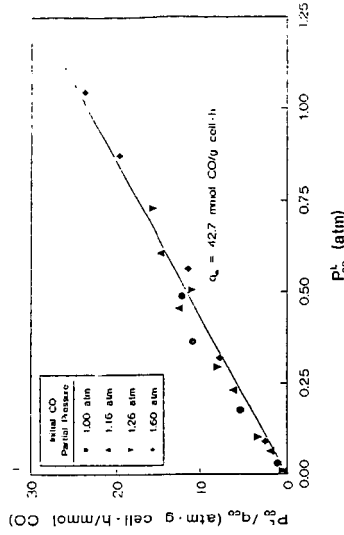


Figure 5. Determination of Monod Model Kinetics for the Rate of CO Uptake by *S. limosus*.

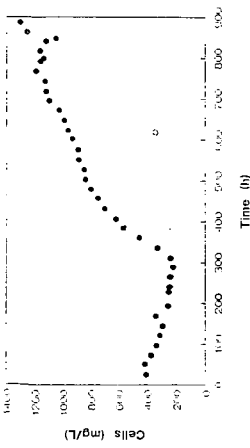


Figure 7. Ethanol and Acetic Acid Concentration Profiles for *E. Limbachi* in the CSTB with Cell Recycle

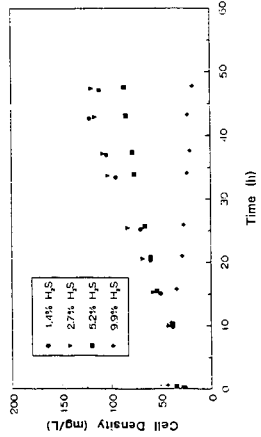


Figure 8. Cell Concentration Profile for *E. Limbachi* in the CSTB with Cell Recycle

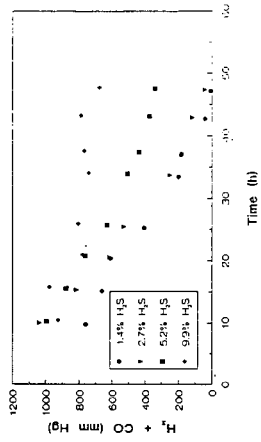


Figure 9. The Effects of H₂S on CO and H₂S in Batch Culture

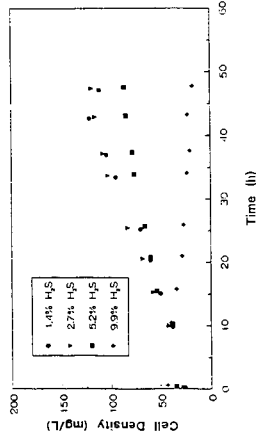


Figure 10. The Effects of H₂S on the Growth of *E. Limbachi* in Batch Culture

COPROCESSING OF COAL AND WASTE RUBBER

Malvina Farcasiu and Charlene M. Smith
U.S. Department of Energy
Pittsburgh Energy Technology Center
P.O. Box 10940, Pittsburgh PA 15236

Keywords: coal, rubber, coprocessing

ABSTRACT

The disposal of used tires, the main source of waste rubber, is an important environmental problem. We describe a method to transform used rubber tires into useful liquid products by coprocessing them with coal. Carbon black, an important constituent in rubber tires, provides a good hydrocracking catalyst during coprocessing. Due to the presence of carbon black in the rubber tires, the yields of liquids obtained by coal-rubber tires coprocessing are superior to those that could be obtained by coprocessing rubber with coal in the absence of carbon black.

INTRODUCTION

Over 200 million used rubber tires are discarded each year in the United States¹. When not indiscriminately dumped, they are usually either stockpiled or landfilled. Neither of these methods of disposal is likely to be accepted in the future, and major efforts are under way to find more environmentally acceptable solutions for the disposal of used rubber tires. Recently, Gillen² and D. J. Stopek, et al.³ reported successful coal-used rubber tires cofiring tests in power plants in Ohio and Illinois, respectively.

A different possible approach for the use of rubber tires is their coprocessing with coal to obtain liquids⁴. In this approach, we can take advantage of both the high hydrogen content of the organic material in rubber tires and of the good solvent properties of the depolymerized rubber to aid coal liquefaction. Also, the carbon black, a major constituent of rubber tires, can act as a catalyst in the process⁵⁻⁷. The liquids produced in coprocessing coal and tires could be a source of transportation fuels, or could be used in the production of new tires by replacing the petroleum-based aromatic oil. The unreacted coal and the carbon black remaining from tires can then be burned.

EXPERIMENTAL

The materials used in these experiments were: Illinois #6 coal, 20 mesh; tread material from a highway-collected rubber tire; vulcanized tread material; styrene-butadiene rubber; cis-polybutadiene rubber; aromatic oil provided by Dr. E. T. McDonell, Michelin America Small Tire Co. Akron, Ohio; elemental sulfur (Fisher Scientific Co.); and carbon black Mogul L (138 m²/g) provided by Cabot Corp. The elemental analyses of tires and of the coal used in these experiments are given in Table 1. The composition of the tread material as provided by E. T. McDonell is given in Table 2.

Liquefaction Experiments. The liquefaction experiments using shredded rubber tire materials and coal were performed in a laboratory shaker autoclave. In all experiments described, the reaction temperature was 425°C, the reaction time was 60 minutes, and the initial hydrogen pressure (at room temperature) was 1000 psi. The relative amounts of materials are given in Tables 3 and 4. In a typical liquefaction experiment the total amount of materials was 6-7 g.

After liquefaction, the liquid and solid products were separated by methylene chloride extraction followed by filtration. After the removal of methylene chloride by evaporation in a rotary evaporator, the residue was extracted with heptane, the soluble part separated again by filtration, and the heptane removed by evaporation in a rotary evaporator.

The conversion was calculated as the percent of the methylene chloride soluble materials vs. the initial organic materials in the reactants. For convenience of discussion, the heptane-soluble fraction will be defined as "oils" and the heptane-insoluble, methylene chloride-soluble fraction of the products as "asphaltenes." The insoluble solids are: unreacted coal, mineral matter from coal, and carbon black and zinc oxide from rubber tires.

The elemental analyses were performed by Huffmann Laboratories, Golden, CO and by PETC.

RESULTS AND DISCUSSION

Several tests were performed to test the concept of coal-rubber tire coprocessing and to assess the properties of the liquids obtained. The organic material from both highway-collected rubber

tire material and the tread material provided by Michelin are converted completely to liquid, heptane-soluble materials when processed alone under the above described conditions. In both cases the gas formation was under 1%. When shredded rubber tire material and Illinois #6 coal were coprocessed, coal conversions to methylene chloride soluble materials were ~51% and ~56% respectively, when the ratio of organic materials from tread and coal was 0.74 : 1 and 1.4 : 1. For comparison, when Illinois #6 was liquefied under the same experimental conditions in the presence of tetralin⁸ (ratio tetralin : coal, 2 : 1, by weight) the coal conversion was 57 %. The percent of heptane-soluble material obtained from coal was 31 % when the liquefaction was performed in the presence of tetralin⁸, and 37 - 41 %, when the liquefaction was performed in the presence of rubber-tread material⁴. The heptane-soluble oils that constitute the majority (~87 %) of the liquefied material are rich in hydrogen (Table 3).

As can be seen from the data in Table 2, carbon black is an important constituent of rubber tire material. From the information received from Dr. McDonnell¹, the usual surface area of the carbon black used in rubber tires is around 100 m²/g. We have found carbon blacks to be good catalysts in hydrocracking reactions⁵⁻⁷. We hypothesized that the carbon black present in rubber tires could exhibit catalytic activity during coal-rubber tire coprocessing. To check this assumption, coprocessing experiments were performed in the presence and in the absence of carbon black. When coal and a mixture of all the components of the tread material described in Table 2 were coprocessed, the conversions were very similar (~71%) to those obtained with the vulcanized tread material, and the gas production was under 1%. However, when the coal was coprocessed with the same components of tread material except carbon black the conversion decreased to 60% and the gas production increased to 6% (Table 4). Elemental analyses of the heptane soluble liquid products obtained in the experiments described in Table 4 are given in Table 5.

Comparative data for conversion to liquids (71% vs. 60%) when the coprocessing is performed in the presence and in the absence of carbon black indicate its role during coprocessing. The reduction in the quantity of gas formed when coprocessing is performed in the presence of carbon black (1% gases) versus in the absence of carbon black (6% gases) suggests the possibility that the aromatic fragments from coal products or rubber are alkylated with aliphatic fragments formed during rubber depolymerization. We have not yet succeeded in the unequivocal identification of such reactions, but

work with model compounds will soon be started.

Work with model compounds⁵⁻⁶ has shown that carbon blacks are good catalysts at temperatures lower than those described in this paper, and that their catalytic activity at constant concentration is dependent on the surface area. Two logical developments of rubber tire-coal coprocessing studies would be 1. Coprocessing at lower temperatures (350-400°C), and 2. Coprocessing in the presence of high surface carbon blacks. The carbon blacks currently used in the rubber industry have surface areas in the range of 100 m²/g, but carbon blacks with surface areas over 1400 m²/g are commercially available⁶.

Data in Table 2 indicate that a heavy petroleum fraction ("aromatic oil") is used in a rather large concentration (20% by wt. in the tread material) in rubber tires. Since an automobile tire contains about 15 pounds of organic materials (i.e., 3 lb aromatic oil), a production of about 200 million rubber tires per year will require about 600 million pounds (273,000 tons) per year of aromatic oils. Preliminary results (Table 6) indicate that at least a part of this oil could be generated from coprocessing coal with used rubber tires, so that a valuable, hydrogen-rich material can be recycled.

From a process viewpoint, it may be advantageous to recycle a part of the liquid product, so that a feed slurry of coal and shredded rubber tires can be manipulated more easily. Also, our data with model compounds^{5,7} indicate that high pressure is not necessary for reactions in the presence of carbon black. Both lines of research deserve further study.

CONCLUSIONS

Our experimental results show that the coprocessing of used rubber tire and coal can provide an alternative use for waste rubber materials. The liquids formed in this coprocessing are hydrogen rich and are a potential source for the aromatic oil component in new tires. Also, these liquids can be a source of transportation fuels.

ACKNOWLEDGEMENTS

We want to express our gratitude to Dr. E. T. McDonell of Michelin America Small Tire Co., Akron, Ohio, for providing us with samples of vulcanized rubber materials, and the components used in the manufacture of rubber tires, as well as for the information

concerning the composition and disposal problems related to rubber tires. We want to thank A. V. Cugini and his research associates at the Pittsburgh Energy Technology Center for their help with shaker bomb experiments.

The technical discussions with Dr. B. Blaustein, PETC, and his editorial help are gratefully acknowledged.

This research was supported in part by an appointment to the Postgraduate Research Training program under Contract DE-AC05-76OR00033 between U.S. DOE and Oak Ridge Associated Universities (C.M. Smith). C. M. Smith's current address: Corning Incorporated Polymer Research Department, Corning, N.Y. 14831.

DISCLAIMER

Reference in the paper to any specific commercial product, process, or service is to facilitate understanding and does not necessarily imply its endorsement or favoring by the United States Department of Energy.

REFERENCES

1. McDonell, E. T.; Michelin America Small Tire Co., personal communication.
2. Gillen, J. E.; Proceedings Eighth Annual International Pittsburgh Coal Conference. The University of Pittsburgh School of Engineering, Center for Energy Research, October 14-18, 1991, p. 859.
3. Stopek, D. J.; Millis, A. K.; Licklider, P. L.; Proceedings Eighth Annual International Pittsburgh Coal Conference. The University of Pittsburgh School of Engineering, Center for Energy Research, October 14-18, 1991, p. 865.
4. Farcasiu, M.; Smith, C. M.; U.S. Patent 5,061,363, October 29, 1991.
5. Farcasiu, M.; Smith, C. M.; Energy and Fuels 1991, 5, 83.
6. Farcasiu, M.; Smith, C. M.; Ladner, E. P.; Sylwester, A. P.; Prepr. Pap. Am. Chem. Soc. Div. Fuel Chem. 1991, 36, 1869.
7. Farcasiu, M.; Smith, C. M.; Hunter, E. A.; 1991 Proceedings of Conference on Coal Science, ed. IEA Coal Research Ltd., Butterworth, Heinemann Ltd. 1991, p. 166.
8. Cugini, A. V., PETC; personal communication.

TABLE 1. Elemental analyses: rubber tires and Illinois #6 coal

Sample	Elemental composition Organic components, wt%			Inorganics wt. %
	C	H	S	
Illinois #6 coal	80.4	5.4	2.1	11
Rubber tire*	82.6	11.0	2.9	34**
Tread material*	85.3	11.0	2.9	34**

* Calculated elemental composition of the organic material after correction for the 34% of inorganic material present in tread material.

** The inorganics present as 34% of the tread consist of carbon black (33) and zinc oxide (1).

TABLE 2. Rubber tire (tread material) composition.

Composition	%
styrene-butadiene rubber	35
cis-polybutadiene rubber	8.5
aromatic oil (from petroleum)	20
carbon black	33
zinc oxide	1
sulfur	1

TABLE 3. Elemental analyses of heptane-soluble products obtained from liquefaction of used rubber tires and tread material.

Sample	Heptane-Soluble Products Elemental Analysis, wt.%		
	C	H	S
Used rubber tire	86.5	10.9	0.4
Illinois #6 / used rubber tire (1/1.4 by wt. organics)	84.5	10.5	0.5
tread material (Michelin)	88.9	10.1	0.1
Illinois #6/tread material (1/0.74 by wt. organics)	87.8	9.7	0.5

TABLE 4. Coprocessing of coal and rubber materials in the presence and absence of carbon black.^a

Sample		#Conversion (wt. %)			Liquids Composition	
Rubber	Coal	All	rubber	coal	Oils	Asphaltenes
1. Tread mat.	none	100	100	-	100	0
2. Tread mat.	yes	71	43	28	89	11
3. Tread comp*	yes	73	43	30	84	16
4. Tread.mod**	yes	60	-	-	87	13

^aReaction conditions: 60 min, 425°C. Weight ratio organic materials in rubber/coal 0.74:1.

1 and 2. Vulcanized tread material (Table 2).

3. Tread material compounds (mixed in the proportion described in Table 2).

4. As 3, but without carbon black.

Based on methylene chloride soluble material.

* <1% gas.

** 6% gas.

TABLE 5. Elemental analyses of heptane-soluble fractions (Expt. identified in Table 4).

Exp.#	Elemental Analysis (wt. %)				
	C	H	N	S	O
1	88.9	10.1	0.25	0.13	1.2
2	87.8	9.7	0.36	0.47	1.7
3	87.5	9.5	0.56	0.47	2.0
4	87.5	9.4	0.36	0.57	2.2

TABLE 6. Comparative elemental analyses of petroleum based "aromatic oil" and heptane-soluble coprocessing products.

Sample	Elemental Analysis (wt.%)			
	C	H	N	S
"Aromatic oil"	86.8	10.2	-	2.28
Heptane-soluble (Table 5, Expt. 2)	87.8	9.7	0.36	0.47

LIQUEFACTION OF A SUBBITUMINOUS COAL IN THE PRESENCE OF NOVEL MICROEMULSION-BASED MOLYBDENUM CATALYSTS

N. Vaidyanathan, E. Boakye, K. Osseo-Asare and L.R. Radovic

Department of Materials Science and Engineering
The Pennsylvania State University, University Park, PA 16802

INTRODUCTION

The state of knowledge in catalysis of direct coal liquefaction has been reviewed recently by Derbyshire (1988). An efficient catalyst for coal solubilization and/or upgrading of coal liquids not only improves the yield and distribution of products but relaxes some of the stringent demands placed upon the (process-derived) solvent. An inexpensive, disposable catalyst, which does not have to be recycled or recovered, is of particular interest for improved process economics (and thus commercialization potential). Use of "dispersed" catalysts (i.e., catalysts which are "unsupported" or initially supported by the coal prior to its dissolution) has been of increasing interest in recent years (Utz et al., 1989; Cugini et al., 1991; Hirschon and Wilson, 1991; Miki et al., 1991; Bi et al., 1991), particularly for the dissolution stage of coal liquefaction, but also for liquid upgrading purposes. In most studies, the relatively expensive molybdenum-based catalysts have been found to provide greater rate enhancement (at comparable catalyst loadings) than the inexpensive iron-based catalysts. (Both are probably most active in their (at least partially) sulfided form.) Derbyshire (1988) correctly concludes, however, that "there is usually insufficient information available on catalyst dispersion and composition to provide a sound basis for direct comparison" and that "the available information on catalyst dispersion is totally inadequate."

The objective of our work is to use a novel approach to synthesize direct liquefaction catalysts of known particle size (and thus known dispersion). It is based on the molecular design of metal-loaded reverse micelles (microemulsions). In particular, the synthesis and catalytic testing of nanosize molybdenum sulfide particles is of interest. In this regard, the approach taken here differs from the early work at the Dow Chemical Company (Moll and Quarderer, 1979) in which micrometer-size particles were obtained by emulsifying a solution of AHM in a recycle oil. The emphasis in this paper, which reports the results of our initial efforts, is on the synthesis and use of molybdenum-based catalyst particles but the techniques being developed should also be generally applicable.

EXPERIMENTAL SECTION

Microemulsion Catalyst Synthesis. Molybdenum sulfide particles were synthesized in three different microemulsion systems: (a) 0.1 M sodium bis (2-ethylhexyl) sulfosuccinate (AOT)/decane/water (b) 0.1 M polyoxyethylene nonylphenyl ether (NP-5)/cyclohexane/water, and (c) 0.4 M NP-5/tetralin/benzyl alcohol/water. The use of an anionic (AOT) and a nonionic (NP-5) surfactant was thus explored. The microemulsions were prepared at room temperature by first adding 10% sulfuric acid to the oil/surfactant solution. The acid-solubilized microemulsion was deoxygenated by bubbling nitrogen through it for 20 min. This procedure was followed by adding 10^{-3} , 10^{-3} and 10^{-2} M ammonium tetrathiomolybdate (ATTM) to the AOT/decane, NP-5/cyclohexane and NP-5/tetralin/benzyl alcohol systems, respectively. Additional information on the microemulsion synthesis procedures are given in a companion publication (Boakye et al., 1992). To investigate the effect of particle size on liquefaction kinetics, the water-to-surfactant molar ratio was varied during microemulsion formulation.

For comparative purposes, molybdenum catalysts were also prepared in a conventional manner, by excess-solution impregnation. The catalyst precursor was ammonium heptamolybdate (AHM). It was dissolved in deionized water, at 1 % (wt) Mo loading. Five grams of coal were added to this solution and stirred overnight at 60 °C. The impregnated coal was dried under vacuum for 48 h at room temperature. In selected experiments, the pH of the solution was adjusted to 2.5 using formic acid.

Coal Liquefaction. Conventional liquefaction experiments were conducted following the procedures used previously at Penn State (Derbyshire et al., 1986; Davis et al., 1991). The coal (2.5 g), tetralin (5 g) and carbon disulfide (0.12 g) were charged into a standard (25 cc) tubing bomb reactor and agitated for 30 min in a preheated fluidized sand bath. The reaction conditions were: 350 ± 2 °C, 1000 psig H_2 (cold). In the case of microemulsion-based NP-5/cyclohexane catalysts, the microemulsion was added to 2.5 g of coal; no tetralin was used. Tetralin was added to the AOT/decane system. The NP-5/tetralin/benzyl alcohol catalyst system was also simply added to 2.5 g of coal in the tubing bomb reactor. "Blank" microemulsions, without the molybdenum catalyst, were also tested.

After reaction, the tubing bomb was rinsed with hexane into a weighed ceramic thimble. The reaction products were extracted with hexane in a conventional Soxhlet extractor assembly for 12-18 h, until the solvent falling back into the flask was absolutely colorless. The hexane was removed in a rotary vacuum evaporator and the product left behind (referred to as oils) was weighed. The thimble with the residue (referred to as residue) was dried and weighed. The reaction yields are thus reported as weight percent oils (hexane solubles) plus gases; gas production at the relatively low temperature of 350 °C was not very significant, however.

RESULTS AND DISCUSSION

A Wyodak subbituminous coal was used in this study. Its properties are summarized in Table 1. Figure 1 shows the plot of the average particle size vs. the water-to-surfactant molar ratio (R) for molybdenum sulfide in the 0.4 NP-5/tetralin/benzyl alcohol microemulsion. It is interesting to note that an optimum R value exists for which a minimum particle size of ca. 40 nm was obtained.

Tables 2 and 3 show the yield of oils (plus gas) in liquefaction tests using the AOT/decane and NP-5/cyclohexane microemulsions. At comparable Mo loadings, the yields are lower for the latter system, possibly due to the absence of a hydrogen donor solvent, whose role is crucial for low-rank coals when an efficient catalyst is not available to meet the relatively high hydrogen demand (Derbyshire and Stansberry, 1987).

Table 4 illustrates the use of NP-5/tetralin microemulsions for R values of 1-4. The oil (plus gas) yield is seen to be remarkably high at low Mo loadings. Furthermore, a comparison with the data in Figure 1, as well as those in Table 3, suggests that there is an optimum water-to-surfactant ratio for which the average particle size is at a minimum and the yield of oils at a maximum. (The oils produced are relatively viscous, suggesting that they contain some higher-molecular-weight (hexane-soluble) components.)

Table 5 was compiled in an attempt to place our initial results into proper perspective. For a subbituminous coal, high oil yields were obtained by Weller and Pelipetz (1951), when the catalyst precursor was added to the coal in an acidic medium. This could be due either to the favorable interaction with the coal or to a more effective sulfidation of the catalyst. It should be noted, however, that our attempt to maximize the dispersion of the catalyst at pH=2.5 by favoring the electrostatic interaction between the positively charged coal surface and molybdate anions (Solar et al., 1990) was not successful.

Hirschon and Wilson (1991) have recently reported relatively high yields (~84%) of toluene-solubles (corresponding roughly to the sum of asphaltenes, oils and gases) for an Illinois No. 6 bituminous coal (425 °C, 500 psi H₂, 20 min) using an organometallic Mo complex, with 0.6 mmol Mo/g coal, i.e., 5.8% Mo. The use of an organometallic Fe complex resulted in yields of ~40% (in the absence of a hydrogen donor solvent), with ~3.4% Fe. Also using "dispersed-phase" Mo catalysts (1000 ppm of ATTM, MoS₃, AHM), Utz et al. (1989) obtained yields of ≤60% heptane-solubles for a bituminous coal (425 °C, 1000 psi H₂, 1 h). Similar results were reported more recently for "dispersed-phase" Fe catalysts by Cugini et al. (1991).

Under appropriately selected conditions, the microemulsion-based catalysts are seen to be able to produce comparable yields of oils at much lower Mo loadings.

CONCLUSIONS

Our initial results on the kinetics of coal liquefaction in the presence of microemulsion-mediated molybdenum sulfide particles are very encouraging. Yields of oils which are equal or superior to those obtained using conventional catalyst preparation techniques are achieved at molybdenum loadings that are lower by one order of magnitude. At a more fundamental level, the variation in the water-to-surfactant molar ratio, during the formulation of the microemulsion system, offers the possibility to vary catalyst particle size and surface area over a wide range. This in turn allows the testing of correlations between liquefaction kinetics and catalyst dispersion.

ACKNOWLEDGMENTS

This study is being supported by the Department of Energy on Contract No. DE-AC22-90PC90054. The coal used was obtained from the Penn State/DOE Coal Sample and Data Bank.

REFERENCES

- Bi, X.-X., Derbyshire, F.J., Eklund, P.C., Hager, G.T. and Stencel, J.M., Proc. Inter. Conf. Coal Sci., 1991, p. 683.
- Boakye, E., Vaidyanathan, N., Radovic, L.R. and Osseo-Asare, K., "Microemulsion-Mediated Synthesis of Nanosize Molybdenum Sulfide Coal Liquefaction Catalysts," ACS Preprints (San Francisco), 1992.
- Burgess, C.E., Artok, L. and Schobert, H.H., ACS Preprints (Div. Fuel Chem.) **36** (2), 462 (1991)
- Cugini, A.V., Utz, B.R., Krastman, D., Hickey, R.F. and Balsone, V., ACS Preprints (Div. Fuel Chem.) **36** (1), 91 (1991).
- Davis, A., Mitchell, G.D., Derbyshire, F.J., Schobert, H.H. and Lin, R., ACS Preprints (Div. Fuel Chem.) **36** (2), 445 (1991).
- Derbyshire, F.J., "Catalysis in Coal Liquefaction," IEA CR/08, London, 1988.
- Derbyshire, F.J., Davis, A., Epstein, M.J. and Stansberry, P.G., Fuel **65**, 1233 (1986).
- Derbyshire, F.J. and Stansberry, P., Fuel **66**, 1741 (1987).
- Hirschon, A.S. and Wilson, Jr., R.B., ACS Preprints (Div. Fuel Chem.) **36** (1), 103 (1991).
- Miki, K., Yamamoto, Y., Inaba, A. and Sato, Y., Proc. Inter. Conf. Coal Sci., 1991, p. 675.
- Moll, N.G. and Quarderer, G.J., U.S. Patent 4,136,013 (1979).
- Solar, J.M., Leon y Leon, C.A., Osseo-Asare, K. and Radovic, L.R., Carbon **28**, 369 (1990).
- Utz, B.R., Cugini, A.V. and Frommell, E.A., ACS Preprints (Div. Fuel Chem.) **34** (4), 1423 (1989).
- Weller, S. and Pelipetz, M.G., Ind. Eng. Chem. **43**, 1243 (1951).

Table 1
 Characteristics of Low-Rank Coal Used in the Liquefaction Experiments

Penn State Sample Bank Number	PSOC 1401
Seam	Lower Wyodak
State	Wyoming
ASTM Rank	Subbituminous B
Mean Maximum Vitrinite Reflectance, %	0.42
Ultimate Analysis, % daf	
Carbon	72.23
Hydrogen	4.59
Nitrogen	1.06
Sulfur (total)	0.29
Oxygen (by difference)	21.83
Proximate Analysis	
Moisture	16.33
Volatile Matter	37.74
Fixed Carbon	41.14
Ash	4.79
Petrographic Composition (% vol, mf)	
Vitrinite	85.0
Liptinite	2.0
Inertinite	13.0

Table 2
 Preliminary Results of Liquefaction Tests with the
 AOT/Decane Microemulsion Catalyst

Run #	Sample	Mo Loading	Yield of Oils (+Gas), %	% Residue
4	Coal/Mo ME	1.2 ppm	33.8	66.2
8	Coal/Mo ME	2.6 ppm	47.9	52.1

Table 3
Results of Liquefaction Tests with the 0.1 M NP-5/Cyclohexane
Microemulsion (ME) Molybdenum Sulfide Catalyst

Run #	Sample	Mo Loading	Yield of Oils (+Gas), %	% Residue ^a
17	Coal/Mo ME (R=0.5)	1.9 ppm	14.1	85.9
18	Coal/Mo ME (R=1)	2.0 ppm	19.9	80.1
19	Coal/Mo ME (R=2)	2.0 ppm	20.5	79.5
20	Coal/Mo ME (R=3)	1.9 ppm	14.4	85.6
21	Coal/ME ^b	0.0 ppm	4.6	95.4

^a Includes preasphaltenes and asphaltenes

^b Surfactant plus cyclohexane alone

Table 4
Results of Liquefaction Tests Using 0.4 M NP-5/Tetralin/Benzyl Alcohol
Microemulsion (ME) Molybdenum Sulfide Catalyst ^a

Run #	Sample	Mo Loading	Yield of Oils (+Gas), %	% Residue ^b
23	Coal/Mo ME (R=1)	58 ppm	78.4	21.6
24	Coal/Mo ME (R=2)	118 ppm	83.2	16.8
26	Coal/Mo ME (R=3)	185 ppm	9.1	90.9
27	Coal/Mo ME (R=4)	243 ppm	9.9	90.1
29	Coal/ME (R=1)	0.0 ppm	7.3	92.7
30	Coal/ME (R=2)	0.0 ppm	5.2	94.8
31	Coal/ME (R=3)	0.0 ppm	2.9	97.1
32	Coal/ME (R=4)	0.0 ppm	6.2	93.8

^a Coal/tetralin = 1/2.5-2.6

^b Includes preasphaltenes and asphaltenes

Table 5
Compilation of Results of Liquefaction Tests on Subbituminous Coals
Using Conventional Catalysts

Author(s)	Coal	Conditions	Catalyst	Yield of Oils (+Gas), %
Weller and Pelipetz (1951)	Subbit. B	450 °C, 1 h 1000 psi H ₂	None	10.4
Weller and Pelipetz (1951)	Subbit. B	450 °C, 1 h 1000 psi H ₂	AHM ^a (1% Mo)	41.1
Weller and Pelipetz (1951)	Subbit. B	450 °C, 1 h 1000 psi H ₂	AHM ^b (1% Mo)	76.5
Epstein (1987) (see Burgess et al., 1991)	Subbit. B	425 °C, 10 min 1000 psi H ₂	None	37.8
Epstein (1987) (see Burgess et al., 1991)	Subbit. B	425 °C, 10 min 1000 psi H ₂	SAM ^c (1% Mo)	24.9
Epstein (1987) (see Burgess et al., 1991)	Subbit. B	Two-stage ^d	None	32.0
Epstein (1987) (see Burgess et al., 1991)	Subbit. B	Two-stage ^d	SAM (1% Mo)	44.0
Burgess and Schobert (see Burgess et al., 1991)	Subbit. B	350 °C, 1 h 1000 psi H ₂	None	11.2
Burgess and Schobert (see Burgess et al., 1991)	Subbit. B	350 °C, 1 h 1000 psi H ₂	SAM (1% Mo)	14.0
Burgess and Schobert (see Burgess et al., 1991)	Subbit. B	350 °C, 1 h 1000 psi H ₂	STM (1% Mo)	14.7
Burgess and Schobert (see Burgess et al., 1991)	Subbit. B	Two-stage ^d	None	16.9
Burgess and Schobert (see Burgess et al., 1991)	Subbit. B	Two-stage ^d	SAM (1% Mo)	21.7
Burgess and Schobert (see Burgess et al., 1991)	Subbit. B	Two-stage ^d	STM (1% Mo)	30.7
This study	Subbit. B	350 °C, 30 min 1000 psi H ₂	AHM/CS ₂ (1% Mo)	70.2
This study	Subbit. B	350 °C, 30 min 1000 psi H ₂	AHM/CS ₂ (1% Mo) ^g	71.1
This study	Subbit. B	350 °C, 30 min 1000 psi H ₂	None	29.1

^a AHM = ammonium heptamolybdate

^b AHM acidified with H₂SO₄

^c SAM = sulfided ammonium molybdate

^d 350 °C, 1 h; 425 °C, 10 min

^e STM = sulfided tetrahydroquinolinium molybdate

^f ATTM = ammonium tetrathiomolybdate

^g pH adjusted to 2.5 during catalyst impregnation

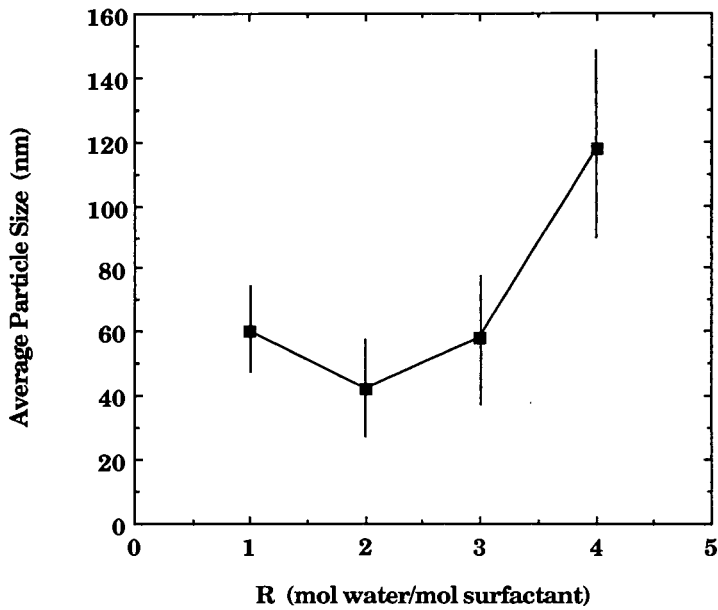


Figure 1. Effect of water-to-surfactant molar ratio (R) on the average particle diameter for the 0.4 M NP-5/tetralin/benzyl alcohol microemulsion.

NEW SYNTHETIC METHODS FOR THE PRODUCTION OF ULTRA-FINE COAL LIQUEFACTION CATALYSTS.

John C. Linehan, Roger M. Bean, Dean W. Matson,
John L. Fulton, and Anne E. Crump

Pacific Northwest Laboratory¹, P.O. Box 999, Richland, WA 99352.

ABSTRACT

Nanometer-sized catalysts have several advantages over conventional micrometer-sized catalysts including higher surface area, better diffusion properties and longer catalytic lifetimes. We have developed methods to produce large quantities of very small iron-oxides using reverse micelle and rapid thermal decomposition of solutes (RTDS) technologies. The synthesis and characterization of these iron-based nanometer-sized catalysts will be presented. The catalytic activity of the iron particles toward model compounds and coals will also be discussed.

INTRODUCTION

There is currently extensive interest in new technologies for coal liquefaction that are economical and environmentally sound. One such new method of interest is the use of highly dispersed, ultra-fine, coal liquefaction catalysts. Of particular interest are catalysts containing iron as the major foundation and catalytic agent because of the low costs involved. A variety of iron containing catalysts and catalyst precursors have been used to liquefy coal and researchers have also shown the utility of highly dispersed iron compounds for the liquefaction of coal.²⁻¹⁰

We describe results from two different catalyst preparation technologies; rapid thermal decomposition of solutes (RTDS) and a modified reverse micelle synthesis. Both of these methods allow selective, gram-scale production of nanometer-sized iron-containing materials. These nanoscale particles have been tested for catalyst selectivity using a model compound.

EXPERIMENTAL

Particle Synthesis

In a typical small scale preparation of iron-oxide from reverse micelles, 12 ml of a 1 M aqueous solution of $\text{FeNH}_4(\text{SO}_4)_2$, 2 g sodium dodecyl sulfate, 150 ml of a 0.12 M isooctane solution of bis(2-ethylhexyl)sulfosuccinate sodium salt (AOT) were mixed together with vigorous stirring. Ammonia or another base was then added to the gold colored homogeneous reverse micellar solution to precipitate the iron-oxide. The iron-oxide product was washed with isooctane, water and acetone. Approximately 1.5 g of clean, dry, iron-bearing product was collected in a typical bench-scale run using this procedure. The RTDS process involves the rapid thermal decomposition of soluble precursors under controlled conditions at elevated pressures. Grams of the desired materials can be produced in minutes with this technique.

Catalyst Testing

The model coal compound naphthyl bibenzylmethane was synthesized using the method developed by Dr. Paul Dowd.¹¹ The synthetic procedure involved the Friedel-Crafts acylation of bibenzyl with 1-naphthoyl chloride in carbon disulfide followed by purification of the naphthyl bibenzyl ketone by column chromatography. The ketone was reduced using the Huang-Minlon modification of the Wolf-Kishner reduction. The purity of the model compound, after column chromatography, was greater than 98% as determined by gas chromatography (GC).

In our typical catalyst testing procedure, adapted from the method of Farcasiu and Smith,¹¹ 25 mg of naphthyl bibenzylmethane, 100 mg of 9,10-dihydrophenanthrene, 3 mg of sulfur, and 3 mg of catalyst were sealed in a pyrex tube under vacuum. The pyrex tube was heated inside a stainless steel bomb in a fluidized sand bath at 400°C for one hour and

then cooled quickly. The contents of the tube were dissolved in a known volume of methylene chloride containing a known amount of tert-butylbenzene as a GC calibration standard. The methylene chloride solution was filtered through silica gel to remove the suspended iron catalyst and analyzed by GC/FID or GC/MS on a 15 m DB-17 column. The GC analysis was conducted with on-column injection at 40°C with a 10°C/minute ramp to 100°C followed by a 5°C/minute ramp to 280°C. The temperature was held at 280°C for 38 minutes.

RESULTS and DISCUSSION

Table I shows sizes and morphologies determined by transmission electron microscopy (TEM) and X-ray diffraction (XRD) of selected iron containing catalysts produced by the RTDS and reverse micelle techniques. The RTDS and reverse micellar synthetic methods have the capability to produce different sizes and morphologies of iron containing catalysts depending upon the reaction conditions.

Iron bearing particle sizes determined by TEM and XRD generally agree for the highly crystalline materials produced. However, large differences are noted between the results of these analytical techniques for catalyst III which has a relatively small crystalline content as determined by dark field TEM and the weakness of the XRD pattern. The few crystallites present in catalyst III are large, >20 nm, which skews the XRD-based size results to larger sizes. Most of the materials produced by both particle formation methods have significant fractions which are not crystalline according to XRD or dark field TEM.

The iron-containing particles produced in the reverse micelle system are observed to be amorphous by both dark field TEM and XRD. Preliminary Mossbauer spectroscopy performed on the iron-oxides generated by the reverse micelle process reveals that α -FeOOH, β -FeOOH or α -Fe₂O₃ can be produced depending upon precipitation method and processing. The bulk aqueous chemistry of iron-oxide production¹² appears to be directly transferable to the reverse micellar system. Upon calcination of the reverse micelle produced iron-oxides at 450°C the primary phase becomes magnetite. The particle size of the materials produced can be as small as 1 nm. Surface area analysis of catalysts I, $S_g=164.77$ m²/g, and catalyst VIII, $S_g=150.68$ m²/g, as measured by the BET method are consistent with the small particle sizes determined by XRD and TEM.

The 298°K and 77°K Mossbauer spectra of catalyst I are shown in Figure 1. Using the methods developed by others, size distributions of the superparamagnetic hematite particles can be obtained with variable temperature Mossbauer.^{2,13-15} The size distribution for catalyst I is 52% > 8.5 nm, 31% between 8.5 and 5 nm and 17% < 5 nm if spherical geometry is assumed. These values agree well with the sizes of the particles determined by TEM and XRD (Table I). Mossbauer spectra of micelle produced α -FeOOH catalysts show no magnetic hyperfine structure even at 77°K. Care must be taken in using the Mossbauer results as a measure of particle size as the critical volume determined from Mossbauer spectroscopy can be due to "superparamagnetic clusters" and do not necessarily correspond to discrete particles.

The results of the catalyst testing are shown in Table II. These show that the materials produced by both RTDS and reverse micellar methods are good, selective, catalysts for carbon-carbon bond scission. While others have discussed the importance of hydration for iron catalysts² we have not attempted to optimize the degree of hydration in our materials. Our materials were tested as produced except for calcination of catalysts VII and VIII. We have found that iron containing materials contaminated with the surfactants from the reverse micelle synthetic method are not good catalysts. Commercial ferric-oxides, such as magnetite, were found not to catalyze the model reaction as well as our magnetite. Conversions of the model compound were typically 20-30%, with selectivity below 80% for commercial magnetite. Some of the best catalyst results are from micellar produced ferric-sulfides without the addition of sulfur, catalysts X and XIII. The structural phase of these ferric sulfides has not yet been determined. They are amorphous by XRD, and their catalytic activity varies with the precipitation technique used.

SUMMARY

Both the RTDS and the reverse micellar techniques can be used to produce catalytic iron containing compounds. The sizes and morphologies of the particles produced by both techniques can be controlled through experimental parameters. In addition, both techniques can produce large quantities of materials. We can produce grams of material in minutes with the RTDS technique, and with the reverse micelle technique we are currently producing greater than 11 grams of material per liter of organic solvent. The amount of material produced per liter is substantially more than the amounts which have been produced in other reverse micelle systems.¹⁶⁻¹⁹

ACKNOWLEDGEMENTS

We thank Dr. Paul Dowd of the University of Pittsburgh for disclosing his synthetic preparation of the model compound and the U.S. Department of Energy, Office of Fossil Energy for supporting this work under contract DE-AC06-76RLO 1830.

REFERENCES

1. Pacific Northwest Laboratory is operated for the U.S. Department of Energy by Battelle Memorial Institute. This work was supported by the U.S. Department of Energy, Office of Fossil Energy under contract DE-AC06-76RLO 1830.
2. Pradham, V. R.; Tierney, J. W.; Wender, I.; and Huffman, G. P., *Energy & Fuels*, **1991**, 5, 497.
3. Pradhan, V. R.; Herrick, D. E.; Tierney, J. W.; and Wender, I., *Energy & Fuels*, **1991**, 5, 712.
4. Suzuki, T.; Yamada, H.; Yunoki, K.; and Yamaguchi, H., in *Proceedings: 1991 International Conference on Coal Science*. Newcastle on the Tyne, UK., **1991**, 703.
5. Miki, K.; Yamamoto, Y.; Inabe, A.; and Sato, Y., in *Proceedings: 1991 International Conference on Coal Science*. Newcastle on the Tyne, UK., **1991**, 675.
6. Bi, X-X; Derbyshire, F. J.; Eklund, P. C.; Hager, G. T.; and Stencel, J. M., *Energy & Fuels*, **1991**, 5, 683.
7. Yokoyama, S.; Yamamoto, M.; Yoshida, R.; Maekawa, Y.; and Kotanigawa, T., *Fuel*, **1991**, 70, 163.
8. Kotanigawa, T.; Yokoyama, S.; Yamamoto, M.; and Maekawa, Y., *Fuel*, **1989**, 68, 618.
9. Kotanigawa, T.; Takahashi, H.; Yokoyama, S.; Yamamoto, M.; and Maekawa, Y., *Fuel*, **1988**, 67, 927.
10. Shabtai, J. S. and Zhang, Y., *1989 International Conference Coal Science, Vol II*, Tokyo **1989**, 807.
11. Farcasiu, M. and Smith, C., *Energy & Fuels*, **1991**, 5, 83.
12. Clarke, N. S. and Hall, P. G., *Langmuir*, **1991**, 7, 672.
13. Morup, S., *Hyperfine Interactions*, **1990**, 60, 959.
14. Huffman, G. P.; Ganguly, B.; Taghiei, M.; Higgins, F. E.; and Shah, N., *preprints, Div. of Fuel Chem., American Chemical Society*, **1991**, 36, 561.

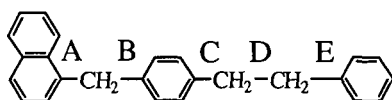
15. Wickman, H. H., in *Mossbauer Effect Methodology*, Ed. I. J. Gruverman, Plenum Press, NY, **1966**, p 39.
16. Wilcoxson, J. P.; Baughmann, R. J.; and Williamson, R. L., in *Proceedings of the Materials Research Society*, Boston, **1990**, 225.
17. Matson, D. W.; Fulton, J. L.; and Smith, R. D., *Materials Letters*, **1987**, 6, 31.
18. Petit, C. and Pileni, M. P., *J. Phys. Chem.*, **1988**, 92, 2282.
19. Kortan, A. R.; Hull, R.; Opila, R. L.; Bawendi, M. G.; Steigerwald, M. L.; Carol, P. J.; and Brus, L. E., *J. Am. Chem. Soc.*, **1990**, 112, 1327.

Table I
Sizes and Morphologies of Representative Iron Catalysts
Produced by RTDS and Reverse Micelle Methods

Catalyst Number	Iron Compound	Phase	Average Particle Size (nm)	
			TEM	XRD
<u>RTDS Derived</u>				
I	Fe ₂ O ₃	Hematite	10-30	11 ± 2
II	Fe ₂ O ₃	Hematite	15-40	23 ± 2
III	Fe ₂ O ₃	Hematite	5-15	44 ± 4
IV	Fe ₂ O ₃	Hematite	30-50	42 ± 4
V	Fe ₃ O ₄	Magnetite	nd	29 ± 3
VI	Fe	α-Iron	nd	6 ± 4
<u>Reverse Micelle Derived</u>				
VII	Fe ₃ O ₄	Magnetite	5-10	10 ± 2
VIII	Fe ₃ O ₄ FeOOH/Fe ₂ O ₃	nd	4-10	nd
IX	FeOOH/Fe ₂ O ₃	nd	4-8	Amorphous
X	Fe ₂ S ₃	nd	8-15	Amorphous
XI	FeOOH/Fe ₂ O ₃	nd	10-20	Amorphous
XII	FeOOH/Fe ₂ O ₃	nd	10-20	Amorphous
XIII	Fe ₂ S ₃	nd	nd	Amorphous

nd- Not determined

Table II
Selected Results of Catalyst Testing Using
the Model Compound :



Naphthyl Bibenzylmethane

Catalyst	% Conversion ^a (±3%)	Selectivity ^b (±3)
None	2-5%	20-60
II	61%	98
III	49%	95
IV	23%	83
VII	67%	92
VIII	77%	89
X	68%	96 ^c
XI	51%	91
XII	70%	94
XIII	70%	98 ^c

a) Conversion is based on the model compound consumed. b) Selectivity is defined as the amount of products arising from cleavage of bonds A or B vs. the total amount of products. $([A]+[B])/([A]+[B]+[C]+[D]+[E])$ c) No sulfur added.

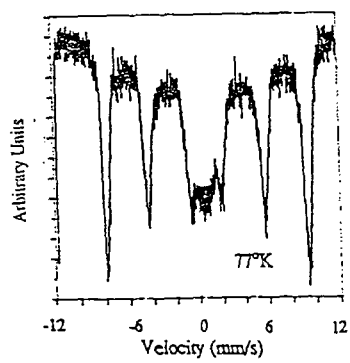
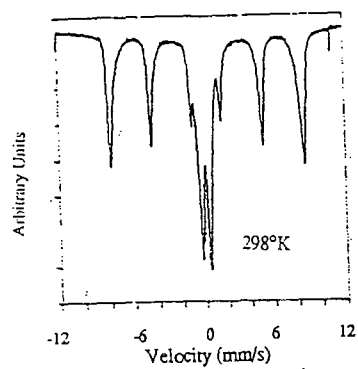


Figure 1. The Mossbauer spectra of catalyst I at room temperature and 77°K.